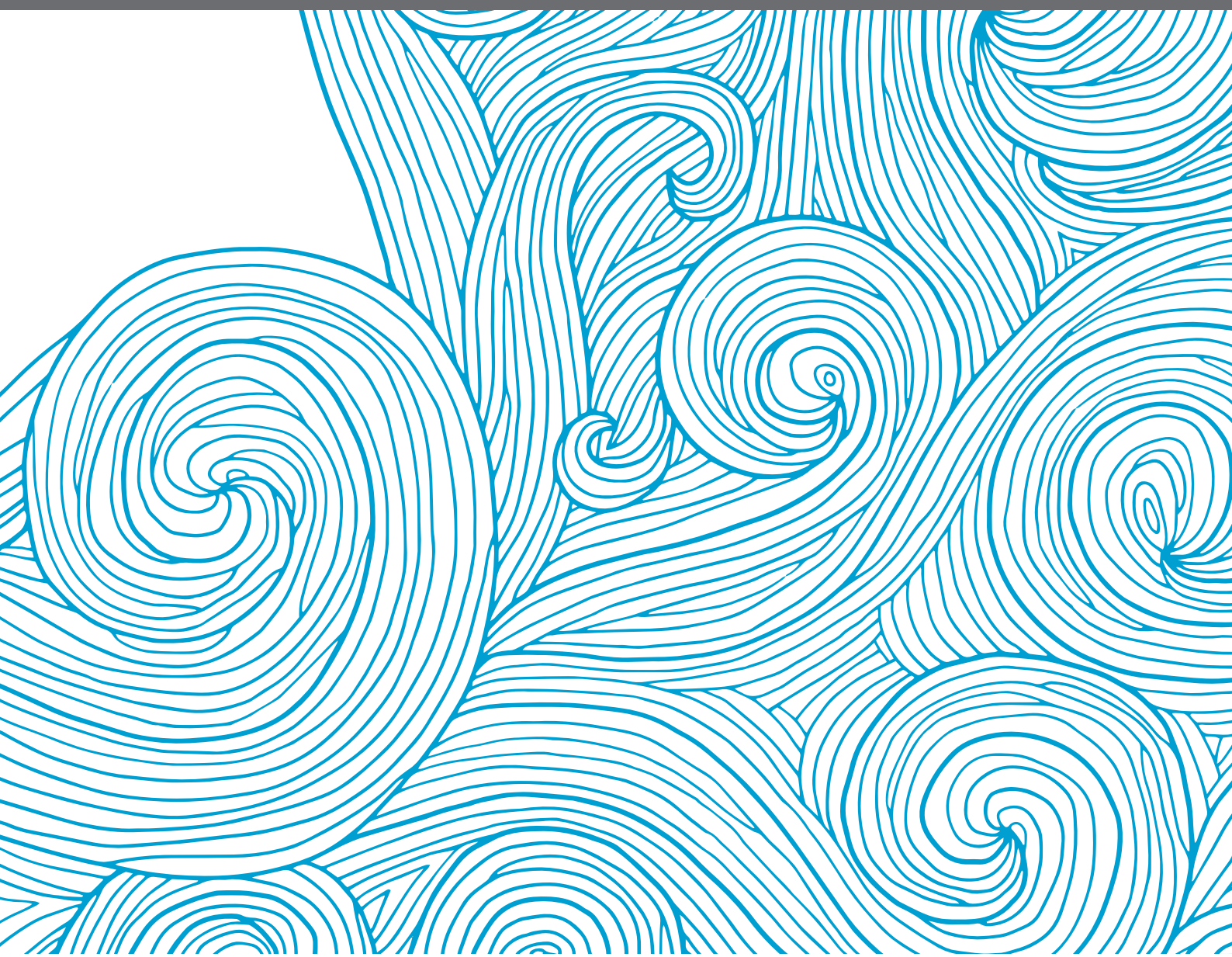
RIVER PLUMES AND ESTUARIES

EDITED BY: Alexander Osadchiev and Alexander Yankovsky
PUBLISHED IN: Frontiers in Marine Science



frontiers Research Topics

Frontiers eBook Copyright Statement

The copyright in the text of individual articles in this eBook is the property of their respective authors or their respective institutions or funders. The copyright in graphics and images within each article may be subject to copyright of other parties. In both cases this is subject to a license granted to Frontiers.

The compilation of articles constituting this eBook is the property of Frontiers.

Each article within this eBook, and the eBook itself, are published under the most recent version of the Creative Commons CC-BY licence. The version current at the date of publication of this eBook is CC-BY 4.0. If the CC-BY licence is updated, the licence granted by Frontiers is automatically updated to the new version.

When exercising any right under the CC-BY licence, Frontiers must be attributed as the original publisher of the article or eBook, as applicable.

Authors have the responsibility of ensuring that any graphics or other materials which are the property of others may be included in the CC-BY licence, but this should be checked before relying on the CC-BY licence to reproduce those materials. Any copyright notices relating to those materials must be complied with.

Copyright and source acknowledgement notices may not be removed and must be displayed in any copy, derivative work or partial copy which includes the elements in question.

All copyright, and all rights therein, are protected by national and international copyright laws. The above represents a summary only. For further information please read Frontiers' Conditions for Website Use and Copyright Statement, and the applicable CC-BY licence.

ISSN 1664-8714
ISBN 978-2-88976-883-7
DOI 10.3389/978-2-88976-883-7

About Frontiers

Frontiers is more than just an open-access publisher of scholarly articles: it is a pioneering approach to the world of academia, radically improving the way scholarly research is managed. The grand vision of Frontiers is a world where all people have an equal opportunity to seek, share and generate knowledge. Frontiers provides immediate and permanent online open access to all its publications, but this alone is not enough to realize our grand goals.

Frontiers Journal Series

The Frontiers Journal Series is a multi-tier and interdisciplinary set of open-access, online journals, promising a paradigm shift from the current review, selection and dissemination processes in academic publishing. All Frontiers journals are driven by researchers for researchers; therefore, they constitute a service to the scholarly community. At the same time, the Frontiers Journal Series operates on a revolutionary invention, the tiered publishing system, initially addressing specific communities of scholars, and gradually climbing up to broader public understanding, thus serving the interests of the lay society, too.

Dedication to Quality

Each Frontiers article is a landmark of the highest quality, thanks to genuinely collaborative interactions between authors and review editors, who include some of the world's best academicians. Research must be certified by peers before entering a stream of knowledge that may eventually reach the public - and shape society; therefore, Frontiers only applies the most rigorous and unbiased reviews.
Frontiers revolutionizes research publishing by freely delivering the most outstanding research, evaluated with no bias from both the academic and social point of view. By applying the most advanced information technologies, Frontiers is catapulting scholarly publishing into a new generation.

What are Frontiers Research Topics?

Frontiers Research Topics are very popular trademarks of the Frontiers Journals Series: they are collections of at least ten articles, all centered on a particular subject. With their unique mix of varied contributions from Original Research to Review Articles, Frontiers Research Topics unify the most influential researchers, the latest key findings and historical advances in a hot research area! Find out more on how to host your own Frontiers Research Topic or contribute to one as an author by contacting the Frontiers Editorial Office: frontiersin.org/about/contact

RIVER PLUMES AND ESTUARIES

Topic Editors:
Alexander Osadchiev, Russian Academy of Sciences, Russia
Alexander Yankovsky, University of South Carolina, United States

Citation: Osadchiev, A., Yankovsky, A., eds. (2022). River Plumes and Estuaries. Lausanne: Frontiers Media SA. doi: 10.3389/978-2-88976-883-7

Table of Contents

05 ***Editorial: River plumes and estuaries***
Alexander Osadchiev and Alexander Yankovsky

08 ***Are Periodic Oscillations of Sea Surface Height Inherent to River Plumes?***
Peter O. Zavialov

17 ***Non-Linear Processes in the Gironde River Plume (North-East Atlantic): Instabilities and Mixing***
Adam Ayouche, Guillaume Charria, Xavier Carton, Nadia Ayoub and Sébastien Theetten

41 ***Mechanisms of Lateral Spreading in a Near-Field Buoyant River Plume Entering a Fjord***
Rebecca A. McPherson, Craig L. Stevens, Joanne M. O'Callaghan, Andrew J. Lucas and Jonathan D. Nash

58 ***Freshwater Composition and Connectivity of the Connecticut River Plume During Ambient Flood Tides***
Michael M. Whitney, Yan Jia, Kelly L. Cole, Daniel G. MacDonald and Kimberly D. Huguenard

79 ***Variability of the Red River Plume in the Gulf of Tonkin as Revealed by Numerical Modeling and Clustering Analysis***
Tung Nguyen-Duy, Nadia K. Ayoub, Patrick Marsaleix, Florence Toublanc, Pierre De Mey-Frémaux, Violaine Piton, Marine Herrmann, Thomas Duhaut, Manh Cuong Tran and Thanh Ngo-Duc

104 ***Structure and Inter-Annual Variability of the Freshened Surface Layer in the Laptev and East-Siberian Seas During Ice-Free Periods***
Alexander Osadchiev, Dmitry Frey, Eduard Spivak, Sergey Shchuka, Natalia Tilinina and Igor Semiletov

124 ***Water Exchange Between the Gulf of Ob and the Kara Sea During Ice-Free Seasons: The Roles of River Discharge and Wind Forcing***
Alexander Osadchiev, Olga Konovalova and Alexandra Gordey

142 ***Response of a Small River Plume on Wind Forcing***
Alexander Osadchiev, Roman Sedakov and Alexandra Barymova

151 ***Regulation of Algal Bloom Hotspots Under Mega Estuarine Constructions in the Changjiang River Estuary***
Yanru He, Yihe Wang and Hui Wu

170 ***Offshore Spreading of a Supercritical Plume Under Upwelling Wind Forcing: A Case Study of the Winyah Bay Outflow***
Alexander E. Yankovsky, Diane B. Fribance, Douglas Cahl and George Voulgaris

186 ***The Impacts of Freshwater Input and Surface Wind Velocity on the Strength and Extent of a Large High Latitude River Plume***
J. Blake Clark and Antonio Mannino

204 ***River Plume Rooted on the Sea-Floor: Seasonal and Spring-Neap Variability of the Pearl River Plume Front***
Haihang Zhi, Hui Wu, Jiaxue Wu, Wenxia Zhang and Yihe Wang

221 ***Long-Term Variability on Suspended Particulate Matter Loads From the Tributaries of the World's Largest Choked Lagoon***
Eduardo C. Bortolin, Juliana Távora and Elisa H. L. Fernandes

238 ***Impact of Wave–Current Interactions on the Detachment of Low-Salinity Water From Changjiang River Plume and Its Subsequent Evolution***
Zhipeng Jiang, Dehai Song, Qinsheng Wei and Yang Ding

257 ***Differential Impact of the Khatanga and Lena (Laptev Sea) Runoff on the Distribution and Grazing of Zooplankton***
Anna Pasternak, Alexander Drits, Elena Arashkevich and Mikhail Flint

274 ***Characterization and classification of estuarine suspended particles based on their inorganic/organic matter composition***
Z. Safar, C. Chassagne, S. Rijnsburger, M. Ibanez Sanz, A. J. Manning, A.J. Souza, T. van Kessel, A. Horner-Devine, R. Flores, M. McKeon and J.D. Pietrzak

frontiers | Frontiers in Marine Science

TYPE Editorial
PUBLISHED 27 July 2022
DOI 10.3389/fmars.2022.986114

Check for updates

OPEN ACCESS

EDITED AND REVIEWED BY
Marta Marcos,
University of the Balearic Islands, Spain

*CORRESPONDENCE
Alexander Osadchiev
osadchiev@ocean.ru

SPECIALTY SECTION
This article was submitted to Coastal Ocean Processes, a section of the journal Frontiers in Marine Science

RECEIVED 04 July 2022
ACCEPTED 12 July 2022
PUBLISHED 27 July 2022

CITATION
Osadchiev A and Yankovsky A (2022) Editorial: River plumes and estuaries. *Front. Mar. Sci.* 9:986114. doi: 10.3389/fmars.2022.986114

COPYRIGHT
© 2022 Osadchiev and Yankovsky. This is an open-access article distributed under the terms of the Creative Commons Attribution License (CC BY). The use, distribution or reproduction in other forums is permitted, provided the original author(s) and the copyright owner(s) are credited and that the original publication in this journal is cited, in accordance with accepted academic practice. No use, distribution or reproduction is permitted which does not comply with these terms.

Editorial: River plumes and estuaries

Alexander Osadchiev[1]* and Alexander Yankovsky[2]

[1]Shirshov Institute of Oceanology, Russian Academy of Sciences, Moscow, Russia, [2]School of the Earth, Ocean and Environment, University of South Carolina, Columbia, SC, United States

KEYWORDS

river plumes, estuaries, coastal processes, buoyancy currents, land-ocean interaction

Editorial on the Research Topic
River plumes and estuaries

River runoff is an important driver of many physical, biological, and geochemical processes in coastal and shelf sea areas. The river-estuary-sea continuum represents a variety of complex interactions between the terrestrial freshwater discharge and ocean water. River estuaries are areas where freshwater discharge initially interacts with seawater. The related estuarine mixing processes define the source properties for river plumes, which in turn determine the plume's structure and govern its subsequent dynamics on the shelf. The intensity of estuarine mixing varies from negligible, when mostly undiluted freshwater discharge inflows directly into a coastal sea, to dominant, which results in significant dilution of river discharge in well-mixed semi-enclosed basins by the time it enters the shelf.

River plumes generally occupy wide, but shallow sea surface layer bounded by sharp density gradient. The area of a river plume is 3-5 orders of magnitude greater than its depth, therefore, even small rivers with discharge rates ~1–10 m^3/s form river plumes with horizontal spatial extents ~10–100 m. Areas of river plumes formed by the largest World rivers are ~100–1000 km^2. Despite relatively small volume of total freshwater runoff to the World Ocean, river plumes occupy up to 1/5 of shelf areas of the World Ocean and substantially influence global fluxes of buoyancy, heat, terrigenous sediments, nutrients, and anthropogenic pollutants, which are discharged into the coastal sea with continental runoff. River plumes are characterized by strong spatial inhomogeneity and high temporal variability caused by external forcing and mixing processes. Regional features (delta/estuary, enclosed bay/open sea, shoreline, bathymetry, etc.) also affect

the morphology and behavior of river plumes. As a result, dynamics and variability of river plumes are key factors for understanding mechanisms of spreading, transformation, and redistribution of continental discharge and river-borne constituents in the coastal sea and their influence on the adjacent continental shelf.

Estuarine processes and river plumes received much attention during the last decades. Previous research provided general concepts of transport and mixing processes in estuaries (e.g., MacCready and Geyer, 2010; Geyer and MacCready, 2014; Burchard et al., 2018) and in river plumes (e.g., Yankovsky and Chapman, 1997; Lentz and Fewings, 2012; Horner-Devine et al., 2015). However, progress in observational sampling methods and in numerical model capabilities have brought new challenges in understanding the structure, dynamics, and variability of estuaries and river plumes, as well as the influence of freshwater discharge on processes in the coastal sea. This was the main motivation to organize this Research Topic.

A collection of 16 papers authored by 69 researchers in total were published in this Research Topic. The majority of these articles were focused on various aspects of the river plume dynamics. The influence of wind and tidal forcing on different river plumes was studied by Osadchiev et al., Yankovsky et al., and Whitney et al. Yankovsky et al. and McPherson et al. demonstrated that tidally-induced internal waves can strongly affect spreading patterns of river plumes. Zavialov described a new mechanism of oscillations of surface level of a small plume. Other related works analyzed the mechanisms that drives lateral spreading of river plumes (McPherson et al.) and mixing across the plume-sea interface (Ayouche et al.; Jiang et al.). Several works described variability of structure of specific river plumes on various temporal scales: synoptic variability of the Yukon plume (Clark and Mannino) synoptic and seasonal variability of the Pearl river plume (Zhi et al.), seasonal variability of the Red river plume (Nguyen-Duy et al.), seasonal and inter-annual variability of the Lena plume (Osadchiev et al.), as well as broad spectrum of meso- and submesoscale processes associated with the Gironde River plume (Ayouche et al,). Estuarine processes addressed in this Research Topic included ocean-estuarine exchange for the Gulf of Ob (Osadchiev et al.) and the Patos Lagoon (Bortolin et al.). Several works studied the influence of river plumes on estuarine and coastal ecosystems: sediment processes in the Rhine plume (Safar et al.) and the Patos Lagoon (Bortolin et al.), algal blooms near the Changjiang Delta (He et al.), distribution and grazing of zooplankton at the Laptev Sea shelf (Pasternak et al.).

Studies of river plumes and estuarine processes are mostly based on *in situ* measurements, remote sensing and numerical modeling. *In situ* measurements represent ground truth for studies of estuaries and river plumes. Generally, they provide discrete data with relatively low spatial and/or temporal resolution. As a result, studies based only on *in situ* measurements often have the inherent spatial or temporal limitations. Satellite and other remotely sensed data, on the other hand, provide sufficient spatial coverage of estuaries and river plumes. However, remote sensing is limited to surface processes and requires validation of sampled characteristics against *in situ* measurements. Numerical modeling reproduces the three-dimensional plume structure with relatively high spatial and temporal resolution. Albeit in many cases it is still not sufficient for many processes including submesoscale dynamics, internal waves, etc. Numerical studies also require thorough validation against *in situ* data, which is often lacking.

The methodology applied in manuscripts published in this Research Topic was either analysis of *in situ* data sets (McPherson et al.; Osadchiev et al.; Osadchiev et al.; Pasternak et al.; Safar et al.; Yankovsky et al.; Zavialov) or numerical modeling (Ayouche et al.; Clark and Mannino; He et al., Jiang et al.; Nguyen-Duy et al.; Whitney et al.; Zhi et al.). Several papers combined remotely sensed data with *in situ* measurements including Osadchiev et al. and Yankovsky et al. who used novel techniques of aerial remote sensing to measure surface currents within river plumes and Bortolin et al. who used satellite data to evaluate turbidity in the Patos Lagoon.

River plumes and estuaries have wide variety of regional features; therefore, it is important to study them in different geographical regions. It was the case of the Research Topic, which papers addressed river plumes and estuaries in the Arctic Ocean (Clark and Mannino; Osadchiev et al.; Osadchiev et al.; Pasternak et al.), in mid-latitudes in Northern (Ayouche et al.; Osadchiev et al.; Safar et al.; Whitney et al.; Zavialov) and Southern (McPherson et al.) hemispheres, in tropical coastal areas in the Eastern Asia (He et al.; Jiang et al.; Nguyen-Duy et al.; Zhi et al.), North America (Yankovsky et al.) and South America (Bortolin et al.).

Recent studies demonstrated that many processes are significantly different for small and large river plumes. Therefore, it is necessary to consider different spatial and temporal scales of transformation of river runoff in the sea and distinguish the obtained regional results for specific river plumes in context of these scales. The papers in the Research Topic covered all spatial scales of river plumes from the largest World rivers (Clark and Mannino; He et al.; Jiang et al.; Osadchiev et al.; Osadchiev et al.; Pasternak et al.; Zhi et al.) to medium-size (Ayouche et al.; Bortolin et al.; Nguyen-Duy et al.; Safar et al.; Yankovsky et al.) and small river plumes (McPherson et al.; Osadchiev et al.; Whitney et al.; Zavialov).

Author contributions

All authors have contributed in equal amounts to this manuscript. All authors contributed to the article and approved the submitted version.

Funding

The funding from Ministry of Science and Higher Education of the Russian Federation, theme FMWE-2021-0001 is acknowledged.

Acknowledgments

We thank all authors, reviewers, and editors that have contributed to this Research Topic.

Conflict of interest

The authors declare that the research was conducted in the absence of any commercial or financial relationships that could be construed as a potential conflict of interest.

Publisher's note

All claims expressed in this article are solely those of the authors and do not necessarily represent those of their affiliated organizations, or those of the publisher, the editors and the reviewers. Any product that may be evaluated in this article, or claim that may be made by its manufacturer, is not guaranteed or endorsed by the publisher.

References

Burchard, H., Schuttelaars, H. M., and Ralston, D. K. (2018). Sediment trapping in estuaries. *Ann. Rev. Mar. Sci.* 10, 371–395. doi: 10.1146/annurev-marine-010816-060535

Geyer, W. R., and MacCready, P. (2014). The estuarine circulation. *Ann. Rev. Fluid Mech.* 46300, 175–197. doi: 10.1146/annurev-fluid-010313-141302

Horner-Devine, A. R., Hetland, R. D., and MacDonald, D. G. (2015). Mixing and transport in coastal river plumes. *Ann. Rev. Fluid Mech.* 47, 569–594. doi: 10.1146/annurev-fluid-010313-141408

Lentz, S. J., and Fewings, M. R. (2102). The wind- and wave-driven inner-shelf circulation. *Ann. Rev. Mar. Sci.* 41, 317–343. doi: 10.1146/annurev-marine-120709-142745

MacCready, P., and Geyer, W. R. (2010). Advances in estuarine physics. *Ann. Rev. Mar. Sci.* 2315, 35–58. doi: 10.1146/annurev-marine-120308-081015

Yankovsky, A. E., and Chapman, D. C. (1997). A simple theory for the fate of buoyant coastal discharges. *J. Phys. Oceanogr.* 27, 1386–1401. doi: 10.1175/1520-0485(1997)027<1386:astftf>2.0.co;2

frontiers in Marine Science

ORIGINAL RESEARCH
published: 13 May 2021
doi: 10.3389/fmars.2021.679323

Are Periodic Oscillations of Sea Surface Height Inherent to River Plumes?

*Peter O. Zavialov**

P. P. Shirshov Institute of Oceanology, Russian Academy of Sciences, Moscow, Russia

We analyze high temporal resolution (10 min) sea surface height (SSH) data records from pressure sensors deployed on the inner shelf within the plumes of the Mzymta and the Vulan, two small-to-medium size rivers in the Russian sector of the Black Sea coast. The SSH was recorded in parallel with meteorological parameters, averaged over the same 10 min intervals. While the low-frequency changes of the SSH at periods of 6 h or longer accounted for about 90% of the total variability and were strongly correlated with the wind, superimposed on them there always existed higher frequency oscillations whose characteristic periods ranged from 70 to 230 min, and the amplitudes spanned between 1 and 19 cm, not correlated with either the wind stress or atmospheric pressure. Furthermore, the amplitudes and the periods of these high-frequency oscillations appeared to be proportional to the horizontal scale of the river plume, as well as to each other. A very simple semi-analytical model focused on the interplay between the plume's mass and the momentum budgets demonstrated that periodic oscillations of the sea surface height should be inherent to river plumes, and also helped to explain the abovementioned dependencies.

Keywords: river plumes, sea surface height, short term variability, *in situ* measurements, small rivers

OPEN ACCESS

Edited by:
Alexander Yankovsky, University of South Carolina, United States

Reviewed by:
Georgia Kakoulaki, Joint Research Centre, Italy
Dimitris Stagonas, University of Cyprus, Cyprus

***Correspondence:**
Peter O. Zavialov
peter@ocean.ru

Specialty section:
This article was submitted to Coastal Ocean Processes, a section of the journal Frontiers in Marine Science

Received: *11 March 2021*
Accepted: *19 April 2021*
Published: *13 May 2021*

Citation:
Zavialov PO (2021) Are Periodic Oscillations of Sea Surface Height Inherent to River Plumes? Front. Mar. Sci. 8:679323. doi: 10.3389/fmars.2021.679323

INTRODUCTION

As important features of the near-shore ocean and major mediators of land-sea interactions, river plumes have long attracted attention and been subject of extensive literature since the 1970s, see, for example, Garvine and Monk (1974), Garvine (1984), Yankovsky and Chapman (1997). Nonetheless, a relatively recent review article by Horner-Devine et al. (2015) described the state-of-the-art knowledge of the fluvial plumes in the sea as follows: "*...although studies [accomplished to date] have clarified many individual processes, a holistic description of the interaction and relative importance of different mixing and transport processes in river plumes has not yet been realized*". This is so partly because of the scarcity of observational data at spatial and temporal resolution sufficient to elucidate the internal structure and variability of plumes, especially small and medium-sized. The dynamics of plumes from small rivers and their response to wind forcing are significantly different from those of large ones (Mestres et al., 2007; Osadchiev and Korshenko, 2017; Osadchiev and Sedakov, 2019). Typically, small plumes are characterized by limited near-field area and do not exhibit a recirculating bulge because of rapid deceleration of the inflowing river stream and quick decay of its inertia (Osadchiev and Zavialov, 2019). In this study, we focus on two small-to-medium size rivers at the Russian coat of the Black Sea.

One particularly notable property of river plumes is their ability of generating internal waves (e.g., Nash and Moum, 2005). Mechanisms responsible for this phenomenon are not yet fully understood. Previous publications focused on this issue mainly referred to horizontally propagating (due to either tidal forcing or momentum gained from a river stream in flush flood events) density fronts generating internal waves when transitioning to subcritical flow (e.g., Stashchuk and Vlasenko, 2009; Osadchiev, 2018; Mendes et al., 2021). However, observations have been reported of internal waves triggered by apparently steady plumes in non-tidal regions and in the absence of supercritical river inflow (e.g., Korotkina et al., 2011; Lavrova and Mityagina, 2017).

The initial motivation for the present study was about investigating the proper variability of the sea surface height (SSH) in plumes. The author is not aware of any previously published works reporting on oscillatory motion of the plume's surface nor elaborating on plausible physical mechanisms of such motion. In a recent study by Branch et al. (2020), the authors obtained analytical and numerical solutions describing the shape of a «plume ridge» assuming its stationary state. They defined the ridge as a result of liftoff process by which buoyant river water separates from the bottom and flows over saltier and denser seawater generating a ridge on the water surface. In what follows, we show that the ridge is subject to vertical oscillations about its mean elevation. To this end, we analyzed high temporal resolution (10 min) data records obtained in field experiments on the inner shelf within the plumes of the Mzymta and the Vulan, two regionally important rivers in the Russian sector of the Black Sea coast. The current meters equipped with pressure sensors were deployed in 3 field experiments in 2008, 2009, and 2011, yielding 3 series of data, about 120 h long each. While the velocity records obtained in these experiments have been analyzed and published before, [see (Korotkina et al., 2011, 2014; Osadchiev and Zavialov, 2013)], the data from the pressure sensors have not.

STUDY AREAS AND DATA

Although relatively small, the Mzymta River and the Vulan River are important rivers of the Russian coast of the Black Sea. The long-term average discharge rate is 49.6 m^3/s (1.6 km^3/year) of the former and 6.4 m^3/s (0.2 km^3/year) of the latter (Dzhaoshvili, 2002). However, the peak runoff during flood events can exceed the mean values by a factor of 10 and more (Alexeevsky et al., 2016). Both rivers are mountainous, with the average altitudes of their catchment basins of 240 m a.s.l. for the Vulan and 1309 m a.s.l. for the Mzymta. The width of the Mzymta estuary at the mouth is about 90 m, and that of the Vulan is approximately 30 m, while the depth at the mouth is about 2 m in both cases. Both rivers form distinct plumes whose typical lengths vary from 0.5 to 2 km for the Vulan and 2 to 5 km for the Mzymta on the long-term average (Zavialov et al., 2014), but much larger values exceeding 15 and even 20 km have also been documented in high discharge periods. Based on available information, the internal Froude number characterizing dynamical behavior of a plume (e.g., Kilcher and Nash, 2010) is below unity for the Vulan indicating subcritical flow, but can be either subcritical or supercritical for the Mzymta depending on discharge conditions. Both study areas are essentially non-tidal, with the maximum tidal amplitude of less than 2 cm (Medvedev and Kulikov, 2016).

The *NorTek Aquadopp 300M* instruments equipped with a set of sensors including a piezoresistive hydrostatic pressure probe were deployed attached to the bottom in the immediate proximity of the river mouths as shown in **Figure 1**. The water depth at the deployment sites was 5 m for the Mzymta mooring and 3 m for the Vulan mooring. The instruments sampled pressure once a second, the data were then converted to 10 min averages. The pressure sensor's precision as specified by the manufacturer was 1.5 10^{-2} dBar, or about 1.5 cm if expressed as the height of the water column. Such a precision was sufficient to resolve small oscilations of the sea surface we focused on whose range (i.e., the doubled amplitude), spanned between about 2 cm to about 30 cm.

The mooring near the Mzymta mouth was in operation twice: first from May 22 through May 27, 2009, yielding a total of 698 10-min averaged pressure readings, secondly, from May 26 through May 31, 2011, resulting in 3450 2-min readings later converted to 690 10-min averages for uniformity. The mooring at the Vulan site functioned only once from October 8 to October 13, 2008, and collected 720 pressure samples as 10-min averages. The total length of the series was 116 h 20 min, 115 h 00 min, and 120 h 00 min for 2009, 2011, and 2008, respectively.

Concurrently with these measurements, all meteorological parameters, including the wind speed and direction and atmospheric pressure, were also recorded by a portable meteorological station temporarily installed on the shore near the river mouths. The *ConradElectronic 2300-15* meteostation was used in all cases at a 10-min sampling rate. The wind data were later converted to wind stress components using the formulas given in (Smith, 1980).

In parallel with the measurements at the moorings, every day of the experiments we used a motorboat R/V *Ashamba* to perform detailed CTD mapping of the sea region adjacent to the river mouths. The sampling area encompassed the river plumes and the surrounding areas of the sea. In addition to the surface-to-bottom vertical profiling by the *SeaBird 19plus* CTD instrument at 15–25 stations daily, we also used a *YSI6600* CTD probe placed into a special 8 dm^3 container on the ship's deck while water from the sea surface was continuously pumped through it, which enabled measuring the surface salinity at high spatial resolution along the track. Accordingly, we were able to produce salinity maps and to estimate the spatial extent of the plume for each individual day of the experiments (excluding 4 days for which such data were not available). The results of this daily mapping of the plumes have been published elsewhere (e.g., Osadchiev and Zavialov, 2013; Zavialov et al., 2014) and will not be discussed in detail in the present article; however, we use them here to estimate the characteristic length of the plume for each day. This length was formally determined as the maximum distance from the river mouth to a specific isohaline contour. For the purposes of this study, the latter was selected as 16.8 psu for the Vulan river in October 2008, and 15.0 psu and 14.5 psu for the Mzymta river in May 2009 and May 2011, respectively, because it was found that these contours corresponded to the maximum horizontal gradient of salinity and hence best represented the

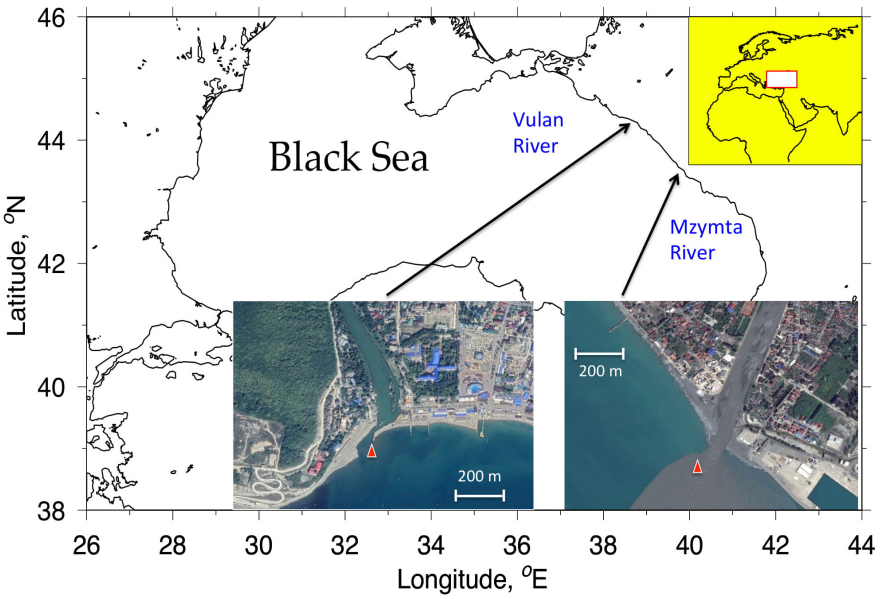


FIGURE 1 | Study areas. The red triangles indicate locations where the moored instruments were deployed.

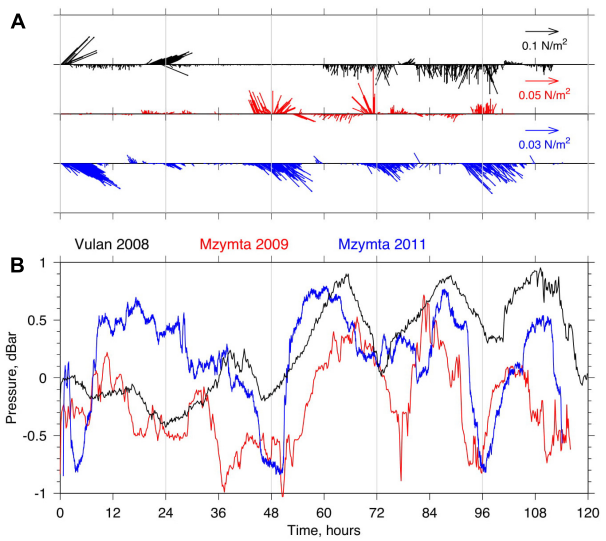


FIGURE 2 | (A) Vector diagrams of wind stress vectors registered by portable meteostation installed near Vulan-2008 (black), Mzymta-2009 (red), and Mzymta-2011 (blue) mooring sites. **(B)** Raw series of water column pressure anomalies (dBar) collected at Vulan-2008 (black), Mzymta-2009 (red), and Mzymta-2011 (blue) mooring sites.

outer limits of the plumes as distinct areas of relatively low salinity surrounding the estuaries.

RESULTS

The original raw data series are shown in **Figure 2** as pressure anomalies (i.e., the instantaneous value minus the average over the entire series) registered by the instruments. It can be seen that absolute pressure records exhibit a combination of energetic variability at relatively low frequency (periods > 6 h) and high amplitude (1dBar) – and much smaller amplitude, higher frequency variability superimposed on it.

Figure 3 depicts the same data shown in **Figure 2**, but high-pass filtered: the series were filtered low-pass with a 6-h-wide moving window, and then the result was subtracted from the original data, thus eliminating the variability at periods longer than 6 h and retaining only higher frequency variability. As it is seen in **Figure 3**, all series exhibit distinct oscillatory pattern whose range, however, is much smaller than the variability in the original series.

We note that, as demonstrated by the CTD measurements, the water density at the locations of the deployments remained nearly constant throughout the observations and varied only slightly within $0.5\ \mathrm{kg\ m^{-3}}$, which implies a change of less than 0.1% of hydrostatic pressure (for a fixed height of the water column). On the other hand, the sea surface height (SSH) change of only 2 cm (which we consider the minimum resolvable by the equipment used) for a water column of 5 m will result in pressure change larger by a factor of 4 at least. We, therefore, assume hereinafter that the observed variability of pressure was totally due to the SSH changes, and pass from pressure units to the units of SSH ($1\ \mathrm{cm} = 10^{-2}$ dBar).

To get some insights as to the origins of the SSH variability, we computed the lagged correlations between the SSH series (low-passed and high-passed) and the wind stress components with the time lags from 0 to 24 h. An example corresponding to the measurements taken in 2011 is shown in **Figure 4**. The figure is based on the series of 687 members, hence, a 99% significance level for the correlation coefficient according to the standard t-statistic test is 0.098, as indicated by yellow shading in the

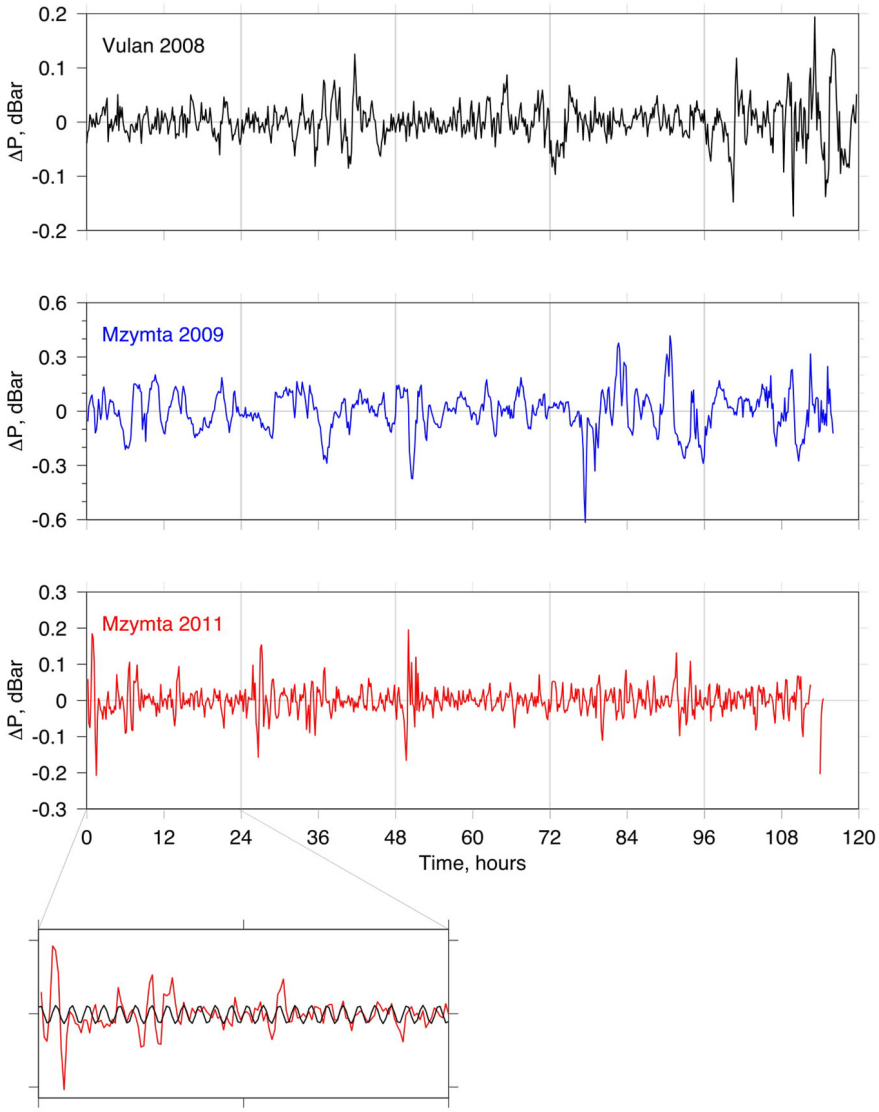


FIGURE 3 | Same data series as in **Figure 2**, but high-pass filtered with 6 h wide moving window filter. The inset in the lower panel illustrates the procedure of finding the harmonic (black) best fitting the observational data (red) over the selected segment of the series (24 h in this case).

plot. It is notable that while the low-passed SSH changes and the components of the wind stress τ show significant synoptic correlation whose shape strongly suggests 24-h periodic breeze forcing, no significant correlation is seen at any time lag for the high-passed SSH series (not even with the high-passed τ, not shown here). We also computed the correlation between the high-passed SSH and the atmospheric pressure (the green curve in **Figure 4**), which also proved insignificant at any temporal lag. The respective figures illustrating the measurements of 2008 and 2009 are not shown here, but they are generally similar to **Figure 4**.

Next, we performed harmonic analysis of the high-passed SSH series using the following approach: we found a harmonic $C\sin(\frac{2\pi}{T}t + \varphi)$ best representing the observational data within a specific time interval by fitting the amplitude C, the period T, and the initial phase φ which would minimize the rms deviation from the data. This procedure is illustrated in **Figure 3** (see the best fitting harmonic in the small inset at the lower panel). The time intervals we selected for this analysis were the 12-h intervals from 8 a.m. to 8 p.m. on the days when observational estimation of the plume size was feasible.

The next step of the analysis was aimed at finding any dependencies that could possibly exist between the oscillation period and amplitude and the length scale of the plume. Unfortunately, *in situ* determination of the plume size required rather extensive CTD mapping, and, consequently, the amount of data we could rely on for this purpose was limited – in total, at our disposal there were only 9 individual days of measurements (see **Table 1**) for which we could infer the plume size estimated through the procedure described in the «Data» section. However,

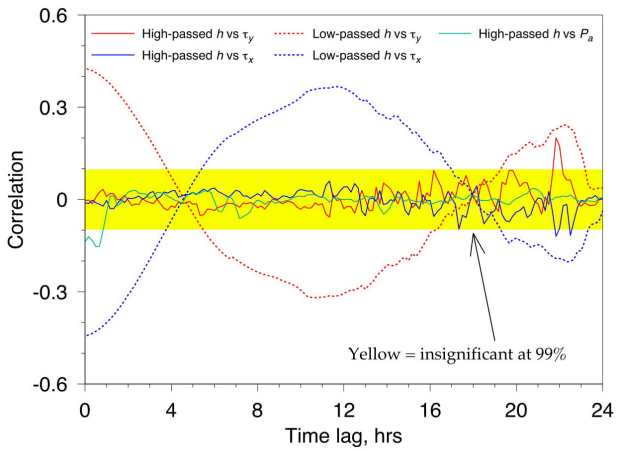


FIGURE 4 | Correlations between high-pass filtered SSH and meridional wind stress series (red, solid); high-pass filtered SSH and zonal wind stress (blue, solid); low-pass filtered SSH and meridional wind stress (red, dotted); low-pass filtered SSH and zonal wind stress (blue, dotted); high-pass filtered SSH and atmospheric pressure (green) as functions of the time lag. Mzymta-2011 experiment. Only values outside the yellow corridor are significant at 99%.

TABLE 1 | Amplitudes and periods of harmonics best fitting the SSH variability data and plume sizes for individual days of observations.

#	River	Date	Amplitude, cm	Period, min	Maximum plume length, m
1	Vulan	October 10, 2008	3.5	152	Unknown
2	Vulan	October 11, 2008	3.0	148	Unknown
3	Vulan	October 12, 2008	3.0	180	1520
4	Vulan	October 13, 2008	8.5	196	Unknown
5	Mzymta	May 22, 2009	7.5	104	3610
6	Mzymta	May 23, 2009	6.0	184	8820
7	Mzymta	May 24, 2009	10.0	180	9450
8	Mzymta	May 26, 2009	12.5	224	14750
9	Mzymta	May 27, 2009	10.5	72	Unknown
10	Mzymta	May 28, 2011	2.5	92	820
11	Mzymta	May 29, 2011	2.0	160	2390
12	Mzymta	May 30, 2011	2.0	128	1910
13	Mzymta	May 31, 2011	1.0	156	1980

as shown in **Figure 5**, the available data suggested that both the period and the amplitude increased with the horizontal size of the plume. While the plume size spanned in a broad interval from 820 to 14750 m, the oscillation periods varied from 72 to 224 min and the ranges from 2.0 to 25.0 cm.

A significantly larger amount of observational evidence is available for investigating the mutual relations between the periods and the amplitudes of the SSH oscillation. To this end, we used 352 6-h wide data subsets distributed through the 3 data series with temporal shifts of 1 h between the neighboring subsets. The results of this analysis are summarized in **Figure 6**. The red bullets in the figure represent averages over 20-min bins of period values, the yellow shading is the respective rms deviation

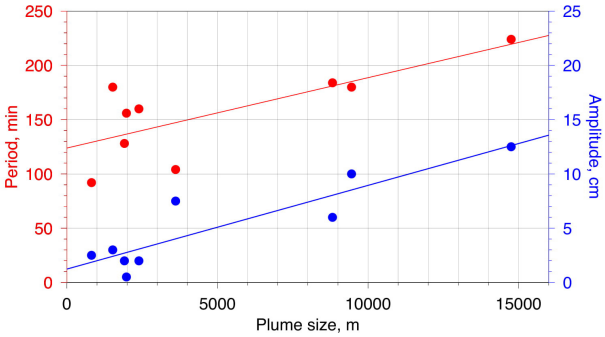


FIGURE 5 | Dependencies of the period (red) and amplitude (blue) of the oscillation harmonic best fitting the data on the plume size for individual days of observations. Straight lines are the respective linear regressions.

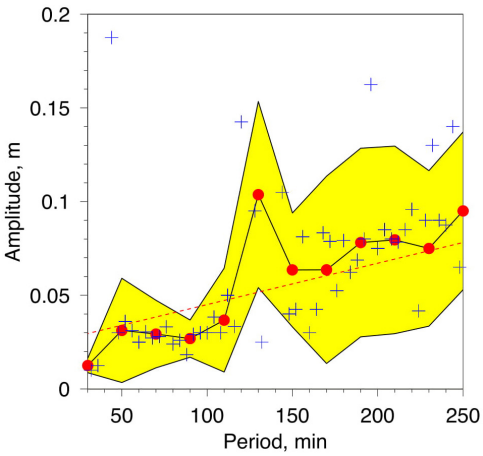


FIGURE 6 | Relation between the period and the amplitude of the oscillation based on 6-h wide subsets of all data series (total of 352 data subsets). Red bullets are the averages over 20-min intervals of period values (dashed line is the respective linear regression, yellow shading indicates the rms deviation corridor), and blue crosses are the averages over 4-min intervals of period values.

corridor, and the blue crosses are averages over 4-min intervals. As it is evident from **Figure 6**, the amplitude generally grows with the period.

DISCUSSION

At this point, let us summarize the main findings that we have obtained from the analysis of the data exposed above.

(i) First: while during the measurements the observed SSH changes in river plumes were dominated by low frequency variability at periods over 6 h, there always existed a smaller amplitude and higher frequency variability at periods 1–4 h superimposed on it.

(ii) Second: while the former was significantly correlated with the wind stress and, hence, likely wind-driven, the latter

exhibited no significant correlation with either wind or atmospheric pressure.

(iii) Third: the amplitudes of the SSH oscillations generally increased with the increase of the periods thereof.

(iv) Fourth: both the periods and the amplitudes of these oscillations appeared to increase as the plume size was getting larger.

What dynamical mechanisms could explain these oscillatory patterns? First of all, it is worthy of reminding that the Black Sea is considered a non-tidal basin. Although previous studies revealed that there actually do exist rudimentary tides with the maximum range of 2–3 cm at the diurnal and semi-diurnal frequencies (Hüseyin, 1993; Medvedev and Kulikov, 2016), neither their periods nor the amplitudes fit in the ranges we have encountered. One possible mechanism might be associated with surface seiches. However, the periods of the seiches typical in the northeastern coastal part of the Black Sea investigated rather thoroughly in previous studies were in the range from 5 to 11 h (Hüseyin, 1993; Ivanov et al., 1996; Medvedev and Kulikov, 2016) and, hence, were significantly longer than those observed in the case of our interest. Another candidate mechanism for oscillatory behavior of SSH, the coastal trapped waves, develop mainly at subinertial frequencies (e.g., Dale and Sherwin, 1996), i.e., at periods over 17 h for the region of this study. For example, the spectra of trapped waves off the coast of Crimea as obtained from direct observations by Ivanov and Yankovsky (1995) peaked at about 27 h. Trapped waves at the superinertial domain have also been predicted for the Black Sea by means of numerical modeling, but their periods exceeded 6 h in a majority of cases (Ivanov et al., 2018). Thus, although the attribution of the short-period oscillations we focus on in this article to seiches or coastal trapped waves cannot be completely ruled out, we deem it unlikely.

We, therefore, hypothesize that the oscillations described above were generated by a mechanism related to the internal dynamics of river plumes themselves. To disclose it, we first consider the following deliberately oversimplified model where the plume is thought of as a box of horizontal size b with the upper lid freely moving along the vertical axis. The height of the plume surface $H(t)$ above the mean sea level depends on time t. Let the plume receive the inflowing water from the river at a constant velocity equal to U_m at the mouth and volume rate Q ($m^3 s^{-1}$), and lose the water through an outlet of the effective cross-section area A with the depth-averaged velocity $U(t)$ which is governed solely by the pressure gradient created by the elevation of the plume surface. Given this, the mass and the momentum budgets read simply

$$b^2 \frac{dH}{dt} = Q - UA \tag{1}$$

and

$$\frac{dU}{dt} = -\frac{1}{\rho}\frac{\partial P}{\partial x} \simeq \frac{g}{b} H \tag{2}$$

where ρ is the water density, P is the pressure, and x is the horizontal coordinate across the plume [hereinafter, we adopt the notation used by Branch et al. (2020)]. Differentiating Eq. (1) by time and using Eq. (2), we immediately obtain:

$$\frac{d^2 H}{dt^2} + \frac{gA}{b^3} H = 0 \tag{3}$$

Obviously, Eq. (3) describes harmonic oscillations with the period equal to:

$$T = 2\pi\sqrt{\frac{b^3}{gA}}. \tag{4}$$

Furthermore, if we assume that $A \simeq bh$, where h is the characteristic depth under the plume, we get:

$$T = \frac{2\pi b}{\sqrt{gh}}. \tag{5}$$

Note that if we consider $h \simeq 10$ m, the slope $\frac{2\pi}{\sqrt{gh}}$ of the linear dependence between T and b is equal to 0.63 s m^{-1}, which compares reasonably well with the value obtained in the observations (0.41 s m^{-1}, see red regression line in **Figure 5**).

Of course, this schematic model is very far from being realistic, as it completely ignores dynamical features that are known to be of great importance for real river plumes, such as friction, as well as advection of momentum (not to mention the Coriollis force, where applicable). It also ignores complex internal structure of a river plume (e.g., Zavialov et al., 2018). Rather than a real plume, the equations above are appropriate for describing the motion of a moving upper lid of a solid tank where water is pumped into at a constant rate from an inbound pipe, and flows out freely through an outbound pipe. Somewhat surprisingly, this representation of the plume, however, oversimplified, does explain (at least, qualitatively) all four properties (i–iv) evident in the observational data. Indeed, harmonic oscillations of the plume surface arise naturally as a solution of Eq. (3); moreover, it follows immediately from Eqs. (4) or (5) that their period

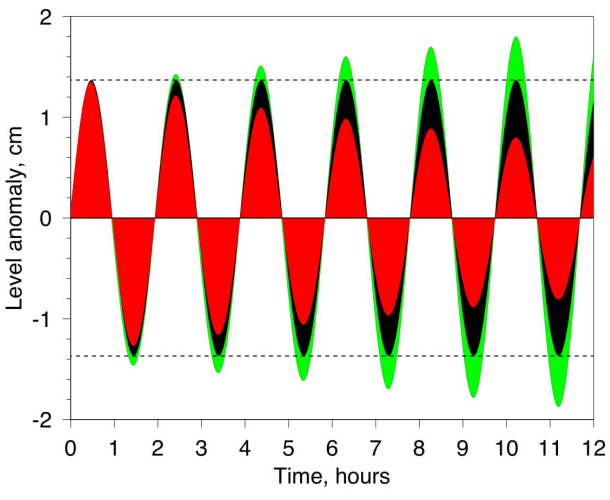


FIGURE 7 | Black: numerical solution of Eqs. (1) and (2); red: numerical solution of Eqs. (1) and (6) for $C_d = 10^{-2}$; green: numerical solution of Eqs. (1) and (6) for $C_d = 6\ 10^{-3}$.

increases with the plume size. The amplitude of the oscillations will depend on the initial conditions, i.e., the initial liftoff of the plume "ridge" (Branch et al., 2020) with respect to the mean level. It seems reasonable to assume that this liftoff is proportional to the river discharge rate Q. On the other hand, the plume size is also generally proportional to Q if other parameters are fixed (e.g., Osadchiev and Zavialov, 2013). From this point of view, both the amplitude and the period are likely to be proportional to b and, therefore, to each other.

In short, the suggested physical mechanism can be described verbally as follows. There are two reference values of the plume surface elevation, one corresponding to the equilibrium of the mass budget, and the other one – to the equilibrium of the momentum budget, and these two "equilibria" generally do not coincide. Consider, for example, the situation where the inflow from the river exceeds the outflow from the plume, so that the plume surface height grows, thus boosting the pressure gradient and the outflow rate. At some point of time, equilibrium with respect to the mass budget is achieved when the total mass flux of water coming from the river into the plume is balanced by the outflow from the plume. However, at that moment, the total force applied to the outflowing water particle is not zero, so that the momentum budget is not equilibrated and the instantaneous outflow velocity that would provide for mass conservation at a stationary plume surface height cannot be maintained and keeps increasing, leading to a drop of the surface height. Subsequently, at some point of time the momentum budget attains equilibrium – but the mass budget no longer does, and the plume volume and hence the surface height resume to increase. This cycle repeats over and over again in the form of periodic oscillations.

We believe that the simple physics outlined above may be a driver of vertical oscillations of the surface in real plumes, even though their dynamics is much more complex. If we consider the other terms of the momentum budget, quantitative details do change, but the general mechanism leading to oscillations remains the same. Indeed, with the nonlinear terms and vertical friction taken into account, Eq. (2) now takes the form

$$\frac{dU}{dt} = -g\frac{\partial H}{\partial x} - U\frac{\partial U}{\partial x} - C_D\frac{U^2}{h} \qquad (6)$$

The second and the third terms in the right-hand side of Eq. (6) represent the advection of momentum and the vertical friction, respectively, C_D is the dimensionless bottom drag coefficient. This form of momentum equation was used in Branch et al. (2020), cf. Eq. (16) therein, except that these authors set the left-hand side to zero to investigate the steady state profile of the plume ridge, while here we retain the temporal derivative in order to describe the ridge oscillations. The dynamics of the plume is fully determined by the momentum Eq. (6) together with the mass conservation Eq. (1).

This system of first-order equations no longer explicitly reduces to the harmonic oscillations Eq. (3), but it can be easily solved numerically. We approximate $\frac{\partial H}{\partial x}$ as $\frac{H}{b}$ and $\frac{\partial U}{\partial x}$ as $b^{-1}\left(U - \frac{Q}{S}\right)$, where S is the cross-sectional area of the inflow at the river mouth. We then start with $H = 0$ and $U = 0$ (for example), and at each time step of the integration set to be equal to $\Delta t = 1$ min first calculate ΔH and the next value of H from Eq. (1), and then ΔU and the next value of U from Eq. (6), continuing this process for 12 h. Examples of numerical solutions obtained thereby are shown in **Figure 7**. The following settings which roughly correspond to real conditions of the Mzymta plume were used for these particular integrations: $b = 7000$ m, $h = 4$ m, $U_m \equiv Q/S = 0.6$ m s^{-1}. In **Figure 7**, the black shaded curve corresponds to the case where the second and the third terms in the right-hand side of Eq. (6) were set to null, i.e., the acceleration of the liquid particle was only balanced by pressure gradient force, and the momentum budget returned to the form of Eq. (2). Not surprisingly, in this case the solution exhibited harmonic oscillations with constant amplitude and the period determined by Eq. (4). Red and green curves in **Figure 7** represent solutions for the complete Eq. (6) with different values of the drag coefficient C_D: for relatively high C_D (red curve), the loss of momentum through bottom friction exceeds the gain of momentum from the river inflow and the amplitude of the oscillation decreases with time – and vise versa, if C_D is relatively low (green curve), the advection of momentum exceeds friction and the amplitude grows. However, as it is clearly seen from **Figure 7**, the inclusion of momentum advection and friction terms into consideration changes neither the oscillatory pattern of vertical displacements of the plume surface, nor the period of these oscillations. The latter is still governed solely by the plume size and the mean depth in the area covered by the plume as prescribed by Eq. (5).

For medium size river plumes like that of the Mzymta where $b \simeq 10^4$ m and $h \simeq 10$ m, formula (5) leads to $T \simeq 100$ min, which, indeed, agrees reasonably well with the SSH observations reported in this study. This order of magnitude estimate is also consistent with our earlier published data on variability of near-bottom velocity in the area adjacent to the Mzymta mouth that revealed pattern of internal waves propagating from the plume at about 0.7 m/s with periods spanning between 2.8 and 4.8 h, which implies the wavelengths between 7 and 12 km (Korotkina et al., 2014). However, for big rivers with $b \geq 10^5$ m, the SSH oscillation period should be of an order constrained by one or several days. Perhaps, historical records from level gauges deployed near the estuaries of major rivers may help to reveal this signal. This, however, is beyond the scope of the present study. Inversely, for very small rivers ($b \simeq 10^2$ m) the expected period could be as short as 1 min or even shorter. Recent drone-borne observations of internal waves from plumes generated by small ducts of the Bzyb River in the northwestern Black Sea seem to be in line with this estimate (Osadchiev et al., 2020).

CONCLUSION

Data from pressure gauges deployed on the inner shelf of the northeastern Black Sea near the mouths of the Mzymta and the Vulan rivers revealed persistent periodic oscillations of the SSH within the river plumes corresponding to periods from 70 to 230 min and not correlated with either wind stress or atmospheric pressure. Although based on limited data,

the available records suggested that both the period and the amplitude of these oscillations increased with the size of the plume. More voluminous observational evidence indicated that the periods and the amplitudes were in direct relation to each other. To interpret the measurements, we devised a simple physical model, which demonstrated that the momentum and the mass budgets of the plume taken together naturally provide for periodic vertical oscillations of the plume surface, and the said oscillations can be deemed an intrinsic property inherent to river plumes. This may have several important implications. In particular, the observed pressure oscillations associated with the SSH variability may represent a forcing mechanism for internal waves generated by river plumes. This, however, requires further investigation.

DATA AVAILABILITY STATEMENT

The original contributions presented in the study are included in the article/supplementary material, further inquiries can be directed to the corresponding author.

AUTHOR CONTRIBUTIONS

The author confirms being the sole contributor of this work and has approved it for publication.

FUNDING

This study was supported by the Ministry of Science and Higher Education of Russia, theme 0128-2021-0001, and the Russian Foundation for Basic Research through Grants 20-55-75002 (data analysis) and 19-55-80004 (plume modeling).

ACKNOWLEDGMENTS

The author thank the crew of R/V *Ashamba*, all participants of the field campaigns, and Dr. A. Subbotin for critical reading of the manuscript.

REFERENCES

Alexeevsky, N. I., Magritsky, D. V., Koltermann, K. P., Krylenko, I. N., and Toropov, P. A. (2016). Causes and systematics of inundations of the Krasnodar territory on the Russian Black Sea coast. *Nat. Hazard. Earth Syst.* 16, 1289–1308. doi: 10.5194/nhess-16-1289-2016

Branch, R. A., Horner-Devine, A. R., Kumar, N., and Poggioli, A. R. (2020). River plume liftoff dynamics and surface expressions. *Water Resources Research* 56, e2019WR026475. doi: 10.1029/2019WR026475

Dale, A. C., and Sherwin, T. J. (1996). The extension of baroclinic coastal-trapped wave theory to superinertial frequencies. *J. Phys. Oceanogr.* 26, 2305–2315. doi: 10.1175/1520-0485(1996)026<2305:teobct>2.0.co;2

Dzhaoshvili, S. H. (2002). *Rivers of the Black Sea, Technical Report no. 71*. European Environmental Agency, 58. Available online at: www.reports.eea.eu.int/technical-report-2002-71

Garvine, R. W. (1984). Radial spreading of buoyant surface plumes in coastal waters. *J. Geophys. Res.* 89, 1989. doi: 10.1029/JC089iC02p01989

Garvine, R. W., and Monk, J. D. (1974). Frontal structure of a river plume. *J. Geophys. Res.* 17, 2251–2259. doi: 10.1029/JC079i015p02251

Horner-Devine, A. R., Hetland, R. D., and MacDonald, D. G. (2015). Mixing and transport in coastal river plumes. *Annu. Rev. Fluid Mech.* 47, 569e594.

Hüseyin, Y. (1993). Analysis of the water level variations in the eastern Black Sea. *J. Coastal Research* 9, 1075–1082.

Ivanov, V. A., and Yankovsky, A. E. (1995). Dynamics of the Crimea shelf waters in summer. *Physical Oceanography* 6, 201–217. doi: 10.1007/BF02197518

Ivanov, V. A., Manilyuk, Y. V., and Cherkesov, L. V. (1996). Seiches in the Black Sea. *Soviet Meteorology and Hydrology* 11, 57–63. (in Russian),

Ivanov, V. A., Shul'ga, T. Y., Plastun, T. V., and Svishcheva, I. A. (2018). Spatial and temporal parameters of the trapped waves in the Black Sea shelf areas. *Physical Oceanography* 25, 280–294. doi: 10.22449/1573-160X-2018-4-280-294

Kilcher, L. F., and Nash, J. D. (2010). Structure and dynamics of the Columbia River tidal plume front. *J. Geophys. Res.* 115, C05S90. doi: 10.1029/2009JC006066

Korotkina, O. A., Zavialov, P. O., and Osadchiev, A. A. (2011). Submesoscale variability of the current and wind fields in the coastal region of Sochi. *Oceanology* 51, doi: 10.1134/S0001437011050109

Korotkina, O. A., Zavialov, P. O., and Osadchiev, A. A. (2014). Synoptic variability of currents in the coastal waters of Sochi. *Oceanology* 54, 545–556. doi: 10.1134/S0001437014040079

Lavrova, O., and Mityagina, M. (2017). Satellite survey of internal waves in the Black and Caspian Seas. *Remote Sensing* 9, 892. doi: 10.3390/rs9090892

Medvedev, I. P., and Kulikov, E. A. (2016). Spectrum of mesoscale sea level oscillations in the northern Black Sea: Tides, seiches, and inertial oscillations. *Oceanology* 56, 6–13. doi: 10.1134/S0001437016010094

Mendes, R., da Silva, J. C. B., Magalhaes, J. M., St-Denis, B., Bourgault, D., Pinto, J., et al. (2021). On the generation of internal waves by river plumes in subcritical initial conditions. *Scientific Reports* 11, 1963. doi: 10.1038/s41598-021-81464-5

Mestres, M., Sánchez-Arcilla, A., and Sierra, J. P. (2007). Modeled dynamics of a small-scale river plume under different forcing conditions. *Journal of Coastal Research* 2010, 84–96. doi: 10.2112/1551-5036-47.sp1.84

Nash, J. D., and Moum, J. N. (2005). River plumes as a source of large-amplitude internal waves in the coastal ocean. *Nature* 437, 400–403. doi: 10.1038/nature03936

Osadchiev, A. A. (2018). Small mountainous rivers generate high-frequency internal waves in coastal ocean. *Scientific Reports* 8, 1–8. doi: 10.1038/s41598-018-35070-7

Osadchiev, A. A., and Korshenko, E. A. (2017). Small river plumes off the north-eastern coast of the Black Sea under average climatic and flooding discharge. *Ocean Sci.* 13, 465–482. doi: 10.5194/os-13-465-2017

Osadchiev, A. A., and Zavialov, P. O. (2013). Lagrangian model of a surface-advected river plume. *Continental Shelf Research* 58, 96–106. doi: 10.1016/j.csr.2013.03.010

Osadchiev, A. A., and Zavialov, P. O. (2019). "Structure and dynamics of plumes generated by small rivers," in *Estuaries and Coastal Zones—Dynamics and Response to Environmental Changes*, ed. J. Pan (London: IntechOpen).

Osadchiev, A. A., and Sedakov, R. O. (2019). Spreading dynamics of small river plumes off the northeastern coast of the Black Sea observed by Landsat 8 and Sentinel-2. *Remote Sensing of Environment* 221, 522–533. doi: 10.1016/j.rse.2018.11.043

Osadchiev, A. A., Barymova, A. A., Sedakov, R. O., Zhiba, R. Y., and Dbar, R. S. (2020). Spatial structure, short-temporal variability, and dynamical features of small river plumes as observed by aerial drones: case study of the Kodor and Bzyp river plumes. *Remote Sensing* 12, 3079. doi: 10.3390/rs12183079

Stashchuk, N., and Vlasenko, V. (2009). Generation of internal waves by a supercritical stratified plume. *J. Geophys. Res.* 114, C01004. doi: 10.1029/2008JC004851

Smith, S. D. (1980). Wind stress and heat flux over the ocean in gale force winds. *J. Phys. Oceanogr.* 10, 709–726. doi: 10.1175/1520-0485(1980)010<0709:wsahfo>2.0.co;2

Yankovsky, A. E., and Chapman, D. C. (1997). A simple theory for the fate of buoyant coastal discharges. *J. Phys. Oceanogr.* 27, 1386–1401. doi: 10.1175/1520-0485(1997)027<1386:astftf>2.0.co;2

Zavialov, P. O., Makkaveev, P. N., Konovalov, B. V., Osadchiev, A. A., Khlebopashev, P. V., Pelevin, V. V., et al. (2014). Hydrophysical and hydrochemical characteristics of the sea areas adjacent to the estuaries of small rivers of the Russian coast of the Black Sea. *Oceanology* 54, 265–280. doi: 10.1134/S0001437014030151

Zavialov, P. O., Pelevin, V. V., Belyaev, N. A., Izhitskiy, A. S., Konovalov, B. V., Krementskiy, V. V., et al. (2018). High resolution LiDAR measurements reveal fine internal structure and variability of sediment-carrying coastal plume. *Estuarine, Coastal and Shelf Science* 205, 40–45. doi: 10.1016/j.ecss.2018.01.008

Conflict of Interest: The author declares that the research was conducted in the absence of any commercial or financial relationships that could be construed as a potential conflict of interest.

Copyright © 2021 Zavialov. This is an open-access article distributed under the terms of the Creative Commons Attribution License (CC BY). The use, distribution or reproduction in other forums is permitted, provided the original author(s) and the copyright owner(s) are credited and that the original publication in this journal is cited, in accordance with accepted academic practice. No use, distribution or reproduction is permitted which does not comply with these terms.

frontiers in Marine Science

ORIGINAL RESEARCH
published: 30 June 2021
doi: 10.3389/fmars.2021.701773

Non-Linear Processes in the Gironde River Plume (North-East Atlantic): Instabilities and Mixing

Adam Ayouche[1]*, *Guillaume Charria*[1], *Xavier Carton*[1], *Nadia Ayoub*[2] and *Sébastien Theetten*[1]

[1] Laboratory for Ocean Physics and Satellite remote sensing (LOPS), UMR6523, Ifremer, Univ. Brest, CNRS, IRD, Brest, France, [2] Laboratoire d'Etudes en Géophysique et Océanographie Spatiales (LEGOS), UMR5566, Université de Toulouse, CNRS, CNES, IRD, Toulouse, France

Instability and mixing are ubiquitous processes in river plumes but their small spatial and temporal scales often limit their observation and analysis. We investigate flow instability and mixing processes in the Gironde river plume (Bay of Biscay, North-East Atlantic ocean) in response to air-sea fluxes, tidal currents, and winds. High-resolution numerical simulations are conducted in March (average river discharge) and in August (low discharge) to explore such processes. Two areas of the Gironde river plume (the bulge and the coastal current) experience different instabilities: barotropic, baroclinic, symmetric, and/or vertical shear instabilities. Energy conversion terms reveal the coexistence of barotropic and baroclinic instabilities in the bulge and in the coastal current during both months. These instabilities are intensified over the whole domain in August and over the inner-shelf in March. The Hoskins criterion indicates that symmetric instability exists in most parts of the plume during both periods. The evolution of the Gironde plume with the summer stratification, tidal currents and winds favors its development. During both seasons, ageostrophic flow and large Rossby numbers characterize rapidly-growing and small-scale frontal baroclinic and symmetric instabilities. The transition between these instabilities is investigated with an EKE decomposition on the modes of instability. In the frontal region of the plume, during both months, symmetric instabilities grow first followed by baroclinic and mixed ones, during wind bursts and/or high discharge events. In contrast, when the wind is weak or relaxing, baroclinic instabilities grow first followed by symmetric and then mixed ones. Their growth periods range from a few hours to a few days. Mixing at the ocean surface is analyzed via Potential Vorticity (PV) fluxes. The net injection of PV at the ocean surface occurs at submesoscale buoyant fronts of the Gironde plume during both months. Vertical mixing at these fronts has similar magnitude as the wind-driven and surface buoyancy fluxes. During both months, the frontal region of the plume is restratified during wind relaxation events and/or high river discharge events through frontogenetic processes. Conversely, wind bursts destratify the frontal plume interior through non-conservative PV fluxes.

Keywords: river plumes, buoyant fronts, (sub)mesoscale instabilities, PV mixing, stratification, Gironde river, Bay of Biscay

OPEN ACCESS

Edited by:
Alexander Yankovsky, University of South Carolina, United States

Reviewed by:
Nuno Vaz, University of Aveiro, Portugal
Peng Cheng, Xiamen University, China

***Correspondence:**
Adam Ayouche
adam.ayouche@ensta-bretagne.org

Specialty section:
This article was submitted to Coastal Ocean Processes, a section of the journal Frontiers in Marine Science

Received: *28 April 2021*
Accepted: *07 June 2021*
Published: *30 June 2021*

Citation:
Ayouche A, Charria G, Carton X, Ayoub N and Theetten S (2021) Non-Linear Processes in the Gironde River Plume (North-East Atlantic): Instabilities and Mixing. Front. Mar. Sci. 8:701773. doi: 10.3389/fmars.2021.701773

1. INTRODUCTION

The Bay of Biscay is a semi-enclosed region in the northeastern Atlantic ocean where ocean flows with different spatial and temporal scales interact and are constrained by a complex bathymetry (a wide continental shelf, several canyons along the slope). The bay receives freshwater from three main rivers (the Loire, the Gironde, and the Adour). The purpose of this paper is to investigate the instability of the Gironde river plume and the associated mixing processes.

The Bay of Biscay is the seat to multiple oceanic phenomena as described in Koutsikopoulos et al. (1998) and Le Boyer et al. (2013). The continental shelf and the open ocean have different dynamics; regional modeling reveals weak cross-slope exchanges (Xu et al., 2015; Graham et al., 2018; Rubio et al., 2018; Akpınar et al., 2020). Over the continental shelf, river runoffs induce density currents and salinity fronts (Lazure and Jegou, 1998; Puillat et al., 2004). The residual circulation over the shelf is due to wind and tidal forcings, leading to density gradients. On the continental slope, nonlinear processes favor the generation of mesoscale [scales $\sim$ O (10–100 km)] and submesoscale [scales $\sim$ O (1–10 km)] structures (Charria et al., 2017; Yelekçi et al., 2017). The open ocean circulation is marked by long-living mesoscale eddies, mainly generated along the continental slope. Such eddies can be shed by the Iberian Poleward current, which flows over canyons (Pingree and Le Cann, 1989; Pingree and Le Cann, 1990; Frouin et al., 1990; Pingree et al., 1999; Garcia-Soto et al., 2002; Serpette et al., 2006; Le Cann and Serpette, 2009).

Using submesoscale permitting numerical models, small-scale oceanic features have been observed in the Bay of Biscay with a seasonal variability (Charria et al., 2017). At the end of winter, the most intense surface features result from mixed layer baroclinic instabilities. These features also display an interannual variability due to winter atmospheric conditions (Charria et al., 2017). In this macro-tidal bay, tides also play a role in the growth of small scale features. For example, Karagiorgos et al. (2020) showed that the semidiurnal tidal harmonics intensify the submesoscale activity in summer, in particular near the Ushant front. Tidal and buoyant fronts are ubiquitous in the Bay of Biscay. Buoyant fronts are observed over the continental shelf due to the interaction between the Loire and Gironde river plumes and the open ocean (Yelekçi et al., 2017). This frontal activity is intense in winter due to the river influence over the inner-shelf. The Loire, Gironde, and Adour rivers are an important source of freshwater, they represent more than 75% of the total river runoff in the bay, with an annual river discharge of 900 $m^3\ s^{-1}$; their plumes reach a noticeable alongshore extension during downwelling favorable wind events (Lazure et al., 2009; Costoya et al., 2017).

When the freshwater flows from the estuary to the open ocean, a river plume is formed. The structure and extent of the river plume result from the river discharge, the local topography, and the influence of winds, tides, and of the Coriolis force. It can be studied in two steps: (1) the offshore spreading and its curvature which lead to the generation of an anticyclonic bulge and (2) the development of a coastal current, both interacting with the topography (Yankovsky and Chapman, 1997). Concerning the bulge, Nof and Pichevin (2001) studied the ballooning of buoyant outflows near a river mouth using numerical and analytical simulations. For large Rossby number outflows, they found that a ballooning anticyclonic gyre forms, which traps most of the freshwater. When the Rossby number of the outflow is smaller than unity, the coastal current transports most of the freshwater which does not accumulate in the bulge. Frictionless processes alter the Potential Vorticity (PV) of the bulge. Isobe (2005) finds that the bulge ballooning is due to near inertial disturbances near the river mouth; these instabilities develop in the anticyclonic gyre fed by an inflow of freshwater. Such instabilities grow in the absence of wind or ambient currents whereas tides stabilize their growth offshore, and also modify the plume structure near the river mouth (Horner-Devine, 2009). When winds are weak, tidal plumes can form as the river plume interacts with tides; this is observed for the Columbia River. In the presence of stronger winds, river plume spreading is sensitive to the wind direction (Kourafalou et al., 1996a,b; Liu et al., 2008; Kastner et al., 2018). When winds are downwelling favorable, low surface salinity waters are advected to the southwest. In contrast, upwelling favorable winds favor large exports of low-salinity water offshore. Under the influence of external forcings, river plumes undergo geostrophic and non-geostrophic instabilities.

Geostrophic and non-geostrophic instabilities can develop in river plumes under favorable conditions. The numerical modeling of the Mississippi-Atchafalaya river plume has revealed that baroclinic instabilities are not observed when the width of the coastal current is too small compared to the local deformation radius and inertial length scale (Hetland, 2017). This study however mentioned that baroclinic unstable flows can be observed in the presence of tides and during winds relaxation periods or through a transition from symmetric instabilities. This instability can also occur as frontal disturbances due to a small salinity anomaly or strong stratification (Jia and Yankovsky, 2012). They indicate that barotropic and baroclinic instabilities can coexist. In this latter study, baroclinic instability played the leading role and could be inhibited with a gentle bottom slope. The onset of such instabilities can also occur after a downwelling favorable wind event (Lv et al., 2020). This study, using numerical simulations, showed that a downwelling favorable wind strengthens the stratification and that symmetric instabilities are generated. After a wind event, the stratification weakens and baroclinic instabilities prevail. For the specific case of the Bay of Biscay, the interaction between the Gironde river plume, tides and winds promote the existence of different instabilities which coexist in different regions of the plume (Ayouche et al., 2020). This study showed that semi-diurnal tides lead to the coexistence of symmetric, barotropic, and baroclinic instabilities in the near field of the plume. Southwesterly winds promote the coexistence of frontal symmetric, baroclinic, and barotropic instabilities in the far field region of the plume. In addition, when the river plume is not constrained by external forcings (high discharge only $\sim$10,000 $m^3\ s^{-1}$), it undergoes symmetric and mixed barotropic/baroclinic instabilities where the Rossby number is large.

River plumes are not only propitious to the development of such instabilities but also play a major role in the exchange

of freshwater with the salty open ocean which induces vertical mixing within different regions of the plume.

In river plumes, a competition between the growth of fronts and local mixing is observed in different regions. The freshwater volume retained behind the front is inversely proportional to mixing rates, near the river mouth (Hetland, 2010). The near-field plume is sensitive to tides and to estuarine discharge. Larger river discharges lead to a decrease in plume mixing, limiting its lateral expansion and inhibiting shear mixing (Cole and Hetland, 2016). Tidal rectification is also a possible mechanism for transport and/or mixing as suggested by Wu and Wu (2018). Tides also lead to the development of Kelvin-Helmholtz billows in the bottom boundary layer which enhance mixing between freshwater and ambient salty waters near the river mouth (MacDonald and Geyer, 2004; Kilcher and Nash, 2010). In the far-field region of the plume the net mixing is less sensitive to tides and more sensitive to increased river discharge in the absence of winds through shear mixing (Cole and Hetland, 2016). In the presence of winds, mixing is efficient in both near field and far field regions (Hetland, 2005). In idealized simulations of the Gironde River plume, interior mixing was evaluated with a restratification budget based on PV mixing (Ayouche et al., 2020). They showed that frontogenetic processes govern the restratification in the near field region of the plume when forced by tides or a high river discharge ($\sim$10,000 m^3 s^{-1}). Frontogenesis is enhanced in the coastal current of the plume when interacting with downwelling favorable winds and the PV is eroded through surface frictionless processes.

Following these previous studies, we analyze the plume dynamics, its instabilities and the associated mixing in the case of the Gironde River. We use diagnostics based on potential vorticity budget and on a Fourier decomposition of the Eddy Kinetic Energy (EKE).

Numerical realistic simulations (with a submesoscale resolving model) are performed with a specific focus on the Gironde river plume. The study is organized around the following four main questions:

1. What are the 3D structure and dynamics of Gironde river plume in high resolution realistic simulations?
2. Which instability processes affect this river plume (nature, mechanism, intensity, and growth)?
3. What are the processes responsible for potential vorticity removal or injection at the ocean boundary layers (surface and bottom) in the river plume?
4. What are the processes explaining the stratification weakening or intensification in the plume?

The paper is organized as follows: the model configuration, simulations and methods are described in section 2. The model validation is presented in section 3. The 3D structure and dynamics of Gironde river plume are detailed in section 4.1. The instabilities are analyzed in sections 4.2 and 4.3; the potential vorticity mixing at the ocean boundaries is analyzed in section 4.4 and the processes explaining the stratification destruction or intensification are explored in section 4.5. The main results are then discussed (section 5) before the main conclusions and perspectives are given.

2. MATERIALS AND METHODS

2.1. Model Configuration

The numerical model used for our realistic simulations is the CROCO model (based on the ROMS model) (Shchepetkin and McWilliams, 2005; Debreu et al., 2012). CROCO is a free-surface, hydrostatic, primitive equation ocean model. Sigma coordinates are used in the vertical with 40 vertical levels. These levels are stretched at the surface with $\theta_s = 5$ and at the bottom with $\theta_b = 0.4$. The bathymetry is a combination of HOMONIM bathymetry from the Shom (https://data.shom.fr/—100 m horizontal resolution) and of EMODNET bathymetry for regions E3 and E4 (https://portal.emodnet-bathymetry.eu—115 m horizontal resolution). The merged bathymetry was smoothed to limit pressure gradient errors. The minimum depth is 8 m (estuaries) and the maximum depth at the western boundary is $\sim$ 4,000 m (**Figure 1A**). Orthogonal curvilinear horizontal coordinates are used with a horizontal resolution of 400 m. The model time step is 15 s with hourly model outputs.

The horizontal and vertical advection of momentum are performed with the Total Variation Diminishing scheme. The tracers horizontal and vertical advection schemes are with the Zico extension fifth order WENO scheme (a weighted ENO with improvements of the weights formula) (Rathan and Naga Raju, 2018). The tracer horizontal advection is rotated along isopycnals. The model turbulent closure scheme is KPP (Large et al., 1994). The background vertical diffusivities (for both momentum and tracers) are $Kv_b = 10^{-5}$ m^2 s^{-1} and $Kt_b = 10^{-6}$ m^2 s^{-1}. Smagorinsky-like viscous and diffusive terms (with molecular viscosities and diffusivities) are implemented. The quadratic Von-Karman law (logarithmic law) is used for bottom friction with a bottom roughness $z_0 = 5$ mm.

Initial conditions and open boundaries are extracted from a daily average of the BACH1000, 1 km resolution, 100 sigma layers, MARS3D simulation (Charria et al., 2017; Akpınar et al., 2020). Open boundaries are parameterized using the Chapman (Chapman, 1985) and Flather scheme (Marchesiello et al., 2001) for 2D components (sea surface height and barotropic velocities). An Orlanski scheme is used for the 3D momentum and tracers (Orlanski, 1976). A sponge layer with 200 grid points is used.

Atmospheric forcing is provided by ERA-Interim (3 h) (Dee et al., 2011). The wind stress is computed from the C_d drag coefficient, model SST, and wind velocities at 10 m using the bulk formulae. The different components of the air-sea heat exchanges are parameterized using bulk definitions. The bulk formulation is based on air temperature, pressure, relative humidity at 2 m, rain and cloud coverage (ERA-Interim). The tidal sea surface elevation and currents with 15 harmonic constituents are imposed along the boundaries using the FES2014 ocean tide atlas (Lyard et al., 2020). In the result section, model outputs are detided using Godin filtering (Godin, 1972). In our study, 2 months (March and August 2008) have been simulated.

The freshwater source salinity and temperature for the Gironde river are estimated as monthly averages (March, August 2019) from the MAGEST *in situ* observing network time series (at 1 m depth; **Figures 1D,E**). Since no MAGEST data were available during the 2008 year, we chose the nearest year where

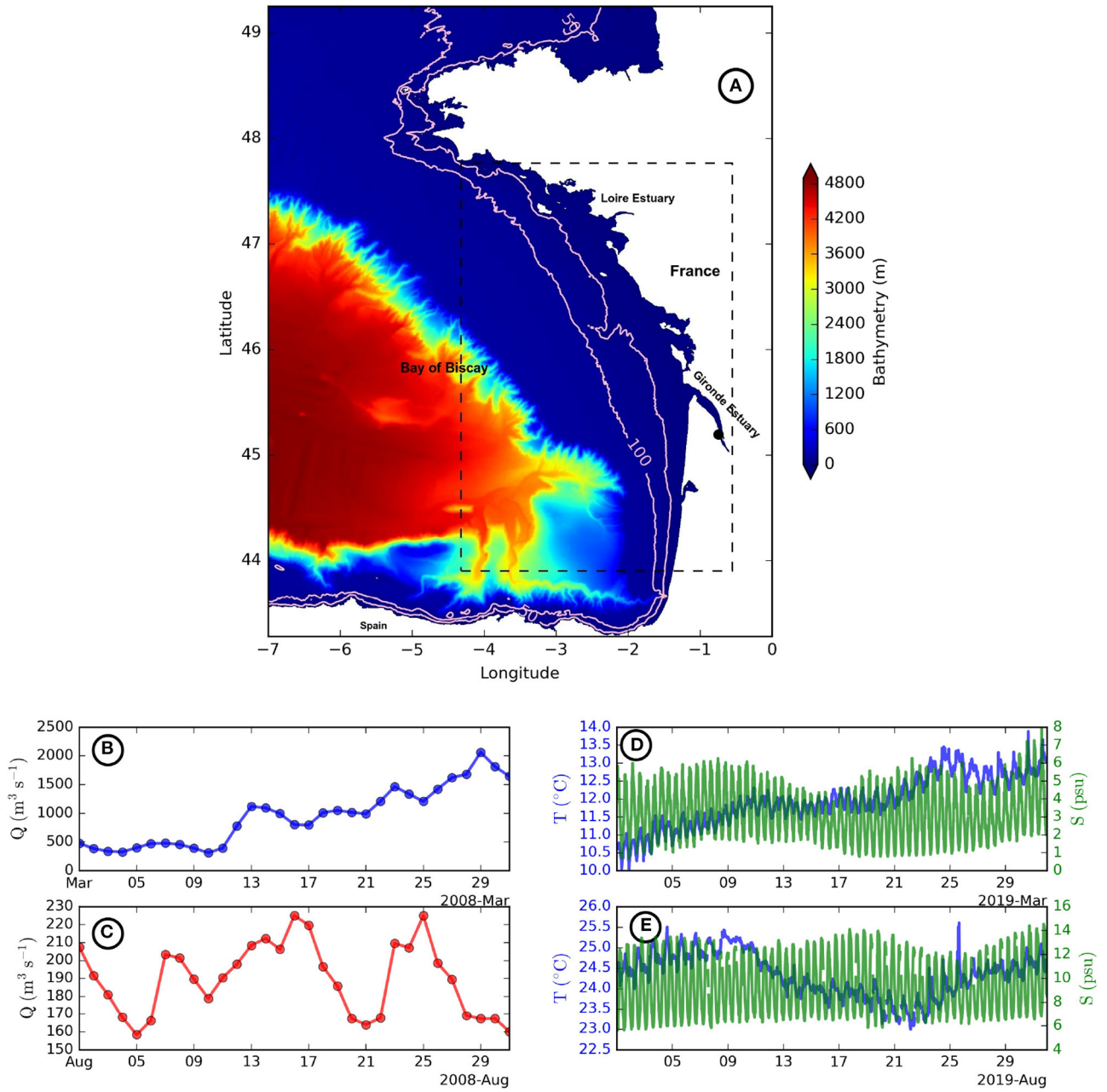


FIGURE 1 | (A) Bathymetry of the Bay of Biscay used in numerical simulations; black dashed box limits the studied region; pink solid contours for the 50 and 100 m isobaths and the black dot in the estuary shows the Pauillac station. Daily values of the Gironde river discharge in March **(B)** and August **(C)**. Time series of the temperature and salinity measured in the Gironde river estuary at the Pauillac station in March **(D)** and August **(E)**.

freshwater source salinity and temperature are available (the 2019 year). The Pauillac station was considered here (location shown in **Figure 1A**) for summer and winter simulations. For the Loire river, temperature and salinity are estimated from the BOBYCLIM climatology (http://www.ifremer.fr/climatologie-gascogne/; Vandermeirsch et al., 2010). River discharges are provided by Banque Hydro France for Dordogne, Garonne (Gironde as a combination of both Dordogne and Garonne rivers) and Loire rivers, and their daily values are shown in **Figures 1B,C**. River inputs (discharge, freshwater source salinity, and temperature) are applied over one grid point at the end of the Gironde and Loire estuaries.

2.2. Methods of Analysis

2.2.1. River Plume Instabilities

The instability mechanisms are analyzed using the transfer of kinetic and potential energy from the mean to the turbulent flows. A scale decomposition is performed (into mean and

perturbations) on the velocity and buoyancy fields. We write $u = \overline{u} + u'$ and $b = \overline{b} + b'$. Overbar and prime denote temporal mean over one day as follows ($\overline{X(t)} = \frac{1}{T}\int_{t-T/2}^{t+T/2} X(t')dt'$) and perturbations relative to the mean flow, respectively. The horizontal (HRS) and vertical (VRS) shear stresses and the vertical buoyancy flux (VBF) (instantaneous values) are expressed as (Gula et al., 2016):

$$HRS = -u'^2\partial_x\overline{u} - u'v'[\partial_y\overline{u} + \partial_x\overline{v}] - v'^2\partial_y\overline{v} \quad (1)$$

$$VRS = -u'w'\partial_z\overline{u} - v'w'\partial_z\overline{v} \quad (2)$$

$$VBF = w'b' \quad (3)$$

Positive HRS, VRS, and VBF values indicate the potential presence of barotropic, vertical shear, and baroclinic instabilities, respectively. A positive HRS [transfer from MKE (mean kinetic energy) to EKE (eddy kinetic energy)] characterizes barotropic instability. A positive vertical buoyancy flux (VBF, transfer from potential to kinetic energy) reveals baroclinic instability. Mixed barotropic and baroclinic instabilities occur when VBF and HRS are positive at the same location. Kelvin-Helmholtz instability is characterized by a positive VRS. More generally, negative values of VBF, VRS, HRS represent a contribution from the perturbation to the mean flow (Kang, 2015; Contreras et al., 2019).

The change of sign of Ertel potential vorticity (Q) (or of its anomaly with respect to a state of rest) is used to indicate instability. Ertel potential vorticity is written as:

$$Q = \boldsymbol{\omega_a}.\nabla b \quad (4)$$

where $\omega_a = \nabla \wedge \boldsymbol{u} + f\boldsymbol{k}$ is the absolute vorticity and $b = -g\frac{\rho}{\rho_0}$ is the buoyancy (ρ_0 is the mean density in our domain).

To understand the relation between river plumes, stratification and shear mixing, we evaluate the Richardson Number:

$$R_i = \frac{N^2}{S^2} \quad (5)$$

where $N^2 = \partial_z b$ is the Brunt-Vaisala frequency and $S^2 = \partial_z u^2 + \partial_z v^2$ is the vertical shear of horizontal velocity. $R_i < 0.25$ indicates the possibility of Kelvin Helmholtz instability (which is one type of vertical shear instability).

The Hoskins (1974) criteria $fQ < 0$) and $R_i < 1$ indicate a potential existence of symmetric instability.

Eddy kinetic energy [$EKE = 0.5*(u'^2 + v'^2)$] was decomposed over different modes of instability as suggested by Stone's theory (Stone, 1970). We decompose perturbations using Fourier analysis onto baroclinic (BC), symmetric (SI), mixed modes (MM; as in Stamper and Taylor, 2016); MM are a combination of SI and BC. We consider the baroclinic mode in the cross-shore direction (independent of the wavenumber l) and the symmetric mode in the along-shore direction (independent of the wavenumber k); the mixed mode is for both directions (wavenumbers different than 0). We express the vertical averaged eddy kinetic energy associated with each mode as follows:

$$\overline{\overline{EKE}^z}(k = 0, l \neq 0) = \frac{1}{2H}\int\int u'^2 + v'^2 dldz \quad (6)$$

$$\overline{\overline{EKE}^z}(l = 0, k \neq 0) = \frac{1}{2H}\int\int u'^2 + v'^2 dkdz \quad (7)$$

$$\overline{\overline{EKE}^z}(k =\neq 0, l \neq 0) = \frac{1}{2H}\int\int\int u'^2 + v'^2 dkdldz \quad (8)$$

Where we express perturbations as:

$$u', v' = (u(z), v(z)) * \exp(\sigma t) * \exp i(kx + ly) \quad (9)$$

H represents the averaged depth of the base of the plume and is expressed as follows (Thomson and Fine, 2003):

$$mld = \frac{\int zN^2 dz}{\int N^2 dz} \quad (10)$$

For each instability, the growth rate σ of instability is expressed as:

$$\sigma = \frac{1}{2(t_i - t_{i-1})}\log(\frac{EKE_i}{EKE_{i-1}}) \quad (11)$$

The same decompositions are performed on the EAPE (Eddy Available Potential Energy) field (Roullet et al., 2014)

$$EAPE = \frac{b'^2}{2N^2} \quad (12)$$

where b' is the buoyancy perturbation field.

2.2.2. Analysis of the River Plume Restratification

We evaluate the ocean restratification in terms of PV mixing and of frontogenesis/frontolysis (Marshall and Nurser, 1992; Marshall et al., 2001; Lapeyre et al., 2006; Thomas and Ferrari, 2008). To describe PV mixing near the surface, we write the evolution equation of PV:

$$\partial_t Q + \nabla.J = 0 \quad (13)$$

where the flux is written $J = wq + \nabla b \wedge \boldsymbol{F} - \omega_a D$. The first term is advective stirring ($Ja = wq$), the second term is frictional mixing ($Jf = \nabla b \wedge \boldsymbol{F}$) and last term is diabatic mixing ($Jd = -\omega_a D$). We write $D = \frac{Db}{Dt} = \partial_t b + u\partial_x b + v\partial_y b + w\partial_z b$. $\boldsymbol{F}$ represents body forces in the Navier-Stokes equations as expressed in Marshall and Nurser (1992).

At the surface, advective stirring can be neglected (via the Haynes and McIntyre impermeability theorem) and we can write $J = Jf + Jd = Jwind + Jttw + Jd_{buoy} + Jbot$.

The frictional term is made of the wind contribution at the surface (Jwind) and of the body force exerted by the bottom (Jbot). The diabatic term is made of the surface buoyancy flux (Jd_{buoy}) and of a wind-driven buoyancy flux term at fronts (Jttw,

where ttw stands for turbulent thermal wind), where Ekman transport can advect dense water over light one (e.g., Thomas and Ferrari, 2008). These four terms are expressed as follows:

$$\mathrm{Jwind} = (\mathrm{f} + \zeta_z)\frac{\mathrm{EBF}}{\mathrm{H}} \tag{14}$$

$$\mathrm{Jttw} = (\mathrm{f} + \zeta_z)\frac{\mathrm{EBF_g}}{\mathrm{H}} \tag{15}$$

$$\mathrm{Jd_{buoy}} = (\mathrm{f} + \zeta_z)\mathrm{B_0H} \tag{16}$$

$$\mathrm{Jbot} = \nabla \mathrm{b} \wedge \boldsymbol{F_b}.\boldsymbol{n} \tag{17}$$

where $\mathrm{EBF} = (\rho \mathrm{f})^{-1}\boldsymbol{\tau^w} \wedge \boldsymbol{k}.\nabla_h \mathrm{b}$ ($\boldsymbol{\tau_w}$ for the surface wind stress) is the Ekman Buoyancy flux. $\mathrm{EBF_g} = -\nu\partial_z \boldsymbol{u}.\partial_z \boldsymbol{u_g}$ is the geostrophic Ekman buoyancy flux. Geostrophic shear is deduced from thermal wind balance, using $\nu = 0.1\mathrm{Hu}^*$, a scaling where $\mathrm{u}^* = \sqrt{\frac{\|\boldsymbol{\tau^w}\|}{\rho}}$ is the wind frictional velocity (Wenegrat et al., 2018). $\mathrm{B_0}$ is the surface buoyancy flux deduced from $\mathrm{D} = \partial_z \mathrm{B}$. $\boldsymbol{F_b}$ represents the body force (the right hand side terms of the Navier-Stokes equations) at the bottom.

We focus on the restratification processes using a Budget of vertical density gradient (Brunt Vaisala frequency). This budget is related to PV fluxes (deduced from a volume integral of Equation 13) and frontogenesis [FRONT = $\partial_t(\zeta_z \mathrm{b})$, where ζ_z is the vertical component of the relative vorticity and b is the buoyancy]. This budget is defined as in Wenegrat et al. (2018) but we include the lateral transport of N^2 across the lateral boundaries since the computation domain is finite and subject to tides and river discharge from the estuary; it is written as:

$$\partial_t \overline{\mathrm{N}^2} + \frac{\mathrm{bvp}|_{z_b}^{z_t}}{\mathrm{h}} = -\frac{1}{fh}(< FRONT >|_{z_b}^{z_t} + < J_d >|_{z_b}^{z_t} + < J_f >|_{z_b}^{z_t} + < J_a >|_{z_b}^{z_t}) \tag{18}$$

where $\overline{\mathrm{N}^2} = \frac{<\mathrm{b}(\mathrm{z}=\mathrm{z_t}) - \mathrm{b}(\mathrm{z}=\mathrm{z_b})>}{\mathrm{h}}$; bvp is the boundary value problem considered here for the advection of N^2 across the lateral boundaries (called Σ); it is expressed as $\mathrm{bvp} = \frac{1}{\Sigma}\int\int \boldsymbol{u}.\boldsymbol{n}\mathrm{N}^2 \mathrm{d}\Sigma$. h represented the thickness (z_t - z_b) of the layer where this budget is evaluated. The brackets (<>) indicate a horizontal averaging over a domain. In our study, this budget is evaluated near the surface and in the frontal region of the Gironde plume.

3. MODEL VALIDATION

3.1. Frontal Dynamics

In this section, the modeled salinity is described for the two simulated months (March and August). Here the salinity evolution is not detided. The horizontal salinity gradients are derived and compared with MODIS chlorophyll concentration gradients (with ∼800 m spatial resolution); this comparison of two different tracers aims at comparing the fronts. Indeed, remotely sensed salinity is not available at high resolution.

First, the spatial distribution of the salinity is explored in the studied region (**Figures 2A,B**). The Gironde river plume is made of two regions: a bulge (an anticyclonic gyre near the river mouth, also called the near field) and a coastal current (also called the far field). When the river discharge rate is nominal (∼1,500 $\mathrm{m^3\ s^{-1}}$), the Gironde river plume is well developed (for instance, in March 2008). Low salinity water from the estuary is advected offshore in the plume, and extends northward, up to a latitude ∼ 46.5°N, via the coastal current. Indeed, low salinity values (with values of about 30) characterize the river water in the open ocean, once it has exited the estuary. This plume remains close to the coast due to wind influence. By contrast, in August, the bulge is small because of the low river discharge (200 $\mathrm{m^3\ s^{-1}}$), and of strong westerlies. Indeed, these westerlies favor the development of a northward coastal current. They constrict the coastal current near the coast while it extends to the northern part of the domain. The plume is bounded by sharp salinity gradients with the high salinity shelf water (34–35 psu). These gradients are observed to oscillate with tides.

Figure 3 shows the horizontal salinity gradient and MODIS chlorophyll gradient in the studied region. The salinity gradient is mainly zonal as $\partial_x \mathrm{S} > \partial_y \mathrm{S}$. In March, salinity fronts are intense inside and outside of the Gironde estuary (**Figure 3A**). Near the Gironde river mouth, they remain close to the coast (longitude ∼ 1.5°W). These fronts are more sensitive to the average river discharge. The river discharge also feeds the coastal current where salinity fronts are intense. In the Gironde river plume, the zonal salinity gradient is largest in the estuary since the river discharge is low in August (**Figure 3B**). In the near field, the Gironde river plume front remains close to the coast (longitude ∼1.5°W). This plume extends to the north (up to a latitude ∼46.5 °N) in the coastal current. Moderate winds and small river discharge constrict the coastal current near the coast. Beyond the river plume front, small scale filaments and eddies are observed.

Then, we compare these modeled salinity fronts to observed chlorophyll fronts (**Figures 3C,D**). In winter, cloud coverage does not allow the observation of the Gironde river plume (**Figure 3C**). Thus, comparisons are carried out outside of this region. South of the Gironde river plume (latitude between 44.5 and 45°N), the observed chlorophyll fronts and modeled salinity fronts locations are similar (longitude ∼1.6°W). On the northern side of the bay, the Loire river plume front (latitude ∼47°N) remains close to the coast in our numerical simulation and in the observed MODIS dataset. The modeled and observed river plume fronts are different in intensity. The location of salinity and chlorophyll fronts is similar outside of the Loire river plume. In August, the turbid Gironde river plume and salinity fronts are similar (**Figure 3D**). In the near field, the chlorophyll gradient maxima is close to the coast (longitude ∼1.5°W). Meanwhile, the chlorophyll front is at the same longitude in the coastal current.

Thus, our numerical simulations reproduce the frontal activity linked with the salinity gradients in the studied region. The main differences between the model and the data are that: (i) in the Gironde river plume, the coastal plume front is closer to the coast in numerical simulations, (ii) small scale eddies and filaments outside the Gironde river plume are not observed in the MODIS dataset. These differences can be due to: (i) different horizontal resolutions, (ii) MODIS chlorophyll data is influenced by biological processes, (iii) uncertainties in MODIS

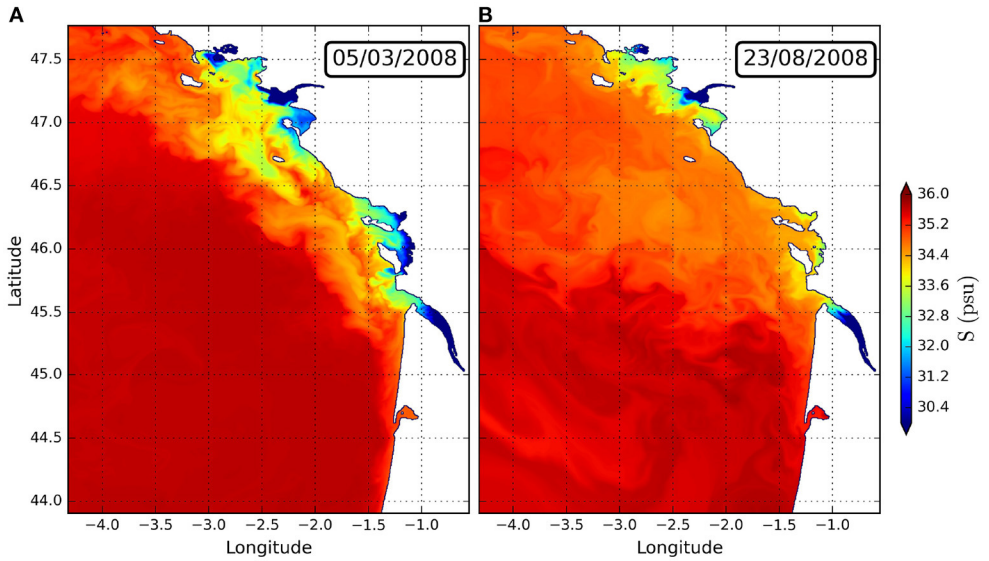


FIGURE 2 | Modeled sea surface salinity at midnight on March 5 **(A)** and on August 23 **(B)** 2008.

chlorophyll data due for instance to cloud coverage, or (iv) the fact that we include only the Loire and Gironde rivers in our numerical simulations. Other rivers, such as the Charente and the Sèvre-Niortaise, located between the Loire and Gironde rivers, may contribute to the total freshwater input and change slightly the coastal current front location due to their small discharges (between 12 and 40 $m^3\ s^{-1}$ in annual average).

3.2. Tidal Dynamics in the Model Simulations

Here, we compute the modeled and observed sea surface height (ssh) anomaly. The ssh anomaly (ssha) is computed as the perturbation from a time mean over the studied periods. Then, we decompose these signals into different tidal harmonics. This decomposition is performed on each tidal constituent and written as

$$\mathrm{ssha(t)} = \sum_{i=0}^{k} a_i \cos(\omega_i t + \phi_i) \tag{19}$$

where a_i are the Fourier coefficients, ω_i is the angular frequency of harmonic i and ϕ_i is its phase.

These decomposed signals are extracted at four locations across the domain. These locations are listed in **Table 1**. In our numerical simulations, we consider the nearest immersed locations to observations. This validation is performed for semi-diurnal (M2, S2, and N2) and for diurnal (K1, O1, Q1) tidal constituents. The amplitudes and phase lags averaged over all tidal gauges for observations and numerical model are first explored (**Figure 4**). The main differences are observed for the semi-diurnal components with an amplitude overestimated by the model of the M2 and N2 harmonics (+∼10 cm in August and March) and an underestimation of the S2 harmonic (−5 to 10 cm) (**Figure 4A**). Simulated diurnal components are close to observations with differences around 1 cm (an underestimation by the model of the O1 harmonic amplitudes by 1 cm, an overestimation of the K1 harmonics by 1–2 cm for both months, with differences of 0.5–1 cm for Q1 harmonic).

In March, the model overestimates the phases lags of several tidal constituents: S2 by 1°, N2 by 1°, and O1 by 2° (**Figure 4B**). It underestimates the M2 by 1°, K1 by 2°, and Q1 by 10° tidal constituents in phase lags. In contrast, during August the model underestimates the S2 by 30°, N2 by 100°, O1 by 5°, and Q1 by 10° tide harmonics as phases lags. But it overestimates the phase lags of the M2 by 20° and K1 by 10° harmonics. In order to evaluate these discrepancies two statistical indicators are defined, the root mean square error (RMSE) and the Willmott refined index (d_i) that we write as

$$\mathrm{RMSE} = \sqrt{\frac{1}{n}\sum_{1}^{n}(P_i - O_i)^2} \tag{20}$$

$$d_i = 1 - \frac{\sum_1^n |P_i - O_i|}{2\sum_1^n |O_i - \overline{O_i}|} \tag{21}$$

when $\sum_1^n |P_i - O_i| \leq 2\sum_1^n |O_i - \overline{O}|$

$$d_i = \frac{2\sum_1^n |O_i - \overline{O_i}|}{\sum_1^n |P_i - O_i|} \tag{22}$$

when $\sum_1^n |P_i - O_i| > 2\sum_1^n |O_i - \overline{O}|$

where the overbar denotes a time average over the studied period and n refers to the number of values for the observed and modeled time series.

The RMSE evaluates the bias between the modeled (P_i) and the observed (O_i) ssh anomaly signals. The refined Willmot

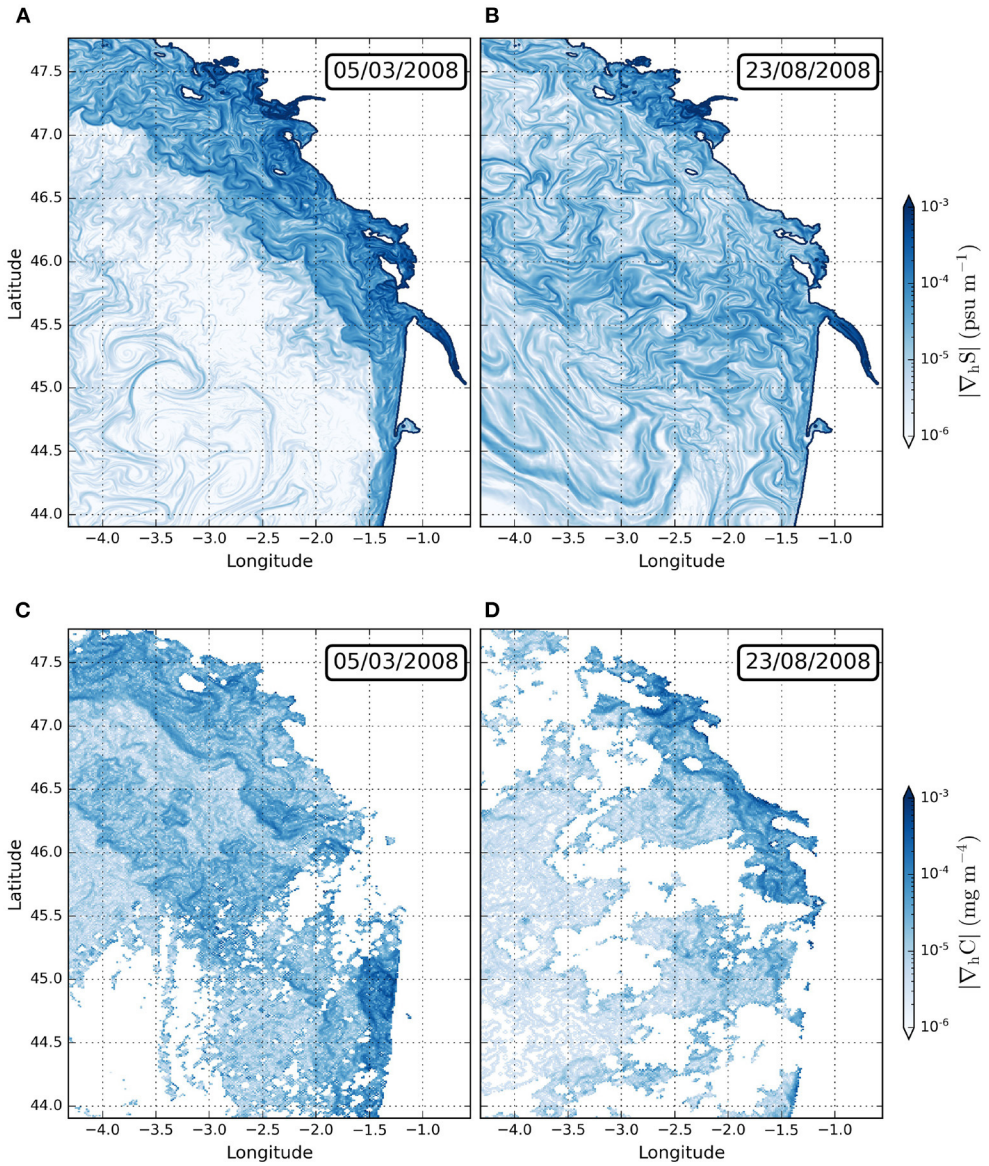


FIGURE 3 | Modeled sea surface salinity gradients the 5 March **(A)** and the 23 August **(B)** 2008; and corresponding observed Sea Surface Chlorophyll-a gradients in March **(C)** and in August **(D)** from MODIS satellite.

TABLE 1 | Geographic location of each tide gauge in the studied domain.

Tide gauges	Latitude [° N]	Longitude[° E]
Arcachon eyrac (Station 1)	44.7	−1.2
Port bloc (Station 2)	46.0	−1.1
Herbaudiere (Station 3)	47.0	−2.2
Saint nazaire (Station 4)	47.3	−2.2

index characterizes the performance of the model to predict the observed values and it is bounded between −1 and 1 (Willmott et al., 2012). The refined Willmott index is less sensitive to outliers. These indicators are computed for each tide gauge and constituent. The RMSE of ssh anomaly is <12 cm at each station for the semi-diurnal tidal constituents in March and August (**Figures 5A,B**). This indicator is above 10 cm for the N2 harmonic during these periods. The RMSE between observations and model ssh anomaly is between 0.5 and 2 cm at each location in March and August for the diurnal tidal constituents. It reaches a maximum of 2 cm for the K1 harmonic near the Gironde (Station 2) and the Loire (Station 3) river plumes in August. The Willmott refined index indicates that the model performance at each location is good ($d_i \geq 0.7$) for most of the semi-diurnal and diurnal tidal constituents in March and August (**Figures 5C,D**). However, the agreement between the numerical and observations

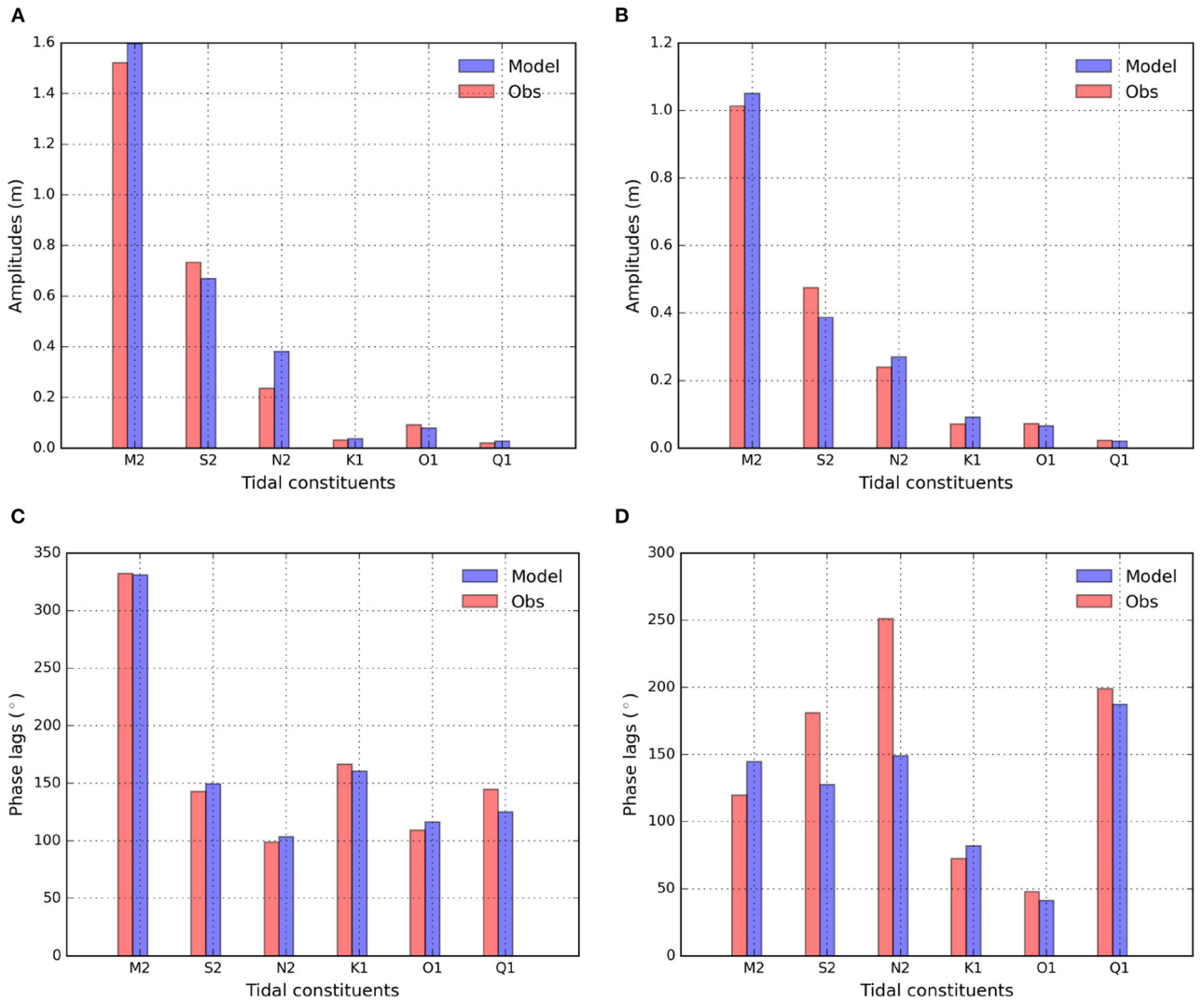


FIGURE 4 | Statistics of the mean tide amplitudes in March **(A)** and in August **(B)** from numerical simulations (blue) and tide gauge observations (red); and the corresponding mean phase lags in March **(C)** and August **(D)** averaged using four tide gauges (see **Table 1**).

is correct ($0.5 \leq d_i < 0.7$) for the N2 harmonic at the 4 stations in March, and near the Gironde river plume (Station 2) in August. This satisfactory performance is also observed for the Q1 harmonic near the Gironde river plume (Station 1). A poor performance of the model ($0 \leq d_i < 0.5$) is observed for the Q1 harmonic at station 1 (near the Gironde river plume) in March. Finally, the model outperformed ($d_i < 0$) for the M2 and N2 harmonics near the Loire river plume (Station 3) in August.

The differences between observed and modeled sea level can be explained by: (i) the location of the tide gauges near the coast, or near islands, where the model grid is too coarse to resolve local processes, or (ii) the sensitivity to the bottom drag parameterization in the numerical model. Simulated tides are sensitive to the bathymetry, the bottom roughness and to the friction law (linear, quadratic, and logarithmic) (Toublanc et al., 2018; Piton et al., 2020).

Despite these differences and since the Bay of Biscay is energetic in M2 and S2 tidal harmonics, the numerical model performance is satisfactory for the simulations of tides.

3.3. Vertical Salinity Structure

Now, we evaluate the salinity distribution in the numerical simulations of March and August 2008, in order to explore the Gironde river plume dynamics. We use observations from cruises carried out during these periods. ECLAIR cruises (Huret et al., 2018) located in front of the Gironde estuary, and achieved in March (10–16th) and August (10–14th) 2008 constitute a unique and valuable dataset to validate the vertical salinity structure in our simulations. The vertical salinity profiles from 13 CTD stations are compared with colocated modeled profiles (**Figure 6**). During the ECLAIR1 cruise in March 2008, a river plume with a limited offshore extent was observed despite the

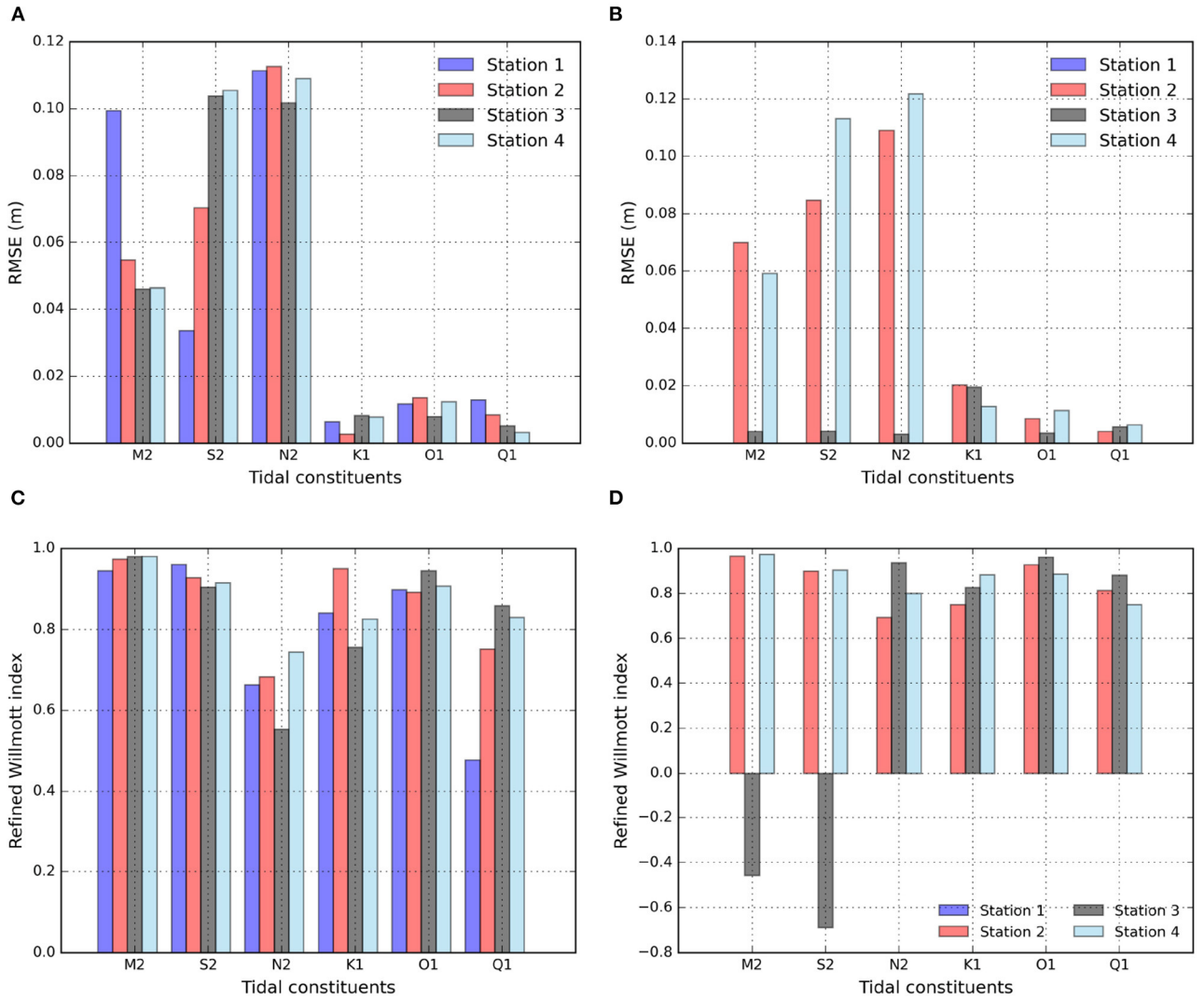


FIGURE 5 | RMSE in March **(A)** and in August **(B)**; and the refined Willmott index in March **(C)** and in August **(D)** between the modeled and observed Sea Surface Height anomaly for each station (detailed in **Table 1**) and M2, S2, N2, K1, O1, and Q1 tidal constituents.

high river discharge season. Profiles 2 and 4 (**Figure 6**) show comparable salinity values with a similar stratification (profile 2 has a lower salinity at the surface originated from the plume). The model overestimates the salinity (+0.1 in profile 2 in the surface layer; +0.1 in profile 4 outside the plume in a vertically mixed water column). In summer, during ECLAIR5, the modeled river plume extends offshore with several low salinity filaments. The river plume reaches a depth of about 30 m (profiles 7 and 13) in the numerical simulation, similar to the observed profiles. In the plume, low salinities between 34.4 and 34.6 are reproduced in the simulations. Deeper, below 40 m depth, the observed and simulated salinities are very close with values around 35.6. The large spatial and temporal variability of the river plume makes the comparison to *in-situ* observations complicated. However, the simulated salinity and vertical gradients are in good agreement with the observations which make us confident about the realism of our simulations of the plume.

4. ANALYSIS OF THE GIRONDE RIVER PLUME STRUCTURE, STABILITY, AND MIXING

4.1. Gironde River Plume Dynamics

The dynamics of the Gironde river plume is first analyzed using the local Rossby number ($R_o \sim \frac{\zeta_z}{f}$, where ζ_z is the vertical component of the relative vorticity and f the Coriolis parameter) at the surface; this is presented in **Figure 7**. This local Rossy number determines the geostrophic or ageostrophic nature of the velocity field of the Gironde river plume. In winter (March), the circulation is mostly anticyclonic in the plume ($\zeta_z < 0$) except : (i) at the river mouth (longitude ∼1.2°W and latitude between 45.5 and 45.6°N), (ii) in the northern part of the coastal current (longitude ∼1.5°W and latitude ∼ 46.2°N), and (iii) offshore of the plume front (longitude ∼ 1.5°W and latitude between 45.75 and 46.2°N; **Figure 7**, left). The circulation is ageostrophic [R_o

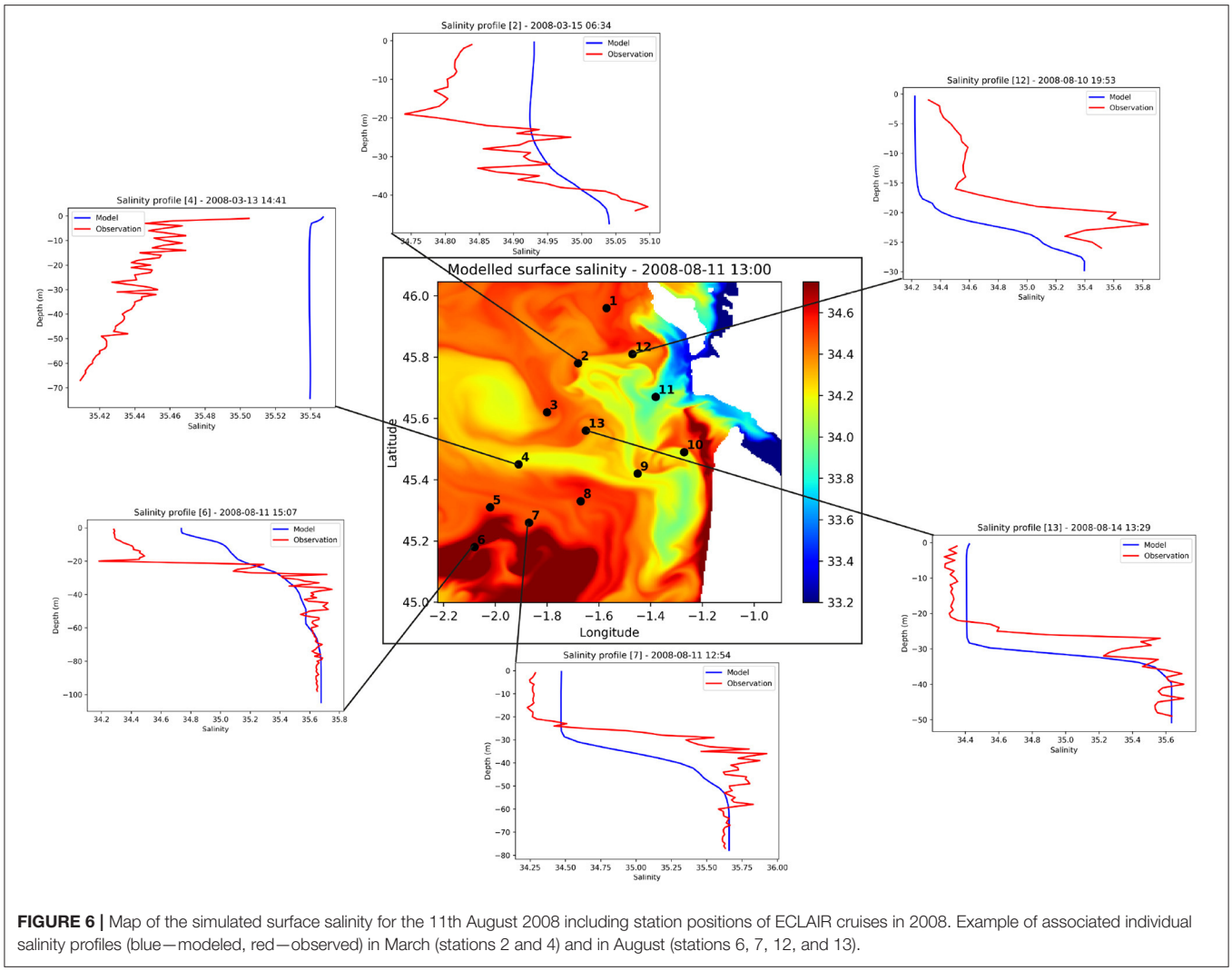


FIGURE 6 | Map of the simulated surface salinity for the 11th August 2008 including station positions of ECLAIR cruises in 2008. Example of associated individual salinity profiles (blue—modeled, red—observed) in March (stations 2 and 4) and in August (stations 6, 7, 12, and 13).

$\sim$ O(1)] at these locations. Moreover, strong negative vorticity ($\frac{\zeta_z}{f} < -1$) is observed in the coastal current. Further offshore, over the continental shelf, the local Rossby number is small, indicating a geostrophic balance. In contrast, when the ocean is stratified (in August), the circulation remains anticyclonic in the river plume except : (i) at the northern corner of the river mouth (longitude $\sim$1.2°W and latitude $\sim$45.6°N), (ii) near the coast south of the Gironde river plume (longitude between 1.2 and 1.5°W and latitude between 45 and 45.4°N), and (iii) at the offshore edge of the plume front (longitude $\sim$ 1.5°W and latitude between 45.4 and 46.2°N; **Figure 7**, right). This (cyclonic) circulation is ageostrophic at the northern (latitude between 45.75 and 46°N) and southern edges of the plume front and in a small filament south of the Gironde, along the coast and to the east. At the southern edge of the plume, a small ageostrophic cyclonic eddy can be observed (longitude $\sim$1.5°W and latitude $\sim$45.4°N) due to recirculation processes. Over the continental shelf and outside of the Gironde river plume, the overall circulation is anticyclonic except at the rim of small eddies and in filaments. The stratification in summer favors the development of anticyclonic eddies over the continental shelf.

Despite the existence of local ageostrophic motions in the Gironde river plume and over the continental shelf, on average (over the box in **Figure 7**), the global Rossby number is small (R_o $\sim$ 0.1) both in March and August. This means that the global circulation over the continental shelf is mostly in geostrophic balance. Therefore, to understand the contrast between these motions, we represent in **Figure 8** the surface averaged time evolution of the wind stress intensity ($\tau = \sqrt{\tau_x^2 + \tau_y^2}$, where τ_x and τ_y are the cross-shore and along-shore wind stress components) and the vertical geostrophic shear. These terms are evaluated in frontal regions bounded by two isopycnals (1,024 and 1024.5 kg m^{-3} in August, 1,025 and 1025.5 kg m^{-3} in March) and are written as

$$S_g^2 = \partial_z u_g^2 + \partial_z v_g^2 = \frac{\partial_y b^2 + \partial_x b^2}{f^2} \quad (23)$$

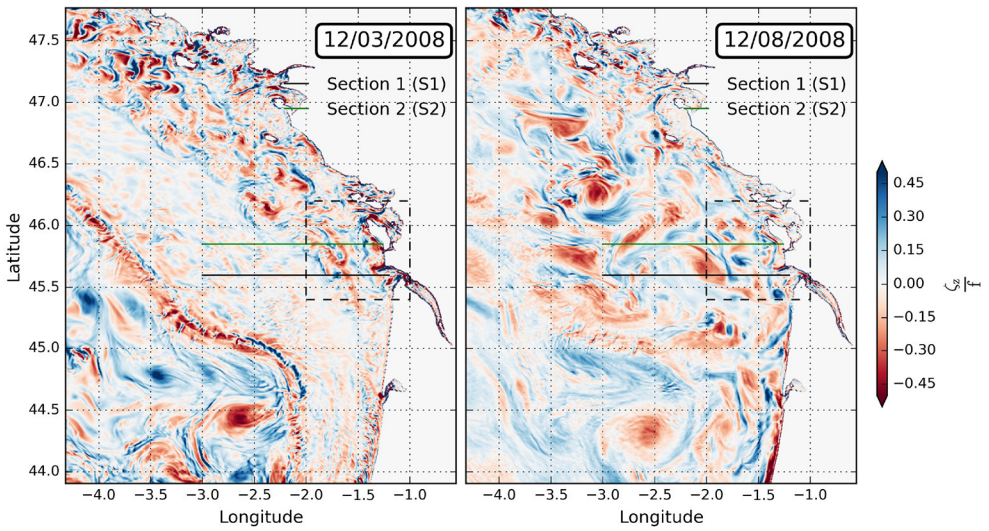


FIGURE 7 | Surface local Rossby number in March **(left)** and in August **(right)** 2008. The black dashed box shows the analyzed delimited region in **Figures 8**, **12**, **15**. The green and black solid lines show the vertical sections represented in **Figures 9**, **10**.

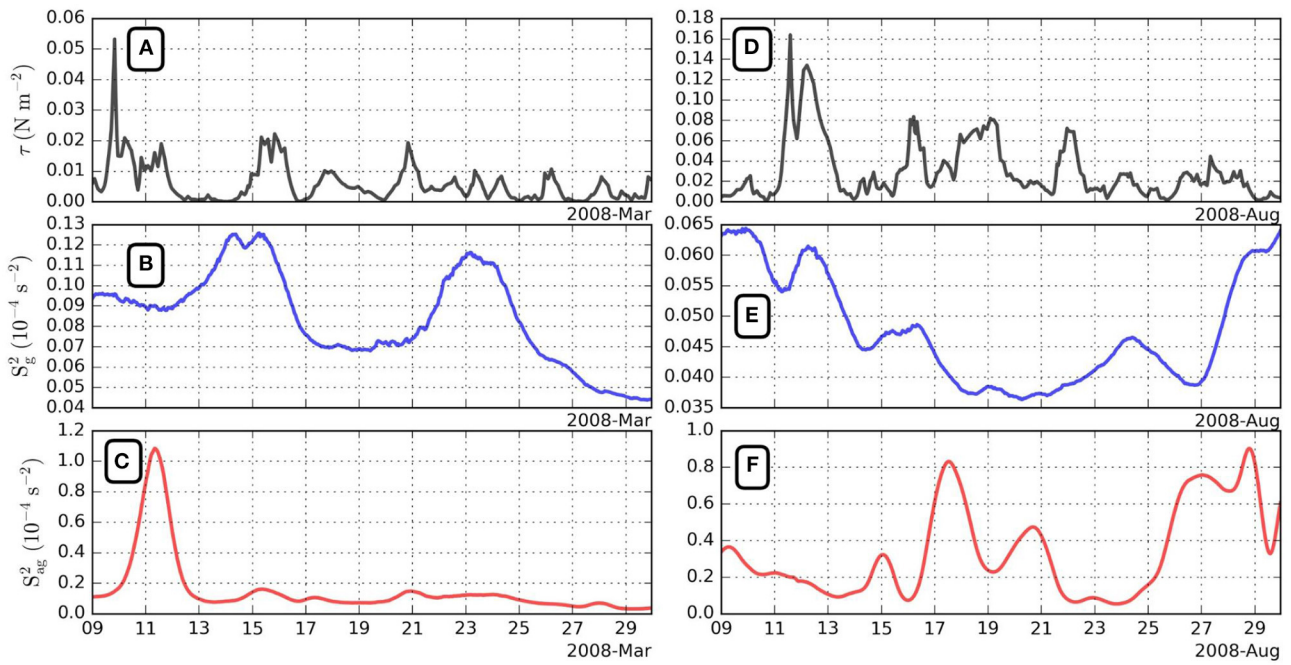


FIGURE 8 | Wind stress intensity in March **(A)** and in August **(D)**. Geostrophic shear in March **(B)** and in August **(E)**. Ageostrophic shear in March **(C)** and in August **(F)**. These quantities are averaged over the box shown in **Figure 7** and between two isopycnals as explained in the text.

where $b = -g\frac{\rho}{\rho_0}$ is the buoyancy (g is the gravity acceleration, ρ is the potential density and ρ_0 is a mean density over the studied domain), and the vertical ageostrophic shear is written as

$$S_{ag}^2 = \partial_z(u - u_g)^2 + \partial_z(v - v_g)^2 \quad (24)$$

In March, a storm is observed during the first half of the month (between March 9th and 13th; **Figure 8A**). During this period and after a lag of $\sim$ 1 day, the vertical ageostrophic shear increases and the geostrophic shear remains steady (**Figures 8B,C**). Then (between 13 and 15th March), a wind relaxation event is observed during which the ageostrophic shear slackens and the geostrophic shear increases. Afterwards (between 15 and 21st March), the geostrophic shear weakens and remains steady during 3 days. Conversely, during the latter period, few moderate wind events are observed with few variations in the ageostrophic shear.

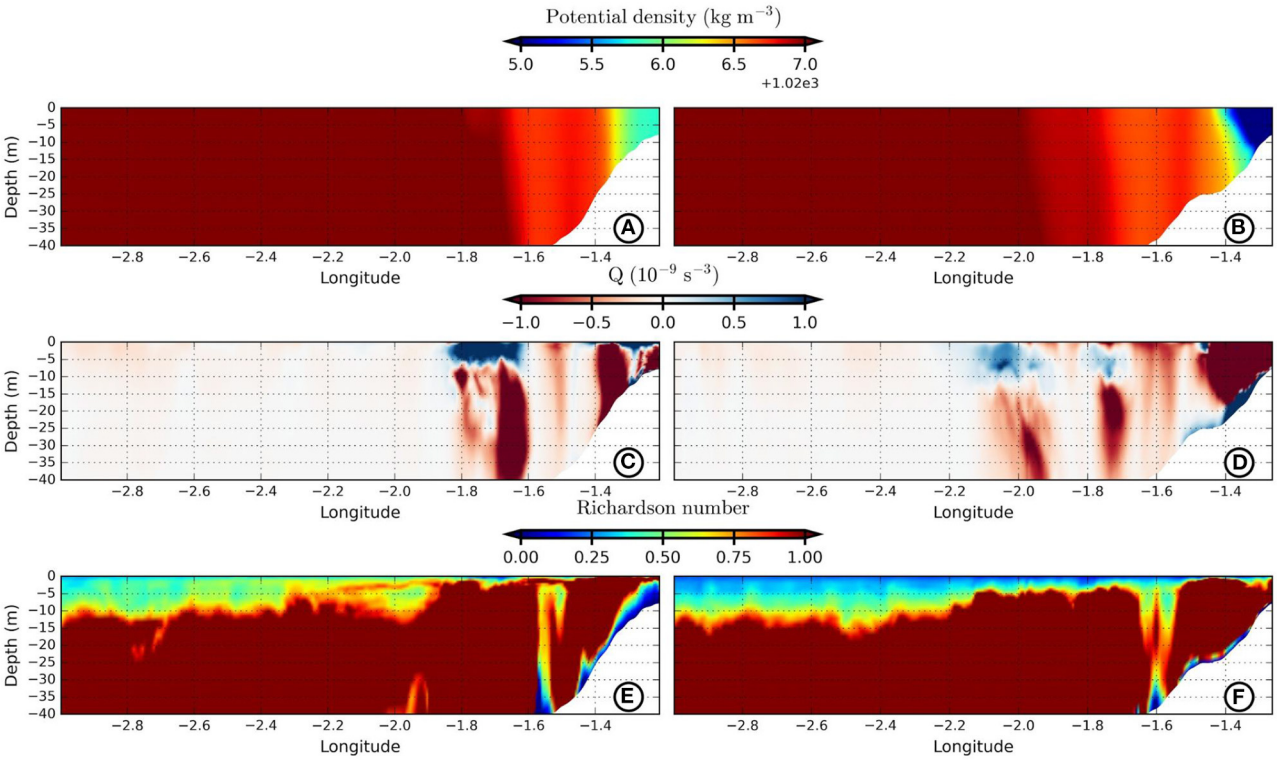


FIGURE 9 | Snapshot (12/03/2008 at midday) of: the Potential density in section 1 **(A)** and in section 2 **(B)** (cf. **Figure 7**), the PV in section 1 **(C)** and in section 2 **(D)** and the Richardson number in section 1 **(E)** and in section 2 **(F)**.

Following this period (between 21 and 23rd March), weak wind events are associated with the growth of geostrophic shear and weak ageostrophic shear. At the end of March, the geostrophic shear decreases noticeably and a weak maximum in the ageostrophic shear is observed. Geostrophic shear growth events are associated with wind relaxation and increase in river discharge (Q $\sim$ 1,000 and 1,500 m^3 s^{-1}, see **Figure 1B**). Meanwhile, the wind conditions in August 2008 are characterized by a series of strong wind events, with an intensity larger than the peak in March (an order of magnitude larger). Therefore, the ageostrophic component predominates largely over the geostrophic shear (an order of magnitude larger) due to these wind conditions and to the weak river discharge during this period (Q $\sim$ 200 m^3 s^{-1}, see **Figures 1C**, **8D**). The increase of the ageostrophic shear during this month is due to previous wind gusts (**Figure 8F**). Moreover, the geostrophic shear increases during wind relaxation events or when the ageostrophic shear slackens (**Figure 8E**). It remains quasi-steady during periods where the ageostrophic shear increases.

Thus, ageostrophic motions prevail in the frontal region of the plume due to (i) a local Rossby number R_o $\sim$ O(1) and (ii) higher (two times larger in March or an order of magnitude larger in August) ageostrophic shear than the geostrophic shear (the geostrophic shear is an order of magnitude larger in March due to the average river discharge >1,000 m^3 s^{-1}). In the Bay of Biscay, ageostrophic motions are more noticeable in winter (March) over the inner shelf (shallower than 100 m) and over the whole continental shelf in summer (August).

4.2. Generation and Occurrence of Instabilities in the Gironde River Plume

In this section, we perform diagnostics to identify and characterize instabilities in the Gironde river plume. First, we evaluate the existence of symmetric instabilities using the Hoskins stability criterion in the near field and the coastal current during March and August. The Hoskins stability criterion is based on negative PV values and a Richardson number smaller than one. Negative PV are related to different instabilities: gravitational, inertial (centrifugal), or symmetric. Gravitational instability requires unstable stratification (negative N^2) which is not the case here since the Richardson number is positive (**Figures 9E,F**). Centrifugal instability requires a negative absolute vorticity which is not the case here either (figure not shown). Hereafter, we will refer to negative PV (Hoskins criteria) as symmetric instabilities since it is mostly dominated by geostrophic and ageostrophic shears. In March, symmetric instabilities exist in different locations of the near field: (i) in the Gironde river plume (longitude between 1.25 and 1.4°W) from the surface to the bottom, (ii) at the offshore edge of the river plume front (longitude $\sim$1.5°W) where large (negative) values are observed near the surface (at 2 m depth), and (iii) offshore of the Gironde river plume (longitudes between 1.6

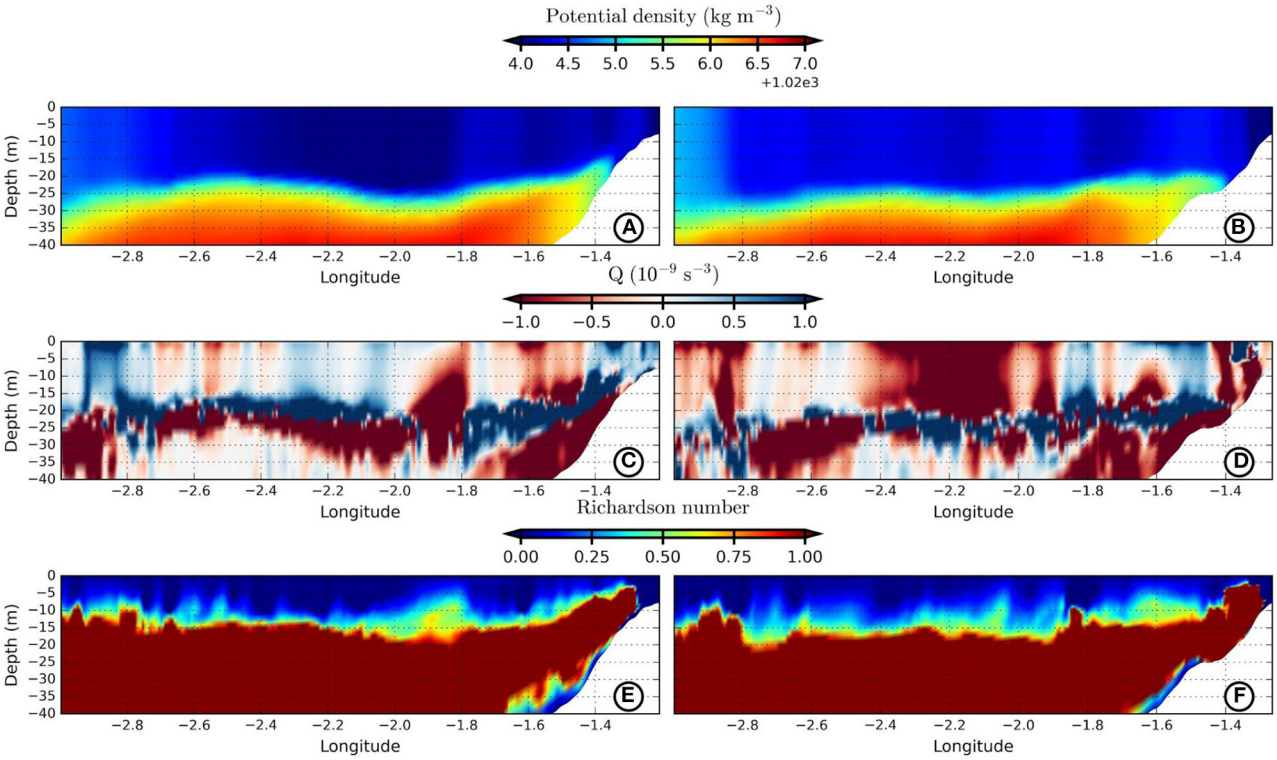


FIGURE 10 | Snapshot August (12/08/2008 at midday) of: the Potential density in section 1 **(A)** and in section 2 **(B)** (cf. **Figure 7**), the PV in section 1 **(C)** and in section 2 **(D)** and the Richardson number in section 1 **(E)** and in section 2 **(F)**.

and 1.8°W) from 10 to 40 m depth (**Figures 9C,E**). In the plume interior, symmetric instabilities are generated via local flow interaction with moderate winds and river discharges inducing vertical sheared horizontal currents. In the offshore part of the plume front, they are also observed and intensified near the surface due to strong buoyancy/salinity gradients and high wind sheared flows since the vertical ageostrophic shear prevails there (see previous section). Offshore of the Gironde river plume, symmetric instabilities may exist from 10 m down to 40 m depth due to interior horizontal sheared currents and weak/homogenized stratification. Near the bottom, vertical shear instabilities may prevail, since the Richardson number is smaller than 0.25, due to high baroclinic tidal currents and steep bathymetric gradients which induce high sheared currents. In this region the freshwater density is lower than 1,026 kg m^{-3} and the plume is bottom attached (isopycnals interact with the bottom) (**Figure 9A**).

In March, in the coastal current, symmetric instabilities also exist at different locations: (i) near the coast (longitude between 1.3 and 1.5°W) in almost the whole water column except in a small layer near the bottom, (ii) at the edge of the plume (longitude ∼ 1.6°W) between the surface and 25 m depth, and (iii) offshore of the plume (longitude between 1.7 and 2°W) between 15 and 40 m depth (**Figures 9D,F**). In the plume interior, symmetric instabilities are intensified near the surface (∼ 5 m depth) via the interaction of the plume with winds, tidal currents and/or the coast. The plume interaction with winds and baroclinic tidal currents enhances the sheared currents intensity and therefore the vertical components of the PV become dominant which induce negative PV. The interaction between the coast and the Gironde plume may also induce processes which may favor the development of such instabilities. At the edge of the plume, symmetric instabilities prevail on the upper 25 m due to frontogenetic processes inducing high salinity gradients, baroclinic tidal currents, and moderate winds favoring intense ageostrophic vertical shear. Meanwhile, offshore of the Gironde plume, these instabilities exist on the upper 10 m via the ageostrophic shear induced by moderate winds. Near the bottom in this region of the plume, since the freshwater interacts with the bottom with densities <1,026 kg m^{-3} as seen in **Figure 9B**, vertical shear instabilities may dominate. The latter instabilities develop due to steep bottom slopes and baroclinic tidal currents which favor strong sheared flows.

In August, symmetric instabilities also exist at different locations of the near field region bounded by different isopycnals. In regions where the density is smaller than 1024.5 kg m^{-3} (**Figure 10A**), they exist at different longitudes: (i) between 1.4 and 1.6°W, (ii) between 1.8 and 2°W, and (iii) far offshore between 2.4 and 2.7°W. These instabilities span the vertical extent of the isopycnal layer, between the surface and 25 m depth (**Figures 10C,E**). Symmetric and vertical shear instabilities coexist from the surface down to ∼10 m depth, since the Richardson number is smaller than 0.25 and the PV is negative, due to the wind activity inducing a high vertical shear. The river

discharge would have a weak influence on those instabilities since small values (∼) 200 m^3 s^{-1} are observed during August. In this isopycnic layer and slightly beneath, symmetric instabilities exist also due to shear interior induced by strong frontogenetic processes generated by tidal currents and/or internal waves. Near the bottom, symmetric and vertical shear instabilities coexist due to strong bathymetric gradients and baroclinic tidal currents.

In the coastal current and during the same period, symmetric instabilities prevail in regions with smaller densities, <1024.5 kg m^{-3} as shown in **Figure 10B**, and at various zonal locations: (i) near the coast (longitude ∼ 1.4°W), (ii) between 1.6 and 1.8°W, (iii) between 1.9 and 2.4°W, and (iv) far offshore with longitudes >2.8°W (**Figures 10D,F**). These instabilities overwhelm almost the entire isopycnic layer and are more intense due to stronger wind bursts compared to a winter situation (an order of magnitude stronger). At the top 10 m, they coexist with vertical shear instabilities, since the Richardson number is smaller than 0.25, due to strong ageostrophic shear which engenders negative PV values. Symmetric instabilities also exist between 10 and 25 m depth in regards of the interaction between the ambient stratification and tidal currents which induce frontogenetic processes and therefore intense horizontal buoyancy gradients. Beneath this isopycnic layer and near the bottom, symmetric and vertical shear instabilities coexist (R_i < 0.25), from 1.4 to 1.6°W longitude, due to steep bottom slopes and tidal currents inducing high ageostrophic shear.

Energy conversion terms are evaluated near the surface, at 5 m depth, during both months to identify the existence and intensity of baroclinic, barotropic, and vertical shear instabilities (**Figure 11**). Positive HRS, VBF, and VRS indicate the existence of barotropic, baroclinic, and vertical shear instabilities, respectively. The VBF and HRS dominate over the VRS term near the river mouth (not shown—VRS values below 10^{-9} m s^{-3}).

In winter, barotropic and baroclinic instabilities coexist at a larger scale over the continental shelf at the rim of eddies and in filaments (**Figure 11A**). Over the continental shelf, winds play a major role in increasing the energy of the mean flow which feeds the perturbations, and therefore the generation of mixed barotropic/baroclinic instabilities is observed. Over the inner-shelf (above 100 m isobath), these mixed instabilities are more intense due to the interaction of density currents induced by Gironde plume and its front, tidal currents and wind bursts. Those interactions sustain the mean flow (buoyancy and momentum) with a high reservoir of energy which feed the perturbations and generate such instabilities.

In summer, mixed barotropic/baroclinic instabilities exist in the near field and the coastal current of the plume, and over the continental shelf (**Figure 11B**). Compared to winter, those instabilities are intensified over the whole domain. In the Gironde plume and since the river discharge is weak, the source of such instabilities is the interaction of the ocean surface layer with tidal currents and wind activity. Those interactions alter the stratification and the momentum which induce perturbations essential to the generation of mixed barotropic/baroclinic instabilities. Over the continental shelf, the mean flow induced by eddies, wind bursts, and internal waves favor the development of these instabilities.

Since the wind and tides contribute to the generation of baroclinic and symmetric instabilities, the relation between these two instabilities in frontal regions of the plume will be explored in the following section.

4.3. Plume Instability

The development of instability can be monitored using the evolution of the energy from buoyancy and momentum perturbations. We then decompose the Eddy Kinetic Energy (EKE) and Eddy Available Potential Energy (EAPE) in three main contributions from: symmetric, baroclinic, and mixed instabilities (**Figure 12**).

In winter, the mixed modes are dominant in both decompositions of EKE and EAPE; they are one order of magnitude larger than the symmetric and baroclinic modes during the first 8 days (see **Figures 12A–C**).

Meanwhile, during the last 2 days of this analyzed period, the three modes feed equally and weakly the perturbations in the 3D eddying state. Through this decomposition, two events are noticed which occur during the second half of March (on the 16th and the 17th). During these periods, peaks in EAPE precede peaks in EKE with a lag of about half a day. The lag is similar for the symmetric and baroclinic modes.

Conversely in August, the symmetric, baroclinic, and mixed modes supply EKE and EAPE significantly with a predominance of the mixed perturbations (**Figures 12D–F**). During this period, three major events can be observed in the EKE decomposition. The first event occurs around August 12th. On this day, the mixed mode grows first with a significant amplitude followed by symmetric and then baroclinic modes. Then, a second event occurs almost 2 days later when the symmetric mode grows first followed by baroclinic and then mixed modes. On August 16th, symmetric and mixed modes contribute equally and nearly at the same time followed by baroclinic modes. Finally, after this active period the three unstable modes have developed nonlinearly and reach a 3D eddying state. In contrast, in the EAPE decomposition only the first event is noticeable. It occurs almost a day later. Similarly to the EKE decomposition, mixed modes increase first followed by symmetric and then baroclinic modes. The lag between EKE and EAPE suggests that a transfer of energy occurs within the same instability mode.

The development of these instabilities is related to the wind activity. A lagged cross-correlation between the EKEs and the wind stress intensity (∼0.7) reveals that the instabilities develop after wind events within a lag ∼18 h in summer and ∼3 days in winter (figure not shown). These lags are different due to a larger wind stress intensity in summer (an order of magnitude larger compared to winter).

Growth rates can be deduced from the evolution of EKE (see Equation 11). Estimated growth rates (**Figure 13**) range from 0.02 to 0.12 h^{-1} (i.e., time scales ranging from 8 to 50 h). In March, the second event grows faster and contributes more to the increase of the EKE (**Figure 13A**). Meanwhile in summer (**Figure 13B**), growth rates are higher for symmetric and baroclinic instabilities (between 0.04 and 0.08 h^{-1} for symmetric instabilities and between 0.04 and 0.1 h^{-1} for baroclinic instabilities). On the opposite, in winter, mixed and

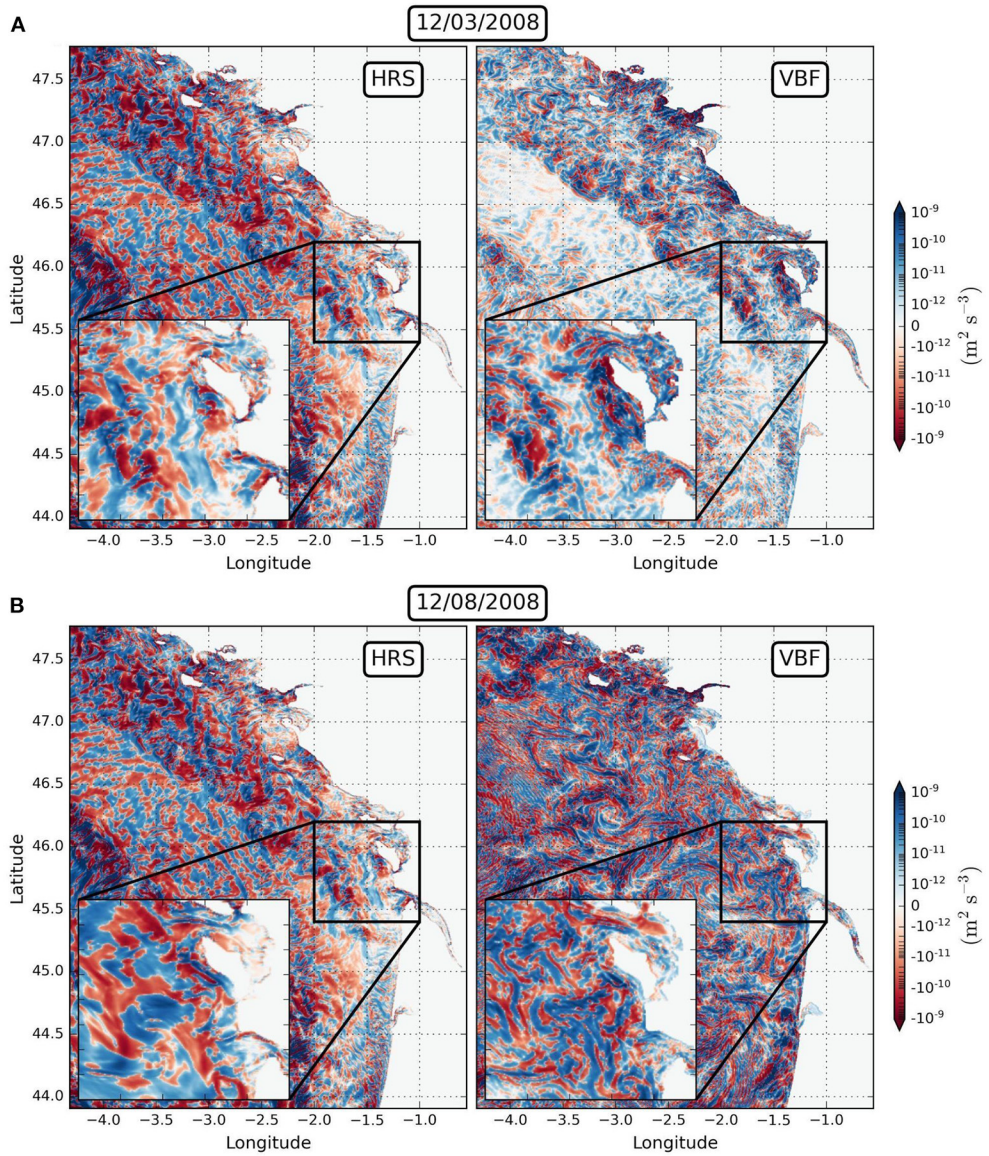


FIGURE 11 | HRS and VBF energy conversion terms at 5 m in March **(A)** and in August **(B)** 2008. The left corner panel indicates a zoom on the region delimited by the black solid box centered on the Gironde river plume.

symmetric instabilities have higher growth rates (between 0.04 and 0.1 h^{-1} for mixed instabilities and between 0.04 and 0.12 h^{-1} for symmetric instabilities).

4.4. Mixing at Ocean Boundaries

To explore the mixing in different ocean layers, the potential vorticity (PV) mixing in Gironde river is first evaluated in the surface and bottom boundary layers, where the isopycnals can outcrop. We averaged over 10 days (between the 10th and the 20th of each month) the surface wind-driven, buoyancy, thermal turbulent wind, and bottom PV fluxes. These fluxes have been evaluated between two outcropping isopycnals (at the surface and at the bottom): between 1,025 and 1025.5 kg m^{-3} in March and between 1,024 and 1024.5 kg m^{-3} in August. **Figure 14** shows the spatial distribution of these fluxes during the two periods.

In March, surface buoyancy fluxes always remove PV from the ocean surface (-Jdbuoy < 0) except at some locations: (i) at the Gironde river mouth (longitude ∼1.5°W and latitude ∼45.6°N) and (ii) at the northern edge of the coastal current (longitude ∼1.5°W and latitude ∼46.2°N) (**Figure 14A**). The wind-driven PV fluxes (-Jdwind) inject and remove potential vorticity from the surface depending on the location. They strongly remove PV at the northern edge of the coastal current and at the offshore edge of the plume. On the opposite, near the river mouth and in the inner edge of the plume front, wind-driven PV is injected. The thermal turbulent wind flux (-Jttw) always injects PV at

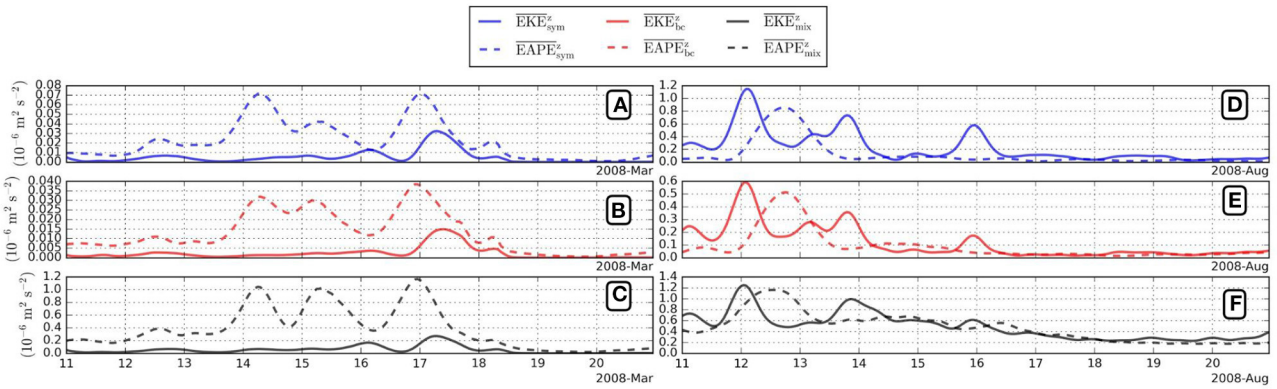


FIGURE 12 | Decomposition of the EKE and the EAPE onto individual modes of instability : symmetric mode (blue color) in March **(A)** and in August **(D)**, baroclinic mode (red color) in March **(B)** and in August **(E)** and mixed mode (black color) in March **(C)** and in August **(F)**. The solid lines characterize the EKE decomposition and dashed lines indicate the EAPE decomposition.

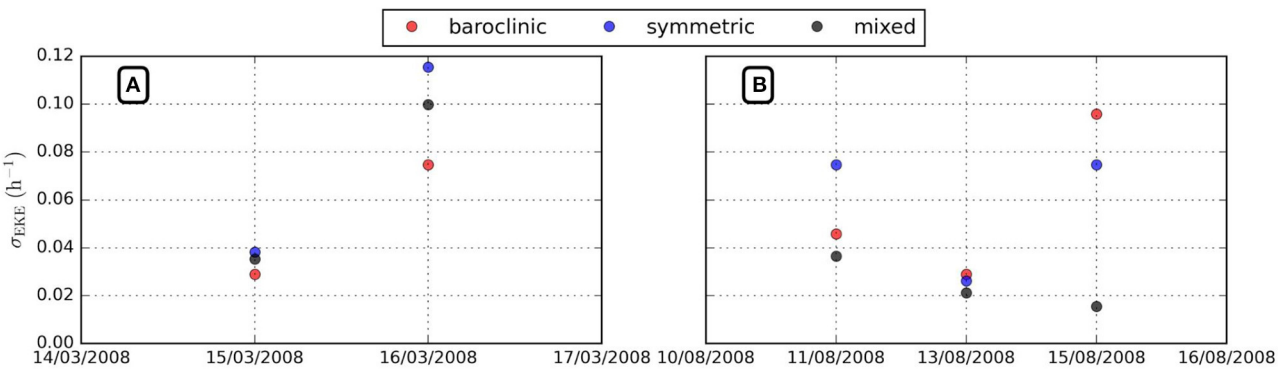


FIGURE 13 | The EKE growth rate of each instability (baroclinic in red, symmetric in blue, and mixed in black) computed between midday (previous day) and midnight in March **(A)** and in August **(B)** 2008.

the ocean surface, suggesting the importance of buoyant fronts induced by the Gironde river in the PV budget. These fluxes have comparable magnitudes ($\sim 10^{-12}$ m s^{-4}); this shows their importance in the freshwater mixing of the Gironde river plume. The bottom fluxes are not important during this period; their magnitudes are smaller ($\sim 10^{-14} < 10^{-12}$ m s^{-4}) than those of the surface fluxes (not shown).

In August, positive and negative surface buoyancy fluxes associated with PV are also observed (**Figure 14B**). They remove PV from the ocean surface (-Jdbuoy < 0): (i) near the river mouth, (ii) at the plume front, and (iii) over the continental shelf. In the latter region, the surface buoyancy PV fluxes show positive and negative patterns in the zonal direction. The wind-driven flux changes sign meridionally at the plume front and over the continental shelf. The thermal turbulent wind fluxes always inject PV in plume fronts when the river discharge is average, in the strong salinity gradients and in filaments over the continental shelf. These fluxes have the same magnitude; they are important sources of mixing at the ocean surface. The bottom PV flux is weak except in small positive strips north and south of the Gironde mouth and near the Loire river plume (not shown).

4.5. Frontal Vertical Mixing in the Water Column

Stratification budgets are analyzed in the plume frontal region (**Figure 15**) in a range of isopycnic layers previously defined (cf section 2.2.2). These budgets are evaluated between 5 and 10 m depth. The stratification budget is related to frontogenesis/frontolysis (intensification/weakening of salinity/density gradients), non-conservative PV fluxes (PV mixing) and advective PV fluxes (stirring processes). Non-conservative PV fluxes are the combination between frictional PV fluxes (related to momentum mixing) and diabatic PV fluxes (related to mass/buoyancy mixing). The bvp term was also considered to close the stratification budget (**Figures 15B,D**). This boundary term was not neglected since we considered that the finite computation domain is subject to tides and river discharge from the estuary. We compare the time variations of N^2 and the total term (sum of bvp and time variations of N^2). In the total term, the time variations of N^2 dominate except during episodic periods in winter (March 13th and 17th, **Figure 1B**) and summer (after August 19th, **Figure 1C**) where the bvp may have an important impact due to an increase of the river discharge.

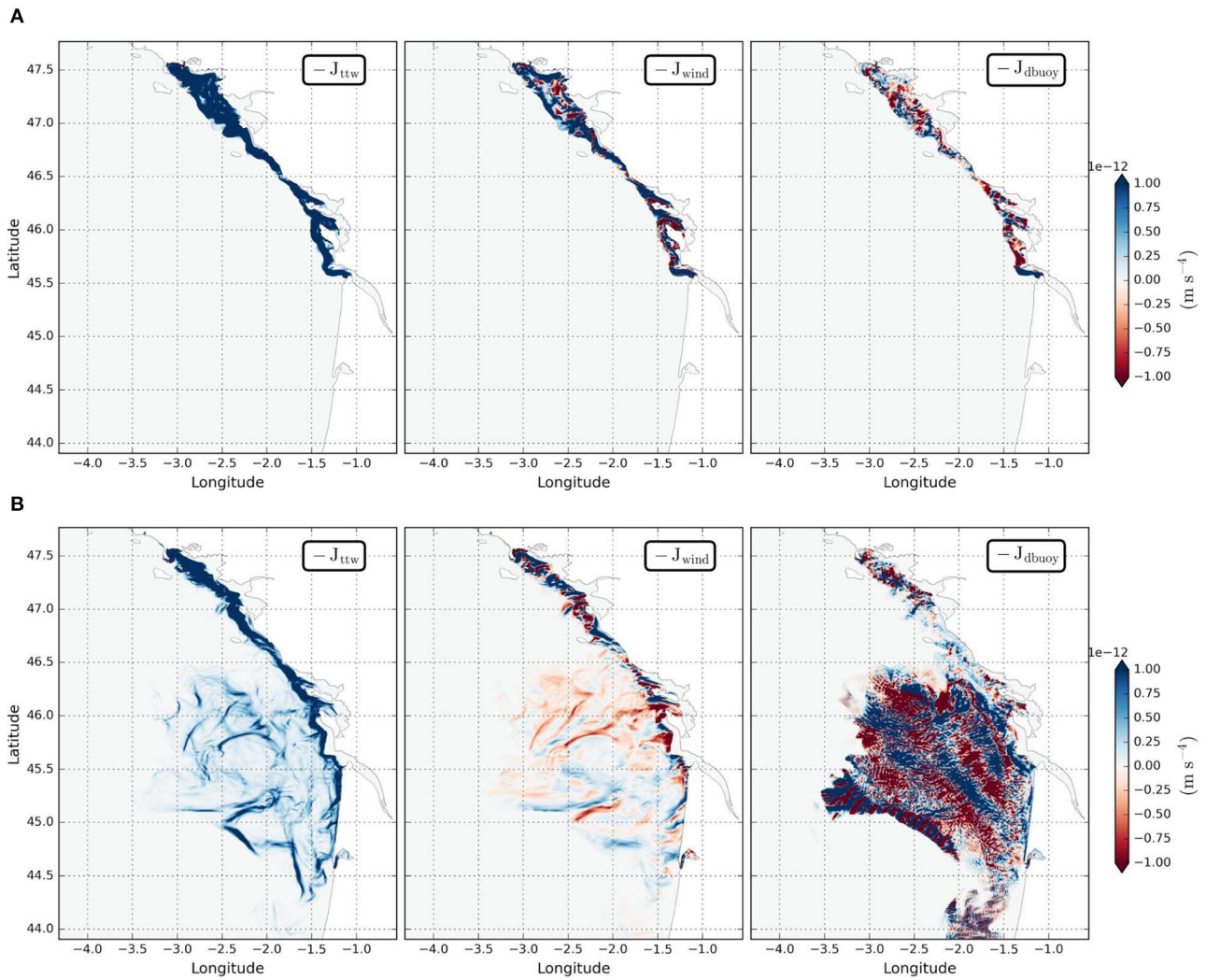


FIGURE 14 | The PV fluxes: thermal turbulent wind (-Jttw), the wind-driven (-Jwind), and the surface buoyancy (-Jdbuoy) in March **(A)** and in August **(B)**.

Hereafter, we will consider the total term to characterize the time rate of the stratification in the plume frontal region.

In winter, two events of restratification and one event of destratification are observed (**Figure 15B**). The first restratification event occurs between March 12th and 14th. This event is associated with an increase of the river discharge and a wind relaxation after a wind burst. Frontogenesis (positive FRONT values) and weak positive advective PV fluxes (positive ADV values) then control the intensification of the stratification. Non conservative PV fluxes as a combination of shear and diabatic mixing, are mutually compensated and do not contribute to the restratification process of the water column between March 12th and 14th (**Figure 15A**). Destratification occurs between March 14th and 16th during a higher river discharge (around 1,000 m^3 s^{-1}) period but it is mainly due to an increase of the wind stress. During this event, non conservative fluxes and frontolysis (negative FRONT values) contribute to the destratification of the water column. Following the latter event (between March the 16th and 18th), a restratification occurs again driven by frontogenesis and slightly positive non conservative fluxes; the latter fluxes are associated with the wind relaxation after the second wind burst and with a high river discharge. After the last restratification event, the stratification variations decrease (or nearly constant) leading to a homogenized water column. The homogenization of the water column happens after the generation of instabilities (**Figures 12A–C**) and during moderate wind events (**Figure 8A**). It is mostly related to upwelling-favorable winds (figure not shown) which favor the flattening of isopycnals (EAPE $\sim$ 0) and therefore the homogenization of the water column. Similar events are also observed in summer when the river discharge remains small (around 200 m^3 s^{-1}). A destratification event develops between August 10th and 12th (**Figure 15C**) associated with an increase of the wind stress. This process is governed

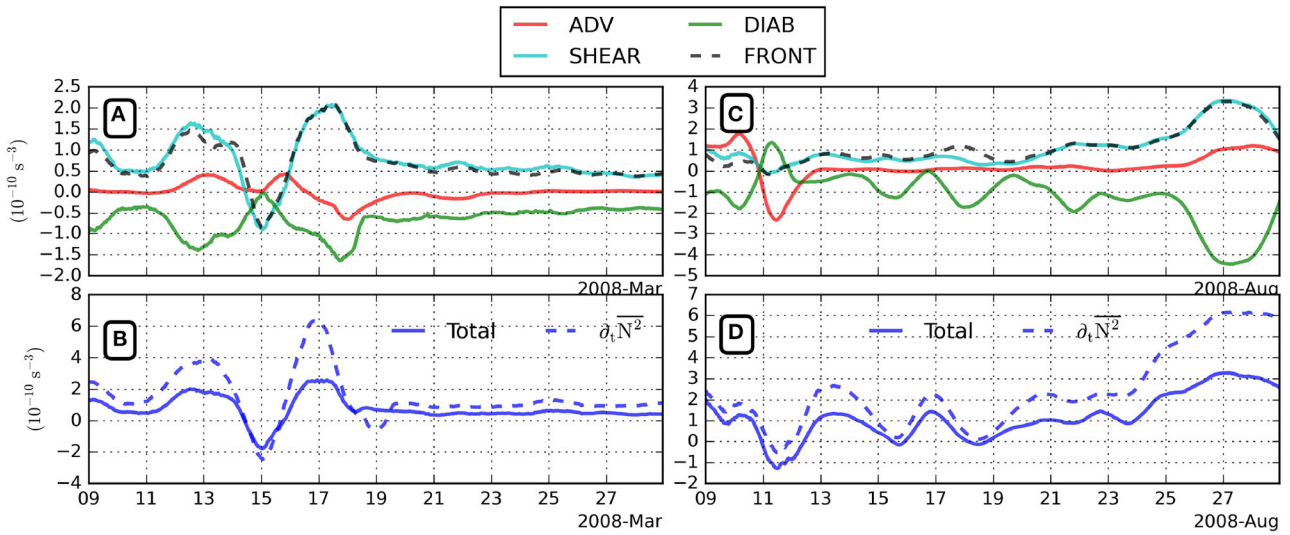


FIGURE 15 | The advective (Ja, solid red), shear (Jf, solid light blue), diabatic (Jd, solid green) PV fluxes and Frontogenesis term (FRONT, dashed black) in March **(A)** and in August **(C)** 2008. The stratification time rate (dashed blue) and the total term ($\partial_t\overline{N^2} + \frac{bvp|_{z_b}^{z_t}}{h}$, solid blue) in March **(B)** and in August **(D)**.

by negative advective PV fluxes and a weak frontolysis. The non conservative PV fluxes are weakly positive (**Figure 15D**). Following this destratification, two successive restratification events (13th and 17th August) occur. During these events, frontogenesis is the major contributor since non conservative fluxes (shear and diabatic mixing) are small and negative. This weak frontogenesis occurs during wind relaxation after wind gusts. It is also related to the weak summer river discharge ($\sim$200 $m^3\ s^{-1}$). Advective (stirring) processes are then close to zero. Finally, between August 24th and the 29th, a noticeable restratification event is observed with an increase of the PV from $10^{-10}\ s^{-3}$ to more than $3 \times 10^{-10}\ s^{-3}$. This increase is concomitant with a river discharge increase (from 160 to 230 $m^3\ s^{-1}$) and a weak wind stress. At that time, vertical advective PV fluxes and frontogenesis are the main sources of this restratification since non conservative fluxes are almost balanced or are weakly negative.

5. DISCUSSION

5.1. Gironde River Plume Fronts

Our high resolution numerical simulation reveals (sub)mesoscale features in the Gironde river plume and over the continental shelf. The shape of the plume appears more complex than previously simulated (Lazure and Jegou, 1998). River plumes fronts have been explored in our simulations using the sea surface salinity gradients which characterize buoyant plumes (Vic et al., 2014; Ayouche et al., 2020). Salinity and chlorophyll fronts show similar locations in the Gironde and in the Loire river plumes. The extension of these plumes has been explored using satellite SST data (2002–2014) in previous studies (Costoya et al., 2016). The former authors showed that the locations of the Gironde and Loire river plumes fronts remain close to the coast which is similar to our findings in this study. These fronts can be pushed shoreward by wind and tides, then suppressing the ballooning of the outflow (Nof and Pichevin, 2001; Isobe, 2005; Ayouche et al., 2020). In the northward coastal current of the Gironde river plume, winds may constrain the plume near the coast both in summer and in winter. Ayouche et al. (2020) showed that in idealized simulations referring to the Gironde river plume, downwelling favorable winds pushed the plume toward the coast and this might be the case in our simulations during episodic wind regimes. The river plume can also be detected from sea surface temperature in winter (Costoya et al., 2016; Yelekçi et al., 2017) when the strong river discharge strengthens the stratification; the mixed layer is then more sensitive to air-sea fluxes. Fronts in winter remain confined over the inner shelf. Their extent is limited offshore at the 100 m isobath, as shown by remote sensing observations (Yelekçi et al., 2017). Plume fronts are less prominent in summer due the weaker river discharges.

5.2. River Plume Dynamics

Inside the river plume, the circulation is mainly in geostrophic balance as observed (Mazzini et al., 2019; Alory et al., 2021) and modeled in other buoyant plumes (Nof and Pichevin, 2001; Ou et al., 2009; Schiller et al., 2011). Locally, the circulation in the river plume is ageostrophic [$R_o \sim O(1)$]. This ageostrophic circulation corresponds to the strongly sheared flows near the plume front (with strong curvature). Isobe (2005) shows that in the bulge, the inertial oscillations are locally constrained by the tidal dynamics. In our simulations, such a mechanism may be at work in the near-field. The friction with the coast and its geometry induce strong negative vorticity ($\frac{\zeta_z}{f} < -1$) in the coastal current due to strong sheared flows. This ageostrophic circulation has been highlighted in idealized simulations (Ayouche et al., 2020; Lv et al., 2020) and is reproduced in the present

realistic simulations. These high Rossby number flows appear during high discharge conditions or during strong wind events. Over the continental shelf and outside the river plume, the ageostrophic circulation remains weak in winter. In summer, at the rim of eddies and in filaments, strong ageostrophic circulation is observed related to a local secondary circulation (McWilliams, 2017).

The local ageostrophic circulation and its contrast with geostrophic processes have been explored in the frontal region of the Gironde river plume. This contrast has been analyzed in terms of vertical shears and linked to the wind stress intensity. We find that wind gusts (high to moderate winds) generate ageostrophic shear in the plume after a period of time (of the order of a day) during both seasons. In contrast, when the wind stress intensity is weak the geostrophic shear predominates. We emphasize the key role of the average river discharge during weak wind events to enhance density currents and therefore their induced vertical geostrophic shear. The wind-driven and geostrophic shear processes are important in the cross-shelf circulation of a coastally trapped plume (Moffat and Lentz, 2012). The river discharge induces alongshore geostrophic currents which carry out the downcoast freshwater transport in the northern Hemisphere (Horner-Devine et al., 2015). The interaction between surface intensified river plumes and downwelling favorable winds induces geostrophic sheared flows (weak to moderate winds) in regions of strong horizontal density gradients (Spall and Thomas, 2016). In their study, high wind conditions induced circulation that prevails over the density current (Spall and Thomas, 2016). In our study, intense winds induce ageostrophic sheared currents that dominate over the density current which is similar to their key findings.

The Gironde river plume transports nutrients, sediments, and pollutants to the open ocean. Once it interacts with the open ocean, a flow barrier is formed: the plume front. This plume front is characterized by intense chlorophyll concentration and salinity/density gradients. Our study reveals also the existence of frontal ageostrophic dynamics related to winds. Such frontal dynamics and hydrology favor the concentration of phytoplankton which feeds marine organisms such as zooplankton and fish (Acha et al., 2004; Morgan et al., 2005). The concentration of nutrients and light fluctuations is sensitive to the nature of the front (convergent or divergent) and therefore influence the size of phytoplankton (Marañón et al., 2012; Marañón et al., 2015). The interactions between the frontal plume dynamics and marine biology using high resolution numerical modeling is a topic of interest for future studies to understand the biophysical dynamics in the Bay of Biscay.

5.3. Development of Instabilities in the River Plume

Energy conversion terms reveal that mixed baroclinic/barotropic instabilities, characterized by positive VBF and HRS, coexist in the near-field and the far-field of the Gironde plume. Such instabilities have a large signature over the inner-shelf (shallower than 100 m) in winter and summer.

In our realistic simulations, we have shown that the generation of such instabilities is due to the interaction between external forcings (tides and winds) and density currents in winter and mostly due to the interaction between external forcings and the surface ocean layer in summer since the river discharge is weak during this period. The combination between the Gironde discharge, tides and winds favors the development of such instabilities in the near and far fields of the plume. Our results confirm what has been shown in previous idealized simulations (Jia and Yankovsky, 2012; Ayouche et al., 2020).

Symmetric instabilities have also been investigated using the Hoskins and Richardson number criteria. These instabilities develop in different regions of the plume,the bulge and the coastal current, when the PV is negative and the Richardson number is smaller than 1. They are generated through the impact of winds on the bulge and coastal current. Symmetric instabilities in our realistic simulations remain close to the coast in winter and extend from the coast to the continental shelf in summer. These instabilities may overwhelm the water column in the bottom-attached plume interior in March and August. In August, symmetric instabilities remain near the surface locally over the continental shelf. Such instabilities have been studied previously in idealized simulations (Ayouche et al., 2020; Lv et al., 2020). In plumes frontal regions interacting with downwelling favorable winds, symmetric instabilities are triggered and restratify the plume interior (Lv et al., 2020). In idealized simulations referring to a Gironde river plume, downwelling winds trigger frontal symmetric instabilities in the coastal current of the plume and semidiurnal tides (M2) favor the generation of these instabilities in the bulge (Ayouche et al., 2020).

Vertical shear instabilities are also simulated ($R_i < 0.25$) near the bottom of the Gironde plume near (bulge) and far (coastal current) fields due to their interaction with steep bottom slopes and strong tidal currents. Their existence in the near field of the plume have been attributed to strong tidal horizontal currents near the bottom (MacDonald and Geyer, 2004; Kilcher and Nash, 2010).

The previous results highlight the possible coexistence of baroclinic and symmetric instabilities in the Gironde plume regions when R_i is smaller than one. Symmetric instabilities can be replaced by baroclinic instabilities when the Richardson number R_i is O(1). To investigate the relation between these instabilities, an EKE modal decomposition has been achieved in frontal regions where large Rossby numbers are observed locally. These instabilities have short growth time ranging from a few hours to a few days. In winter, they occur after moderate wind bursts, during relaxation events, with a transition from symmetric to baroclinic instability. Indeed, symmetric instabilities grow first followed by mixed instabilities and then baroclinic instabilities after different wind events. During this period, the turbulent activity is transferred from the EAPE to the EKE for each instability (baroclinic, symmetric, and mixed). This transition corroborates the classical Lorentz cycle (Lorenz, 1955). The origin of such instabilities is due to the interaction between density currents and the wind activity in the Gironde plume.

In summer, these instabilities also occur after wind events. The growth time is slightly weaker than in winter, due to low

river discharge, but it keeps the same order of magnitude. These growths have been associated with three wind events. During the first event (moderate winds), symmetric instabilities grow first followed by baroclinic and then mixed instabilities. During the other two events, the wind is weak and therefore baroclinic instabilities grow first followed by symmetric and mixed instabilities. During this month, a transfer occurs from the EKE to the EAPE for each instability and this might be due to the presence of internal waves and their interactions with the Gironde plume. In our simulations, these decompositions reveal that frontal baroclinic instability exists through a transition from symmetric instabilities. The EKE decomposition indicates that mixed instabilities (symmetric and baroclinic instabilities) also exist but with a slower growth.

Baroclinic instabilities may exist during wind relaxation events or through a symmetric instability transition (Hetland, 2017; Lv et al., 2020). Following Stone (1970) classification, the presence of Richardson numbers between 0.84 and 1 locally in the plume during both simulated periods may explain the development of mixed baroclinic/symmetric instabilities. Another classification allows exploring the growth of non-geostrophic baroclinic instabilities based on the slope Burger number (Qu and Hetland, 2020). In further studies, the exploration of the slope Burger number in realistic simulations would help to detail the instability growth rate sensitivity.

5.4. Mixing in Ocean Boundary Layers

In our study, we retain non-linearities in the computation of PV fluxes since ageostrophic circulation is important at the river plume front compared with previous studies which neglected these non-linearities (Wenegrat et al., 2018). The three main sources of PV mixing at the surface of the ocean are buoyancy, thermal turbulent wind and wind-driven fluxes. These fluxes are similar in intensity during both months; this emphasizes their importance in the frontal region PV budget of the Gironde river plume. The main source of PV mixing at the surface of the ocean are buoyancy/salinity fronts since thermal wind fluxes always inject the PV during both periods. They are localized in the frontal region at the edge of the plume for both periods and at the rim of eddies and in filaments over the continental shelf in summer. Thermal turbulent wind PV fluxes are related to density currents that are enhanced during average to high river discharge periods, typically in winter. The latter results are limited to the bounding isopycnals defining the frontal region. Thermal turbulent wind PV fluxes are also enhanced during wind relaxation periods when the geostrophic shear increases, and when the ageostrophic circulation weakens (during both periods). This result has also been observed in the far field of the Chesapeake Bay plume during weak wind periods (Mazzini et al., 2019).

The wind-driven and surface buoyancy fluxes inject and extract PV from the frontal region of the river plume. In winter, these fluxes remain close to the coast. Surface buoyancy fluxes are injecting PV closer to the river mouth due to some local warming from the Gironde estuary and at the northern edge of the coastal current due to air-sea fluxes. Such injections of surface buoyancy fluxes are also observed in summer due to warmer temperature from the atmosphere and from the Gironde estuary. Extreme events can play a role in those surface buoyancy fluxes as observed during hurricanes. For example, Hurricane Irma in 2017 impacted the stability in the Amazon-Orinoco river plume by reducing the SST cooling and energizing the air-sea fluxes (Rudzin et al., 2020). Surface buoyancy fluxes are also observed over the continental shelf as patterns of positive and negative fluxes that result from the air-sea interactions and internal tides oscillations. Internal waves, due to strong semi-diurnal tidal currents (Pichon and Corréard, 2006), have been observed over the continental shelf of the Bay of Biscay in late summer and they are reproduced in our simulations.

Wind-driven fluxes are sensitive to the wind direction and intensity. They are highly variable in space and time in the frontal region of the plume. In winter, these fluxes inject PV at the inner edge of the plume front and remove potential vorticity north of the coastal current and at the offshore edge of the plume front. While in summer, injection and removal of PV vary along the front (meridional direction). Over the continental shelf, positive and negative fluxes are mainly compensated. The PV removal and injection vary depending on whether the wind is along-front or cross-front and on the induced frontal symmetric instabilities. The injection of PV by winds can be also observed during periods when the wind is weak and the geostrophic shear increases. The wind-driven removal/destruction of PV by winds has been observed in ocean fronts when the wind is downfront which induces an upward flux at the sea surface (Thomas, 2005). The latter have also been observed for weak to moderate downfront winds interacting with buoyant coastal plumes (Spall and Thomas, 2016).

Since the frontal region of the plume is interacting with the bottom most of the time in our simulation, bottom PV fluxes have been analyzed. They remain relatively weak and are not expected to contribute effectively to the PV mixing of the plume frontal region.

5.5. River Plume Interior Mixing

In the ocean interior, the mixing has been characterized by frontogenesis and PV mixing processes in the Gironde river plume frontal region. In winter, during river discharge intensification periods and/or wind relaxation events, the frontogenesis prevails and the plume interior restratification is intensified. In contrast, destratification is characterized by non conservative fluxes (diabatic and shear mixing) and frontolysis through wind intensification periods. These budgets have been evaluated in idealized simulations characterizing the Gironde river plume in a winter regime (Ayouche et al., 2020). In their study, they show that downwelling favorable winds with average discharge favor the destratification in the coastal current (far field) of the plume. The former authors also show that semi-diurnal tides generate intense fronts (frontogenesis) near the river mouth (near-field region) that restratify the plume. Conversely, in a stratified regime (summer season), weak restratification events are observed during wind relaxation due to the small river discharge. The destratification in summer is also linked to a high wind event inducing frontolysis and the growth of ageostrophic shear. Similar results have been

observed in idealized simulations in stratified buoyant coastal plumes where the wind stress is linked to the reduction of PV and therefore to destratification (Spall and Thomas, 2016; Lv et al., 2020). In their study, the restratification processes are observed during wind relaxation periods when the geostrophic shear becomes dominant.

6. CONCLUSION

The Gironde river plume appears as a complex system under the influence of varying forcings: the river discharge, wind stress fluctuations, tide related processes. The interaction of all these nonlinear processes strongly shapes the development of instabilities and the mixing efficiency in the river plume.

Based on high resolution numerical simulations, we highlighted the buoyant frontal activity at meso- and sub-mesoscale with a contrasted seasonal activity. This buoyant frontal dynamics is linked with geostrophic (driven by river discharge) and ageostrophic (associated with wind stress) motions. The geostrophic balanced circulation exists in the river plume interior (in the near field and the coastal current) whereas the ageostrophic circulation occurs locally in the frontal regions. Exploring two seasons (winter and summer), numerical simulations indicate that ageostrophic features are more intense over the inner shelf (shallower than 100 m) in winter and extend to the whole continental shelf in summer. Our understanding of geostrophic and ageostrophic dynamics is giving insights for future observations of coastal ocean submesoscale through satellite altimetry (e.g., SWOT mission).

These nonlinear processes favor the development and coexistence of instabilities (baroclinic, frontal symmetric, and barotropic) in different regions of the river plume. We simulated these instabilities. We observed baroclinic and symmetric instabilities in frontal regions. Such instabilities are growing in a mixed mode (co-existing) or through a transition sequence between symmetric and baroclinic instabilities linked with wind events. These instabilities can also develop in the near field or the coastal current (with a signature in energy and PV fluxes). Other instabilities such as barotropic instability are also find to coexist with baroclinic and symmetric instabilities, in the near field and the coastal current due to the interaction between Gironde river plume and moderate to high wind gusts, tidal currents and river discharge growth.

The potential source of the mixing in river plumes is sustained through different processes (ocean fronts, air/sea interactions, and wind dynamics). Based on our simulations, the mixing appears mainly linked to the frontal dynamics at the edge of the river plume. The analysis of PV fluxes in the ocean interior and at the surface at small temporal (hourly fields) and spatial (400 m resolution) scales allows quantifying the mixing. PV fluxes are driven by density currents (frontogenesis), heat fluxes, internal waves and wind forcings (non conservative, i.e., shear and diabatic, mixing processes). The estimate of the PV budget relies on approximations and hypotheses (see section 2.2.2). Besides, mixing processes in the simulations are highly sensitive to model parameterizations. Therefore, future efforts should be oriented toward *in situ* measurements that would help us to assess or tune some model parameterizations and to test some of our hypotheses. In the near future, *in situ* experiments will be proposed to measure the turbulent mixing (i.e., turbulence microstructure measurements) to improve model parametrization for the river plume in tidally-driven coastal environments.

DATA AVAILABILITY STATEMENT

The raw data supporting the conclusions of this article will be made available by the authors, without undue reservation.

AUTHOR CONTRIBUTIONS

AA, GC, and XC designed the study. AA, GC, XC, and NA contributed to the writing. AA performed most of the analyses. ST develops the previous CROCO configuration used for this analysis. All authors contributed to the article and approved the submitted version.

FUNDING

This work has been driven with the support of Brittany region. This study is part of the COCTO project (SWOT science team program) funded by the CNES. The Ph.D. thesis of A. Ayouche was funded by Brittany region and Ifremer. Model simulations were carried out with GENCI (French National High-Performance Computing Organization) computational resources administered at the CINES (National Computing Center for Higher Education).

ACKNOWLEDGMENTS

The authors thank Sabine Schmidt for providing the MAGEST *in situ* observations. MAGEST Verdon station was part of the DIAGIR project.

REFERENCES

Acha, E. M., Mianzan, H. W., Guerrero, R. A., Favero, M., and Bava, J. (2004). Marine fronts at the continental shelves of austral South America - Physical and ecological processes. *J. Mar. Syst.* 44, 83–105. doi: 10.1016/j.jmarsys.2003.09.005

Akpınar, A., Charria, G., Theetten, S., and Vandermeirsch, F. (2020). Cross-shelf exchanges in the northern Bay of Biscay. *J. Mar. Syst.* 205:103314. doi: 10.1016/j.jmarsys.2020.103314

Alory, G., Da-Allada, C. Y., Djakouré, S., Dadou, I., Jouanno, J., and Loemba, D. P. (2021). Coastal upwelling limitation by onshore geostrophic flow in the gulf of guinea around the Niger river plume. *Front. Mar. Sci.* 7:1116. doi: 10.3389/fmars.2020.607216

Ayouche, A., Carton, X., Charria, G., Theettens, S., and Ayoub, N. (2020). Instabilities and vertical mixing in river plumes: application

to the Bay of Biscay. *Geophys. Astrophys. Fluid Dyn.* 114, 650–689. doi: 10.1080/03091929.2020.1814275

Chapman, D. C. (1985). Numerical treatment of cross-shelf open boundaries in a barotropic coastal ocean model. *J. Phys. Oceanogr.* 15, 1060–1075. doi: 10.1175/1520-0485(1985)015<1060:NTOCSO>2.0.CO;2

Charria, G., Theetten, S., Vandermeirsch, F., Yelekçi, O., and Audiffren, N. (2017). Interannual evolution of (sub)mesoscale dynamics in the Bay of Biscay. *Ocean Sci.* 13, 777–797. doi: 10.5194/os-13-777-2017

Cole, K. L., and Hetland, R. D. (2016). The effects of rotation and river discharge on net mixing in small-mouth kelvin number plumes. *J. Phys. Oceanogr.* 46, 1421–1436. doi: 10.1175/JPO-D-13-0271.1

Contreras, M., Pizarro, O., Dewitte, B., Sepulveda, H. H., and Renault, L. (2019). Subsurface mesoscale eddy generation in the ocean off central Chile. *J. Geophys. Res.* 124, 5700–5722. doi: 10.1029/2018JC014723

Costoya, X., Fernández-Nóvoa, D., deCastro, M., and Gómez-Gesteira, M. (2017). Loire and Gironde turbid plumes: Characterization and influence on thermohaline properties. *J. Sea Res.* 130, 7–16. doi: 10.1016/j.seares.2017.04.003

Costoya, X., Fernández-Nóvoa, D., deCastro, M., Santos, F., Lazure, P., and Gómez-Gesteira, M. (2016). Modulation of sea surface temperature warming in the Bay of Biscay by Loire and Gironde rivers. *J. Geophys. Res.* 121, 966–979. doi: 10.1002/2015JC011157

Debreu, L., Marchesiello, P., Penven, P., and Cambon, G. (2012). Two-way nesting in split-explicit ocean models: algorithms, implementation and validation. *Ocean Model.* 49–50, 1–21. doi: 10.1016/j.ocemod.2012.03.003

Dee, D. P., Uppala, S. M., Simmons, A. J., Berrisford, P., Poli, P., Kobayashi, S., et al. (2011). The era-interim reanalysis: configuration and performance of the data assimilation system. *Q. J. R. Meteorol. Soc.* 137, 553–597. doi: 10.1002/qj.828

Frouin, R., Fiúza, A. F. G., Ambar, I., and Boyd, T. J. (1990). Observations of a Poleward surface current off the coasts of Portugal and Spain during winter. *J. Geophys. Res.* 95, 679–691. doi: 10.1029/JC095iC01p00679

Garcia-Soto, C., Pingree, R. D., and Valdés, L. (2002). Navidad development in the southern Bay of Biscay: Climate change and Swoddy structure from remote sensing and *in situ* measurements. *J. Geophys. Res.* 107, 28-1–28-29. doi: 10.1029/2001JC001012

Godin, G. (1972). *The Analysis of Tides*. Toronto, ON; Buffalo, NY: University of Toronto Press.

Graham, J. A., Rosser, J. P., O'Dea, E., and Hewitt, H. T. (2018). Resolving shelf break exchange around the European northwest shelf. *Geophys. Res. Lett.* 45, 12,386–12,395. doi: 10.1029/2018GL079399

Gula, J., Molemaker, M., and Mcwilliams, J. (2016). Topographic generation of submesoscale centrifugal instability and energy dissipation. *Nat. Commun.* 7:12811. doi: 10.1038/ncomms12811

Hetland, R. (2005). Relating river plume structure to vertical mixing. *J. Phys. Oceanogr.* 35, 1667–1688. doi: 10.1175/JPO2774.1

Hetland, R. D. (2010). The effects of mixing and spreading on density in near-field river plumes. *Dyn. Atmos. Oceans* 49, 37–53. doi: 10.1016/j.dynatmoce.2008.11.003

Hetland, R. D. (2017). Suppression of baroclinic instabilities in buoyancy-driven flow over sloping bathymetry. *J. Phys. Oceanogr.* 47, 49–68. doi: 10.1175/JPO-D-15-0240.1

Horner-Devine, A. (2009). The bulge circulation in the Columbia river plume. *Contin. Shelf Res.* 29, 234–251. doi: 10.1016/j.csr.2007.12.012

Horner-Devine, A. R., Hetland, R. D., and MacDonald, D. G. (2015). Mixing and transport in coastal river plumes. *Annu. Rev. Fluid Mech.* 47, 569–594. doi: 10.1146/annurev-fluid-010313-141408

Hoskins, B. J. (1974). The role of potential vorticity in symmetric stability and instability. *Q. J. R. Meteorol. Soc.* 100, 480–482. doi: 10.1002/qj.49710042520

Huret, M., Bourriau, P., Doray, M., Gohin, F., and Petitgas, P. (2018). Survey timing vs. ecosystem scheduling: degree-days to underpin observed interannual variability in marine ecosystems. *Prog. Oceanogr.* 166, 30–40. doi: 10.1016/j.pocean.2017.07.007

Isobe, A. (2005). Ballooning of river-plume bulge and its stabilization by tidal currents. *J. Phys. Oceanogr.* 35, 2337–2351. doi: 10.1175/JPO2837.1

Jia, Y., and Yankovsky, A. (2012). The impact of ambient stratification on freshwater transport in a river plume. *J. Mar. Res.* 70, 69–92. doi: 10.1357/002224012800502408

Kang, D. (2015). Energetics of eddy-mean flow interactions in the Gulf Stream region. *J. Phys. Oceanogr.* 45, 1103–1120. doi: 10.1175/JPO-D-14-0200.1

Karagiorgos, J., Vervatis, V., and Sofianos, S. (2020). The impact of tides on the Bay of Biscay dynamics. *J. Mar. Sci. Eng.* 8:617. doi: 10.3390/jmse8080617

Kastner, S. E., Horner-Devine, A. R., and Thomson, J. (2018). The influence of wind and waves on spreading and mixing in the Fraser river plume. *J. Geophys. Res.* 123, 6818–6840. doi: 10.1029/2018JC013765

Kilcher, L. F., and Nash, J. D. (2010). Structure and dynamics of the Columbia river tidal plume front. *J. Geophys. Res.* 115:C05S90. doi: 10.1029/2009JC006066

Kourafalou, V. H., Lee, T. N., Oey, L.-Y., and Wang, J. D. (1996a). The fate of river discharge on the continental shelf: 2. transport of coastal low-salinity waters under realistic wind and tidal forcing. *J. Geophys. Res.* 101, 3435–3455. doi: 10.1029/95JC03025

Kourafalou, V. H., Oey, L.-Y., Wang, J. D., and Lee, T. N. (1996b). The fate of river discharge on the continental shelf: 1. modeling the river plume and the inner shelf coastal current. *J. Geophys. Res.* 101, 3415–3434. doi: 10.1029/95JC03024

Koutsikopoulos, C., Beillois, P., Leroy, C., and Taillefer, F. (1998). Temporal trends and spatial structures of the sea surface temperature in the Bay of Biscay. *Oceanol. Acta* 21, 335–344. doi: 10.1016/S0399-1784(98)80020-0

Lapeyre, G., Klein, P., and Hua, B. L. (2006). Oceanic restratification forced by surface frontogenesis. *J. Phys. Oceanogr.* 36, 1577–1590. doi: 10.1175/JPO2923.1

Large, W. G., McWilliams, J. C., and Doney, S. C. (1994). Oceanic vertical mixing: A review and a model with a nonlocal boundary layer parameterization. *Rev. Geophys.* 32, 363–403. doi: 10.1029/94RG01872

Lazure, P., Garnier, V., Dumas, F., Herry, C., and Chifflet, M. (2009). Development of a hydrodynamic model of the Bay of Biscay. Validation of hydrology. *Contin. Shelf Res.* 29, 985–997. doi: 10.1016/j.csr.2008.12.017

Lazure, P., and Jegou, A.-M. (1998). 3d modelling of seasonal evolution of Loire and Gironde plumes on Biscay bay continental shelf. *Oceanol. Acta* 21, 165–177. doi: 10.1016/S0399-1784(98)80006-6

Le Boyer, A., Charria, G., Cann, B., Lazure, P., and Marié, L. (2013). Circulation on the shelf and the upper slope of the Bay of Biscay. *Contin. Shelf Res.* 55, 97–107. doi: 10.1016/j.csr.2013.01.006

Le Cann, B. and Serpette, A. (2009). Intense warm and saline upper ocean inflow in the Southern Bay of Biscay in Autumn-winter 2006–2007. *Contin. Shelf Res.* 29, 1014–1025. doi: 10.1016/j.csr.2008.11.015

Liu, W.-C., Chen, W.-B., Cheng, R. T., and Hsu, M.-H. (2008). Modelling the impact of wind stress and river discharge on Danshuei river plume. *Appl. Math. Model.* 32, 1255–1280. doi: 10.1016/j.apm.2007.03.009

Lorenz, E. N. (1955). Available potential energy and the maintenance of the general circulation. *Tellus* 7, 157–167. doi: 10.3402/tellusa.v7i2.8796

Lv, R., Cheng, P., and Gan, J. (2020). Adjustment of river plume fronts during downwelling-favorable wind events. *Contin. Shelf Res.* 202:104143. doi: 10.1016/j.csr.2020.104143

Lyard, F. H., Allain, D. J., Cancet, M., Carrére, L., and Picot, N. (2020). FES2014 global ocean tides atlas: design and performances. *Ocean Sci. Discuss.* 2020, 1–40. doi: 10.5194/os-2020-96

MacDonald, D. G., and Geyer, W. R. (2004). Turbulent energy production and entrainment at a highly stratified estuarine front. *J. Geophys. Res.* 109:C05004. doi: 10.1029/2003JC002094

Mara nón, E., Cerme no, P., Latasa, M., and Tadonléké, R. D. (2012). Temperature, resources, and phytoplankton size structure in the ocean. *Limnol. Oceanogr.* 57, 1266–1278. doi: 10.4319/lo.2012.57.5.1266

Marañón, E., Cermeño, P., Latasa, M., and Tadonléké, R. D. (2015). Resource supply alone explains the variability of marine phytoplankton size structure. *Limnol. Oceanogr.* 60, 1848–1854. doi: 10.1002/lno.10138

Marchesiello, P., McWilliams, J. C., and Shchepetkin, A. (2001). Open boundary conditions for long-term integration of regional oceanic models. *Ocean Model.* 3, 1–20. doi: 10.1016/S1463-5003(00)00013-5

Marshall, J., Jamous, D., and Nilsson, J. (2001). Entry, flux, and exit of potential vorticity in ocean circulation. *J. Phys. Oceanogr.* 31, 777–789. doi: 10.1175/1520-0485(2001)031<0777:EFAEOP>2.0.CO;2

Marshall, J. C., and Nurser, A. J. G. (1992). Fluid dynamics of oceanic thermocline ventilation. *J. Phys. Oceanogr.* 22, 583–595. doi: 10.1175/1520-0485(1992)022<0583:FDOOTV>2.0.CO;2

Mazzini, P. L. F., Chant, R. J., Scully, M. E., Wilkin, J., Hunter, E. J., and Nidzieko, N. J. (2019). The impact of wind forcing on the thermal wind shear of a river plume. *J. Geophys. Res.* 124, 7908–7925. doi: 10.1029/2019JC015259

McWilliams, J. C. (2017). Submesoscale surface fronts and filaments: secondary circulation, buoyancy flux, and frontogenesis. *J. Fluid Mech*. 823, 391–432. doi: 10.1017/jfm.2017.294

Moffat, C., and Lentz, S. (2012). On the response of a buoyant plume to downwelling-favorable wind stress. *J. Phys. Oceanogr*. 42, 1083–1098. doi: 10.1175/JPO-D-11-015.1

Morgan, C., De Robertis, A., and Zabel, R. (2005). Columbia River plume fronts. I. Hydrography, zooplankton distribution, and community composition. *Mar. Ecol. Prog. Ser*. 299, 19–31. doi: 10.3354/meps299019

Nof, D., and Pichevin, T. (2001). The ballooning of outflows. *J. Phys. Oceanogr*. 31, 3045–3058. doi: 10.1175/1520-0485(2001)031<3045:TBOO>2.0.CO;2

Orlanski, I. (1976). A simple boundary condition for unbounded hyperbolic flows. *J. Comput. Phys*. 21, 251–269. doi: 10.1016/0021-9991(76)90023-1

Ou, S., Zhang, H., and Wang, D.-x. (2009). Dynamics of the buoyant plume off the Pearl river estuary in summer. *Environ. Fluid Mech*. 9, 471–492. doi: 10.1007/s10652-009-9146-3

Pichon, A., and Corréard, S. (2006). Internal tides modelling in the Bay of Biscay: comparisons with observations. *Sci. Mar*. 70, 65–88. doi: 10.3989/scimar.2006.70s165

Pingree, R., and Le Cann, B. (1989). Celtic and armorican slope and shelf residual currents. *Prog. Oceanogr*. 23, 303–338. doi: 10.1016/0079-6611(89)90003-7

Pingree, R., Sinha, B., and Griffiths, C. (1999). Seasonality of the European slope current (Goban spur) and ocean margin exchange. *Contin. Shelf Res*. 19, 929–975. doi: 10.1016/S0278-4343(98)00116-2

Pingree, R. D., and Le Cann, B. (1990). Structure, strength and seasonality of the slope currents in the Bay of Biscay region. *J. Mar. Biol. Assoc. United Kingdom* 70, 857–885. doi: 10.1017/S0025315400059117

Piton, V., Herrmann, M., Lyard, F., Marsaleix, P., Duhaut, T., Allain, D., et al. (2020). Sensitivity study on the main tidal constituents of the gulf of Tonkin by using the frequency-domain tidal solver in t-UGOM. *Geosci. Model Dev*. 13, 1583–1607. doi: 10.5194/gmd-13-1583-2020

Puillat, I., Lazure, P., Jégou, A., Lampert, L., and Miller, P. (2004). Hydrographical variability on the French continental shelf in the Bay of Biscay, during the 1990s. *Contin. Shelf Res*. 24, 1143–1163. doi: 10.1016/j.csr.2004.02.008

Qu, L., and Hetland, R. (2020). Nongeostrophic baroclinic instability over sloping bathymetry: Buoyant flow regime. *J. Phys. Oceanogr*. 50, 1937–1956. doi: 10.1175/JPO-D-19-0145.1

Rathan, S., and Naga Raju, G. (2018). A modified fifth-order weno scheme for hyperbolic conservation laws. *Comput. Math. Appl*. 75, 1531–1549. doi: 10.1016/j.camwa.2017.11.020

Roullet, G., Capet, X., and Maze, G. (2014). Global interior eddy available potential energy diagnosed from Argo floats. *Geophys. Res. Lett*. 41, 1651–1656. doi: 10.1002/2013GL059004

Rubio, A., Caballero, A., Orfila, A., Hernández-Carrasco, I., Ferrer, L., González, M., et al. (2018). Eddy-induced cross-shelf export of high CHL-a coastal waters in the se Bay of Biscay. *Remote Sens. Environ*. 205, 290–304. doi: 10.1016/j.rse.2017.10.037

Rudzin, J. E., Chen, S., Sanabia, E. R., and Jayne, S. R. (2020). The air-sea response during hurricane Irma's (2017) rapid intensification over the amazon-orinoco river plume as measured by atmospheric and oceanic observations. *J. Geophys. Res*. 125:e2019JD032368. doi: 10.1029/2019JD032368

Schiller, R. V., Kourafalou, V. H., Hogan, P., and Walker, N. D. (2011). The dynamics of the Mississippi river plume: Impact of topography, wind and offshore forcing on the fate of plume waters. *J. Geophys. Res*. 116:C06029. doi: 10.1029/2010JC006883

Serpette, A., Cann, B., and Colas, F. (2006). Lagrangian circulation of the north Atlantic central water over the abyssal plain and continental slopes of the Bay of Biscay: description of selected mesoscale features. *Sci. Mar*. 70, 27–42. doi: 10.3989/scimar.2006.70s127

Shchepetkin, A. F., and McWilliams, J. C. (2005). The regional oceanic modeling system (ROMS): a split-explicit, free-surface, topography-following-coordinate oceanic model. *Ocean Model*. 9, 347–404. doi: 10.1016/j.ocemod.2004.08.002

Spall, M. A., and Thomas, L. N. (2016). Downfront winds over buoyant coastal plumes. *J. Phys. Oceanogr*. 46, 3139–3154. doi: 10.1175/JPO-D-16-0042.1

Stamper, M., and Taylor, J. (2016). The transition from symmetric to Baroclinic instability in the eady model. *Ocean Dyn*. 67, 65–80. doi: 10.1007/s10236-016-1011-6

Stone, P. H. (1970). On non-geostrophic Baroclinic stability: Part II. *J. Atmos. Sci*. 27, 721–726. doi: 10.1175/1520-0469(1970)027<0721:ONGBSP>2.0.CO;2

Thomas, L., and Ferrari, R. (2008). Friction, frontogenesis, and the stratification of the surface mixed layer. *J. Phys. Oceanogr*. 38, 2501–2518. doi: 10.1175/2008JPO3797.1

Thomas, L. N. (2005). Destruction of potential vorticity by winds. *J. Phys. Oceanogr*. 35, 2457–2466. doi: 10.1175/JPO2830.1

Thomson, R. E., and Fine, I. V. (2003). Estimating mixed layer depth from oceanic profile data. *J. Atmos. Ocean. Technol*. 20, 319–329. doi: 10.1175/1520-0426(2003)020<0319:EMLDFO>2.0.CO;2

Toublanc, F. T., Ayoub, N., Lyard, F., Marsaleix, P., and Allain, D. (2018). Tidal downscaling from the open ocean to the coast: a new approach applied to the Bay of Biscay. *Ocean Model*. 124, 16–32. doi: 10.1016/j.ocemod.2018.02.001

Vandermeirsch, F., Charraudeau, M., Bonnat, A., Fichaut, M., Maillard, C., Gaillard, F., et al. (2010). "Bay of Biscay's temperature and salinity climatology," in *XII International Symposium on Oceanography of the Bay of Biscay* (Plouzané).

Vic, C., Berger, H., Tréguier, A.-M., and Couvelard, X. (2014). Dynamics of an equatorial river plume: theory and numerical experiments applied to the Congo plume case. *J. Phys. Oceanogr*. 44, 980–994. doi: 10.1175/JPO-D-13-0132.1

Wenegrat, J. O., Thomas, L. N., Gula, J., and McWilliams, J. C. (2018). Effects of the submesoscale on the potential vorticity budget of ocean mode waters. *J. Phys. Oceanogr*. 48, 2141–2165. doi: 10.1175/JPO-D-17-0219.1

Willmott, C. J., Robeson, S. M., and Matsuura, K. (2012). A refined index of model performance. International *J. Climatol*. 32, 2088–2094. doi: 10.1002/joc.2419

Wu, T., and Wu, H. (2018). Tidal mixing sustains a bottom-trapped river plume and buoyant coastal current on an energetic continental shelf. *J. Geophys. Res*. 123, 8026–8051. doi: 10.1029/2018JC014105

Xu, W., Miller, P. I., Quartly, G. D., and Pingree, R. D. (2015). Seasonality and interannual variability of the European slope current from 20years of altimeter data compared with *in situ* measurements. *Remote Sens. Environ*. 162, 196–207. doi: 10.1016/j.rse.2015.02.008

Yankovsky, A., and Chapman, D. (1997). A simple theory for the fate of buoyant coastal discharges. *J. Phys. Oceanogr*. 27, 1386–1401. doi: 10.1175/1520-0485(1997)027<1386:ASTFTF>2.0.CO;2

Yelekçi, Ö., Charria, G., Capet, X., Reverdin, G., Sudre, J., and Yahia, H. (2017). Spatial and seasonal distributions of frontal activity over the French continental shelf in the Bay of Biscay. *Contin. Shelf Res*. 144, 65–79. doi: 10.1016/j.csr.2017.06.015

Conflict of Interest: The authors declare that the research was conducted in the absence of any commercial or financial relationships that could be construed as a potential conflict of interest.

Copyright © 2021 Ayouche, Charria, Carton, Ayoub and Theetten. This is an open-access article distributed under the terms of the Creative Commons Attribution License (CC BY). The use, distribution or reproduction in other forums is permitted, provided the original author(s) and the copyright owner(s) are credited and that the original publication in this journal is cited, in accordance with accepted academic practice. No use, distribution or reproduction is permitted which does not comply with these terms.

frontiers in Marine Science

ORIGINAL RESEARCH
published: 20 July 2021
doi: 10.3389/fmars.2021.680874

Mechanisms of Lateral Spreading in a Near-Field Buoyant River Plume Entering a Fjord

Rebecca A. McPherson[1]*, *Craig L. Stevens*[1,2], *Joanne M. O'Callaghan*[2], *Andrew J. Lucas*[3] *and Jonathan D. Nash*[4]

[1] Department of Physics, University of Auckland, Auckland, New Zealand, [2] National Institute of Water and Atmospheric Research, Wellington, New Zealand, [3] Scripps Institution of Oceanography and Department of Mechanical and Aerospace Engineering, University of California, San Diego, San Diego, CA, United States, [4] College of Earth, Ocean and Atmospheric Sciences, Oregon State University, Corvallis, OR, United States

Observations collected from a fast-flowing buoyant river plume entering the head of Doubtful Sound, New Zealand, were analysed to examine the drivers of plume lateral spreading. The near-field plume is characterised by flow speeds of over 2 ms^{-1}, and strong stratification ($N^2 > 0.1\ s^{-2}$), resulting in enhanced shear which supports the elevated turbulence dissipation rates ($\epsilon > 10^{-3}\ W\ kg^{-1}$). Estimates of plume lateral spreading rates were derived from the trajectories of Lagrangian GPS surface drifters and from cross-plume hydrographic transects. Lateral spreading rates derived from the latter compared favourably with estimates derived from a control volume technique in a previous study. The lateral spreading of the plume was driven by a baroclinic pressure gradient toward the base of the plume. However, spreading rates were underestimated by the surface drifters. A convergence of near-surface flow from the barotropic pressure gradient concentrated the drifters within the plume core. The combination of enhanced internal turbulence stress and mixing at the base of the surface layer, and the presence of steep fjord sidewalls likely reduced the rate of lateral spreading relative to the theoretical spreading rate. The estimates of plume width from the observations provided evidence of scale-dependent dispersion which followed a 4/3 power law. Two theoretical models of dispersion, turbulence and shear flow dispersion, were examined to assess which was capable of representing the observed spreading. An analytical horizontal shear-flow dispersion model generated estimates of lateral dispersion that were consistent with the observed 4/3 law of dispersion. Therefore, horizontal shear dispersion appeared to be the dominant mechanism of dispersion, thus spreading, in the surface plume layer.

Keywords: river plume, plume spreading, stratified flows, dispersion, drifters

OPEN ACCESS

Edited by:
Alexander Yankovsky, University of South Carolina, United States

Reviewed by:
Daniel MacDonald, University of Massachusetts Dartmouth, United States
Guoxiang Wu, Ocean University of China, China
Michael Whitney, University of Connecticut, United States

***Correspondence:**
Rebecca A. McPherson
rmcp393@aucklanduni.co.nz

Specialty section:
This article was submitted to Coastal Ocean Processes, a section of the journal Frontiers in Marine Science

Received: *15 March 2021*
Accepted: *27 May 2021*
Published: *20 July 2021*

Citation:
McPherson RA, Stevens CL, O'Callaghan JM, Lucas AJ and Nash JD (2021) Mechanisms of Lateral Spreading in a Near-Field Buoyant River Plume Entering a Fjord. Front. Mar. Sci. 8:680874. doi: 10.3389/fmars.2021.680874

1. INTRODUCTION

Buoyant river plumes inject large freshwater discharges and terrigenous material into the coastal ocean. Such input, particularly sediment, pollutants and nutrients, can have significant environmental implications. For example, the high nutrient content of water runoff from agricultural lands can cause algal blooms, with adverse effects on marine life (Durand et al., 2002). Similarly, treated wastewater is often discharged into adjacent waters which leads to residual

nutrient and contaminant loading (Roberts, 1999; Hunt et al., 2010). Accurate predictions of the ultimate fate and impact of the riverine waters and related material require an understanding of the plume dynamics over a broad range of spatial scales, typically considered in terms of near and far-field processes.

The near-field region, immediately seawards of the plume discharge point, is where the momentum-dominated initial river discharge transitions into a buoyancy-forced plume. The dynamics in this near-field region are governed by turbulent mixing, driven by the initial momentum anomaly which enhances velocity shear, and lateral spreading (Hetland, 2005, 2010). The mid-field region occurs after the inflow momentum is depleted by these near-field processes, before transitioning into the far-field plume that can extend hundreds of kilometers from the river mouth. The far-field plume region is influenced by buoyancy, wind stress and rotation (Hetland, 2005). An understanding of the near-field processes, which compete to determine the plume structure and ultimate redistribution of energy and momentum in the plume (Hetland, 2005; MacDonald et al., 2007; MacDonald and Chen, 2012; McPherson et al., 2020), is necessary to properly characterise the local plume behaviour and understand the implications for the larger coastal ocean.

Turbulent mixing and lateral spreading in the near-field plume region are closely linked (MacDonald et al., 2007; Hetland, 2010). Vertical mixing of low-momentum, high density ambient water into the buoyant plume decelerates the plume, reduces shear and decreases the density anomaly which in turn slows the rate of spreading (McCabe et al., 2009; Kilcher et al., 2012; MacDonald and Chen, 2012). Lateral spreading, on the other hand, accelerates the plume due to a shoaling of the surface layer and enhances stratified-shear turbulence (Hetland, 2005; MacDonald and Chen, 2012). The role of turbulent mixing in the near-field region of the plume system studied in this paper was quantified by McPherson et al. (2020) using direct measurements and a control volume method. A momentum budget determined that the deceleration of the plume was controlled by turbulence stress, with enhanced turbulent kinetic energy (TKE) dissipation rates (ϵ) at the base of the plume (maximum $\epsilon > 10^{-3}$ W kg^{-1}) (McPherson et al., 2019). Quantifying the role of lateral spreading in the presence of enhanced rates of turbulent mixing is therefore necessary to characterise the dynamics which govern near-field plume structure.

Spreading dynamics have been examined primarily using numerical simulations, which have proved useful for estimating plume spreading rates and determining plume structure (Hetland and MacDonald, 2008; McCabe et al., 2009; Hetland, 2010; MacDonald and Chen, 2012). These model results generally compare well with direct measurements of plume spreading obtained using hydrographic surveys and Lagrangian GPS surface drifters (McCabe et al., 2008; Chen et al., 2009; Kakoulaki et al., 2020). However, while the observational methods demonstrate similar trends, the drifters are also susceptible to slippage and other near-field processes such as shear or rotation, which influence the perceived lateral spreading rates. A control volume approach using observations (MacDonald et al., 2007) has also been validated for estimating spreading rates, and tends to compare better to model results than drifter deployments (Chen et al., 2009). However, few studies have focused explicitly on identifying the mechanisms governing lateral spreading.

The physical mechanisms responsible for plume spreading can be examined by quantifying horizontal dispersion. While advection governs the rate of travel and the direction in which the plume evolves from a source, dispersion determines the lateral and vertical structure of the plume (Stacey et al., 2000; Jones et al., 2008). When the vertical dimension is constrained by a boundary or stratified layer, such as in the coastal ocean, vertically well-mixed conditions are quickly reached and the dispersion of scalars tends to occur primarily in the lateral direction (Okubo, 1971).

The mechanisms responsible for horizontal dispersion can be combined into a single empirical law which relates the rate of diffusion [the dispersion coefficient, K_h (m^2 s^{-1})] of a tracer plume to its size (l), i.e., the dispersion is scale-dependent (Richardson, 1926; Okubo, 1971). Therefore, the dispersion coefficient can be expressed generally as,

$$K_h = \alpha l^n \tag{1}$$

where the parameters α and n are empirical, and the value of n defines the scale-dependence of the dispersion. These empirical constants incorporate the effects of meteorological (e.g., wind speed, direction) and oceanographic (e.g., stratification, ambient currents and turbulence) influences, as well as measurement errors. The coefficient α is related to the turbulence dissipation rate (ϵ), as the energy transfer between scales is constant (Okubo, 1968; Stacey et al., 2000). By applying these parameters to models of dispersion, each which represent different dispersion mechanisms, the drivers of K_h can be determined (Stacey et al., 2000; Spydell et al., 2007). Note that the nomenclature adopted in this study defines dispersion as the combined processes by which turbulence causes irreversible mixing.

Measurements of dispersion in the open ocean have found that $K_h \propto l^{4/3}$ in a field of homogenous turbulence (Stommel, 1949; Batchelor, 1950). Studies of dispersion in the surface waters of lakes and oceans (Stommel, 1949; Okubo, 1971; LaCasce and Bower, 2000; Stevens et al., 2004) and in shelf seas (Jones et al., 2008; Moniz et al., 2014) have corroborated this $n = 4/3$ power law. Furthermore, Stacey et al. (2000) and Fong and Stacey (2003) found that the initial growth of a near-bed coastal plume also obeyed the 4/3 law, indicating that open ocean dispersion theory can be applicable in the near-shore coastal environment. However, the stratification in near-field river plume systems, where a freshwater surface layer overlies a coastal ambient layer, is generally stronger than in the open ocean and lakes (Fischer et al., 1979; Nash et al., 2009; Osadchiev, 2018). This stratification constrains the vertical component of velocity fluctuations which alters the form of dispersion (Fischer et al., 1979; Jones et al., 2008; McPherson et al., 2019). Therefore, it is important to understand the driving mechanisms for dispersion in a stratified near-field river plume setting, and compare them to those postulated by the 4/3 power law.

The objective of this study is to quantify the lateral plume spreading rate in the near-field region of a buoyant river plume. The sheltered fjord setting reduces the background energy input

from wind and tides, providing an idealised system in which to examine near-field plume dynamics. Fjord–river interactions can been directly applied to coastal plumes as the two systems share many common features, whereby a freshwater inflow interacts with a coastal ambient (Garvine, 1987; O'Callaghan and Stevens, 2015). The evolution of the plume width and lateral spreading rate in the near-field are obtained directly from GPS surface drifters and lateral hydrographic data, and then compared with the control volume derived estimates from McPherson et al. (2020). The role that the fjord setting, with its steep sidewalls, plays in influencing the lateral spreading of the plume is also examined. Moreover, the forces that drive lateral spreading in the near-field are determined using horizontal dispersion coefficients, obtained from direct observations and numerical analysis.

2. FIELD SETTING

Doubtful Sound is a glacial fjord located in the far south-west of New Zealand (45.3° S, 167° E, **Figure 1**). The fjord is approximately 35 km long, typically <1 km wide and has a maximum depth of 450 m south of Secretary Island (**Figure 1B**). At the seaward entrance of Doubtful Sound lies a sill approximately 120 m deep, and a second shallower sill (30 m) exists near the head of the fjord, at the entrance to Deep Cove. Deep Cove itself is 3.6 km long and approximately 1 km wide, with a maximum depth (126 m) occurring within 50 m of the shoreline (**Figure 1C**). The tides in the region are predominantly semi-diurnal with ranges of 1.5 and 2.5 m for neap and spring tides, respectively, with tidal velocities between 3 and 5 cms^{-1} (Walters et al., 2001).

A freshwater tailrace carries discharge from the Manapouri hydroelectric power station into the head of Deep Cove (**Figure 1C**). The tailrace is the third largest river flow in New Zealand with an average inflow of $Q = 420\ m^3\ s^{-1}$. Peak surface plume speeds are over 2 ms^{-1} (McPherson et al., 2019) and comparable to the maximum outflow velocity of the Columbia River (Nash et al., 2009). The continuous tailrace inflow into the fjord represents an excess of twice the natural run-off, driven by an annual rainfall >7 m (Bowman et al., 1999), and results in highly stratified conditions. The freshwater input can produce similar vertical density gradients to those observed in major rivers such as the Columbia and Mzymta Rivers (Kilcher et al., 2012; Osadchiev, 2018). The depth of the freshwater surface layer is typically between 2 and 3 m thick (Gibbs, 2001).

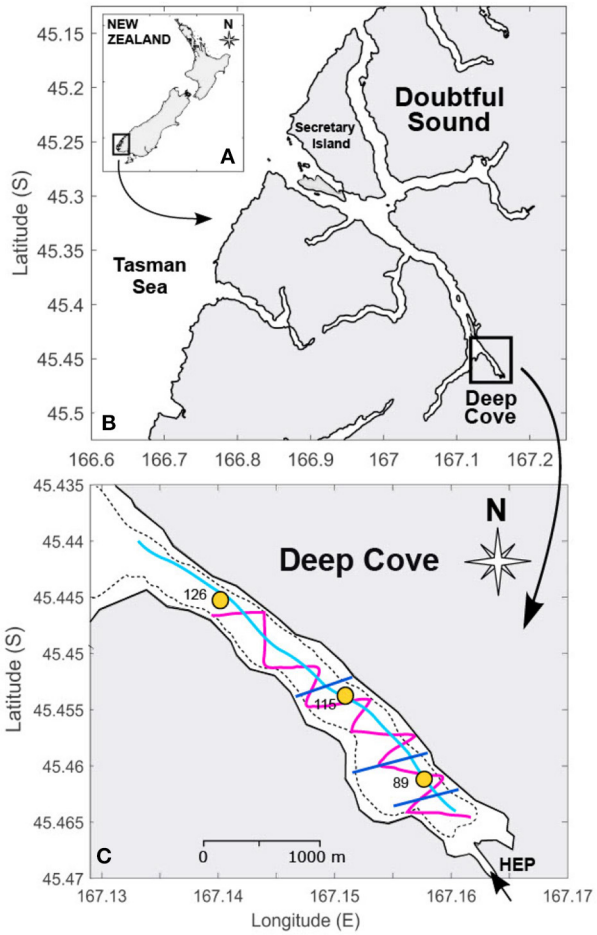


FIGURE 1 | Location map of **(A)** New Zealand with the south-west Fiordland region highlighted, **(B)** Doubtful Sound and **(C)** Deep Cove showing the longitudinal (light blue), lateral (dark blue) and 'zig-zag' (pink) vessel transects. The placement of the September 2015 moorings are the circles. The arrow indicates the tailrace inflow from the Manapouri hydroelectric power station (HEP) and the thin dashed line is the 50 m depth contour. The lateral transects are 0.2 km, 0.5 km and 1.5 km downstream of the tailrace discharge point, respectively.

3. METHODS AND ANALYSIS

The present observations were made during a 2-week long field campaign in March 2016. Over this period, tailrace discharge rates into Deep Cove were high and relatively steady ($Q \approx 530\ m^3\ s^{-2}$) and the tidal range varied from 0.5 to 1.2 m (**Figure 2**). A range of instrumentation and observational techniques were applied to obtain a spatial distribution of the density and velocity fields within Deep Cove. The coordinate system used here is based in a channel reference frame, where x is the along-channel coordinate increasing with distance from the discharge point ($x = 0$) toward the end of Deep Cove, and y is the across-channel coordinate. This reference frame maintains consistency between the calculation of lateral plume spreading rates using the different methods outlined below.

3.1. Vessel-Based Survey

A sequence of vessel-based observations within Deep Cove were repeated over the course of the field campaign. Along-channel transects were aligned with the main river discharge, lateral transects cut through the plume perpendicular to its trajectory, and oblique ('zig-zag') transects captured both lateral and longitudinal plume evolution (**Figure 1C**). At least six consecutive lateral transects were repeated during each sampling period (**Figure 2**). Horizontal velocity estimates were obtained

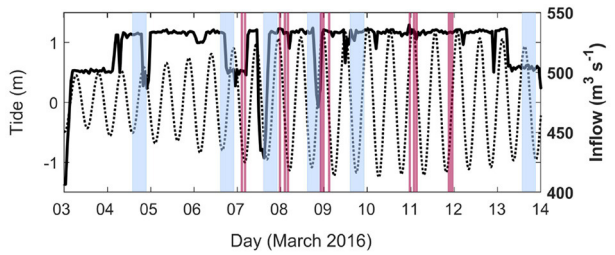


FIGURE 2 | Hourly tailrace discharge rate (solid line) and tide (dashed) for the duration of the field experiment. Peak spring tide occurred on 11 March. The blue shaded boxes indicate the timing of the GPS drifter experiments and the red were the across-channel vessel transects.

from a vessel-mounted ADCP (RDI Workhorse, 600 kHz) which sampled water velocities in 1 m vertical bins from 2.5 to 41.4 m. Near-surface velocities were obtained by applying a linear fit to the velocity data to extrapolate from 2.5 m to the surface. The extrapolated velocity profiles had compared well to *in-situ* near-surface velocity measurements from previous field campaigns (McPherson et al., 2019), and were in good agreement with surface plume velocities estimated by the Lagrangian GPS drifters. Currents were rotated according to the local bathymetry to determine along-channel (u) and across-channel (v) velocities. A weighted 10 m 'bowchain' was attached to the vessel which comprised temperature (RBRsolo) and CTD loggers (RBRconcerto) sampling at 2 and 5 Hz, respectively. High-resolution profiles of practical salinity and temperature were obtained from continuously profiling 'tow-yoed' CTD loggers (RBRconcerto). These data enabled estimation of the buoyancy frequency from the measured density profiles,

$$N = \sqrt{-\frac{g}{\rho}\frac{\partial \rho}{\partial z}} \tag{2}$$

where ρ is the potential density.

The lateral transects of temperature from the bowchain were used to quantify vertical (K_z) and lateral (K_y) diffusion by estimating the change in thickness and width of the plume over distance, respectively. While salinity is generally used to identify and track freshwater plumes in coastal systems (Hetland, 2005), the persistent low-salinity surface layer observed throughout Deep Cove and the wider fjord region, resulting from the tailrace inflow and high rainfall (Gibbs, 2001), makes the distinction between the buoyant plume and freshwater surface layer less pronounced in the salinity field than in temperature (**Figures 3C–E**). Thus, temperature was used to define the plume boundaries in this study (**Figures 3A,B**). The diffusion components were therefore estimated by,

$$K_y = \frac{\Delta y_\mathrm{p}^2}{t_t} \qquad \text{and} \qquad K_z = \frac{\Delta z_\mathrm{p}^2}{t_t}, \tag{3}$$

where t_t is the time taken for the plume to flow between each transect, y_p is the width of the plume at its base and z_p is the plume depth. The base of the plume is defined as the depth of maximum stratification. The depth of the plume is then defined as the distance from the base of the plume to the maximum height of the bounding isotherm.

3.2. GPS Drifters

Lagrangian measurements of near-surface currents were made during six GPS drifter experiments. The plume discharge rate and wind speeds for each experiment are detailed in **Table 1**, and wind direction was consistently up-fjord due to the surrounding steep topography. The headwaters of the fjord absorb the momentum of tidal oscillations (O'Callaghan and Stevens, 2015) and tides do not influence near-field mixing here (McPherson et al., 2019), thus the tidal impact on drifter trajectories is not considered.

The drifters each had a cylindrical drogue of height 0.5 m and diameter 0.2 m, and were ballasted to measure the upper 0.5 m of the water column by a small spherical float. Wind slippage was minimal as the float had little exposure to wind above the surface water level. Each drifter was equipped with a GPS receiver (Columbia V-900 GPS data logger) which recorded every 1 s. The GPS devices have a position accuracy up to 1.5 m, depending on satellite coverage. The drifters were released approximately 10 m apart across the width of the tailrace discharge point and were recovered after $\sim$ 1 h. A total of 8 drifters were deployed in the first two experiments then, due to the loss of a GPS receiver, 7 drifters were deployed and retrieved in the subsequent four experiments.

The drifters were used to quantify the plume lateral spreading rate by estimating the change in plume width with distance from the discharge point, following a similar approach applied by Chen et al. (2009). The normalized plume width is given by W/W_0, where W is the plume width at a given location and W_0 is the width of the plume at a reference location. For drifter data, W is evaluated as the standard deviation of the distances between all drifters in the cross-plume direction at the given location. The plume width is then normalized by W_0. For each GPS drifter deployment, W_0 is taken as the first estimate of plume width (W) closest to the tailrace discharge point. This choice of W_0 enables W/W_0 for each drifter deployment to be compared, despite the variability in the deployment locations of the drifters in each experiment. For the lateral transects, $W_0 = 100$ m, which is the measured distance of the width of the tailrace discharge point (McPherson et al., 2020). Here, W is calculated along each drifter track at intervals of 10 m from the reference point. The uncertainty limits are the minimum and maximum standard deviations of all the subsets of the deployed drifters at each 10 m interval. The drifter method of estimating plume spreading is independent of drifter speed as plume width is evaluated as the distance between drifter tracks at a specified point from the reference point, and not at a given time.

Lateral dispersion is then quantified from the continuous convergence and divergence of drifters from the center of the plume. The standard deviation of the distance between the drifters and the plume centerline (σ_r), defined as the average

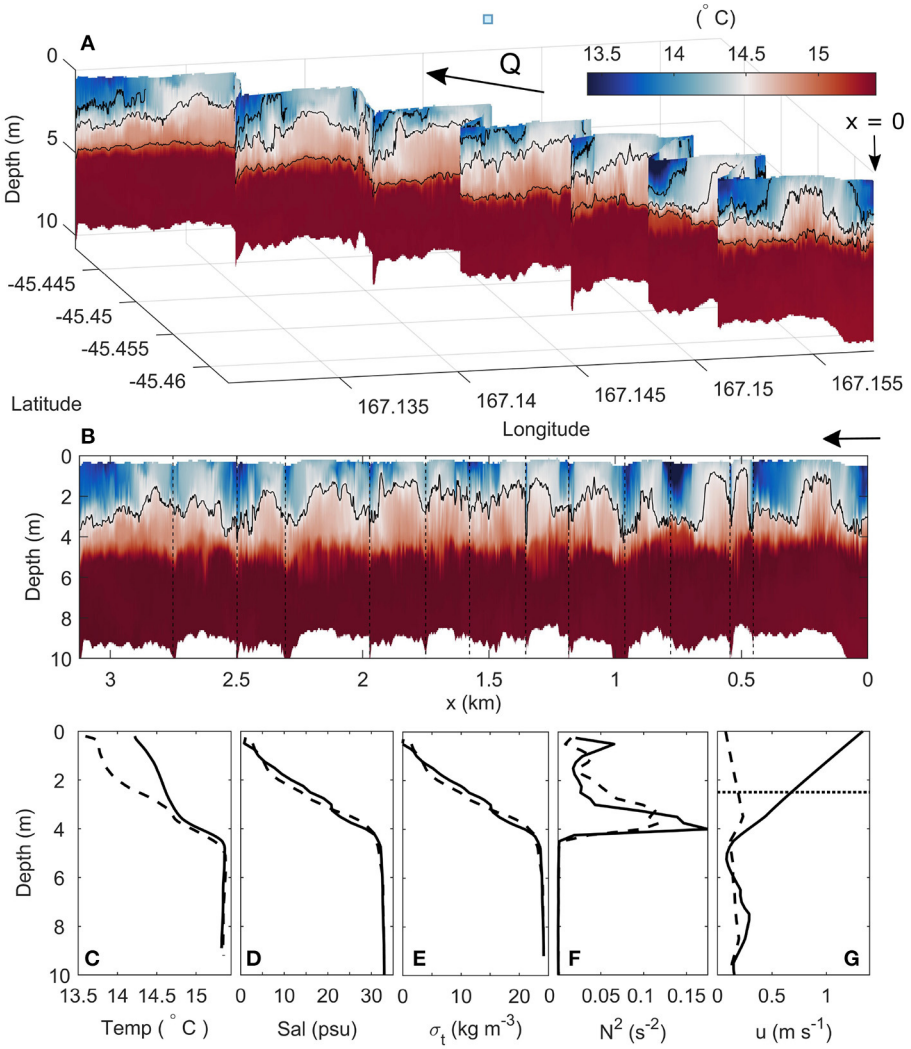


FIGURE 3 | (A) Vertical and spatial distribution of temperature within Deep Cove, and **(B)** the expanded temperature timeseries of **(A)** with respect to distance from the discharge point. The horizonal lines in **(B)** separate each transect. Mean profiles of **(C)** temperature, **(D)** salinity, **(E)** density (σ_t), **(F)** buoyancy frequency-squared (N^2), and **(G)** along-channel velocity (u) from inside (solid) and outside (dashed) the plume. The path of the transect relative to the fjord in **(A)** can be seen in **Figure 1C**. The 14, 14.5 and 15° C isotherms are shown in **(A)**, and the 14.5° C isotherm in **(B)**. The dotted line in **(G)** shows the depth above which the velocity was interpolated. The arrows in **(A)** and **(B)** indicate the direction of tailrace inflow (Q), from right to left.

drifter track, was used to calculate the diffusion coefficient,

$$K_h(l) = \frac{d{\sigma_r}^2(t_d)}{2dt} \quad (4)$$

where t_d is the diffusion time (i.e., the time elapsed since the individual drifter deployment) and $l = 3\sigma_r$ is the scale of diffusion (Okubo, 1971). Horizontal plume spreading is generally anisotropic thus $\sigma_r = \sqrt{(\sigma_x^2 + \sigma_y^2)}$, where σ_x, σ_y denote the standard deviations in the along and across-channel directions, respectively (Stocker and Imberger, 2003).

3.3. Moored Timeseries Data

Contributions to results in section 5.3.1 were from three near-surface moorings deployed in September 2015 (**Figure 1C**). Further details about this field campaign can be found in McPherson et al. (2019). Velocity measurements were obtained from an upwards-facing Acoustic Doppler Current Profiler at 10 m (ADCP; RDI Workhorse, 600 kHz), set to record an ensemble every 3 min in 2 m vertical bins. Spectral analysis was conducted on the velocity observations (Emery and Thomson, 2001) in which the time series was split into half-overlapping intervals equivalent to the inertial frequency, and the spectrum was computed using Welch's periodogram method.

3.4. Control Volume Methods

Plume lateral spreading rates can also be quantified using the control volume method, where measured quantities are connected to plume dynamics over a defined finite region of

TABLE 1 | Summary of drifter deployments and conditions.

Day (March 2016)	Wind speed (ms^{-1})	Discharge ($m^3\ s^{-1}$)	Total retrieved
04	5.6–6.8	515	8
06	0.8–2.4	527	8
07	1.5–1.8	501	7
08	4.8–6.0	530	7
09	2.3–2.6	532	7
13	4.1–5.3	536	7

the flow field, termed a control volume. Freshwater conservation is applied to estimate plume width (b) in the control volume region (MacDonald and Geyer, 2004; Chen et al., 2009). Details of the control volume over the near-field plume region in Deep Cove can be found in McPherson et al. (2020). Horizontal scale-dependent dispersion is then determined from the growth of b with distance from the tailrace discharge point,

$$b(x) = ((2-n)\beta b_0^{1-n}x + b_0^{2-n})^{1/(2-n)} \quad (5)$$

where $\beta = 12\alpha/(Ub_0)$ represents the magnitude of dispersion using the mean along-channel velocity U, and b_0 is the initial plume width (Fong and Stacey, 2003). A non-linear least squares fit of the control volume estimates of b to Equation (5) is taken and both β and n are treated as adjustable parameters. By optimising for n and α using this fit, these parameters can be compared to the empirical estimates from Equation (4). The method has been used to estimate horizontal dispersion in both near-coastal systems and the open ocean (Stacey et al., 2000; Fong and Stacey, 2003; Jones et al., 2008; Moniz et al., 2014).

4. RESULTS

4.1. Near-Field Water Column Structure

Observations from the bowchain and tow-yoed CTD showed a highly-stratified upper water column with a 2 m thick freshwater ($\sigma_t \approx 1$ kg m^{-3}) surface layer overlaying a sharp density interface, and a dense, oceanic ambient ($\sigma_t = 24$ kg m^{-3}) below 5 m (**Figures 3B–E**). The zig-zag temperature transects illustrate the evolving structure and path of the buoyant plume within the surface layer (**Figure 3A**). The 3 m thick plume was observed in the surface layer as a core of water approximately 1° C warmer than the 13.6°C ambient surface layer (**Figures 3A–C**). The plume boundary can thus be defined by an isotherm of 14.5°C. Maximum plume temperatures were found at the base of the surface layer, toward the core of the plume ($\sim$ 14.9°C) where warmer water was entrained from the ambient below (15.5°C) (**Figure 3C**). The plume was confined to the surface layer by strong salinity-induced stratification ($N^2 = 10^{-1}$ s^{-2}) in the pycnocline (**Figure 3F**). Generally weaker values were observed within the plume layer ($N^2 = 10^{-2}$ s^{-2}) and reduced toward zero with depth below the interface to 10 m.

The velocity structure of the near-field region was characterised by a fast-flowing surface plume with speeds over 1.5 ms^{-1}, which overlay a relatively stationary ambient below 5 m (**Figure 3G**). The ambient surface layer currents were weak ($<$ 0.1 ms^{-1}), thus the outer plume boundary can also be defined by speeds of 0.2 ms^{-1}. The near-surface velocity field shows the plume decelerates as it propagates downstream. Maximum surface velocities at the plume centerline decreased from 1.05 ms^{-1} to 0.2 km downstream of the tailrace discharge point to 0.81 and 0.65 ms^{-1} at 0.5 and 1.5 km downstream, respectively, (**Figure 4A**). Flow speeds tended toward zero with lateral distance from the plume centerline, into the surrounding surface ambient. The near-surface plume measurements compared well to the velocities derived from the GPS drifters, estimated as the time derivative of the coordinate position. The drifters initially moved at speeds of $\sim$ 1.7 ms^{-1} near the tailrace discharge point and decreased to approximately 0.6 ms^{-1} toward the seaward end of Deep Cove (**Figure 5**). Maximum speeds of over 2 ms^{-1} were recorded near the discharge point.

4.2. Techniques for Evaluating Lateral Plume Spreading

4.2.1. GPS Drifters

Estimates of plume width derived from the 6 GPS drifter deployments indicate an evolving plume structure as the plume propagates downstream (**Figure 6**). The drifter tracks show consistent behaviour over sections of the trajectories, with the plume width thinning and thickening over the same intervals. A general reduction in plume width from $W/W_0 = 1$ between the tailrace discharge point to 1 km downstream is observed in all transects, reaching a minimum of $W/W_0 = 0.2$, before the plume begins to spread laterally and W/W_0 increases toward 1 at 1.5 km. The three deployments that propagated further downstream show an overall decrease in W/W_0 toward 2.5 km. However, little to no lateral plume spreading occurred over the length of Deep Cove. The estimates of W/W_0 at the end of each transect were generally smaller than 1, with fluctuations of W/W_0 between $0.7 and 0.9$ over the length of each deployment. This reflects the observed drifter trajectories where the majority of drifters remained within 10 m of each other over the duration of each experiment (**Figure 5**). The maximum $W/W_0 = 3.4$ occurred during the 04 March experiment when two drifters were detrained from the mean flow and diverged from the body of the drifter pack at approximately 1 km downstream from the inflow (**Figure 5A**).

4.2.2. Lateral Vessel Transects

The lateral spreading and evolving structure of the surface plume can be clearly identified in mean transects of temperature and velocity at increasingly downstream locations. Near the tailrace discharge point, the buoyant plume was a distinct symmetrical core of warmer water ($>$ 14.5° C) within the 3 m thick ambient surface layer (**Figure 7a**). The surface layer overlays a sharp thermocline and well-mixed 15.5° C ambient water below 4 m. The plume width at 0.2 km from the discharge point was 268 m, compared to a fjord width of approximately 800 m. At 0.5 km downstream, the width of the near-symmetric core had increased to 312 m (**Figure 7b**) while, farther downstream at 1.5 km, the plume had spread almost uniformly across the vessel transect and

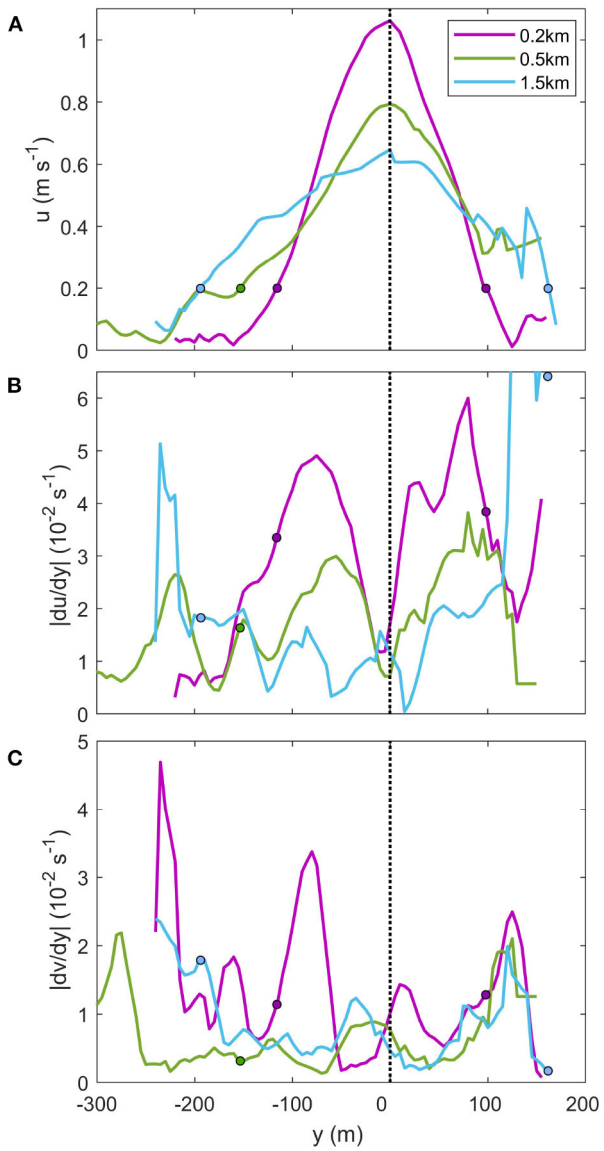


FIGURE 4 | The evolving mean **(A)** across-stream velocity, and velocity shear of **(B)** along-channel and **(C)** across-channel velocities at downstream locations from the discharge point. Velocities are from 2.5 m below the surface. The across-channel distance (y) is relative to the centre of the plume, defined as the location of maximum u. The coloured circles represent the location of the plume edge, defined by 0.2 ms^{-1}. **(A)** The mean velocity transects were averaged over at least six consecutive lateral transects from the vessel-mounted ADCP on 09 March 2016.

had a width of 371 m (**Figure 7c**). The thermocline had become more diffuse with distance from the inflow and thickened down to 4.5 m.

The evolution of the near-surface velocity field also shows the lateral spreading of the plume. At the tailrace discharge point, the plume has a near-Gaussian appearance which flattens and spreads laterally as it propagates downstream (**Figure 4A**). The distance between the outer plume boundaries, here defined by 0.2 ms^{-1}, increased laterally from 225 to 355 m over the 1.3 km distance. Along and across-channel velocity shear at the base of the plume were derived using the vessel-mounted ADCP. Strong velocity shear occurs at either side of the plume centerline at each downstream transect, with peaks corresponding the location of the plume edges (0.2 ms^{-1}, **Figure 4A**), before tending toward zero both toward the plume centerline and into the surrounding ambient. Maximum values of $|du/dy| \approx |dv/dy| \approx 10^{-2}$ s^{-1} peaked within 0.2 km of the tailrace discharge point, where plume speeds were greatest ($u > 1$ ms^{-1}) (**Figure 4**). The peaks of velocity shear decreased with distance from the discharge point as the plume decelerated and moved laterally away from the centreline as the plume spread. Farther downstream at 1.5 km, the maximum $|du/dy|$ and $|dv/dy|$ decreased by half and peaked toward the edges of the transect where the plume boundaries were approached (**Figures 4B,C**).

4.3. Techniques for Evaluating Dispersion

4.3.1. GPS Drifters

A diffusion diagram provides a means of predicting the rate of lateral spreading and the scale-dependence of the dispersion rates. Dispersion rates for the plume derived from the GPS drifters (using Equation 4) are shown as a function of their scale. As expected, the lateral component of dispersion (K_y) was much larger than the longitudinal dispersion (K_x) component, and both K_x and K_y increased with the scale of mixing (**Figure 8**). Estimates of $K_x = 0.3 - 1.0$ m^2 s^{-1} were observed at diffusion scales of $0 < l < 120$ m, while K_y was at least one order of magnitude greater for larger scales, ranging from $K_y = 1.4 - 14.1$ m^2 s^{-1} between $10^2 < l < 10^3$ m. Expressing the estimates in the form of $K_h = \alpha l^n$ (Equation 1), the line of best fit yielded $\alpha = 0.0017$ m$^{2/3}$ s^{-1} and $n = 1.38 \pm 0.23$. The errorbars show 95% confidence intervals of the slope over 1,000 bootstrap samples. Most of the latitudinal and longitudinal diffusion estimates fall within the 95% confidence intervals on either side of the predicted values.

4.3.2. Lateral Vessel Transects

Estimates of plume dispersion rates from the lateral vessel transects of temperature (**Figure 7**) can also be obtained. Using the 14.5° C isotherm as the plume boundary and applying Equation (3), the results provided an alternate estimate of $K_y = 29.8$ m^2 s^{-1} and a vertical diffusion component of $K_z = 1.4 \times 10^{-4}$ m^2 s^{-1} for the distance between the 0.2 and 1.5 km transects. This K_z is comparable to the vertical diffusivity measured in other river plumes (Hetland, 2005; Horner-Devine et al., 2009) which suggests that Equation (3) provides an accurate first-order estimate of bulk diffusion. The K_y estimates derived from both **Figure 7** and other repeated lateral transects of temperature agree well with the drifter-derived horizontal diffusion results (**Figure 8**).

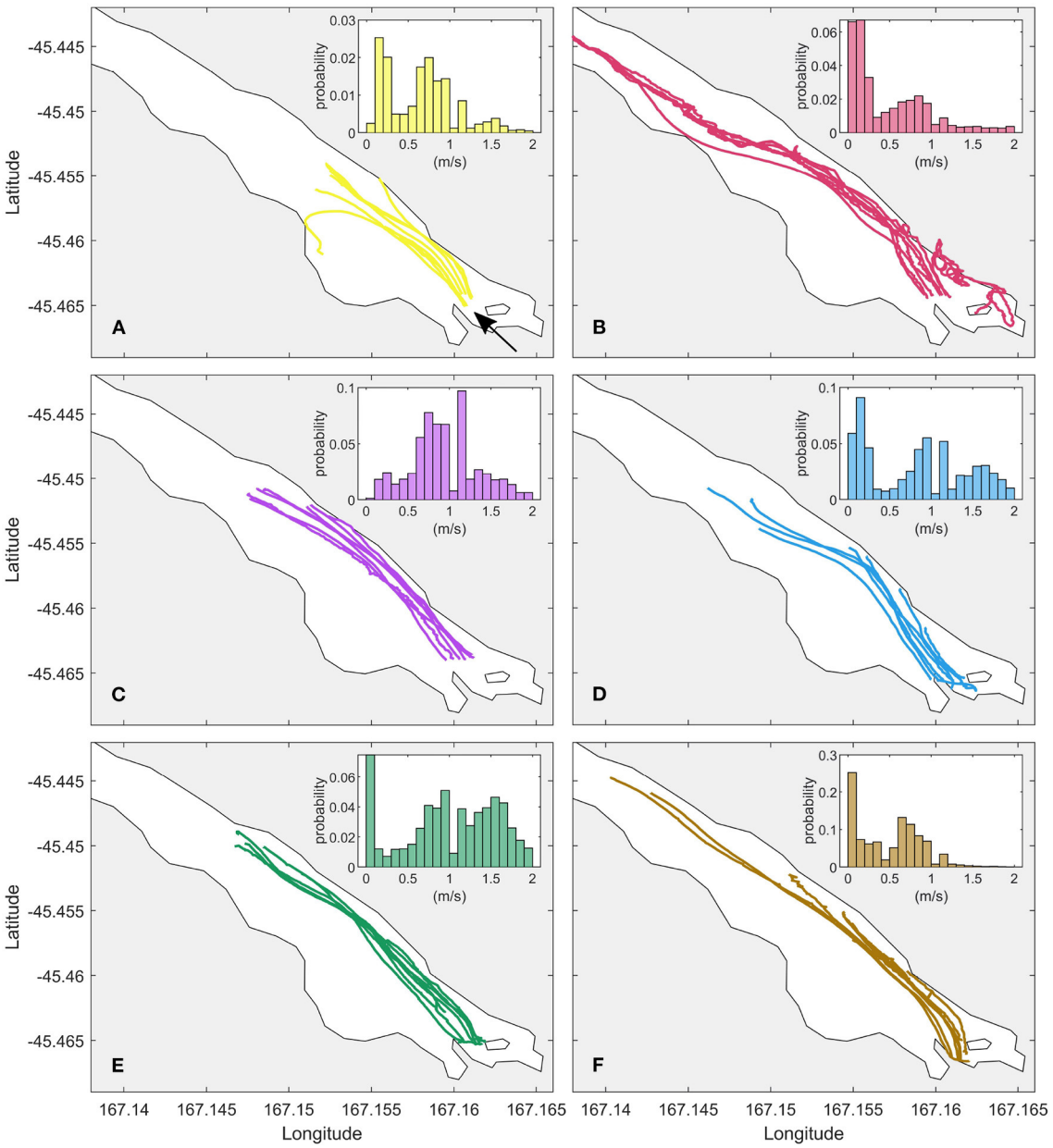


FIGURE 5 | The trajectories of the multiple GPS drifters released near the entrance of the tailrace discharge point, where **(A–F)** are the six deployments, corresponding to the days outlined in **Table 1**, respectively. On the upper right corner of each plot is a histogram of flow velocities of all the drifters in each experiment (ms^{-1}). The histograms are normalised by the maximum of the distribution. The arrow in **(A)** indicates the tailrace discharge point and the direction of flow.

5. DISCUSSION

5.1. Comparison of Spreading Rates Between Techniques

The rate of plume lateral spreading was quantified using two different observational methods; Lagrangian GPS drifters which measured near-surface plume velocities directly (**Figure 6**) and lateral transects of temperature and velocity fields (**Figures 4**, **7**). These directly observed results can then be compared to estimates of plume width determined by a control volume method. This control volume technique used hydrographic observations from along and across-fjord transects, and is detailed in McPherson et al. (2020).

Estimates of plume width derived from the across-channel hydrographic transects generally compared well to the estimates derived from the control volume method (**Figure 9**). The control volume results show that W/W_0 increased from 1 close to the tailrace discharge point to $W/W_0 = 1.8$ over 3 km downstream, indicating that the plume spread laterally in the near-field region as it propagated seaward. The estimates of W/W_0 derived

from the repeated lateral transects of temperature and velocity, using 14.5 ° C and 0.2 ms^{-1} as the definitions of the plume boundary, respectively, correspond well at the three downstream locations. They all show a consistent increase in W/W_0 over the along-channel distance and are in good agreement with the control volume plume width estimates. The estimates of W/W_0 derived from the average GPS drifter trajectory (**Figure 6**) are generally smaller than the other observed values, suggesting an underestimation of plume width using this method.

While a general increase in W/W_0 over the length of Deep Cove was observed in both the control volume and transect data, the variability in the measurements highlights an evolving along-channel lateral spreading rate (db/dx). Over the total 3 km near-field region, $db/dx = 0.045$ from the control volume estimates. However, this rate increases and decreases over different sections of Deep Cove. All methods show an agreement in the evolving pattern of db/dx in the initial 1.5 km, with weaker horizontal spreading rates in the first 0.5 km and an increase toward 1.5 km. Further downstream, there is a slowing of plume spreading toward the end of Deep Cove. The highest lateral spreading rates are generally derived from between the lateral transects of temperature and velocity, with $db/dx \approx 0.05$ between 0.2 and

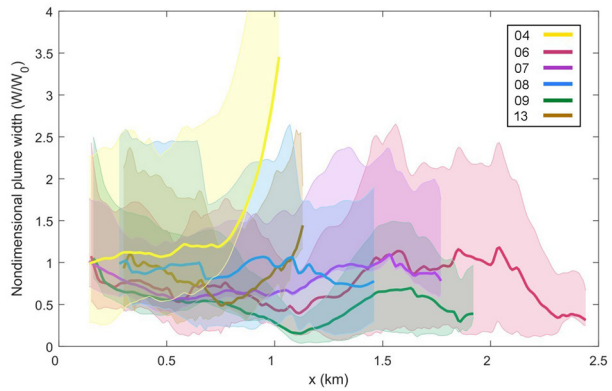


FIGURE 6 | The non-dimensional plume width (W/W_0) for each GPS drifter experiment with respect to along-channel distance from the discharge point (x). The shaded regions indicate the uncertainty for each deployment. The drifter trajectories were averaged over 10 m.

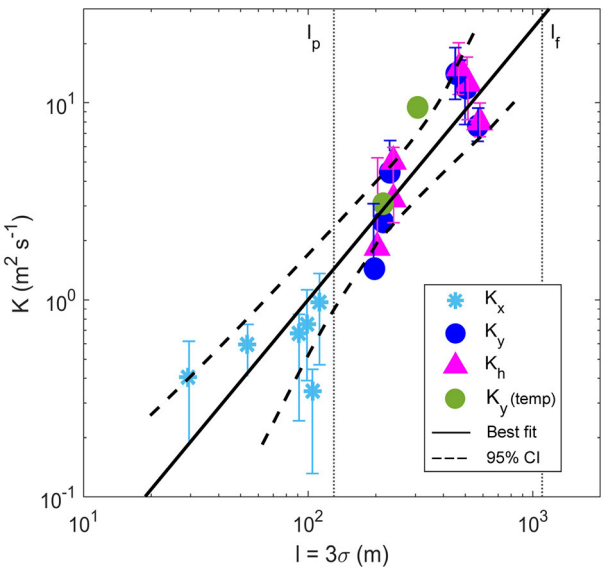


FIGURE 8 | Okubo-style diffusion diagram of mean lateral (K_y, circles), longitudinal (K_x, stars) and total diffusion (K_h, triangles) against the scale of diffusion (l). All diffusion component estimates were derived from the 6 GPS drifter trajectories (**Figure 5**) and K_y from two sets of mean lateral temperature transects at the three downstream locations (green) (**Figure 1C**). Error bars denote a 95% bootstrap confidence interval of the slope (dashed lines). The two vertical lines (dotted) represent the average width of the plume (l_p) and the fjord (l_f).

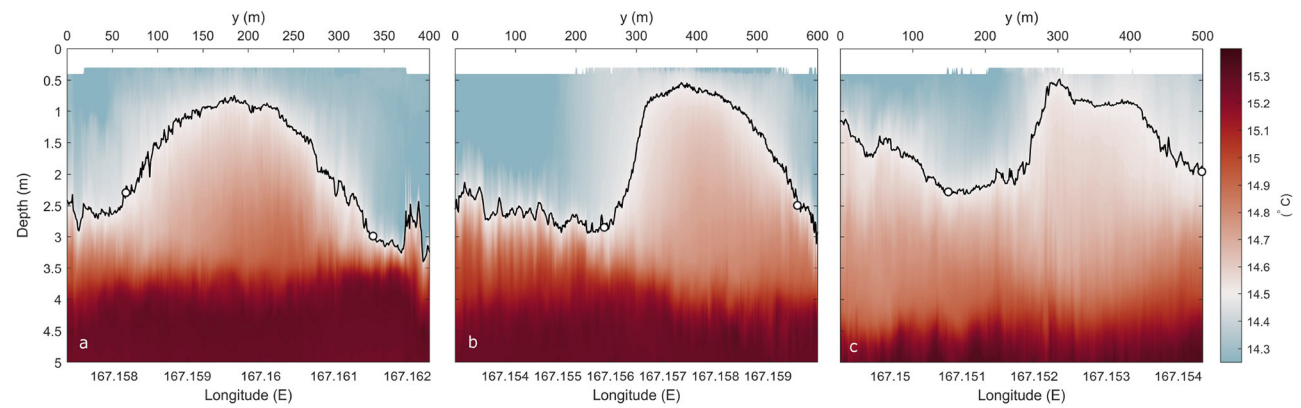


FIGURE 7 | Mean vertical distribution of temperature of across-channel transects in the near-field plume region taken **(a)** 0.2 km, **(b)** 0.5 km and **(c)** 1.5 km downstream of tailrace discharge point. The plume boundary was defined by the isotherm 14.5°C (black lines), and the plume edge is indicated by the white circles on the isotherm. These edges were determined from the gradient of the depth of the isotherm. Temperature was recorded by the bowchain and averaged over at least six consecutive lateral transects.

0.5 km increasing to between 0.04 and 0.09 between 0.5 and 1.5 km. Estimates of db/dx from the control volume method are at the lower range over the same intervals, peaking at 0.05 at 1.5 km. While the corresponding horizontal spreading rate from the GPS drifters also shows this evolution of db/dx, with an initial weaker db/dx and an increased rate between 0.5 and 1.5 km, the estimates of db/dx remain one order of magnitude smaller than the control volume estimates over the length of the track. The good agreement between the estimates of plume width and db/dx from the control volume and lateral vessel transects (**Figure 9**) indicates that either the drifters underestimated the plume width, or in fact quantified a different process that was locked to the near-surface.

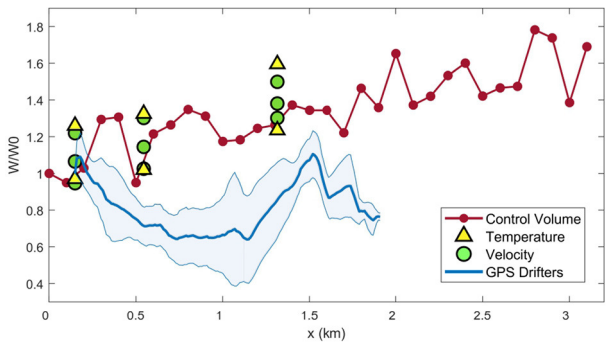


FIGURE 9 | The evolution in non-dimensional plume width (W/W_0) with distance from the discharge point estimated by three observational methods: lateral transects of temperature (triangles) and velocity (circles), a control volume method (red) (McPherson et al., 2020) and the average W/W_0 calculated from the six GPS drifter deployments (**Figure 6**) (blue). The estimate of W for each method was normalized by W_0, where $W_0 = 100$ m for the transects and control volume, and $W_0 = W(1)$ for the drifter deployments. The average plume width from the drifters was estimated with a minimum of three measurements for a standard deviation (shaded blue area).

This change in db/dx in space is not surprising as the spreading rate is determined by the initial momentum from the variable plume inflow (**Figure 2**), the density difference between the freshwater surface layer and ambient water below, and the degree of vertical mixing at the interface (Chen et al., 2009). Thus the effect of the enhanced shear-driven mixing observed at the base of the plume (McPherson et al., 2019) which weakens the density gradient at the interface as the plume propagates downstream (**Figure 7**) would in turn reduce the lateral spreading rate.

The discrepancy between the results can be examined by considering what the GPS drifters actually measured in this field setting. While estimates of lateral spreading from drifters in other river plume systems have generally compared well to results from numerical and other observational techniques (Hetland and MacDonald, 2008; Chen et al., 2009; McCabe et al., 2009), drifters are also susceptible to meteorological and other oceanographic factors. A drifter consisting solely of a surface float with no drogue provides velocities and a trajectory that are a combination of surface advection, Stokes drift (an extra wave-induced force at the water surface) and direct wind forcing (Lumpkin et al., 2017). However, the impact of these external forcings on the GPS drifters used in the experiments conducted in Deep Cove were minimized by their design. The effects of wind on the trajectories of the drifters in Deep Cove was reduced by having very little of the drifter visible above the water, by conducting the GPS drifter experiments when wind speeds were low (**Table 1**), and by including a ballast centered at 0.5 m beneath the surface. The ballast also ensured the drifter was largely unaffected by the motion due to drift beneath the surface-wave-driven Stokes layer.

In Deep Cove, the drifters tended to remain clustered together within the body of the plume with no evidence of horizontal

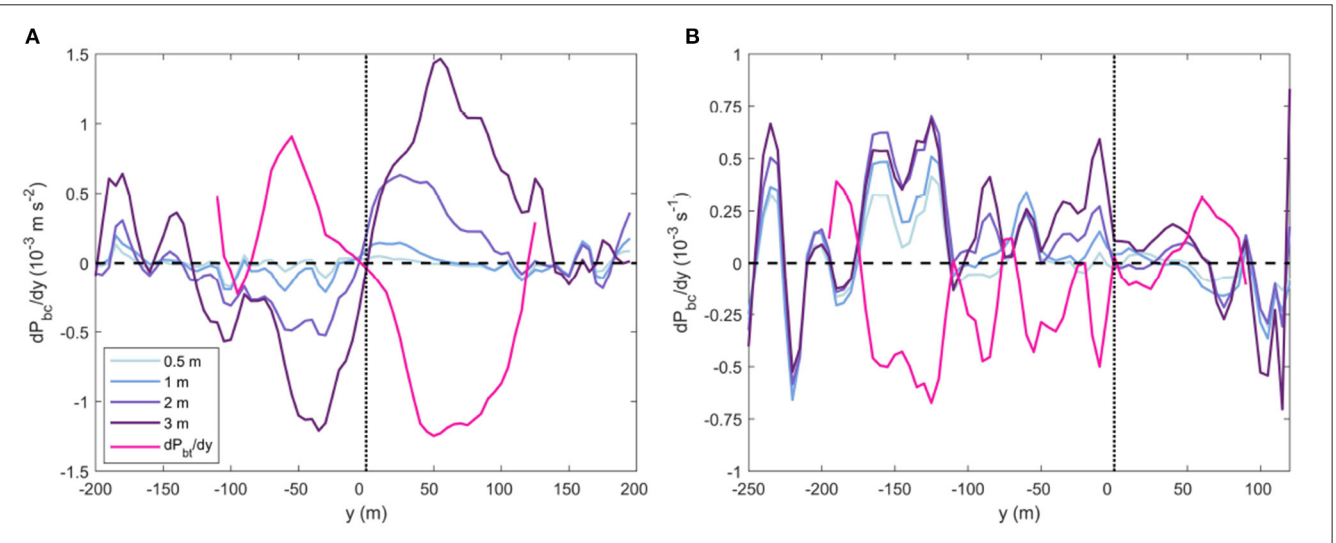


FIGURE 10 | Horizontal baroclinic pressure gradient from within the plume layer at 0.5, 1, 2, and 3 m below the water surface, and barotropic pressure gradient (pink) at **(A)** 0.25 km and **(B)** at 1.5 km downstream of the tailrace discharge point (**Figure 1C**). The vertical dashed lines illustrates the centre of the plume.

spreading (**Figure 5**). Over the initial 1 km, all drifter trajectories tended to show a decrease in plume width, before increasing further again downstream (**Figure 6**). The high flow speeds measured by the drifters (**Figure 5**) indicate the drifters remained within the main flow. The clustering of the drifters near the plume centerline is likely caused by a convergence of surface flow that concentrated the drifters in regions of high velocity within the center of the plume (Hetland and MacDonald, 2008).

The density and pressure gradients in the surface layer suggest this convergence of surface water occurred in the initial 1 km. Density and pressure in the surface layer are greatest within the center of the plume (**Figure 3E**) due to the enhanced entrainment of high density ambient water into the low density surface plume, driven by strong vertical mixing (McPherson et al., 2019). This vertical mixing creates a horizontal density gradient at the base of the plume. The corresponding horizontal baroclinic pressure gradient component is therefore greatest at 3 m below the surface, and peaked on either side of the plume centreline at both 0.25 and 1.5 km downstream of the inflow (**Figure 10**). The baroclinic pressure gradients tends toward zero at the surface. The barotropic pressure gradient also displays corresponding peaks at eiher side of the plume centerline, though the peaks of either pressure component are of an opposite sign.

By combining the across-channel baroclinic and barotropic pressure gradients, the total across-channel pressure gradient determines the direction and magnitude of the near-surface flow (**Figure 11**). At the surface, the total pressure gradient is dominated by the barotropic component, as the baroclinic pressure gradient is weakest at 0.5 m (**Figure 11A**). The positive total pressure gradient to the left of the plume centerline and the negative to the right indicates a strong flow converging toward the center of the plume. With depth, the baroclinic component increases and begins to influence the total pressure gradient, thus the direction of near-surface flow. A lateral diverging flow from the centre of the plume is already apparent at 2 m, while there is still exists a stronger converging flow outside 50 m (**Figure 11C**). At 3 m, the baroclinic component dominates the total pressure gradient (**Figure 11D**). This results in a strong lateral flow of plume water away from the centerline, driving the lateral spreading of the plume. The lateral velocity gradient (dv/dy) also illustrates diverging velocities at 2.5 m below the surface, peaking at the edges of the plume (**Figure 4C**).

This balance of flow convergence toward the plume centerline at the near-surface and divergence from the centerline at the plume base can also be demonstrated in the Gaussian shape of the near-field plume in the lateral transects of temperature (**Figure 7**). The wider base illustrates the lateral spreading of the plume driven by the baroclinic pressure gradient, while the narrowing toward the water surface indicates the near-surface convergence.

Further downstream at 1.5 km, the role of the pressure gradient components are reversed (**Figure 10B**). The barotropic component drives a near-surface divergence of flow while the corresponding baroclinic pressure gradient shows a convergence of flow, the strength of which increases with depth. The barotropic pressure gradient tends to dominate throughout the surface layer which drives a total lateral spreading of the plume. This near-surface divergence of flow from the plume centerline is also reflected in the GPS drifter trajectories which show an increase of plume width from 1 to 1.5 km. The rate of plume spreading over this distance derived from the GPS drifters compared relatively well to db/dx from the control volume estimates (**Figure 9**). Toward the end of Deep Cove, the drifters measured a decrease in plume width (**Figure 9**) which suggests another reversal of the lateral pressure components and a convergence of near-surface flow.

These horizontal density, pressure and velocity gradients (**Figures 3B**, **4**, **10**, **11**), and the structure of the plume (**Figure 7**), suggests that the GPS drifters, drogued to the upper 0.5 km, were concentrated within the plume core over the intial 1 km by near-surface convergence, driven by the barotropic pressure gradient. The clustering of drifters about the plume centerline and within the main flow (**Figure 4**) meant that both the plume width and lateral spreading rate were not accurately measured, but also that the drifters were then dominated by the strong along-channel advection, which was a dominant component of the plume dynamics along the whole 3 km near-field region (McPherson et al., 2020). This resulted in an underestimation of the overall

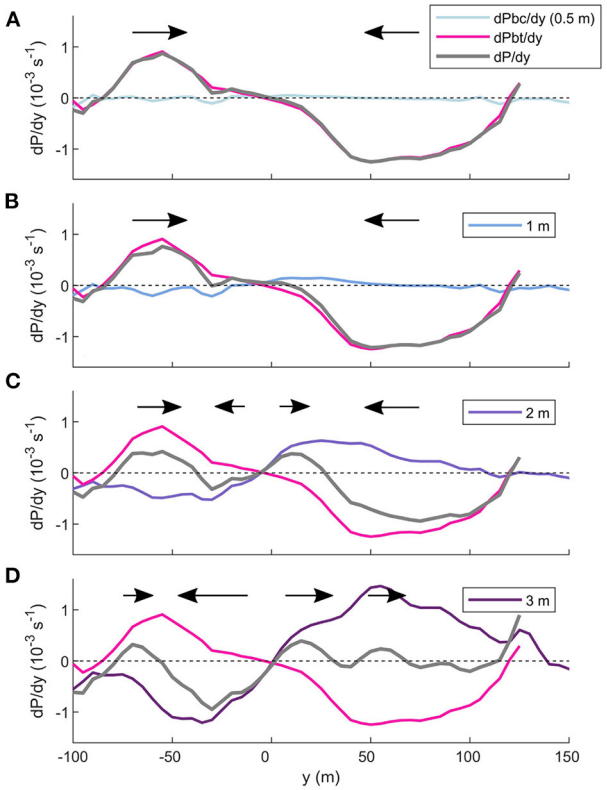


FIGURE 11 | The balance of pressure gradient components within the surface layer at 0.2 km from the tailrace discharge point. The barotropic (pink) and baroclinic components sum to equal the total pressure gradient (grey). The baroclinic component is calculated at **(A)** 0.5 m, **(B)** 1 m, **(C)** 2 m, and **(D)** 3 m below the surface. The black arrows indicate the direction of the flow across the mean transect as a result of the total pressure gradient. The size of the tail of the arrow scales with the strength of the flow.

lateral spreading rate by the drifters in comparison to the other observational methods (**Figure 9**). Further downstream, the barotropic pressure gradient acted to diverge the near-surface flow away from the centerline which produced a comparable lateral spreading rate to the other observational methods employed, before converging again toward the end of Deep Cove.

5.2. Comparison With Other River Plume Systems

While the drifters converged toward the plume centerline at the near-surface and tended to underestimate the plume width, the results from the hydrographic transects and control volume also suggest a slower lateral spreading rate than typically found in near-field settings. The coastal river plumes conventionally studied generally show radial expansion and splaying streamlines (Hetland and MacDonald, 2008; McCabe et al., 2009; Kakoulaki et al., 2020), and adhere to a horizontal spreading rate for a two-layer gravity current of $\sqrt{(g'H)/2}$ (Farmer et al., 2002). In the near-field region of Deep Cove, where g' is calculated using an across-channel $\Delta\sigma_t$ from **Figure 3E**, this equates to a bulk horizontal spreading rate of $\sim$ 0.19 ms^{-1}. With a mean along-channel plume velocity of 0.8 ms^{-1}, the plume would theoretically spread by $\sim$ 450 m over the 3 km near-field region ($db/dx = 0.15$). However, the observational results did not agree with these estimates. The plume width increased from 105 to 240 m over the length of Deep Cove, with a total spreading rate that was slower than theoretical rate by one order of magnitude ($db/dx = 0.045$ m^{-1}, **Figure 9**).

The difference between these lateral spreading rates could be attributed in part to the intense vertical mixing at the base of the plume in Deep Cove. Enhanced turbulent mixing has been shown to drive interfacial stress which is a dominant force acting to decelerate the near-field plume (Chen et al., 2009; McCabe et al., 2009; McPherson et al., 2020). The deceleration is controlled by entraining low-momentum ambient water into the surface layer, simultaneously mixing high-density ambient water into the freshwater surface layer, thus reducing the density gradient and slowing lateral spreading (Hetland, 2010). In comparison to typical estimates of ϵ in coastal environments, the measurements observed in the near-field region of Deep Cove are orders of magnitude greater. The highly stratified interface ($N^2 = 10^{-1}$ s^{-2}, **Figure 3F**) supports the intense shear generated by the high flow speeds ($u > 1.5$ ms^{-1}, **Figure 3G**), resulting in surface-intensified turbulence ($\epsilon > 10^{-3}$ W kg^{-1}) (McPherson et al., 2019). This corresponds to enhanced surface-intensified turbulence stress, over one order of magnitude greater than the peak stress in the Columbia River (Kilcher et al., 2012).

Comparing the balance of terms in a near-field momentum budget between Deep Cove and the Columbia River shows that the enhanced vertical mixing in Deep Cove is likely linked to the reduced corresponding lateral spreading rate. In the Columbia River, where internal stress was weaker, the role of lateral spreading in balancing the total momentum budget was much greater than in Deep Cove. The spreading term balanced the acceleration terms in the surface layer, and the internal stress divergence drove the deceleration. This translates to a greater lateral spreading rate in the Columbia River, $db/dx = 0.16$ (Kilcher et al., 2012), which was one order of magnitude larger than in Deep Cove. In Deep Cove however, where turbulence stress was high, the spreading term was negligible and the internal stress similarly controlled the plume deceleration. The balance of dynamics in each near-field setting suggests that the increase in internal stress reduces the spreading rate. When the internal stress increases relative to the other near-field processes, the enhanced turbulence at the interface drives a reduction in the density difference between the ambient and surface and therefore a reduced lateral spreading rate. Thus, the high ϵ in Deep Cove could be responsible for the slower horizontal spreading than typically observed for near-field plumes with weaker turbulent mixing.

While the enhanced turbulent mixing at the base of the plume in the near-field is likely to reduce the rate of lateral plume spreading, the surrounding topography and its impact on plume evolution is also relevant in this system. The trajectories of the GPS drifters highlight the proximity of the fjord sidewalls to the mean plume flow (**Figure 5**). While the role of the sidewalls on the lateral plume spreading rate cannot be quantified, they are able to explain the circulation pattern in the surface layer by driving the barotropic pressure gradient and convergence of near-surface flow. The plume spreads laterally, from high to low pressure, as it propagates downstream (**Figure 10**). However, the sidewalls act as a physical barrier which prevents the continued and uninhibited lateral spreading of the plume. As the strong vertical density gradients (**Figures 3E,F**) also prohibit the downwelling of the surface ambient water, the surface water is then pushed up against the fjord sidewalls and increases the water height there. This creates a barotropic pressure gradient across the width of Deep Cove which drives the water back toward the center of the fjord and the plume. However, as the baroclinic pressure gradient is zero at the surface but greater than the barotropic component at 3 m (**Figure 11**), the water converges at the surface but is forced to diverge laterally at the base of the plume.

However, a uniform convergence of near-surface flow along the fjord was not observed. The lateral pressure gradient components showed a transition from near-surface convergence in the initial 0.25 km to divergence further downstream at 1.5 km (**Figure 10**) which was reflected in the trajectories of the GPS drifters as they propagated downstream (**Figure 6**). This along-channel change in near-surface flow could also be attributed to the sidewalls driving a form of oscillatory motion, such as a seiche, which propagates throughout the fjord basin. The initial expansion of the plume as it enters the fjord, no longer confined by the tailrace channel, forces the surrounding ambient water toward the fjord sidewalls. The barotropic pressure gradient is formed as described above and drives the near-surface convergence. However, this returning flow toward the center of plume could also be an oscillation which continues to propagate downstream and move laterally, impacting the barotropic pressure gradient and thus the drivers of plume spreading, reflected in the trajectories of the GPS drifters. However, the current spatial and temporal resolution

of the data is unable to fully resolve any basin-wide oscillatory motion and its impact on the plume. The change in the fjord topography also impacts the plume spreading. The fjord is wider between 0.25 and 1 km as a bay exists to the south of the inflow (**Figure 1C**), before narrowing further downstream. As described above, the sidewalls restrict lateral spreading of both the plume and the surface ambient, thus any narrowing or widening of the sidewalls relative to the location of the plume would also affect the lateral pressure gradients and spreading.

There have been no observational field studies of the spreading dynamics of topographically-constrained plumes; river plumes typically studied generally exhibit a discharge perpendicular to the coast with no lateral boundaries (Yankovsky, 2000; Hetland and MacDonald, 2008; Chen et al., 2009; Kakoulaki et al., 2020). However, a change in drifter patterns was observed when GPS and modelled drifters, deployed near the mouth of a weakly-stratified tidal inlet, left the constrained tidal channel and reached the mouth of the inlet (Spydell et al., 2015). Within the channel, the drifters were generally retained in the main flow while, upon exiting the inlet, the lateral spreading rates increased. While a decrease in flow velocities with downstream distance was observed, which could balance the increase in horizontal spreading, the impact of the channel walls on the drifter trajectories and spreading rate were not considered. It is not unlikely that the same barotropic pressure gradient, from the increased sea surface height at the sidewalls of the channel, produced a convergence of flow which contributed to the drifters clustering together in the main flow. Though the fjord sidewalls appear to influence the near-surface circulation in Deep Cove, the relative roles of the enhanced turbulence and topography on the reduced lateral spreading rate relative to other plume systems remains unclear.

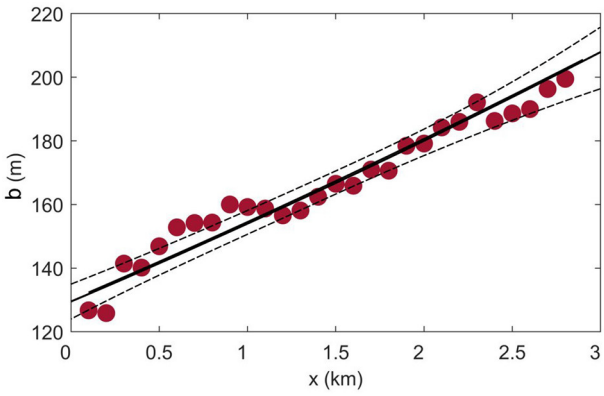


FIGURE 12 | Plume width (b) as a function of distance from the tailrace discharge point. The best-fit line with scale-dependency $n = 1.39 \pm 0.35$ (solid) was determined using the length-scale model of Equation (5). Dashed lines are the 95% confidence limits of the line of best fit.

5.3. Lateral Dispersion

While advection governs the evolution and transport of the along-channel flow (Kilcher et al., 2012; McPherson et al., 2020), diffusion processes determine the across-channel transport in the near-field. Thus the processes responsible for the observed lateral spreading of the plume (**Figure 9**) can be examined by quantifying horizontal dispersion. A number of theoretical models describe dispersion by defining different drivers. The plume growth is characterised by an exponent of $n = 4/3$ which is the value expected for three-dimensional turbulence (Fong and Stacey, 2003). Turbulence theory postulates that dispersion depends on the length scale of the motions and rate of turbulent dissipation (Batchelor, 1952), while shear-flow theory considers vertical diffusion in a horizontally sheared flow, driven by turbulence, as the governing process (Taylor, 1953; Fischer et al., 1979). Both theories are capable of producing a 4/3 power law, suggestive of scale-dependent growth (Stommel, 1949; Batchelor, 1950), and both are assessed here, to determine which is capable of representing the observed lateral spreading.

The scale-dependence of the observed lateral dispersion must be first examined to determine if the $n = 4/3$ power law is met, thus if these models are suitable. The slope of the best-fit of the lateral diffusion estimates, n, defines the scale-dependence of the dispersion. The diffusion diagram is first examined, which combines estimates of diffusion from the GPS drifters and hydrographic transects (**Figure 8**). Based on scale, the estimates of lateral diffusion observed here are comparable to other plume inflows (Yankovsky, 2000; Hunt et al., 2010). The line of best-fit applied to these estimates yielded $n = 1.38 \pm 0.23$. This observed n is not inconsistent with, and indeed compares relatively well to, the theoretical $n = 4/3$ which suggests scale-dependent behaviour following the 4/3 law.

Furthermore, the plume width model (Equation 5), using estimates of b derived from the control volume, can also be used to quantify the plume's scale-dependent lateral dispersion. A non-linear least-squares fit of b is applied to Equation (5), setting $b_0 = 128$ m and $U = 1.1$ ms^{-1}, and optimising for n and β, gives a best-fit of $n = 1.39 \pm 0.35$ and $\beta = 0.024 \pm 0.005$ (**Figure 12**). Most of the plume width estimates fall within the 95% confidence intervals on either side of the predicted values given the optimised parameters. The close agreement of n between the diffusion diagram and plume width model results indicate that, within statistical certainty, $n = 4/3$, and independently supports the empirical dispersion coefficient from the diffusion diagram. Thus, both turbulence and shear-driven theoretical models can be examined in order to determine the drivers of lateral dispersion.

5.3.1. Dispersion From Turbulence Theory

The initial dispersion in the near-field plume is governed by a 4/3 power law, which is the exponent expected for three-dimensional turbulence. Furthermore, the enhanced turbulent mixing observed in the near-field of this system and its dominant role in controlling the structure and behaviour of the plume (McPherson et al., 2019, 2020), including its likely impact on the reduction of lateral plume spreading, motivates the analysis of dispersion first using turbulence theory. The turbulence model can be examined based on its assumption that dispersion depends on the length scale of turbulence, i.e., the plume lateral length scale is related to the distance from the discharge point (Equation

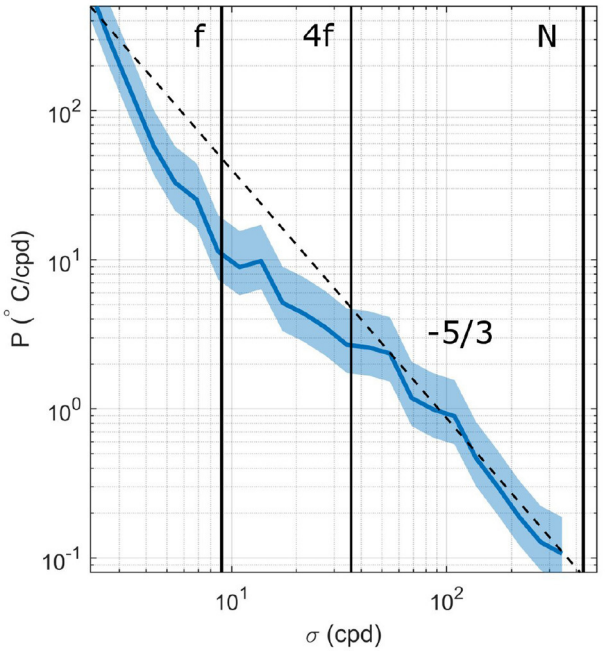


FIGURE 13 | Power spectral density measurements of the along-channel near-surface flow ($z = 2$ m) approximately 1 km downstream from the tailrace discharge point. The vertical lines indicate the focus on the [f,N] range, and the −5/3 slope is shown as the dashed line. Variability lies within the 95% confidence interval (shaded region around the spectrum). The time series was split into half-overlapping intervals equivalent to the inertial frequency.

5). Fixing $n = 4/3$, thus eliminating n as a fitting coefficient in Equation (5), gives $\beta = 0.023 \pm 0.002$, where β is the magnitude of horizontal dispersion. This value of β is comparable to results from a near-bed plume in coastal waters where $\beta = 0.02$ (Stacey et al., 2000) and $\beta = 0.036$ (Fong and Stacey, 2003), suggesting the turbulence theory produces reasonable estimates of dispersion for a near-field buoyant plume.

However, the underlying assumption of the theory that the motions driving dispersion are found in the inertial subrange, thus turbulence governs lateral dispersion, must be considered. The length-scale model assumes that the plume is dispersed by three-dimensional turbulence structures, i.e., as the plume grows in scale, it is dispersed by progressively larger eddies (Fong and Stacey, 2003). To examine the scale of the dispersive motions in the surface layer, spectral analysis was conducted on velocity observations from the near-surface mooring deployed approximately 1 km downstream of the tailrace discharge point. The spectral fall-off rate varied with frequency (σ). A steep spectral slope of –3 was observed throughout the low-frequency range of the band ($\sigma < f$, where f is the Coriolis frequency) and transitioned to a slope of -5/3 for the higher frequency band ($\sigma > 4f$) (**Figure 13**). The –5/3 slope suggests a mean dominance of turbulence in the surface layer.

In the surface layer of a stratified river plume, the largest eddies scale with the depth of the surface layer due to the strong salinity-induced stratification (McPherson et al., 2019). The vertical velocity fluctuations are constrained to the thickness of the surface layer and, as the width of the plume far exceeds the vertical scales, forces the turbulence to be essentially two-dimensional (in the horizontal plane). The vertical plume scales which correspond to $f = 10^3$ cpd (Tennekes and Lumley, 1972) fall outside of the inertial subrange thus the length-scale assumption is invalid. Therefore, while turbulence is in part responsible for the observed dispersion in the near-field plume region, hence $n = 4/3$ and a $-5/3$ energy spectrum, the lateral dispersion cannot be adequately described by turbulence theory.

5.3.2. Shear Flow Dispersion

An alternative to turbulence-driven dispersion is shear flow dispersion, which also yields a 4/3 power law dependence (Fischer et al., 1979). Shear dispersion arises from vertical mixing acting upon horizontally sheared flow (Taylor, 1953) and has been observed to be an important mechanism of dispersion in lakes and the ocean (LaCasce and Bower, 2000; Stocker and Imberger, 2003; Stevens et al., 2004; Moniz et al., 2014). The flow conditions in the near-field region support shear-flow dispersion, i.e., the strong velocity shear on either side of the plume centreline ($|du/dy| = 10^{-2}$ s^{-1}) highlights the presence of a sheared region between the plume interior and ambient surface layer (**Figure 4B**). These shear regions were most pronounced at 0.2 km from the tailrace discharge point and weakened with distance downstream as the plume decelerated. This deceleration was due to the entrainment of stationary ambient water into the fast-flowing surface layer by enhanced vertical mixing ($\epsilon > 10^{-3}$ W kg^{-1}) which exists throughout the near-field region (McPherson et al., 2020). Thus this combination of processes allows for the existence of shear-flow dispersion (Young et al., 1982).

Estimates of horizontal shear dispersion for a mean flow in the along-channel (x) direction can be derived (Fischer et al., 1979),

$$K_x = 1.5 c_2 (\partial u/\partial y)^2 \kappa_y t_e^2 \quad (6)$$

where $c_2 = 0.037$ (Saffman, 1963), t_e is the elapsed time, and κ_y is the horizontal diffusivity associated with the small-scale motions (Okubo and Ebbesmeyer, 1976). An equivalent expression applies for the across-channel (y) direction. The near-surface flow speeds were estimated from the lateral velocity transects, and estimates of $\kappa_x = 0.3$ and $\kappa_y = 0.2$ m^2 s^{-1} were derived using the GPS drifters. The resultant horizontal along and across-channel shear dispersion coefficients, $K_x = 0.2$ and $K_y = 15.8$ m^2 s^{-1}, respectively, were the same order of magnitude as the empirical estimates of K_x and K_y from drifters and hydrographic transects (**Figure 8**). Furthermore, the magnitude of K_h from the horizontal shear dispersion coefficients was over 90% of the maximum dispersion coefficient from empirical estimates. This suggests that horizontal shear dispersion was the dominant mechanism responsible for the observed lateral dispersion in the surface layer of the near-field plume.

6. SUMMARY

This study presents estimates of the lateral spreading rate of a near-field buoyant plume discharged into the head of a fjord. The plume system is characterised by flow speeds of over 2 ms^{-1}, and strong stratification ($N^2 > 0.1\ s^{-2}$), resulting in enhanced shear which supports the elevated turbulence dissipation rates ($\epsilon > 10^{-3}\ W\ kg^{-1}$) at the base of the surface layer. The plume spreads horizontally at a rate of $db/dx = 0.045$ from the tailrace discharge point to 3 km downstream, which is one order of magnitude weaker than the theoretical spreading rate. This discrepancy is likely attributed to a combination of the enhanced internal stress and the presence of the fjord sidewalls. The vertical mixing at the interface drives a reduction in the density gradient between the dense ambient and freshwater surface layer and slows lateral spreading. The fjord sidewalls create a barotropic pressure gradient which drives a convergence of near-surface flow back toward the center of the fjord and the plume. The enhanced vertical mixing and reduced lateral spreading rates in Deep Cove highlight the interplay between these governing processes in a highly stratified and turbulent near-field plume system, and how their balance determines the ultimate structure and behaviour of the plume.

Results showed good agreement of estimates of plume widths between the cross-plume hydrographic data and estimates derived from a control volume method, while the GPS surface drifters underestimated the plume lateral spreading rate over the initial 2 km by a factor of ~ 10. This discrepancy was the result of a change in the dominance of pressure gradient components with depth. At the near-surface, a strong barotropic pressure gradient drove flow convergence toward the center of the plume and concentrated the drifters in regions of high velocity in the plume core. There, the drifters were dominated by along-channel advection and did not effectively measure lateral processes. Toward the base of the plume, a baroclinic pressure gradient dominated the barotropic component and drove lateral flow divergence at the interface. Further downstream, the barotropic pressure gradient component drove lateral spreading at both the near-surface and base of the plume. Both the control volume and lateral transects measured plume width at the plume base thus captured this lateral spreading.

Empirical diffusion estimates indicated that the lateral dispersion of this near-field plume increased with distance from the source, consistent with scale-dependent dispersion. A turbulence model and shear-flow dispersion model independently corroborated the 4/3 law of dispersion, which indicates that open ocean dispersion theory can be applicable in the near-shore coastal environment where stratification and vertical mixing are elevated. The strong stratification constrains the vertical dispersion of scalars while turbulence, which dominates the surface layer, acts on the strong horizontal shear between the plume interior and ambient surface layer to drive lateral dispersion. Horizontal shear dispersion that was responsible for over 90% of total diffusion within the surface layer. These results can be applied to other estuarine and coastal regimes as dispersion govern the fate of scalars, such as nutrients and contaminants, discharged into the coastal ocean. The presence of the steep fjord sidewalls means that these drivers of lateral spreading can also be applied to constrained systems, such as tidal inlets where tidal forcing produces strong currents in relatively narrow channels.

However, the work also highlights the sensitivity of observational methods to highly energetic systems and the complexity of the interactions between near-field physical processes such as plume mixing, shear and spreading. The combination of observational techniques appears to resolve and isolate lateral plume spreading, and quantify shear-driven dispersion. However, further numerical work is required to determine the relative role that turbulent mixing and lateral boundaries play to constrain the horizontal spreading. Improved understanding of these issues will also enable a better understanding of the behaviour and evolution of the near-field plume, and the ultimate fate and impact of the riverine waters.

DATA AVAILABILITY STATEMENT

The original contributions presented in the study are included in the article/supplementary materials, further inquiries can be directed to the corresponding author/s.

AUTHOR CONTRIBUTIONS

RM, CS, JO'C, and AL collcted the data. AL and JN contributed instrumentation and support to the field campaign, which was planned by RM and CS. RM treated and analysed the data, and wrote the manuscript. RM, CS, and JO'C discussed the results. CS, AL, and JN reviewed the previous drafts of the manuscript. All authors contributed to the article and approved the submitted version.

FUNDING

This research has been supported by the New Zealand Royal Society Marsden Fund (grant no. NIW-1301-2015) and the New Zealand Sustainable Seas National Science Challenge (project no. 4.2.2). The National Institute of Water and Atmospheric Research Strategic Science Investment Fund, and supported by the National Institute of Water and Atmospheric Research (NIWA).

ACKNOWLEDGMENTS

We would like to thank Brett Grant, Mike Brewer, Tyler Hughen, and June Marion, who helped with the 2016 field experiments, and Meridian Energy for providing the tail-race flow data. We thank the Reviewers for their extensive comments which where very helpful in improving the manscript. Bill Dickson and Sean Heseltine from the University of Otago skippered the vessels for the duration of the field campaign. Also thanks to Natalie Robinson for the use and field practice of the GPS drifters.

REFERENCES

Batchelor, G. K. (1950). The application of the similarity theory of turbulence to atmospheric diffusion. *Q. J. R. Meteorol. Soc.* 76, 133–146. doi: 10.1002/qj.49707632804

Batchelor, G. K. (1952). Diffusion in a field of homogeneous turbulence. *Math. Proc. Cambridge Philos. Soc.* 48, 345–362. doi: 10.1017/S0305004100027687

Bowman, M., Dietrich, D., and Mladenov, P. (1999). "Predictions of circulation and mixing in Doubtful Sound, arising from variations in runoff and discharge from the Manapouri power station," in *Coastal Ocean Prediction*, Vol. 56, *Coastal and Estuarine Studies*, ed C. N. K. Mooers (Washington, DC: American Geophysical Union), 59–76.

Chen, F., MacDonald, D. G., and Hetland, R. D. (2009). Lateral spreading of a near-field river plume: Observations and numerical simulations. *J. Geophys. Res.* 114:C07013. doi: 10.1029/2008JC004893

Durand, N., Fiandrino, A., Fraunié P., Ouillon, S., Forget, P., and Naudin, J. J. (2002). Suspended matter dispersion in the Ebro ROFI: an integrated approach. *Contin. Shelf Res.* 22, 267–284. doi: 10.1016/S0278-4343(01)00057-7

Emery, W. J., and Thomson, R. E. (2001). *Data Analysis Methods in Physical Oceanography*. 2nd edn, Amsterdam: Elsevier.

Farmer, D., Pawlowicz, R., and Jiang, R. (2002). Tilting separation flows: a mechanism for intense vertical mixing in the coastal ocean. *Dyn. Atmosph. Oceans* 36, 43–58. doi: 10.1016/S0377-0265(02)00024-6

Fischer, H., List, J., Koh, C., Imberger, J., and Brooks, N. (1979). *Mixing in Inland and Coastal Waters*. New York, NY: Academic Press.

Fong, D. A., and Stacey, M. T. (2003). Horizontal dispersion of a near-bed coastal plume. *J. Fluid Mech.* 489:S002211200300510X. doi: 10.1017/S002211200300510X

Garvine, R. W. (1987). Estuary plumes and Ffonts in shelf waters: a layer model. *J. Phys. Oceanogr.* 17, 1877–1896. doi: 10.1175/1520-0485(1987)017<1877:EPAFIS>2.0.CO;2

Gibbs, M. T. (2001). Aspects of the structure and variability of the low-salinity-layer in Doubtful Sound, a New Zealand fiord. *N. Z. J. Mar. Freshwater Res.* 35, 59–72. doi: 10.1080/00288330.2001.9516978

Hetland, R. D. (2005). Relating river plume structure to vertical mixing. *J. Phys. Oceanogr.* 35, 1667–1688. doi: 10.1175/JPO2774.1

Hetland, R. D. (2010). The effects of mixing and spreading on density in near-field river plumes. *Dyn. Atmos. Oceans* 49, 37–53. doi: 10.1016/j.dynatmoce.2008.11.003

Hetland, R. D., and MacDonald, D. G. (2008). Spreading in the near-field Merrimack River plume. *Ocean Model.* 21, 12–21. doi: 10.1016/j.ocemod.2007.11.001

Horner-Devine, A. R., Jay, D. A., Orton, P. M., and Spahn, E. Y. (2009). A conceptual model of the strongly tidal Columbia River plume. *J. Mar. Syst.* 78, 460–475. doi: 10.1016/j.jmarsys.2008.11.025

Hunt, C. D., Mansfield, A. D., Mickelson, M. J., Albro, C. S., Geyer, W. R., and Roberts, P. J. (2010). Plume tracking and dilution of effluent from the Boston sewage outfall. *Mar. Environ. Res.* 70, 150–161. doi: 10.1016/j.marenvres.2010.04.005

Jones, N. L., Lowe, R. J., Pawlak, G., Fong, D. a., and Monismith, S. G. (2008). Plume dispersion on a fringing coral reef system. *Limnol. Oceanogr.* 53, 2273–2286. doi: 10.4319/lo.2008.53.5_part_2.2273

Kakoulaki, G., MacDonald, D. G., and Cole, K. (2020). Calculating lateral plume spreading with surface Lagrangian drifters. *Limnol. Oceanogr. Methods* 18, 346–361. doi: 10.1002/lom3.10356

Kilcher, L. F., Nash, J. D., and Moum, J. N. (2012). The role of turbulence stress divergence in decelerating a river plume. *J. Geophys. Res. Oceans* 117:C05032. doi: 10.1029/2011JC007398

LaCasce, J. H., and Bower, A. (2000). Relative dispersion in the subsurface North Atlantic. *J. Mar. Res.* 58, 863–894. doi: 10.1357/002224000763485737

Lumpkin, R., Özgökmen, T., and Centurioni, L. (2017). Advances in the application of surface drifters. *Ann. Rev. Mar. Sci.* 9, 59–81. doi: 10.1146/annurev-marine-010816-060641

MacDonald, D. G., and Chen, F. (2012). Enhancement of turbulence through lateral spreading in a stratified-shear flow: development and assessment of a conceptual model. *J. Geophys. Res. Oceans* 117:C05025. doi: 10.1029/2011JC007484

MacDonald, D. G., and Geyer, W. (2004). Turbulent energy production and entrainment at a highly stratified estuarine front. *J. Geophys. Res.* 109:C05004. doi: 10.1029/2003JC002094

MacDonald, D. G., Goodman, L., and Hetland, R. D. (2007). Turbulent dissipation in a near-field river plume: a comparison of control volume and microstructure observations with a numerical model. *J. Geophys. Res.* 112:C07026. doi: 10.1029/2006JC004075

McCabe, R. M., Hickey, B. M., and MacCready, P. (2008). Observational estimates of entrainment and vertical salt flux in the interior of a spreading river plume. *J. Geophys. Res.* 113:C08027. doi: 10.1029/2007JC004361

McCabe, R. M., MacCready, P., and Hickey, B. M. (2009). Ebb-tide dynamics and spreading of a large river plume. *J. Phys. Oceanogr.* 39, 2839–2856. doi: 10.1175/2009JPO4061.1

McPherson, R. A., Stevens, C. L., and O'Callaghan, J. M. (2019). Turbulent scales observed in a River Plume entering a Fjord. *J. Geophys. Res. Oceans* 124, 9190–9208. doi: 10.1029/2019JC015448

McPherson, R. A., Stevens, C. L., O'Callaghan, J. M., Lucas, A. J., and Nash, J. D. (2020). The role of turbulence and internal waves in the structure and evolution of a near-field river plume. *Ocean Sci.* 16, 799–815. doi: 10.5194/os-16-799-2020

Moniz, R. J., Fong, D. A., Woodson, C. B., Willis, S. K., Stacey, M. T., and Monismith, S. G. (2014). Scale-dependent dispersion within the stratified interior on the shelf of northern Monterey Bay. *J. Phys. Oceanogr.* 44, 1049–1064. doi: 10.1175/JPO-D-12-0229.1

Nash, J. D., Kilcher, L. F., and Moum, J. N. (2009). Structure and composition of a strongly stratified, tidally pulsed river plume. *J. Geophys. Res.* 114:C00B12. doi: 10.1029/2008JC005036

O'Callaghan, J. M., and Stevens, C. L. (2015). Transient river flow into a fjord and its control of plume energy partitioning. *J. Geophys. Res. Oceans* 120, 3444–3461. doi: 10.1002/2015JC010721

Okubo, A. (1968). Some Remarks on the importance of the shear effect on horizontal diffusion. *J. Oceanogr. Soc. Jpn* 24, 60–69. doi: 10.5928/kaiyou1942.24.60

Okubo, A. (1971). Oceanic diffusion diagrams. *Deep Sea Res. Oceanogr. Abstracts* 18, 789–802. doi: 10.1016/0011-7471(71)90046-5

Okubo, A., and Ebbesmeyer, C. C. (1976). Determination of vorticity, divergence, and deformation rates from analysis of drogue observations. *Deep Sea Res. Oceanogr. Abstracts* 23, 349–352. doi: 10.1016/0011-7471(76)90875-5

Osadchiev, A. A. (2018). Small mountainous rivers generate high-frequency internal waves in coastal ocean. *Sci. Rep.* 8, 16609. doi: 10.1038/s41598-018-35070-7

Richardson, L. F. (1926). Atmospheric diffusion shown on a distance-neighbour graph. *Proc. R. Soc. A Math. Phys. Eng. Sci.* 110, 709–737. doi: 10.1098/rspa.1926.0043

Roberts, P. J. W. (1999). Modeling mamala bay outfall plumes. I: near field. *J. Hydraulic Eng.* 125, 564–573. doi: 10.1061/(ASCE)0733-9429(1999)125:6(564)

Saffman, P. G. (1963). The effect of wind shear on horizontal spread from an instantaneous ground source. *Q. J. R. Meteorol. Soc.* 89, 293–295. doi: 10.1002/qj.49708938016

Spydell, M., Feddersen, F., Guza, R. T., and Schmidt, W. E. (2007). Observing surf-zone dispersion with drifters. *J. Phys. Oceanogr.* 37, 2920–2939. doi: 10.1175/2007JPO3580.1

Spydell, M. S., Feddersen, F., Olabarrieta, M., Chen, J., Guza, R. T., Raubenheimer, B., et al.. (2015). Observed and modeled drifters at a tidal inlet. *J. Geophys. Res. Oceans* 120, 4825–4844. doi: 10.1002/2014JC010541

Stacey, M. T., Cowen, E. A., Powell, T. M., Dobbins, E., Monismith, S. G., and Koseff, J. R. (2000). Plume dispersion in a stratified, near-coastal flow: measurements and modeling. *Contin. Shelf Res.* 20, 637–663. doi: 10.1016/S0278-4343(99)00061-8

Stevens, C. L., Lawrence, G. A., and Hamblin, P. F. (2004). Horizontal dispersion in the surface layer of a long narrow lake. *J. Environ. Eng. Sci.* 3, 413–417. doi: 10.1139/s04-035

Stocker, R., and Imberger, J. (2003). Horizontal transport and dispersion in the surface layer of a medium-sized lake. *Limnol. Oceanogr.* 48, 971–982. doi: 10.4319/lo.2003.48.3.0971

Stommel, H. (1949). Horizontal diffusion due to oceanic turbulence. *J. Mar. Res.* 8, 199–225.

Taylor, G. (1953). Dispersion of soluble matter in solvent flowing flowly through a tube. *Proc. R. Soc. A Math. Phys. Eng. Sci.* 219, 186–203. doi: 10.1098/rspa.1953.0139

Tennekes, H. T., and Lumley, J. L. (1972). *A First Course in Turbulence* Vol. 58. Cambridge, MA: MIT Press.

Walters, R. A., Goring, D. G., and Bell, R. G. (2001). Ocean tides around New Zealand. *N. Z. J. Mar. Freshwater Res.* 35, 567–579. doi: 10.1080/00288330.2001.9517023

Yankovsky, A. E. (2000). The cyclonic turning and propagation of buoyant coastal discharge along the shelf. *J. Mar. Res.* 58, 585–607. doi: 10.1357/002224000321511034

Young, W. R., Rhines, P. B., and Garrett, C. J. R. (1982). Shear-flow dispersion, internal waves and horizontal mixing in the ocean. *J. Phys. Oceanogr.* 12, 515–527. doi: 10.1175/1520-0485(1982)012<0515:SFDIWA>2.0.CO;2

Conflict of Interest: The authors declare that the research was conducted in the absence of any commercial or financial relationships that could be construed as a potential conflict of interest.

Copyright © 2021 McPherson, Stevens, O'Callaghan, Lucas and Nash. This is an open-access article distributed under the terms of the Creative Commons Attribution License (CC BY). The use, distribution or reproduction in other forums is permitted, provided the original author(s) and the copyright owner(s) are credited and that the original publication in this journal is cited, in accordance with accepted academic practice. No use, distribution or reproduction is permitted which does not comply with these terms.

frontiers in Marine Science

ORIGINAL RESEARCH
published: 11 October 2021
doi: 10.3389/fmars.2021.747191

Freshwater Composition and Connectivity of the Connecticut River Plume During Ambient Flood Tides

Michael M. Whitney[1], Yan Jia[1], Kelly L. Cole[2], Daniel G. MacDonald[3] and Kimberly D. Huguenard[2]*

[1] Department of Marine Sciences, University of Connecticut, Groton, CT, United States, [2] Department of Civil and Environmental Engineering, University of Maine, Orono, ME, United States, [3] Civil and Environmental Engineering, University of Massachusetts Dartmouth, Dartmouth, MA, United States

The Connecticut River plume interacts with the strong tidal currents of the ambient receiving waters in eastern Long Island Sound. The plume formed during ambient flood tides is studied as an example of tidal river plumes entering into energetic ambient tidal environments in estuaries or continental shelves. Conservative passive freshwater tracers within a high-resolution nested hydrodynamic model are applied to determine how source waters from different parts of the tidal cycle contribute to plume composition and interact with bounding plume fronts. The connection to source waters can be cut off only under low-discharge conditions, when tides reverse surface flow through the mouth after max ambient flood. Upstream plume extent is limited because ambient tidal currents arrest the opposing plume propagation, as the tidal internal Froude number exceeds one. The downstream extent of the tidal plume always is within 20 km from the mouth, which is less than twice the ambient tidal excursion. Freshwaters in the river during the preceding ambient ebb are the oldest found in the new flood plume. Connectivity with source waters and plume fronts exhibits a strong upstream-to-downstream asymmetry. The arrested upstream front has high connectivity, as all freshwaters exiting the mouth immediately interact with this boundary. The downstream plume front has the lowest overall connectivity, as interaction is limited to the oldest waters since younger interior waters do not overtake this front. The offshore front and inshore boundary exhibit a downstream progression from younger to older waters and decreasing overall connectivity with source waters. Plume-averaged freshwater tracer concentrations and variances both exhibit an initial growth period followed by a longer decay period for the remainder of the tidal period. The plume-averaged tracer variance is increased by mouth inputs, decreased by entrainment, and destroyed by internal mixing. Peak entrainment velocities for younger waters are higher than values for older waters, indicating stronger entrainment closer to the mouth. Entrainment and mixing time scales (1–4 h at max ambient flood) are both shorter than half a tidal period, indicating entrainment and mixing are vigorous enough to rapidly diminish tracer variance within the plume.

Keywords: river plume, freshwater, tides, tracers, variance, mixing

OPEN ACCESS

Edited by:
Alexander Yankovsky, University of South Carolina, United States

Reviewed by:
Adam Ayouche, Laboratoire de Physique des Océans et de Télédétection par Satellite (LOPS), France
Elizabeth Brasseale, University of California, La Jolla, United States

****Correspondence:***
Michael M. Whitney
michael.whitney@uconn.edu

Specialty section:
This article was submitted to Coastal Ocean Processes, a section of the journal Frontiers in Marine Science

Received: *25 July 2021*
Accepted: *13 September 2021*
Published: *11 October 2021*

Citation:
Whitney MM, Jia Y, Cole KL, MacDonald DG and Huguenard KD (2021) Freshwater Composition and Connectivity of the Connecticut River Plume During Ambient Flood Tides. Front. Mar. Sci. 8:747191. doi: 10.3389/fmars.2021.747191

INTRODUCTION

Rivers deliver terrestrial freshwater, nutrients, sediments, and contaminants to the marine environment (Meybeck, 2003). River plumes influence the physical dynamics, biogeochemistry, ecosystems and fisheries in coastal and open-ocean waters (e.g., Dittmar and Kattner, 2003; Hickey et al., 2010; Grimes, 2001). Due to these manifold effects on the marine environment, it is critically important to continue studying and improving the understanding of river plumes. The structure, mixing, and transport of river plumes has been studied extensively, as described in several research reviews (O'Donnell, 2010; Chant, 2011; Hetland and Hsu, 2013; Horner-Devine et al., 2015). Particular attention has been devoted to the main plume front, a region characterized by strong surface convergence, downwelling, and mixing of the plume with ambient waters (e.g., Garvine, 1974a; Garvine and Munk, 1974; O'Donnell et al., 1998; Marmorino and Trump, 2000; Orton and Jay, 2005). Flow within the plume can overtake the propagating plume front, thereby creating a large intake region of plume waters that interacts with the front (e.g., Garvine, 1974a; Mazzini and Chant, 2016). This connectivity with the front can extend all the way back to the river mouth, can be short-circuited by developing interior fronts, or can be limited by many other processes including tides, winds, ambient currents, and changing source conditions (e.g., McClimans, 1978; Garvine, 1984; O'Donnell, 2010; Chant, 2011; Huguenard et al., 2016; Cole et al., 2020). The degree of connectivity between river source waters and bounding fronts merits further study. The degree of source-front connectivity likely varies considerably for different plumes and forcing situations. The approach of Cole et al. (2020) provides guidance for plume connectivity studies. The transport, mixing, and trapping of pollutants, sediments, nutrients, and plankton within the plume is influenced by when and where source waters reach the plume front. Thus, identifying times and locations of particularly strong or weak source-front connectivity within plumes is important for understanding coastal biogeochemical distributions.

Tides modulate many river plumes. Strong tidal currents within rivers can reverse flow, preventing freshwater from exiting the mouth during river flood tides and intensifying freshwater outflow during ebbs. Two well-studied examples of ebb-pulsed plumes entering ambient environments with weaker tides are the Columbia River (e.g., Cudaback and Jay, 1996; Hickey et al., 1998; Horner-Devine et al., 2009; Nash et al., 2009; Kilcher and Nash, 2010; Akan et al., 2018) and the Merrimack River (e.g., MacDonald et al., 2007; Hetland and MacDonald, 2008; Chen et al., 2009; Kakoulaki et al., 2014; Cole et al., 2020). Ebb-pulse outflows also have been studied for smaller plumes (e.g., Luketina and Imberger, 1987; Pritchard and Huntley, 2006). Other tidal plumes are swept back and forth by strong ambient tidal currents in the receiving waters of the adjacent estuary, sea, or continental shelf (e.g., Spicer et al., 2021). The combination of tidally pulsed outflows through the mouth and swift ambient tidal currents along the coast can cut off plume waters from the river source and create a series of discrete tidal plume pulses (de Ruijter et al., 1997). Two formative examples are the Connecticut River plume (e.g., Garvine, 1974b; Garvine and Munk, 1974; Garvine, 1977; O'Donnell et al., 1998; Ackelson and O'Donnell, 2011; Jia and Whitney, 2019) and the Rhine region of freshwater influence (e.g., van Alphen et al., 1988; Simpson and Souza, 1995; de Ruijter et al., 1997; Hessner et al., 2001). Flow reversals and mixing by strong ambient tides also have been studied for smaller plumes (e.g., Bricker et al., 2006; Basdurak et al., 2020). Plume connectivity and overall behavior in these situations depends on the relative magnitudes of the subtidal mouth outflow velocity, plume propagation speed (scaled by the internal wave speed), and river and ambient tidal current amplitudes as well as the relative phasing of river and ambient tides. These factors influence which portions of the tidal cycle have a plume fed by source waters, a plume starved or cut off from the source, or no plume at all.

The present study investigates the composition of and connectivity within the Connecticut River plume, an important example of plumes influences by strong ambient tides. The Connecticut, named after a Native American word meaning 'on the long tidal river' (Trumbull, 1881), is the largest freshwater source flowing into Long Island Sound (LIS, **Figure 1A**). Average annual discharge (from 2009 to 2019) is 600 m^3/s and average monthly discharge ranges from 1294 m^3/s in April down to 304 m^3/s in September (USGS 01193050, Middle Haddam, CT). The Connecticut River has a tidal salt-wedge estuary with a salinity intrusion that typically extends 5–15 km from the mouth (Meade, 1966; Garvine, 1975; Ralston et al., 2017). The navigational channel is bounded by two jetties (collectively referred to as the Saybrook Jetty) extending beyond the mouth (**Figure 1B**). Planetary vorticity ($f = 9.6 \times 10^{-5}$ s^{-1}) does not exert a strong influence on the mouth outflow, indicated by a large Rossby number associated with the relatively fast outflow velocities O(0.1–1 m/s) through the 1 km wide mouth. Plume waters enter into the ambient macrotidal environment of eastern LIS, where tidal currents are O(1 m/s) with substantial spring-neap variability (O'Donnell et al., 2014). Ambient tides are predominantly rectilinear and shore-parallel near the coast, but have more ellipticity in the deeper waters farther offshore within the Sound (Bennett et al., 2010). Tides advect plume waters eastward during ambient ebbs and westward during flood tides (Garvine, 1974b; Garvine and Munk, 1974). The present study focuses on the plume that forms during ambient flood tides. During this tidal stage, the plume can pass over Long Sand Shoal, which is within 5 km from shore and stretches 10 km westward from the river mouth (**Figure 1B**; Ellis and Gen, 1874; Poppe et al., 2000). Higher river discharge decreases salinities and increases the extent of the plume (**Figures 2A,B**; Garvine, 1974b). After high discharge events (e.g., tropical storm Irene flooding), coherent plumes formed during prior tidal cycles are evident farther offshore (**Figure 2C**; Whitney et al., 2014). Connecticut River water persists in LIS after it is no longer part of a dynamically distinct tidal river plume. Some of its freshwater joins the LIS estuarine outflow and progresses through Block Island Sound onto the continental shelf within several days (Jia and Whitney, 2019). The rest of the Connecticut River water takes longer months-long routes through LIS, where it comprises most of the freshwater residing in the large estuary (Deignan-Schmidt and Whitney, 2018; Jia and Whitney, 2019). Despite

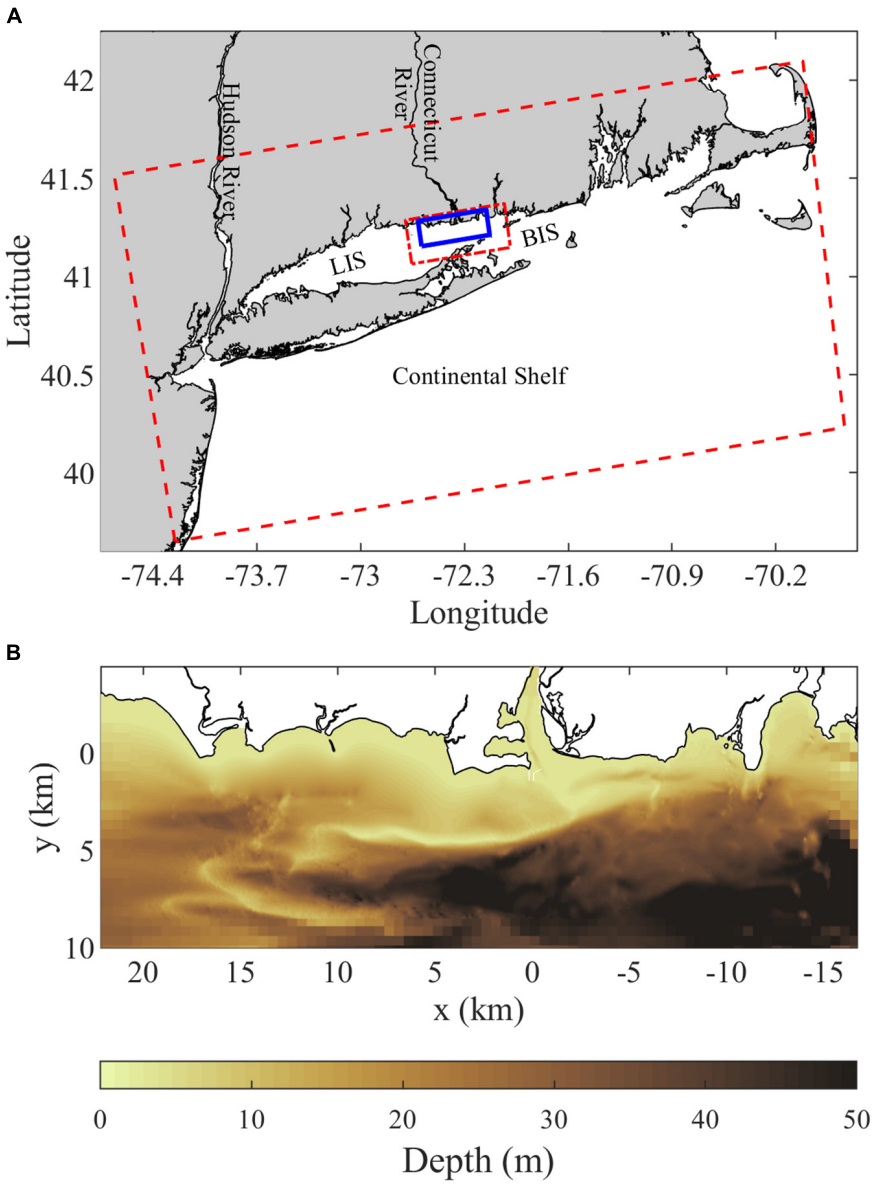


FIGURE 1 | (A) Location map showing the Connecticut River, Long Island Sound (LIS), Block Island Sound (BIS), and the continental shelf along with the outer (dashed red), intermediate (short-long dashed red), and inner highest-resolution (solid blue) grid domains. **(B)** Bathymetry within the inner grid domain, the Saybrook Jetties immediately outside the Connecticut River mouth show as thin white lines and are land points in the model.

the many studies on the Connecticut River plume, the degree of connectivity between the front and the rest of the plume is still unknown. Early models imply connectivity extending from the front all the way back to the river source (Garvine, 1974a; 1984). This high connectivity may be representative of frontal areas near the mouth, such as the upstream front. As the front travels farther from the mouth, however, increasingly large velocities within the plume would be necessary for water to travel from the mouth to the leading edge front before ambient tidal conditions switch from flood to ebb (or vice versa). Thus it is probable that less plume water interacts with the downstream front as the plume grows during a tidal cycle, resulting in relatively weak plume-front connectivity as seen for the Merrimack plume (Cole et al., 2020).

The main objectives of this study on the Connecticut River plume formed during ambient flood tidal conditions are: 1) determining the contributions of river source waters from different parts of the tidal cycle and 2) quantifying the degree and spatial distribution of connectivity of these source waters with the bounding plume fronts. A high-resolution numerical modeling approach is taken. The character of the tidal plume will be described to provide context for the subsequent analysis. Conservative passive freshwater tracers are employed as a key tool for studying plume composition and connectivity. A tracer

variance budget also is applied to describe how the plume entrains waters and is mixed during the tidal cycle. The main case with low discharge during neap tides is compared to other cases with higher discharge and/or spring tides. Results are discussed relative to other plumes in weaker ambient tidal environments to emphasize how strong ambient tides can reshape the plume and patterns of source-front connectivity.

MATERIALS AND METHODS

Model Setup

The Regional Ocean Modeling System (ROMS, Haidvogel et al., 2000, 2008) is applied to model the Connecticut River plume and surrounding waters. ROMS is a free-surface, hydrostatic, primitive-equation model that evolves the governing momentum, mass, and tracer conservation equations in finite-differenced form. The applied advection schemes are 3rd-order upstream for 3D momentum, 4th-order centered for 2D (depth-averaged) and vertical momentum, and the Wu and Zho (2010) 3rd-order scheme for salinity, temperature, and passive tracers. Vertical turbulent viscosity and diffusivity are parameterized with the generic length scale method k-epsilon closure scheme. Note that salinity is calculated with the Practical Salinity Scale, thus reported salinities are dimensionless.

The outer (mother) grid domain includes the tidal extent of the Connecticut River (and other rivers), LIS, Block Island Sound, and a large portion of the adjacent continental shelf (**Figure 1A**). Full details of the outer model configuration are included in Jia and Whitney (2019). The horizontal resolution is 500 m within LIS and vertical resolution is supplied by 30 sigma levels evenly distributed through the water column. Outer model bathymetry is derived from the NOAA 3 arc-second United States Coastal Relief Model. The outer model is forced along the open ocean boundaries with eight semi-diurnal and diurnal tidal coefficients from the OSU TOPEX/Poseidon Global Inverse Solution (Egbert and Erofeeva, 2002) and subtidal velocities, temperatures, and salinities from the Hybrid Coordinate Ocean Model (Chassignet et al., 2008). Chapman (1985) and Flather (1976) boundary conditions are applied for surface elevation and 2D velocities along the open boundaries. Radiation with nudging open boundary conditions are applied for 3D velocities, temperature, and salinity. Surface winds, humidity, air temperature, surface pressure, net shortwave radiation, and downward longwave radiation are supplied by the North American Regional Reanalysis (NARR, Mesinger et al., 2006). Bulk flux formulae (Fairall et al., 2003) are applied within ROMS to compute surface fluxes of momentum and sensible, latent, and longwave heat. Jia and Whitney (2019) describe how the NARR temperatures were modified to better align with NOAA buoy observations. Daily river discharge for the Connecticut and 78 other rivers are derived from USGS streamgage records. Jia and Whitney (2019) validated tidal performance with tidal harmonic analysis at NOAA coastal stations along LIS and with depth-averaged tidal current observations throughout LIS (Bennett et al., 2010).

This study adds a nested intermediate grid with 100 m resolution and an inner grid with 20 m horizontal resolution

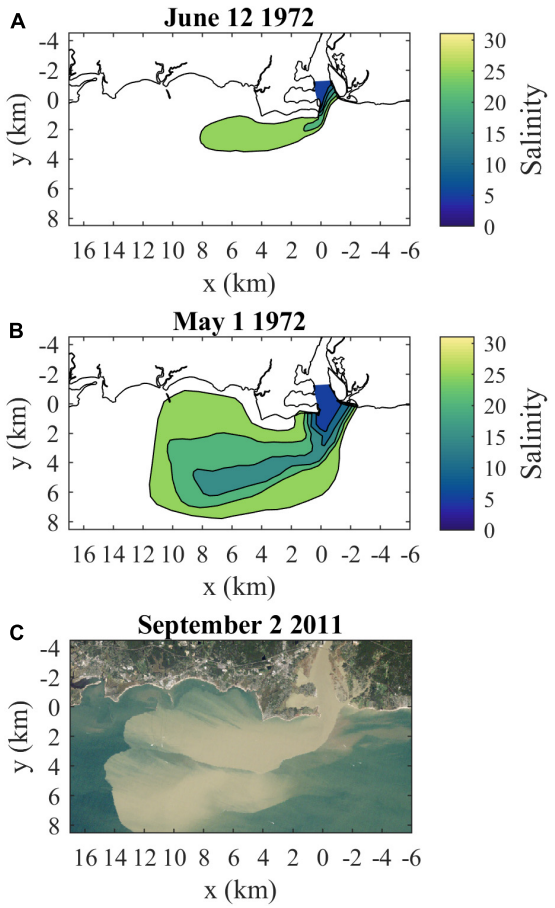


FIGURE 2 | Connecticut River plume observations: **(A)** surface salinities at high slack (near spring tide) for moderate discharge (720 m^3/s) conditions (from Figure 15 in Garvine, 1974b), **(B)** surface salinities at high slack (near neap tide) for high discharge (1580 m^3/s) conditions (from Figure 13b in Garvine, 1974b), and **(C)** a true-color Landsat 5 satellite image coincident with max ambient flood tide (near spring tide) during high discharge (1633 m^3/s) and sediment load from tropical storm Irene (from Figure 2 in Whitney et al., 2014). Discharges in parentheses are daily data from USGS station 01184000 (Thompsonville, CT) multiplied by 1.086 to represent total Connecticut River discharge. The salinity contour interval is 5, as in Garvine (1974b).

covering the lower Connecticut River estuary and the tidal plume region (**Figure 1A**). The nested runs are initialized with a mother grid simulation that spans at least 2.5 years prior to nesting. The nested runs each are evolved for only 1.5 days, these short runs are sufficient to capture the intratidal evolution of the plume. Light wind periods are selected and then wind stress is set to zero to remove all immediate wind influence during the short nested runs. Four cases are analyzed that are combinations of low and high discharge and neap and spring tides. Connecticut River discharge (Q_R) is set at 250 and 1500 m^3/s for low and high discharge cases, respectively. The dates and details of these cases are summarized in **Table 1**. The low discharge and neap tide case is analyzed in greatest detail as it produces the most compact plume and pairs with new observational efforts. Instantaneous fields (in ROMS 'history' files) output at 20-min

TABLE 1 | Comparison of nested model runs: forcing, surface mouth and plume characteristics, and plume-averaged quantities.

	Low-discharge, neap-tide	Low-discharge, spring-tide	High-discharge, neap-tide	High-discharge, spring-tide
Analysis start date (month/day/year)	8/28/2013	8/21/2013	4/6/2014	3/30/2014
Connecticut River Discharge (Q_R, m^3/s)	250	250	1500	1500
Ambient tidal current amp. (U_{Ta}, m/s)	0.75	1.00	0.75	1.25
Ambient tidal excursion (L_{Ta}, km)	10.7	14.2	10.7	17.8
Surface conditions at river mouth				
Tidal current amplitude (V_{Tm}, m/s)	0.70	0.75	0.50	0.65
Tidal-averaged velocity (V_D, m/s)	0.25	0.25	0.80	0.80
Lag from ambient tides (t_{lag}, hour)	3.1	2.1	1.0	1.0
Flow reversal time span (t_{rev}, hour)	4.8	4.9	0	0
Sal. diff., max ambient flood (ΔS_m)	20	16	23	25
Internal wave speed (c_m, m/s)	0.55	0.49	1.32	0.97
Froude number, max river ebb (Fr_m)	1.7	2.0	1.0	1.5
Surface plume characteristics at max ambient flood				
Downstream extent (L_p, km)	8.5	10.0	9.5	11.5
Salinity diff., downstream (ΔS_d)	5	4	14	11
Internal wave speed (c_p)	0.27	0.25	0.46	0.41
Ambient tidal Froude number (Fr_{Ta})	2.7	4.1	1.6	3.1
Velocity, downstream (u_d, m/s)	1.10	1.40	1.10	1.50
Downstream Froude number (Fr_d)	4.0	5.7	2.4	3.7
Downstream front velocity (u_f, m/s)	0.96	0.80	0.90	1.26
Interior water velocity (u_i, m/s)	1.05	1.21	1.00	1.45
Plume-averaged characteristics based on combined tracer field at max ambient flood				
Entrainment velocity (w_e, mm/s)	1.2	2.0	1.0	2.0
Entrainment time scale (T_e, hour)	2.2	1.9	4.1	1.9
Concentration ($\overline{C}$)	0.013	0.004	0.026	0.027
Variance ($\overline{C'^2}$)	0.0019	0.0002	0.0082	0.0069
Rate of variance change (10^{-5} s^{-1})	−0.0483	−0.0074	−0.0714	−0.1526
Mouth variance input (10^{-5} s^{-1})	0.0144	0.0005	0.0655	0.0963
Entrainment of variance (10^{-5} s^{-1})	−0.0220	−0.0026	−0.0511	−0.0899
Mixing of variance ($-M/V_p$, 10^{-5} s^{-1})	−0.0407	−0.0053	−0.0858	−0.1590
Mixing time scale (T_{mix}, hour)	1.3	1.1	2.7	1.2

intervals are analyzed. Results are mapped on an *x*-*y* grid with the origin at center channel of the river mouth, the positive *x* axis is oriented along the coast in the direction of LIS flood tides (approximately west-southwestward), and the positive *y* axis is pointed down-river and offshore (approximately south-southeastward) (**Figure 1**).

Freshwater Tracers and Plume Characteristics

Freshwaters from the Connecticut River are tracked with conservative passive tracers using the tracer routines included within ROMS. The passive tracers are evolved in the Eulerian framework and are akin to continuous dye fields. Tracer concentrations are normalized so that they represent the fraction of the tracked freshwater. Individual freshwater tracers are released at an hourly interval spanning a tidal cycle. Each tracer is imposed as an hour-long release at the up-river boundary of the inner grid (4 km up-river from the mouth) with the same volume flux and freshwater fraction of the Connecticut River waters flowing through the boundary over the release time interval. There are no other interior or boundary tracer sources. There are no tracer sinks; therefore, concentrations of these conservative passive tracers decrease only through dilution. The hourly tracers are summed to create a combined tracer that tracks all the recently discharged Connecticut River freshwater within the plume. Plume waters are identified as including all locations (both horizontal and vertical) outside of the Connecticut River mouth where the combined freshwater tracer concentration exceeds a low threshold value (C_0) set to 10^{-6} for standard analysis. In practice, the plume boundaries change little with an order of magnitude increase or decrease of C_0 because of typically sharp concentration gradients at plume fronts. Plume volume (V_p) and area at the surface (A_p) are calculated within the plume boundaries. The average plume depth (H_p) can be calculated as V_p/A_p. Plume length (L_p) is calculated as the farthest downstream extent of the tracer plume. The plume width (W_p) is reported as the farthest offshore extent of the main plume marked by a sharp surface front and does not include more diffuse tracer waters farther offshore that are included within V_p. Plume perimeter (P_p) is calculated as the total length of the plume boundary at the surface. The composition of plume boundary points in terms of individual freshwater tracers is used to quantify connectivity between the plume fronts and source waters released at different times of the tidal cycle.

Plume volume changes due to the volume flux through the mouth (Q_m, with positive into the plume) and entrainment volume flux into the plume (Q_e, positive into the plume):

$$\frac{dV_p}{dt} = Q_m + Q_e \quad (1)$$

Q_m is calculated as the section integral of the v velocity component through the mouth where there is tracer (with higher concentration than C_0), operationally v is multiplied by a binary coefficient that is set to one if the tracer is present above the concentration threshold and zero otherwise. The instantaneous Q_m can either be into or out of the plume, but represents a net source to the plume overall. The entrainment flux adds water with zero tracer concentration to the plume. V_p, its rate of change dV_p/dt, and Q_m are calculated directly from model output fields and Q_e is solved for as the unknown in (1). The plume-averaged entrainment velocity (w_e) is calculated by dividing Q_e by the plume surface area:

$$w_e = \frac{1}{A_p}\left(\frac{dV_p}{dt} - Q_m\right) \quad (2)$$

Note that, despite the suggestive notation, entrainment does not have to occur exclusively through vertical velocities; entrainment velocities are locally normal to plume boundaries. The analysis is completed with the combined tracer to represent conditions for the entire plume. Individual hourly tracer fields identify the plume regions associated with source waters distinguished by river release time. Thus, corresponding analysis of individual hourly tracers indicates the entrainment within different parts of the plume.

Freshwater Tracer Variance Budgets

Analysis of salinity variance has been applied to studying mixing in estuaries and coastal waters (e.g., Burchard and Rennau, 2008; Li et al., 2018; MacCready et al., 2018; Wang and Geyer, 2018; Burchard, 2020; Warner et al., 2020). Analogous tracer variance analysis is applied to the freshwater tracers described above. The first step is decomposing tracer concentration (C) into a spatial-mean value ($\overline{C}$) and deviations from the mean (C') such that $C = \overline{C} + C'$. The tracer variance is defined as $\left(C - \overline{C}\right)^2$ which equals C'^2. The spatial mean may be taken over a fixed volume (e.g., an estuary or part of a continental shelf) or a time-varying volume tracking a water mass (e.g., a river plume). Most prior published examples analyze fixed volumes extending throughout the water column, whereas the present analysis considers expanding control volumes encompassing river plumes. In this application, the plume control volume (V_p) is the region with freshwater tracer concentrations above the threshold value ($C_0 = 10^{-6}$, as described above). The control volume only extends throughout the water column where the plume interacts with the bottom, otherwise there is a sub-surface interface between plume and ambient waters. The plume-averaged concentration ($\overline{C}$) is calculated as:

$$\overline{C} = \frac{1}{V_p}\int C\, dV_p \quad (3)$$

Following MacCready et al. (2018), the volume-integrated tracer variance budget is:

$$\frac{d}{dt}\int C'^2 dV_p = -\int u_n C'^2 dA_b - \int 2K(\nabla C')^2 dV_p \quad (4)$$

where, u_n is the outward normal velocity through the bounding area (A_b) of the control volume, K is the eddy diffusivity, and $\nabla C'$ is the concentration gradient. K is written as a scalar in (4) for simplicity (as in MacCready et al., 2018), but a more detailed representation involves a diagonal diffusivity tensor with different horizontal and vertical eddy diffusivities (e.g., Li et al., 2018). Alternately, horizontal diffusion is sometimes considered negligible and only vertical diffusion is included (e.g., Warner et al., 2020). The final integrand in (4) represents the tracer mixing per unit volume; it is symbolized with χ in some prior studies (e.g., Wang and Geyer, 2018; Burchard, 2020). The term on the left-hand side of (4) can change both because of tracer variance changes and plume volume changes. The first term on the right-hand side of (4) is the advective transport of variance through the control volume boundaries. Note that (4), does not include a term representing diffusive transport of tracer variance across the boundary between the plume and ambient waters. This diffusive transport is implicitly considered negligible relative to advective transport in (4), but the diffusive transport of tracer variance is considered in other studies (e.g., Burchard, 2020; Wang et al., 2021). The final term in (4) is the dissipation of variance by mixing inside the control volume; it can be symbolized as $-M$ for 'mixing'; M is positive definite. The M notation follows MacCready et al. (2018) except in that study M is a tidal-averaged quantity, whereas here it is tidally varying. In the present application, M is calculated (as described below) such that it includes vertical and horizontal physical mixing as well as numerical diffusion arising from discretization errors associated with the advection scheme (Burchard and Rennau, 2008).

For the plume control volume, transport through the plume boundaries can be partitioned into contributions through the river mouth and by plume entrainment. The mouth will tend to have higher concentrations than the plume and therefore have a strong tracer variance signature. With an outflow through the mouth cross-sectional area (A_m) and into the tracer plume, the velocity through the mouth (v_m) is positive and adds both volume and tracer variance to the plume. Entrained water comes from outside the tracer plume and its tracer concentration equals the low threshold value (C_0). The corresponding variance of entrained water is $C'^2_e = \left(C_0 - \overline{C}\right)^2$ and the entrainment tracer variance flux is $C'^2_e Q_e$, a positive flux. Substituting this information into (4), the volume-integrated tracer budget for the tracer plume is:

$$\frac{d}{dt}\int C'^2 dV_p = +\int v_m C'^2 dA_m + C'^2_e Q_e - M \quad (5)$$

Note that, $C_0 \ll \overline{C}$ since an exceedingly small C_0 has been selected (i.e., the entrained water has nearly zero tracer concentration) and $C'^2_e \approx \overline{C}^2$. Therefore, the entrainment tracer variance flux is approximately $\overline{C}^2 Q_e$. This approximation is used

when describing results and discussing generalization of tracer variance budgets for other plumes. In summary, (5) indicates that river inputs and entrainment both increase volume-integrated variance, while mixing within the plume reduces it.

Analyzing the volume-averaged (rather than volume-integrated) budget provides a different perspective that isolates changes in tracer variance and facilitates intercomparison of results for different plumes. A first step is defining the volume-averaged variance:

$$\overline{C'^2} = \frac{1}{V_p}\int C'^2 dV_p \tag{6}$$

With this definition, the term on the left-hand side of (5) can be expressed as the time derivative of the product of the volume-averaged variance and plume volume (7, the intermediate step). Then the product rule for derivatives can be applied and the plume volume budget (1) can be substituted to separately show the contributions associated with changing volume-averaged tracer variance, mouth volume inputs, and entrained volume flux (7).

$$\frac{d}{dt}\int C'^2 dV_p = \frac{d}{dt}\left(\overline{C'^2}V_p\right) = V_p\frac{d}{dt}\overline{C'^2} + \overline{C'^2}Q_m + \overline{C'^2}Q_e \tag{7}$$

It also is useful to define the flux-weighted average tracer variance at the mouth:

$$C'^2_m = \frac{1}{Q_m}\int v_m C'^2 dA_m \tag{8}$$

With this definition, the first term on the right-hand side of (5) can be expressed as:

$$\int v_m C'^2 dA_m = C'^2_m Q_m \tag{9}$$

Dividing the volume-integrated tracer variance budget (5) by V_p and substituting in expressions from (6), (7), (8), and (9) yields the volume-averaged tracer variance budget:

$$\frac{d}{dt}\overline{C'^2} = +\left(C'^2_m - \overline{C'^2}\right)\frac{Q_m}{V_p} + \left(C'^2_e - \overline{C'^2}\right)\frac{Q_e}{V_p} - \frac{M}{V_p} \tag{10}$$

It can be seen from this balance that a volume source from the mouth tends to increase plume-averaged tracer variance as long as there is higher variance at the mouth ($C'^2_m/\overline{C'^2} > 1$), as would be the case for high-concentration source waters. Since C'^2_e is approximately $\overline{C}^2$ for small C_0, entrainment will tend to increase plume-averaged tracer variance when the variance is smaller than plume-averaged concentration squared ($\overline{C'^2}/\overline{C}^2 < 1$); otherwise $\overline{C'^2}/\overline{C}^2 > 1$ and the entrainment term is negative and tends to decrease $\overline{C'^2}$. The mixing term is simply divided by V_p and remains negative as it represents the internal destruction of tracer variance. The relationship between (5) and (10) is similar to the relationship between heat and temperature budgets in the sense that any net advective inflow will increase heat and volume-integrated tracer variance yet the same inflow can either increase or decrease temperature and volume-averaged tracer variance depending on whether the inflow has higher or lower scalar values than the control-volume average. Both perspectives are useful, but the volume-averaged budget (10) is analyzed in this study to focus on tracer variance changes.

The model provides the information to directly calculate all terms in tracer variance balances (5) and (10). The computational approach in this study applies model results to directly calculate all but the final term in (5) and (10). Then M is solved as the unknown in (5) and divided by V_p for the final term in (10). This calculation method for M ensures that the tracer variance budget closes exactly and that M represents the total mixing in the model, which includes physical mixing and numerical mixing from advection scheme discretization errors. Analyzing the combined tracer fields provides the tracer variance budget associated with the entire active plume. Analyzing individual hourly tracers indicates the tracer variance budgets of plume regions associated with different source waters, distinguished by river release time.

RESULTS

Salinity and Velocity

For the standard case with low discharge and neap tides, the along-estuary currents in LIS (2 km east of the river mouth within 4 km from shore) indicate the ambient LIS tidal amplitude (U_{Ta}) is 0.75 m/s (**Figure 3A**). With the time origin at the onset of ambient flood tide the time-varying ambient velocity (u_a) can be approximated as:

$$u_a = U_{Ta}\sin\left(\frac{2\pi}{T}t\right) \tag{11}$$

where, t is time, T is the tidal period (12.42 h for the dominant semidiurnal lunar tides), and u_a is positive during flood tide. The corresponding ambient tidal excursion ($L_{Ta} = U_{Ta}T/\pi$) is 10.7 km.

The surface flow is outward through the mouth for much of the tidal cycle (**Figure 3A**). The tidal-averaged surface velocity at the mouth (V_D, following the notation in de Ruijter et al., 1997) is 0.25 m/s and the mouth tidal amplitude (V_{Tm}) is 0.70 m/s. The V_D/V_{Tm} ratio is 0.36 and meets the $V_D/V_{Tm} < 1$ 'pinching off criterion' for flow reversal at the mouth and shutoff of plume source waters (de Ruijter et al., 1997). The surface velocity at the mouth (v_m) can be approximated as the combination of the steady flow and sinusoidal tidal variations:

$$v_m = V_D - V_{Tm}\sin\left(\frac{2\pi}{T}(t - t_{lag})\right) \tag{12}$$

where, t_{lag} it the lag time of the mouth tides relative to ambient tides, such that a positive lag indicates ambient flood leads the mouth flood tide. Note that v_m is negative while the flood tide reverses the flow to inward through the mouth. The ambient flood tides lead mouth flood tides by approximately $\frac{1}{4}$ of the tidal cycle for this model run (**Figure 3A**, t_{lag} = 3.1 h). As found in de Ruijter et al. (1997), trigonometric investigation of (12) indicates the mouth flow reversal time span (t_{rev}) is:

$$t_{rev} = \frac{T}{\pi}\text{acos}\left(V_D/V_{Tm}\right) \tag{13}$$

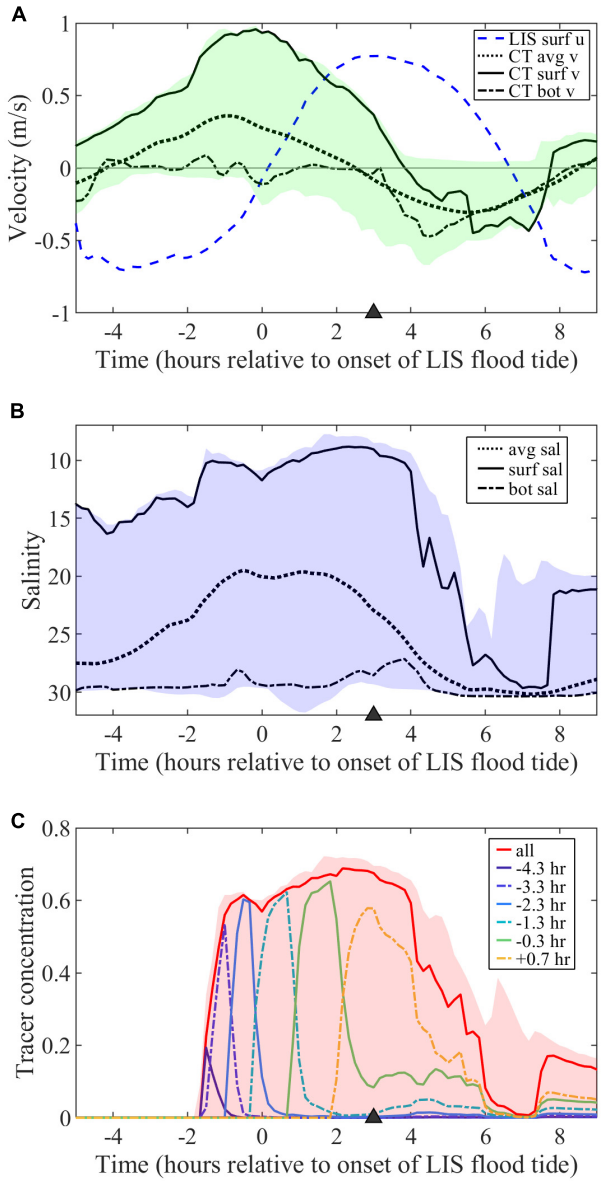


FIGURE 3 | (A) Time series of along-estuary velocity (u, positive for LIS flood tides) at surface in LIS and depth- (avg), surface- (surf), and near-bottom- (bot) averaged across-estuary velocities (*v*, positive out of mouth) through the Connecticut (CT) River mouth. Shading indicates the *v* range over the mouth cross-section. **(B)** Depth-, surface-, and near-bottom-averaged salinities at the mouth with shading indicating the mouth salinity range. **(C)** Surface freshwater tracer concentrations at the mouth for hourly tracers (labeled according to first release times) and the combination of all hourly tracers (labeled 'all') along with the combined tracer range. The triangle (here and in other figures with time series) marks the timing of the max ambient flood surface maps and sections in subsequent figures.

For this low-discharge neap-tide case, t_{rev} is 4.8 h; indicating the plume is cut off from source waters for at least 38% of the tidal cycle. Since this study focuses on plumes during ambient flood tides, it is useful to express the time interval when there is a mouth reversal during ambient flood tides. With equations (11), (12), and (13), this mouth-reversal during ambient-flood time interval can be expressed as:

$$\max\left(0, \frac{T}{4} + t_{lag} - \frac{t_{rev}}{2}\right) < t < \min\left(\frac{T}{2}, \frac{T}{4} + t_{lag} + \frac{t_{rev}}{2}\right) \quad (14)$$

For this model run, flow at the mouth is reversed throughout late ambient flood beginning at $t = (T\text{-}t_{rev})/2$ (t = 3.8 h). This indicates the plume is fed by source waters during early and max ambient flood tides, but is cut off from the source during late flood.

Mouth surface-averaged salinity falls from 14.0 to 8.8 throughout mouth ebb tides, then increases to 29.6 near the end of mouth flood (**Figure 3B**). Bottom-averaged salinities at the mouth remain salty throughout the tidal cycle (27.2–30.4). By the end of mouth ebb, which corresponds to max ambient flood, the bulk vertical salinity difference (ΔS_m, between surface- and bottom-averaged values) is 19.5. The corresponding bulk density difference ($\Delta\rho_m$) can be approximated as $\rho_o\beta\Delta S_m$ (with reference density ρ_o and haline-contraction coefficient $\beta = 7.7 \times 10^{-4}$) using a salinity-based linear equation of state. The scale for the first-mode internal wave speed at the mouth (c_m) is $(g'h_m)^{1/2}$, where $g' = g\Delta\rho_m/\rho_o$, g is gravitational acceleration (9.8 m/s^2), and h_m is the upper-layer thickness scale. With the $\Delta\rho_m$ expression, $c_m = (g\beta\Delta S_m h_m)^{1/2}$. For ΔS_m = 20.0 and h_m = 2 m (representative of mouth conditions), c_m = 0.55 m/s. The internal Froude number associated with the mouth surface outflow is $Fr_m = v_m/c_m$. The outflow is supercritical during most of mouth ebb with Fr_m reaching 1.7 at max ebb, which is coincident with the onset of ambient flood tide. During early ambient flood tide, Fr_m transitions from supercritical to subcritical prior to mouth flow reversal near max ambient flood.

Near the start of ambient flood tide, the plume has expanded 6 km outward from the mouth with a western (downstream, relative to ambient flood tidal flow) bias in lower salinities, higher velocities, and sharper boundaries (**Figure 4A**). The flow of low-salinity source waters is bifurcated by Saybrook Jetty outside the mouth and bifurcation effects are evident out to the plume boundary. The lowest salinities on the eastern (upstream) side are within 2 km from the mouth, but more diffuse plume waters associated with the prior ambient ebb extend to 5 km eastward along the coast. The sharp boundary on the downstream side bends around farther offshore and the highest velocities (0.9 m/s) and lowest salinities (20) are near the middle of this front. The Froude number in the downstream frontal zone (Fr_d) exceeds two, for ΔS_d = 8.5 and h_d = 2 m, indicating supercritical flow. Two hours later at max ambient flood (**Figure 4B**), the plume stretches 8 km downstream ($L_p > L_{Ta}/2$), extends 4.5 km offshore, has higher salinities than before, and remains connected to source waters. Velocities within the plume increase downstream from 0.7 to 1.1 m/s and are predominantly westward except the offshore flow near the mouth. The plume is supercritical, the plume internal wave speed (c_p) is 0.27 m/s and Fr_d = 4.0 with ΔS_d = 5.0 and h_d = 2 m. The sum of c_p and U_{Ta} is consistent with the total plume velocity near the downstream front, indicating plume propagation is superimposed on the ambient currents. The upstream front near the mouth has the sharpest salinity contrast and the ambient flood flow (0.75 m/s) converges with

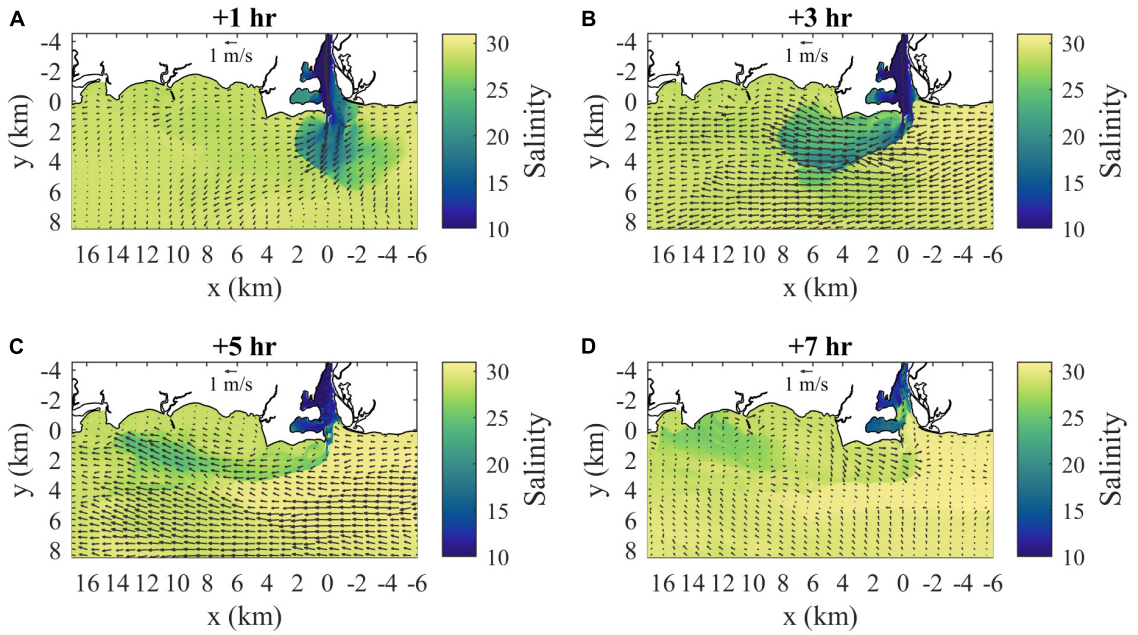


FIGURE 4 | Surface velocity (arrows) and salinity (shaded) maps for **(A)** 1 h, **(B)** 3 h, **(C)** 5 h, and **(D)** 7 h after the onset of ambient flood tide. Velocity arrows are shown for every 40th point (800 m spacing) and every 20th point (400 m spacing) in *x* and *y*, respectively.

the offshore plume flow. The propagation of the upstream front has been arrested by the opposing tidal flow because the Froude number associated with ambient tides ($Fr_{Ta} = U_{Ta}/c_p$) exceeds one. Plume salinities increase downstream along the offshore boundary, but remain lower than inshore. The downstream front is clearly defined and the plume overtakes the slower ambient waters. Two hours later during late ambient flood (**Figure 4C**), the plume has extended to 14 km from the mouth (farther than L_{Ta}) and is bending toward the coast. Flow is reversed at the mouth and velocities increase along the plume to 0.9 m/s near the downstream front, approximately double the weakening ambient tidal flow. The plume, now cut off from source waters, has higher salinities than before and the lowest salinities are in a partially disconnected area (7–14 km downstream), where the minimum salinity is 24.2. The plume remains supercritical, with Fr_d exceeding three for $\Delta S_d = 4.5$ and $h_d = 2$ m. Two hours later as ambient tides switch to ebb (**Figure 4D**), the freshwater supply still is cut off and the remnants of the plume are evident. In the plume area, the salinity difference has diminished ($\Delta S_d < 2.0$) and velocities have reversed with the tides.

Velocities and salinities at max ambient flood tide are examined in further detail in **Figures 5**, **6**, respectively. With a closer view of surface conditions (**Figures 5A**, **6A**), the main plume and ambient flow features can still be seen and a secondary more diffuse plume farther offshore (from $y = 4.5$ to 8 km) with a convergent downstream front is evident. The mouth velocity field (**Figure 6B**) indicates the outflow is within 1–2 m from the surface where salinities are lowest (**Figure 5B**). There is stratification throughout the channel water column. The nearfield section shows the sharp offshore salinity front (**Figure 5C**) which has strong convergence of the cross-shore flow (**Figure 6C**). The surface-intensified freshwater layer increases thickness from the coast out to the offshore front, contrary to large-scale buoyancy-driven plumes (e.g., Yankovsky and Chapman, 1997). The salinity front is farther offshore and not as sharp in the farfield section (**Figure 5D**), but there is still strong flow convergence (**Figure 6D**). The freshwater layer plunges deeper just inshore of Long Sand Shoal, likely due to plume interaction with bathymetry along the shoal.

Freshwater Tracers

Surface concentrations of freshwater tracers at the mouth (**Figure 3C**) show the pulses associated with hourly tracer releases. Peak concentrations range from 0.20 to 0.65; the hourly tracers with the highest peak concentrations (>0.60) are mixed less within the river estuary before reaching the mouth. The tracers that first appear at the mouth during early mouth ebb (late ambient ebb) were released during late river flood. Concentrations peak at the mouth about an hour after peaking at the release point 4 km upriver. The final tracer appearing at the mouth was released during late river ebb (early ambient flood). Despite all being imposed as hour-long pulses, the time interval of elevated concentrations at the mouth increases substantially for each subsequent tracer. The combined tracer increases during late ambient ebb, remains high through max ambient flood, and drops through late ebb.

By max ambient flood the plume is composed of a variety of source waters, mostly originally released in the river during ambient ebb tide (**Figure 7A**). Average freshwater ages are calculated as the time interval between the average tracer release time at each location (determined by the concentration-weighted average of all tracers) and the mapped time (3 h into ambient

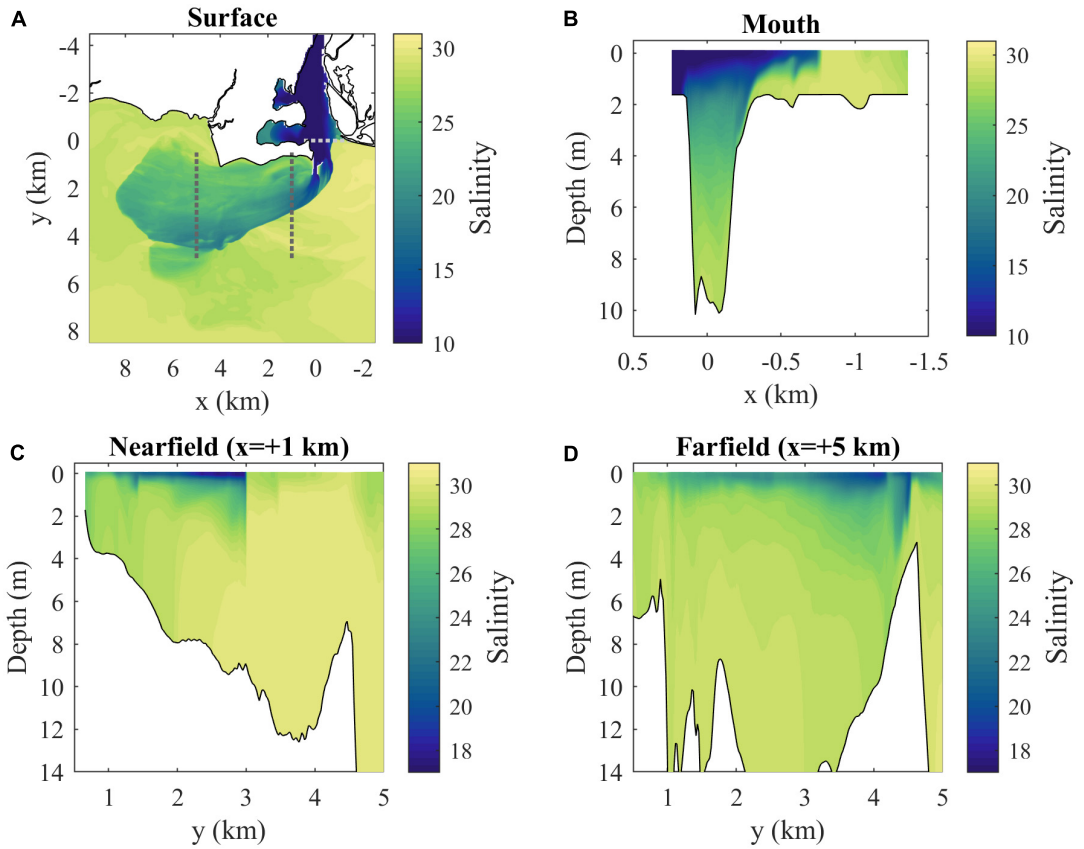


FIGURE 5 | (A) Surface salinity map with locations of cross-sections (dotted lines) and **(B)** mouth, **(C)** nearfield, and **(D)** farfield salinity sections at max ambient flood (3 h after onset of LIS flood tide).

flood). Freshwater age increases along the plume, with the oldest water (with earliest release time) at the downstream tip. The offshore secondary plume has the oldest waters, indicating it is a relic of the prior ebb plume. Overall, the upstream plume boundary has the youngest freshwater, the downstream boundary has the oldest, and the offshore and inshore boundaries have a downstream progression from younger to older waters. The mouth section (**Figure 7B**) indicates the outflowing surface layer has the youngest waters. The nearfield section (**Figure 7C**) shows age decreases toward the offshore front with some vertical variability, whereas the farfield section (**Figure 7D**) shows less spatial variability in water age.

Higher combined tracer concentrations correspond to lower salinity, so surface concentrations highlight the same plume patterns (**Figure 8A**) as the surface salinity field (**Figure 5A**). The texture of plume composition is better seen with maps of the hourly tracers. By max ambient flood, the two tracers introduced during late river flood and exiting the mouth in late ambient ebb (**Figure 8B**) either are in the secondary offshore plume (a relic of the prior ebb plume) or have been incorporated in the new flood plume. Concentrations increase from <0.001 at the mouth to 0.05 toward the downstream front. These source waters are mostly disconnected from the mouth at this time, but some tracer remains trapped in coves along the river. The two early river ebb tracers, exiting the mouth from late ambient ebb into early ambient flood, (**Figure 8C**) are distributed throughout the plume and tend to increase in concentration from 0.02 along the coast to 0.12 toward the offshore front. The tracers introduced later in river ebb (**Figure 8D**) enter the plume later in ambient flood. These tracers are present in highest concentrations (>0.30) near the mouth, particularly along the arrested upstream front, and extend only halfway downstream into the plume. Overall, the downstream half of the plume only includes source waters introduced from late river flood to early river ebb, while the upstream half is composed of a greater variety of source waters with the late river ebb waters at highest concentrations. It is evident that all tracers interact with some portions of the plume boundaries, but the downstream front only sees older waters.

The plume perimeter grows linearly over the ambient flood tidal cycle (**Figure 9A**). The perimeter of each individual tracer field also approximately grows linearly with time, but the growth rate decreases for later tracers. How much each tracer interacts with plume fronts is quantified by the percent of the plume boundary with each hourly tracer present (**Figure 9B**). Each tracer goes through an initial period (lasting 1.5 to 3 h) of increasing interaction with plume boundaries. Frontal connectivity is highest for the oldest waters (present when the early ambient flood plume forms), with prevalence at the front

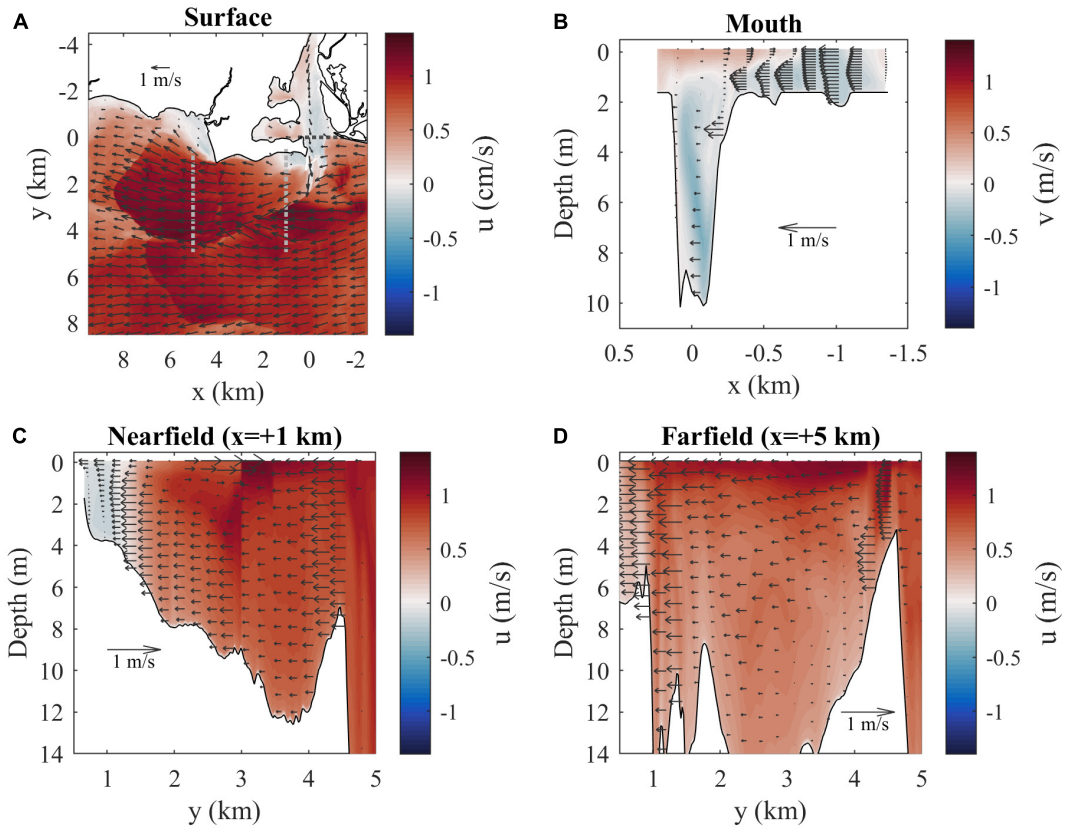


FIGURE 6 | (A) Surface velocity map (u is shaded and arrows indicate horizontal velocity vectors) with locations of cross-sections (dotted lines). Velocity arrows are shown for every 40th point (800 m spacing) and every 20th point (400 m spacing) in *x* and *y*, respectively. **(B)** Mouth, **(C)** nearfield, and **(D)** farfield velocity sections (flow through sections is shaded and arrows indicate the horizontal velocity component across sections) at max ambient flood. Horizontal spacing for velocity arrows is every 8th point (160 m) across the mouth and every 12th point (240 m) across the other sections. Vertical spacing for arrows is every other vertical grid point.

exceeding 80%. Frontal connectivity is lowest for the youngest waters (entering as the ambient flood progresses), which interact with only 20% of the plume front. Overall, frontal connectivity is proportional to water age.

Tracking the perimeter allows for analysis of downstream front advancement relative to ambient and interior plume waters. At max ambient flood, the downstream front advance velocity (u_f) is 0.96 m/s, which is 0.21 m/s faster than U_{Ta} and is 94% of $U_{Ta}+c_p$. The interior water (the leading edge of the −0.3 h tracer release, **Figure 8D**) advance velocity (u_i) is 1.05 m/s, which is 0.09 m/s faster than the downstream plume front is advancing. Thus, the plume front is overtaking ambient water while interior waters are more gradually closing the gap at relative velocity u_i - u_f. The interior waters, however, are not traveling quickly enough to reach the downstream plume front by the end of ambient flood.

Plume volume (**Figure 10A**) grows at an increasing rate over time throughout ambient flood tide, reflecting a combination of plume lengthening, widening, and deepening. As for perimeters, the volumes and increase rates of individual tracers are higher for earlier tracer releases than later ones. Following (1), plume volumes increase only due to entering source waters and entraining ambient waters. After source inputs are shutoff (when $Q_m = 0$), plume volume exponentially increases due only to entrainment with an e-folding time scale (T_e) equal to the average plume depth divided by the entrainment velocity:

$$T_e = H_p/w_e \tag{15}$$

Since $H_p = V_p/A_p$ and $w_e = Q_e/A_p$, T_e also can be expressed as V_p/Q_e. Note that T_e can be time variable, as both the entrainment velocity and plume depth can vary. Plume-averaged entrainment velocities, calculated with (2), are 0.7–2.0 mm/s with variability during the tidal cycle (**Figure 10B**). Most of the tracers have entrainment velocities within about the same range (0.7–2.3 mm/s), indicating a similar entrainment efficiency to each other and the plume as a whole. The younger waters included in the latest two tracer releases have notably higher peak entrainment velocities (3.3–3.8 mm/s). Since these younger waters are concentrated in the upstream half of the plume (**Figure 8D**), the result indicates more vigorous entrainment in the nearfield plume. The linear increase in average plume depth over time (not shown) results in a linear increase in plume entrainment time scale (T_e) from 1 to 6 h from the onset to the end of ambient flood tides, so plume volume exponentially increases at a slower rate over time.

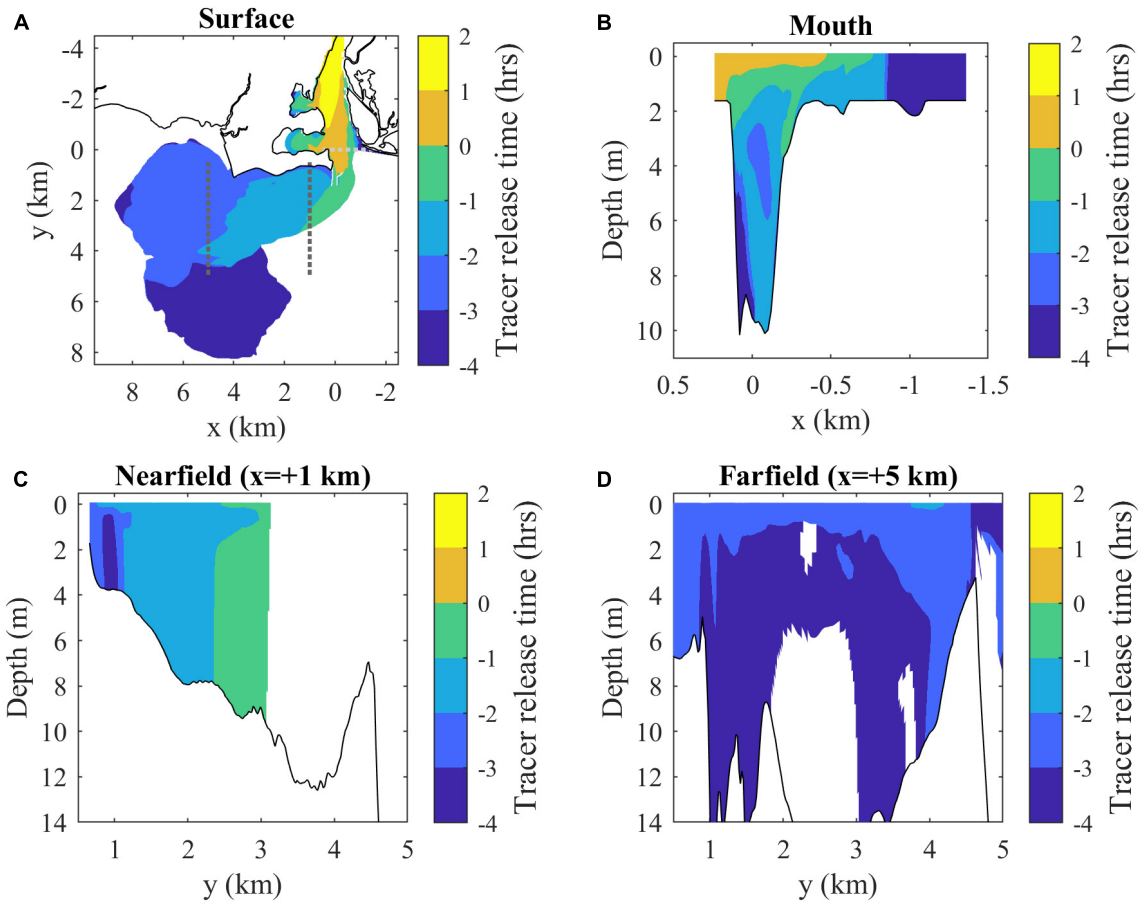


FIGURE 7 | (A) Surface map and **(B)** mouth, **(C)** nearfield, and **(D)** farfield sections of average freshwater composition indicated by average release times of tracers present in each location at max ambient flood. Tracer release times are expressed relative to the onset of ambient flood tides (as in **Figure 3**). Average freshwater age can be calculated by subtracting the average release times from 3 h (the mapped time). Shaded contouring only includes locations where the combined tracer concentration is above the $C_0 = 10^{-6}$ threshold.

Volume-averaged tracer concentrations within the plume ($\overline{C}$, **Figure 11A**), calculated with (3), initially increase (for 0.5–1 h) due to source water supply and then decrease due to dilution by continued entrainment of ambient waters. Peak plume-averaged concentrations range from 0.035 to 0.085, with a 0.060 peak for the combined tracer. Concentrations exponentially decay at the same rate (set by T_e) at which plume volume increases. Note that the decay in concentrations is only due to dilution, as the conservative nature of these tracers precludes imposed exponential tracer loss or other interior tracer sinks. By the end of ambient flood, average tracer concentrations decrease to <0.004, which are $<5\%$ of their peak average concentrations and $<0.4\%$ of the undiluted unit concentration. Thus, entrainment leads to a voluminous but highly diluted plume by the end of ambient flood tide.

Freshwater Tracer Variance Budgets

The freshwater tracer variance budgets assess how source water inputs, entrainment, and mixing affect plume evolution over time. The analysis is completed over the expanding plume control volume, defined as the region where the combined freshwater tracer concentrations exceed the threshold value ($C_0 = 10^{-6}$). The plume control volume boundaries are shown in **Figures 7**, **8A**. At the mouth (**Figure 7B**) and in the nearfield (**Figure 7C**), the control volume extends throughout the water column. Farther downstream (**Figure 7D**), the plume does not reach the bottom in all locations. Volume-averaged tracer variances ($\overline{C'^2}$, **Figure 11B**) follow patterns similar to volume-averaged tracer concentrations (**Figure 11A**), with an initial increase pattern and a long decay period through the rest of the tidal cycle. Peak tracer variances range from 0.002 to 0.021 and are two to three times larger than the corresponding squared peak concentration values (i.e., $\overline{C'^2}/\overline{C}^2 > 1$). By the end of ambient flood tide, tracer variances decrease to $<10^{-4}$, which are $<1\%$ their peak concentrations.

The volume-averaged tracer variance budgets (10) track how $\overline{C'^2}$ changes. The rate of change for the combined tracer variance (**Figure 12A**) is positive with a peak during the initial period of concentration and variance increase (**Figure 11**) and then is negative with smaller magnitude during the longer decay period. Mouth input (**Figure 12B**) is the single largest term and the only

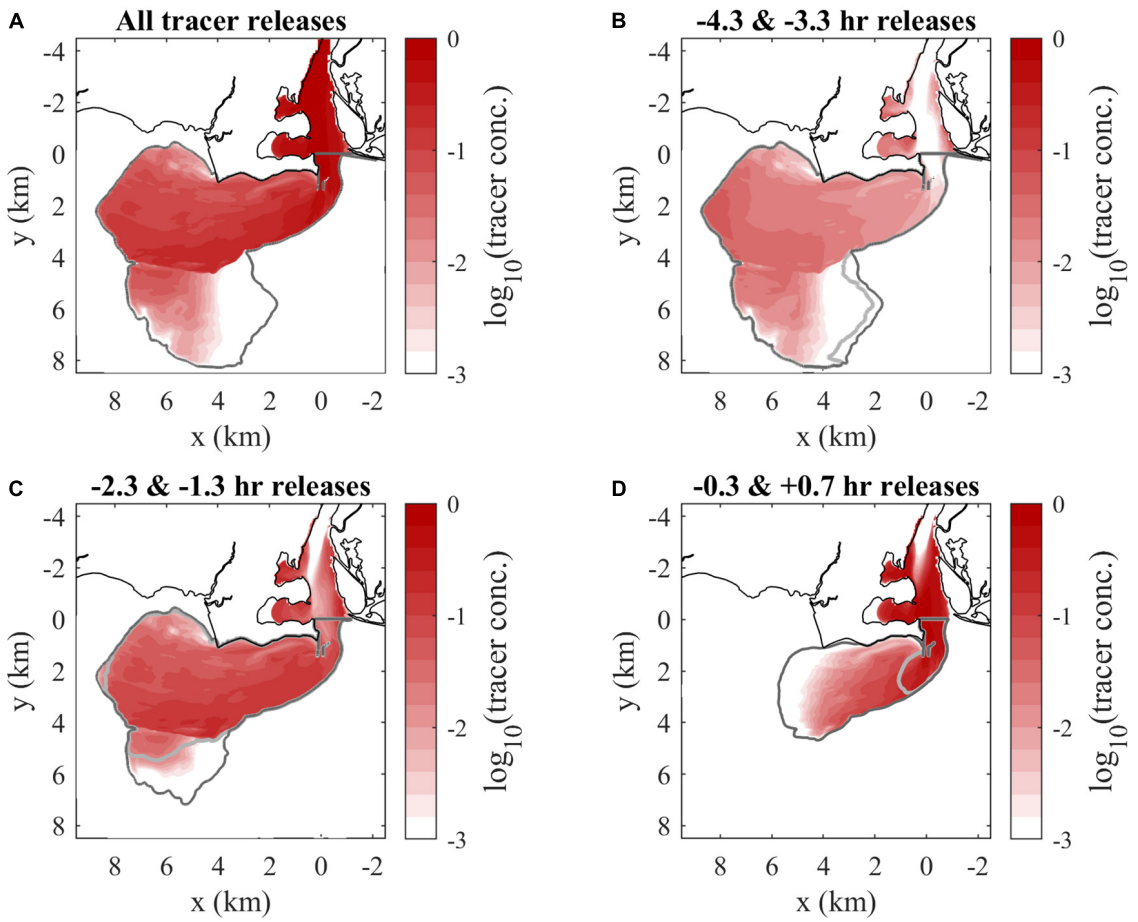


FIGURE 8 | Surface tracer concentration maps at max ambient flood of **(A)** the combination of all hourly tracers, **(B)** late river flood releases, **(C)** early river ebb releases, and **(D)** max and late river ebb releases. Tracers are designated by first release times (relative to the onset of ambient flood tide). The darker and lighter gray lines indicate the boundaries (the $C_0 = 10^{-6}$ tracer concentration contour, outside of the river) of the earlier and later releases included in each panel, respectively. Tracer concentrations are shown on a logarithmic scale.

one that acts to increase $\overline{C'^2}$, as it adds high concentration water with higher tracer variance than the plume average. Entrainment (**Figure 12C**) brings in low concentration water (at the C_0 threshold value) and tends to decrease $\overline{C'^2}$. The entrainment term in (10) is negative because $\overline{C'^2}/C_e'^2 > 1$. As described earlier, an approximately equivalent condition is $\overline{C'^2}/\overline{C}^2 > 1$ because $C_e'^2$ is approximately $\overline{C}^2$ for small C_0. The $\overline{C'^2}/\overline{C}^2 > 1$ condition is met for this plume, but this does not have to be the case in general. The internal mixing term (**Figure 12D**) always acts to destroy tracer variance; the term grows smaller while $\overline{C'^2}$ decreases and V_p increases. This mixing within the plume control volume reflects vertical and/or horizontal mixing that tends to homogenize tracer concentrations within the plume. Dividing the tracer variance by the absolute value of the mixing term in (10) yields a mixing time scale:

$$T_{mix} = \overline{C'^2} V_p / M \tag{16}$$

T_{mix} is 1.3 h and T_e is 2.2 h at max ambient flood, indicating mixing (**Figure 12D**) is about twice as powerful as entrainment (**Figure 12C**) in reducing tracer variance at this stage of plume evolution. Sensitivity testing indicates tracer variance budgets at max ambient flood are similar when higher concentration threshold values (up to $C_0 = 10^{-3}$) are applied, but the term magnitudes approximately double (increasing by a factor of 2.1–2.2) from the original $C_0 = 10^{-6}$ to the $C_0 = 10^{-3}$ results. For all tested C_0, mixing is approximately twice (1.8 to 1.9 times) the entrainment at max ambient flood. During early ambient flood (1 h after the onset of flood tide), however, sensitivity testing indicates the mixing to entrainment ratio increases from 0.6 to 1.5 from the $C_0 = 10^{-6}$ to the $C_0 = 10^{-3}$ results. The volume-averaged variance budgets for the hourly tracer are broadly similar (**Figure 12**). The entrainment and mixing terms contribute about equally to reducing variance for the combined tracer and most hourly tracers. Entrainment is more than double the mixing term for the two latest tracer releases; this is consistent with the higher associated entrainment velocities (**Figure 10B**, described above) for younger waters in the nearfield plume. Overall, tracer variance inputs from the mouth exceed reductions *via* entrainment and mixing only during an initial 0.5- to 1-h

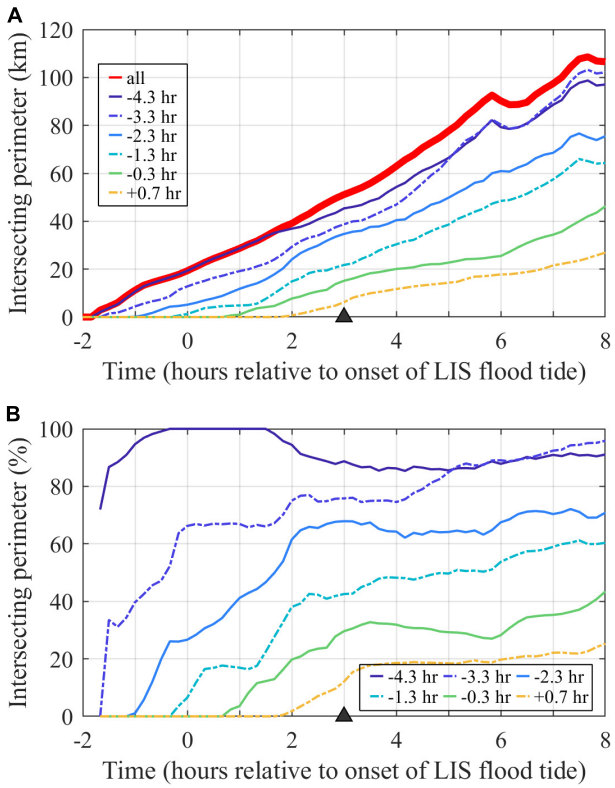


FIGURE 9 | Time series of tracers at the surface plume boundary. **(A)** The entire plume perimeter is indicated by the perimeter of the combined tracer (labeled 'all'), as contoured in **Figure 8A** at the max ambient flood time (marked with a triangle), and each other line shows the portion of the plume perimeter with an hourly tracer present (at least at 10^{-7} concentration). **(B)** The percent of the plume perimeter with each hourly tracer present, calculated by dividing time series for each hourly tracer in the upper panel by the plume perimeter time series. Tracers are labeled by first release times.

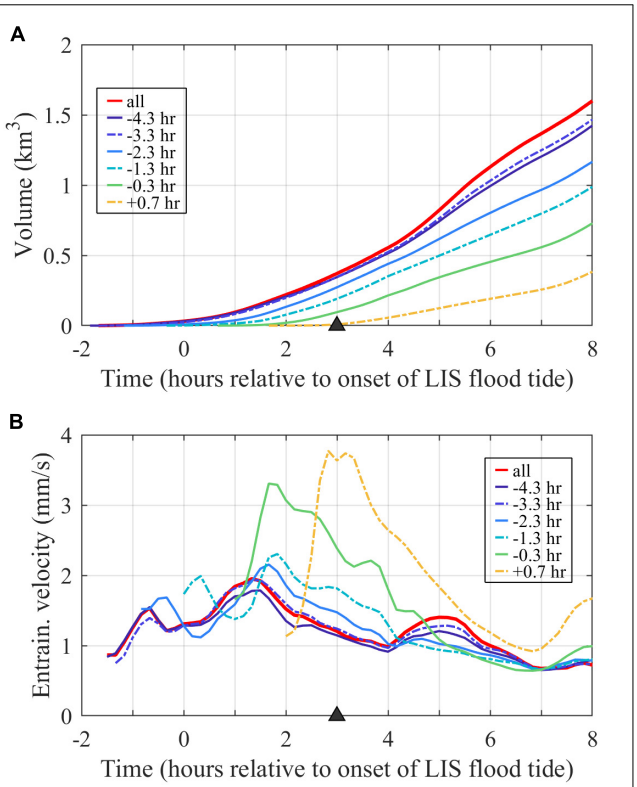


FIGURE 10 | Time series of **(A)** plume volume (assessed with the combined tracer, labeled 'all') and volumes associated with individual tracer waters and **(B)** spatial-averaged entrainment velocities for the entire plume (labeled 'all') and plume regions associated with individual tracers. Tracers are labeled by first release times.

period; tracer variance is eroded throughout the rest of the ambient flood tide.

Other Discharge and Tide Conditions

The standard case is representative of summer low discharge conditions during neap tides. By comparison, the low-discharge spring-tide case increases ambient tidal currents by 33% (**Table 1**). Tides through the river mouth increase by a smaller amount (7%) and t_{lag} is shorter (**Table 1**). Surface flow reverses an hour earlier during spring tides; therefore, the plume is cut off from source waters prior to max ambient flood. Consistent with stronger river tides, the bulk vertical salinity difference at the mouth is smaller (ΔS_m = 16.0) and the Froude number at the mouth is larger (Fr_m = 2.0) (**Table 1**). The plume is somewhat longer (10 km length), narrower (3.5 km width), and has a lower downstream salinity anomaly (ΔS_d = 4.0) during spring tides (**Figure 13** and **Table 1**), but the dimensions and salinity anomaly are within 30% of the neap plume characteristics. The spring-tide plume is supercritical with Fr_d exceeding five. Comparing the high-discharge neap-tide case to the standard case indicates how river mouth and plume conditions change with six times stronger discharge (**Table 1**). Even though ambient tides are the same, river tides are weaker with a shorter t_{lag} (**Table 1**). The tidal-averaged flow exceeds the river tidal amplitude ($V_D/V_{Tm} < 1$), so currents do not reverse and the 'pinching off criterion' (de Ruijter et al., 1997) is not met. Consequently, the plume is fed by source waters throughout the tidal cycle. Completely freshwater reaches the mouth (**Table 1**) and low-salinity water occupies the entire water column in the channel (not shown). The fresher and thicker mouth outflow (ΔS_m = 23.0, h_m = 10 m) has a faster c_m (1.32 m/s), but source conditions are still at least critical at max ambient flood (**Table 1**). The main plume is somewhat longer (9.5 km length) and wider (5.5 km width), but the much higher salinity anomaly (ΔS_d = 14.0) and the more apparent offshore relic plume are the most conspicuous changes relative to the low-discharge plume (**Figure 13** and **Table 1**). The stronger salinity anomaly increases c_p to 0.46 m/s and decreases Fr_d to 2.4, but the plume still is supercritical at max ambient flood. Even with a stronger c_p, ambient tides still arrest the upstream front ($Fr_{Ta} > 1$). Comparing the high-discharge runs with neap and spring tides indicates a qualitatively similar spring-neap tidal dependence as shown for the two low-discharge runs.

Intercomparison of the four model runs at max ambient flood (**Figure 13** and **Table 1**) indicates the mouth outflow and plume

velocities always become supercritical during part of the tidal cycle. Under low-discharge conditions, the tidal plume is fed by source waters until max ambient flood, when flow reversal at the mouth cuts off the source water supply. During high-discharge, the plume maintains a connection with source waters because the mouth surface flow always is outward. The plume at max ambient flood is always faster than ambient tidal currents (i.e., $u_d > U_{Ta}$), and longer than the time-integral of the tidal flow (i.e., $L_p > L_{Ta}/2$). Plume salinities decrease with weaker tides and particularly with higher discharge. Plume dimensions, however, are less sensitive to changing tidal and discharge forcing. The upstream extent is limited because ambient tidal currents arrest the opposing plume propagation, as $Fr_{Ta} > 1$ in all runs. The downstream extent of the tidal plume always is within 20 km from the mouth, which is less than twice the ambient tidal excursion.

The hourly freshwater tracers released within each run indicate the composition and connectivity within the plume under various forcing conditions. In all cases, water age increases downstream and offshore to a lesser degree (**Figure 14**). The downstream front has older waters, the upstream front has younger waters, and the main offshore front and more gradual inshore boundary span young to old waters. The oldest waters are found in the relic offshore plume (**Figure 14**). At max ambient flood, the plumes are chiefly composed of source waters released in the river during the preceding ambient ebb. The oldest water ages are detected during neap tides, particularly within the relic plume that persists under high-discharge conditions. The low-discharge spring-tide plume has the narrowest age range because the oldest waters have been mixed away and the youngest waters are cut off from the plume by the mouth flow reversal (**Figure 14**). The plume front advances downstream faster than ambient tidal currents in all runs, but the u_f advancement velocity is somewhat less than (64–94%) $U_{Ta}+c_p$. Interior waters in all runs, assessed with the hourly tracer closest to but not at the downstream front, approach the downstream front with a relative velocity ($0.09 < u_i < 0.19$ m/s) at max ambient flood (**Table 1**). The interior waters, however, are not traveling quickly enough to reach the downstream plume front by the end of ambient flood. Thus, the downstream front always has the lowest overall connectivity with source waters, as interaction is limited to waters that exited the mouth by early ambient ebb. In stark contrast, the arrested upstream front has high connectivity, as all freshwaters exiting the mouth immediately interact with this boundary. Thus, energetic ambient tides lead to a strong upstream-to-downstream asymmetry in source-front connectivity.

Analysis of the plume volume budgets, identified with the combined tracer fields, indicates how the entrainment velocity and the associated e-folding time scale vary among runs. The w_e values for both spring-tide cases (1.0–1.2 mm/s) are approximately the same and are about twice the w_e values for neap-tide cases (2.0 mm/s) (**Table 1**). The w_e tidal dependence, and lack of sensitivity to discharge, point to entrainment driven by tidal shear. The entrainment time scale (T_e) at max ambient flood is about the same (2 h) for all but the high-discharge neap-tide plume, which has double the T_e. For the combined tracer at max ambient flood, $\overline{C} \geq 0.026$ in both high discharge runs; these values are at least double the concentration in the standard

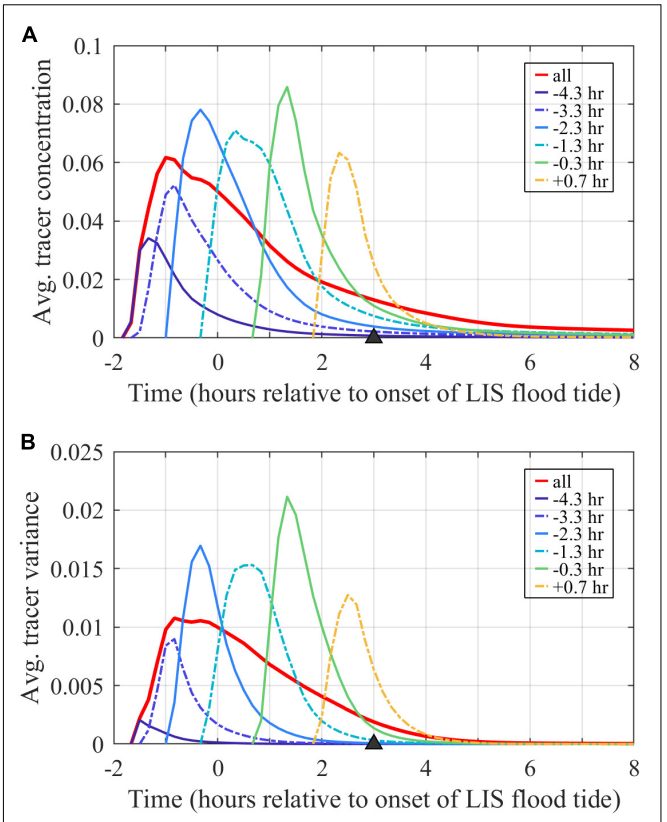


FIGURE 11 | Time series of volume-averaged **(A)** tracer concentrations and **(B)** tracer variances. Values for the entire plume volume are calculated with the combined tracer (labeled 'all'). Averages are associated with the volumes bounded by each tracer outside of the river. Tracers are labeled by first release times.

low-discharge neap-tide run ($\overline{C} = 0.013$) and several times greater than in the low-discharge spring-tide run ($\overline{C} = 0.004$) (**Table 1**). Note that the higher concentration values in the high-discharge cases correspond to lower plume salinities. Both high discharge runs also have much higher variance at max ambient flood ($\overline{C'^2} \geq 0.0069$) than the low-discharge neap-tide run ($\overline{C'^2} = 0.0019$) and the low-discharge spring-tide run ($\overline{C'^2} = 0.0002$) (**Table 1**). The ratio $\overline{C'^2}/\overline{C}^2$ at max ambient flood ranges from 9.5 to 12.5 (**Table 1**) and $\overline{C'^2}/\overline{C}^2 > 1$ during the entire ambient flood tide in all cases.

Tracer variance budgets are qualitatively similar, but term magnitudes vary by orders of magnitude among runs. In all runs, $\overline{C'^2}$ is increased only by mouth inputs and is decreased both by entrainment and mixing (**Table 1**). Entrainment decreases tracer variance because C'^2_e is approximately $\overline{C}^2$ and $\overline{C'^2}/\overline{C}^2 > 1$ for all tidal and discharge conditions explored; indicating that the plume remains in the same regime in this regard. By max ambient flood, mixing is about twice as strong as entrainment and T_{mix} (1–2 h) is shorter than T_e. Both time scales are less than half the tidal cycle, indicating mixing and entrainment are vigorous enough to rapidly diminish tracer variance within the plume.

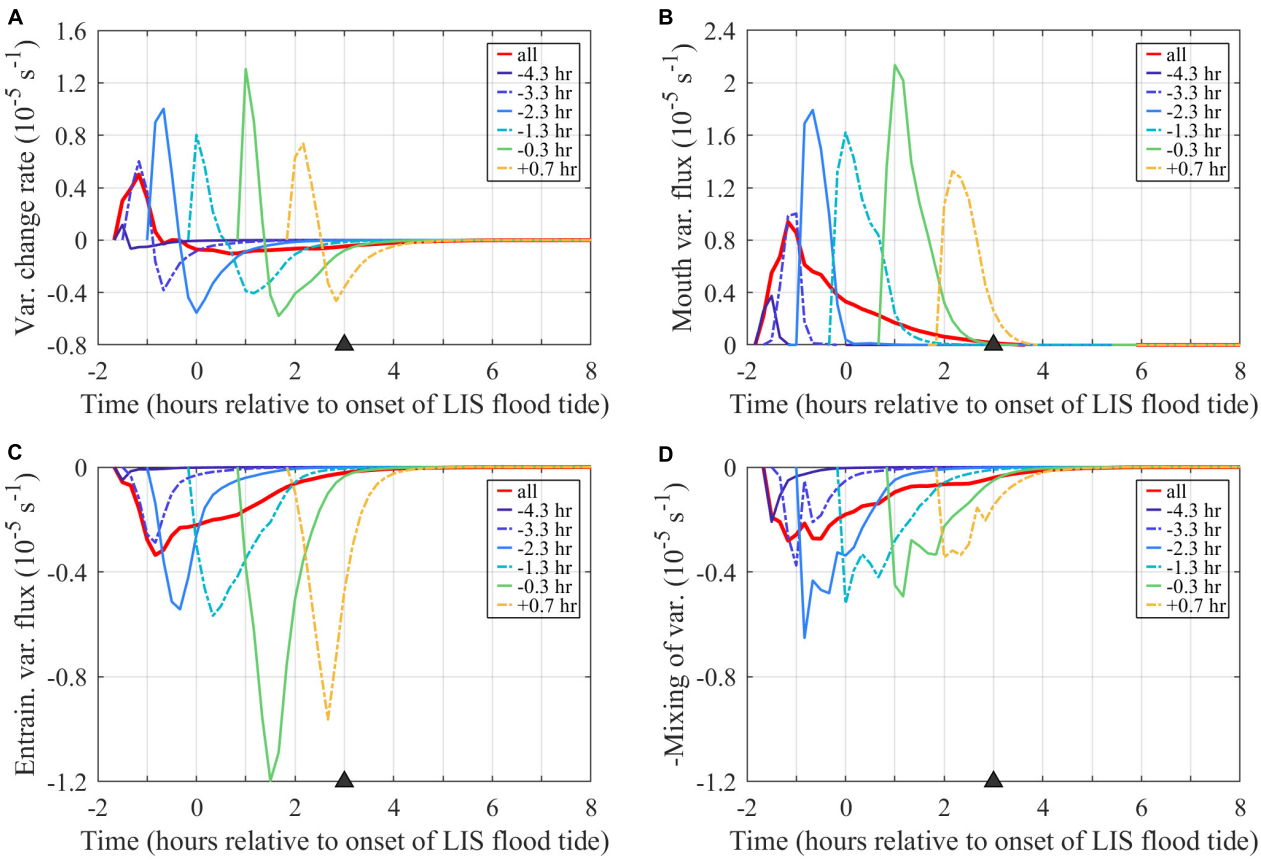


FIGURE 12 | Time series of terms in the volume-averaged tracer variance budget (10): **(A)** rate of change, **(B)** mouth flux, **(C)** entrainment, and **(D)** mixing ($-M/V_p$). The entrainment and mixing terms are graphed with half the *y*-axis range of the rate of change and mouth terms. Term units are (concentration units)^2 (10^{-5} s^{-1}), where the concentration units are non-dimensional because tracers are source water fractions. Volume averages include the entire region bounded by each tracer outside the river. The combined tracer (labeled 'all') includes the entire plume. Tracers are labeled by first release times.

DISCUSSION

This study investigates the Connecticut River plume formed during ambient flood tides. Observations (e.g., Garvine, 1974b; **Figure 2**) and model results indicate strong plume salinity variability with forcing conditions, but the downstream extent of the tidal plume always is within 20 km from the mouth. The plume length is strikingly short in comparison to plumes exiting other estuaries with similar river discharge ranges. For comparison, the buoyant outflow from the Delaware Bay can stretch over 100 km along the coast during buoyancy driven conditions (e.g., Whitney and Garvine, 2006). The key difference is the Connecticut River plume forms in a much stronger ambient tidal environment. Tidal advection during flood increases downstream transport and extent, but plume length ultimately is limited by ebb currents strong enough to arrest and then reverse the plume. Simple estimates are useful for characterizing plume length generally for other tidally reversing plumes. The frontal advancement velocity is approximated as the internal wave speed superimposed on the ambient tidal velocity: $u_f \approx c_p + u_a$, where u_a can be expressed in terms of a sinusoidal tide as in (11). Integrating over half a tidal cycle (either flood or ebb) yields $L_p \approx (T/2)(c_p + 2U_{Ta}/\pi)$, where $2U_{Ta}/\pi$ is the mean tidal current during one phase (flood or ebb) of the tide. Writing c_p in terms of the salinity anomaly as before, the ratio of the plume length to the tidal excursion (L_{Ta}, as defined earlier) is approximately:

$$\frac{L_p}{L_{Ta}} \approx \left(\frac{\sqrt{g\beta \Delta S_p H_p}}{2U_{Ta}/\pi} + 1 \right) \tag{17}$$

Plumes experiencing substantial tidal reversals are expected to be approximately within two tidal excursions from the mouth ($L_p < 2L_{Ta}$) because c_p should be less than $2U_{Ta}/\pi$ in these strong tidal regimes. For the Connecticut River, $2L_{Ta}$ ranges from 22 km during neap tides up to 36 km during spring tides. The actual plume extent is smaller mostly because c_p typically is much less than $2U_{Ta}/\pi$, particularly during spring tides.

Results indicate the downstream front has very limited connectivity with interior waters. These waters are approaching the front with an overtake velocity equaling the difference between the interior water velocity and the frontal advancement velocity: $\Delta u = u_i - u_f$. This overtake velocity does not depend on the ambient tidal velocity. The time available for interior waters

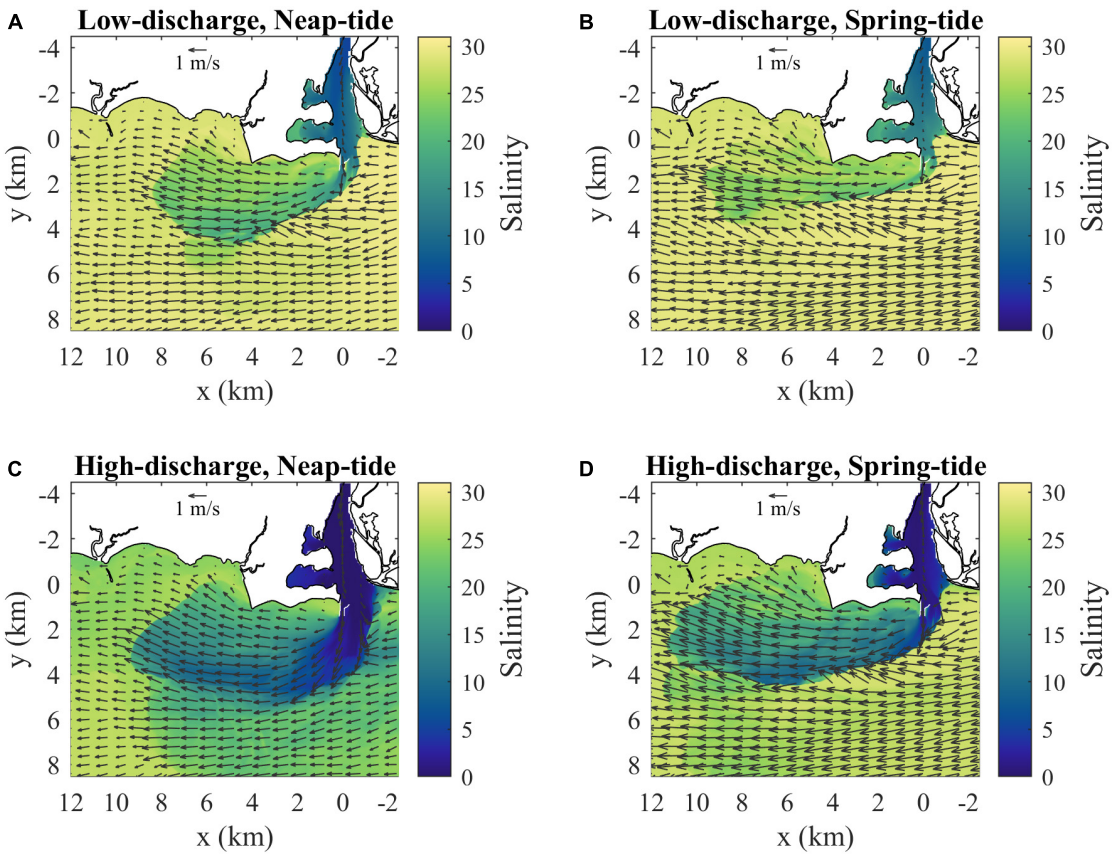


FIGURE 13 | Surface velocity (arrows) and salinity (shaded) maps at max ambient flood for **(A)** low discharge during neap tides (as in **Figure 4B**), **(B)** low discharge during spring tides, **(C)** high discharge during neap tides and **(D)** high discharge during spring tides. Velocity arrows are shown for every 40th point (800 m spacing) and every 20th point (400 m spacing) in *x* and *y*, respectively.

to travel from the mouth to the advancing front position (x_f) is at most the time between when the interior water first exits the mouth (t_i) and when the ambient tidal phase (in this case flood) ends at $T/2$. The downstream extent of the interior water (x_i) is less than x_f while approaching the front and equals x_f after reaching the front, if that occurs. Assuming constant u_i and u_f for simplicity, the condition for reaching the front by the end of the tidal phase is $u_i(T/2\text{-}t_i) \geq u_f T/2$. Expressed as a velocity ratio, the condition for interior water interacting with the downstream front is:

$$\frac{u_i}{u_f} \geq \frac{1}{1 - 2t_i/T} \tag{18}$$

Note that u_f and u_i, respectively can be scaled as c_p+u_a and $\Delta u+u_f$, so there is an implicit dependence on ambient tidal currents that tends to reduce u_i/u_f with stronger tides. Late-flood interior water exits the mouth with $t_i \geq T/4$ and (18) indicates that these waters can only reach the downstream front if $u_i/u_f \geq 2$. This is a difficult threshold to meet, so it is unlikely that late-stage waters interact with the downstream front of tidally reversing plumes. For the Connecticut River plume, three of the runs have $u_i/u_f \leq 1.2$ (**Table 1**), so $t_i \leq 1$ h to reach the downstream front. For the low-discharge spring-tide case, $u_i/u_f = 1.5$ and $t_i \leq 2$ h to overtake the front. Thus, interaction with the downstream front is limited to source waters exiting the mouth by early ambient flood. The tracers are identified by the first time they are released within the river, which can be several hours earlier than when they exit the mouth. For the standard low-discharge neap-tide case, the tracer released at −1.3 h is the youngest tracer with $t_i \leq 1$ h (**Figure 3C**) and, consistent with the u_i/u_f value and (18), it is the youngest water to interact with the downstream front (**Figure 8C**).

The present results are most directly comparable to the Cole et al. (2020) plume connectivity study. Cole et al. (2020) studies the Merrimack River plume, which is fed by a river-ebb pulse of fresh source waters and evolves in a much lower-energy ambient tidal environment than the Connecticut River plume experiences. Simulated tracers injected at the Merrimack River mouth indicate that only source waters released within the first 2 h ($t_i \leq 2$ h) overtake the front within a half tidal cycle after plume formation. This limited frontal connectivity is similar to results for the downstream front of the Connecticut River plume. A key difference between the plumes is weak ambient tides allow the Merrimack plume to spread almost radially outward from the mouth, while strong ambient tides arrest the upstream front ($Fr_{Ta} > 1$) in the Connecticut plume and elongate it in the tidally

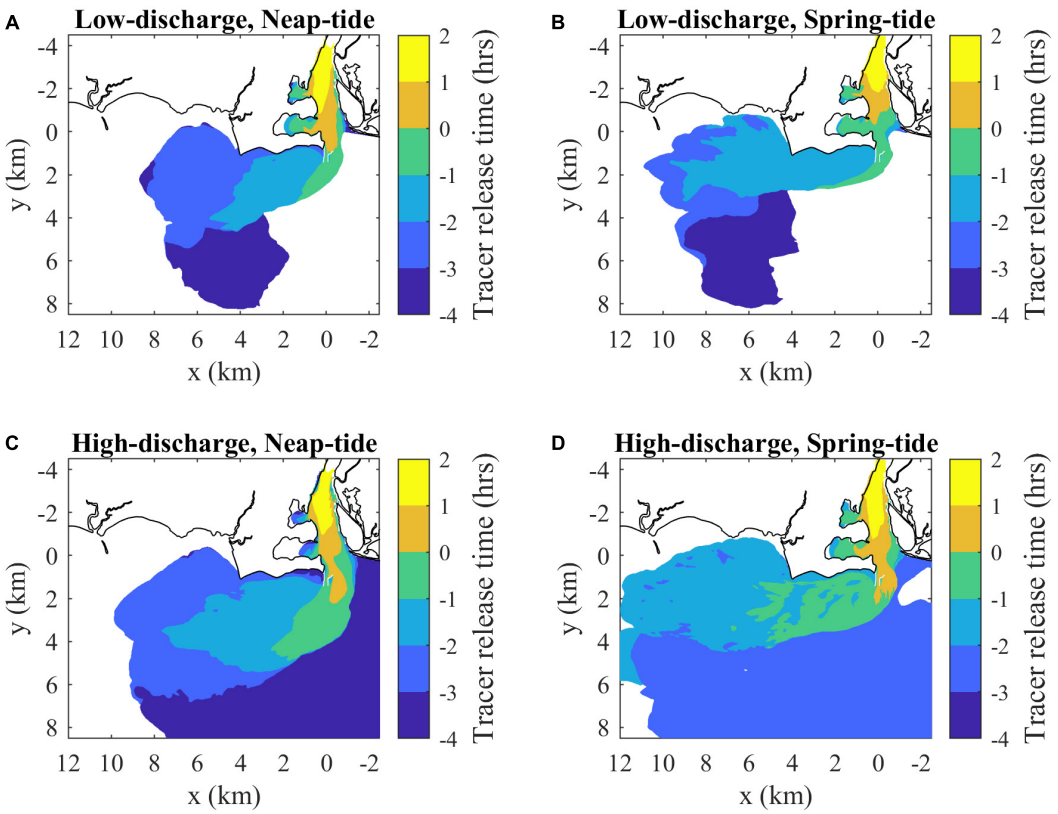


FIGURE 14 | Surface maps of average freshwater composition (indicated by average release times of tracers present in each location at max ambient flood) for **(A)** low discharge during neap tides (as in **Figure 7A**), **(B)** low discharge during spring tides, **(C)** high discharge during neap tides and **(D)** high discharge during spring tides. Tracer release times are expressed relative to the onset of ambient flood tides (as in **Figure 7**). Average freshwater age can be calculated by subtracting the average release times from 3 h (the mapped time).

downstream direction. The Connecticut's arrested upstream front has strong and immediate connectivity with all source waters exiting the mouth. There is no part of the Merrimack plume front that has such strong connectivity. The strong connectivity is not guaranteed for all plumes with an arrested upstream front, as it is possible for later source waters to slip past in the plume interior without interacting with the bounding front. For the Connecticut plume, energetic ambient tides lead to large differences in connectivity and source-water composition along the bounding plume front. It is likely other plumes with a tidally arrested upstream front (where $Fr_{Ta} > 1$) exhibit a similar transition from youngest to oldest waters progressing from the upstream front, along the offshore and onshore fronts, and to the downstream front. Consequently, such plumes will have more source-front connectivity than plumes in weaker ambient tidal environments, but the downstream front still will have very limited connectivity. Relative to plumes in weak ambient tidal regimes, the Connecticut River plume and other tidally reversing plumes should have key differences with respect to the fate and transport of pollutants, sediments, and biogeochemical substances. The relatively short length of tidally reversing plumes should tend to keep the highest concentrations close to the mouth. Spatial gradients of substances along the river can result in large differences in transport pathways. Material passing through the mouth in late ambient ebb or early flood will tend to be transported the farthest in plumes formed during ambient flood tides; this material can be processed at the downstream front. Substances in late-flood source waters would tend to remain closer to the mouth and only interact with the arrested upstream front. The strong connectivity of the arrested upstream front and its constrained location make it a good location for studying the frontal processing of pollutants, sediments, and biogeochemical substances. Future research incorporating plume biogeochemistry and source-front connectivity characteristics would help advance the understanding of plume effects on coastal ecosystem dynamics. It is also important to connect processes acting within the tidally reversing active plume to tracking substances over longer time scales (e.g., days to months), after plume waters have been extensively mixed with ambient waters.

Entrainment and mixing occur throughout the Connecticut River plume; as indicated by the results that concentrations and variances for all hourly tracers diminish quickly (**Figure 11**). The plume-averaged tracer variance budgets (10) for the combined tracer are qualitatively similar for all runs: tracer variance is increased by mouth inputs, decreased by entrainment, and destroyed by internal mixing. Mouth inputs increase tracer variance because source waters have higher concentrations than the plume (leading to $C'^2_m/\overline{C'^2} > 1$), a common situation

for plumes. Entrainment decreases tracer variance because $\overline{C'^2}/C'^2_e > 1$; this condition is approximately $\overline{C'^2}/\overline{C}^2 > 1$ because C'^2_e is approximately $\overline{C}^2$ for small C_0. The $\overline{C'^2}/\overline{C}^2 > 1$ condition should be met by other strongly mixed low-concentration plumes. The tracer variance budget terms vary by orders of magnitude among runs (**Table 1**). It is useful to simplify and scale the budget in a way that collapses results for the investigated range of tidal and discharge conditions. For $C'^2_m/\overline{C'^2} \gg 1$ and $\overline{C'^2}/\overline{C}^2 \gg 1$, the mouth input term and entrainment term in (10) are approximately $C'^2_m Q_m/V_p$ and $-\overline{C'^2}Q_e/V_p$, respectively. These simplifications are reasonable approximations for the Connecticut River plume results. Analysis of tracer variance budgets of other plumes should include evaluating the $C'^2_m/\overline{C'^2}$ and $\overline{C'^2}/\overline{C}^2$ ratios. The latter ratio is larger for strongly mixed low-concentration (low freshwater fraction) plumes, while the former ratio will be greater than one for any case with much higher concentration (fresher) source waters than the plume. The estimated mouth input term ($C'^2_m Q_m/V_p$) at $t = 0$ h (onset of ambient floods) can be used to scale the time-varying terms in (10). This mouth-based scaling reduces term magnitude differences among runs from orders of magnitude to approximately a factor of two. The successful collapsing of budget results indicates a dose-response relationship, whereby stronger tracer variance inputs by source waters have correspondingly larger variance decreases by entrainment and destruction *via* internal mixing.

Plume-averaged tracer budgets are valuable for analyzing plume evolution as a whole, but combine together horizontal and vertical processes as well as processes occurring in different regions of the plume. Future analysis of the Connecticut River plume should explore the decomposition of tracer variance into its horizontal and vertical parts, as introduced in Li et al. (2018) and applied in other studies (e.g., Wang and Geyer, 2018; Warner et al., 2020). The vertical tracer variance is particularly useful since it is directly related to stratification and it may be more readily applied to understanding biogeochemical processes in plumes. Analyzing spatial variations of tracer variance and budget terms as in Li et al. (2018) and other works (e.g., Warner et al., 2020) would help highlight important areas for variance advection and dissipation. The multiple tracer approach applied in the present study already allows for distinguishing between near-field and far-field plume regions. The mixing term in the tracer budgets for the present study includes the total mixing acting in the model, which includes physical mixing and numerical mixing associated with the advection scheme. Several studies have shown that numerical mixing can be comparable to physical mixing (e.g., Burchard and Rennau, 2008; Li et al., 2018; Burchard et al., 2021; Wang et al., 2021) and the ratio of numerical to physical diffusivities can have pronounced spatial variability within estuaries and plumes (Burchard et al., 2021).

Mixing in idealized tidal plumes representative of the Connecticut River plume and other situations has been studied in more detail in Spicer et al. (2021), following the turbulent buoyancy flux approach of Pritchard and Huntley (2006). Spicer et al. (2021) finds that bottom-generated tidal mixing dominates over mixing associated with buoyant plume shear if the estuarine Richardson number ($Ri_E = {c_m}^2 V_D/{U_{Ta}}^3$; modified from Fischer (1972) to use ambient tides) divided by the mouth Rossby number ($Ro_m = V_D/(fW_m)$, where W_m is mouth width) is less than one ($Ri_E/Ro_m < 1$). Provided that $c_p \leq c_m$, this condition is satisfied when the product of the ambient tidal Froude number squared and the corresponding Rossby number exceeds one (${Fr_{Ta}}^2 Ro_{Ta} > 1$, where $Ro_{Ta} = U_{Ta}/(fW_m)$), which is true for all model runs in this study. Thus, the Connecticut River plume belongs in the class of plumes strongly influenced by tidal mixing (Spicer et al., 2021).

Other plumes in energetic ambient tidal environments, whether generated during flood or ebb, are expected to share similarities with the Connecticut River plume. These tidally reversing plumes should be within two tidal excursions from the mouth, be cut off from source waters while flow reverses at the mouth, have limited connectivity at the downstream front, strong connectivity along the arrested upstream front, and rapid entrainment and mixing that reduces the plume buoyancy signature over intratidal time scales. Follow-up work should compare the present results to connectivity within the Connecticut's ambient ebb plume. Future research should extend the connectivity and tracer analysis approach to the transport and processing of pollutants, sediments, and biogeochemical material by the Connecticut River plume and other plumes in energetic ambient tidal environments.

DATA AVAILABILITY STATEMENT

The original contributions presented in the study are publicly available. This data can be found here: https://opencommons.uconn.edu/marine_sci/12.

AUTHOR CONTRIBUTIONS

MW led this research, completed analysis, constructed figures, and wrote this manuscript with input from co-authors. YJ completed the hydrodynamic model runs, contributed to analysis, and edited and suggested improvements to the manuscript. KC, DM, and KH contributed to the ideas underpinning this research, helped set the scope of this manuscript, and improved the manuscript through their suggestions. All authors contributed to the article and approved the submitted version.

FUNDING

This research was supported by the NSF Ocean Sciences Physical Oceanography grant 1756578.

ACKNOWLEDGMENTS

The manuscript was improved by the helpful suggestions of the reviewers and editor.

REFERENCES

Ackelson, S. G., and O'Donnell, J. (2011). Small-scale variability in suspended matter associated with the Connecticut River plume front. *J. Geophys. Res.* 116:C10013. doi: 10.1029/2011JC007053

Akan, Ç, McWilliams, J. C., Moghimi, S., and Özkan-Haller, H. T. (2018). Frontal dynamics at the edge of the Columbia River plume. *Ocean Modell.* 122, 1–12. doi: 10.1016/j.ocemod.2017.12.001

Basdurak, N. B., Largier, J. L., and Nidzieko, N. J. (2020). Modeling the dynamics of small-scale river and creek plumes in tidal waters. *J. Geophys. Res.* 125:e2019JC015737. doi: 10.1029/2019JC015737

Bennett, D. C., O'Donnell, J., Bohlen, W. F., and Houk, A. (2010). Tides and overtides in long Island Sound. *J. Mar. Res.* 68, 1–35. doi: 10.1357/002224010793079031

Bricker, J. D., Okabe, I., and Nakayama, A. (2006). Behavior of a small pulsed river plume in a strong tidal cross-flow in the Akashi strait. *Environ. Fluid. Mech.* 6, 203–225. doi: 10.1007/s10652-005-3480-x

Burchard, H. (2020). A universal law of estuarine mixing. *J. Phys. Oceanogr.* 50, 81–93. doi: 10.1175/JPO-D-19-0014.1

Burchard, H., Gräwe, U., Klingbeil, K., Koganti, N., Lange, X., and Lorenz, M. (2021). Effective diahaline diffusivities in estuaries. *J. Adv. Model. Earth Sys.* 13. doi: 10.1029/2020MS002307

Burchard, H., and Rennau, H. (2008). Comparative quantification of physically and numerically induced mixing in ocean models. *Ocean Modell.* 20, 293–311. doi: 10.1016/j.ocemod.2007.10.003

Chant, R. J. (2011). "Interactions between estuaries and coasts: river plumestheir formation transport and dispersal," in *Treatise on Estuarine and Coastal Science*, Vol. 2, eds E. Wolanski and D. McLusky (Amsterdam: Elsevier), 213–235. doi: 10.1016/B978-0-12-374711-2.00209-6

Chapman, D. C. (1985). Numerical treatment of cross-shelf open boundaries in a barotropic coastal ocean model. *J. Phys. Oceanogr.* 15, 1060–1075. doi: 10.1175/1520-04851985015<1060:NTOCSO<2.0.CO;2

Chassignet, E. P., Hurlburt, H. E., Smedstad, O. M., Halliwell, G. R., Hogan, P. J., Wallcraft, A. J., et al. (2008). The HYCOM (hybrid coordinate ocean model) data assimilative system. *J. Mar. Syst.* 65, 60–83. doi: 10.1016/j.jmarsys.2005.09.016

Chen, F., MacDonald, D. G., and Hetland, R. D. (2009). Lateral spreading of a near-field river plume: observations and numerical simulations. *J. Geophys. Res.* 114:C07013. doi: 10.1029/2008JC004893

Cole, K. L., MacDonald, D. G., Kakoulaki, G., and Hetland, R. D. (2020). River plume source-front connectivity. *Ocean Modell.* 150:101571. doi: 10.1016/j.ocemod.2020.101571

Cudaback, C. N., and Jay, D. A. (1996). "Formation of the columbia river plume-hydraulic," in *Buoyancy Effects on Coastal and Estuarine Dynamics*, Vol. 53, eds D. G. Aubrey and C. T. Friedrichs (Washington, DC: American Geophysical Union), 139–154. doi: 10.1029/CE053p0139

de Ruijter, W. P., Visser, A. W., and Bos, W. G. (1997). The Rhine outflow: a prototypical pulsed discharge plume in a high energy shallow sea. *J. Mar. Systems* 12, 263–276. doi: 10.1016/S0924-7963(96)00102-9

Deignan-Schmidt, S. R., and Whitney, M. M. (2018). A model study on the summertime distribution of river waters in long island sound. *Estuaries Coasts* 41, 1002–1020. doi: 10.1007/s12237-017-0348-5

Dittmar, T., and Kattner, G. (2003). The biogeochemistry of the river and shelf ecosystem of the Arctic Ocean: a review. *Mari. Chem.* 83, 103–120. doi: 10.1016/S0304-4203(03)00105-1

Egbert, G. D., and Erofeeva, S. Y. (2002). Efficient inverse modeling of barotropic ocean tides. *J. Atmosph. Oceanic Tech.* 19, 183–204. doi: 10.1175/1520-04262002019<0183:EIMOBO<2.0.CO;2

Ellis, and Gen, T. G. (1874). *The Causes of the Formation of Bars at the Mouths of Rivers, as Shown in An Examination of the Connecticut River, Van Nostrand's Eclectic Engineering Magazine*. Available online at: https://search.proquest.com/docview/357141998 (accessed October 1, 1874).

Fairall, C. W., Bradley, E. F., Hare, J. E., Grachev, A. A., and Edson, J. B. (2003). Bulk parameterization of air–sea fluxes: updates and verification for the COARE algorithm. *J. Climate* 16, 571–591. doi: 10.1175/1520-04422003016<0571:BPOASF<2.0.CO;2

Fischer, H. (1972). Mass transport mechanisms in partially stratified estuaries. *J. Fluid Mech.* 53, 671–687. doi: 10.1017/S0022112072000412

Flather, R. A. (1976). A tidal model of the northwest European continental shelf. *Memoires de la Soc. R. des Sci. de Liege* 10, 141–164.

Garvine, R. W. (1974a). Dynamics of small-scale oceanic fronts. *J. Phys. Oceanogr.* 4, 557–569. doi: 10.1175/1520-04851974004<0557:DOSSOF<2.0.CO;2

Garvine, R. W. (1974b). Physical features of the Connecticut River outflow during high discharge. *J. Geophys. Res.* 79, 831–846.

Garvine, R. W. (1975). The distribution of salinity and temperature in the Connecticut River estuary. *J. Geophys. Res.* 80, 1176–1183. doi: 10.1029/JC080i009p01176

Garvine, R. W. (1977). Observations of the motion field of the Connecticut River plume. *J. Geophys. Res.* 82, 441–454. doi: 10.1029/JC082i003p00441

Garvine, R. W. (1984). Radial spreading of buoyant, surface plumes in coastal waters. *J. Geophys. Res.* 89, 1989–1996. doi: 10.1029/JC089iC02p01989

Garvine, R. W., and Munk, J. D. (1974). Frontal structure of a river plume. *J. Geophys. Res.* 79, 2251–2259. doi: 10.1029/JC079i015p02251

Grimes, C. B. (2001). Fishery production and the Mississippi River discharge. *Fisheries* 26, 17–26. doi: 10.1577/1548-84462001026<0017:FPATMR<2.0.CO;2

Haidvogel, D. B., Arango, H., Budgell, W. P., Cornuelle, B. D., Curchitser, E., Di Lorenzo, E., et al. (2008). Ocean forecasting in terrain-following coordinates: formulation and skill assessment of the Regional Ocean modeling system. *J. Comput. Phys.* 227, 3595–3624. doi: 10.1016/j.jcp.2007.06.016

Haidvogel, D. B., Arango, H. G., Hedstrom, K., Beckmann, A., Malanotte-Rizzoli, P., and Shchepetkin, A. F. (2000). Model evaluation experiments in the North Atlantic basin: simulations in nonlinear terrain-following coordinates. *Dynam. Atmos. Oceans* 32, 239–281.

Hessner, K., Rubino, A., Brandt, P., and Alpers, W. (2001). The Rhine outflow plume studied by the analysis of synthetic aperture radar data and numerical simulations. *J. Phys. Oceanogr.* 31, 3030–3044. doi: 10.1175/1520-04852001031<3030:TROPSB<2.0.CO;2

Hetland, R., and MacDonald, D. (2008). Spreading in the near-field Merrimack River plume. *Ocean Modell.* 21, 12–21. doi: 10.1016/j.ocemod.2007.11.001

Hetland, R. D., and Hsu, T.-J. (2013). "Freshwater and sediment dispersal in large river plumes," in *Biogeochemical Dynamics at Large River-Coastal Interfaces: Linkages With Global Climate Change*, eds T. S. Bianchi, M. A. Allison, and Cai W-J (New York: Springer), 55–85. doi: 10.1017/CBO9781139136853

Hickey, B. M., Kudela, R. M., Nash, J. D., Bruland, K. W., Peterson, W. T., MacCready, P., et al. (2010). River influences on shelf ecosystems: introduction and synthesis. *J. Geophys. Res.* 115:112. doi: 10.1029/2009JC005452

Hickey, B. M., Pietrafesa, L. J., Jay, D. A., and Boicourt, W. C. (1998). The Columbia River plume study: subtidal variability in the velocity and salinity fields. *J. Geophys. Res: Oceans* 103, 339–368.

Horner-Devine, A. R., Hetland, R. D., and MacDonald, D. G. (2015). Mixing and transport in coastal river plumes. *Ann. Rev. Fluid Mech.* 47, 569–594. doi: 10.1146/annurev-fluid-010313-141408

Horner-Devine, A. R., Jay, D. A., Orton, P. M., and Spahn, E. Y. (2009). A conceptual model of the strongly tidal Columbia River plume. *J. Mar. Sys.* 78, 460–475. doi: 10.1016/j.jmarsys.2008.11.025

Huguenard, K. D., Bogucki, D. J., Ortiz-Suslow, D. G., Laxague, N. J. M., MacMahan, J. H., Özgökmen, T. M., et al. (2016). On the nature of the frontal zone of the Choctawhatchee bay plume in the Gulf of Mexico. *J. Geophys. Res.* 121, 1322–1345. doi: 10.1002/2015JC010988

Jia, Y., and Whitney, M. M. (2019). Summertime Connecticut River water pathways and wind impacts. *J. Geophys. Res.* 124, 1897–1914. doi: 10.1029/2018JC014486

Kakoulaki, G., MacDonald, D., and Horner-Devine, A. R. (2014). The role of wind in the near field and midfield of a river plume. *Geophys. Res. Lett.* 41, 5132–5138. doi: 10.1002/2014GL060606

Kilcher, L. F., and Nash, J. D. (2010). Structure and dynamics of the Columbia River tidal plume front. *J. Geophys. Res.* 115:58. doi: 10.1029/2009JC006066

Li, X., Geyer, W. R., Zhu, J., and Wu, H. (2018). The transformation of salinity variance: a new approach to quantifying the influence of straining and mixing on estuarine stratification. *J. Phys. Oceanogr.* 48, 607–623. doi: 10.1175/JPO-D-17-0189.1

Luketina, D. A., and Imberger, J. (1987). Characteristics of a surface buoyant jet. *J. Geophys. Res.* 92, 5435–5447. doi: 10.1029/JC092iC05p05435

MacCready, P., Geyer, W. R., and Burchard, H. (2018). Estuarine exchange flow is related to mixing through the salinity variance budget. *J. Phys. Oceanogr.* 48, 1375–1384. doi: 10.1175/JPO-D-17-0266.1

MacDonald, D. G., Goodman, L., and Hetland, R. D. (2007). Turbulent dissipation in a near-field river plume: a comparison of control volume and microstructure observations with a numerical model. *J. Geophys. Res.* 112:51. doi: 10.1029/2006JC004075

Marmorino, G. O., and Trump, C. L. (2000). Gravity current structure of the Chesapeake Bay outflow plume. *J. Geophys. Res.* 105, 28847–28861. doi: 10.1029/2000JC000225

Mazzini, P. L. F., and Chant, R. J. (2016). Two-dimensional circulation and mixing in the far field of a surface advected river plume. *J. Geophys. Res. Oceans* 121, 3757–3776. doi: 10.1002/2015JC011059

McClimans, T. A. (1978). Fronts in fjords. *Geophys. Astrophys. Fluid Dynam.* 11, 23–34. doi: 10.1080/03091927808242649

Meade, R. H. (1966). Salinity variations in the Connecticut River. *Water Resour. Res.* 2, 567–579. doi: 10.1029/WR002i003p00567

Mesinger, F., DiMego, G., Kalnay, E., Mitchell, K., Shafran, P. C., Ebisuzaki, W., et al. (2006). North American regional reanalysis. *Bull. Am. Meteorolog. Soc.* 87, 343–360.

Meybeck, M. (2003). Global analysis of river systems: from Earth system controls to Anthropocene syndromes. *Philosoph. Trans. R. Soc. London B Biol. Sci.* 358, 1935–1955. doi: 10.1098/rstb.2003.1379

Nash, J. D., Kilcher, L. F., and Moum, J. N. (2009). Structure and composition of a strongly stratified, tidally pulsed river plume. *J. Geophys. Res.* 114:42. doi: 10.1029/2008JC005036

O'Donnell, J. (2010). "The dynamics of estuary plumes and fronts," in *Contemporary Issues in Estuarine Physics*, ed. A. Valle Levinson (Cambridge: Cambridge Univ. Press), 186–246. doi: 10.1017/CBO9780511676567

O'Donnell, J., Marmorino, G. O., and Trump, C. L. (1998). Convergence and downwelling at a river plume front. *J. Phys. Oceanogr.* 28, 1481–1495. doi: 10.1175/1520-04851998028<1481:CADAAR<2.0.CO;2

O'Donnell, J., Wilson, R. E., Lwiza, K., Whitney, M. M., Bohlen, W. F., Codiga, D., et al. (2014). "The physical oceanography of long island sound," in *Long Island Sound: Prospects for the Urban Sea*, ed. J. S. Latimer (Springer), 79–158. doi: 10.1007/978-1-4614-6126-5_3

Orton, P. M., and Jay, D. A. (2005). Observations at the tidal plume front of a high-volume river outflow. *Geophys. Res. Lett.* 32:L11605. doi: 10.1029/2005GL022372

Poppe, L. J., Knebel, H. J., Mlodzinska, Z. J., Hastings, M. E., and Seekins, B. A. (2000). Distribution of surficial sediment in Long Island Sound and adjacent waters: texture and total organic carbon. *J. Coast. Res.* 16, 567–574.

Pritchard, M., and Huntley, D. (2006). A simplified energy and mixing budget for a small river plume discharge. *J. Geophys. Res. Oceans* 111:C03019. doi: 10.1029/2005JC002984

Ralston, D. K., Cowles, G. W., Geyer, W. R., and Holleman, R. C. (2017). Turbulent and numerical mixing in a salt wedge estuary: Dependence on grid resolution, bottom roughness, and turbulence closure. *J. Geophys. Res. Oceans* 122, 692–712. doi: 10.1002/2016JC011738

Simpson, J. H., and Souza, A. J. (1995). Semidiurnal switching of stratification in the region of freshwater influence of the Rhine. *J. Geophys. Res.* 100, 7037–7044. doi: 10.1029/95JC00067

Spicer, P., Cole, K. L., Huguenard, K., MacDonald, D. G., and Whitney, M. M. (2021). The effect of bottom – generated tidal mixing on tidally pulsed river plume. *J. Phys. Oceanogr.* 51, 2223–2241.

Trumbull, J. H. (1881). *Indian Names of Places Etc., in and On the Borders of Connecticut: With Interpretations of Some of Them*. Available online at: https://books.google.com/books?id=JS8TAAAAYAAJ&num=10. (accessed July 1, 2021)

van Alphen, J. S. L. J., de Ruijter, W. P. M., and Borst, J. C. (1988). "Outflow and three-dimensional spreading of rhine river water in the netherlands coastal zone," in *Physical Processes in Estuaries*, eds J. Dronkers and W. van Leussen (Berlin: Springer), doi: 10.1007/978-3-642-73691-9_5

Wang, T., and Geyer, W. R. (2018). The balance of salinity variance in a partially stratified estuary: implications for exchange flow, mixing, and stratification. *J. Phys. Oceanogr.* 48, 2887–2899. doi: 10.1175/JPO-D-18-0032.1

Wang, T., Wei, Z., Jiang, W., Xu, T., Chen, J., and Bian, C. (2021). Quantification of numerical mixing in coastal ocean models through an offline method. *Ocean Eng.* 222:108588. doi: 10.1016/j.oceaneng.2021.108588

Warner, J. C., Geyer, W. R., Ralston, D. K., and Kalra, T. (2020). Using tracer variance decay to quantify variability of salinity mixing in the hudson river estuary. *J. Geophys. Res.* 125:e2020JC016096. doi: 10.1029/2020JC016096

Whitney, M. M., and Garvine, R. W. (2006). Simulating the delaware bay buoyant outflow: comparison with observations. *J. Phys. Oceanogr.* 36, 3–21. doi: 10.1175/JPO2805.1

Whitney, M. M., Jia, Y., McManus, P. M., and Kunz, C. J. (2014). Sill effects on physical dynamics in eastern long Island sound. *Ocean Dynam.* 64, 443–458. doi: 10.1007/s10236-013-0681-6

Wu, H., and Zho, J. (2010). Advection scheme with 3rd high-order spatial interpolation at the middle temporal level and its application to saltwater intrusion in the Changjiang Estuary. *Ocean Modell.* 33, 33–51. doi: 10.1016/j.ocemod.2009.12.001

Yankovsky, A. E., and Chapman, D. C. (1997). A simple theory for the fate of buoyant coastal discharges. *J. Phys. Oceanogr.* 27, 1386–1401. doi: 10.1175/1520-04851997027<1386:ASTFTF<2.0.CO;2

Conflict of Interest: The authors declare that the research was conducted in the absence of any commercial or financial relationships that could be construed as a potential conflict of interest.

Publisher's Note: All claims expressed in this article are solely those of the authors and do not necessarily represent those of their affiliated organizations, or those of the publisher, the editors and the reviewers. Any product that may be evaluated in this article, or claim that may be made by its manufacturer, is not guaranteed or endorsed by the publisher.

Copyright © 2021 Whitney, Jia, Cole, MacDonald and Huguenard. This is an open-access article distributed under the terms of the Creative Commons Attribution License (CC BY). The use, distribution or reproduction in other forums is permitted, provided the original author(s) and the copyright owner(s) are credited and that the original publication in this journal is cited, in accordance with accepted academic practice. No use, distribution or reproduction is permitted which does not comply with these terms.

frontiers in Marine Science

ORIGINAL RESEARCH
published: 12 November 2021
doi: 10.3389/fmars.2021.772139

Variability of the Red River Plume in the Gulf of Tonkin as Revealed by Numerical Modeling and Clustering Analysis

Tung Nguyen-Duy[1,2], Nadia K. Ayoub[1], Patrick Marsaleix[1], Florence Toublanc[1], Pierre De Mey-Frémaux[1], Violaine Piton[1,3], Marine Herrmann[1,2], Thomas Duhaut[1], Manh Cuong Tran[4,5] and Thanh Ngo-Duc[2]*

[1] LEGOS, Université de Toulouse, CNES, CNRS, IRD, UPS, Toulouse, France, [2] LOTUS Laboratory, University of Science and Technology of Hanoi, Vietnam Academy of Science and Technology, Hanoi, Vietnam, [3] Ecological Engineering Laboratory, Ecole Polytechnique Fédérale de Lausanne, Lausanne, Switzerland, [4] Laboratory of Oceanology and Geosciences, CNRS UMR 8187, Université du Littoral Côte d'Opale, University of Lille, IRD, Wimereux, France, [5] Center for Oceanography, Vietnam Administration of Seas and Islands, Hanoi, Vietnam

OPEN ACCESS

Edited by:
Alexander Yankovsky, University of South Carolina, United States

Reviewed by:
Xavier Carton, Université de Bretagne Occidentale, France
Yan Jia, University of Connecticut, United States

***Correspondence:**
Tung Nguyen-Duy
nguyenduytung@hotmail.com

Specialty section:
This article was submitted to Coastal Ocean Processes, a section of the journal Frontiers in Marine Science

Received: *07 September 2021*
Accepted: *13 October 2021*
Published: *12 November 2021*

Citation:
Nguyen-Duy T, Ayoub NK, Marsaleix P, Toublanc F, De Mey-Frémaux P, Piton V, Herrmann M, Duhaut T, Tran MC and Ngo-Duc T (2021) Variability of the Red River Plume in the Gulf of Tonkin as Revealed by Numerical Modeling and Clustering Analysis. Front. Mar. Sci. 8:772139. doi: 10.3389/fmars.2021.772139

We study the daily to interannual variability of the Red River plume in the Gulf of Tonkin from numerical simulations at high resolution over 6 years (2011–2016). Compared with observational data, the model results show good performance. To identify the plume, passive tracers are used in order to (1) help distinguish the freshwater coming from different continental sources, including the Red River branches, and (2) avoid the low salinity effect due to precipitation. We first consider the buoyant plume formed by the Red River waters and three other nearby rivers along the Vietnamese coast. We show that the temporal evolution of the surface coverage of the plume is correlated with the runoff (within a lag), but that the runoff only cannot explain the variability of the river plume; other processes, such as winds and tides, are involved. Using a K-means unsupervised machine learning algorithm, the main patterns of the plume and their evolution in time are analyzed and linked to different environmental conditions. In winter, the plume is narrow and sticks along the coast most of the time due to the downcoast current and northeasterly wind. In early summer, the southwesterly monsoon wind makes the plume flow offshore. The plume reaches its highest coverage in September after the peak of runoff. Vertically, the plume thickness also shows seasonal variations. In winter, the plume is narrow and mixed over the whole water depth, while in summer, the plume can be detached both from the bottom and the coast. The plume can deepen offshore in summer, due to strong wind (in May, June) or specifically to a recurrent eddy occurring near 19°N (in August). This first analysis of the variability of the Red River plume can be used to provide a general picture of the transport of materials from the river to the ocean, for example in case of anthropogenic chemical substances leaked to the river. For this purpose, we provide maps of the receiving basins for the different river systems in the Gulf of Tonkin.

Keywords: Red River, river plume, coastal ocean modeling, K-means, clustering analysis, passive tracers, unsupervised learning

INTRODUCTION

River plume can be defined in a general way as the region of the coastal ocean where its properties and dynamics are affected by the river runoff (Horner-Devine et al., 2015). Though the river runoff is small compared to the whole ocean water volume, it can impact both the physics and biogeochemistry of the coastal ocean depending on the discharge, the properties of the ocean area (bathymetry, bottom roughness) and external forcing (air-sea fluxes, open ocean influence). Furthermore, rivers carry sediments and anthropogenic contaminants from agriculture and industrial activities. Therefore, there is a need to better understand the fate of the river water from the estuaries to the ocean. It is the first step toward the study of the dispersion of the possible contaminations and toward the design of strategies for monitoring and managing the water quality and the health of ecosystems. These are particularly crucial issues in densely populated areas, such as many deltaic regions of Southeast Asia, including the Gulf of Tonkin.

The Gulf of Tonkin (16.9°N – 21.9°N, 105.6°E – 110°E) is a small shelf sea located east of Vietnam and south of China with depth less than 100 m (**Figure 1A**). It is a meso-tidal region, dominated by diurnal constituents (K1, O1) as described for instance by Nguyen et al. (2014) and Piton et al. (2020). The ocean circulation of the Gulf of Tonkin (hereafter GOT) has been examined by several authors (e.g., Ding et al., 2013; Gao et al., 2014; Rogowski et al., 2019; for a recent review see Piton et al., 2021). Using model results and observational data, they all agree that the winter circulation at the gulf scale is cyclonic and driven by wind. However, in summer, the circulation is not so well explained. Wu et al. (2008) showed that the flow through Hainan Strait has an impact on the circulation in summer: if it is inflow, the circulation is mainly cyclonic and vice versa. From high-resolution model pluri-annual simulations, Piton et al. (2021) found a basin-scale anticyclonic circulation in summer. They also suggest that the surface circulation is mainly ageostrophic, as a consequence from the monsoon wind forcing, except along the Vietnamese coast where the southward coastal current has a dominant density-driven component.

One of the expected drivers of the dynamics is the freshwater input from the continent. In the GOT, several rivers feed the gulf. The main one is the Red River (hereafter RR) system. It is formed by 3 tributaries that connect at Son Tay (**Figure 1B**) and then split again into several distributaries. On average, the RR's runoff accounts for more than 60% of the total runoff in GOT (**Figure 1C**).

In spite of its importance, to date, studies focusing on the RR plume are still scarce. Gao et al. (2013) showed that the coastal plume was found near the northern and western coasts of the gulf in winter while spreading eastward and offshore in summer. Rogowski et al. (2019) analyzed the mean seasonal circulation and suggested that the southwesterly wind direction which is prominent during the summer monsoon is the main mechanism preventing downcoast advection of the RR plume. However, that study did not attempt to explain further the temporal variations of the RR plume. In this study, we propose to take the analysis a step further and examine the plume variability in the mid-field and far-field regions (as defined by Horner-Devine et al., 2015) in more detail, using high-resolution simulations and an unsupervised learning method.

The objectives of this study are (1) to propose a method to identify the RR plume in the GOT from the model outputs, (2) to describe its development and characterize its variability at different scales and (3) to attempt to describe the physical processes at work. To do this, we use numerical simulations combined with cluster analysis. In section "Methods, Model, and Data," the model configurations, data sources and the unsupervised learning algorithm used to classify the main pattern of the plume (K-means) are described. The model is then evaluated against several observational data sets in section "General Circulation and Model Assessment." In section "River Plume in GOT: Identification and Variations of Area," several methods to identify the plume in the GOT are compared which allows us to select the most appropriate one given our purposes. On that basis, the river plume variability at different time scales is examined in section "Variability of the RR Plume," illustrating the effect of key physical processes. A discussion on the plume classification and a description of the receiving basins from the different river systems in the GOT are presented in section "Discussion," followed by conclusions in section "Conclusion."

METHODS, MODEL, AND DATA

SYMPHONIE Model and General Configuration

SYMPHONIE is a numerical model that solves the primitive, Boussinesq, hydrostatic equations of the ocean circulation (Marsaleix et al., 2006, 2008) on a curvilinear bipolar (Bentsen et al., 1999). Arakawa C-grid with regular sigma vertical levels. The QUICKEST scheme is used for advection and diffusion of tracers (Neumann et al., 2011), while horizontal advection and diffusion of momentum are respectively computed with a 4th order centered and a bi-harmonic scheme, and vertical advection of momentum by a 2nd order centered scheme (Damien et al., 2017). The k-epsilon turbulence closure scheme is implemented as in Michaud et al. (2012).

Our reference configuration, hereafter called **GOT_REF**, is an update of the configuration of Piton et al. (2021). The model domain covers the GOT area. Due to the variable horizontal grid, the coastal area near the RR mouths has a fine horizontal resolution of 300 m, while near the open boundary, the grid size can increase to 4500 m (**Figure 2A**). As the coastal area adjacent to the RR delta is characterized by a complex topography, with many islands and islets, a considerable effort has been devoted to the construction of the model bathymetry and shorelines and is described in Piton et al. (2020). In particular, the bathymetry is reconstructed from GEBCO 2014 combined with other sources and field surveys. The bottom drag coefficient follows a logarithmic law (Blumberg and Mellor, 1987), depending upon the bottom roughness length which is set to 1 mm. The parametrization for the solar penetration depth (as described for instance by

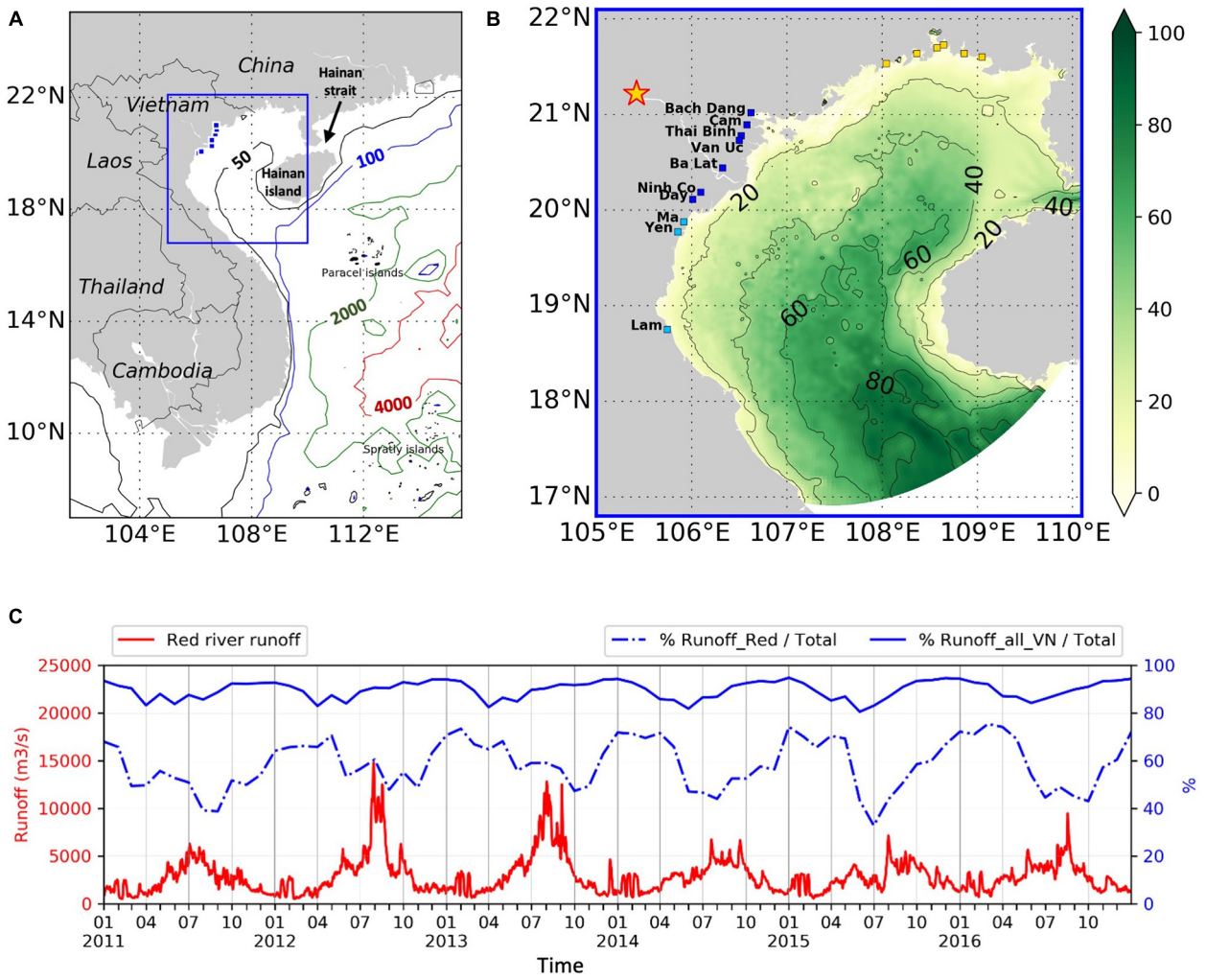


FIGURE 1 | (A) Location of the Gulf of Tonkin. Blue dots show the location of the river mouths of the Red River system. Contour lines indicate the bathymetry of the area. **(B)** Model domain with bathymetry. The star indicates the location of Son Tay hydrological station at the apex of the delta. Blue boxes show the most upstream points where the runoffs flow to the model. Cyan and yellow boxes show the location of other river mouths in the south and north of RR, respectively. **(C)** Daily Red River discharge in the model configuration, from National Hydro-Meteorological Service data (red curve, left y-axis). Blue dashed line: Percentage of Red River runoff compared to total runoff (sum of runoff from Red River, other rivers in Vietnam, rivers in China). Blue line: percentage of all rivers in Vietnam (including Red and other rivers in the GOT) compared to total runoff. Blue lines are referred to the right y-axis.

Maraldi et al., 2013) distinguishes the red and near-infrared radiations which are absorbed in surface layers (e-folding length scale: l = 0.35 m), and shorter wavelengths (mostly visible and ultraviolet) which penetrate deeper (e-folding length scale from less than 4 m along the coastline up to 15 m in the deeper region of the GOT).

Lateral boundary conditions, as described in Toublanc et al. (2018), allow the model to be nested into a larger scale model. At the open boundary, tidal surface elevation and current at K1, O1, P1, Q1, K2, M2, N2, S2, M4 frequencies from the tidal atlas FES2014 (Lyard et al., 2021) are taken into account as in Pairaud et al. (2008). The model is also forced by daily averages of sea surface height (SSH), 3D zonal velocity (u), meridional velocity (v), temperature (T) and salinity (S) fields, from the global analysis (hereafter 'OGCM') produced by Mercator-Océan International and provided by Copernicus Marine Service (CMEMS) at a resolution of 1/12°. CMEMS T, S fields are adjusted to recover consistency with tidal physics before being used at the open-boundary conditions of the model (**APPENDIX A**).

At the surface, boundary conditions are provided by an atmospheric model and fluxes of momentum, heat and freshwater are computed using the bulk formulae of Large and Yeager (2004). Operational ECMWF analyses (with a spatial resolution of 1/8°) are used to provide 3-h wind, precipitation, solar energy, atmospheric temperature, dew-point temperature, surface pressure.

As the present study focuses on the fate of continental water into the coastal ocean, a specific effort has been deployed on the

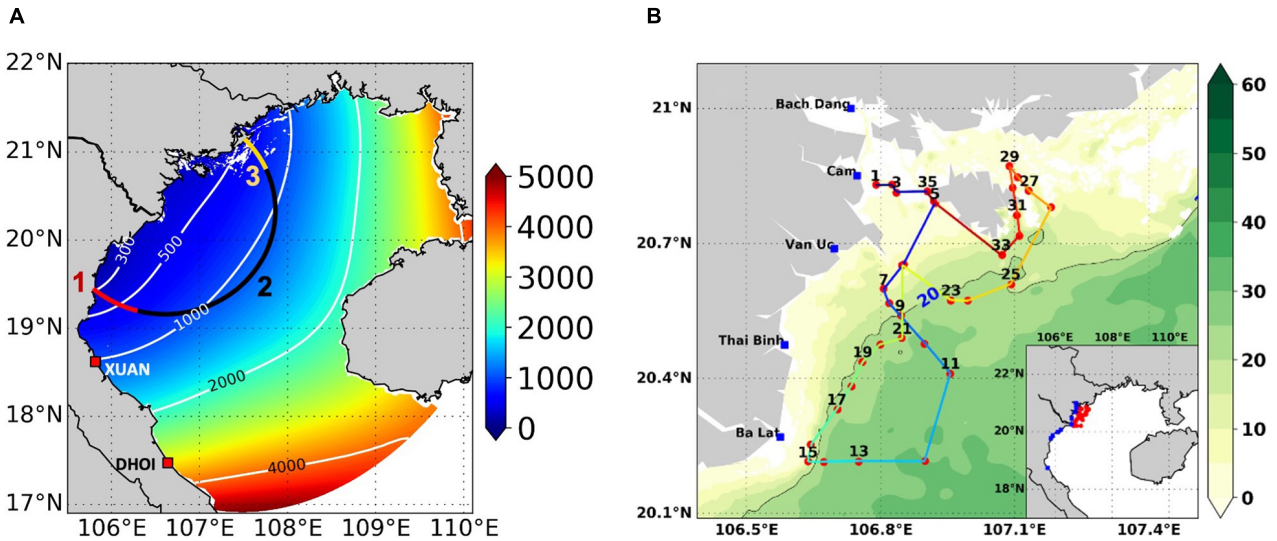


FIGURE 2 | (A) Grid cell size (m). Red squares show the location of HFR antennas. (1, 2, 3): Sections used to calculate the tracer transport. VITEL **(B)** CTD stations location. Red dots indicate the station locations, while blue points indicate the river mouths' locations.

river runoffs implementation; section "River Configurations" is dedicated to its description.

The model is run from 2010 to 2016, starting from the ocean state condition as provided by the global OGCM on 01/01/2010. The time step is set at 2 min. Further analyses are calculated during 2011–2016 (i.e., following a 1-year spinup). The model outputs include daily averaged variables as well as instantaneous fields every 12 h. Unless otherwise specified, both components of the current are detided based on an online harmonic analysis. A summary of the general configuration is available in **Table 1**.

Two other simulations are performed over the same period:

- a twin simulation without river forcing (GOT_NORIV) to assess the impact of the river runoff on the coastal circulation; all other forcings and parameters are the same as in GOT_REF.
- a twin simulation without tides (GOT_NOTIDE) to assess the impact of tides on the main patterns of the river plume variability; all other forcings and parameters are the same as in GOT_REF.

River Configurations

In most modeling studies to date, the RR was set up with only one mouth (or input grid point) using monthly or annual climatological runoff because more realistic runoff at the hydrological station was unavailable (Ding et al., 2013; Gao et al., 2013). In this study and in Piton et al. (2021), the river condition is configured as realistically as possible. Firstly, the delta is represented taking into account seven input grid points representing the mouths of the main RR delta distributaries (Bach Dang, Cam, Van Uc, Thai Binh, Ba Lat, Ninh Co., Day) (**Figure 1B**). Secondly, the daily RR runoff is obtained from the National Hydro-Meteorological Service (NHMS) of Vietnam at Son Tay hydrological station which is located at the apex of the RR delta. The discharge is distributed across the seven distributaries based on the results of Vinh et al. (2014) (Bach Dang (7%), Cam (13.2%), Van Uc (14.5%), Thai Binh (6.4%), Ba Lat (30.3%), Ninh Co (5.6%), Day (23.0%)). Furthermore, each river mouth is connected to a channel in the model to allow the water entering the coastal ocean with realistic salt and temperature properties and realistic stratification. The length of the channels (35–45 km, depending on the channel) is chosen to exceed the saltwater intrusion, which is approximately 30 km from the mouth (Nguyen Thi Hien et al., 2020). The results from GOT_REF confirm that the salty water never reaches the end of the channel, even in the low discharge period. The river runoff is converted into a vertically sheared current at the most upstream point of the channel (**APPENDIX B**); there the salinity of the river flow is 0 and the temperature varies seasonally from 17°C (in February) to 29°C (in August).

TABLE 1 | General characteristics of GOT_REF.

Name	Features
Grid points	429 * 600
Grid size	300 m (near the coast), 4500 m (near the boundary)
No. of vertical layers	20
Boundary conditions	global OGCM
Atmospheric conditions	ECMWF analysis (1/8°, 3 h)
Tidal forcing	FES2014 (K1, O1, P1, Q1, K2, M2, N2, S2, M4)
Light attenuation	Varying by space (~1 m near the coast and 15 m offshore)
Bottom roughness	1 mm
Timestep	2 min
Time	2010 – 2016

Other Vietnamese rivers (Ma, Yen, Lam) at the south of the Red River delta (hereafter referred to as the 'southern rivers') are also taken into account (**Figure 1B**). As daily runoffs were not available to us, we prescribe monthly climatological runoffs from NHMS. At the north of the Red River delta, 6 rivers (hereafter referred to as the 'northern rivers') are accounted for (**Figure 1B**), based on the data given by Gao et al. (2013). In general, the runoff of the Red River system alone accounts for 60% of the total runoff to the gulf, while adding other rivers runoff in Vietnam accounts for around 90% of the total runoff (**Figure 1C**). In detail, the average discharge for the Red River system in low (December, January, February) and high (July, August, September) discharge period equals to 1632 m^3/s and 4959 m^3/s, respectively. For the southern rivers, this value is 365 and 2043 m^3/s. For the northern rivers, it is 164 m^3/s and 1103 m^3/s. It is clearly shown that for the Red River, the ratio between high and low discharge seasons is only 3 times, this ratio is 5.6 times for the southern rivers and 6.7 times for the northern rivers. The lower ratio of the Red River can be due to the presence of several hydrological dams upstream.

In order to simulate the pathways of the river water into the GOT, passive tracers are used. Tracers act as dyes, i.e., they do not affect the dynamics. In total, there are 3 tracers (or three colors) meant to distinguish the inputs from the different river systems. The first tracer is added to the runoff of all the Red River distributaries at constant concentration (100 arbitrary unit/m^3). The second one is added at the other rivers in the south and the third one at the rivers in the north of Red River, with the same concentration (100 arbitrary unit/m^3). Since tracers are injected with the runoff, they are also submitted to the 1 year of spin-up.

Observational Data Sets Used to Evaluate the Simulation

In situ Data

We use temperature (T) and salinity (S) profiles measured at 35 CTD stations (**Figure 2B**) during the VITEL cruise which took place in July 2014 (Ouillon, 2014). We further use CTD measurements of T, S acquired repeatedly at 10 stations along a 25 km cross-shelf section by Vietnamese and US teams from Center for Oceanography (CFO) and Oregon State University (Rogowski et al., 2019). This dataset, hereinafter referred to as CFO data, consists in 20 timeframes between September 2015 and July 2016.

We compare the simulated tidal amplitude and phase with historical tidal measurements from 13 stations (whose location is indicated in **Figure 3**). The dataset stems from the International Hydrographic Organization[1].

High-Frequency Radar Measurements

We use surface velocity data from the high-frequency radar (hereafter HFR) system based on two antennas located at 18.62°N (XUAN site) and 17.47°N (DHOI site) (**Figure 2A**) along the coast and operated by the Center for Oceanography, Vietnam Administration of Sea and Islands (CFO, VASI). The data consists of daily maps of zonal and meridional components of the surface current, over the year 2015, built by Tran et al. (2021). The radial velocity measurements are gap-filled, interpolated onto a 6-km rectangular grid and detided as described by Tran et al. (2021). As explained in Rogowski et al. (2019), the summer coverage is lesser than in winter because of low sea state conditions; therefore uncertainties on the interpolated velocities are larger in summer. Comparisons with *in situ* measurement over a 12-day period indicate a mean bias of 3 cm/s and an RMS difference of 10 cm/s (Tran et al., 2021); we use these values as rough estimates of the data uncertainties. HFR data is representative of currents at 2.4 m below the surface (Tran et al., 2021); as a consequence, for the model assessment, we estimate the model current at 2.4 m before interpolating it over the HFR grid.

Altimetric Data

Tidal constituents computed from satellite altimetric data provide a rich dataset to evaluate the simulated tides offshore. Along-track amplitudes and phases are calculated from the long time series of sea surface height obtained from satellite altimetry (TOPEX/Poseidon, Jason 1–2) by using harmonic analysis. We use the dataset described in Lyard et al. (2021).

K-Means Unsupervised Learning Algorithm for Time Series Pattern Analysis

Many different methods exist to analyze the main characteristics of time series, such as statistical, spectral and classification methods. In terms of classification, there are several methods. For example, Self-Organizing Maps method is used to describe the river plume patterns by Vaz et al. (2018) for the Tagus River and Falcieri et al. (2014) for the Po River. Here, we apply another method, K-means, to analyze not only the plume patterns but the associated forcing conditions.

K-means clustering analysis (KMA) is a popular unsupervised learning method (Hastie et al., 2001) that allows to classify objects (observations, model outputs) into different groups, given a measure of dissimilarity.

The aim of this method is to iteratively identify clusters by their centroid (the means) then minimize the distance between each member of the cluster and the centroid of that cluster. The procedure of this method is made of six steps.

Step 1: Choose the number of clusters to compute.
Step 2: Allocate random numbers as the centroids of the clusters.
Step 3: Calculate the distance from each member to the centroids, using the Euclidian distance (see **APPENDIX C** for more details).
Step 4: compare these distances, then assign the member to the cluster corresponding to the minimum distance.
Step 5: for each cluster, re-calculate the centroid based on the mean of all members which belong to that cluster.
Step 6: repeat step 3 to 5 until the clusters no longer change.

This method has been used in several past studies in coastal oceanography. Solabarrieta et al. (2015) used it

[1]https://www.iho.int/

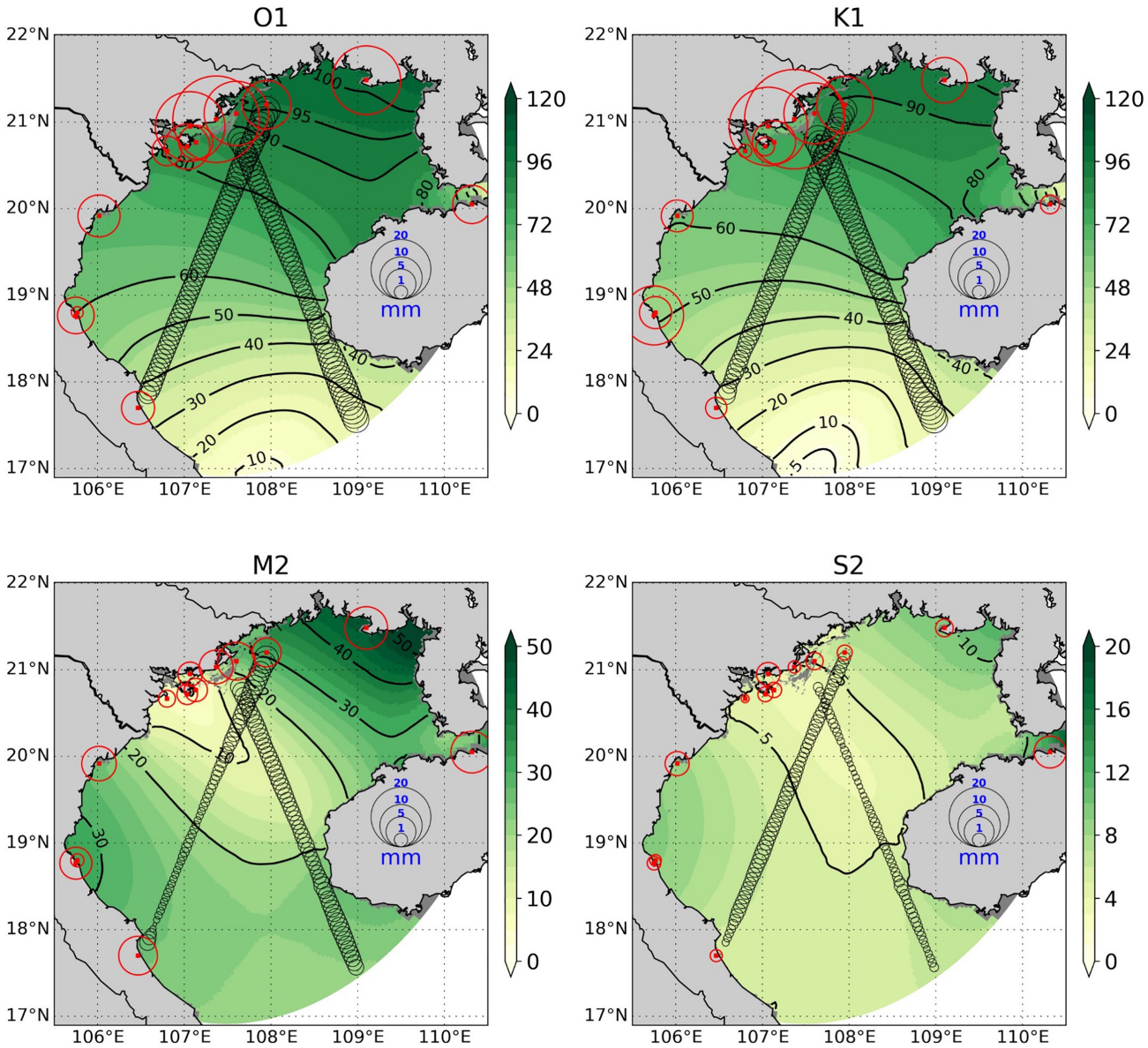


FIGURE 3 | Amplitude of the tidal constituent (in colors, cm) from GOT_REF. Each figure shows the complex error (mm), calculated from the amplitude and phase, between model result and observational data for 4 main tidal constituents (O1, K1, M2, S2). Black circles show errors compared to altimetry data, while red circles indicate errors compared to the tidal gauges data.

to examine the relationship between wind and surface circulation in the Bay of Biscay. They found that most of the current patterns are related to a specific wind pattern in the study area. Chen et al. (2017) identified the area of Pearl river plume by applying the K-means clustering to a summer climatological turbidity image. Sonnewald et al. (2019) used it to classify different regions based on the barotropic vorticity.

In this study, we use KMA to identify the main patterns of the plume and their temporal variations using daily model outputs. To do this, we use the KMA as implemented in the scikit-learn library coded in python (Pedregosa et al., 2011).

In the KMA method, the number of clusters is not fixed automatically, it is chosen depending on the application. The number of clusters should lead to an easy interpretation of the classification, since the objective is to reduce the dimension of the ensemble of scenes to analyze, without eliminating too much variability. In this study, we choose 4 clusters. The method to identify the number of clusters is described in **APPENDIX C**.

We applied KMA to the "masked river plume." Firstly, plumes are identified using tracers (as described in section "River Plume in GOT: Identification and Variations of Area"). Then, for a given day (a scene), each grid point where the plume is considered to be present is masked with 1, while other points are masked with 0.

The results of the classification are shown and analyzed in section "Variability of the RR Plume."

GENERAL CIRCULATION AND MODEL ASSESSMENT

The main objectives of this section are to provide a general description of the patterns of the seasonal circulation at the scale of the GOT from GOT_REF, to assess the consistency of model results with previous studies (or evidence their specificities) and to provide a qualitative assessment by comparing to observations. As a description of the general circulation and model verification (in particular using satellite data) have been provided recently by Piton et al. (2021) from a very similar configuration, we do not provide a detailed analysis. We introduce the section by a discussion of the first Rossby radius, continue with the basin-scale circulation, evaluation of tidal elevation and with the comparison to *in situ* temperature and salinity data and surface current velocity from high-frequency radars in the area of the RR plume.

First Baroclinic Rossby Radius of Deformation

The first baroclinic Rossby radius of deformation (Rd) sets the scale of mesoscale baroclinic instabilities and, as such, should be resolved by the numerical circulation models (see for instance Greenberg et al., 2007). In river plume dynamics, Rd in the near-field or far-field (coastal current) is used to estimate the relative impact of Coriolis force on the plume dynamics with respect to other forcing (runoff, ambient current). For instance, Yankovsky and Chapman (1997) showed that for surface-advected plumes, the offshore extension is more than four Rossby radii.

In this study, Rd is computed from the mean seasonal field of temperature and salinity from our simulation over 2011–2016. The calculation is made by solving a Sturm-Liouville problem as described for instance in Chelton et al. (1998). We use the method developed by F. Lyard at LEGOS for free surface vertical modes of the internal pressure and described for instance in Nugroho (2017). At depths larger than 60 m, the Rossby radius decreases from 10 to 13 km in April–September (**Figure 4A**) to 4–7 km in October–March (**Figure 4B**). In shallower areas, it decreases from 3–8 to 1–5 km. Such a seasonal variation is expected as the stratification is stronger in April–September with higher air temperature. A large spatial variability is also observed; by construction it is correlated to the bathymetric variations. In particular, a striking feature is the eastward extension of the shelf, between the Bach Long Vi island and the coast; the Rd does not exceed 4 km there. Close to the coast in both summer and winter monsoon periods, it can drop to less than 1 km. Moreover, the Rd spatial variability also reflects some patterns of the circulation. For instance, a strong mixing occurs west of Hainan, mostly due to tides, as suggested in the literature (e.g., Nguyen et al., 2014; Piton et al., 2020) and in agreement with the local maximum of the K1 and O1 current in our simulation (**Supplementary Figure 1**). As a consequence, the Rd is only a few hundred meters west of Hainan Island. On the other hand, the RR runoff leads to an increase of stratification along the Vietnamese coast south of 21°N which has a clear signature in a locally larger Rd (∼4–5 km) in the October–March period.

Assuming that the effective resolution is roughly between six and ten times its grid resolution, we can evaluate the model's ability to resolve Rd. Rd is well resolved in the northwest quarter of our domain where the mesh is well refined in summer, and along the Vietnamese coast between 19 and 21°N in winter. However, if we consider that the scales of interest are about 4 times the Rossby radius, then the model resolution is sufficient between 18 and 21°N.

General Circulation

Mean Surface Circulation

The current in the GOT has been studied with mainly a focus on the northern region, due to the lack of observational data in the south (Wu et al., 2008; Ding et al., 2013; Gao et al., 2014). Recently, thanks to the deployment of a high-frequency radar system, the surface circulation in the southwestern area has been documented (Rogowski et al., 2019; Tran et al., 2021). However, the variability of the general surface and subsurface circulation remains relatively undocumented over the whole gulf and more specifically along the Vietnamese coasts.

Figure 5A shows the mean surface current from November to March from GOT_REF for the 2011–2016 period. The circulation in this winter monsoon period is dominated by the gulf-scale cyclonic gyre, as reported by several authors (Ding et al., 2013; Gao et al., 2014; Rogowski et al., 2019; Piton et al., 2021). The coastal current along Vietnam originates from the merging at 20°N of the westward flow from Hainan Strait and a coastal current from the northernmost shelf. It flows downcoast down to the southern boundary of the domain. It is the dominant feature of the surface circulation with a mean amplitude of about 30 cm/s. South of Hainan Island, an inflow from the South China Sea is simulated in the deepest part of the area with a decreasing intensity from November to March. This inflow is deflected westward and joins the coastal current south of 19°N, creating a small-scale cyclonic gyre as in Ding et al. (2013).

In April, the summer monsoon sets in and lasts until August. The southward coastal current weakens and becomes intermittent (**Figure 5B**). When present, it is deflected eastward at ∼18°N; it then splits into 2 branches. The first one forms a cyclonic circulation in the central basin. The second branch feeds an intense current south of Hainan that flows out from the gulf. This corresponds to the circulation scheme described by Gao et al. (2014) and Rogowski et al. (2019), but, in our simulation, the current variability is large at daily and interannual time scales.

In September and October (**Figure 5C**), the coastal current is southward again from 21°N to the southern boundary where it exits the gulf. It reaches its maximum amplitude (∼35 cm/s) and width. Besides, the circulation is characterized by two inflows with large velocity (∼30 cm/s): one from Hainan Strait and the other from the southern boundary in the deep region.

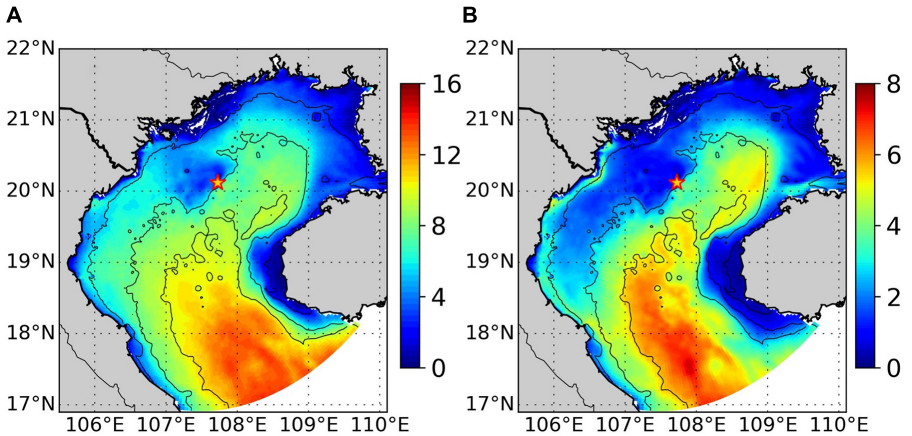


FIGURE 4 | (A,B) The first baroclinic Rossby radius of deformation (km), over the period 2011 – 2016, computed from the temperature and salinity profiles averaged from April to September **(A)** and October to March **(B)**. Contour lines indicate the bathymetry. Star shows the location of Bach Long Vi island. *Note: Different color bar scales.*

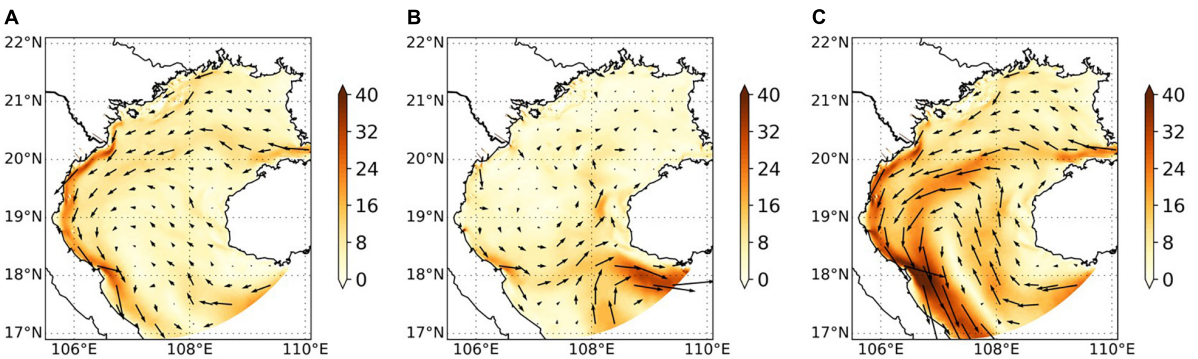


FIGURE 5 | Means of the detided daily surface current (cm/s) simulated by GOT_REF. **(A)** November – March average. **(B)** April – August average. **(C)** September – October average.

Horizontal Transport

The horizontal transport displays a similar seasonal cycle as the surface current. From September to March, the general circulation is cyclonic, with a large downcoast transport over the shelf in the west. From April to August, the transport inside the gulf weakens significantly. The main specific patterns are a cyclonic gyre in the central area.

The flow direction during the summer monsoon through Hainan Strait is discussed in several papers (Shi et al., 2002; Gao et al., 2013; Chen et al., 2017). In our simulation, the flux is inflow from September to April and an outflow during the summer monsoon. It varies between −0.18 Sv and +0.15 Sv at 110 E, with significant daily and interannual variability (not shown). Our results however are consistent with the situation described by Wu et al. (2008); in case of inflow the circulation is mainly cyclonic, while in case of outflow the overall circulation is anticyclonic.

Besides, the gulf is fed all year long by an inflow from the southern boundary, which is maximum in summer monsoon period. From September to December, it enters through the east and either penetrates northward in the gulf or is deflected westward and joins the coastal current. The rest of the year it enters through the center, is deflected eastward and generates a large outflow south of Hainan Island.

Model Assessment

Evaluation of Tides

The simulated amplitudes in terms of sea surface elevation for the four main tidal constituents (O1, K1, M2, S2) are shown in **Figure 3**. O1 and K1 have the same amplitude distribution. The amplitude is largest in the north (100 cm and 95 cm for O1 and K1, respectively) and decreases to its lowest value at the south of the gulf, near the boundary. M2 has two peaks of amplitude. One peak is located in the north (50 cm) and another peak is located at 19°N (30 cm) along the Vietnamese coast. The lowest amplitude is located near RR mouths. These patterns are similar to the ones found by Nguyen et al. (2014) and Piton et al. (2020). We also examined the tidal currents (see **Supplementary Figure 1**): the O1 and K1 tidal currents are the strongest west and south of Hainan Island and in the Hainan Strait (more than 50 cm/s). Near the Vietnamese coast, they are weaker and range from 10 to 20 cm/s. They reach a local maximum (∼ 30 cm/s) along the coast at ∼18°N, 106.5°E. M2 tidal currents vary between 10 and

20 cm/s, with a local maximum close to the Ba Lat mouth. S2 currents have a similar spatial distribution but smaller amplitude (<4 cm/s close to the RR mouths).

The simulated tides show remarkable comparisons to along-track altimetric data (**Figure 3**): the root mean squares of the complex errors (i.e., the model-data misfits) over the domain are as low as 2.6 cm, 2.8 cm, 1.3 cm, 0.7 cm for O1, K1, M2 and S2, respectively. These values correspond to 5.0%, 6.0%, 7.4%, and 12.9% of the signal. The model-data misfits are homogeneous in the center of the basin. They are the largest near the coast as expected due to the larger uncertainty of both the altimetry data near the coast and due to the uncertainty of model bathymetry in the very shallow area. These values are comparable to those obtained by Piton et al. (2020) with the T-UGOm tidal model over the same domain (2.6 cm, 3.5 cm, 3.0 cm, and 1.2 cm for O1, K1, M2 and S2, respectively) and to those of Nguyen et al. (2014).

Compared to historical tidal gauges data, the complex error is larger: 18.3, 20.9, 6.2, and 2.3 cm for O1, K1, M2, S2, respectively (**Figure 3**). There are several reasons for these higher errors. Firstly, the observation period for the tidal gauges data that are available is relatively short (15 days to 1 year) and may not be long enough to be accurate and representative of 'mean' tides. Secondly, the largest errors are observed in the area of the RR delta where the extremely complicated coastline with the presence of thousands of small islands makes the accurate representation of tides a challenge for such a configuration. Compared to Piton et al. (2020), GOT_REF performs better for M2 (6.8 cm) and S2 (3.5 cm), but gives poorer results for K1 (10.2 cm) and O1 (10.2 cm). Future work will be dedicated to tuning the properties of the channels (see section "River Configurations") to better simulate the propagation of the tidal wave in the delta.

Comparisons With High-Frequency Radar Currents

Figure 6 shows the data from the HFRs and from GOT_REF in different seasons in 2015, as well as the maps of correlation between simulated and observed u and v over the whole time series (1 year).

In January, the main observed coastal current is southward, with an amplitude of ∼ 30 cm/s at the coast and decreasing offshore. The model shows the same current direction, but its amplitude is underestimated by 20 cm/s (**Figures 6A,B**). In April, the coastal current is less intense, but the northward current at 107–107.5°E is stronger. In GOT_REF, both the southward and northward circulations are observed, with a persistent underestimation of the coastal current regarding the HFR data (**Figures 6C,D**). In May, the coastal current reverses north of 19°N in both the observations and simulation. At around 18°N, the simulated downcoast current is deflected eastward consistently with the HFR observations. However, both at 19°N and 18°N the simulated current is stronger than in the HFR data (**Figures 6E,F**). In July, HFR data show a nearly closed circulation. The coastal current flows southward at 19°N, then rotates at 18°N and flows northward and finally joins the coastal current at 19°N again. In GOT_REF, the circulation shows a more complex pattern, with a northward current (of ∼20 cm/s) at 19°N and a large temporal variability (**Figures 6G,H**). In October, HFR data show a similar current pattern as in January, with a strong southward coastal current (∼40 cm/s). The model shows very good consistency, with the strongest velocity near 18°N (**Figures 6I,J**).

The temporal correlation between simulated and observed daily fields of u and v is higher for u offshore (∼0.5) (**Figure 6K**), while the correlation for v is better near the coast (>0.6) (**Figure 6L**). The larger misfits between the model and data at ∼19°N seem to come from a larger spatial variability of the simulated u component (not shown) than the observed one. In particular, as discussed in section "Variability of the RR Plume," this area is characterized by some eddy activity in summer which may not be resolved by the HFR observations or may be out of phase with the observations.

Temperature and Salinity Profiles From *in situ* Measurements

Figure 7 shows the salinity and temperature profiles from the VITEL campaign and the GOT_REF simulation. Although it is a very shallow area, the bathymetry of the model is quite accurate compared to the depth of the CTD data. The largest bathymetry misfit is reached at stations 26 to 30 where the model is too shallow by ∼10 m. Since the campaign took place in summer (July), there is a strong stratification in both salinity and temperature profiles. At the surface, the observed salinity can be as low as 15, while at the bottom it is around 34. The mean value at all points is 28.7. The model performance is good, with a correlation R = 0.88 computed from all profiles, but the mean value is overestimated by 0.7. The model overestimates the surface salinity at stations located in the shallowest area. This suggests that the river runoff is underestimated or that the simulated mixing in the estuaries is too strong, possibly due to local errors on the tidal representation.

The observed temperature goes up to 33°C at the surface and 27°C at the bottom, with a mean value of 30.3°C. The mean bias of the model is low (0.2°C), although the temperature is overestimated at both the surface and bottom at some stations. Overall, R is 0.72.

The comparison with the T, S profiles from the CFO campaigns is not described in detail as we get similar results to those described by Piton et al. (2021) in a similar configuration of the model. For all the 20 sections available, the mean biases (absolute value) between data and model are 0.61 and 0.71°C for S and T respectively, and the mean correlations 0.81 and 0.72. The comparisons suggest that the model runoff is not high enough (as already suggested by the comparison with the VITEL data), or the background salinity provided by the boundary condition is too high. The vertical mixing seems underestimated also. Overall, despite small biases, the model reproduces accurately the seasonal conditions even in the very shallow area.

RIVER PLUME IN GOT: IDENTIFICATION AND VARIATIONS OF AREA

This section will first review some past studies on plume identification then explains our method to identify the plume

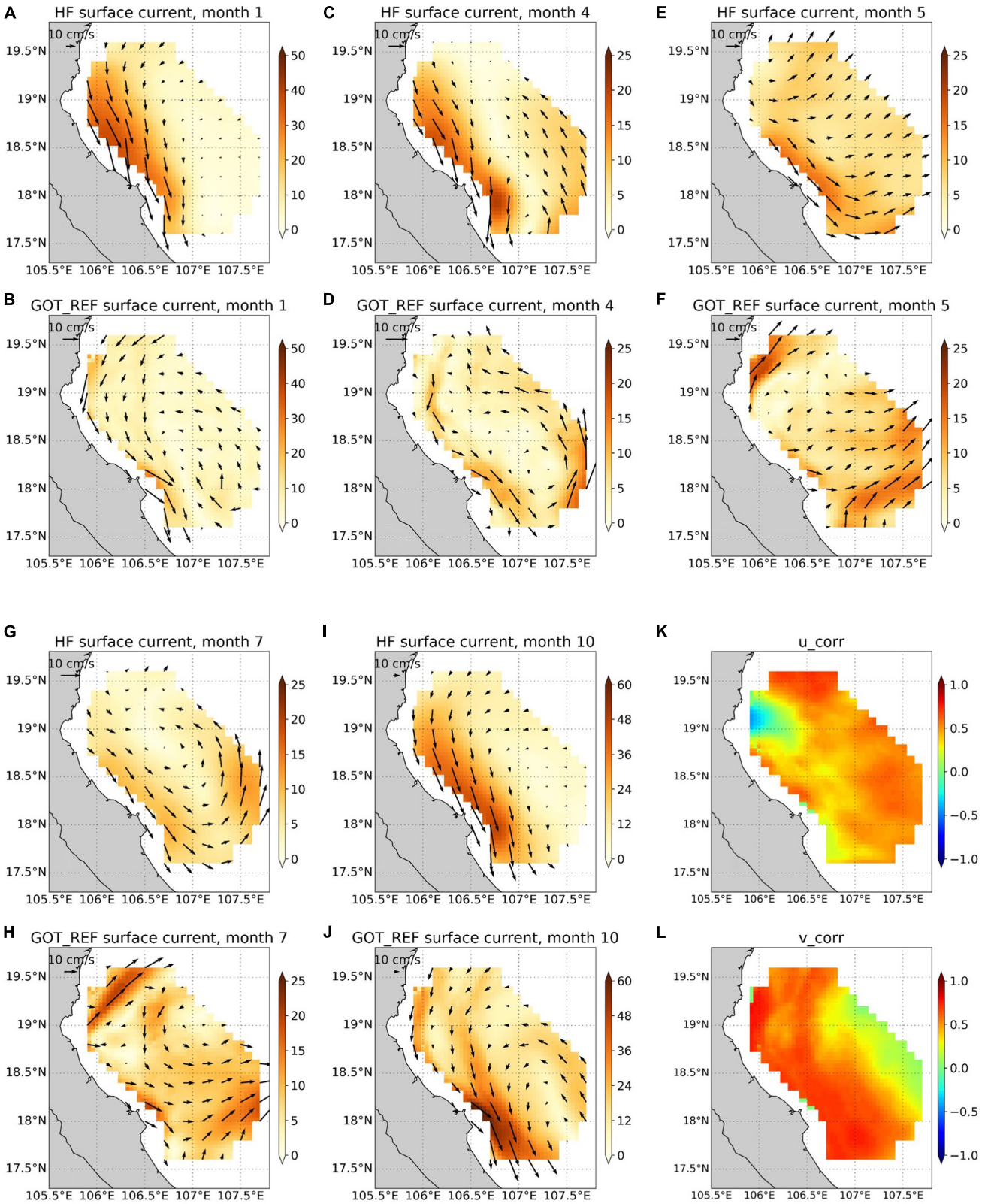


FIGURE 6 | Surface current from HFR data **(A,C,E,G,I)** and model simulations **(B,D,F,H,J)** for different months of 2015 (Jan, Apr, May, Jul, Oct) (cm/s). Temporal correlation of u and v **(K,L)** computed from daily currents. *Note: Different color bar scales.*

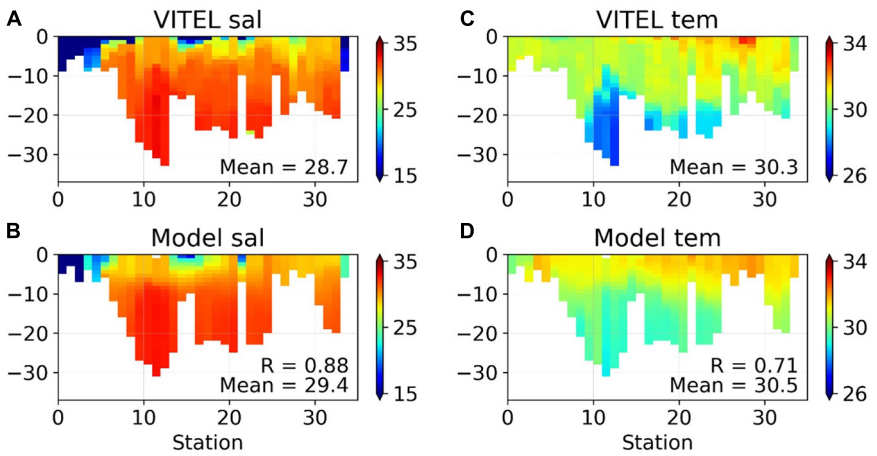


FIGURE 7 | Profiles of salinity from VITEL data **(A)** from GOT_REF **(B)**. **(C,D)** Same but for temperature.

locally in the GOT. Then, the resulting variations of the plume area in the period 2011–2016 are analyzed.

A Brief and Non-exhaustive Review of Past Studies

There are no clear criteria to identify a river plume in general. Usually, such criteria involve sea surface salinity (hereafter SSS) because the river plume has a lower surface salinity than the surrounding ambient waters. However, due to different environmental conditions, the reference salinity is difficult to set in a general enough manner. In some studies, the authors may choose a suitable value based on their knowledge and experience; however, the choice is seldom justified in a rigorous way. This may lead to a situation where different authors choose different values for the same plume, depending on the observational or modeling approach and the objectives. For example, for the Columbia river plume, Liu et al. (2009) use SSS = 29 to detect the plume, while Burla et al. (2010) use the value of SSS = 28 and in MacCready et al. (2009) the plume is identified using SSS < 31.

Other authors defined other criteria to identify the plume. Otero et al. (2008) use the highest horizontal gradient of mixed layer depth to classify the river plume area in the Northwest Iberia and then use the SSS value of 35.6 that coincides with this maximum gradient. Another approach to identify river plumes is based on ocean color satellite images that reveal turbid water masses rich in Chlorophyll, suspended matter, or colored dissolved organic matter (e.g., Chen et al. (2017) for the Pearl River).

To our knowledge, there have been very few studies dedicated to the RR plume, so there is no published reference ambient salinity value. Rogowski et al. (2019) locate the RR plume using monthly means of ocean color maps from MODIS. In tropical areas, the presence of clouds is however a limitation to the use of optical products to investigate the sea surface variability at time scales shorter than a month.

Stratification Index and SSS Threshold

To identify the RR plume, different methods are in consideration in this paper. Firstly, we apply a method based on the Stratification Index (hereafter SI), assuming that the river water forms a buoyant layer over the ocean water. This index was first proposed by Hansen and Rattray (1966) for estuary classification. It is defined as the relative difference between the surface and bottom salinity (eq. 1). In this paper, we tested this method with a threshold of 0.1. If SI equals or exceeds 0.1, the water column is defined as belonging to the river plume. The time series of the daily plume area for all the rivers in GOT based on SI is shown in **Figure 8A**. As expected, the river plume area varies with the river runoff. In July–August (high runoff period), the plume area reaches its highest value, while it is lowest in December–January (low runoff period).

$$SI = \frac{salinity_{bottom} - salinity_{surface}}{vertical\ mean\ salinity} \quad (1)$$

However, there is one major drawback to the SI method. Vertical salinity sections indicate that the plume in the GOT consists of 2 zones. One is the very shallow coastal area where the plume is mixed over the entire water column; in the second one, farther offshore, the plume is detached from the bottom and stays on top of the high salinity water. SI being based on the difference between the salinity at the top and the bottom of the water column, it cannot detect the plume zone in the shallow area where it is totally mixed. In the low runoff period, as we will show in section "Variability of the RR Plume," the downcoast current and the northeasterly wind make the plume stick to the coast; in such a case, the whole plume is well-mixed and SI is not helpful since the calculated area is close to zero (**Figure 8A**).

To deal with that problem, in a second step, we considered using SI as a proxy to find the suitable SSS that can be used as the plume indicator. After several experiments, we selected the value of SSS = 30. In high runoff period, this criterion defines a plume with a similar pattern offshore to the one deduced from the SI

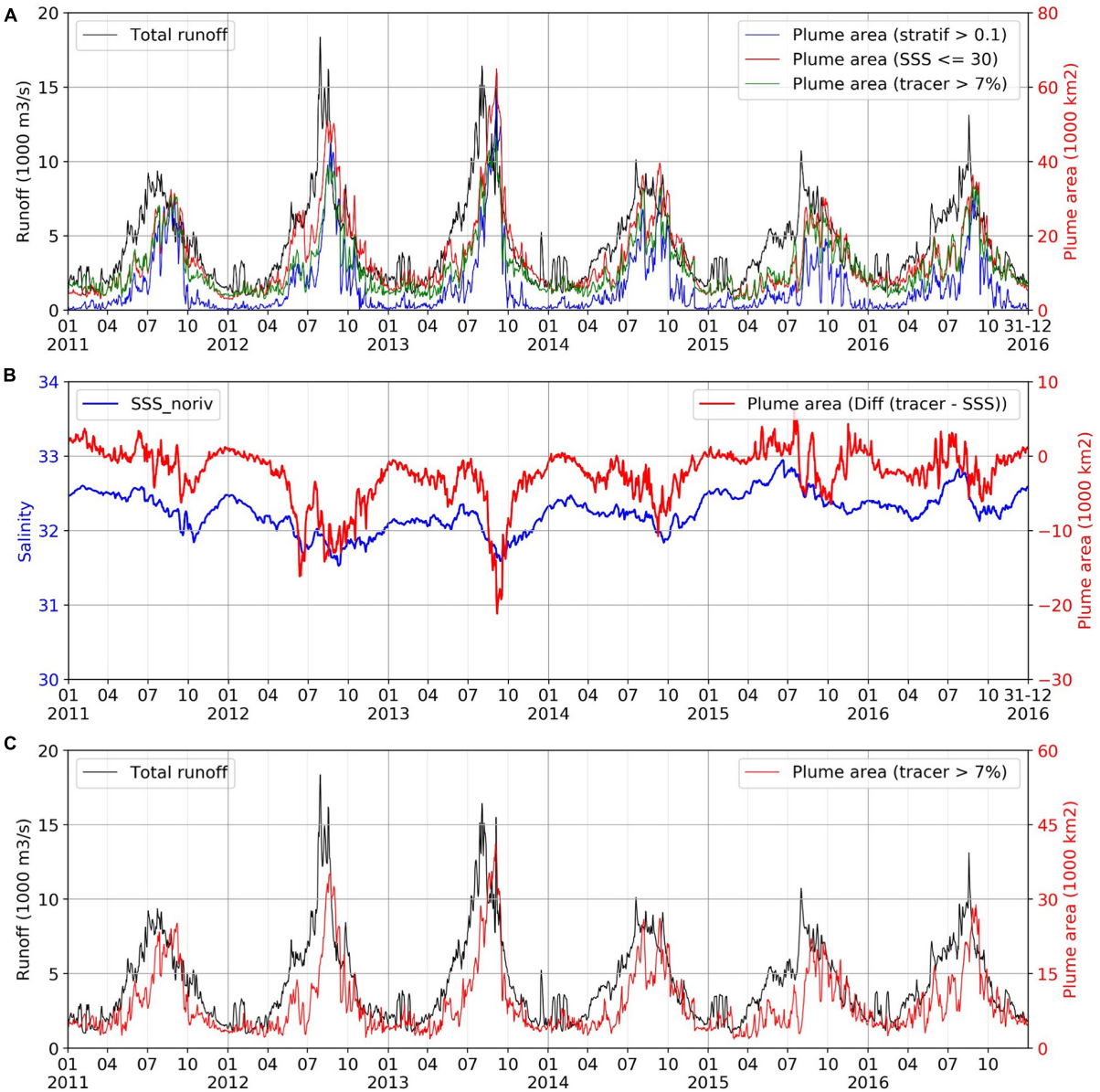


FIGURE 8 | (A) Total runoff (in m^3/s) and plume area (in km^2) for all the rivers in the Gulf of Tonkin. The plume area is calculated using the Stratification Index (blue), SSS (red) and tracer concentration (green). **(B)** Spatially averaged SSS over the whole domain (in blue) from the simulation without river (GOT_NORIV), and difference of river plume area between SSS and tracer methods (in red). **(C)** Daily runoff and plume area for the Red River and Southern rivers.

criterion. In the low runoff period, this discriminant value also captures the narrow plume area that runs along the coast (**Figure 8A**).

Using SSS, the envelope of river plumes created by all the rivers in the GOT was generally identified. However, this "stratification-based SSS" method has in turn two drawbacks. Firstly, it cannot distinguish the plumes created by the different rivers that feed the GOT. Secondly, the SSS criterion may be slightly biased at seasonal time scales by the effect of precipitation. Indeed, the precipitation has seasonal variations due to the monsoon system. The average precipitation from January to March is 1.8 mm/day, while it is 5 times higher (9.4 mm/day) from August to October (calculated from ECMWF daily precipitation over 2011–2016).

Passive Tracers

As an alternative method, we use passive tracers that behave in the model as any buoyancy-free particle or passive chemical from the rivers (as explained in section "River Configurations"). This is particularly relevant to identify the coastal area influenced by the river input of contaminants and to distinguish the freshwater input from other sources than the river such as advection by coastal current and other coastal runoffs [see for instance

Wang et al. (2014) for the Copper River in the Gulf of Alaska] or to study mixing between the plume and ambient waters [e.g., Vlasenko et al. (2013) for the Columbia River]. As for the SSS criteria, the choice of a tracer concentration threshold to define the plume is author-dependent. In Vlasenko et al. (2013), the river plume is identified as the area where the concentration exceeds 10 units/m^3 while in Wang et al. (2014), the threshold is 5 units/m^3. In our study, several experiments led to identify the river plume as the area where the concentration exceeds 7 unit/m^3, which best fits with the area identified by the criterion on SSS in the low runoff period (dry season).

As indicated in section "Observational Data Sets Used to Evaluate the Simulation," 3 tracers were added, respectively to the RR distributaries, the southern rivers and the northern rivers. **Figure 8A** shows the plume area for all the rivers in the GOT calculated by summing the three tracers' concentrations. The plume areas computed from the SSS and tracer criteria have a similar trend in both the low and high runoff periods. However, in the high runoff period, especially during the peaks in 2012 and 2013, the plume area calculated from the tracer is much lower than from the SSS. This difference can go up to over 20,000 km^2 (**Figure 8B**). **Figure 8B** also shows the SSS of the twin simulation without any river runoff (GOT_NORIV). Even with no river, the SSS shows significant variations between 31 and 33. The low sea surface salinity often happens in summer, which is in the rainy season. It is minimum in 2012 and 2013, which are also the years when the runoff reaches the highest peaks (**Figure 8A**), hinting at a correlation between local precipitation and runoff in both years. The SSS drop in the GOT_NORIV run has a similar trend than the difference of plume area calculated by the two methods, which suggests that this difference could be indeed due to precipitation.

In conclusion, for our objectives, the method based on the passive tracers seems the most appropriate to help identify the RR plume among the three methods investigated in this study. It can capture the plume in both the highly stratified zone and the shallow mixed zone. Besides, it can distinguish the plumes created by different rivers (as discussed in section "Discussion").

Temporal Variability of the Plume Area

South of 20°N, the RR plume is quickly joined by the plumes of the southern rivers (Ma, Yen and Lam, **Figure 1**), creating a unique buoyant plume which extends southward along the coast most of the year. In this section and in the following we therefore analyze the variability of the resulting plume from the RR and the three southern rivers together. Section "Discussion" will discuss the receiving basins by distinguishing the RR from the other rivers, thanks to the multi-tracer approach.

Figure 8C shows the evolution of the cumulated runoff from the Red, Lam, Yen and Ma rivers and the corresponding plume area from 2011 to 2016. As expected, the plume area follows the same variations as the river runoff, albeit with a time lag. In summer, when the runoff is high, the peak of the plume area occasionally reaches more than 40,000 km^2 (about 27% of the GOT area), while in winter, it sometimes falls below 2,000 km^2. Due to the interannual variability of the runoff, the plume area varies significantly between different years. The river plume area peak in 2013 (41,000 km^2) is nearly twice as large as the peak in 2015 (22,000 km^2). Both the total discharge and the plume area undergo a strong variability at shorter time scales of a few days as well.

Figure 8C also shows two more characteristics of the plume variability. Firstly, a higher runoff does not ensure a larger river plume area. In 2012, the runoff peak is higher than in 2013, while the plume extension in 2013 is larger. Similarly, although the rainy seasons in 2014 and 2015 are characterized by similar runoffs, the plume area in 2015 is much lower than in 2014. Secondly, there is a time lag between the runoff peak and the peak of the plume area. This lag is also described in Rogowski et al. (2019). Depending on the year, it can be up to 1 month (in 2013). In 2015 and 2016, the plume area is relatively small until July and reaches its peak value rapidly within a few days. In short, both the time lag and plume area do not appear directly correlated to the runoff intensity (i.e., a higher runoff will not necessarily create a larger plume area about 1 month later). Such a variability evidences the fact that river runoff intensity is not the only factor driving the plume size and variability. Wind variability and its impact on the surface circulation and mixing is likely to be another driver, as we show in the next section.

Figure 8C displays as well some interannual variability in both the runoff and the plume area variations. The years 2015–2016 were marked by an intense El Nino event. Generally, El Nino events lead to decreased rainfall, drought and saltwater intrusion in deltas in Vietnam (Sutton et al., 2019). **Figure 8C** does not evidence a drastic drop in the 2015–2016 runoff with respect to 2014 and 2011. However, the SSS signal in the GOT_NORIV run is significantly different in 2015–2016 with respect to the previous years (**Figure 8B**): the mean SSS stays above 32 and the seasonal signal is inverted with a maximum SSS in summer. El Nino is likely to influence the coastal circulation, through alteration of wind and air-sea fluxes of freshwater and heat. The specific influence of ENSO on the coastal plume will be investigated in future studies as we focus in this paper on seasonal and shorter time scales.

VARIABILITY OF THE RR PLUME

Spatial Patterns of the Plume

In the previous section, the river plume in GOT has been identified using passive tracers. We have documented the time variations of the total surface area and compared them to the runoff variations. Now, the seasonal variability of the plume spatial patterns is examined using KMA.

Figure 9 shows the spatial distribution of frequency of occurrence of the plume within each of the 4 clusters calculated from the plume area from 2011 to 2016, and the temporal evolution of the clusters, revealing both seasonal and interannual variations. The main variables of interest (SSS, wind, surface current, SSH) are averaged over the period corresponding to each cluster and are shown in **Figure 10**.

The first cluster usually occurs from October to March and appears on 992 days (45.3%) in 6 years. In this cluster, the plume is very narrow and is mostly confined to the shallow area (depth $<$ 20 m). 75% of the time that the plume occurs,

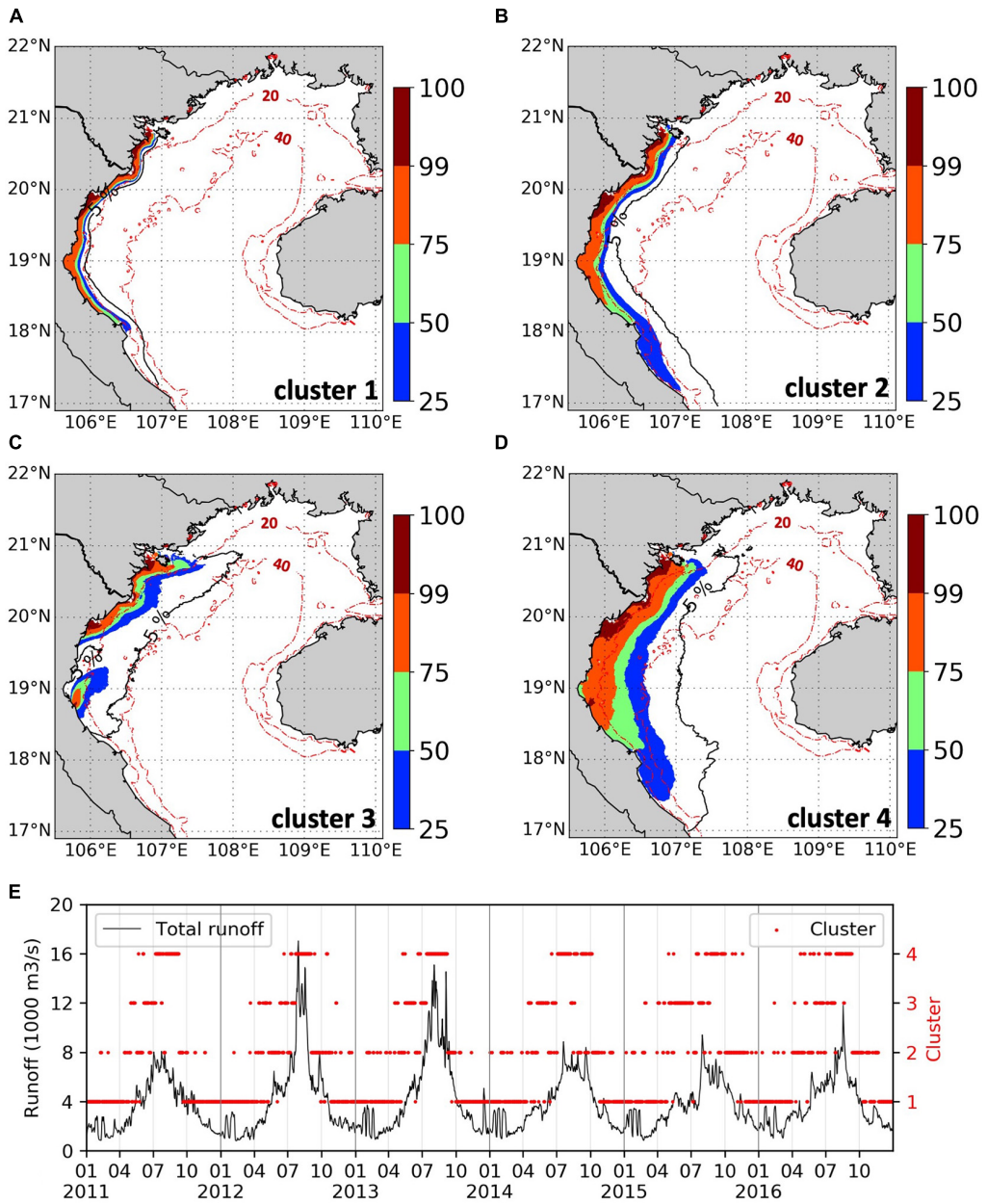


FIGURE 9 | Frequency of occurrence of the plume within cluster 1 **(A)**, cluster 2 **(B)**, cluster 3 **(C)**, cluster 4 **(D)**. For instance, for cluster 1: at a given point, a frequency of 25 means that over the whole period when cluster 1 is present, the plume is present at this point 25% of the time. **(E)** Temporal distribution of each cluster (in red) and the runoff from Red and Southern rivers (in black).

at 19°N, it extends to 105.8E (∼20 km from the coast) while 25% of the plume extends to 105.85E (∼25 km from the coast) (**Figure 9A**). If the runoff (or other forcing) undergoes strong fluctuations, the plume area should also vary. In this cluster, the difference between the spatial occupancy of 25% and 75% is small: it means that the forcing condition is relatively stable. The simultaneous occurrence of several conditions can explain the relatively small extent of the plume in this cluster. Firstly, it happens in the lowest runoff period (average discharge over the cluster equal to 2197 m^3/s). Secondly, the wind is strong and from the north-east (winter monsoon, **Figure 10A**), which is downwelling-favorable. At the GOT scale, the mean wind velocity is 6.4 m/s; it is stronger than in any other cluster, even near the coast (it reaches ∼ 5.7 m/s on average inside the red box shown on **Figure 10A**). The coastal surface current is southward, with a mean speed larger than 20 cm/s between 20.5 and 17.5°N (**Figure 10E**); consistently with the strong monsoon wind, the current also reaches its largest intensity in cluster 1. All these conditions favor the low salinity (SSS < 30) water to be confined to the coast and to extend southward

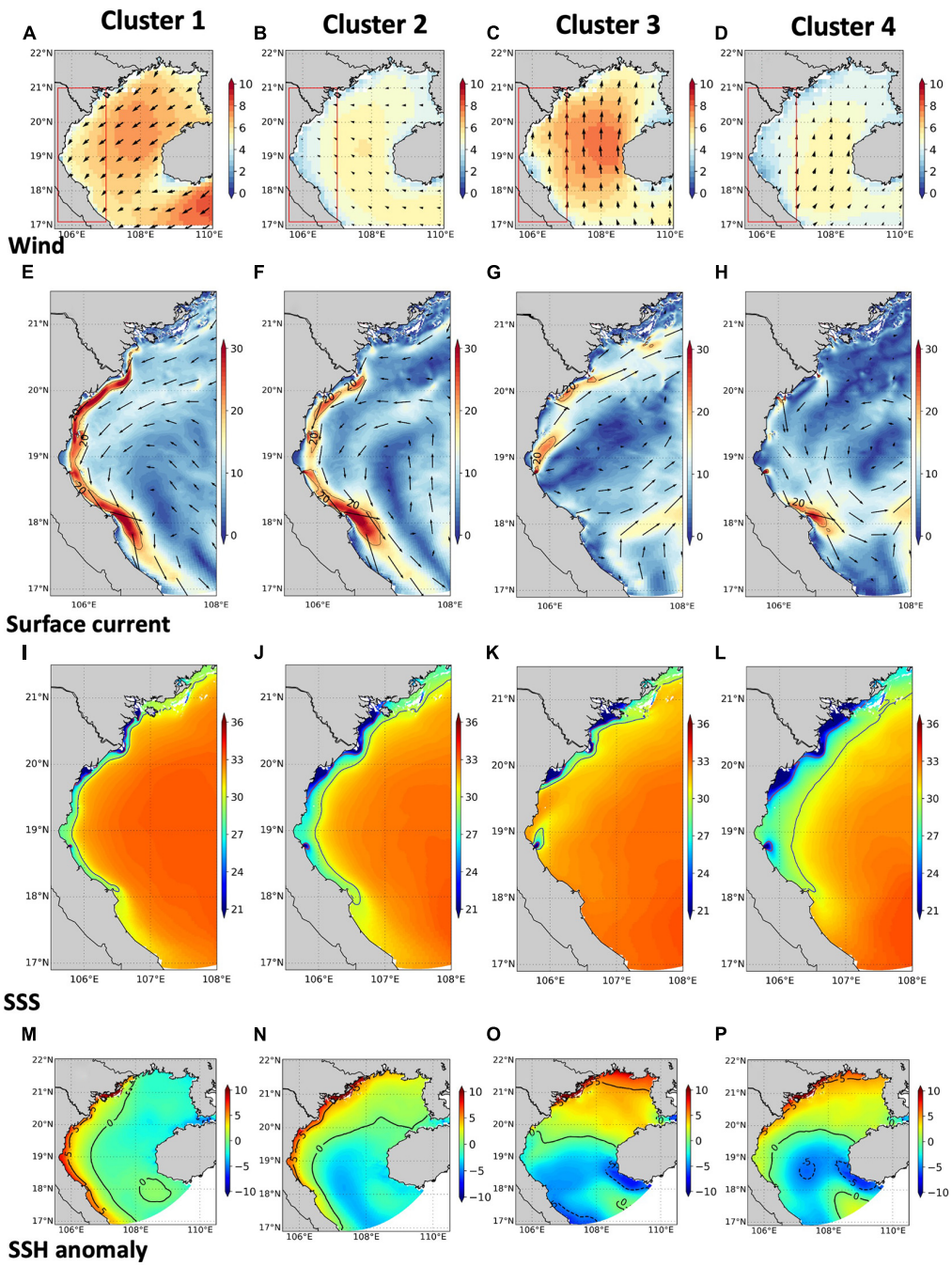


FIGURE 10 | (A–D) Wind conditions (m/s) corresponding to the 4 clusters. **(E–H)** and **(I–L)** Same as **(A–D)** but for surface current (cm/s) and SSS. **(M–P)** SSH anomaly with respect to the mean over the basin for each cluster (cm).

all along the coast (**Figure 10I**). We also observe a cross-shore gradient of SSH with an elevation larger than 5 cm with respect to the basin-averaged SSH (**Figure 10M**). Here, the coastal current is fed by buoyant river waters which contribute to the geostrophic component of the current. Indeed, in the GOT_NORIV simulation, the surface current in cluster 1 is 10 to 15 cm/s weaker; the SSH is 1 to 4 cm lower (not shown). Similarly, Piton et al. (2021) estimate that the geostrophic contribution to the downcoast surface current reaches up to 60% in December-February.

The second cluster appears on and off throughout the year, with a slightly greater rate of occurrence in April and September (usually before the occurrence of cluster 3 and after the one of cluster 4), and accounts for 518 days (23.6%). It happens mostly in late spring and early winter, i.e., during the seasonal transition of the monsoon. This suggests that cluster 2 represents

a transition regime for the river plume. In this cluster, the river plume extends both further offshore and further southward compared to cluster 1. 75% of the time, the plume extends to 105.85°E (∼25 km from the coast) while 25% of the time, it extends to 106°E (∼40 km from the coast). The low salinity strip defined by the 30 isohaline is about twice as wide as in cluster 1 (**Figure 10J**). 50% of the time, the plume reaches 18°N, which is the same as in cluster 1, while 25% of the time, it extends as south as 17.1°N (**Figure 9B**). The higher spatial coverage of the plume area in this cluster can be explained by the higher runoff (4020 m^3/s) than in cluster 1 (2197 m^3/s). Also, in this cluster, the wind direction is from the southeast, therefore different with respect to cluster 1 (**Figure 10B**). The wind speed is weak, with a mean speed of 4.3 m/s near the coast (4.7 m/s at the gulf scale). The downwelling effect is relaxed and the light plume water can spread seaward. The coastal current is still flowing southward but is weaker than in cluster 1. As in cluster 1 and cluster 4 (see below), it is locally intensified, around 106.5°E, 18°N. The tidal current is intensified there as well (**Supplementary Figure 1**), probably because this is an area where the shelf is thinning and the coastline draws a cape. When present, the coastal current may be intensified there, through the same processes as for the tidal current. Another assumption is that interactions between tides and the coastal current occur there and result in an intensification of the local circulation.

The third cluster, which happens primarily in June and July (315 days, 14.4%), has a different shape with respect to clusters 1 and 2 (**Figure 9C**). In this cluster, the plume is advected northward and seaward. This is also the cluster in which the river plumes from the various rivers are disjoint. It corresponds to the period when the runoff increases with the mean value equal to 4631 m^3/s and the summer monsoon wind reaches its strongest intensity. The mean gulf-scale wind speed is 5.7 m/s (5.6 m/s inside the box). It blows northeastward therefore corresponding to upwelling conditions. The surface coastal current is not present anymore south of ∼18.7°N; at 18°N the surface current is oriented seaward, with weak speed (∼10–15 cm/s). North of 18.7°N, the coastal current is reversed, flowing northward, with a weaker speed than in cluster 2 (∼15 cm/s), but locally intensified by the river runoffs. Although the average runoff is larger than for cluster 2, the very low salinity strip (SSS < 25) is smaller than in cluster 2, suggesting that strong mixing is taking place, either vertically due to wind-induced turbulent kinetic energy or horizontally. **Figure 9C** shows that 5% of the time, the plume reaches the 40 m isobath, and indeed the salinity over this area is decreased with respect to cluster 2, supporting the hypothesis of lateral mixing and/or stirring. The involved processes are assumed to be at daily timescales or shorter (inertial, tidal time scales) and are discussed in section "Variability of the Plume Dynamics at Daily Time Scales."

The fourth cluster exhibits the largest spatial coverage and occurs mostly in August and September (367 days, 16.7%), that is at the peak of the high runoff season (the mean runoff over this cluster reaches 7336 m^3/s). In this cluster, the plume extends the farthest offshore. At 19°N, it can extend to more than 100 km from the coast. 75% of the plume extends to ∼55 km from the coast, while 25% of the plume extends to 100 km from the coast. 5% of the plume can extend as far east as 107.0°N, which is 145 km from the coast (**Figure 9D**). In this cluster, the mean wind pattern is still upwelling-favorable, i.e., capable of driving the plume offshore (**Figure 10D**). However, the wind speed is less intense: 4.5 m/s at the gulf scale and 4.0 m/s inside the box only. It is the period with the lowest wind speed and the weakest coastal current; the latest is downcoast again. Its speed does not exceed 10 cm/s (except around 106.5°E, 18°N where it is locally accelerated up to more than 20 cm/s as in clusters 1 and 2, **Figure 10H**). The plume is surface-advected, which is verified by the analysis of the plume thickness in the next section. The large runoff during the August–September period is responsible for the very low salinity (SSS < 25) simulated along the coast between 21°N and 19.5°N. As for cluster 3, the salinity over the whole shelf in the western half of the GOT is decreased in this cluster, with respect to the previous one, indicating a larger extent of the river water influence than the one formalized by the plume definition that we adopted in section "River Plume in GOT: Identification and Variations of Area." In other words, even highly diluted in the ocean waters, the river water is still influencing the ocean SSS. The comparison between the reference run and the run without runoff (GOT_NORIV) confirms that the runoff influences the SSS all over the gulf in clusters 2, 3 and 4 (**Supplementary Figure 2**), with the largest influence in cluster 4 (more than 1 west of 107°N and north of ∼20.5°N). The SSH shows a small elevation between the center of the basin and the Vietnamese coast, consistently with a weak downcoast circulation (**Figure 11P**). In GOT_NORIV, the SSH east of 107°E is decreased by 1 to 2.5 cm with respect to REF (not shown), while the surface current only differs from the REF run locally and the differences are smaller than for cluster 1 (and to a lesser extent for cluster 2), therefore suggesting a weak contribution of the riverine waters to the circulation in late summer.

We estimate the export of riverine waters by computing the daily fluxes of dye concentration (for the RR and southern rivers) through three sections (**Figure 2A**). We then average the fluxes over the periods of the cluster to obtain a mean daily flux for each cluster. We found that the highest offshore flux (section 2) occurs in cluster 3 (∼402,000 unit/s), while the largest downcoast flux (section 1) is in cluster 2. Overall the largest exports are across section 1 in clusters 2 (473,532 unit/s) and 4 (431,408 unit/s). The flux across section 3 is much smaller in all the clusters; it is the largest (northward) in cluster 3 (76,000 unit/s).

Plume Thickness

We define the plume thickness as the maximum depth at which water is found with a tracer concentration greater than 7 unit/m^3. It is computed daily. **Figure 11** shows the time evolution of plume thickness and temperature at 5 m along the 19°N section. For the sake of clarity, we show years 2013 and 2014 only, representative of high and low discharge conditions respectively, but similar conclusions would be drawn for the other years (**Supplementary Figure 3**).

As we have seen in the previous section, from September to March, the plume is narrow and elongated along the coast due to the winter monsoon downwelling winds. During that period the plume is bottom attached, i.e., it is filling the whole water

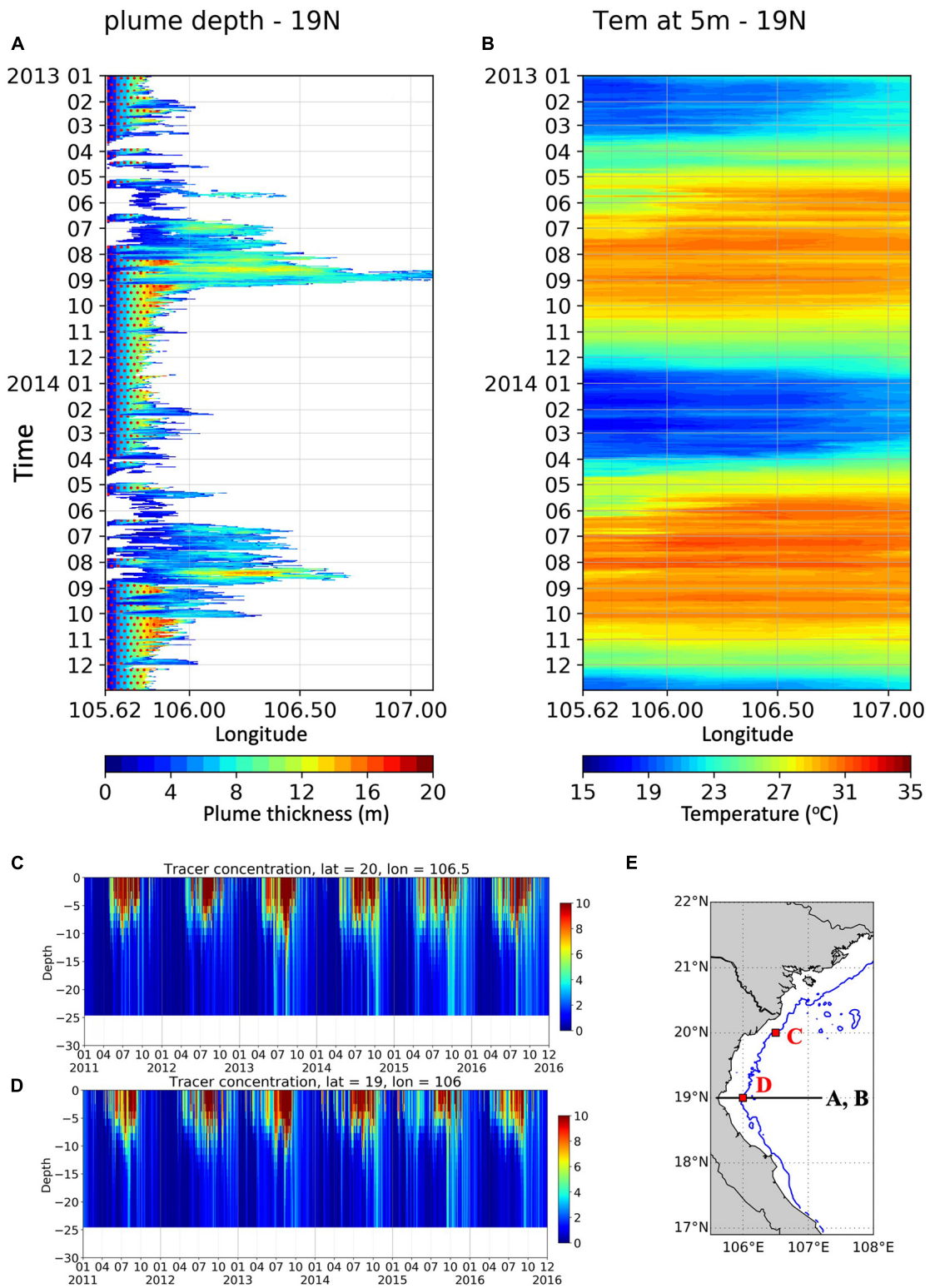


FIGURE 11 | (A) Plume thickness (m) at 19°N section from 2013 to 2014. Red points indicate the area where the plume is present over the whole depth. **(B)** Temperature (°C) at 5 m at the same section as **(A)**. **(C,D)** Tracer concentration over time at two coastal points. The location of the section and the points are shown in panel **(E)**.

column with a thickness of the order of 10 m at 20°N and 15 m at 19°N (**Figure 11A**). Several factors can explain such a thickness: first the downwelling winds tend to create a convergent flow onshore; secondly the vertical mixing may be enhanced by the bottom-generated turbulence resulting from the strong coastal current (Wiseman and Garvine, 1995). Wiseman and Garvine (1995) also suggest that onshore Ekman flow may result in dense ocean water overriding buoyant plume water, therefore creating instabilities and mixing.

From May on, the monsoon changes to southwesterly wind, driving the plume northward and detaching it from the coast and from the bottom. We observe that events where the plume detaches from the coast at 19°N coincide with the temperature at the coast colder than seaward (**Figure 11B**). This supports the assumption that the southerly monsoon winds generate a coastal upwelling. The offshore extension of the low-temperature signal is less than 40 km. This summer upwelling was also simulated by Gao et al. (2013) for 2007, and is likely to be responsible for the detachment of the plume from the coast. When detached, the plume thickness increases from ∼4 m onshore to about 10 m seaward. Sometimes in May-August, the plume is thickening offshore to 12–15 m (**Figure 11A**). That deepening may be due to strong winds events that increase the mixing offshore in the upwelling region or to the increase of river discharge.

In mid-August, we observe a strong plume deepening. In 2013, the plume is still attached to the coast, contrary to 2014 (**Figure 11A**). This difference can be due to two reasons. Firstly, the runoff in 2013 is higher than in 2014. Secondly, the wind in 2014 is stronger than in 2013 (not shown). However, both deepening events appear to be linked with a seasonally recurrent anti-cyclonic eddy developing near 19°N, which is examined in more detail in the next section.

We also look into detail at the temporal evolution of the tracer concentration over the water column at some points near the coast (**Figures 11C–E**). After a peak discharge in summer, from October until November or December (depending on the year), the tracer is rapidly mixed down to the bottom (∼25 m) at a low concentration (3–5 unit/m^3). Then, from January to March, the concentration gets close to zero, except for some sporadic events of a few days.

Variability of the Plume Dynamics at Daily Time Scales

The cluster analysis allowed to identify clear seasonal patterns of the plume variability, but the analysis of the plume thickness variability highlighted a strong variability at daily time scales as well. In particular, the plume is observed to spread seaward in spring and summer, which is synonymous of export of fresh water and riverine materials from the coastal zone to the interior of the GOT. Those sporadic events are represented by the 5% of plume occurrence in **Figure 9**. **Figures 12A–C** illustrates some of these events for three dates in June 2012. They show that the river waters spread within the whole basin, with a low concentration though. They extend as far east as Hainan coasts. As the forcings (wind, runoff, tides) are also strongly variable, it is not possible to disentangle their respective impacts. Besides, the plume seems to be shaped by small-scale circulation patterns over the whole shelf, suggesting that mesoscale or submesoscale activity strongly influences the horizontal transport as well as the dilution.

In particular, at 19°N, we observe a recurrent anticyclonic eddy as mentioned in the previous section. **Figures 12D,E** shows the relative surface vorticity and the plume thickness on 11 and 15 August 2014. The eddy is depicted by the minimum of negative surface vorticity. It appears clearly that the plume is deepening at the center of the eddy, with a difference of thickness reaching 8 m between the edge and the center for instance on 15 August 2014. In our simulation, this eddy generally happens in August, when the wind direction is southwest, which is upwelling-favorable, and the runoff is high. Then, this eddy disappears when the coastal southward current develops again and/or the wind is not favorable anymore. Its lifetime varies from a few days to ∼15 days; its diameter is about 50 km, i.e., much larger than the first Rossby radius. There is no mention about such an eddy from the HFR analysis (Rogowski et al., 2019; Tran et al., 2021); the availability and resolution of the HFR measurements may be too limited to depict such a pattern. The formation mechanism of this eddy is unclear. The comparison with GOT_NORIV shows that most of the time, without the river, some vorticity gradients can be depicted, suggesting a weak anticyclonic structure which vanishes on a shorter time scale (for instance in 2013, 6 days in GOT_NORIV instead of 8 days in GOT_REF) (**Supplementary Figure 4**). The anticyclone seems strongly connected to the Lam river plume. Bottom topography may be another forcing factor. Indeed a small island is present at 106°N and is likely to influence the river flow. Both the buoyant Lam river plume and the island may generate instabilities of the coastal flow that could lead to the eddy development.

Impact of Tides

The influence of tides in shaping the far field plume is investigated by comparing the reference simulation GOT_REF with the simulation without tides (GOT_NOTIDE). We first compute the total area of the plume from all the Vietnamese rivers (including the RR). On average, the plume in GOT_REF is 5% larger than in GOT_NOTIDE, with the largest differences found in the high discharge period (not shown). Significant differences (∼10%) are observed during the summer of 2011 and 2012, with the plume being larger in the GOT_REF run; over the remaining period, the differences are weaker.

We performed a KMA analysis on the GOT_NOTIDE outputs for 4 clusters; the resulting clusters are very close to the ones from GOT_REF, both in terms of spatial structures and temporal distribution (**Supplementary Figure 5**). The main differences are found in clusters 3 and 4, that is during the summer monsoon and high runoff period. Without tides, the plume spreads more to the north. In cluster 4, the plume spreads a bit further to the south without tides.

Besides, of equal importance are the tidal effect on vertical mixing (already inside the estuaries) and frontal activities (Guarnieri et al., 2013). The impact of tides on the vertical mixing is investigated by comparing the tracer concentration between

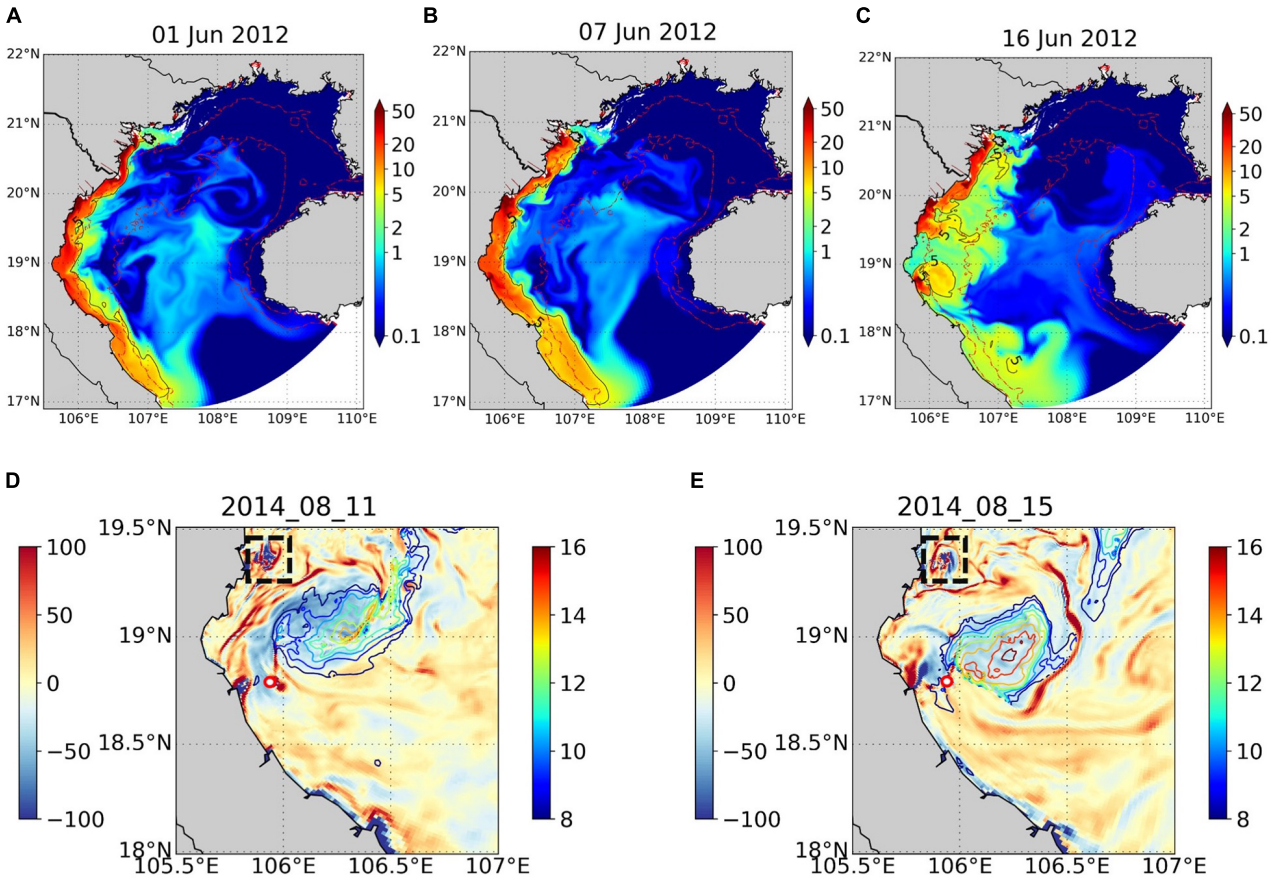


FIGURE 12 | (A–C) Surface tracer concentration on 01 June 2012 **(A)**, 07 June 2012 **(B)**, and 16 June 2012 **(C)**. **(D,E)** Relative surface vorticity ($10^{-6}s^{-1}$) (contour fill, left color bar) and plume thickness (m) (line, right color bar) on 11 and 15 August 2014. The black box and red circle indicate the location of two islands.

GOT_REF and GOT_NOTIDE (**Figure 13**). The tidal influence differs depending on the area: along the coast, just north of the mouth (close to ∼21°N), it is larger without tides at both surface and bottom (>4 unit/m^3). Everywhere else, the bottom concentration is larger with tides (>0.5 unit/m^3). At the surface, the concentration is smaller at the mouths (>4 unit/m^3) and larger in the plume (0.5–1 unit/m^3) in the run with tides. Over the shelf, the impact is small; in clusters 3 and 4 we observe a larger surface concentration (>0.5–1 unit/m^3) in the run without tides at ∼ 107–108°E and ∼ 20°N. These differences are small but significant with regard to the concentrations in GOT_REF (**Figure 13**): the values are 5–50 unit/m^3 (resp. 1–20 unit/m^3) in the plume and 0.5–10 unit/m^3 (resp. 0.1–1 unit/m^3) over the shelf west of 108°E at surface and at the bottom, respectively.

We interpret the results as follows: tides enhance the vertical mixing, which explains the larger concentration at the bottom in GOT_REF. However, tides also enhance the export of riverine waters offshore at the mouth, hence the slightly larger surface concentration values in GOT_REF in the plume and the smaller concentration close to the mouth. The plume reaches the small coastal area north of the RR mouths only in the absence of tides as mentioned previously, so the surface and bottom concentrations are larger in GOT_NOTIDE.

DISCUSSION

In this section, we summarize our findings, presenting them with paradigms found in the literature on plume dynamics (classification) or on environmental applications (receiving basins).

Classification

Several attempts have been made in the past to classify buoyant coastal runoffs with the objective of deriving general dynamical properties and to compare different plume systems. Garvine (1995) introduced the Kelvin number (K) which is defined as the ratio of the typical cross-shore scale of the buoyant runoff (usually taken as the estuary mouth width) over the local internal Rossby radius. K measures the importance of rotation: for $K < 1$, the influence of earth rotation on the plume dynamics is not significant and the river outflow forms energetic jets whose direction is controlled by local bathymetry and coastline (Hetland and Hsu, 2013). When $K > 1$, the Coriolis effect is dominant and the plume flows downcoast forming a coastal current; for large K, the downcoast flow may be insensitive to wind-driven motion in the opposite direction (Wiseman and Garvine, 1995).

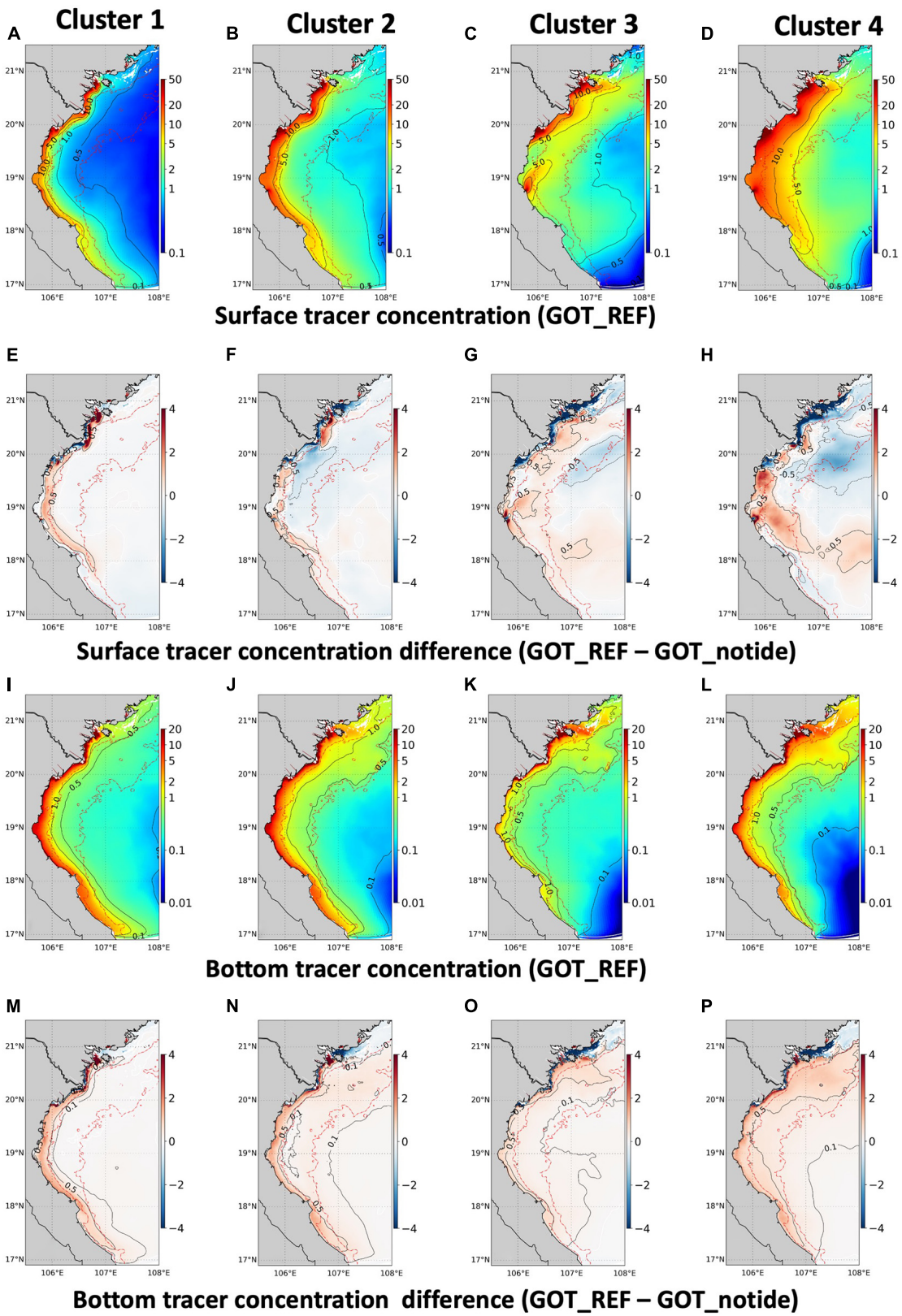


FIGURE 13 | (A–D) Maps of mean surface tracer concentration correspond for 4 clusters. **(E–H)** Difference of surface tracer concentration between GOT_REF and GOT_NOTIDE correspond for 4 clusters. **(I–L)** Same as **(A–D)** but at the bottom. **(M–P)** Same as **(E–H)** but at the bottom.

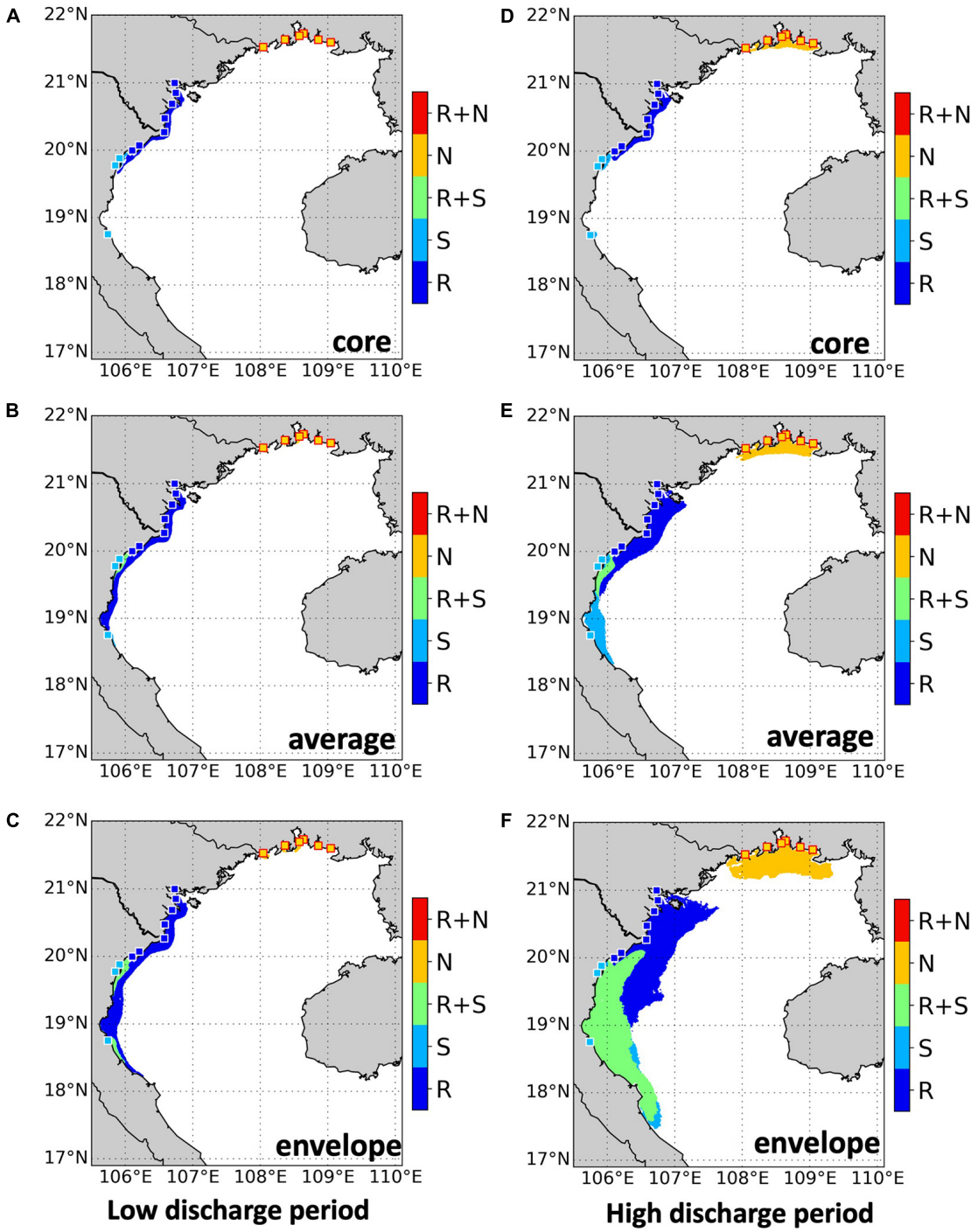


FIGURE 14 | The "receiving basins" from different rivers. The "core of the receiving basin" is the area where the plume is present at least 90% of the time **(A)**, the "average receiving basin" is the area where the plume is present at least 50% of the time **(B)**, "the envelop of the receiving basin" is the area where the plume is present at least 10% of the time **(C)**, all in low runoff period. **(D–F)** Same as **(A–C)** but in high runoff period. The location of the rivers is indicated by little boxes with the same color as the corresponding receiving basins. Explanation: (R): Red River plume, (S): plume of the rivers south of the RR delta, (N): the rivers north of the RR delta, (R+S): both R and S are present, (R+N): both R and N are present.

Very close to the RR mouths, the internal Rossby radius is between 1.5 and 5 km. Given the typical width of the distributaries mouths in our configuration (from 0.6 to 2.5 km), the Kelvin numbers vary between 0.5 and 1. Therefore in theory, bulges could be formed and the impact of the Coriolis force should be small. Close to the mouth, the currents for each cluster

do not show evidence of bulge formation. The outflow from the Cam river is very much constrained by the bathymetry and coastline. At the Van Uc and Ba Lat mouths, the outflow forms a kind of jet. In clusters 1 and 2, the plume is deflected downcoast and merges into the strong (wind-generated) coastal current (not shown). At the mouth of the Lam river, we identified daily scenes where the outflow has the shape of a bulge with a recirculating current (not shown). There the Kelvin number is estimated around 0.35, so a recurrent bulge might possibly be formed.

However, as in other delta systems, the typical length scale of the plume, and therefore the Kelvin number K, is not defined unambiguously, according to whether one considers the individual mouths or the system created by the merging plumes. Indeed, the plumes of the Red River distributaries (plus the Ma and Yen rivers) interact and merge in all clusters except cluster 3. Therefore, the overall fate of the Red River is likely to be better described by considering the system as a whole, as suggested by the 'menagerie' of plumes summarized by Horner-Devine et al. (2015; their **Figure 5**).

The Receiving Basin of Different Rivers in the GOT

As described in section "Observational Data Sets Used to Evaluate the Simulation," the introduction of several tracers allows us to follow the pathway of different river systems: Red River, the rivers south of the RR delta (SR) and the rivers north of the RR delta (NR). This information is helpful for many practical purposes and environmental applications (e.g., contaminant dispersion, water quality). Mapping the 'receiving basin' of a river is a useful tool to estimate the zone of influence of dissolved or particulate terrestrial inputs, with the aim to design evaluation strategies of the coastal ocean ecological status and to build scenarios for the preservation or restoration of vulnerable areas. This is done, for instance, by Menesguen et al. (2018) in a numerical study to identify the source of eutrophication in the Bay of Biscay and the English Channel and to design a strategy of nutrient load reduction within European institutions directives framework. In this study, we define the "receiving basin" for different rivers from the passive tracer content with the same threshold as defined in section "River Plume in GOT: Identification and Variations of Area" (concentration > 7 unit/m^3), but this time we apply it to each river system. The calculation is made for the high runoff/summer monsoon period (July–August–September, hereafter JAS) and for the low runoff/winter monsoon season (December–January–February, hereafter DJF) from 2011 to 2016 (**Figure 14**). The choice to work with 'classical' seasons, and not on the clusters of section "Variability of the RR Plume," is motivated by the concern to provide maps that can be easily used by the readers of this article. For each season, the "core of the receiving basin" is the area where the plume is present at least 90% of the time, the "average receiving basin" where the plume is present at least 50% of the time, "the envelope of the receiving basin" where the plume is present at least 10% of the time. **Figure 14** also shows areas where the cores/averages/envelopes of the receiving basins for two different river systems superimpose.

In the low runoff period (DJF, **Figures 14A–C**), the receiving basins are very narrow and elongated along the coast. While the envelope of the RR receiving basin can extend to approximately 18.2°N and mix with the plume of SR, its core appears mostly at the river mouths. In all cases, the receiving basins of NR is not detected with this choice of threshold for the tracer concentration (see below).

In the high runoff period (JAS, **Figures 14D–F**), the envelopes of the receiving basins of RR and SR are connected. South of 19°N, the plumes of RR and SR are fully mixed and their envelopes are indistinguishable. North of 19°N, the eastward extension of the RR envelope exceeds the one of the SR envelope and extends as eastward as 107.5°E. The receiving basin of NR appears north of 21°N but does not connect with the RR one. The average basins show different characteristics than the envelopes: while the SR influence can reach 18.3°N, the RR basin does not extend further south than 19.3°N.

In **Figure 14**, there is no connection between the RR and NR. However, it does not mean that they do not interact with each other. If we consider a lower threshold to identify the plume (e.g., 3 unit/m^3), the envelopes of NR and RR are connected both in low and high discharge periods (not shown). This suggests that the NR waters are strongly and quickly diluted. This also means that depending on the objectives of the study, and therefore on the choice of the tracer concentration threshold, the basins will be connected or not.

As written before, the information about receiving basins can help in case of water quality monitoring or contamination leakage. This analysis leads to 2 concluding remarks. Firstly, the freshwater along the Vietnamese coasts tends to flow southward and to exit the gulf. However, the freshwater from all the rivers tends to dilute to under 7% before it leaves the domain. This means that in case of contaminant leakage, the contaminants tend to mix and affect the gulf's water quality locally mostly. Secondly, the RR average receiving basin extends further southward and in a wider coastal strip than the SR basin during the low runoff season, while the SR basin extends further southward and further eastward (south of 19.5°N) than the RR basin during the high runoff period (**Figures 14B,E**). In both cases though, the RR runoff is higher than the SR runoff. These contrasted situations highlight the importance of wind and coastal circulation on shaping the receiving basin and consequently, on the fate of terrestrial inputs depending on their origin (SR or RR rivers systems).

CONCLUSION

We presented a comprehensive study of the plume formed by the waters from the Red River and three nearby rivers in the GOT using numerical simulation, in a realistic high-resolution configuration over the period 2011–2016. Compared to various observational data, the model shows good results. We then compare several methods to identify the river plume in the study area. We found that identification through passive (dye-like) tracers is preferable since it allows to distinguish the runoff influence from the precipitation one and to distinguish

the runoff from different rivers as well. The runoff shows large seasonal and interannual variability. It usually reaches the highest value in August and lowest in February, in phase with the monsoon system. At the surface, the plume area shows similar variations. However, the plume area reaches its peak in September, which is about 1 month later than the peak of runoff.

To identify the main spatial patterns of variability, we apply a clustering method to daily scenes of the model outputs where the plume is defined from the tracer concentration (>7 arbitrary unit/m^3). The cluster analysis identifies the plume regimes and their period of occurrence without having to pre-define these periods as one would do when computing seasonal averages for instance. Besides it allows identifying transition regimes (e.g., cluster 2).

The plume pattern of the first cluster is characteristic of the November–March period: the plume is narrow and contained within the inner shelf (bottom depth < 20 m), due to low runoff and downwelling wind (winter monsoon) with an intense downcoast current. The second pattern is mainly observed in the transition period of the monsoon (April, May, October) and is wider than the first pattern; both the relaxation of the winter monsoon and the weaker coastal current allow the plume to spread further offshore than in cluster 1. The third pattern occurs when the summer monsoon is the strongest and the runoff increases. The wind is upwelling favorable; the plumes are advected northward and detach locally from the coast. It is the only pattern where the plumes from the different rivers are disconnected. The final pattern coincides with the highest runoff period and the summer monsoon relaxation. The plumes are connected again in a pool of low salinity waters with the largest coverage, spreading both offshore and southward. Overall, we found that this hydrological system with multiple source points and a strong seasonal variability of along-shore wind is similar to the one for instance described by Kourafalou et al. (1996) in the Southern Atlantic Bight along the US coast.

The vertical variability of the plume is examined as well. In winter, the plume is usually mixed over the whole water depth. When the summer monsoon arrives at the end of March, the plume starts to detach from the bottom and spreads offshore as a surface buoyant layer. The plume can detach from the coast near 19°N when a coastal upwelling develops. It may deepen offshore also. In particular, the plume is strongly deepened in the middle of August when trapped in a recurrent eddy near 19°N.

The cluster analysis therefore evidenced at least three regimes. In winter regime, the plumes of all the Vietnamese rivers are connected in a well-mixed freshwater strip which is contained to the coast; the downcoast current is likely to act like a barrier preventing exchanges of riverine water and material cross-shore toward the center of the gulf. In early summer, the upwelling winds lead to a reverse circulation, where the plumes are advected northward and slightly offshore; the plumes are partly disconnected from each other. In the late summer regime, the wind relaxes and the large amount of freshwater due to the annual runoff peak spreads at the surface, reaching the maximal offshore and southward extension.

The impact of tides on the shape of the plume has been explored using a dedicated simulation without tides; we found that the general shape of the plume is not significantly influenced by tides, except in the Ha Long Bay area during the high runoff period (clusters 3 and 4). The main forcings of the far-field plume are the wind and basin-scale circulation. However, tides impact the vertical structure of the plume: they enhance the vertical mixing hence the riverine water concentration in the bottom layer. They also lead to a larger export offshore or the riverine water at the surface close to the mouth during the high discharge season. The influence of tides is obviously not limited to the far field; first, tides determine the buoyancy of the river water entering the ocean. Then, in the near and mid-field area, the bottom friction induced by tides is likely to impact the local dynamics and mixing, therefore influencing the plume properties in the far-field as well. An in-depth analysis of the tidal processes, of the tides-river flow interactions and of their impact on the velocity, shear and stratification in the estuaries and at the mouths was beyond the scope of this paper. It will be the topic of a future study aimed at better understanding the shape and dynamics of the outflow in the near and mid fields. The dynamics at the mouth is also highly important for sediment dynamics close to the mouth area.

Small-scale patterns of the coastal circulation, such as the recurrent eddy observed at 19°N in August, are also involved in the dilution and fate of the riverine water in the ocean. Submesoscale features due to instabilities within the plume or at the fronts may also develop and influence the mixing as found in other systems (e.g., Horner-Devine et al., 2015; Ayouche et al., 2021 this issue). Such small-scale processes should be examined in dedicated studies.

At last, this study provides some reference information about the river plume variability, showing in particular the role of the wind. In such a context, ensemble simulations will be useful to assess the sensitivity of our results due to the uncertainty of the forcing conditions (wind and runoff).

DATA AVAILABILITY STATEMENT

The raw data supporting the conclusions of this article (i.e., the model simulations) will be made available by the authors without undue reservation.

AUTHOR CONTRIBUTIONS

TuN-D, NA, PM, and PDM-F contributed to the conception and scientific design of the study. PM provided the model. VP, MH, TD, and PM developed the previous GOT configuration used for this analysis. MT provided the HFR data. TuN-D, NA, and FT performed most of the analyses. TuN-D wrote the first draft of the manuscript. NA wrote sections of the manuscript. All authors actively contributed to manuscript revision, read, and approved the submitted version.

FUNDING

TuN-D Ph.D. thesis is funded by the "Programme d'Excellence" of the French Embassy of Vietnam and by IRD ARTS program. This work is a contribution to the LMI LOTUS project (http://lotus.usth.edu.vn) and to the SWOT COCTO-FO project funded by CNES (French Spatial Agency). This work has used HPC resources from CALMIP/France (grant 2020-p1119) and HILO at the University of Science and Technology of Hanoi (USTH). Support from IRD, CNES, CNRS, and USTH is gratefully acknowledged.

ACKNOWLEDGMENTS

CFO CTD data used in this study was collected by the Vietnam Center for Oceanography (CFO, VASI) in the framework of the United States–Vietnam collaboration project: "Gulf of Tonkin Circulation study" (NICOP N62909-15-1-2018), financed by the Office of Naval Research (ONR). The VITEL (VIetnam TELédétection remote sensing) campaign has been funded by CNES; we are grateful to S. Ouillon for providing the T/S data. The historical tidal gauges dataset stems from the International Hydrographic Organization (https://www.iho.int/, last access: November 2, 2019) and is available upon request at https://www.admiralty.co.uk/ukho/tidal-harmonics (last access: November 2, 2019). The altimetric tidal constituents were provided to us by F. Lyard (LEGOS). We also acknowledge F. Lyard for the use of his code to compute the Rossby Radius and for his expertise on the model's bathymetry field. This study has been conducted using ECMWF product (www.ecmwf.int) and E.U. Copernicus Marine Service Information (product: GLOBAL_ANALYSIS_FORECAST_PHY_001_024, available at https://resources.marine.copernicus.eu/?option=com_csw&view=details&product_id=GLOBAL_ANALYSIS_FORECAST_PHY_001_024). Many thanks to C. Nguyen and D. Gazen for the help with the model and computing facilities at LAERO (Toulouse). The SYMPHONIE code and the code to compute the Rossby radius are distributed by the SIROCCO French national service website (https://sirocco.obs-mip.fr/), hosted by the Observatoire Midi-Pyrénées, Toulouse, France.

SUPPLEMENTARY MATERIAL

The Supplementary Material for this article can be found online at: https://www.frontiersin.org/articles/10.3389/fmars.2021.772139/full#supplementary-material

REFERENCES

Ayouche, A., Charria, G., Carton, X., Ayoub, N., and Theetten, S. (2021). Nonlinear processes in the Gironde river plume (North-East Atlantic): instabilities and mixing. *Front. Mar. Sci.* 8:701773. doi: 10.3389/fmars.2021.701773

Bentsen, M., Evensen, G., Drange, H., and Jenkins, A. D. (1999). Coordinate transformation on a sphere using conformal mapping. *Mon. Weather Rev.* 127, 2733–2740.

Blumberg, A. F., and Mellor, G. L. (1987). "A description of a three–dimensional coastal ocean circulation model," in *Three-Dimensional Coastal Ocean Models*, ed. N. S. Heaps (Washington, DC: American Geophysical Union), doi: 10.1029/CO004p0001

Burla, M., Baptista, A. M., Zhang, Y., and Frolov, S. (2010). Seasonal and interannual variability of the Columbia river plume: a perspective enabled by multiyear simulation databases. *J. Geophys. Res.* 115:C00B16. doi: 10.1029/2008JC004964

Chelton, D. B., deSzoeke, R. A., Schlax, M. G., El Naggar, K., and Siwertz, N. (1998). Geographical variability of the first baroclinic rossby radius of deformation. *J. Phys. Oceanogr.* 28, 433–460.

Chen, Z., Gong, W., Cai, H., Chen, Y., and Zhang, H. (2017). Dispersal of the Pearl river plume over continental shelf in summer. *Estuar. Coast. Shelf Sci.* 194, 252–262. doi: 10.1016/j.ecss.2017.06.025

Csanady, G. T. (1982). *Circulation in the Coastal Ocean*. Dordrecht: Springer, 281. doi: 10.1007/978-94-017-1041-1

Damien, P., Bosse, A., Testor, P., Marsaleix, P., and Estournel, C. (2017). Modeling postconvective submesoscale coherent vortices in the Northwestern Mediterranean Sea. *J. Geophys. Res. Oceans* 122, 9937–9961. doi: 10.1002/2016JC012114

Ding, Y., Chen, C., Beardsley, R. C., Bao, X., Shi, M., Zhang, Y., et al. (2013). Observational and model studies of the circulation in the Gulf of Tonkin, South China Sea. *J. Geophys. Res. Oceans* 118, 6495–6510. doi: 10.1002/2013JC009455

Falcieri, F. M., Benetazzo, A., Sclavo, M., Russo, A., and Carniel, S. (2014). Po river plume pattern variability investigated from model data. *Cont. Shelf Res.* 87, 84–95. doi: 10.1016/j.csr.2013.11.001

Gao, J., Shi, M., Chen, B., Guo, P., and Zhao, D. (2014). Responses of the circulation and water mass in the Beibu Gulf to the seasonal forcing regimes. *Acta Oceanol. Sin.* 33, 1–11.

Gao, J., Xue, H., Chai, F., and Shi, M. (2013). Modeling the circulation in the Gulf of Tonkin, South China Sea topical collection on the 4th international workshop on modelling the ocean in Yokohama, Japan 21–24 May 2012. *Ocean Dyn.* 63, 979–993. doi: 10.1007/s10236-013-0636-y

Garvine, R. W. (1995). A dynamical system for classifying buoyant coastal runoffs. *Cont. Shelf Res.* 15, 1585–1596.

Greenberg, D. A., Dupont, F., Lyard, F. H., Lynch, D. R., and Werner, F. E. (2007). Resolution issues in numerical models of oceanic and coastal circulation. *Cont. Shelf Res.* 27, 1317–1343. doi: 10.1016/j.csr.2007.01.023

Guarnieri, A., Pinardi, N., Oddo, P., Bortoluzzi, G., and Ravaioli, M. (2013). Impact of tides in a baroclinic circulation model of the Adriatic Sea. *J. Geophys. Res. Oceans* 118, 166–183. doi: 10.1029/2012JC007921

Hansen, D. V., and Rattray, M. (1966). New dimensions in estuary classification. *Limnol. Oceanogr.* 11, 319–326. doi: 10.4319/lo.1966.11.3.0319

Hastie, T., Tsbshirani, R., and Friedman, J. (2001). *The Elements of Statistical Learning: Data Mining, Inference, and Prediction*. New York, NY: Springer, 533.

Hetland, R. D., and Hsu, T.-J. (2013). "Freshwater and sediment dispersal in large river plumes," in *Biogeochemical Dynamics at Large River–Coastal Interfaces: Linkages with Global Climate Change*, eds T. S. Bianchi, M. A. Allison, and W.-J. Cai (New York, NY: Springer), 55–85.

Horner-Devine, A. R., Hetland, R. D., and MacDonald, D. G. (2015). Mixing and transport in coastal river plumes. *Annu. Rev. Fluid Mech.* 47, 569–594. doi: 10.1146/annurev-fluid-010313-141408

Kourafalou, V. H., Lee, T. N., Oey, L.-Y., and Wang, J. D. (1996). The fate of river runoff on the continental shelf: 2. Transport of coastal low–salinity waters under realistic wind and tidal forcing. *J. Geophys. Res.* 101, 3435–3455. doi: 10.1029/95JC03025

Large, W. G., and Yeager, S. (2004). *Diurnal to Decadal Global Forcing for Ocean and Sea–Ice Models: The Data Sets and Flux Climatologies,* NCAR Technical Note, NCAR/TN-460+STR. Boulder, CO: National Center for Atmospheric Research. doi: 10.5065/D6KK98Q6

Liu, Y., MacCready, P., and Hickey, B. M. (2009). Columbia river plume patterns in summer 2004 as revealed by a hindcast coastal ocean circulation model. *Geophys. Res. Lett.* 36:L02601. doi: 10.1029/2008GL036447

Lyard, F. H., Allain, D. J., Cancet, M., Carrère, L., and Picot, N. (2021). FES2014 global ocean tide atlas: design and performance. *Ocean Sci.* 17, 615–649. doi: 10.5194/os-17-615-2021

MacCready, P., Banas, N. S., Hickey, B. M., Dever, E. P., and Liu, Y. (2009). A model study of tide– and wind–induced mixing in the Columbia river estuary and plume. *Cont. Shelf Res.* 29, 278–291. doi: 10.1016/j.csr.2008.03.015

Maraldi, C., Chanut, J., Levier, B., Ayoub, N., De Mey, P., Reffray, G., et al. (2013). NEMO on the shelf: assessment of the Iberia–Biscay–Ireland configuration. *Ocean Sci.* 9, 745–771. doi: 10.5194/os-9-745-2013

Marsaleix, P., Auclair, F., and Estournel, C. (2006). Considerations on open boundary conditions for regional and coastal ocean models. *J. Atmos. Ocean. Technol.* 23, 1604–1613. doi: 10.1175/JTECH1930.1

Marsaleix, P., Auclair, F., Floor, J. W., Herrmann, M. J., Estournel, C., Pairaud, I., et al. (2008). Energy conservation issues in sigma–coordinate free–surface ocean models. *Ocean Model.* 20, 61–89. doi: 10.1016/j.ocemod.2007.07.005

Menesguen, A., Dussauze, M., and Dumas, F. (2018). Designing optimal scenarios of nutrient loading reduction in a WFD/MSFD perspective by using passive tracers in a biogeochemical–3D model of the English Channel/Bay of Biscay area. *Ocean Coast. Manage.* 163, 37–53. doi: 10.1016/j.ocecoaman.2018.06.005

Michaud, H., Marsaleix, P., Leredde, Y., Estournel, C., Bourrin, F., Lyard, F., et al. (2012). Three–dimensional modelling of wave–induced current from the surf zone to the inner shelf. *Ocean Sci.* 8, 657–681. doi: 10.5194/os-8-657-2012

Neumann, L. E., Šimůnek, J., and Cook, F. J. (2011). Implementation of quadratic upstream interpolation schemes for solute transport into HYDRUS–1D. *Environ. Model. Softw.* 26:11. doi: 10.1016/j.envsoft.2011.05.010

Nguyen, N. M., Marchesiello, P., Lyard, F., Ouillon, S., Cambon, G., Allain, D., et al. (2014). Tidal characteristics of the Gulf of Tonkin. *Cont. Shelf Res.* 91, 37–56. doi: 10.1016/j.csr.2014.08.003

Nguyen Thi Hien, A., Vu Minh Cat, B., and Roberto Ranzi, C. (2020). "Upstream effects on salinity dynamics in the Red River Delta," in *APAC 2019*, eds N. Trung Viet, D. Xiping, and T. Thanh Tung (Singapore: Springer), 1439–1443.

Nugroho, D. (2017). *The Tides in a General Circulation Model in the Indonesian Seas.* Ph.D. thesis. Toulouse: Univ. Paul Sabatier 3.

Otero, P., Ruiz-Villarreal, M., and Peliz, A. (2008). Variability of river plumes off Northwest Iberia in response to wind events. *J. Mar. Syst.* 72, 238–255. doi: 10.1016/j.jmarsys.2007.05.016

Ouillon, S. (2014). *VITEL–NORTH Cruise, RV Alis*. doi: 10.17600/14004100

Pairaud, I. L., Lyard, F., Auclair, F., Letellier, T., and Marsaleix, P. (2008). Dynamics of the semi–diurnal and quarter–diurnal internal tides in the Bay of Biscay. Part 1: barotropic tides. *Cont. Shelf Res.* 28, 1294–1315. doi: 10.1016/j.csr.2008.03.004

Pedregosa, F., Varoquaux, G., Gramfort, A., Michel, V., Thirion, B., Grisel, O., et al. (2011). Scikit–learn: machine learning in python. *J. Mach. Learn. Res.* 12, 2825–2830.

Piton, V., Herrmann, M., Lyard, F., Marsaleix, P., Duhaut, T., Allain, D., et al. (2020). Sensitivity study on the main tidal constituents of the Gulf of Tonkin by using the frequency–domain tidal solver in T–UGOm. *Geosci. Model Dev.* 13, 1583–1607. doi: 10.5194/gmd-13-1583-2020

Piton, V., Herrmann, M., Marsaleix, P., Duhaut, T., Ngoc, T. B., Tran, M. C., et al. (2021). Influence of winds, geostrophy and typhoons on the seasonal variability of the circulation in the Gulf of Tonkin: a high–resolution 3D regional modeling study. *Reg. Stud. Mar. Sci.* 45:101849. doi: 10.1016/j.rsma.2021.101849

Reffray, G., Fraunié, P., and Marsaleix, P. (2004). Secondary flows induced by wind forcing in the Rhône region of freshwater influence. *Ocean Dyn.* 54, 179–196. doi: 10.1007/s10236-003-0079-y

Rogowski, P., Zavala-Garay, J., Shearman, K., Terrill, E., Wilkin, J., and Tran, H. L. (2019). Air-sea-land forcing in the Gulf of Tonkin: assessing seasonal variability using modern tools. *Oceanography* 32, 150–161. doi: 10.5670/oceanog.2019.223

Shi, M., Chen, C., Xu, Q., Lin, H., Liu, G., Wang, H., et al. (2002). The role of Qiongzhou Strait in the seasonal variation of the South China Sea circulation. *J. Phys. Oceanogr.* 32, 103–121. doi: 10.1175/1520-04852002032<0103:TROQSI<2.0.CO;2

Solabarrieta, L., Rubio, A., Cárdenas, M., Castanedo, S., Esnaola, G., Méndez, F. J., et al. (2015). Probabilistic relationships between wind and surface water circulation patterns in the SE Bay of Biscay. *Ocean Dyn.* 65, 1289–1303. doi: 10.1007/s10236-015-0871-5

Sonnewald, M., Wunsch, C., and Heimbach, P. (2019). Unsupervised learning reveals geography of global ocean dynamical regions. *Earth Space Sci.* 6, 784–794. doi: 10.1029/2018EA000519

Sutton, W. R., Srivastava, J. P., Rosegrant, M., Thurlow, J., and Sebastian, L. (2019). *Striking a Balance, Managing El Niòo and la Nìòa in Vietnam Agriculture,* RepNo 132068. Washington, DC: World Bank.

Toublanc, F., Ayoub, N. K., Lyard, F., Marsaleix, P., and Allain, D. J. (2018). Tidal downscaling from the open ocean to the coast: a new approach applied to the Bay of Biscay. *Ocean Model.* 124, 16–32. doi: 10.1016/j.ocemod.2018.02.001

Tran, M. C., Sentchev, A., and Nguyen, K. C. (2021). Multi-scale variability of circulation in the Gulf of Tonkin from remote sensing of surface currents by high-frequency radars. *Ocean Dyn.* 71, 175–194. doi: 10.1007/s10236-020-01440-x

Vaz, N., Rodrigues, J. G., Mateus, M., Franz, G., Campuzano, F., Neves, R., et al. (2018). Subtidal variability of the Tagus river plume in winter 2013. *Sci. Total Environ.* 627, 1353–1362. doi: 10.1016/j.scitotenv.2018.01.325

Vinh, V. D., Ouillon, S., Thanh, T. D., and Chu, L. V. (2014). Impact of the Hoa Binh dam (Vietnam) on water and sediment budgets in the Red river basin and delta. *Hydrol. Earth Syst. Sci.* 18, 3987–4005. doi: 10.5194/hess-18-3987-2014

Vlasenko, V., Stashchuk, N., and McEwan, R. (2013). High–resolution modelling of a large–scale river plume. *Ocean Dyn.* 63, 1307–1320. doi: 10.1007/s10236-013-0653-x

Wang, Y., Xue, H., Chai, F., Chao, Y., and Farrara, J. (2014). A model study of the Copper river plume and its effects on the northern Gulf of Alaska topical collection on the 5th International Workshop on Modelling the Ocean (IWMO) in Bergen, Norway 17–20 June 2013. *Ocean Dyn.* 64, 241–258. doi: 10.1007/s10236-013-0684-3

Wiseman, W. J., and Garvine, R. W. (1995). Plumes and coastal currents near large river mouths. *Estuaries* 18:509. doi: 10.2307/1352368

Wu, D., Wang, Y., Lin, X., and Yang, J. (2008). On the mechanism of the cyclonic circulation in the Gulf of Tonkin in the summer. *J. Geophys. Res. Oceans* 113, 2–11. doi: 10.1029/2007JC004208

Yankovsky, A. E., and Chapman, D. C. (1997). A simple theory for the fate of buoyant coastal runoffs. *J. Phys. Oceanogr.* 27, 1386–1401.

Conflict of Interest: The authors declare that the research was conducted in the absence of any commercial or financial relationships that could be construed as a potential conflict of interest.

Publisher's Note: All claims expressed in this article are solely those of the authors and do not necessarily represent those of their affiliated organizations, or those of the publisher, the editors and the reviewers. Any product that may be evaluated in this article, or claim that may be made by its manufacturer, is not guaranteed or endorsed by the publisher.

Copyright © 2021 Nguyen-Duy, Ayoub, Marsaleix, Toublanc, De Mey-Frémaux, Piton, Herrmann, Duhaut, Tran and Ngo-Duc. This is an open-access article distributed under the terms of the Creative Commons Attribution License (CC BY). The use, distribution or reproduction in other forums is permitted, provided the original author(s) and the copyright owner(s) are credited and that the original publication in this journal is cited, in accordance with accepted academic practice. No use, distribution or reproduction is permitted which does not comply with these terms.

frontiers in Marine Science

ORIGINAL RESEARCH
published: 10 December 2021
doi: 10.3389/fmars.2021.735011

Structure and Inter-Annual Variability of the Freshened Surface Layer in the Laptev and East-Siberian Seas During Ice-Free Periods

Alexander Osadchiev[1,2], Dmitry Frey[1,3], Eduard Spivak[4], Sergey Shchuka[1,2], Natalia Tilinina[1] and Igor Semiletov[4,5]*

[1] Shirshov Institute of Oceanology, Russian Academy of Sciences, Moscow, Russia, [2] Moscow Institute of Physics and Technology, Dolgoprudny, Russia, [3] Marine Hydrophysical Institute of RAS, Sevastopol, Russia, [4] V.I. Il'Ichev Pacific Oceanological Institute, Far Eastern Branch of the Russian Academy of Sciences, Vladivostok, Russia, [5] Institute of Ecology, Higher School of Economics, Moscow, Russia

This work is focused on the structure and inter-annual variability of the freshened surface layer (FSL) in the Laptev and East-Siberian seas during ice-free periods. This layer is formed mainly by deltaic rivers among which the Lena River contributes about two thirds of the inflowing freshwater volume. Based on *in situ* measurements, we show that the area of this FSL during certain years is much greater than the area of FSL in the neighboring Kara Sea, while the total annual freshwater discharge to the Laptev and East-Siberian seas is 1.5 times less than to the Kara Sea (mainly from the estuaries of the Ob and Yenisei rivers). This feature is caused by differences in morphology of the estuaries and deltas. Shallow and narrow channels of the Lena Delta are limitedly affected by sea water. As a result, undiluted Lena discharge inflows to sea from multiple channels and forms relatively shallow plume, as compared to the Ob-Yenisei plume, which mixes with subjacent saline sea water in deep and wide estuaries. Due to small vertical extents of FSL in the Laptev and East-Siberian seas, wind conditions strongly affect its spreading and determine its significant inter-annual variability, as compared to relatively stable FSL in the Kara Sea. During years with prevailing western and northern winds, FSL is localized in the southern parts of the Laptev and East-Siberian seas due to southward Ekman transport, meridional extent (<250 km) and area (~250,000 km^2) of FSL are relatively small. During years with strong eastern winds FSL spreads northward over large area (up to 500,000 km^2), its meridional extent increases up to 500–700 km. At the same time, area and position of FSL do not show any dependence on significant variability of the annual river discharge volume and ice coverage during warm season.

Keywords: river plume, freshened surface layer, stratification, Lena River, Laptev Sea, East-Siberian Sea, Arctic Ocean

OPEN ACCESS

Edited by:
Andrea Cucco, National Research Council (CNR), Italy

Reviewed by:
Nino Krvavica, University of Rijeka, Croatia
Rui Caldeira, Agência Regional para o Desenvolvimento da Investigação Tecnologia e Inovação (ARDITI), Portugal

****Correspondence:***
Alexander Osadchiev
osadchiev@ocean.ru

Specialty section:
This article was submitted to Coastal Ocean Processes, a section of the journal Frontiers in Marine Science

Received: *01 July 2021*
Accepted: *22 November 2021*
Published: *10 December 2021*

Citation:
Osadchiev A, Frey D, Spivak E, Shchuka S, Tilinina N and Semiletov I (2021) Structure and Inter-Annual Variability of the Freshened Surface Layer in the Laptev and East-Siberian Seas During Ice-Free Periods. Front. Mar. Sci. 8:735011. doi: 10.3389/fmars.2021.735011

INTRODUCTION

The shallow Laptev and East-Siberian seas are located in the Eastern Arctic and comprise approximately a quarter of the Arctic shelf (**Figure 1**). These seas receive large river discharge that forms sea-wide freshened surface layer (FSL). This FSL is the largest freshened surface layer in the World Ocean in terms of area (Kang et al., 2013) and is among the largest freshwater reservoirs

in the Arctic Ocean in terms of volume (Haine et al., 2015; Williams and Carmack, 2015). As a result, knowledge about structure and variability of this FSL is essential for assessment of large-scale freshwater transport in the Arctic Ocean, which plays a key role in stratification and ice formation (Polyakov et al., 2013; Carmack et al., 2015, 2016). Spreading and transformation of freshwater discharge in the Arctic Ocean also affects many physical, biological, and geochemical processes in the Eastern Arctic, including water circulation, transport of dissolved and suspended sediments, primary productivity, anthropogenic pollution, acidification, and deposit of terrigenous material (Li et al., 2009; Yamamoto-Kawai et al., 2009; McLaughlin and Carmack, 2010; Semiletov et al., 2011, 2012, 2016; Tremblay et al., 2011; Dudarev et al., 2015; Nummelin et al., 2016; Dubinina et al., 2019a,b; Pogojeva et al., 2021; Yakushev et al., 2021).

Generally, river discharge and wind forcing control structure, dynamics, and variability of river plumes (Garvine, 1987; O'Donnell, 1990; Whitney and Garvine, 2005), including those formed by large rivers (Grodsky et al., 2014; Vic et al., 2014; Fournier et al., 2017; Osadchiev, 2017). However, various regional features, such as coastline configuration, river mouth morphology, bathymetry, interaction between neighboring river plumes, sea ice, among others, strongly affect river plumes, which results in significant variety of spreading and mixing patterns of river plumes in the World Ocean (Horner-Devine et al., 2015). This fact supports necessity of regional field studies of river plumes in different climatic and oceanographic conditions.

General spreading pattern of FSL in the Laptev and East-Siberian seas was described in previous works. Berezovskaya et al. (2002); Dmitrenko et al. (2005)Dmitrenko et al. (2008), and Janout et al. (2020) showed that atmospheric vorticity in the study area controls variability of spreading of FSL on inter-annual and quasi-decadal timescales. Fofonova et al. (2015) demonstrated that even moderate wind forcing (>6 m/s) strongly affects dynamics of the Lena plume, while tides play secondary role in plume dynamics. Osadchiev et al. (2020b) revealed that intensity of freshwater transport from the Laptev Sea to the East-Siberian Sea during ice-free periods is governed by eastward Ekman transport at the southeastern Laptev Sea and is prone to large synoptic variability.

However, in these studies, limited attention was paid to vertical structure of FSL in the Laptev and East-Siberian seas, including its seasonal and inter-annual variability. The processes of initial mixing between freshwater and seawater near river deltas and formation of FSL also remain largely unstudied. The objective of this study is to make progress at these aspects using extensive *in situ* data set collected at this remote region with hard climatic conditions and short ice-free season. This study continues our previous research of river plumes and FSL's in the Eastern Arctic focused, first, on regional processes and specific river plumes (Ob, Yenisei, Khatanga, Lena, Indigirka, and Kolyma) (Osadchiev, 2017; Osadchiev et al., 2017, 2019, 2020a,c, 2021b; Spivak et al., 2021) and, second, on large-scale freshwater transport in the Eastern Arctic (Osadchiev et al., 2020b, 2021a).

In this study, we analyze continuous surface measurements and surface measurements at hydrographic stations performed during 17 field surveys in 1999–2019 (**Table 1**). Also, we describe in detail vertical structure of FSL during ice-free season obtained from *in situ* measurements at hydrographic stations along the zonal and meridional transects across this layer performed in 2007, 2008, 2011, 2016, and 2019 (**Figure 1**, colored circles). In order to reveal dependences between the position and vertical structure of FSL and the external forcing conditions, we analyze freshwater discharge from the Lena Delta, wind forcing, and ice conditions in Laptev and East-Siberian seas during summer and autumn.

The main strength of this study consists in analysis of very extensive *in situ* dataset for studying FSL. Satellite products can potentially support determination of spatial extents and internal structure of FSL, however, satellite data is useful only if it is validated against *in situ* data. Despite certain progress in deriving sea surface salinity from satellite measurements in the Arctic Ocean, these products demonstrate proper accuracy only for high salinity values (>28–30), while there is no evidence that they operate well at salinities <25, which are typical for FSL (Matsuoka et al., 2016; Olmedo et al., 2018; Tang et al., 2018; Supply et al., 2020). In particular, satellite-derived sea surface salinity at the study area analyzed recently by Tarasenko et al. (2021) was not properly validated against *in situ* salinity data for low-saline shelf areas. As a result, the presented satellite-derived salinity distributions did not reproduce sharp salinity gradients typical for the outer border of FSL. The area of FSL was overestimated due to artifacts of satellite-derived salinity, and the resulting temporal variability of FSL is speculative. The latter demonstrates crucial importance of *in situ* salinity measurements for study FSL's in the Arctic Ocean.

The paper is organized as follows. Section "Study Area, Data, and Methods" provides general information about the study region and describes the extensive *in situ* data set analyzed in this work, as well as atmospheric reanalysis, river discharge, and satellite-derived ice coverage data. The relation between atmospheric forcing, river discharge, and ice conditions, on the one hand, and the spatial extents and vertical structure of FSL in the Laptev and East-Siberian seas, on the other hand, is analyzed in section "Results." Influence of morphology of freshwater sources, i.e., river deltas, as well as external forcing conditions on structure, dynamics, and variability of FSL are discussed in section "Discussion." The conclusions are presented in section "Conclusion."

STUDY AREA, DATA, AND METHODS

Study Area

The Laptev and East-Siberian seas are marginal and shallow seas in the Eastern Arctic Ocean (**Figure 1**). The Laptev Sea is located between the Siberian coast in the south, the Taymyr Peninsula and Severnaya Zemlya Archipelago in the west, and the New Siberian Islands in the east. The East-Siberian Sea is located between the Siberian coast in the south, the New Siberian Islands in the west, and the Wrangel Island in the east. Approximately half of the Laptev Sea and almost the whole area of the East-Siberian Sea rest on the continental shelf. The majority of this

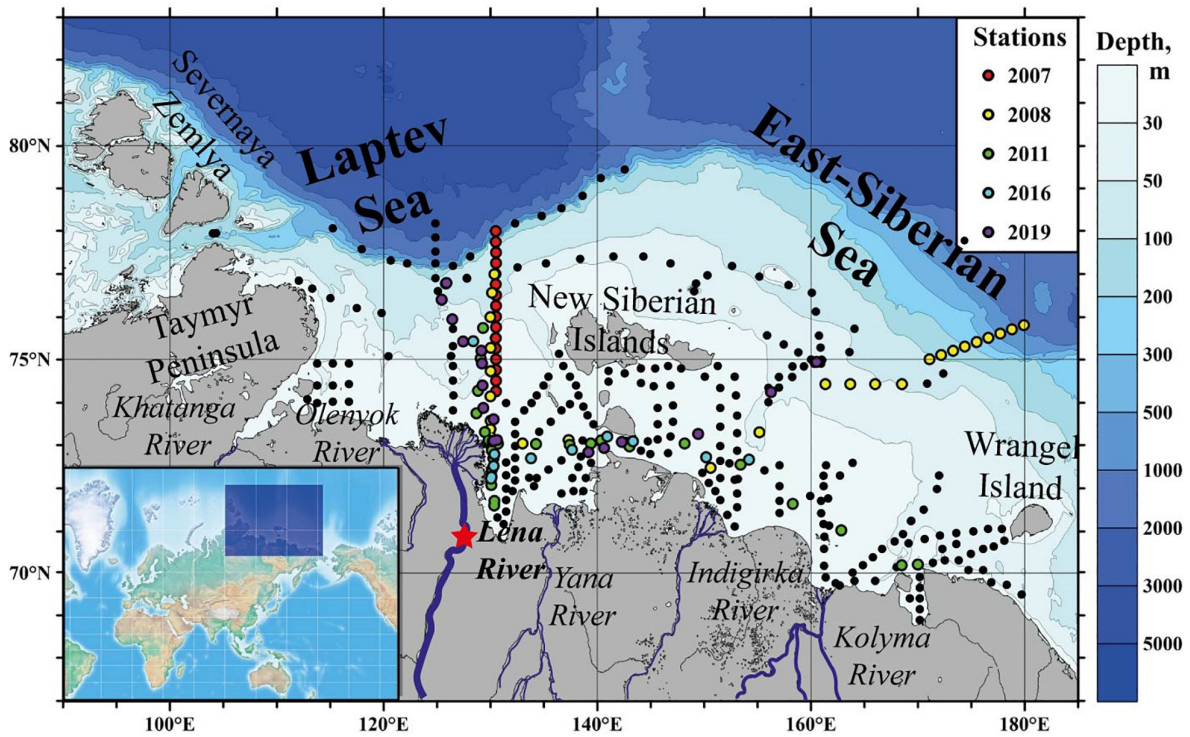


FIGURE 1 | Study area; main rivers inflowing to the Laptev and East-Siberian seas (blue lines); locations of hydrographic stations (black dots) and stations were vertical thermohaline measurements were organized in zonal and meridional transects (color dots); location of the gauge station at the Lena River (red star). The inset shows location of the study area at the World map.

TABLE 1 | Periods, research vessels, areas of field work, and types of *in situ* measurements of oceanographic surveys.

Periods	Research vessel	Area of field work	Type of *in situ* measurements
9–24 September 1999	Dunay	Laptev Sea	Hydrographic stations
24 August – 27 September 2000	Nikolay Kolomeytsev	Laptev and East-Siberian seas	Hydrographic stations
13–23 September 2003	Ivan Kireev	East-Siberian Sea	Continuous surface measurements
24 August – 14 September 2004	Ivan Kireev	East-Siberian Sea	Hydrographic stations
6–24 September 2005	Auga	East-Siberian Sea	Hydrographic stations
26 August – 20 September 2006	Kapitan Dranitsyn	Laptev Sea	Hydrographic stations
14–30 September 2007	Viktor Buynitskiy	Laptev Sea	Continuous surface measurements, meridional hydrographic transect
23 August – 18 September 2008	Yakov Smirnitskiy	Laptev and East-Siberian seas	Continuous surface measurements, zonal and meridional hydrographic transects
18 August – 3 September 2009	Kapitan Dranitsyn	Laptev Sea	Continuous surface measurements
13 September – 8 October 2011	Akademik Lavrentyev	Laptev and East-Siberian seas	Continuous surface measurements, zonal and meridional hydrographic transects
13–21 September 2012	Victor Buynitskiy	Laptev Sea	Continuous surface measurements
23 July – 3 August 2014	Oden	Laptev and East-Siberian seas	Continuous surface measurements
6–17 September 2015	Akademik Mstislav Keldysh	Laptev Sea	Continuous surface measurements, towed measurements
20 September – 20 October 2016	Akademik Lavrentyev	Laptev and East-Siberian seas	Continuous surface measurements, zonal and meridional hydrographic transects
2–20 September 2017	Akademik Mstislav Keldysh	Laptev and East-Siberian seas	Continuous surface measurements
3–17 October 2018	Akademik Mstislav Keldysh	Laptev Sea	Continuous surface measurements and hydrographic stations
23 September – 13 October 2019	Akademik Mstislav Keldysh	Laptev and East-Siberian seas	Continuous surface measurements, zonal and meridional hydrographic transects

shelf area is shallower than 50 m. The shelf break is located 100–200 km far from the continental shore in the western part of the Laptev Sea. The shelf width increases to 700–1,000 km in the eastern part of the Laptev Sea and in the East-Siberian Sea.

The Laptev and East-Siberian seas receive 750–820 and 200–250 km^3 of river discharge annually, respectively. The majority of these volumes is provided by discharges from large deltaic rivers, namely, the Lena (590 km^3), Olenyok (36 km^3), and Yana (36 km^3) rivers in the Laptev Sea and the Kolyma (136 km^3) and Indigirka (61 km^3) rivers in the East-Siberian Sea (Gordeev et al., 1996; Pavlov et al., 1996). The Khatanga River (105 km^3) is the only large estuarine river in this region, which inflows to the southwestern Laptev Sea (Osadchiev et al., 2020a). Approximately 90% of annual river runoff inflows to the Laptev and East-Siberian seas in June – October and forms large FSL in these seas (Polyakov et al., 2003; Semiletov et al., 2005).

The Laptev and East-Siberian seas are covered by ice during the majority of year. Melting out of sea ice at the southern parts of the Laptev and East-Siberian seas along the Siberian coast occurs in June–July. Ice cover in the offshore parts of these seas shows significant inter-annual variability. According to satellite sea ice products, during certain years (e.g., 2013, 2014, and 2018) the southern boundary of ice cover was located less than 200–300 km far from the Siberian coast in the middle of September. The opposite situation was observed in 2012, 2017, and 2019, when almost the whole area of the Laptev and East-Siberian seas was free of ice in August–October. Ice formation starts in the end of October and from the middle of November these seas are covered by ice.

General water circulation at the shallow shelf areas in the Laptev and East-Siberian seas is wind-driven (Pavlov et al., 1996; Berezovskaya et al., 2002; Dmitrenko et al., 2005, 2008; Fofonova et al., 2015) with important role of barotropic wind-induced upwelling events (Dmitrenko et al., 2001; Osadchiev et al., 2020c). In absence of strong wind forcing, the Coriolis force and large salinity gradient between FSL and ambient shelf water induce eastward baroclinic flow along the coast, which induces large-scale freshwater transport from the Laptev Sea to the East-Siberian Sea and further to the Chukchi Sea (Munchow et al., 1999; Weingartner et al., 1999; Carmack et al., 2015; Osadchiev et al., 2020b). A large part of FSL is also transported northward across the shelf break to the central part of the Arctic Ocean as a part of the Transpolar Drift current (Ekwurzel et al., 2001; Guay et al., 2001; Schlosser et al., 2002; Charette et al., 2020). Tidal circulation in the Laptev and East-Siberian seas is governed by semidiurnal tides (Kowalik and Proshutinsky, 1994; Kagan et al., 2008, 2010). Tidal-induced mixing affects FSL to a certain extent (Fofonova et al., 2015). However, it is less intense at the inner shelf (Padman and Erofeeva, 2004; Janout and Lenn, 2014) and during the ice-free period (Dmitrenko et al., 2012), except the southwestern part of the Laptev Sea, which receives discharge from the Khatanga River (Osadchiev et al., 2020a).

In this study, we consider two types of water masses with different thermohaline and dynamical properties, which compose FSL in the Laptev and East-Siberian seas. We distinguish a number of mesoscale river plumes (Lena plume, Kolyma plume, Khatanga plume, etc.) and one joint region of freshwater influence (Laptev/East-Siberian ROFI) (Osadchiev and Zavialov, 2019; Osadchiev et al., 2021a). River plumes are low-saline water masses with spatial extents ∼10–100 km, which are adjacent to river deltas and estuaries. River plumes represent initial transformation of freshwater discharge in the sea, i.e., residence time of river water within a river plume is less than several weeks. As a result, structure and dynamics of a river plume have quick response to variability of river discharge rate. The Laptev/East-Siberian ROFI, on the opposite, is a relatively stable water mass with spatial extents ∼1000 km. Residence time of river water within the ROFI is large, therefore the ROFI shows variability on seasonal and inter-annual temporal scales. The Lena plume and the plumes formed by smaller rivers on the study area are embedded into the Laptev/East-Siberian ROFI. River plumes together with the ROFI compose FSL in the Laptev and East-Siberian seas. Analogously to the Kara Sea, we determine river plumes as water areas with salinities <15 and the Laptev/East-Siberian ROFI as the area with salinities between 15 and 25 (Osadchiev et al., 2021a).

Data and Methods

In this work, we analyzed an extensive *in situ* data set, which was collected in 1999–2019 during 17 oceanographic surveys in the Laptev and East-Siberian seas (**Table 1**). Continuous measurements of salinity in the surface layer (2–3 m depth) were carried during 12 cruises in 2003, 2007–2009, 2011–2012, and 2014–2019. These measurements were performed along the ship track using a shipboard pump-through system equipped with a thermosalinograph (*SBE 21 SeaCAT*) with a frequency of 1 Hz. Vertical thermohaline measurements analyzed in this study were performed using a CTD instrument (*SBE 911plus*) at a 24 Hz sampling rate. These measurements were organized along quasi-meridional (in 2007, 2008, 2011, 2016, and 2019) and quasi-zonal (in 2008, 2011, 2016, and 2019) transects starting from the eastern part of the Lena Delta (**Figure 1**, color dots). Also we used surface salinity data collected at hydrographic stations distributed in the southeastern Laptev Sea and the southwestern East-Siberian Sea (not organized in zonal or meridional transects), which were performed in 1999, 2000, 2004, 2005, and 2006. Continuous measurements of vertical thermohaline structure along the ship track were performed by a towed CTD instrument (*Idronaut 320 Plus*) along the eastern part of the Lena Delta in 2015. The CTD instrument was installed into a streamlined and dynamically balanced body, which was towed along the ship track aside of the ship wake and was repeatedly lowered and raised between the sea surface and the bottom. The measurement rate was 27 cycles per second. The horizontal towing velocity was about 2 m s^{-1}, while the vertical lowering/raising velocity was about 1 m s^{-1}. Horizontal/vertical resolution of the obtained CTD data is about 0.5/0.25 m. The CTD-data were processed based on standard programming package (*SBE Data Processing*, version 7.26.7) using recommended settings (Sea-Bird Electronics, 2017).

Wind forcing conditions and atmospheric pressure during 1999–2019 were examined using ERA5 atmospheric reanalysis with a 0.25° spatial and hourly temporal resolution (Hersbach et al., 2020). The ERA5 reanalysis data were downloaded from the European Centre for Medium-Range Weather Forecasts

(ECMWF) website[1]. The Lena River discharge measurements analyzed in this study were acquired during 1999–2019 in the most downstream gauge station located in Kyusyur (**Figure 1**, red star), which is approximately 300 km far from the sea. Therefore, we shifted the daily discharge rates measured at this station by 7 days onward to obtain the freshwater discharge rate from the Lena Delta to the Laptev Sea according to estimate of the flow speed in the lower part of the Lena River (0.5 m/s) during the beginning of the freshet period (Kääb et al., 2013). The river discharge data were downloaded from the Arctic Great Rivers Observatory (ArcticGRO) website[2]. The sea ice data retrieved for 1999–2019 from satellite products were downloaded from the Arctic and Antarctic Research Institute (AARI) website[3].

RESULTS

Atmospheric Forcing, River Discharge, and Ice Conditions

Monthly averaged wind forcing conditions and sea level pressure shortly before and during the field surveys when detailed measurements of the vertical structure of FSL were performed along the zonal and meridional transects (2007, 2008, 2011, 2016, and 2019) are shown in **Figures 2**, **3**. **Figure 2** shows prevailing western and northern winds at the shelf area of the Laptev and East-Siberian seas in August–September 2007 (average wind speed 4–6 m/s) and in September–October 2016 (6–9 m/s). **Figure 3** shows opposite wind conditions for 2008, 2011, and 2019. In particular, eastern and southern winds prevailed at the shelf area in August–September 2008 (average wind speed 5–7 m/s). Strong eastern winds prevailed in August 2011 (7–9 m/s) followed by moderate winds with complex pattern (western in the Laptev Sea and eastern in the East-Siberian Sea) in September 2011 (4–5 m/s) and strong eastern wind in October 2011 (9–10 m/s). Strong eastern winds prevailed in August–September 2019 (6–9 m/s), which then switched to western winds in October 2019.

The main sources of fresh water in the Laptev and East-Siberian seas are river discharge and ice melting. The role of annual precipitation (100–300 mm) is negligible, because it is mostly provided during the cold season, when the seas are covered by ice (Pavlov et al., 1996). Due to low air temperatures over these seas (<5°C during ice-free season), evaporation also play insignificant role in the regional freshwater balance (Pavlov et al., 1996; Lambert et al., 2019). Discharge rate of the Lena River is characterized by a distinct freshet in June–July (up to 80,000–140,000 m^3/s) followed by steady decrease of discharge until November (5,000–10,000 m^3/s) and low discharge period in December–May (2,000–3,000 m^3/s) (**Figure 4A**). Total freshwater runoff from the Lena River in May–October during the last 20 years significantly varied from 390 km^3 (2019), 420 km^3 (2003), and 440 km^3 (2011) to 600–610 km^3 (2007, 2008, 2016, and 2018) (**Figure 4B**). Seasonal discharge variability of other rivers inflowing to the Laptev and East-Siberian seas is similar to that of the Lena River with short-term summer freshet and drought in winter and spring (Pavlov et al., 1996).

Ice conditions in the Laptev and East-Siberian seas also have large inter-annual variability. **Figure 5** shows ice coverage in the Laptev and East-Siberian seas in the middle of July, August, and September for 2007, 2008, 2011, 2016, and 2019. In 2007 central parts of both seas were free of ice from the second half of July. In 2008, on the opposite, ice coverage was very extensive until the second half of August, ice melted in the central parts of these seas only in the middle of September. In 2011 and 2019, sea ice remained in the central East-Siberian Sea until the middle of September, while the Laptev Sea was free of ice by the middle of July. The opposite situation, i.e., ice-free East-Siberian Sea and ice-covered Laptev Sea by the middle of September, was observed in 2016.

Spatial Extents of Freshened Surface Layer

In this study, we address structure and spatial extents of the Lena plume (salinity <15) formed in the southeastern Laptev Sea and the Laptev/East-Siberian ROFI (salinity between 15 and 25), which occupy wide area in the eastern Laptev Sea and the western East-Siberian Sea. Analogously to FSL formed in the Kara Sea, we determine the isohaline of 15 as the boundary between the Lena plume and the Laptev/East-Siberian ROFI, while the isohaline of 25 represents the boundary between the Laptev/East-Siberian ROFI and the ambient sea (Osadchiev et al., 2021a).

Figure 6 shows the analyzed salinity dataset collected during 12 oceanographic field surveys in 2003–2019 with good spatial coverage of continuous *in situ* measurements in the surface layer along the ship track. The whole dataset was split into two groups according to predominant western/eastern winds at the study area defined by positive/negative zonal component of average wind speed. Predominant eastern winds result in distinct northward spreading of both the Lena plume and the ROFI (**Figure 6a**). Predominant western winds, on the opposite, press the Lena plume and the ROFI to the Siberian coast (**Figure 6b**).

Figure 7 demonstrates locations of isohalines of 15 and 25 in the surface layer in the study area, which were reconstructed using discrete measurements at hydrologic stations and continuous measurements along the ship track. The reconstructed isohalines of 15 and 25 strictly correspond to areas covered by *in situ* measurements and were not extended arbitrary elsewhere. If measurements were limited to the southeastern part of the Laptev Sea (as in 1999 and 2005), only locations of the isohaline of 15 were drawn. If measurements were limited to one meridional transect from the Lena Delta (as in 2006 and 2015), locations of the isohalines of 15 and 25 were drawn only at this transect. Despite certain bias of detection of location of these isohalines based on discrete stations and individual ship tracks, the obtained data provides important information about positions, shapes, and sizes of the Lena plume and the Laptev/East-Siberian ROFI during the considered periods. A half of the considered field surveys took place in September (in several

[1]https://www.ecmwf.int/en/forecasts/datasets/archive-datasets/reanalysis-datasets/era5

[2]https://arcticgreatrivers.org/data/

[3]http://www.aari.ru/odata/_d0015.php?mod=1

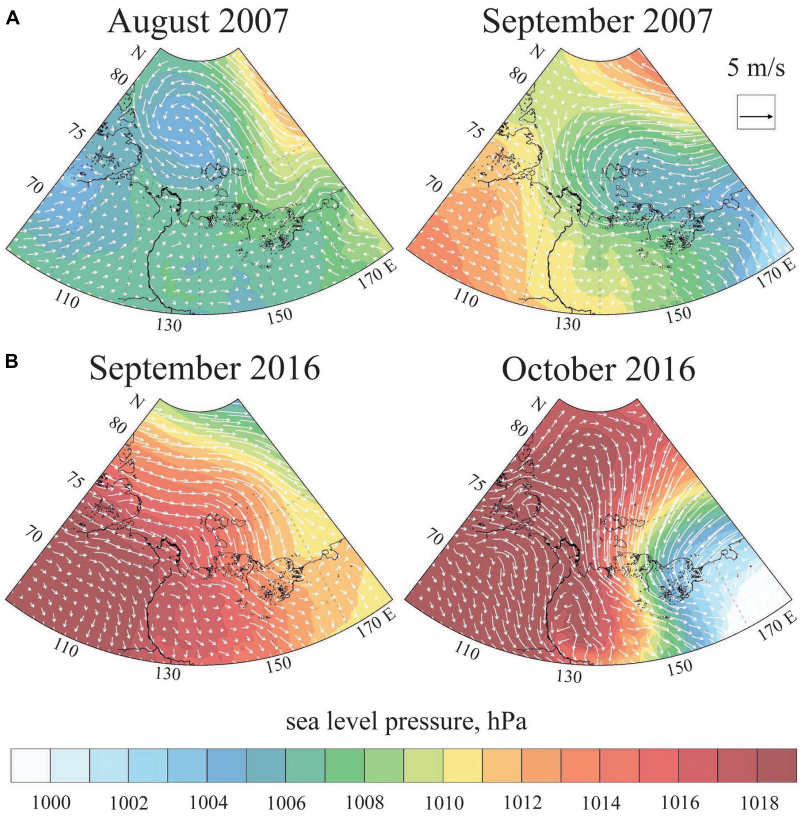


FIGURE 2 | Monthly averaged wind forcing (arrows) and sea level pressure (color) in the Laptev and East-Siberian seas in August and September 2007 **(A)**, and September and October 2016 **(B)**.

cases including a few days in August or October) (**Table 1**). Therefore, the obtained data set is representative of inter-annual variability (in September of different years) of spatial extents of the Lena plume and the Laptev/East-Siberian ROFI. Surface freshening attributed to sea ice can also bias determination of borders of the Lena plume and the Laptev/East-Siberian ROFI. However, according to Bauch et al. (2013) meltwater provides significant (compared to river discharge) freshening of surface layer only at salinities >30. Therefore, we presume that the detected locations of the isohalines of 15 and 25 are not affected by melting of sea ice in the study area during late summer and autumn.

The most extensive continuous measurements of surface salinity in the study area were made in 2008, 2011, 2016, and 2019 (**Figure 8**). During these surveys, the ship tracks covered wide areas in the eastern Laptev Sea and in the western East-Siberian Sea from 90°E in the west to 180°E in the east and from the Siberian coast in the south to 78°N in the north. Also, the detailed vertical thermohaline measurements were performed along zonal and meridional transects during these surveys. As a result, these transects performed in August/September 2008, September/early October 2011, September/October 2016, and late September/October 2019 provide certain information about the seasonal variability of the Lena plume and the Laptev/East-Siberian ROFI as further described in section "Discussion." The northern boundary of FSL in the Laptev Sea was located below 76°N in 2000, 2007, 2009, 2014, 2016, and 2018 while in 2008, 2011, and 2015 salinities <25 were registered reaching as far as 77–78°N (**Figure 7**). The eastern and western boundaries of FSL varied less significantly, salinities <25 were observed between the longitudes of 120°E and 170°E (**Figure 7**). Despite the fact that reconstruction of the isohaline of 25 is speculative to a certain extent, extensive continuous measurements of surface salinity revealed very large FSL in 2008, 2011, and 2019 with area of 400,000–500,000 km^2 (calculated according to the isohaline of 25), while in 2016 FSL was pressed to the Siberian coast and occupied almost twice less area (**Figure 8**). According to our assessment, the meridional extent of FSL varied from 250–350 km in 2016 to 600–700 km in 2008, 2011, and 2019. The zonal extent of FSL was 1,300–1,500 km.

The Lena plume also showed large variability of area and position (**Figures 6–8**). In 1999, 2000, 2009, 2011, 2015, and 2016 the northern boundary of the plume was located at the latitudes of 72.5–73°N and the plume occupied relatively small area (20,000–40,000 km^2) adjacent to the eastern part of the Lena Delta (**Figures 7**, **8b,c**). In 2005, 2008, 2012, 2017, and 2019, on the opposite, the northern plume boundary was located at the latitude above of 75°N (**Figures 7**, **8a,d**). During 2008 and 2017 the Lena plume was reaching the New Siberian Islands and its area was 120,000–150,000 km^2 (**Figures 7**, **8a**). Therefore, the

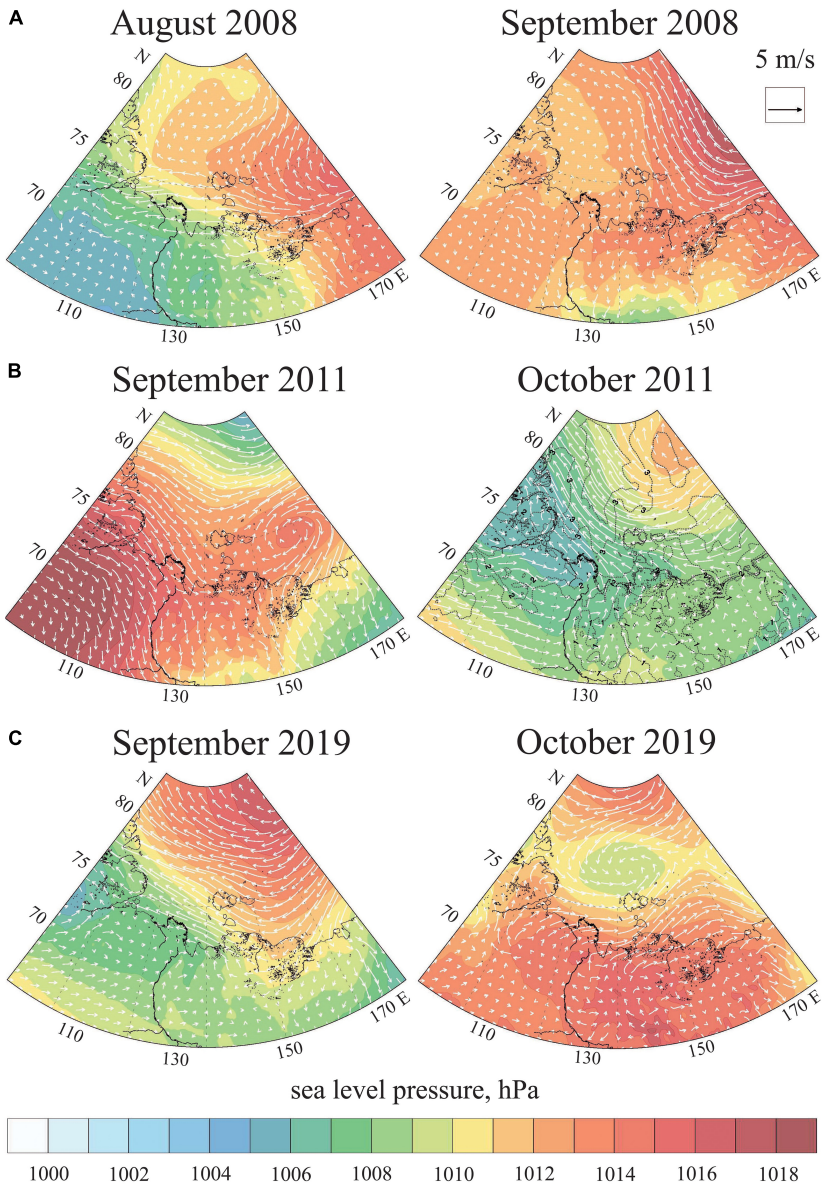


FIGURE 3 | Monthly averaged wind forcing (arrows) and sea level pressure (color) in the Laptev and East-Siberian seas in August and September 2008 **(A)**, September and October 2011 **(B)**, and September and October 2019 **(C)**.

meridional extent of the Lena plume varied from 150 km (1999, 2011, 2015, and 2016) to 400 km (2008 and 2019), while its zonal extent varied from 100 km (1999 and 2011) to 400–500 km (2008 and 2017) (**Figures 7**, **8**).

Vertical Structure of Freshened Surface Layer

The vertical structure of FSL in the Laptev and East-Siberian seas was studied based on the vertical thermohaline measurements performed at hydrographic stations along the zonal and meridional transects. The most southern and western stations of these transects were located near the eastern part of the Lena Delta, which provides the majority of discharge from the Lena Delta to the Laptev Sea (Fedorova et al., 2015). As a result, these transects crossed the central part of FSL and are representative of its vertical structure. **Figures 9–12** show large differences among the vertical thermohaline structure of FSL observed in 2007, 2008, 2011, 2016, and 2019.

In September 2007 the most southern station of the meridional transect was located at the latitude of 74.2°N, i.e., 100 km northward from the Lena Delta (**Figures 9A**, **10A**). Salinities along the transect were >25, so FSL was located southward from the transect (**Figure 9A**). In September–October 2016 low salinities at the meridional transect were registered only near the Lena Delta, while at the most southern station outside

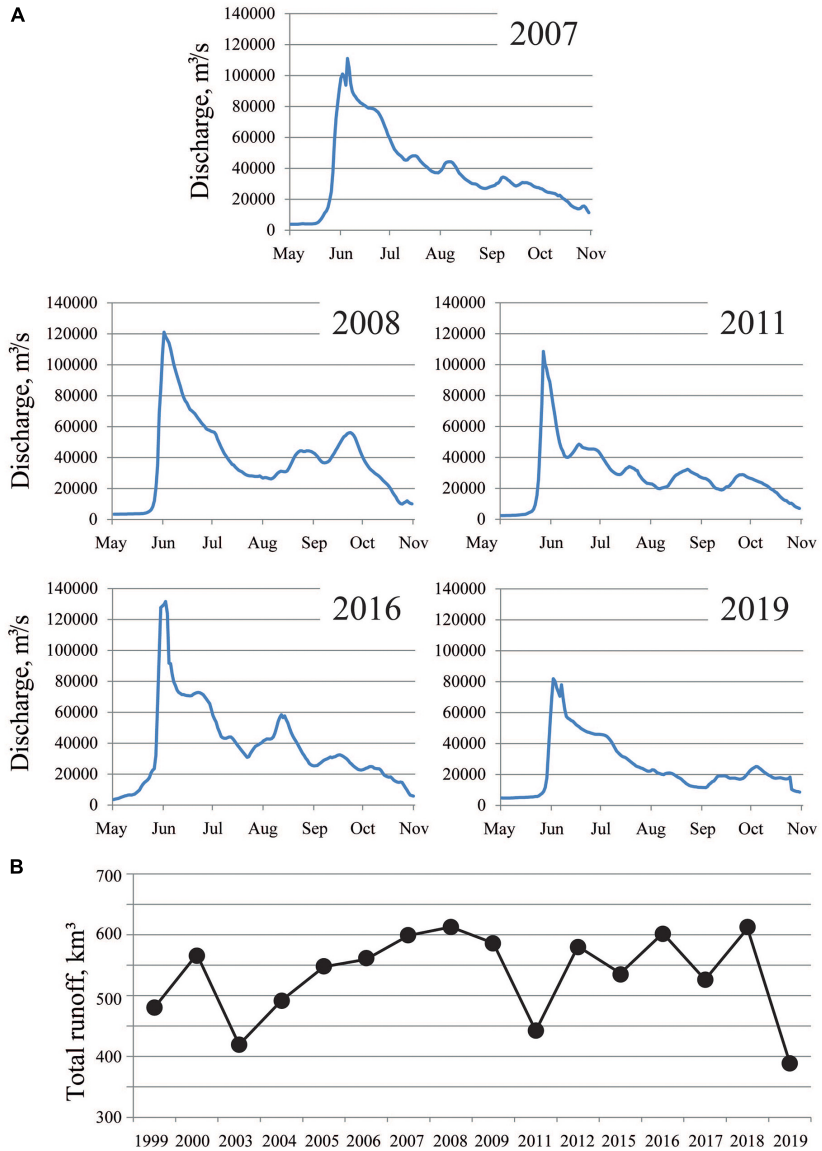


FIGURE 4 | Discharge rates of the Lena River in May–October measured at the gauge station in Kyusyur in 2007, 2008, 2011, 2016, and 2019 **(A)** and total river runoff in May–October between 1999 and 2019 **(B)**.

the delta region located at the latitude of 75.5°N salinities exceeded 26 (**Figure 9D**). FSL near the delta was well mixed and occupied the whole water column from surface to sea bottom (15–20 m deep). Surface salinities of this layer steadily increased from 1–2 to 17, while temperatures decreased from 3 to 0°C (**Figure 10D**). Continuous salinity measurements along the ship track showed that the isohaline of 25 in the surface layer was located at the latitude of 74.8°N indicating the northern boundary of FSL. The zonal transect in 2016 was stretched along the sea coast reaching the longitude of 154°E (**Figure 11C**). Similarly to the southern part of the meridional transect, FSL was well mixed and occupied the whole water column from surface to sea bottom (15–20 m deep) along the whole zonal transect. Surface salinities were 11–16 in the Laptev Sea, eastward from the Laptev Strait it increased to 18–24. Temperatures along the zonal transect were equal to 0–2°C, except in the proximity of the Lena Delta where it was 2–3°C (**Figure 12C**).

By contrast to 2007 and 2016, in August 2008 FSL propagated more than 500 km northward from the Lena Delta, salinities <25 were observed until the end of the meridional transect at the latitude of 77°N (**Figure 9B**). The depth of FSL steadily decreased from 12 m near the delta to 5 m at the most northern station of the transect. The majority of volume of this layer was formed by the fresh (5–15) and warm (4–10°C) Lena plume (**Figures 9B**, **10B**). In eastward direction, the Lena plume reached the Laptev Strait, while FSL was observed along the zonal transect until the longitude of 164°E (**Figure 11A**). The depth of this layer along

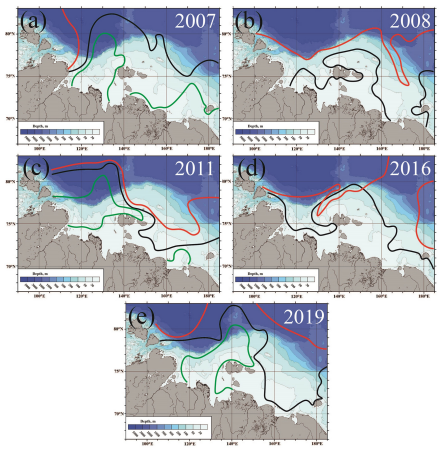


FIGURE 5 | Position of the seasonal sea ice edge in the Laptev and East-Siberian seas on 15 July (green line), 15 August (black line), and 15 September (red line) in 2007 **(a)**, 2008 **(b)**, 2011 **(c)**, 2016 **(d)**, and 2019 **(e)**.

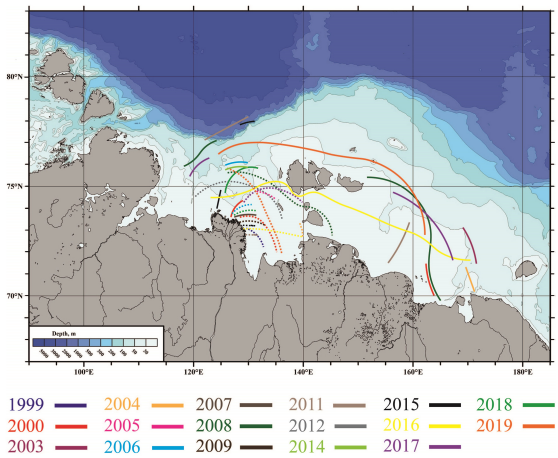


FIGURE 7 | Locations of the isohalines of 15 (dashed lines) and 25 (solid lines) in the Laptev and East-Siberian seas detected by *in situ* measurements of 17 oceanographic field surveys.

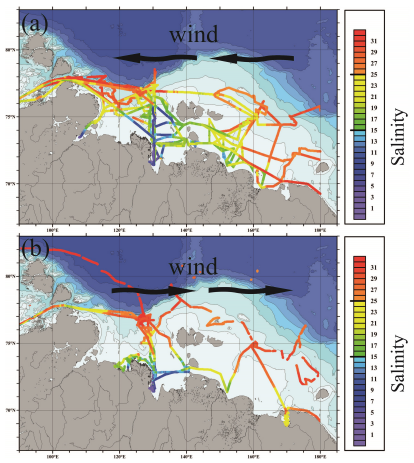


FIGURE 6 | Salinity in the surface layer along the ship tracks in 2003, 2008, 2011, 2012, 2015, 2017, and 2019 **(a)** and in 2007, 2009, 2014, 2016, and 2018 **(b)** with predominant eastern **(a)** and western **(b)** winds in the Laptev and East-Siberian seas during ice-free period.

the zonal transect varied between 10 and 15 m, its temperatures decreased from 10°C near the Lena Delta to 0°C at the central East-Siberian Sea (**Figures 11A**, **12A**).

FSL also occupied large area in the Laptev and East-Siberian seas in September 2011 and October 2019. In 2011 salinities <25 were observed until the end of the meridional transect at the latitude of 75.8°N (**Figure 9C**), while in 2019 the isohaline of 25 was located at the latitude of 76.2°N (**Figure 9E**). The depth of FSL varied between 12 and 20 m in 2011, in 2019 its depth was 9–11 m along the whole transect. The northern boundary of the Lena plume was located at the latitude of 72.6°N in 2011 and of 74.6°N in 2019. FSL propagated eastward reaching the longitude of 156°E along the coast in 2011 (**Figure 11B**) and reaching the longitude of 159°E at the central East-Siberian Sea in 2019 (**Figure 11D**). This layer was well mixed along the zonal transects and occupied the whole water column until the depths of 20–25 m during both surveys. Temperatures of this layer were 0–3°C during both surveys (**Figures 10C,E**, **12B,D**). Note that the Lena plume was not detected along the zonal transect in 2011 presumably because of the complex pattern of the wind in September 2011. The change of eastern/western prevailing winds in August–September 2011 (**Figure 3B**) presumably limited the eastward spread of the plume.

High-resolution vertical structure of FSL in vicinity of the Lena Delta was studied based on thermohaline measurements by a towed CTD instrument in the beginning of September 2015. These measurements were performed along the 145 km long meridional transect located on a distance of 25 km eastward from the eastern shore of the Lena Delta (**Figure 13**). Surface salinities along the transect varied from 10 to 15 at the southern and central parts of the transect to 15–20 at the northern part of the transect (**Figure 13A**). The lowest salinities (0–4) and the highest temperatures (7–9°C) along the transect were registered in the surface layer vicinity the large deltaic channels indicating low mixed freshwater discharge from them. Strong stratification was observed, first, between the Lena plume and the ROFI at the depth of 5–8 m in the central and southern parts of the transect and, second, between the ROFI and the subjacent saline sea at the depth of 10–15 m along the whole transect.

The high-resolution salinity structure reconstructed in vicinity of the Lena Delta demonstrates low intensity of mixing between the inflowing river discharge and the subjacent sea water. First, vertical extent of the Lena plume is stable along the transect. Depth of the plume only slightly increases from 5 to 6 m in vicinity of large deltaic channels (indicated by the lowest salinities) to 7–8 m at the southern part of the transect on a distance of 50 km from the main freshwater sources. Second, horizontal salinity gradient is large only in vicinity of the large deltaic channels. Depth of ROFI is also stable and is equal to 10–11 m along the transect except its northern part, where

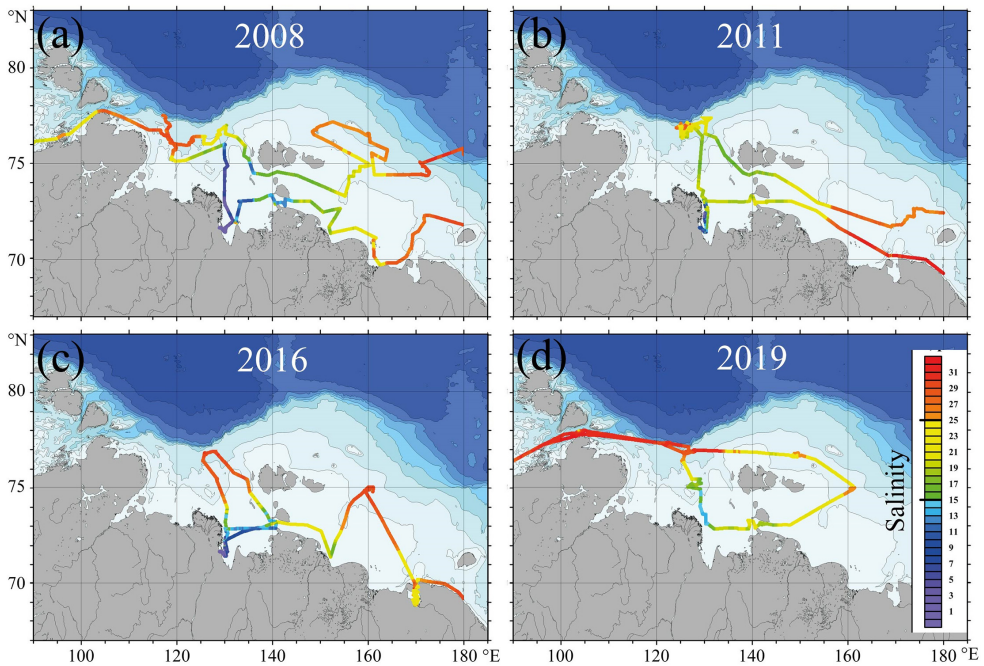


FIGURE 8 | Salinity in the surface layer in the Laptev and East-Siberian seas along the ship tracks on 23 August – 18 September 2008 **(a)**, 13 September – 8 October 2011 **(b)**, 20 September – 20 October 2016 **(c)**, and 27 September – 13 October 2019 **(d)**.

it increases to 15 m. Note that this structure is observed in the beginning of September, i.e., 3 months after the freshet period, which demonstrates that strong vertical stratification and small vertical extent of FSL is still maintained during the low discharge period.

DISCUSSION

In situ measurements (**Figures 6**, **7**) during ice-free periods show significant inter-annual variability of FSL in the Laptev and East-Siberian seas with two typical spreading patterns, which were explicitly addressed in previous studies (Berezovskaya et al., 2002; Dmitrenko et al., 2005, 2008, 2010; Janout et al., 2020). During years with predominant western/eastern winds in the study area, FSL is forced to move eastward/northward and have relatively small/large meridional extents (**Figure 6**). Detailed salinity measurements in the study area made in 2007, 2008, 2011, 2016, and 2019 provide new information about spatial extents and vertical structure of FSL (**Figures 8–12**). In 2008, 2011, and 2019, FSL occupied large area in the Laptev and East-Siberian seas, its meridional and zonal extents were 500–600 km and 1,200–1,300 km, respectively (**Figures 6–8**). Eastern and southern winds prevailed at the shelf area of the Laptev and East-Siberian seas in August-September 2008. In 2011 and 2019, the atmospheric circulation was rather variable. Eastern winds prevailed in August and October 2011, while winds presented a complex pattern in September 2011, namely, western winds in the Laptev Sea and eastern winds in the East-Siberian Sea. Similarly, eastern winds prevailed in August and September 2019 followed by western winds in October 2019. Nevertheless, both in 2011 and 2019, eastern winds occurred at the shelf area during longer period than western winds. In 2007 and 2016 during predominant western and northern winds, FSL was stretched along the Siberian coast, its meridional extent was <250 km, i.e., twice less as compared to the first pattern, while its zonal extent was >1,000 km which is similar to the first pattern. The observed inter-annual variability of FSL in the Laptev and East-Siberian seas is much greater as compared to FSL formed in the Kara Sea, which occupies relatively stable area every year (Osadchiev et al., 2021a). Moreover, the area of FSL in the Laptev and East-Siberian seas during certain years is almost twice greater than the area of FSL in the neighboring Kara Sea, while the total annual freshwater discharge to the Laptev and East-Siberian seas (∼1,000 km^3) is much less than to the Kara Sea (∼1,500 km^3) (Gordeev et al., 1996; Osadchiev et al., 2021a).

In contrast to wind forcing conditions, large inter-annual variability of river discharge rate and ice coverage during warm season does not show any relation to variability of area, position, and depth of FSL. The lowest freshet discharge peak and the lowest total runoff volume from the Lena River among the considered years occurred in 2011 and 2019 (**Figure 4**) and was accompanied by large area of FSL in the Laptev and East-Siberian seas (**Figure 7**). Total runoff volume from the Lena River in 2007, 2008, and 2016 was similar (and 1.5 times higher than in 2011 and 2019) (**Figure 4**), while area of FSL was large in 2008 and small in 2007 and 2016 (**Figure 7**). In particular, area of this layer in 2016 was two times smaller than in 2008 and 2019. The smallest depth of FSL in the Laptev Sea was observed in 2008

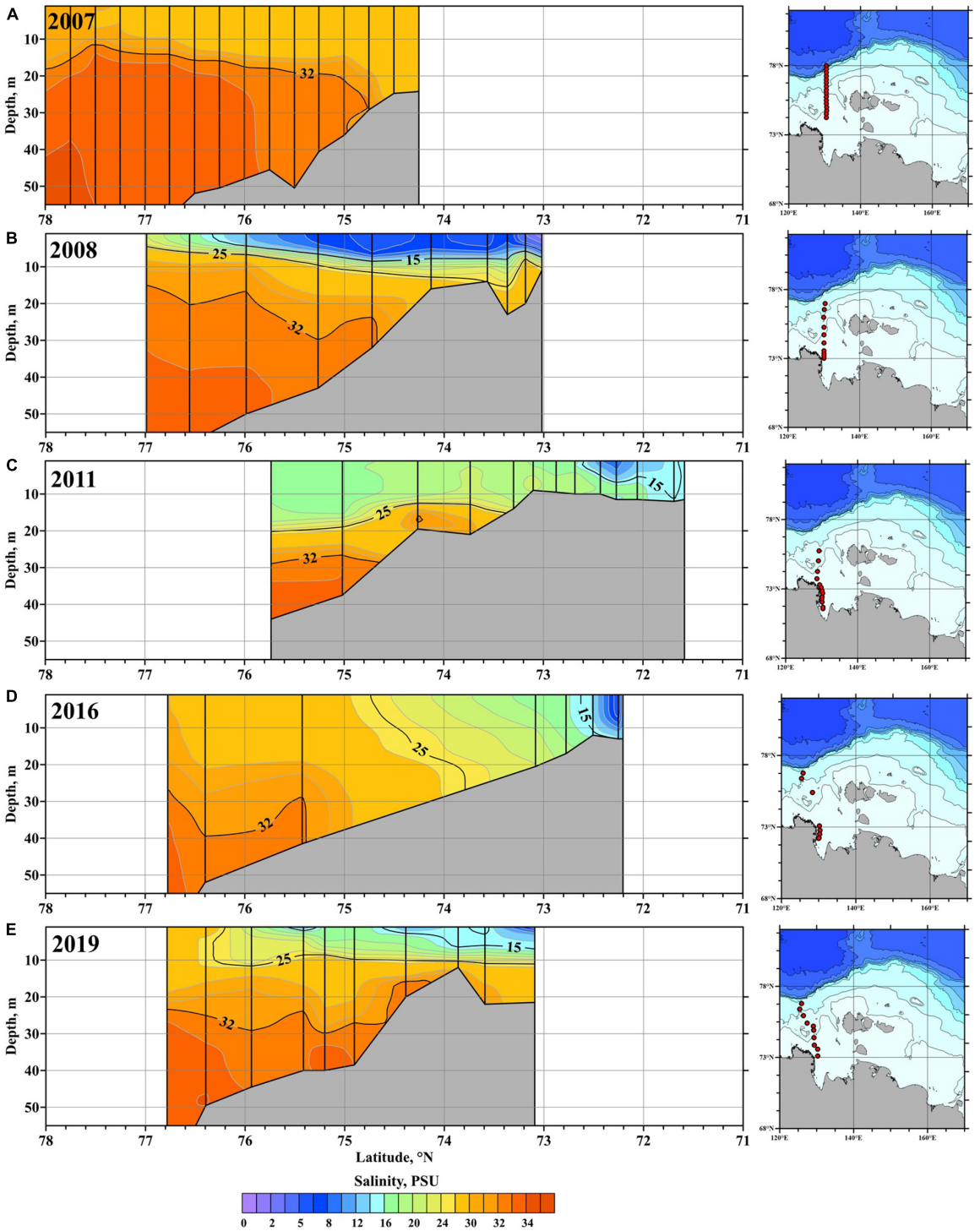


FIGURE 9 | The vertical salinity structure along the meridional transects in the Laptev Sea on 14–30 September 2007 **(A)**, 23–25 August 2008 **(B)**, 19–26 September 2011 **(C)**, 25 September – 2 October 2016 **(D)**, and 6–13 October 2019 **(E)**. The isohalines of 15, 25, and 32 are shown by bold lines. Locations of the stations are shown by black vertical lines. Locations of the transects are shown in the right insets.

and 2019 (**Figure 9**) with significantly different river discharge conditions (**Figure 4**). Inter-annual variability of seasonal ice coverage also does not show any relation to variability of area of FSL. Large/small area of FSL was observed during years with extensive summer ice coverage (2008/2016), as well as during years with early ice melting (2019/2007).

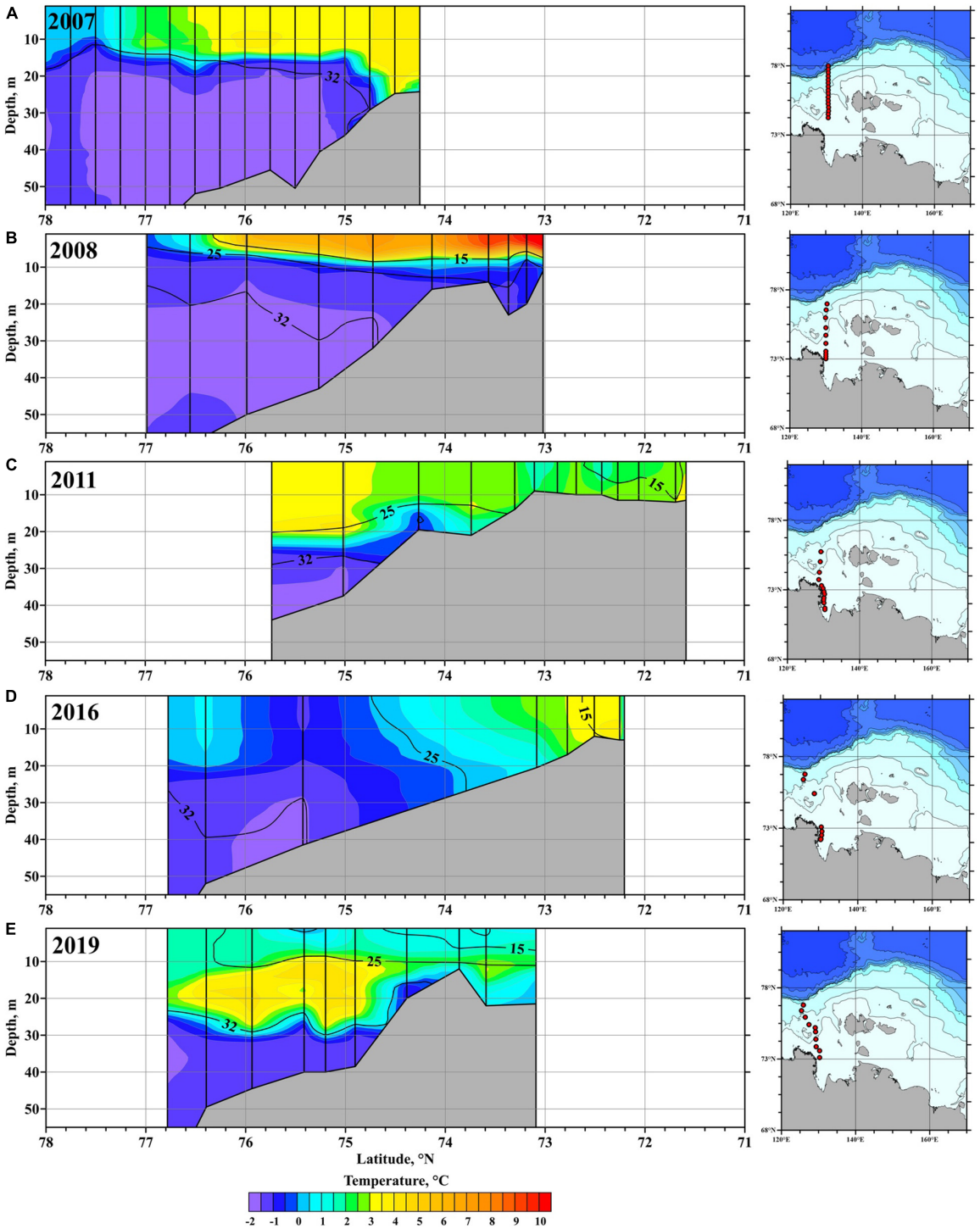


FIGURE 10 | The vertical temperature structure along the meridional transects in the Laptev Sea on 14–30 September 2007 **(A)**, 23–25 August 2008 **(B)**, 19–26 September 2011 **(C)**, 25 September – 2 October 2016 **(D)**, and 6–13 October 2019 **(E)**. The isohalines of 15, 25, and 32 are shown by bold lines. Locations of the stations are shown by black vertical lines. Locations of the transects are shown in the right insets.

The Lena plume is spreading as a low saline (<15) and stratified water mass in the study area during and shortly after the freshet period of the Lena River. In particular, it occupied almost the whole volume of FSL in the Laptev Sea in August 2008 (**Figure 9B**), while no well-developed ROFI was observed along this transect. Then in September 2011 and October 2019

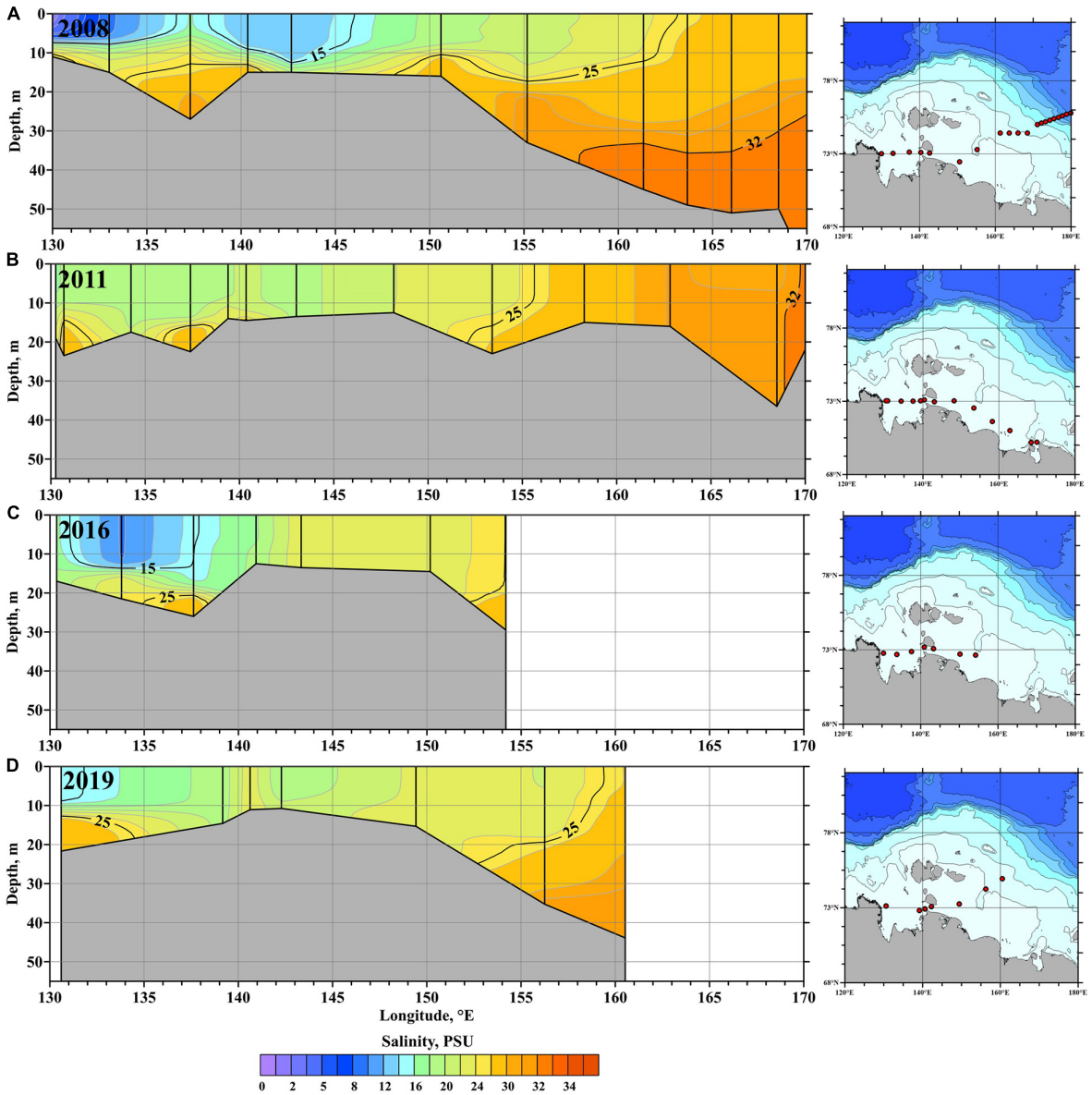


FIGURE 11 | The vertical salinity structure along the zonal transects in the Laptev and East-Siberian seas on 25–30 August 2008 **(A)**, 30 September – 3 October 2011 **(B)**, 2–9 October 2016 **(C)**, and 3–6 October 2019 **(D)**. The isohalines of 15, 25, and 32 are shown by bold lines. Locations of the stations are shown by black vertical lines. Locations of the transects are shown in the right insets.

the Lena plume transforms to ROFI due to mixing with subjacent saline sea water (**Figures 9C,E**). This seasonal transformation is also demonstrated by location of the isohaline of 15 during different months in different years even though it strongly depends on wind forcing (**Figures 6**, **7**). During years with predominant western and northern winds, FSL is stretched along the coast and salinities <15 are registered only southward from the latitude of 74°N, i.e., in vicinity of the Lena Delta (**Figures 6**–**8**). On the opposite, during years with predominant eastern and southern winds (**Figure 6a**), the isohaline of 15 moves southward from 76.5°N in August 2008 to 75°N in September 2005, September 2012, September 2015, and September 2017 and to 74°N in October 2011, October 2018, and October 2019 (**Figures 7**, **8a,b,d**). As a result, in September and October in 2011, 2016, and 2019 the Lena plume is registered at relatively small area in the southeastern Laptev Sea adjacent to the eastern part of the Lena Delta, while the majority of the area of FSL corresponds to the Laptev/East-Siberian ROFI (**Figure 8**). Similar seasonal transformation of the Ob-Yenisei plume to the Kara ROFI occurs in the Kara Sea (Osadchiev et al., 2021a).

The depth of the Lena plume in the Laptev Sea in August (5–8 m) (**Figure 9B**) is twice less than the depth of the Ob-Yenisei plume in the Kara Sea in August (12–15 m) (Osadchiev et al., 2021a). This feature is caused by difference in morphology of

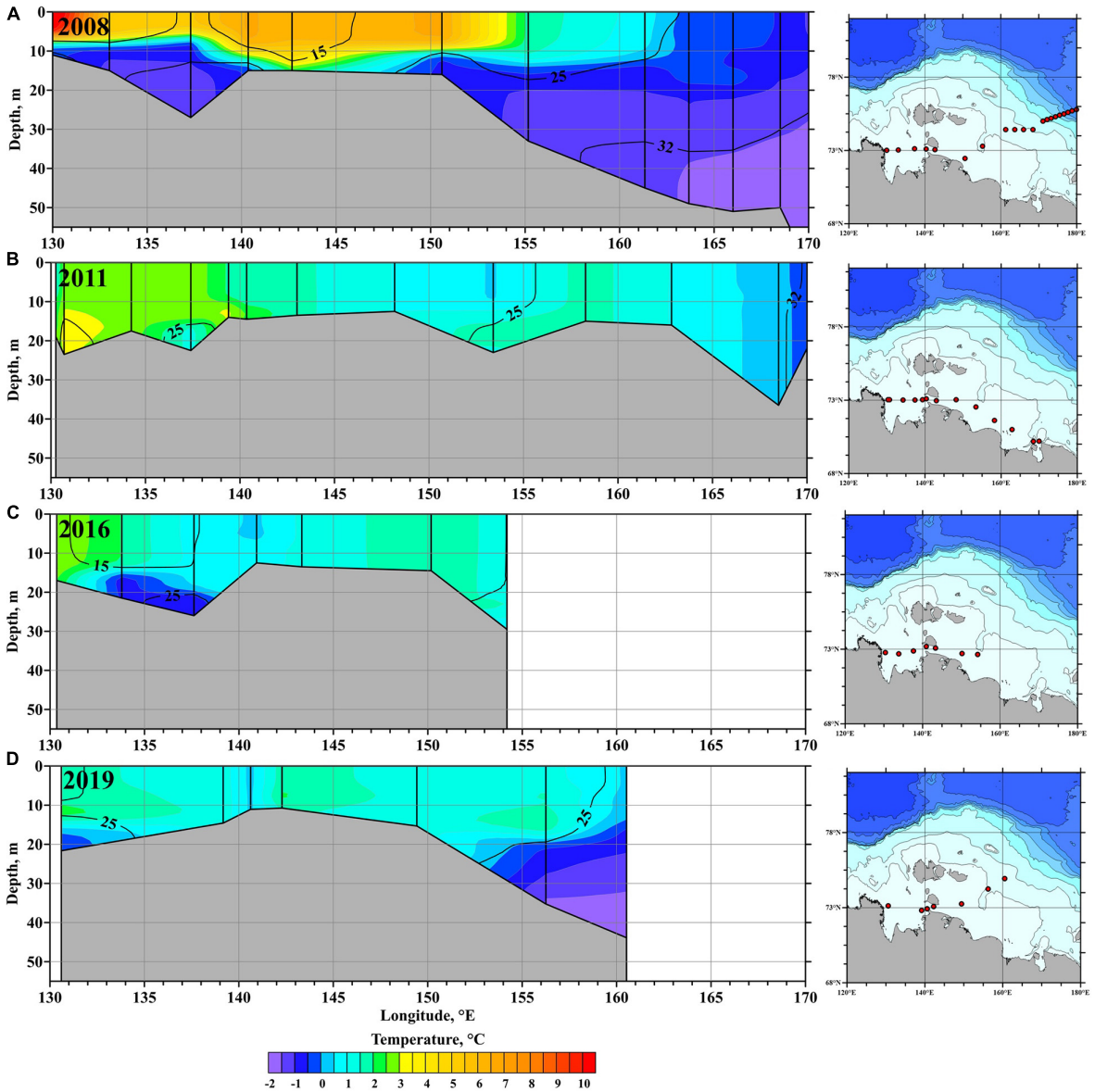


FIGURE 12 | The vertical temperature structure along the zonal transects in the Laptev and East-Siberian seas on 25–30 August 2008 **(A)**, 30 September – 3 October 2011 **(B)**, 2–9 October 2016 **(C)**, and 3–6 October 2019 **(D)**. The isohalines of 15, 25, and 32 are shown by bold lines. Locations of the stations are shown by black vertical lines. Locations of the transects are shown in the right insets.

estuarine and deltaic freshwater sources of these river plumes. The Ob and Yenisei rivers inflow to the Kara Sea through wide (30–60 km) and deep (15–20 m) estuaries, which results in formation of a deep river plume. The liftoff area of FSL within these estuaries, i.e., the area where this layer loses contact with the sea bottom, determines initial vertical extent of the river plume. *In situ* measurements show that liftoff occurs within the Ob and Yenisei gulf and sea depths in these areas are equal to 10–15 m (Osadchiev et al., 2021a). As a result, discharges from the Ob and Yenisei rivers experience intense mixing with saline seawater within their large estuaries before freshened water inflow to open sea.

Different situation is observed at the Lena Delta. The Lena River inflows to the Laptev Sea through numerous narrow (up to several km) and shallow (up to 2–3 m) deltaic branches along the 250 km segment of sea shore (Are and Reimnitz, 2000; Alekseevskii et al., 2014; Fedorova et al., 2015; Fuchs et al., 2021b). *In situ* measurements show that seawater does not inflow even to the largest and deepest deltaic branches and salinity within the Lena Delta is equal to zero from surface to bottom (Semiletov et al., 2011; Fuchs et al., 2021a). Moreover, in the open sea in the shallow (<5 m) vicinity of the Lena Delta salinity is also <1 from surface to bottom even during the low discharge period in winter and spring

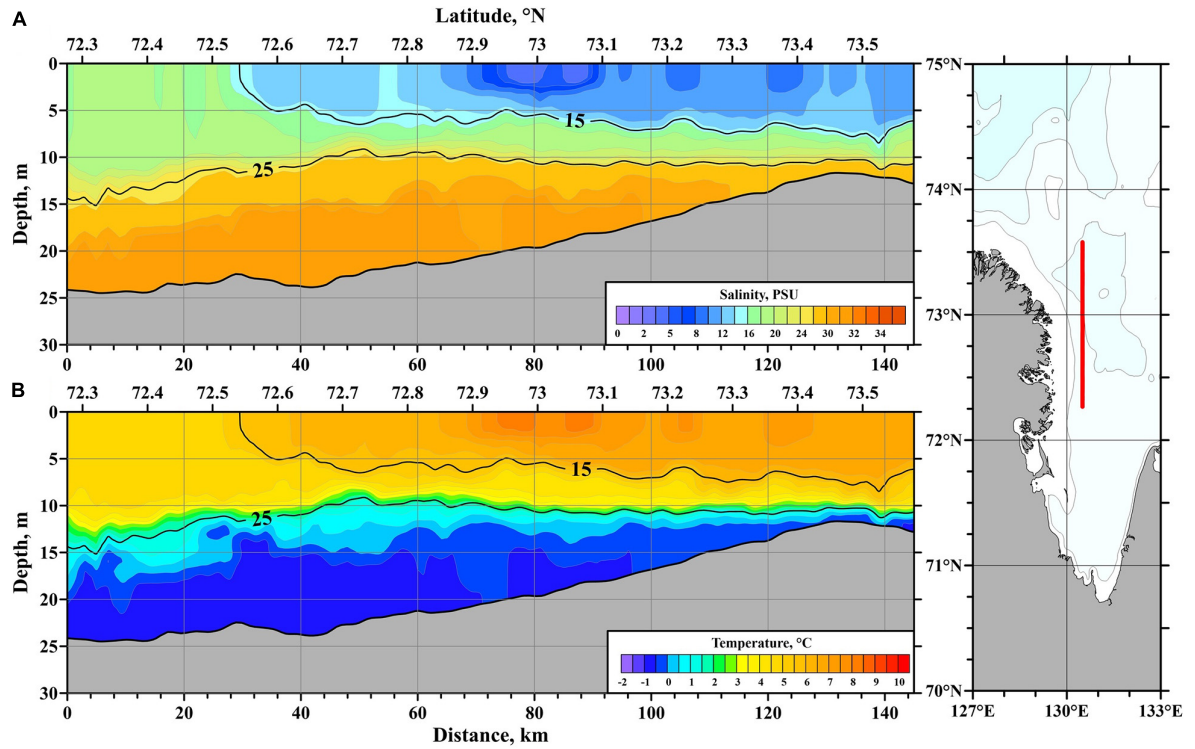


FIGURE 13 | The vertical salinity **(A)** and temperature **(B)** structure along the eastern shore of the Lena Delta on 7–8 September 2015. The isohalines of 15 and 25 are shown by bold lines. Location of the transect is shown in the right inset.

(Charkin et al., 2011; Fuchs et al., 2021a; Spivak et al., 2021). As a result, the undiluted Lena discharge inflows to sea from multiple channels and forms a narrow (10–15 km wide) stripe of zero-saline water from surface to bottom along the Lena Delta. *In situ* measurements demonstrate that this process occurs at least along the 150 km eastern part of the delta (**Figure 13**) which receives the majority of river discharge (80–90% of total Lena discharge). It can be also the case of several segments at the northeastern and southwestern parts of the Lena Delta, both areas receive 5–10% of total Lena discharge. Therefore, initial mixing of the Lena river discharge and saline seawater occurs at the open sea, once the zero salinity water propagates off the shallow vicinity of the delta to the sea deeper than 5 m.

Tidal circulation in the spreading areas of both FSL's in the Kara Sea and in the Laptev and East-Siberian seas is low, average tidal velocities do not exceed 0.2 m/s (Kagan et al., 2008, 2010). Maximal velocities of tidal currents in the Ob and Yenisei gulfs are equal to 0.4–0.5 m/s and 0.3–0.4 m/s, respectively (Voinov, 2002; Osadchiev et al., 2020a). Velocity shear between freshened surface layer and saline bottom layer within the Ob and Yenisei gulfs have similar magnitudes equal to 0.3–0.5 m/s, respectively. Maximal velocities of tidal currents in the area adjacent to the Lena Delta are equal to 0.1 m/s (Fofonova et al., 2014, 2015; Kagan and Timofeev, 2020).

Based on these velocity assessments we can calculate Froude numbers for the Ob-Yenisei and Lena plumes, which are indicative of mixing intensity (Horner-Devine et al., 2009; Geyer and MacCready, 2014). Freshwater Froude number for the Ob and Yenisei gulfs is calculated using the formula $Fr_f = \frac{U_f}{\sqrt{gSH \cdot 7.7 \times 10^{-4}}}$, where U_f is the velocity shear between surface and bottom layers, g is the gravity acceleration, S is the salinity of the bottom layer, H is the depth of the estuary (Geyer and MacCready, 2014). In case of the Ob and Yenisei gulfs these numbers vary from $\frac{0.3}{\sqrt{10 \cdot 30 \cdot 10 \cdot 7.7 \times 10^{-4}}} \sim 0.2$ to $\frac{0.5}{\sqrt{10 \cdot 30 \cdot 10 \cdot 7.7 \times 10^{-4}}} \sim 0.3$. The tidal Froude number for the Ob-Yenisei and Lena plumes is calculated using the formula $Fr_t = \frac{U_t}{\sqrt{g' h}}$, where U_t is the average tidal velocity, h is the depth of the river plume, $g' = g\frac{\rho_s - \rho_f}{\rho_s}$ is the reduced gravity within the plume, ρ_p and ρ_s are the densities of the plume and saline sea, respectively. In case of the Ob-Yenisei and Lena plumes these numbers are equal to $\frac{0.2}{\sqrt{10 \cdot (1024-1004)/1024}} \sim 0.45$ and $\frac{0.1}{\sqrt{10 \cdot (1024-1004)/1024}} \sim 0.2$, respectively. This result shows that the Lena discharge inflows to sea undiluted, while the Ob and Yenisei discharges are substantially mixed with saline seawater within their estuaries. Therefore, the Lena plume experiences lower tidal mixing in the open sea than the Ob-Yenisei plume.

In order to assess mixing of FSL in the Kara, Laptev, and East-Siberian seas, we calculated the vertical distribution of freshwater fraction $F = (S_0 - S)/S_0$ along the meridional and zonal transects from surface to the isohaline of 32, where S

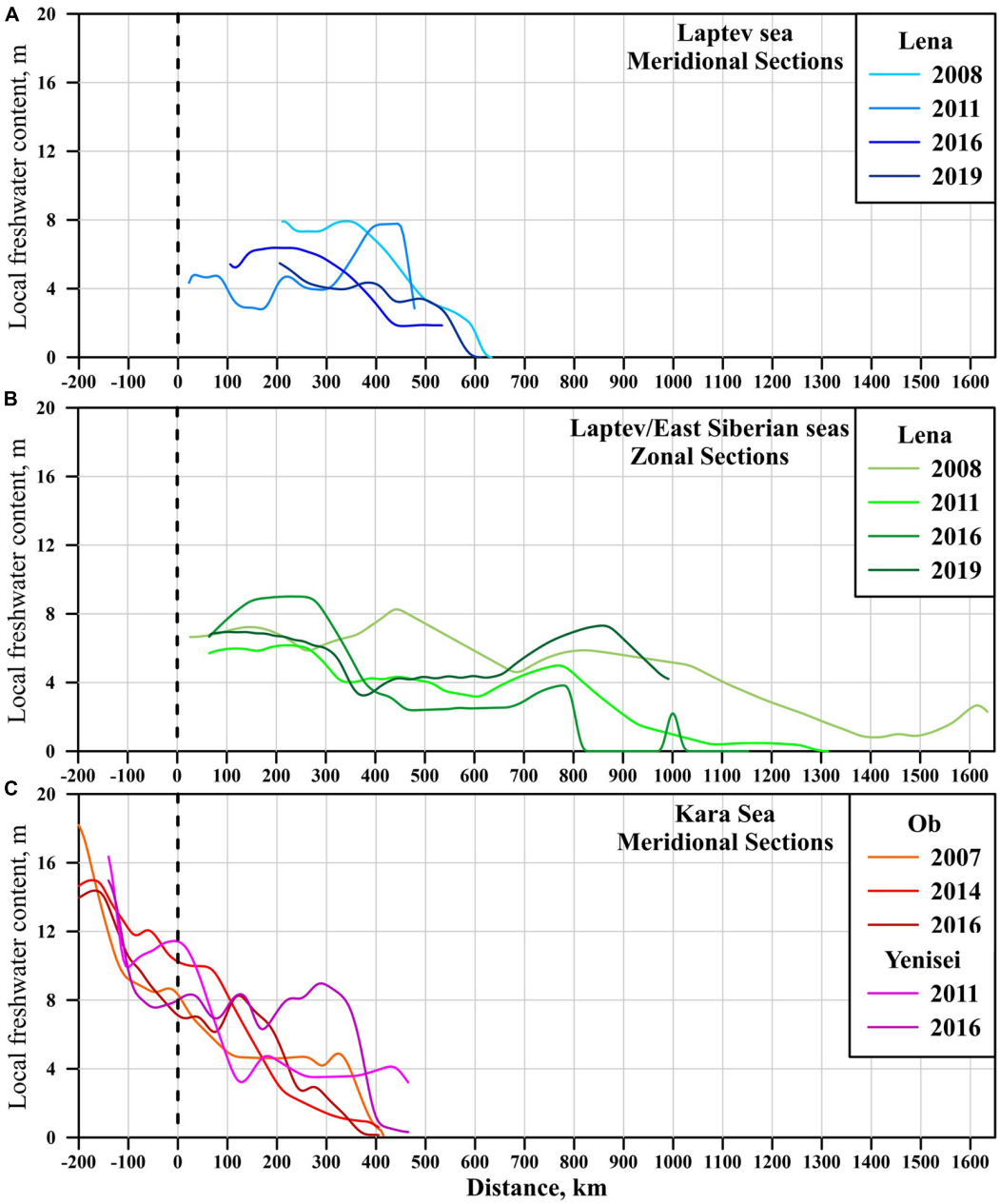


FIGURE 14 | Local freshwater content along the meridional transects in the Laptev Sea **(A)**, the zonal transects in the Laptev and East-Siberian seas **(B)**, the meridional transects in the Kara Sea **(C)** [from Osadchiev et al. (2021a)]. The dashed line indicates boundary of the open sea, i.e., the Lena Delta shoreline in **(A,B)** and the seaward boundaries of the Ob and Yenisei gulfs in **(C)**.

is the observed salinity, $S_0 = 32$ is the reference ambient sea water salinity according to typical salinity of ambient saline sea water at the study region (Pavlov et al., 1996). F represents the volume fraction of freshwater in the surface layer that produced the observed salinity after mixing with ambient saline sea water (Nash et al., 2009). Then, based on the reconstructed distributions of F, we calculated the local freshwater content $L(x) = \int_{-h(x)}^{o} F(x,z)dz$, along the transects, that is, freshwater content in the water column, where x and z are the horizontal (along a transect) and vertical coordinates, respectively, $F(x, z)$ is the freshwater fraction at the point (x, z), $h(x)$ is the sea depth.

Figure 14 illustrates that distribution of freshwater content in the Laptev and East-Siberian seas is significantly different from that observed in the Kara Sea. First, freshwater content near freshwater source in the Laptev Sea (4–8 m near the Lena Delta) (**Figures 14A,B**) is much lower than in the Ob (10–18 m) and Yenisei (8–16 m) gulfs (**Figure 14C**; Osadchiev et al., 2021a).

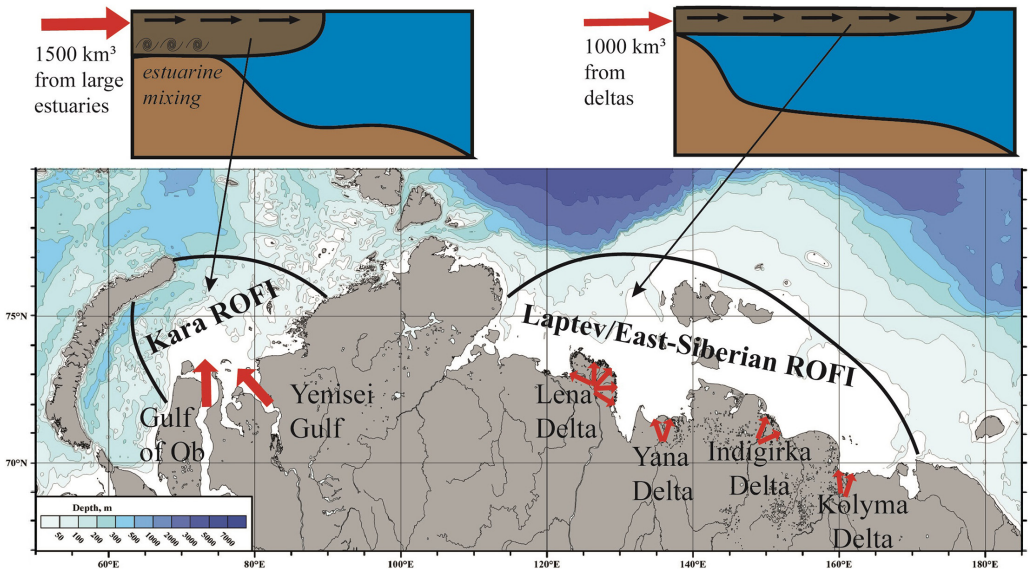


FIGURE 15 | Schematic of formation of deep Kara ROFI by discharges from large estuaries and shallow Laptev/East-Siberian ROFI by discharges from deltas.

Second, freshwater content is more stable in the Laptev and East-Siberian seas. It varies mainly between 5 and 9 m near the Lena Delta indicating low intensity of mixing of the river discharge and saline seawater in this area. Then freshwater content decreases to 3–4 m at the distance of 350–500 km in meridional direction (**Figure 14A**) and at the distance of 800–1,100 km in zonal direction (**Figure 14B**) from the Lena Delta. In the Kara Sea the local freshwater content abruptly drops to 8–12 m within the northern parts of the estuaries and then decreases to 4 m on a distance of 100–400 km from the estuaries in meridional direction (**Figure 14C**).

Large freshwater discharge to the Kara Sea from the Ob and Yenisei rivers experiences intense mixing in the estuaries and adjacent areas and forms 12–15 m deep Ob-Yenisei plume. This plume is expanding in the sea during June-July and occupies relatively stable area (200,000–250,000 km^2) in the central Kara Sea until the end of the ice-free season, as shown by Osadchiev et al. (2021a). Freshwater discharge from the Lena River to the Laptev Sea is almost twice less, than from the Ob and Yenisei rivers. However, this discharge experiences low mixing near the Lena Delta due to, first, small depth of the deltaic channels and the sea area adjacent to the delta, and, second, lower tidal mixing at the open sea. As a result, 5–8 m deep Lena plume is spreading on extremely large area in the Laptev and East-Siberian seas (up to 500,000 km^2) during and shortly after the freshet period. Due to its smaller vertical extent, the Lena plume is more affected by wind forcing than the Ob-Yenisei plume. Therefore, wind forcing conditions govern its spreading pattern and cause significant inter-annual variability of its position and spatial extents, which is not the case of FSL formed in the Kara Sea.

Ice melting, which occurs in the Laptev and East-Siberian seas much later than in the Kara Sea, also contributes to formation of FSL in the study area. This process increases freshwater content and increases stratification in this layer in the areas located far from the river deltas. In particular, we speculate that local peaks of freshwater content associated with ice melting were registered in the central Laptev Sea in 2011 along the meridional transect (**Figure 14A**) and in the central East-Siberian Sea in 2019 along the zonal transect (**Figure 14B**).

CONCLUSION

This work is focused on the freshened surface layer (FSL) formed in the Laptev and East-Siberian seas by large continental runoff mainly from the Lena River and several smaller deltaic rivers (Kolyma, Indigirka, Olenyok, and Yana). Based on *in situ* measurements, we study spatial extents and vertical structure of this layer during ice-free periods. Freshwater discharge from numerous shallow and narrow channels located along the 250-km segment of the Lena Delta forms shallow Lena plume, which initial depth does not exceed 10 m. During and shortly after the freshet period, the Lena plume is spreading over wide area in the Laptev and East-Siberian seas. Then in late summer and autumn it transforms into the Laptev/East-Siberian ROFI and determines position of FSL in these seas, which zonal extent exceeds 1,000 km. Position and area of this layer strongly depends on the local wind forcing conditions during the ice-free periods. Prevailing western and northern winds at the shelf area force this water along the Siberian shore. In this case, FSL is localized in the southern parts of the Laptev and East-Siberian seas, its meridional extent (<250 km) and area (~250,000 km^2) are relatively small. On the opposite, FSL spreads over large area in the central parts of these seas (up to 500,000 km^2) under eastern wind forcing at the sea shelf. In this case meridional extent of FSL increases up to 500–700 km.

The Laptev/East-Siberian ROFI is the largest ROFI formed by continental discharge in the World Ocean (Kang et al., 2013), albeit it does not receive the largest volume of freshwater discharge. In particular, freshwater discharge to the neighboring Kara Sea is 1.5 times greater than to the Laptev and East-Siberian seas, while the area of the Kara ROFI is less than the area of

the Laptev/East-Siberian ROFI. We demonstrate that it can be even twice less during certain years. This feature is caused by differences in distribution of freshwater content in these ROFI's formed by estuarine and deltaic rivers (**Figure 15**). Due to low intensity of mixing of freshwater discharge from narrow and shallow deltaic channels of the Lena River with subjacent sea, as compared to large estuaries of the Ob and Yenisei rivers, the Lena plume experience significantly lower mixing near its source than the Ob-Yenisei plume. As a result, freshwater content in the Lena plume does not significantly decrease near the delta, while freshwater content in the Ob-Yenisei plume halves within the Ob and Yenisei estuaries. Therefore, the Lena River forms shallow river plume with stable freshwater content, while the Ob and Yenisei rivers form twice deeper plume with abruptly decreasing freshwater content. Shallow Lena plume is significantly affected by wind forcing conditions, which results in large inter-annual variability of its position and spatial extents.

The Laptev and East-Siberian seas are strongly influenced by the ongoing climate change in the Arctic Ocean, including increase of discharge of the Lena River and decrease of seasonal ice-coverage (Peterson et al., 2002; Lehner et al., 2012; Haine et al., 2015; Nummelin et al., 2016). Earlier melting of sea ice in summer and longer ice-free season will increase the role of wind forcing and can modify the existing spreading patterns of FSL. Based on the obtained results, we assume that changes in hydrological regime and total runoff volume of the Lena River will not significantly affect structure and spreading patterns of FSL in these seas, because these characteristics do not depend on the current large inter-annual variability of freshwater discharge from the Lena River. However, these issues require additional studies using numerical modeling.

In this study, we demonstrate that morphology of river estuaries/deltas plays very important role in structure and spatial extents of the large FSL. This factor can be of the same importance as freshwater discharge rate and wind forcing. Thus, the comparison between FSL's in the Kara Sea and in the Laptev and East-Siberian seas described in this work can be the case for other FSL's formed by large rivers in the World Ocean. In particular, large deltaic rivers, such as Lena and Ganges/Brahmaputra, form the first and the second largest ROFI's in the World Ocean, respectively (Kang et al., 2013). The related studies are essential for assessment of many physical, biological, and geochemical processes, which occur in coastal and shelf areas affected by discharges of large rivers.

DATA AVAILABILITY STATEMENT

The original contributions presented in the study are included in the article/**Supplementary Material**, further inquiries can be directed to the corresponding author/s.

AUTHOR CONTRIBUTIONS

AO designed the study. DF organized the database. AO, DF, ES, SS, and IS collected, processed, and performed the analysis of the *in situ* data. NT collected, processed, and performed the analysis of the meteorological data. AO and DF wrote the first draft of the manuscript. ES, SS, NT, and IS wrote sections of the manuscript. All authors contributed to manuscript revision, read, and approved the submitted version.

FUNDING

This research was funded by the Ministry of Science and Higher Education of the Russian Federation, theme 0128-2021-0001 (collecting of *in situ* data), Russian Science Foundation, project 21-77-30001 (processing of *in situ* data) and project 21-17-00278 (processing of sea ice data and study of dynamical processes), and Russian Foundation for Basic Research, project 20-35-70039 (study of FSL) and project 20-35-70025 (processing of meteorological data).

SUPPLEMENTARY MATERIAL

The Supplementary Material for this article can be found online at: https://www.frontiersin.org/articles/10.3389/fmars.2021.735011/full#supplementary-material

REFERENCES

Alekseevskii, N. I., Aibulatov, D. N., Kuksina, L. V., and Chetverova, A. A. (2014). The structure of streams in the Lena delta and its influence on streamflow transformation processes. *Geogr. Nat. Resour.* 35, 63–70. doi: 10.1134/s1875372814010090

Are, F., and Reimnitz, E. (2000). An overview of the Lena River Delta settings: geology, tectonics, geomorphology, and hydrology. *J. Coast. Res.* 16, 1083–1093.

Bauch, D., Hölemann, J. A., Nikulina, A., Wegner, C., Janout, M. A., Timokhov, L. A., et al. (2013). Correlation of river water and local sea-ice melting on the Laptev Sea shelf (Siberian Arctic). *J. Geophys. Res. Oceans* 118, 550–561. doi: 10.1002/jgrc.20076

Berezovskaya, S. L., Dmitrenko, I. A., Gribanov, V. A., Kirillov, S. A., and Kassens, H. (2002). Distribution of river waters over the Laptev Sea Shelf under different atmospheric circulation conditions. *Dokl. Earth Sci.* 386, 804–808.

Carmack, E. C., Winsor, P., and Williams, W. (2015). The contiguous panarctic riverine coastal domain: a unifying concept. *Progr. Oceanogr.* 139, 13–23.

Carmack, E. C., Yamamoto–Kawai, M., Haine, T. W., Bacon, S., Bluhm, B. A., Lique, C., et al. (2016). Freshwater and its role in the Arctic Marine System: sources, disposition, storage, export, and physical and biogeochemical consequences in the Arctic and global oceans. *J. Geophys. Res. Biogeosci.* 121, 675–717. doi: 10.1002/2015JG003140

Charette, M. A., Kipp, L. E., Jensen, L. T., Dabrowski, J. S., Whitmore, L. M., Fitzsimmons, J. N., et al. (2020). The transpolar drift as a source of riverine and shelf-derived trace elements to the Central Arctic Ocean. *J. Geophys. Res. Oceans* 125:e2019JC015920. doi: 10.1029/2019JC015920

Charkin, A. N., Dudarev, O. V., Semiletov, I. P., Kruhmalev, A. V., Vonk, J. E., Sánchez-García, L., et al. (2011). Seasonal and interannual variability of sedimentation and organic matter distribution in the Buor-Khaya Gulf: the primary recipient of input from Lena River and coastal erosion in the southeast Laptev Sea. *Biogeoscience* 8, 2581–2594. doi: 10.5194/bg-8-2581-2011

Dmitrenko, I. A., Holemann, J. A., Kirillov, S. A., Berezovskaya, S. L., and Kassens, H. (2001). Role of barotropic sealevel changes in current formation on the eastern shelf of the Laptev Sea. *Dokl. Earth Sci.* 377, 243–249.

Dmitrenko, I. A., Kirillov, S. A., Bloshkina, E., and Lenn, Y.-D. (2012). Tide-induced vertical mixing in the Laptev Sea coastal polynya. *J. Geophys. Res.* 117:C00G14. doi: 10.1029/2011JC006966

Dmitrenko, I. A., Kirillov, S. A., Krumpen, T., Makhotin, M., Abrahamsen, E. P., Willmes, S., et al. (2010). Wind-driven diversion of summer river runoff preconditions the Laptev Sea coastal polynya hydrography: evidence from summer-to-winter hydrographic records of 2007–2009. *Cont. Shelf Res.* 30, 1656–1664. doi: 10.1016/j.csr.2010.06.012

Dmitrenko, I., Kirillov, S., and Tremblay, L. B. (2008). The long-term and interannual variability of summer fresh water storage over the eastern Siberian shelf: Implication for climatic change. *J. Geophys. Res.* 113:C03007. doi: 10.1029/2007JC004304

Dmitrenko, I., Kirillov, S., Eicken, H., and Markova, N. (2005). Wind-driven summer surface hydrography of the eastern Siberian shelf. *Geophys. Res. Lett.* 32:L14613. doi: 10.1029/2005GL023022

Dubinina, E. O., Miroshnikov, A. Y., Kossova, S. A., and Shchuka, S. A. (2019b). Modification of the Laptev Sea freshened shelf waters based on isotope and salinity relations. *Geochem. Int.* 57, 1–19. doi: 10.1134/S001670291901004X

Dubinina, E. O., Miroshnikov, A. Y., Kossova, S. A., and Flirt, M. V. (2019a). Numerical estimations of desalinated seawater modification using waters of the Laptev Sea shelf as an example. *Dokl. Earth Sci.* 484, 109–113. doi: 10.1134/S1028334X19010264

Dudarev, O. V., Charkin, A. N., Semiletov, I. P., Pipko, I. I., Pugach, S. P., Chernykh, D. V., et al. (2015). Peculiarities of the present-day morpholithogenesis on the Laptev Sea Shelf: semenovskaya shoal (Vasema Land). *Dokl. Earth Sci.* 462, 510–516. doi: 10.1134/S1028334X15050116

Ekwurzel, B., Schlosser, P., Mortlock, R. A., Fairbanks, R. G., and Swift, J. H. (2001). River runoff, sea ice meltwater, and Pacific water distribution and mean residence times in the Arctic Ocean. *J. Geophys. Res. Oceans* 106, 9075–9092. doi: 10.1029/1999JC000024

Fedorova, I., Chetverova, A., Bolshiyanov, D., Makarov, A., Boike, J., Heim, B., et al. (2015). Lena Delta hydrology and geochemistry: long-term hydrological data and recent field observations. *Biogeoscience* 12, 345–363. doi: 10.5194/bg-12-345-2015

Fofonova, V., Androsov, A., Danilov, S., Janout, M., Sofina, E., and Wiltshire, K. H. (2014). Semidiurnal tides in the Laptev Sea Shelf zone in the summer season. *Cont. Shelf Res.* 73, 119–132. doi: 10.1016/j.csr.2013.11.010

Fofonova, V., Danilov, S., Androsov, A., Janout, M., Bauer, M., Overduin, P., et al. (2015). Impact of wind and tides on the Lena River freshwater plume dynamics in the summer sea. *Ocean Dyn.* 65, 951–968. doi: 10.1007/s10236-015-0847-573

Fournier, S., Vialard, J., Lengaigne, M., Lee, T., Gierach, M. M., and Chaitanya, A. V. S. (2017). Modulation of the ganges-brahmaputra river plume by the indian ocean dipole and eddies inferred from satellite observations. *J. Geophys. Res. Oceans* 122, 9591–9604. doi: 10.1002/2017JC013333

Fuchs, M., Palmtag, J., Juhls, B., Overduin, P. P., Grosse, G., Abdelwahab, A., et al. (2021b). High-resolution bathymetry models for the Lena Delta and Kolyma Gulf coastal zones. *Earth Syst. Sci. Data Discuss.* doi: 10.5194/essd-2021-256

Fuchs, M., Ogneva, O., Sanders, T., Schneider, W., Polyakov, V., Becker, O. O., et al. (2021a). "CACOON sea – water sampling along the sardakhskaya channel and near shore of the Laptev Sea," in *Reports on Polar and Marine Research, Russian-German Cooperation: Expeditions to Siberia in 2019, Bremerhaven*, eds M. Fuchs, D. Bolshiyanov, M. N. Grigoriev, A. Morgenstern, and A. Dill (Bremerhaven: Alfred Wegener Institute), 141–149. doi: 10.48433/BzPM_0749_2021

Garvine, R. W. (1987). Estuary plumes and fronts in shelf waters: a layer model. *J. Phys. Oceanogr.* 17, 1877–1896.

Geyer, W. R., and MacCready, P. (2014). The estuarine circulation. *Annu. Rev. Fluid Mech.* 46, 175–197. doi: 10.1146/annurevfluid-010313-141302

Gordeev, V. V., Martin, J. M., Sidorov, J. S., and Sidorova, M. V. (1996). A reassessment of the Eurasian river input of water, sediment, major elements, and nutrients to the Arctic Ocean. *Am. J. Sci.* 296, 664–691. doi: 10.2475/ajs.296.6.664

Grodsky, S. A., Reverdin, G., Carton, J. A., and Coles, V. J. (2014). Year-to-year salinity changes in the Amazon plume: contrasting 2011 and 2012 Aquarius/SACD and SMOS satellite data. *Remote Sens. Environ.* 140, 14–22. doi: 10.1016/j.rse.2013.08.033

Guay, C. K., Falkner, K. K., Muench, R. D., Mensch, M., Frank, M., and Bayer, R. (2001). Wind-driven transport pathways for Eurasian Arctic river discharge. *J. Geophys. Res.* 106, 11469–11480. doi: 10.1029/2000JC000261

Haine, T. W., Curry, B., Gerdes, R., Hansen, E., Karcher, M., Lee, C., et al. (2015). Arctic freshwater export: status, mechanisms, and prospects. *Glob. Planet. Change* 125, 13–35. doi: 10.1016/j.gloplacha.2014.11.013

Hersbach, H., Bell, B., Berrisford, P., Hirahara, S., Horányi, A., Muñoz-Sabater, J., et al. (2020). The ERA5 global reanalysis. *Q. J. R. Meteorol. Soc.* 146, 1999–2049. doi: 10.1002/qj.3803

Horner-Devine, A. R., Hetland, R. D., and MacDonald, D. G. (2015). Mixing and transport in coastal river plumes. *Annu. Rev. Fluid Mech* 47, 569–594. doi: 10.1146/annurev-fluid-010313-141408

Horner-Devine, A. R., Jay, D. A., Orton, P. M., and Spahn, E. Y. (2009). A conceptual model of the strongly tidal columbia river plume. *J. Mar. Syst.* 78, 460–475. doi: 10.1016/j.jmarsys.2008.11.0

Janout, M. A., and Lenn, Y. (2014). Semidiurnal tides on the Laptev Sea shelf with implications for shear and vertical mixing. *J. Phys. Oceanogr.* 44, 202–219. doi: 10.1175/JPO-D-12-0240.1

Janout, M. A., Holemann, J., Laukert, G., Smirnov, A., Krumpen, T., Bauch, D., et al. (2020). On the variability of stratification in the freshwater-influenced Laptev Sea region. *Front. Mar. Sci.* 7:543489. doi: 10.3389/fmars.2020.543489

Kääb, A., Lamare, M., and Abrams, M. (2013). River ice flux and water velocities along a 600 km-long reach of Lena River, Siberia, from satellite stereo. *Hydrol. Earth Syst. Sci.* 17, 4671–4683. doi: 10.5194/hess-17-4671-2013

Kagan, B. A., and Timofeev, A. A. (2020). Dynamics and energetics of tides in the Laptev Sea: the results of high-resolving modeling of the surface semidiurnal tide M2. *Fundament. Prikl. Gidrofiz* 13, 15–23. doi: 10.7868/S2073667320010025

Kagan, B. A., Romanenkov, D. A., and Sofina, E. V. (2008). Tidal ice drift and ice-generated changes in the tidal dynamics/energetic on the Siberian continental shelf. *Cont. Shelf Res.* 28, 351–368. doi: 10.1016/j.csr.2007.09.004

Kagan, B. A., Timofeev, A. A., and Sofina, E. V. (2010). Seasonal variability of surface and internal M2 tides in the Arctic Ocean. *Izv. Atmos. Ocean. Phys.* 46, 652–662. doi: 10.1134/S0001433810050105

Kang, Y., Pan, D., Bai, Y., He, X., Chen, X., Chen, C. T. A., et al. (2013). Areas of the global major river plumes. *Acta Oceanol. Sin.* 32, 79–88. doi: 10.1007/s13131-013-0269-5

Kowalik, Z., and Proshutinsky, A. Y. (1994). "The arctic ocean tides," in *The Polar Oceans and Their Role in Shaping the Global Environment, Geophysics Monography Series*, Vol. 85, eds O. M. Johannessen, R. D. Muench, and J. E. Overland (Washington, DC: AGU), 137–158. doi: 10.1029/GM085p0137

Lambert, E., Nummelin, A., Pemberton, P., and Ilıcak, M. (2019). Tracing the imprint of river runoff variability on Arctic water mass transformation. *J. Geophys. Res. Oceans* 124, 302–319.

Lehner, F., Raible, C. C., Hofer, D., and Stocker, T. F. (2012). The freshwater balance of polar regions in transient simulations from 1500 to 2100 AD using a comprehensive coupled climate model. *Clim. Dyn.* 39, 347–363. doi: 10.1007/s00382-011-1199-6

Li, W. K. W., McLaughlin, F. A., Lovejoy, C., and Carmack, E. C. (2009). Smallest algae thrive as the Arctic Ocean freshens. *Science* 326:539. doi: 10.1126/science.1179798

Matsuoka, A., Babin, M., and Devred, E. C. (2016). A new algorithm for discriminating water sources from space: a case study for the southern Beaufort Sea using MODIS ocean color and SMOS salinity data. *Remote Sens. Environ.* 184, 124–138. doi: 10.1016/j.rse.2016.05.006

McLaughlin, F. A., and Carmack, E. C. (2010). Nutricline deepening in the Canada Basin, 2003–2009. *Geophys. Res. Lett.* 37:L24602. doi: 10.1029/2010GL045459

Munchow, A., Weingartner, T. J., and Cooper, L. W. (1999). The summer hydrography and surface circulation of the East Siberian Shelf Sea. *J. Phys. Oceanogr.* 19, 2167–2182.

Nash, J. D., Kilcher, L. F., and Moum, J. N. (2009). Structure and composition of a strongly stratified, tidally pulsed river plume. *J. Geophys. Res* 114:C00B12. doi: 10.1029/2008JC005036

Nummelin, A., Ilicak, M., Li, C., and Smedsrud, L. H. (2016). Consequences of future increased Arctic runoff on Arctic Ocean stratification, circulation, and sea ice cover. *J. Geophys. Res. Oceans* 121, 617–637. doi: 10.1002/2015JC011156

O'Donnell, J. (1990). The formation and fate of a river plume: a numerical model. *J. Phys. Oceanogr.* 20, 551–569.

Olmedo, E., Gabarro, C., Gonzalez-Gambau, V., Martinez, J., Ballabrera-Poy, J., Turiel, A., et al. (2018). Seven years of SMOS sea surface salinity at high latitudes: variability in Arctic and sub-Arctic regions. *Remote Sens.* 10:1772. doi: 10.3390/rs10111772

Osadchiev, A. A. (2017). Spreading of the amur river plume in the amur liman, the sakhalin gulf, and the strait of tartary. *Oceanology* 57, 376–382. doi: 10.1134/S0001437017020151

Osadchiev, A. A., and Zavialov, P. O. (2019). "Structure and dynamics of plumes generated by small rivers," in *Estuaries and Coastal Zones – Dynamics and Response to Environmental Changes*, ed. J. Pan (London: IntechOpen), doi: 10.5772/intechopen.87843

Osadchiev, A. A., Izhitskiy, A. S., Zavialov, P. O., Kremenetskiy, V. V., Polukhin, A. A., Pelevin, V. V., et al. (2017). Structure of the buoyant plume formed by Ob and Yenisei river discharge in the southern part of the Kara Sea during summer and autumn. *J. Geophys. Res. Oceans* 122, 5916–5935. doi: 10.1002/2016JC012603

Osadchiev, A. A., Asadulin, E. E., Miroshnikov, A. Y., Zavialov, I. B., Dubinina, E. O., and Belyakova, P. A. (2019). Bottom sediments reveal inter-annual variability of interaction between the Ob and Yenisei plumes in the Kara Sea. Sci. Rep. 9:18642. doi: 10.1038/s41598-019-55242-3

Osadchiev, A. A., Konovalova, O. P., and Gordey, A. S. (2021b). Water exchange between the Gulf of Ob and the Kara Sea during ice-free seasons: the roles of river discharge and wind forcing. *Front. Mar. Sci.* Available online at: https://www.frontiersin.org/articles/10.3389/fmars.2021.741143/abstract

Osadchiev, A. A., Frey, D. I., Shchuka, S. A., Tilinina, N. D., Morozov, E. G., and Zavialov, P. O. (2021a). Structure of freshened surface layer in the Kara Sea during ice-free periods. *J. Geophys. Res. Oceans* 126:e2020JC016486. doi: 10.1029/2020JC016486

Osadchiev, A. A., Pisareva, M. N., Spivak, E. A., Shchuka, S. A., and Semiletov, I. P. (2020b). Freshwater transport between the kara, laptev, and east-siberian seas. *Sci. Rep.* 10:13041. doi: 10.1038/s41598-020-70096-w

Osadchiev, A. A., Medvedev, I. P., Shchuka, S. A., Kulikov, M. E., Spivak, E. A., Pisareva, M. N., et al. (2020a). Influence of estuarine tidal mixing on structure and spatial scales of large river plumes. *Ocean Sci.* 16, 1–18. doi: 10.5194/os-16-1-2020

Osadchiev, A. A., Silvestrova, K. P., and Myslenkov, S. A. (2020c). Wind-driven coastal upwelling near large river deltas in the Laptev and East-Siberian seas. *Remote Sens.* 12:844. doi: 10.3390/rs12050844

Padman, L., and Erofeeva, S. (2004). A barotropic inverse tidal model for the Arctic Ocean. *Geophys. Res. Lett.* 31:L02303. doi: 10.1029/2003GL019003

Pavlov, V. K., Timokhov, L. A., Baskakov, G. A., Yu, M., Kulakov, V.K. Kurazhov, Pavlov, P. V., et al. (1996). *Hydrometeorological Regime Of The Kara, Laptev, And East-Siberian Seas.* Technical Memorandum, APL-UW TM 1-96. St, Seattle, WA: Applied Physics Laboratory, University of Washington.

Peterson, B. J., Holmes, R. M., McClelland, J. W., Vorosmarty, C. J., Lammers, R. B., Shiklomanov, A. I., et al. (2002). Increasing river discharge to the Arctic ocean. *Science* 298, 2171–2173. doi: 10.1126/science.1077445

Pogojeva, M., Zhdanov, I., Berezina, A., Lapenkov, A., Kosmach, D., Osadchiev, A., et al. (2021). Distribution of floating marine macro-litter in relation to oceanographic characteristics in the Russian Arctic Seas. *Mar. Pollut. Bull.* 166:112201. doi: 10.1016/j.marpolbul.2021.112201

Polyakov, I. V., Pnyushkov, A. V., Rember, R., Padman, L., Carmack, E. C., and Jackson, J. M. (2013). Winter convection transports Atlantic water heat to the surface layer in the eastern Arctic Ocean. *J. Phys. Oceanogr.* 43, 2142–2155. doi: 10.1175/JPO-D-12-0169.1

Polyakov, I., Walsh, D., Dmitrenko, I., Colony, R., and Timokhov, L. (2003). Arctic Ocean variability derived from historical observations. *Geophys. Res. Lett.* 30:1298. doi: 10.1029/2002GL016441

Schlosser, P., Newton, R., Ekwurzel, B., Khatiwala, S., Mortlock, R., and Fairbanks, R. (2002). Decrease of river runoff in the upper waters of the Eurasian Basin, Arctic Ocean, between 1991 and 1996: evidence from δ18O data. *Geophys. Res. Lett.* 29, 31–34. doi: 10.1029/2001gl013135

Sea-Bird Electronics (2017). *SEASOFT-V2: SBE Data Processing User's Manual.* Bellevue, DC: Sea-Bird Electronics, 177.

Semiletov, I. P., Pipko, I. I., Shakhova, N. E., Dudarev, O. V., Pugach, S. P., Charkin, A. N., et al. (2011). Carbon transport by the Lena River from its headwaters to the Arctic Ocean, with emphasis on fluvial input of terrestrial particulate organic carbon vs. carbon transport by coastal erosion. *Biogeoscience* 8, 2407–2426. doi: 10.5194/bg-8-2407-2011

Semiletov, I. P., Shakhova, N. E., Sergienko, V. I., Pipko, I. I., and Dudarev, O. V. (2012). On carbon transport and fate in the East Siberian Arctic land–shelf–atmosphere system. *Environ. Res. Lett.* 7:015201. doi: 10.1088/1748-9326/7/1/015201

Semiletov, I., Dudarev, O., Luchin, V., Charkin, A., Shin, K.-H., and Tanaka, N. (2005). The East Siberian Sea as a transition zone between Pacific-derived waters and Arctic shelf waters. *Geophys. Res. Lett.* 32:L10614. doi: 10.1029/2005GL022490

Semiletov, I., Pipko, I., Gustafsson, Ö, Anderson, L. G., Sergienko, V., Pugach, S., et al. (2016). Acidification of East Siberian Arctic Shelf waters through addition of freshwater and terrestrial carbon. *Nat. Geosci.* 9:361. doi: 10.1038/ngeo2695

Spivak, E. A., Osadchiev, A. A., and Semiletov, I. P. (2021). Structure and variability of the Lena river plume in the south-eastern part of the Laptev Sea. *Oceanology* 61, 832–836. doi: 10.1007/978-3-030-25674-6

Supply, A., Boutin, J., Vergely, J.-L., Kolodziejczyk, N., Reverdin, G., Reul, N., et al. (2020). New insights into SMOS Sea Surface Salinity retrievals in the Arctic Ocean. *Remote Sens. Environ.* 249:112027. doi: 10.1016/j.rse.2020.112027

Tang, W., Yueh, S., Yang, D., Fore, A., Hayashi, A., Lee, T., et al. (2018). The potential and challenges of using Soil Moisture Active Passive (SMAP) sea surface salinity to monitor Arctic Ocean freshwater changes. *Remote Sens.* 10:869. doi: 10.3390/rs10060869

Tarasenko, A., Supply, A., Kusse-Tiuz, N., Ivanov, V., Makhotin, M., Tournadre, J., et al. (2021). Properties of surface water masses in the Laptev and the East Siberian seas in summer 2018 from in situ and satellite data. *Ocean Sci.* 17, 221–247. doi: 10.5194/os-17-221-2021

Tremblay, J. E., Belanger, S., Barber, D. G., Asplin, M., Martin, J., Darnis, G., et al. (2011). Climate forcing multiplies biological productivity in the coastal Arctic Ocean. *Geophys. Res. Lett.* 38:L18604. doi: 10.1029/2011GL048825

Vic, C., Berger, H., Treguier, A. M., and Couvelard, X. (2014). Dynamics of an equatorial river plume: theory and numerical experiments applied to the Congo plume case. *J. Phys. Oceanogr.* 44, 980–994. doi: 10.1175/JPO-D-13-0132.1

Voinov, G. (2002). "Tide and tidal streams," in *Polar Seas Oceanography: An Integrated Case Study of the Kara Sea*, eds V. A. Volkov, O. M. Johannessen, V. E. Borodachev, G. N. Voinov, L. H. Pettersson, L. P. Bobylev, et al. (Berlin: Springer), 147–216.

Weingartner, T. J., Danielson, S., Sasaki, Y., Pavlov, V., and Kulikov, M. (1999). The siberian coastal current: a wind and buoyancy forced coastal current. *J. Geophys. Res.* 104, 29697–29713. doi: 10.1029/1999JC900161

Whitney, M. M., and Garvine, R. W. (2005). Wind influence on a coastal buoyant outflow. *J. Geophys. Res.* 110:C03014. doi: 10.1029/2003jc002261

Williams, W. J., and Carmack, E. C. (2015). The 'interior' shelves of the Arctic Ocean: physical oceanographic setting, climatology and effects of sea-ice retreat on cross-shelf exchange. *Progr. Oceanogr.* 139, 24–31. doi: 10.1016/j.pocean.2015.07.008

Yakushev, E., Gebruk, A., Osadchiev, À, Pakhomova, S., Lusher, A., Berezina, A., et al. (2021). Microplastics distribution in the eurasian arctic is affected by atlantic waters and siberian rivers. *Commun. Earth Environ.* 2:23. doi: 10.1038/s43247-021-00091-0

Yamamoto-Kawai, M., McLaughlin, F. A., Carmack, E. C., Nishino, S., Shimada, K., and Kurita, N. (2009). Surface freshening of the Canada Basin, 2003–2007: river runoff versus sea ice meltwater. *J. Geophys. Res.* 114:C00A05. doi: 10.1029/2008JC005000

Conflict of Interest: The authors declare that the research was conducted in the absence of any commercial or financial relationships that could be construed as a potential conflict of interest.

Publisher's Note: All claims expressed in this article are solely those of the authors and do not necessarily represent those of their affiliated organizations, or those of the publisher, the editors and the reviewers. Any product that may be evaluated in this article, or claim that may be made by its manufacturer, is not guaranteed or endorsed by the publisher.

Copyright © 2021 Osadchiev, Frey, Spivak, Shchuka, Tilinina and Semiletov. This is an open-access article distributed under the terms of the Creative Commons Attribution License (CC BY). The use, distribution or reproduction in other forums is permitted, provided the original author(s) and the copyright owner(s) are credited and that the original publication in this journal is cited, in accordance with accepted academic practice. No use, distribution or reproduction is permitted which does not comply with these terms.

frontiers in Marine Science

ORIGINAL RESEARCH
published: 15 December 2021
doi: 10.3389/fmars.2021.741143

Water Exchange Between the Gulf of Ob and the Kara Sea During Ice-Free Seasons: The Roles of River Discharge and Wind Forcing

Alexander Osadchiev[1,2]*, *Olga Konovalova*[3] and *Alexandra Gordey*[1,2]

[1] Shirshov Institute of Oceanology, Russian Academy of Sciences, Moscow, Russia, [2] Moscow Institute of Physics and Technology, Dolgoprudny, Russia, [3] Marine Research Center at Lomonosov Moscow State University, Moscow, Russia

The Gulf of Ob is among the largest estuaries in the World Ocean in terms of area, watershed basin, and freshwater discharge. In this work, we describe the roles of river discharge and wind forcing on the water exchange between the Gulf of Ob and the Kara Sea during ice-free seasons. This work is based on the extensive *in situ* measurements performed during 10 oceanographic surveys in 2007–2019. Due to large river runoff (~530 km^3 annually) and low tidal forcing (<0.5 m/s), the estuarine processes in the Gulf of Ob during the ice-free season are generally governed by gravitational circulation. Local wind forcing significantly affects general estuarine circulation and mixing only in rare cases of strong winds (~10 m/s). On the other hand, remote wind forcing over the central part of the Kara Sea regularly intensifies estuarine—sea water exchange. Eastern winds in the central part of the Kara Sea induce upwelling in the area adjacent to the Gulf of Ob, which increases the barotropic pressure gradient between the gulf and the open sea. As a result, intense and distant (120–170 km) inflows of saline water to the gulf occur as compared to the average conditions (50–70 km). Remote wind forcing has a far stronger impact on saltwater intrusion into the Gulf of Ob than the highly variable river discharge rate. In particular, saltwater reaches the shallow central part of the gulf only during upwelling-induced intense inflows. In the other periods (even under low discharge conditions), fresh river water occupies this area from surface to bottom. The upwelling-induced intense inflows occur on average during a quarter of days (July to October) when the gulf is free of ice. They substantially increase the productivity of phytoplankton communities in the gulf and modify the taxa ratio toward the increase of brackish water species and the decrease of freshwater species.

Keywords: estuarine circulation, salt-wedge estuary, remote upwelling, stratification, phytoplankton communities, Gulf of Ob, Kara Sea

OPEN ACCESS

Edited by:
Anas Ghadouani, University of Western Australia, Australia

Reviewed by:
Adam Ayouche, Laboratoire de Physique des Océans et de Télédétection par Satellite (LOPS), France
Hans Burchard, Leibniz Institute for Baltic Sea Research (LG), Germany
Heqin Cheng, East China Normal University, China
Nils Edvin Asp, Federal University of Pará, Brazil

***Correspondence:**
Alexander Osadchiev
osadchiev@ocean.ru

Specialty section:
This article was submitted to Coastal Ocean Processes, a section of the journal Frontiers in Marine Science

Received: *14 July 2021*
Accepted: *12 November 2021*
Published: *15 December 2021*

Citation:
Osadchiev A, Konovalova O and Gordey A (2021) Water Exchange Between the Gulf of Ob and the Kara Sea During Ice-Free Seasons: The Roles of River Discharge and Wind Forcing. Front. Mar. Sci. 8:741143. doi: 10.3389/fmars.2021.741143

INTRODUCTION

The Gulf of Ob is located in the southern part of the Kara Sea and is among the largest river estuaries in the World Ocean (**Figure 1**). The Gulf of Ob is long (850 km) and narrow (30–80 km), and its area is about 41,000 km^2, while the area of its watershed basin is 3,320,000 km^2 (~2.2% of Earth's land). The Gulf of Ob receives approximately 530 km^3 (16,800 m^3/s on average) of freshwater discharge annually, namely, 430 km^3 (13,600 m^3/s) from the Ob River and 100 km^3 (3,200 m^3/s)

from the Taz River, the Pur River, and smaller rivers (Gordeev et al., 1996; Pavlov et al., 1996). This large freshwater volume accounts for ∼15% of the total freshwater runoff to the Arctic Ocean (Guay et al., 2001) and ∼1.5% of the total freshwater runoff to the World Ocean (Oki and Kanae, 2006).

The majority of runoff from the rivers inflowing to the Gulf of Ob is provided during the flooding period from May to September (Pavlov et al., 1996). Maximal discharge to the gulf is registered at the end of May and is induced by ice melting in the watershed area of the gulf (**Figure 1C**). However, the decrease of river runoff usually is very slight till the end of September. For certain years, discharge during the secondary rain-induced peak can be the same or higher in the beginning of September than in May (Osadchiev et al., 2021a).

The rivers inflowing to the gulf are frozen from November to May, which result in a relatively low discharge rate in winter and spring (2,000–5,000 m^3/s) (**Figure 1C**). The Gulf of Ob is covered by ice from October to November till May to June, and the water temperature of the surface layer during this period is 0°C. The average temperature of the surface layer in July and September is 2–3°C, while in August it increases up to 8°C (Gladysh et al., 2017). Tidal circulation in the gulf is dominated by the semidiurnal tide (Kagan et al., 2010). Tidal amplitudes during the ice-free periods are 100–140 cm in the northern part of the Gulf of Ob, and they decrease to 60–80 cm in the central part of the gulf and to 20–50 cm in the southern part of the gulf (Voinov, 2016).

River water occupies the whole water column in the southern and central part of the Gulf of Ob during ice-free periods. The northern part of the gulf is a typical salt-wedge estuary with a large salinity gradient between the freshened surface layer and the saline bottom layer formed by water inflow from the Kara Sea. The location of the frontal zone between freshwater and saline water in the bottom layer shows distinct seasonal variability governed by large seasonal variability of the river discharge rate (Lapin, 2011; Lapin et al., 2015), which is a common feature of river estuaries (Hansen and Rattray, 1965; Moller et al., 2001; Chawla et al., 2008; Miranda et al., 2017).

In this study, we demonstrate that wind forcing can strongly modify the estuarine—ocean exchange in the Gulf of Ob in particular that can exceed the role of seasonal variability of the river discharge rate. In contrast to typical shallow estuaries, this process is induced by remote wind forcing, while local winds limitedly affect the general circulation in the gulf. Based on *in situ* salinity measurements performed during 10 different oceanographic surveys in the Gulf of Ob in 2007–2019 and satellite observations, we show that upwelling events in the central part of the Kara Sea adjacent to the Gulf of Ob induce intense and distant inflows of saline seawater to the gulf. We focus on *in situ* measurements performed in the Gulf of Ob in August 2019, which revealed the most intense and distant inflow of saline seawater into the gulf, and demonstrate that these intense inflows of saline water to the gulf significantly affect qualitative and quantitative characteristics of the local phytoplankton communities.

The paper is organized as follows. Section 2 provides the detailed information about the *in situ*, satellite, river discharge, and wind forcing data used in this study. The relation between the external forcing conditions and the intensity of inflow of saline seawater to the gulf is described in Section 3 with an emphasis on the intense inflow registered in August 2019. The influence of inflows of saline water on the biological structure of the gulf, as well as the assessment of its variability on synoptic, seasonal, and inter-annual time scales, is analyzed and discussed in Section 4, followed by conclusions in Section 5.

DATA AND METHODS

The salinity *in situ* data used in this study were collected during 10 oceanographic surveys in the Gulf of Ob in September 2007, August and September 2010, September 2013, August and September 2014, July 2016, and July and August 2019 (Lapin, 2011; Lapin et al., 2015; Drits et al., 2016, 2017; Borisenko et al., 2021; Osadchiev et al., 2021a; **Table 1** and **Figure 2**). The vertical salinity structure was measured at the hydrographic stations in the northern and central part of the Gulf of Ob using a CTD instrument (*SBE 911plus*) at 0.2-m spatial resolution. Based on these measurements, we reconstructed the locations of the isohaline of five in the bottom layer of the Gulf of Ob (**Table 1**, arrows in **Figure 2**). This value is indicative of the intensity of an inflow of saline seawater to the Gulf of Ob and is analyzed in this study.

Biological *in situ* data used in this study were collected during the three oceanographic surveys in the Gulf of Ob in September 2007, September 2014, and August 2019 (Sukhanova et al., 2010; Flint and Poyarkov, 2015; Flint et al., 2020; **Table 1**). In these surveys, qualitative (list of species and abundance of taxa) and quantitative (total abundance and biomass) characteristics were registered at the selected stations. Water sampling was performed with Niskin bottles from surface, halocline, and bottom layers. The water probes were concentrated and preserved in phormamide or Lugol's iodine solution. Measurements were performed using light microscopes. Phytoplankton abundance was registered by calculating the cells in Najott (10^{-5} L) and Fuchs–Rosenthal (3.2×10^{-6} L) chambers three times for each sample. The biomass of microalgae was calculated from cell volume using the method of geometric similarity of figures (Hillebrand et al., 1999).

The wind forcing conditions in this study area were examined using *in situ* measurements at the meteorological station of Seyakha located in the central part of the Gulf of Ob (indicated by the red circle in **Figure 1**) and the ERA5 atmospheric reanalysis with a 0.25° spatial and hourly temporal resolution (Hersbach et al., 2020). To evaluate the influence of wind forcing on estuarine circulation, we calculated the four time integrals of wind stress $W = \int \tau \times dt$ during the periods of downwelling (western wind, $\tau_x > 0$), upwelling (eastern wind, $\tau_x < 0$), offshore (southern wind, $\tau_y > 0$), and onshore (northern wind, $\tau_y < 0$) wind forcing. In particular, the upwelling integral of wind stress W_u is the result of integration of zonal wind stress τ_x only during the periods when $\tau_x < 0$.

The discharge data used in this study were obtained at the most downstream gauge station on the Ob River in Salekhard,

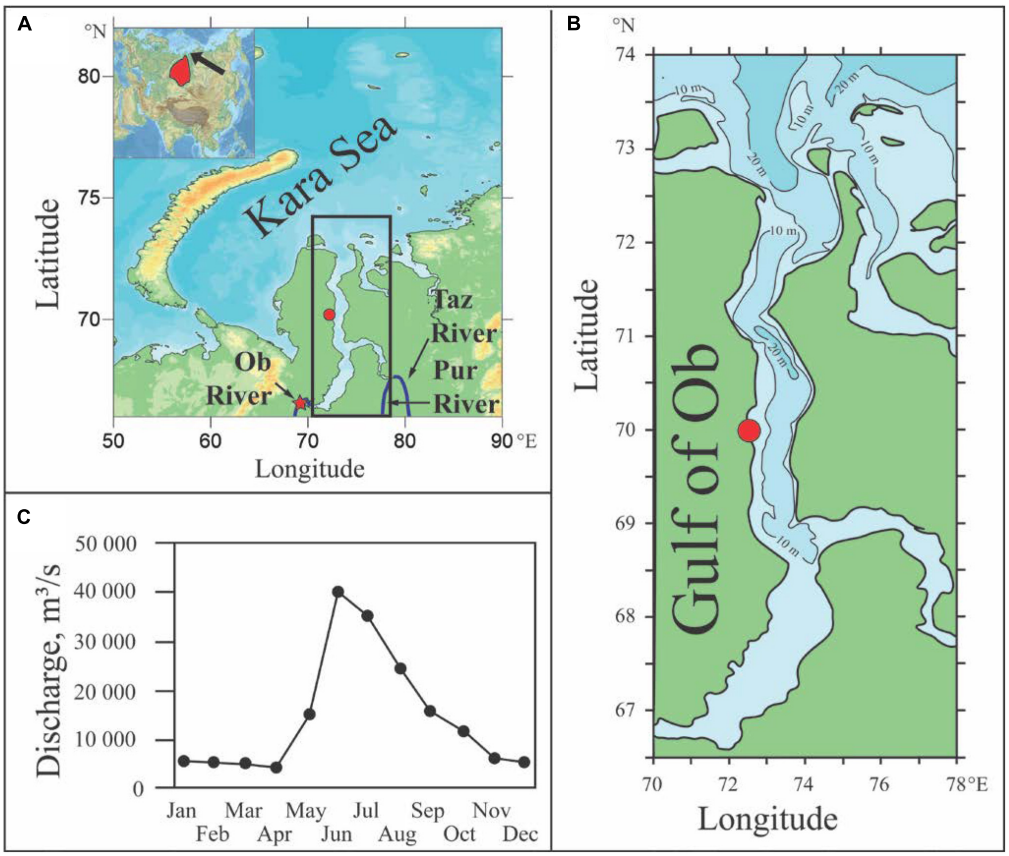


FIGURE 1 | Location of the Gulf of Ob (indicated by the black box) in the Kara Sea (the black arrow at the inset); the main rivers inflowing to the Gulf of Ob; the gauge station in Salekhard (the red star) and the meteorological station in Seyakha (the red circle); the watershed area of the Gulf of Ob shown at the Eurasian map (the red area at the inset) **(A)**; bathymetry of the Gulf of Ob **(B)**; and mean annual hydrograph of the Ob, Pur, and Taz rivers **(C)**.

which is located at the southern edge of the Gulf of Ob (indicated by the red star in **Figure 1**). In this study, we address the processes in the central and northern part of the gulf; therefore, we have to analyze the timing of runoff entering this region. The distance between Salekhard and the study area is ∼750 km. Therefore, we shifted the hydrograph measured in Salekhard by 30 days onward according to estimates of the average flow speed in the Gulf of Ob and Yenisei gulfs (0.3 m/s; Harms and Karcher, 1999).

Satellite data used in this study include Sentinel-2 optical imagery, MODIS optical imagery and thermal data, and AVISO altimetry data.

RESULTS

Gravitational, Tidal, and Wind Forcing in the Gulf of Ob

The Gulf of Ob is a classical positive estuary with a general seaward transport of freshened riverine water in the surface layer and a landward transport of saline seawater in the bottom layer. During the ice-free season, salinity in the Gulf of Ob is equal to 0 from surface to bottom in the shallow (<10 m) southern and central part of the estuary. Further northward, in the northern part of the gulf, the river flow detaches from the bottom and forms a freshened surface layer with depth ∼10 m (Lapin, 2011; Osadchiev et al., 2021a). Surface salinity steadily increases within the northern part of the gulf and is equal to 4–10 when it outflows to the open sea (Osadchiev et al., 2021a). Salinity of the bottom layer within the northernmost part of the gulf is 30–32 and decreases landward.

Circulation and mixing in river estuaries generally are governed by gravitational forcing (due to salinity difference in river water and seawater), tidal forcing, and wind forcing. The relatively shallow Gulf of Ob receives very large freshwater discharge, which results in strong longitudinal density gradient (Osadchiev et al., 2021a). On the opposite, tidal circulation in the gulf is relatively low, the maximal tidal velocities are 0.4–0.5 m/s (Pavlov et al., 1996; Vvedensky et al., 2017). In the absence of wind forcing, the estuarine dynamical and mixing regime determined by the buoyancy and tidal forcing can be characterized by two dimensionless parameters, namely, the freshwater Froude number $Fr_f = \frac{U_R}{\sqrt{\beta g S H}}$ and the mixing parameter $M = \frac{C_D U_T^2}{w N_0 H^2}$, where U_R is the inflowing river velocity, U_T is the amplitude of the depth-averaged estuarine tidal velocity, w is the estuarine

TABLE 1 | Periods, research vessels, and locations of the isohaline of five in the bottom layer during 10 oceanographic surveys in 2007–2019.

Period	Research vessel	Data reference	Location of the isohaline of 5 in the bottom layer
23-25.09.2007	Akademik Mstislav Keldysh	Sukhanova et al., 2010; Osadchiev et al., 2021a	72.1°N
5-9.08.2010	OTA-777	Lapin, 2011	72.1°N
23-26.09.2010	OTA-777	Lapin, 2011	72.0°N
3-5.09.2013	Professor Shtokman	Drits et al., 2017	71.6°N
16-20.08.2014	Professor Shtokman	Flint and Poyarkov, 2015; Osadchiev et al., 2021a	72.3°N
13-21.09.2014	Briz	This paper (biology) Lapin et al., 2015	72.3°N
18-20.07.2016	Akademik Mstislav Keldysh	Sukhanova et al., 2018; Osadchiev et al., 2021a	71.6°N
16-18.07.2019	Akademik Mstislav Keldysh	Flint et al., 2020; Borisenko et al., 2021	72.1°N
8-10.08.2019	Kartesh	This paper (hydrology)	71.7°N
18-20.08.2019	Kartesh	This paper (biology and hydrology)	71.0°N

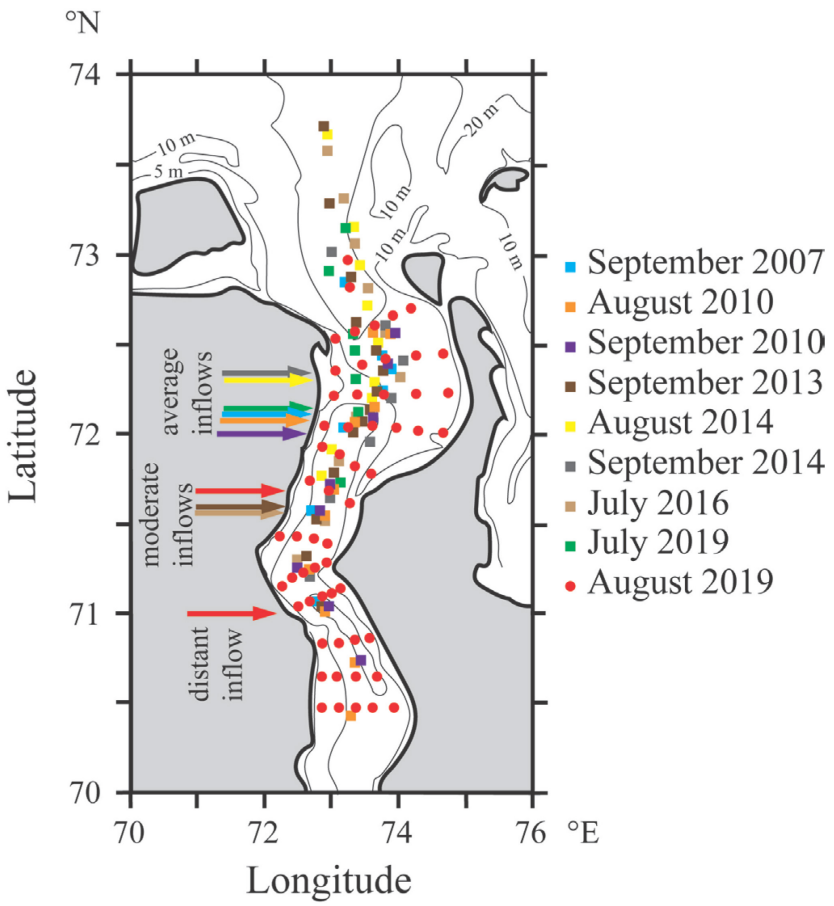


FIGURE 2 | Hydrographic stations of 10 oceanographic field surveys conducted in the Gulf of Ob in 2007–2019 (circles for the two surveys in August 2019, squares for all other cruises). Arrows indicate southernmost detected locations of the isohaline of five in the bottom layer of the Gulf of Ob. Note that the two surveys in August 2019 are indicated by two red arrows.

tidal frequency, S is the ambient sea salinity, H is the depth of an estuary, g is the gravity acceleration, β is the saline contraction coefficient prescribed equal to 7.7×10^{-4}, C_D is the quadratic drag coefficient for wind stress parameterization prescribed equal to 10^{-3}, and $N_0 = \sqrt{\frac{\beta g S}{H}}$ is the buoyancy frequency for maximum top-to-bottom salinity variation in an estuary (Geyer and MacCready, 2014). Values of these parameters for the Gulf of Ob are as follows: $Fr_f \sim 0.3/(7.7 \times 10^{-4} \times 10 \times 32 \times 15)^{0.5} \sim 0.6$, $M \sim 10^{-3} \times (0.4)^2/[2.3 \times 10^{-5} \times (7.7 \times 10^{-4} \times 10 \times 32/15)^{0.5} \times (15)^2] \sim 0.4$. The obtained estimations demonstrate that the Gulf of Ob is a typical salt-wedge estuary with strong vertical stratification due to very large freshwater runoff during the ice-free season, while tidal forcing limitedly affects circulation and mixing in the gulf.

The influence of wind forcing on the estuarine processes in the Gulf of Ob was assessed using the dimensionless Wedderburn number $We = \frac{\tau L}{\Delta \rho g H^2}$, where τ is the along-estuary wind stress, L is the length of the considered segment of the estuary, and $\Delta\rho$ is the density difference over L (Monismith, 1986; Chen and Sanford, 2009; Lange and Burchard, 2019). Once the along-estuary wind speed is large enough so that $We \sim 1$, the role of wind forcing is comparable with the role of gravitational circulation (Geyer, 1997; Chen and Sanford, 2009; Lange and Burchard, 2019; Lange et al., 2020). In case of the northern part of the Gulf of Ob with a two-layer stratification induced by saline inflows, $We \sim \tau \times 150 \times 10^3/6 \times 10 \times (20)^2 = \tau \times 6.25$. According to *in situ* measurements of wind forcing at the meteorological station of Seyakha, the average monthly wind speed in the study area from July to October in 2005–2020 varies between 5.5 and 5.7 m/s, while the maximal registered wind speed is 20 m/s. No prevailing wind direction is registered during the warm period; the repeatability of all eight compass wind directions is 10–15%. Therefore, for the study area we consider the average along-estuary wind speed equal to 5 m/s. In this case, $We \sim 0.04 \times 6.25 = 0.25$, which shows that under average wind forcing the estuarine circulation is governed mainly by gravitational circulation.

Local wind forcing affects estuarine circulation and mixing in case of strong along-estuary wind speed ∼10 m/s because in this case $We \sim 0.16 \times 6.25 = 1$. In particular, strong up-estuary wind is expected to intensify estuarine circulation and increase stratification, while strong down-estuary wind tends to induce wind straining (Chen and Sanford, 2009; Lange and Burchard, 2019). Indeed, Osadchiev and Sedakov (2019) reported that strong northern winds reverse surface flow in the northwestern part of the gulf, i.e., change its predominant flow direction from northward to southward. However, the along-estuary wind speed exceeds 10 m/s during only 4% of days during the ice-free season; therefore, the local wind forcing significantly modifies general circulation and mixing in the Gulf of Ob only in rare cases.

While showing no modification in general estuarine circulation, moderate local wind forcing has a certain influence on circulation in the surface layer in the northern part of the Gulf of Ob during ice-free periods, which can be detected at optical satellite imagery (**Figure 3**). The general northward flow is observed within the southern and central part of the gulf occupied by fresh river water from surface to bottom. Circulation in the deeper and wider northern part of the gulf is more complex. According to the coastline and local bathymetry, riverine water propagates northward in this part of the gulf along its western shore as a narrow stream (10–25 km wide) (illustrated by solid black arrows in **Figure 3b**). Inflows of more saline water from the open sea to the northern part of the gulf occur along its eastern shore (illustrated by dashed black arrows in **Figure 3b**). Note that the estuarine—sea salinity difference is only several units of salinity, which is by an order of magnitude smaller than the salinity difference between the surface and bottom layer at this area. The anticyclonic circulation pattern is distinctly observed during moderate southern and eastern winds (**Figures 3a–d**). Northern and western winds, on the opposite, hamper the anticyclonic circulation and cause the formation of multiple mesoscale eddies and complex frontal zones at the periphery of the riverine stream and in the northeastern part of the gulf (**Figures 3e,f**). However, the influence of local wind forcing on the mesoscale structure of surface circulation in this area requires additional study.

Seawater Inflows to the Gulf of Ob

The intensity of inflow of saline seawater to the Gulf of Ob (indicated by the location of the isohaline of five in the bottom layer) shows large variability during the considered field surveys (**Table 1** and **Figures 2**, **4**). In most cases, saline seawater reached the latitude of 72.0–72.3°N (**Figure 4A**). More distant inflow (i.e., distant from the open sea) was observed in September 2013 and July 2016 (71.6°N) (hereafter referred to as "moderate inflows") (**Figure 4B**); the most distant inflow was registered in August 2019 (71.0°N) (hereafter referred to as "intense inflow"). Moreover, this distant inflow was observed in progress, on August 8–10, 2019 saline water was registered at the latitude of 71.7°N (**Figure 4C**), and 10 days later it reached 71.0°N (**Figure 4D**).

Previous studies of this process by Lapin (2011) and Lapin et al. (2015) based on three field surveys (August 2010, September 2010, and September 2014) reported significantly smaller variability of the salt-water intrusion to the gulf (72.0–72.3°N) and its association with the seasonal variability of river discharge. However, an analysis of more extensive *in situ* data demonstrates no direct dependence between the intensity of seawater inflow and the river discharge rate, including both instant discharge (**Figure 5A**) and average discharge rates from the beginning of summer freshet till the periods of oceanographic field surveys (**Figure 5B**).

The distances of seawater propagation to the gulf among different years with similar discharge conditions varied by ∼50 km in July (light brown and green squares in **Figure 5**), ∼150 km in August (yellow square and red circles), and ∼70 km in September (dark brown and gray squares). On the other hand, similar inflow distances (72.1°N) were registered in July 2019 (green square in **Figure 5**), August 2010 (orange square), and September 2007 (cyan square) with significantly different discharge conditions. Finally, two of the three cases with distant inflows of saline water to the gulf, namely, a moderate inflow in July 2016 (light brown square in **Figure 5**) and an intense inflow in August 2019 (red circles), were registered during high discharge conditions (25,000–30,000 m^3/s). The moderate inflow in September 2013 (dark brown square in **Figure 5**), however, occurred during the drought period (11,000 m^3/s) of the year with relatively low annual runoff. The correlation coefficient between the inflow intensity and river discharge is −0.1 (**Figure 6A**), and the correlation coefficient between the inflow intensity and average discharge from the beginning of summer freshet till the periods of oceanographic field surveys is 0.

As discussed earlier, local winds limitedly affect the circulation in the bottom layer due to strong gravitational forcing and vertical stratification in the northern part of the Gulf of Ob. The saline inflow distances also do not show any dependence on the along-estuary wind stress, and the related correlation

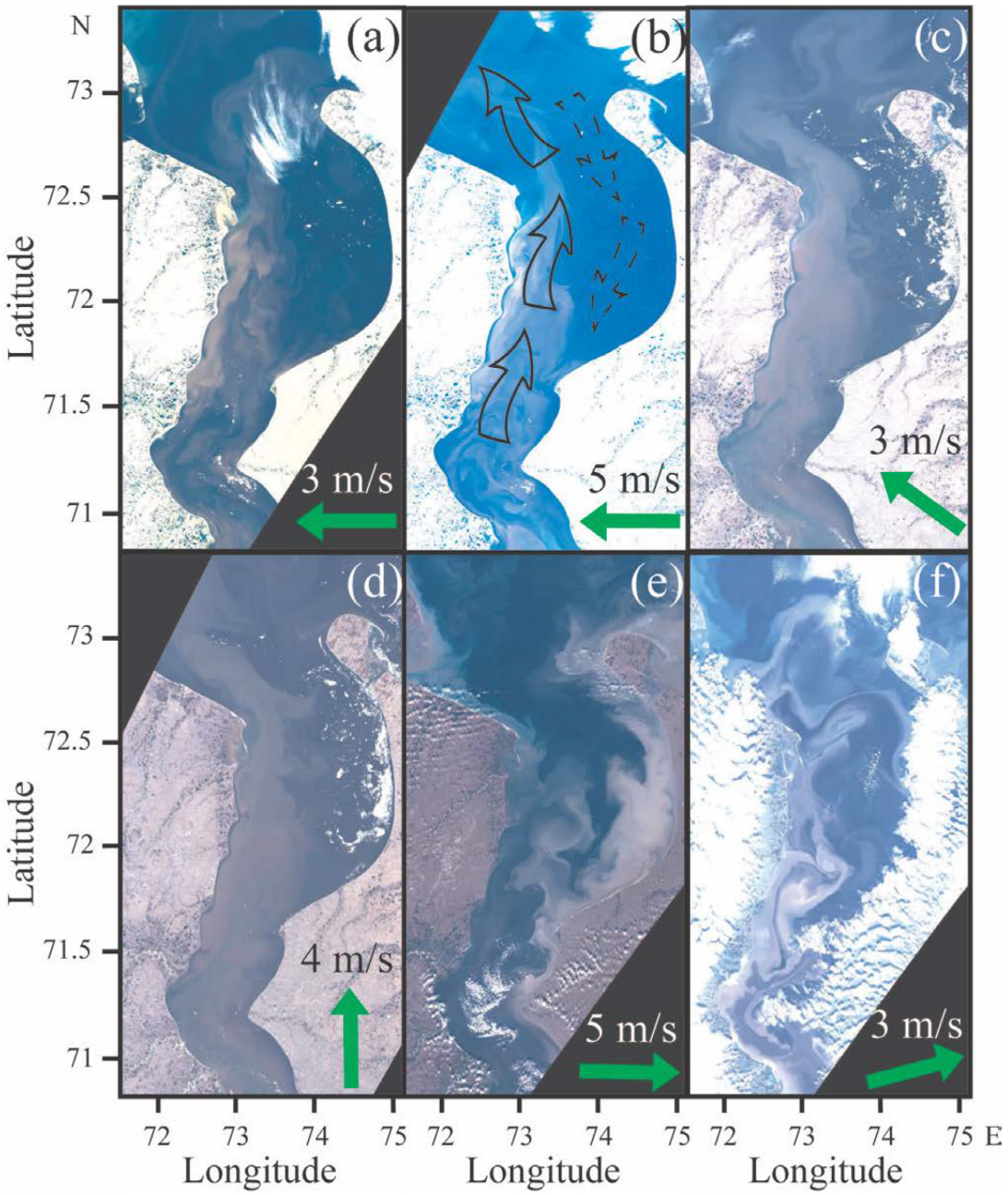


FIGURE 3 | Sentinel-2 optical satellite images of the northern part of the Gulf of Ob acquired on July 4, 2016 **(a)**, July 7, 2016 **(b)**, July 7, 2017 **(c)**, July 16, 2017 **(d)**, September 6, 2018 **(e)**, and August 16, 2020 **(f)**. Green arrows indicate wind forcing during the observation periods. Solid black arrows in panel **(b)** indicate the flow of riverine water from the gulf to the open sea, and dashed black arrows indicate the flow of saline water from the open sea to the gulf.

coefficient is 0.2 (**Figure 6B**). To evaluate the influence of remote wind forcing on saltwater intrusion to the gulf, we calculated the time integrals of downwelling (W_d), upwelling (W_u), offshore (W_{of}), and onshore (W_{on}) wind stress. These wind speed integrals were calculated over the central part of the Kara Sea (73.75–75.5°N, 65.0–85.0°E). The integration is performed over 10 days preceding the middays of the field surveys. Note that the downwelling and offshore wind integrals are positive, and the upwelling and onshore wind integrals are negative. However, to compare all the four wind integrals, we operate with their absolute values, which are shown in **Figure 7**.

Among the four wind integrals, only the upwelling wind shows a good correlation (0.5) with the inflow distance, while the correlations of the downwelling (0.1), onshore (0.2), and offshore (0) winds were low. Large absolute values of the upwelling wind integral (and the respective low values of the downwelling wind

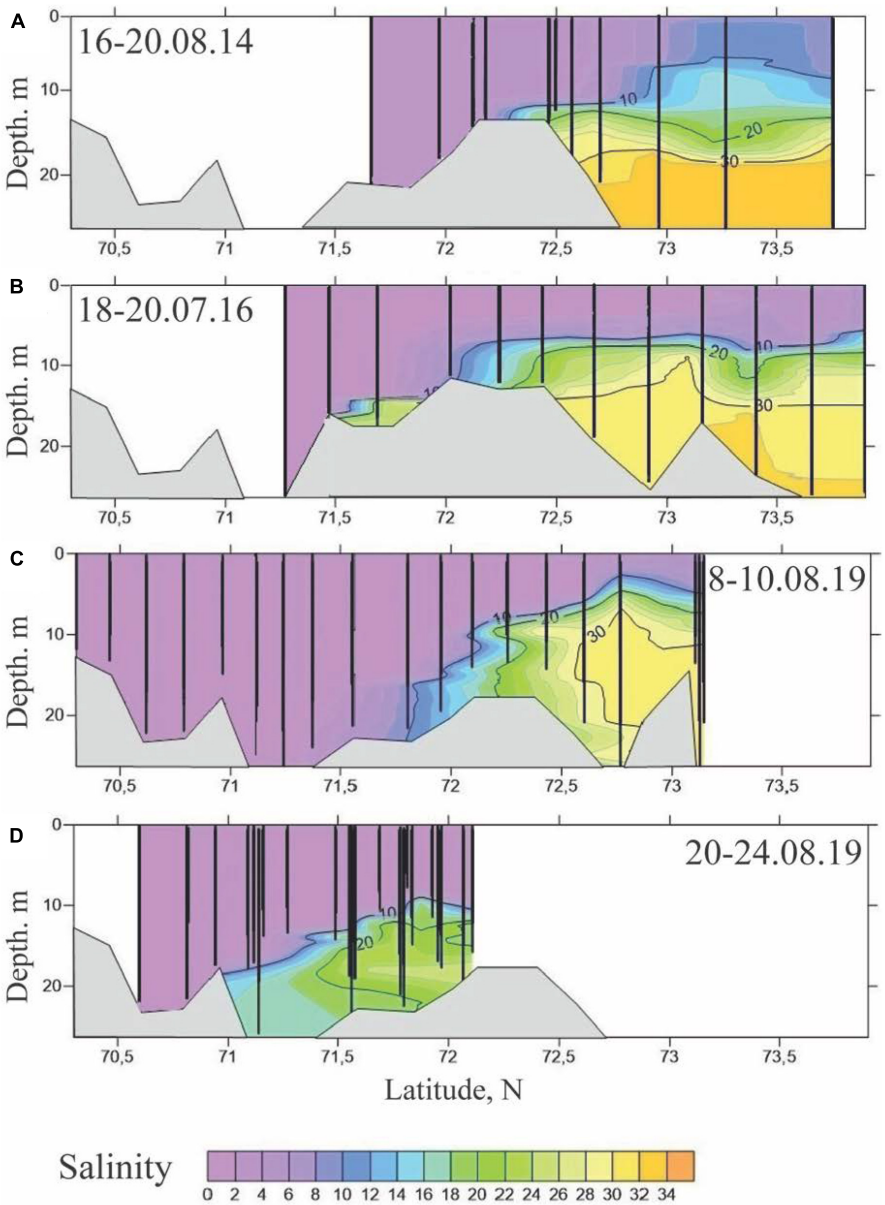


FIGURE 4 | Salinity structure along the transect in the Gulf of Ob on August 16–20, 2014 **(A)**, July 18–20, 2016 **(B)**, August 8–10, 2019 **(C)**, and August 20–24, 2019 **(D)**. Black vertical lines represent salinity measurements at the hydrographic stations.

integral) explain two of the three distant inflows, namely, in July 2016 and August 2019, which were preceded by strong eastern winds. On the other hand, the other wind forcing conditions (except September 2013) were not accompanied by distant inflows, saline waters in these cases propagated only till the latitudes of 72.0–72.3°N. The third registered distant inflow, which occurred in September 2013 (71.6°N), was not preceded by upwelling winds (**Figure 7**). However, it occurred during the drought period in September, and the discharge of the Ob River in 2013 was very low as compared to the other years (**Figure 5**). In particular, the total runoff during the summer freshet in 2013 (270 km^3 or 17,000 m^3/s) was by ∼20% lower than the average value in 2007–2019 (325 km^3 or 20,500 m^3/s). Therefore, we associate this moderate inflow with low discharge conditions, i.e., low gravitational forcing, as described by Lapin (2011).

Upwelling Events in the Central Part of the Kara Sea

Strong eastern winds in July 2016 and August 2019 induced upwelling circulation in the central part of the Kara Sea, including the area adjacent to the Gulf of Ob. This process is manifested by the formation of positive sea level anomaly in the central part of the Kara Sea northward from the Gulf

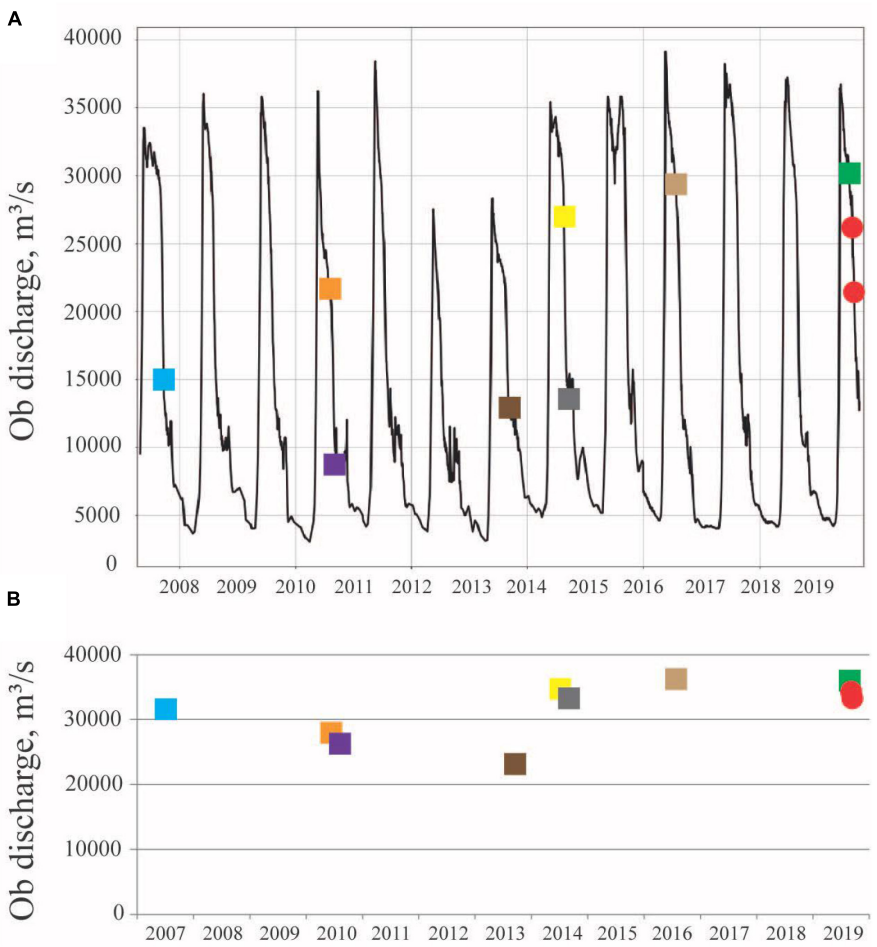


FIGURE 5 | Discharge of the Ob River to the Gulf of Ob in 2007–2019 **(A)** and average discharge from the beginning of summer freshet till the periods of oceanographic field surveys **(B)**. Colored squares and circles in panel **(A)** indicate periods of the oceanographic field surveys as shown in **Figure 2**. Note that the two surveys in August 2019 are indicated by two red circles.

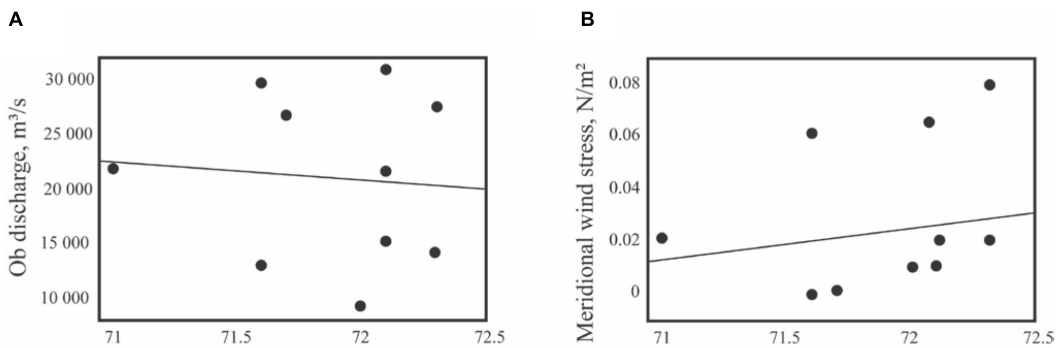


FIGURE 6 | Relations between the discharge rates of the Ob River **(A)** and the along-estuarine wind stress **(B)** with registered distances of saline inflows to the Gulf of Ob during the considered field surveys. Black lines represent the linear trends.

of Ob, which is visible at satellite altimetry data (**Figure 8**). Offshore (northward) flow in the surface layer within the Ob–Yenisei plume and onshore (southward) flow in the bottom layer increased the estuary—sea pressure gradient, which resulted in intensified saltwater intrusion to the gulf. This mechanism of impact of upwelling/downwelling wind events over the open sea

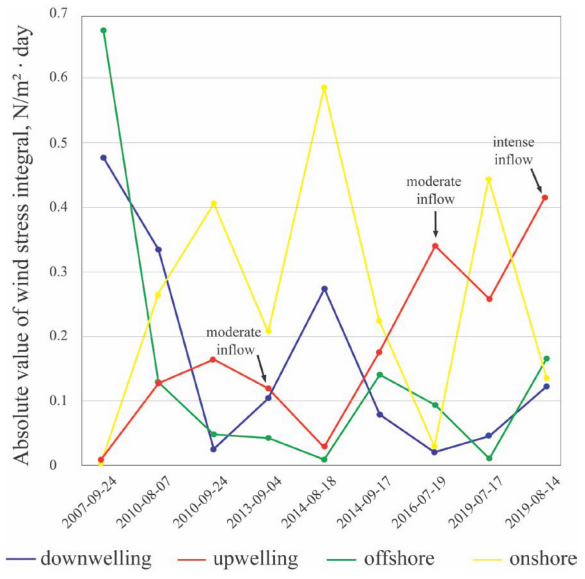


FIGURE 7 | The absolute values of time integrals of downwelling (blue), upwelling (red), offshore (green), and onshore (yellow) wind stress at the central part of the Kara Sea preceding the periods of *in situ* measurements. Black arrows indicate cases with moderate and intense inflows.

on estuarine—sea water exchange was reported earlier for many regions in the World Ocean (Stigebrandt, 1990; Aure et al., 1996; Monteiro and Largier, 1999; Hickey et al., 2002; Hickey and Banas, 2003; Gilcoto et al., 2007) and was explicitly described and analyzed by Giddings and MacCready (2017).

Generally, upwelling events strengthen the barotropic gradient, which increase the horizontal density gradient and the estuarine circulation, and strengthen the baroclinic gradient, which induce the upstream transport of increased salinities. The role of the barotropic effect in the increased saltwater intrusion will be more important because salinity in the bottom layer in front of the Gulf of Ob does not change significantly. The observed variability of salinity is 30–33, which corresponds to variability of density 1,024–1,027 kg/m^3, i.e., ∼0.3% of relative variation. The role of the barotropic pressure gradient typically dominates the role of the baroclinic pressure gradient in water exchange processes in large estuaries (Osadchiev, 2017; Zavialov et al., 2020).

Coastal upwelling events are often manifested at optical and thermal satellite imagery by areas of cold (and sometimes turbid) water along the shore once the bottom layer penetrates up to the sea surface near the coast (Osadchiev et al., 2020c). However, during the upwelling events in the Kara Sea, the cold and saline bottom layer does not reach the surface layer near the Gulf of Ob because it is blocked by the Ob plume in this area. Nevertheless, the bottom layer reaches the surface layer eastward from the Gulf of Ob along the coast of Taymyr Peninsula. Therefore, the formation of a turbid and cold stripe in this area visible at satellite imagery (indicated by white arrows in **Figure 9**) is an indicator of general upwelling circulation in the central part of the Kara Sea. Note that no cloud-free satellite imagery is available for the beginning of August 2019; therefore, in **Figure 9** we showed satellite imagery on July 2019, which are the closest dates to the period of field survey with cloud-free images.

In this study, we selected the integration period for the wind speed equal to 10 days because the best correlation between the wind and inflow conditions was provided. This period is a reasonable time lag between atmospheric forcing in the central part of the Kara Sea and the response of the estuarine circulation in the Gulf of Ob. In particular, the period of response of surface layer circulation to wind forcing in the central part of the Kara Sea is equal to several days (Osadchiev et al., 2017), similar temporal periods are registered in the Laptev and East-Siberian seas (Osadchiev et al., 2020c). The onset of the inflow of saline seawater to the gulf located 200–300 km southward from the central part of the Kara Sea requires approximately a week of additional time. The response period of estuarine inflow to remote upwelling winds reported in Giddings and MacCready (2017) is equal to 8 days, which is also consistent with our averaging period equal to 10 days.

In situ measurements performed in the study area confirm that an intense inflow to the gulf in the middle of August 2019 was induced by upwelling winds and was formed during a relatively short time period (**Figures 4C,D**). Variable wind conditions observed in the study area in the first half of July 2019 were accompanied by typical low-inflow conditions (72.1°N) registered on July 16–18, 2019. Then, strong eastern and northeastern winds dominated in the central part of the Kara Sea from July 30, 2019 to August 8, 2019 (**Figure 8B**). It induced an intense inflow of saline seawater to the gulf till the latitude of 71.7°N registered on August 8–10. After August 8 upwelling winds ceased; however, the inertial flow of saline water in the bottom layer in the Gulf of Ob reached the latitude of 71.0°N, which was registered on August 18–20. In July 2016, upwelling winds dominated the regional atmospheric circulation for 8 days in a row and ceased 4 days before the *in situ* measurements. Thus, in both cases distant inflows of saline water to the Gulf of Ob were formed during 8–10 days by the prevailing upwelling winds in the central part of the Kara Sea. However, the upwelling wind forcing was stronger in the first half of August 2019 ($|W_u| = 0.4$–0.6 N/m^2 × day) than in July 2016 (0.3–0.5 N/m^2 × day), as a result, the inflow was more intense in August 2019 (71.0°N) than in July 2016 (71.6°N).

DISCUSSION

Frequency and Duration of Upwelling Events

The analysis of *in situ* data and wind forcing conditions shows that the moderate/strong upwelling winds in the central part of the Kara Sea induce the moderate/intense inflows of saline seawater to the Gulf of Ob. To estimate the frequency and duration of these inflows, we calculated the absolute value of upwelling wind stress integral $|W_u|$ for every day for the ice-free seasons (July to October) in 1979–2020 using the ERA5 wind reanalysis. Based on the conditions $0.4 > |W_u| > 0.3$ N/m^2 × day for moderate inflows and $|W_u| > 0.4$ N/m^2 × day for intense

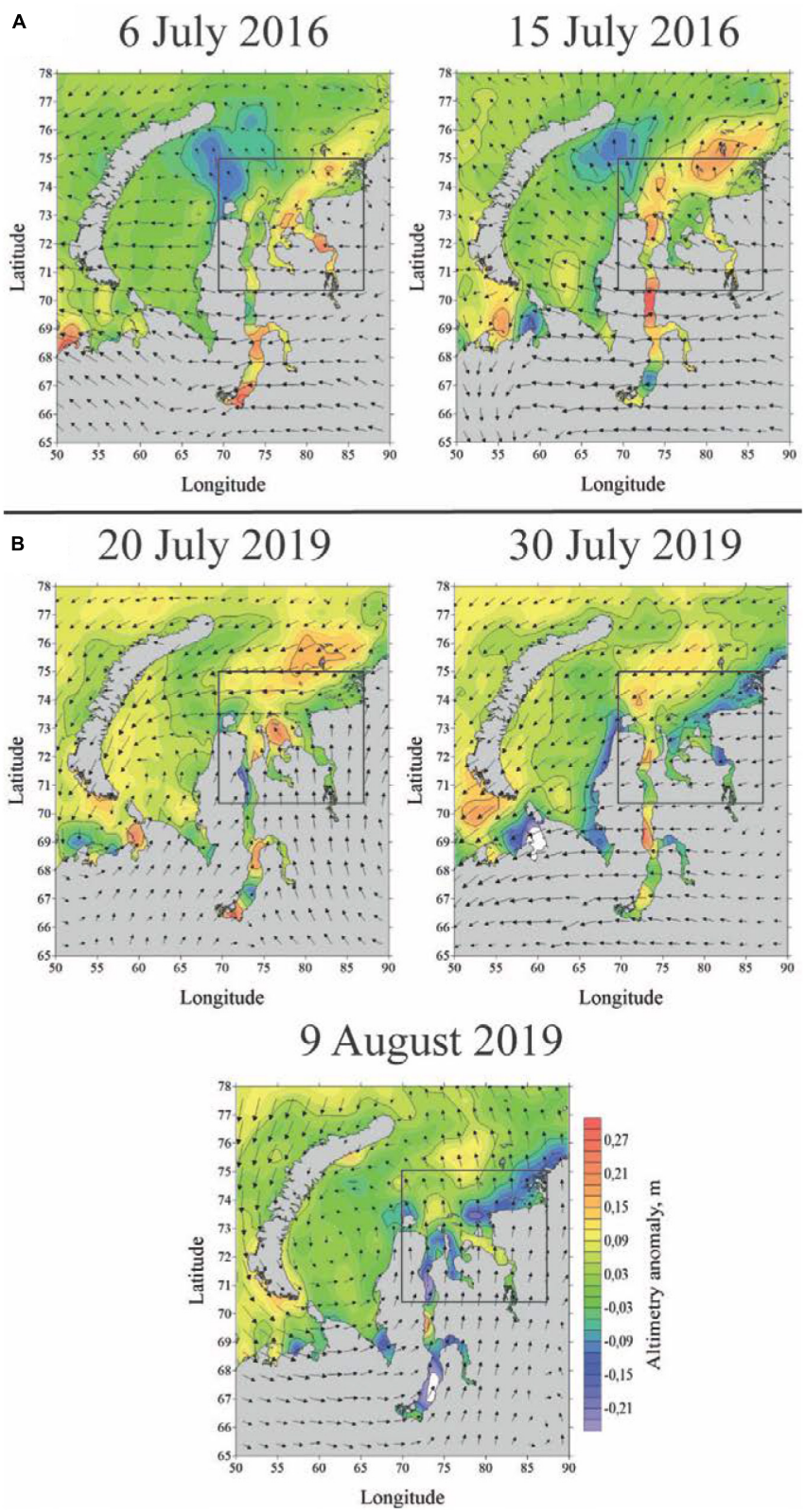


FIGURE 8 | AVISO satellite altimetry anomaly in the Kara Sea on July 6 and July 15, 2016 **(A)**, on July 20, July 30, and August 9, 2019 **(B)**. Black arrows indicate wind direction. Black rectangles indicate the location of area as shown in **Figure 9**.

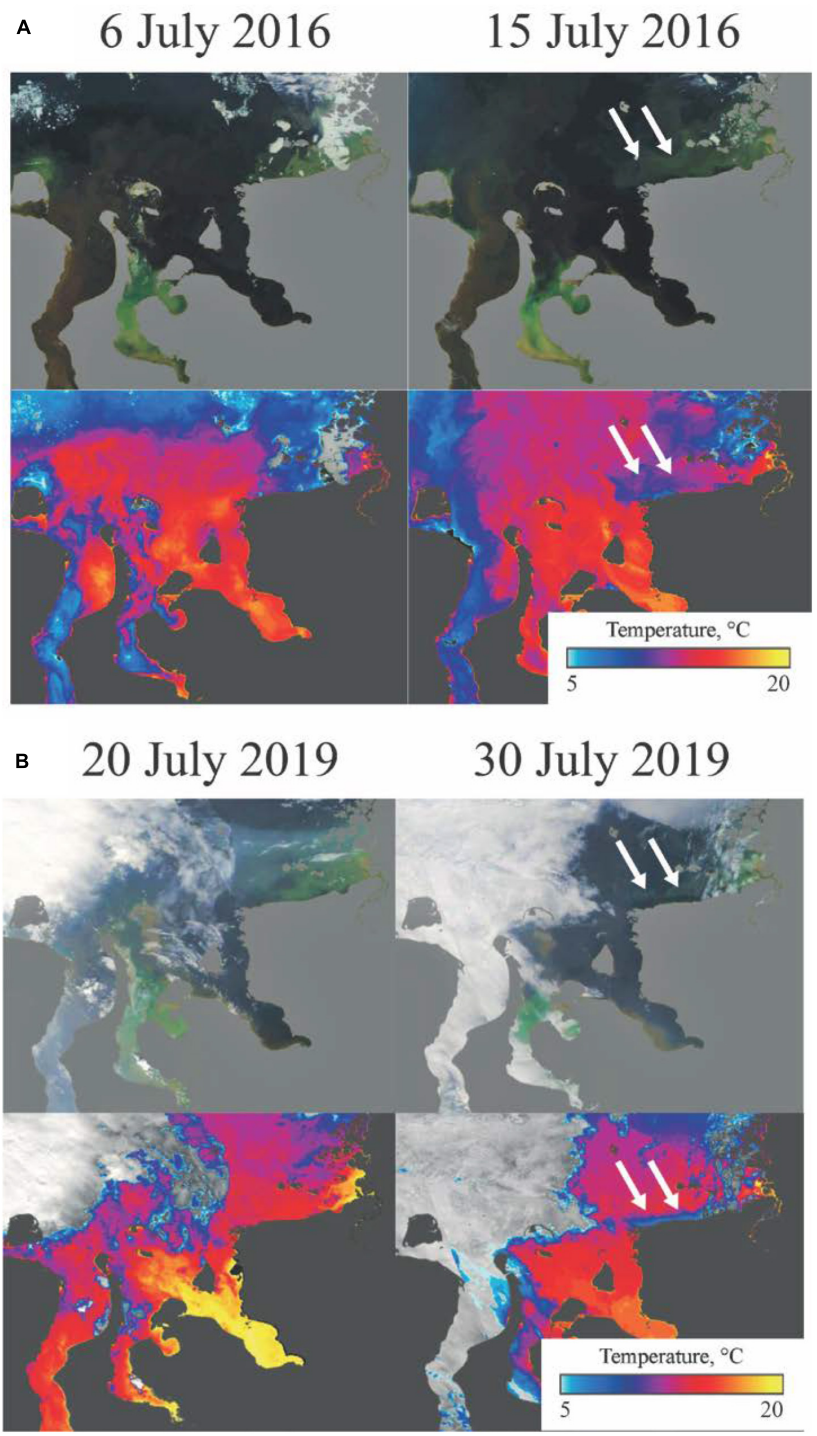


FIGURE 9 | MODIS optical imagery (top panels) and sea surface temperature (bottom panels) in the central part of the Kara Sea on July 6 and July 15, 2016 **(A)**, on July 20 and July 30, 2019 **(B)**. White arrows indicate the location of cold (at thermal images) and turbid (at optical images) surface water along the coast, which manifest upwelling along the Taymyr Peninsula.

inflows, we assessed the periods of wind forcing favorable for the formation of distant inflows to the gulf (**Figure 10**).

Both moderate and intense inflows occurred on average during 26% of days from July to October steadily increasing from 17% in July to 24 and 28% in August and September and then to 35% in October. This feature is caused by intensification of atmospheric circulation in the study region in autumn as compared to summer conditions. The intense inflows have

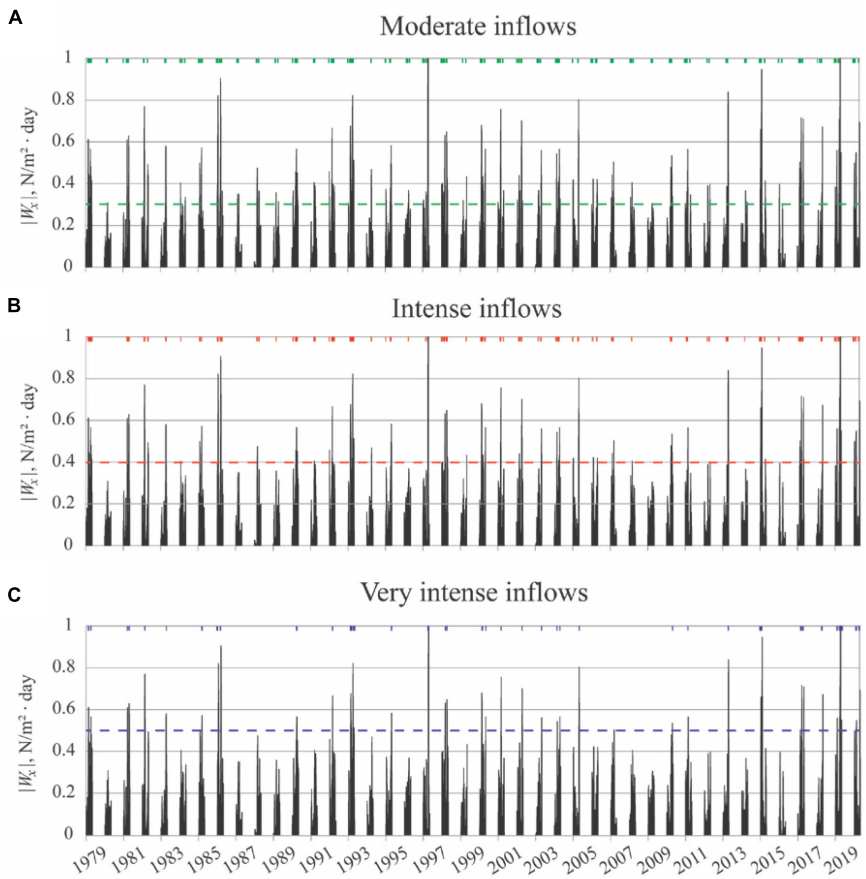


FIGURE 10 | Absolute value of upwelling wind stress integral in the central part of the Kara Sea calculated from the ERA5 atmospheric reanalysis, indicating periods of upwelling-induced moderate inflows (green bars) **(A)**, intense inflows (red bars) **(B)**, and very intense inflows (blue bars) **(C)** to the Gulf of Ob during ice-free seasons (July to October) in 1979–2020. Note that these estimations are based on wind data and not based on *in situ* measurements.

almost the same frequency (14% from July to October, 6% in July, 14% in August, 14% in September, and 22% in October) as the moderate inflows (12% from July to October, 11% in July, 10% in August, 14% in September, and 13% in October). Extremely intense inflows ($|W_u| > 0.5$ N/m^2 × day), which were not yet detected by *in situ* measurements, occur relatively rarely (5% from July to October, 1% in July, 6% in August, 5% in September, and 9% in October), but they can result in even more distant salt intrusion to the gulf than the observed extent to 71.0°N. The duration of the distant inflows varied from several days to 1 month. The total annual duration of periods of distant inflows varied from 67 days in 1979 and 64 days in 1993 to 5 days in 1999 and 9 days in 2009 due to significant inter-annual variability of local atmospheric circulation (**Figure 11**).

Phytoplankton Communities in the Gulf of Ob

Phytoplankton populations in the Gulf of Ob were addressed in a number of studies during the previous years. Phytoplankton productivity strongly depends on hydrological regime in the gulf and, therefore, has distinct seasonal variability. The spring bloom, which is formed mainly by diatoms shortly after ice melting, shifts to a steady decrease of abundance and biomass till the ice formation period (Makarevich, 2008). Generally, three zones with different phytoplankton communities are distinguished, namely, the freshwater zone with maximal productivity, the frontal zone with a distinct two-layered structure and bottom salinities increasing from 5–6 to 18–20 characterized by an abrupt decrease of productivity, and the saline zone with highly variable phytoplankton characteristics (Druzhkov and Makarevich, 1996; Makarevich et al., 2003; Sukhanova et al., 2010, 2018). However, the field surveys, which are reported in these papers, were performed during different seasons and were limited to certain zones within the gulf, i.e., not covering all the three zones within one survey. As a result, the dependence of phytoplankton communities on highly variable salinity conditions in the gulf still remains unaddressed.

The intensity of propagation of saline seawater to the Gulf of Ob affects local phytoplankton communities and, therefore, modifies the biological productivity in the gulf. In this study, we compare the characteristics of phytoplankton communities observed during the same successional season in the central and northern part of the Gulf of Ob in September 2007,

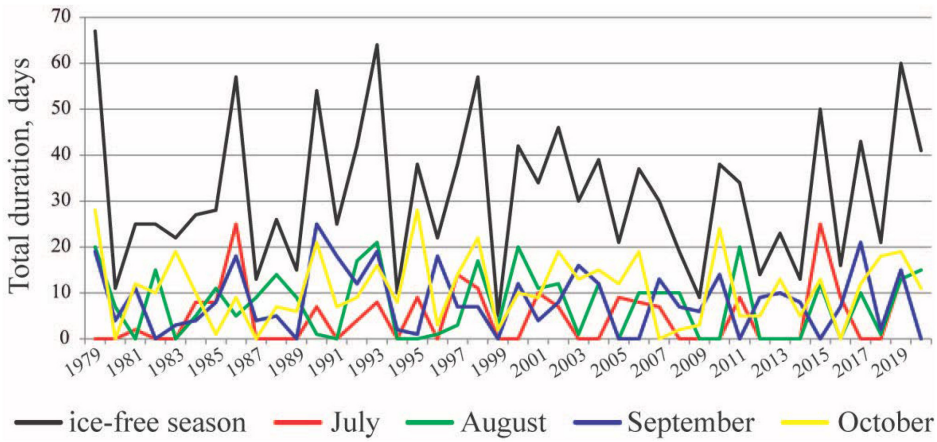


FIGURE 11 | Total annual durations of upwelling-induced distant inflow periods calculated from the ERA5 atmospheric reanalysis during July (red line), August (green line), September (blue line), October (yellow line), and during the whole ice-free season (black line) in 1979–2020. Note that these estimations are based on wind data and not based on *in situ* measurements.

September 2014, and August 2019 during different seawater inflow conditions. In the first and second case, the inflow of saline seawater to the gulf was small, while the third case was accompanied by the development of an intense inflow. As a result, the distribution of phytoplankton in both 2007 and 2014 was significantly different from that in 2019.

Figure 12 illustrates the biomass of phytoplankton and number of cells at the stations along the transects in the gulf. In 2007 and 2014, the maximal biomass and the maximal number of cells were registered in the fresh zone of the gulf (in 2014 also the second maximum of biomass was registered ∼15 km northward from the fresh zone), while further northward the productivity of phytoplankton communities steadily decreases. In particular, in September 2007, the biomass of phytoplankton decreased by 10 times (from 207 to 21 mg/m^3) with an increase of bottom salinity from 0 to 12. In August 2019, on the opposite, the maximal biomass of phytoplankton (1,200 mg/m^3) was observed not in the fresh zone, but at bottom salinities of 10–18. Southward from this area, phytoplankton biomass steadily decreased to 400–600 mg/m^3 in the fresh zone. The number of cells in August 2019 also decreased from 1,000–1,500 million at the latitudes of 71.6–72.2°N to 200–400 in the fresh zone at the latitudes of 70.8–71.4°N.

The qualitative characteristics of phytoplankton communities at different zones within the Gulf of Ob during the considered periods are illustrated by their taxonomical structure certain stations (**Figure 13**). We show the distribution of taxa *Bacillariophyta*, *Dinophyta*, and *Chlorophyta*, while Flagellatae determines a group of flagellated unicellular organisms comprising *Cryptophyta* and *Euglenophyta*. The other taxa in **Figure 13** determine mainly *Cyanobacteria* and other minor taxa. The typical distribution of phytoplankton taxa in the study area described in previous studies was observed in September 2007 and September 2014. Freshwater diatoms, green algae, and cyanobacteria dominate in the fresh zone with the presence of *Euglenophyta* and a small amount of freshwater dinoflagellates. The genus *Aulacoseira* is the most abundant among the freshwater diatoms in the Gulf of Ob. It has a proportional number of cells and biomass and is registered in all seasons. The amount of green algae is decreased in the frontal zone, euglenids steadily disappear, and the amount of dinophytes steadily increases toward the open sea, while the diatoms dominate. At the same time, algae of the genus *Aulacoseira*, which are able to live in brackish water, still dominate in the phytoplankton community of the frontal zone together with other brackish and marine species of the genera *Thalassionema*, *Thalassiosira*, etc. The marine zone of the gulf is characterized by an increase in the amount of dinophytes, which dominate together with diatoms (genera *Thalassionema*, *Thalassiosira*, *Chaetoceros*, etc.). Phylum *Cryptophyta* also contributes to the phytoplankton community in the marine zone, while *Chlorophyta*, *Euglenophyta*, and *Cyanobacteria* are almost completely absent. The largest difference in the taxonomical structure of the phytoplankton communities between September 2007 and September 2014 consists of a significantly lower amount of large diatom algae in the later stage, which results in different ratios of number of cells and biomass (**Figure 13**).

The distribution of phytoplankton communities in the Gulf of Ob in August 2019 was significantly different from those observed in September 2007 and September 2014. Dominance of diatom algae was maximal in August 2019. Diatoms provided 80–98% of total biomass at the majority of stations with bottom salinities equal to 20–25, which were located at the latitudes of 71.6–72.4°N. This large share was associated with an increase in the amount of brackish water species of the genera *Thalassionema*, *Thalassiosira*, *Melosira*, etc. The share of species of *Aulacoseira* was 52–76%, while in 2007 this share at the same salinities was equal to 24–34%.

In accordance with the abovementioned successional cycle, the spring bloom after ice melting occurs due to the development of diatoms, as was observed at the end of July 2016 (Sukhanova et al., 2018). Blooming occurs due to diatoms of all ecological

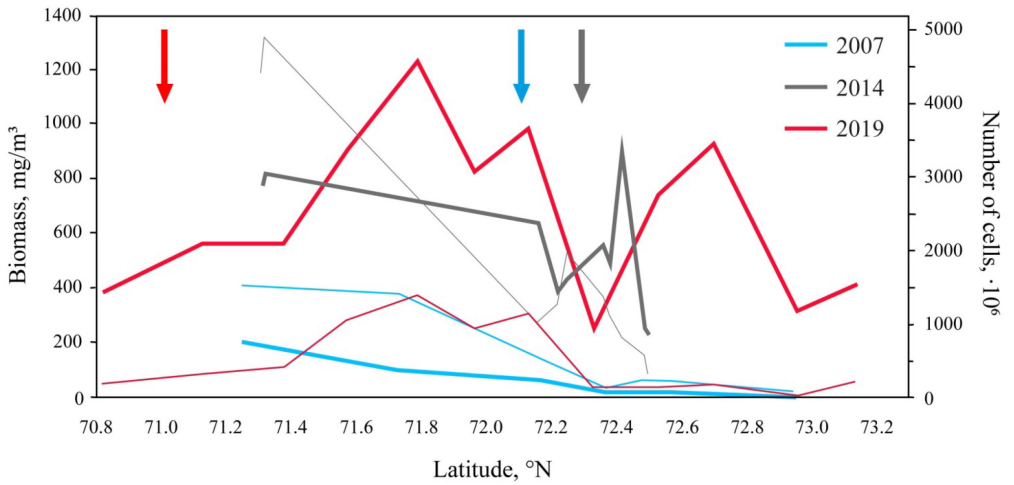


FIGURE 12 | Phytoplankton biomass (thick lines) and the number of cells (thin lines) in 2007 (blue), 2014 (gray), and 2019 (red). Arrows indicate southernmost detected locations of the isohaline of five in the bottom layer in the Gulf of Ob.

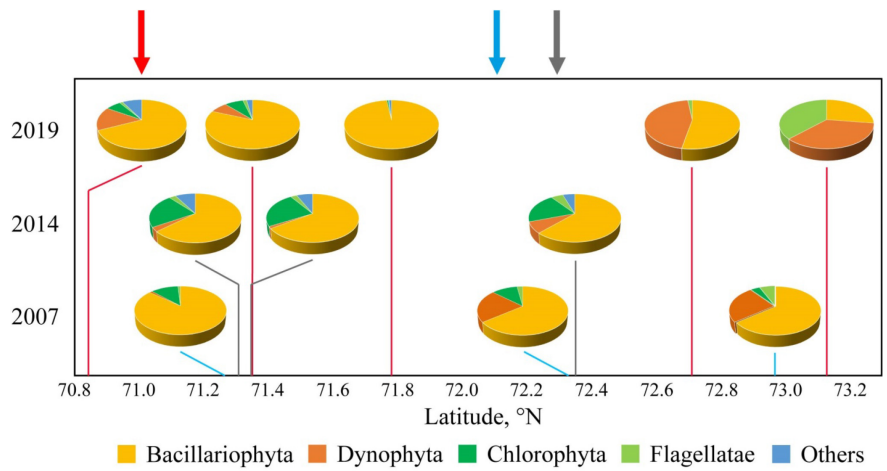


FIGURE 13 | Taxonomical structure of phytoplankton communities in 2007 (blue), 2014 (gray), and 2019 (red) at different zones within the Gulf of Ob. Arrows indicate southernmost detected locations of the isohaline of five in the bottom layer of the Gulf of Ob.

groups, namely, freshwater, marine, and brackish. It is followed by a decline in quantitative indicators and an increase of species ratio of freshwater algae due to *Cyanophyta* and *Chlorophyta* in the frontal zone, as was observed in September 2007 and September 2014. In September 2019, on the opposite, the number of diatoms remained high throughout seasonal, salinity and longitudinal distribution in the gulf, the same was observed for common indices of abundance and biomass. At the same time, the taxonomic diversity of the extended frontal zone decreases in contrast to euryhaline or brackish water diatom species (Olli et al., 2019). This feature can be caused by two factors. First, the distant advection of saline seawater results in the development of brackish water algae at a large area in the Gulf of Ob. Second, upwelling-advected seawater is especially rich in nutrients because active reproduction of diatoms at this season can occur only in the presence of high silicon content in seawater, which is non-typical for this area (Ardyna and Arrigo, 2020). The freshwater species are almost absent at the saline zone of the gulf in August 2019, which is typical for the open part of the Kara Sea. *Dinophyta* and *Cryptophyta* phylums together with marine diatom species dominated in this zone in August 2019. In September 2007 and September 2014, however, freshwater species of green and euglena algae were present in the surface layer of the saline zone.

CONCLUSION

In this study, we address the water exchange between the Gulf of Ob and the open part of the Kara Sea during ice-free periods. Based on the analysis of the extensive *in situ* measurements performed in 2007–2019, we reconstruct a dependency between

the distance of saline water inflow to the gulf and external forcing conditions. We show that the large freshwater runoff during the warm season causes the domination of gravitational circulation in the gulf and the formation of a strong two-layered stratification in the northern part of the gulf. Under average climatic conditions, saline seawater occupies the bottom layer only till the latitudes of 72.0–72.3°N. Further southward, the gulf water have zero salinity from surface to bottom. Seasonal and inter-annual variability of the freshwater runoff results in northern-southern shifts of this boundary between saline and fresh water in the bottom layer, albeit not exceeding 50–70 km. In particular, in 2013, which is characterized by the lowest annual discharge conditions among the analyzed years and the second lowest freshet runoff in the last 25 years, this boundary was located at the latitude of 71.6°N. In the presence of large longitudinal density gradient and vertical stratification, tidal circulation and local wind forcing limitedly affect the general structure of estuarine circulation. Strong wind forcing over the Gulf of Ob can modify estuarine circulation and mixing in case of strong northern or southern winds (∼10 m/s), albeit these conditions occur in only 4% of days during the ice-free season.

The estuarine processes in the Gulf of Ob experience a much stronger influence from remote wind forcing, namely, upwelling winds over the central part of the Kara Sea can cause intense and distant inflows of saline seawater to the Gulf of Ob. In this case, the offshore flow in the surface layer in the area adjacent to the Gulf of Ob and the onshore flow in the bottom layer increase the estuarine—sea barotropic pressure gradient, which results in the intensified transport of seawater to the gulf. Under these conditions, the observed distance of salt intrusion to the gulf is 120–170 km and depends on the intensity and duration of the related upwelling event. This process has synoptic variability, i.e., the response period of an estuarine inflow to remote upwelling wind is equal to 1–2 weeks. Particularly, in August 2019, the southern border of saline seawater in the gulf moved from 71.7°N to 71.0°N, i.e., it was shifted by ∼80 km in less than 10 days. The upwelling-induced inflow of saline seawater is a typical process in the Gulf of Ob, these inflows occur for a quarter of days during the ice-free season. The frequency of these inflows increases from 17% in July to 35% in October, which indicates that the estuarine—sea water exchange significantly intensifies in autumn.

The results obtained for the water exchange between the Gulf of Ob and the Kara Sea can be applied for other coastal areas where large estuarine rivers inflow to sea. Once a large river discharge dominates estuarine circulation and stratification, local wind straining and surface mixing are not strong enough to affect estuarine processes. However, the same wind speed can affect circulation in the adjacent ocean, which is less stratified and has smaller pressure gradient. Thus, remote upwelling can be the only wind-induced process that can influence circulation in stable estuaries, which receive a large amount of freshwater discharge. Also, we want to highlight the fundamental difference between the response of circulation at stratified inner-shelf on upwelling- and downwelling-favorable wind forcing (Lentz and Fewings, 2012). The wind-induced upwelling circulation results in the formation of a constant inflow of high-saline water toward the shore, which maintains the inner-shelf stratification. Once this process occurs in front of a large estuary, it stably enhances the estuarine—sea water exchange. The wind-induced downwelling circulation, on the opposite, causes the onshore flow of freshened water, which tends to inhibit stratification and to weaken the cross-shelf circulation at the inner-shelf. However, freshwater discharge from a large estuary supports stratification. As a result, downwelling circulation occurs seaward from the estuary and limitedly affects the estuarine—sea water exchange.

The upwelling-induced distant salt intrusions strongly modify biological productivity in the Gulf of Ob. First, the distant intrusions of nutrient-rich seawater refresh the content of nutrients in the gulf. Once nutrients are naturally released in the biogeochemical cycle, algae rapidly multiply that results in an additional bloom, which is similar to the spring situation. On the other hand, the upwelling-induced distant salt intrusions significantly enhance the phytoplankton productivity within the gulf by an increase of biomass of just several species of brackish water or euryhaline species of diatoms. Therefore, long-term and frequent upwelling events during certain months and years would cause a shift in taxonomical structure or decrease of species richness in phytoplankton community together with an increase of its quantitative features. As a result, the distribution of species will shift to a similar group of zooplankton, which has adaptation for life in the brackish water conditions (Drits et al., 2017). Finally, frequent upwelling events can strongly modify seasonal variability of plankton communities and food webs within the Gulf of Ob, which is typical for estuaries (Moller et al., 2009). Species richness is an important indicator for the assessment of the anthropogenic influence on the Gulf of Ob; therefore, the effect of an upwelling-induced shift should be considered while estimating the cumulative impact of industrial development in the gulf on the local ecosystem.

The circulation and mixing regimes in the Gulf of Ob are fundamentally different during winter-spring and summer-autumn seasons due to two main factors. First, very large seasonal variability of freshwater discharge (>10 times between cold and warm seasons) provides a dramatic increase of the longitudinal density gradient and the vertical stratification in the gulf during the warm season. Second, the ice coverage in the cold season isolates water in the gulf (as well as in the Kara Sea) from atmospheric forcing and increases mixing of the surface layer as compared to the warm season. As a result, during winter time circulation and vertical stratification in the gulf relax, while salinity increases. However, in this study, we focused on the estuarine processes in the Gulf of Ob only during the warm season. The related processes during the cold season remain almost unaddressed due to the lack of *in situ* measurements and require a specific study.

The distant inflows of saline seawater can strongly affect the delivery and fate of suspended sediments in the Gulf of Ob. The average concentration of total suspended matter in the Ob runoff is ∼0.4 g/m^3, which results in the annual sediment discharge of 16.5 × 10^6 tons (Gordeev et al., 1996). Mixing of river runoff and saline seawater causes the intense sedimentation deposit in the northern part of the gulf (43–1,120 g/m^2 day), in particular, the sediment accumulation velocity within the ship channel is up to 0.2–0.35 m/year (Logvina et al., 2012; Gladysh et al., 2017;

Vvedensky et al., 2017). As a result, frequent and intense inflows of saline seawater to this area can induce the resuspension of bottom sediments and significantly modify local transport and deposition pathways, which was reported for many river estuaries (Festa and Hansen, 1978; Burchard and Baumert, 1998; Li et al., 2011; Burchard et al., 2018) and the adjacent coastal regions (Osadchiev et al., 2016; Osadchiev and Korshenko, 2017).

The results of this study also have certain implications for the ongoing engineering activities in the Gulf of Ob caused by an increase of regional maritime shipping in the last decade. The ship channel (50 km long, 500–600 m wide, and 15 m deep) was constructed in 2015 and connects the central (71.9°N) and northern (72.6°N) part of the gulf. Several previous studies used numerical modeling to assess the influence of this channel on salt intrusion to the central part of the gulf (Dianskiy et al., 2015; Vvedensky et al., 2017). Our results demonstrate that the distance of seawater inflow through the ship channel as a gravity current under average conditions as well as the volume of salt intrusion are negligible as compared to those provided by regular upwelling-induced inflows described in this study.

Finally, the process of mixing of saline seawater and river discharge in the Gulf of Ob determines the initial formation of the Ob–Yenisei plume, which spreads over a wide area in the Kara Sea and is among the largest freshwater reservoirs in the Arctic Ocean. As a result, the study on the formation of the Ob–Yenisei plume is important for understanding many local processes in the Kara Sea, including circulation (Osadchiev et al., 2017, 2020a, 2021a), sediment transport (Osadchiev et al., 2019), carbon cycle and acidification (Polukhin, 2019), anthropogenic pollution (Pogojeva et al., 2021; Yakushev et al., 2021), as well as the large-scale freshwater transport in the Eastern Arctic (Haine et al., 2015; Janout et al., 2015; Carmack et al., 2016; Nummelin et al., 2016; Osadchiev et al., 2020b, 2021b).

DATA AVAILABILITY STATEMENT

The ERA5 reanalysis data were downloaded from the European Centre for Medium-Range Weather Forecasts (ECMWF) website https://www.ecmwf.int/en/forecasts/datasets/reanalysis-datasets/era5. The river discharge data were downloaded from the Arctic Great Rivers Observatory (ArcticGRO) website https://arcticgreatrivers.org/data/. The wind data from the Seyakha meteorological station were downloaded from https://rp5.ru/. The Sentinel-2 L2 products were downloaded from the Copernicus Open Access Hub (https://scihub.copernicus.eu/). The MODIS L1b products were downloaded from the NASA web repository (https://ladsweb.modaps.eosdis.nasa.gov/). The AVISO altimetry products were downloaded from the AVISO web repository (https://www.aviso.altimetry.fr/).

AUTHOR CONTRIBUTIONS

AO designed the study. AO and OK organized the database and wrote the first draft of the manuscript. AO, OK, and AG performed the analysis of the *in situ* and meteorological data. All authors contributed to manuscript revision, read, and approved the submitted version.

FUNDING

This research was funded by the Ministry of Science and Higher Education of the Russian Federation, theme 0128-2021-0001 (collecting of in situ data), the Grant of the President of the Russian Federation for state support of young Russian scientists-candidates of science, research project MK-98.2020.5 (processing of in situ data), and the Russian Foundation for Basic Research 20-35-70039 (study of FSL).

ACKNOWLEDGMENTS

The authors would like to thank Yamal LNG company for support of field survey in the Gulf of Ob in August 2019.

REFERENCES

Ardyna, M., and Arrigo, K. R. (2020). Phytoplankton dynamics in a changing Arctic Ocean. *Nat. Clim. Chang.* 10, 892–903. doi: 10.1038/s41558-020-0905-y

Aure, J., Molvær, J., and Stigebrandt, A. (1996). Observations of inshore water exchange forced by a fluctuating offshore density field. *Mar. Poll. Bull.* 33, 112–119. doi: 10.1016/S0025-326X(97)00005-2

Borisenko, G. V., Makkaveev, E. P., and Stunzhas, P. A. (2021). Concentration and diffusion of nutrients in the interpore–bottom water system of the Ob River estuary. *Oceanology* 61, 25–33. doi: 10.1134/S0001437020060028

Burchard, H., and Baumert, H. (1998). The formation of estuarine turbidity maxima due to density effects in the salt wedge. A hydrodynamic process study. *J. Phys. Oceanogr.* 28, 309–321.

Burchard, H., Schuttelaars, H. M., and Ralston, D. K. (2018). Sediment trapping in estuaries. *Annu. Rev. Mar. Sci.* 10, 371–395. doi: 10.1146/annurev-marine-010816-060535

Carmack, E. C., Yamamoto–Kawai, M., Haine, T. W., Bacon, S., Bluhm, B. A., Lique, C., et al. (2016). Freshwater and its role in the Arctic Marine System: Sources, disposition, storage, export, and physical and biogeochemical consequences in the Arctic and global oceans. *J. Geophys. Res. Biogeosci.* 121, 675–717. doi: 10.1002/2015JG003140

Chawla, A., Jay, D. A., Baptista, A. M., Wilkin, M., and Seaton, C. (2008). Seasonal variability and estuary-shelf interactions in circulation dynamics of a river-dominated estuary. *Estuar. Coasts* 31, 269–288. doi: 10.1007/s12237-007-9022-7

Chen, S. N., and Sanford, L. P. (2009). Axial wind effects on stratification and longitudinal salt transport in an idealized, partially mixed estuary. *J. Phys. Oceanogr.* 39, 1905–1920. doi: 10.1175/2009JPO4016.1

Dianskiy, N., Fomin, V., Kabatchenko, I., Litvinenko, G., and Gusev, A. (2015). "Assessing the impact of the planned approach channel to the seaport Sabetta on salinity changes in the Gulf of Ob," in *Proceedings of the 23rd International Conference on Port and Ocean Engineering under Arctic Conditions*, (Trondheim: University of Science and Technology (NTNU)), 1–12.

Drits, A. V., Pasternak, A. F., Nikishina, A. B., Semenova, T. N., Sergeeva, V. M., Polukhin, A. A., et al. (2016). The dominant copepods Senecella siberica and *Limnocalanus macrurus* in the Ob estuary: ecology in a high-gradient environment. *Polar Biol.* 39, 1527–1538. doi: 10.1007/s00300-015-1878-6

Drits, A., Pasternak, A., and Flint, M. (2017). Distribution and grazing of dominant zooplankton species in the Ob estuary: Influence of the runoff regime. *Estuar. Coasts* 40, 1082–1095. doi: 10.1007/s12237-016-0201-2

Druzhkov, N. V., and Makarevich, P. R. (1996). *Spatiotemporal Organization of Phytocenosis in Open Shelf Waters of the Western Arctic, Ecosystems of the Pelagic Zone of the Western Arctic Seas*. Apatity: Kol'sk, 37–72.

Festa, J. F., and Hansen, D. V. (1978). Turbidity maxima in partially mixed estuaries: a two-dimensional numerical model. *Estuar. Coast. Mar. Sci.* 7, 347–359. doi: 10.1016/0302-3524(78)90087-7

Flint, M. V., and Poyarkov, S. G. (2015). Comprehensive research on the Kara Sea ecosystem (128th cruise of Research Vessel Professor Shtokman). *Oceanology* 55, 657–659. doi: 10.1134/S0001437015040074

Flint, M. V., Poyarkov, S. G., Rimsky-Korsakov, N. A., and Miroshnikov, A. Y. (2020). Ecosystems of Siberian Arctic Seas-2019: Spring processes in the Kara Sea (Cruise 76 of the R/V Akademik Mstislav Keldysh). *Oceanology* 60, 134–137. doi: 10.1134/S0001437020010105

Geyer, W. R. (1997). Influence of wind on dynamics and flushing of shallow estuaries. *Estuar. Coast. Shelf Sci.* 44, 713–722. doi: 10.1006/ecss.1996.0140

Geyer, W. R., and MacCready, P. (2014). The estuarine circulation. *Annu. Rev. Fluid Mech.* 46, 175–197. doi: 10.1146/annurev-fluid-010313-141302

Giddings, S. N., and MacCready, P. (2017). Reverse estuarine circulation due to local and remote wind forcing, enhanced by the presence of along-coast estuaries. *J. Geophys. Res. Oceans* 122, 10184–10205. doi: 10.1002/2016JC012479

Gilcoto, M., Pardo, P. C., Alvarez-Salgado, X. A., and Perez, F. F. (2007). Exchange fluxes between the Ria de Vigo and the shelf: A bidirectional flow forced by remote wind. *J. Geophys. Res.* 112:C06001. doi: 10.1029/2005JC003140

Gladysh, V. A., Logvina, E. A., Nesterov, A. V., and Kubishkin, N. V. (2017). Assessing the intensity of lithodynamic processes in the seaway navigation canal of the sabetta port. *Eng. Surv.* 4, 36–45. doi: 10.25296/1997-8650-2017-4-36-44

Gordeev, V. V., Martin, J. M., Sidorov, J. S., and Sidorova, M. V. (1996). A reassessment of the Eurasian river input of water, sediment, major elements, and nutrients to the Arctic Ocean. *Am. J. Sci.* 296, 664–691. doi: 10.2475/ajs.296.6.664

Guay, C. K., Falkner, K. K., Muench, R. D., Mensch, M., Frank, M., and Bayer, R. (2001). Wind-driven transport pathways for Eurasian Arctic river discharge. *J. Geophys. Res.* 106, 11469–11480. doi: 10.1029/2000JC000261

Haine, T. W. N., Curry, B., Gerdesc, R., Hansend, E., Karcherce, M., Lee, C., et al. (2015). Arctic freshwater export: status, mechanisms, and prospects. *Glob. Planet. Change* 125, 13–35. doi: 10.1016/j.gloplacha.2014.11.013

Hansen, D. V., and Rattray, M. (1965). Gravitational circulation in straits and estuaries. *J. Mar. Res.* 23, 104–122.

Harms, I. H., and Karcher, M. J. (1999). Modeling the seasonal variability of circulation and hydrography in the Kara Sea. *J. Geophys. Res.* 104, 13431–13448. doi: 10.1029/1999jc900048

Hersbach, H., Bell, B., Berrisford, P., Hirahara, S., Horányi, A., Muñoz-Sabater, J., et al. (2020). The ERA5 global reanalysis. *Q. J. R. Meteorol. Soc.* 146, 1999–2049. doi: 10.1002/qj.3803

Hickey, B. M., and Banas, N. S. (2003). Oceanography of the US Pacific Northwest coastal ocean and estuaries with application to coastal ecology. *Estuaries* 26, 1010–1031. doi: 10.1007/BF02803360

Hickey, B. M., Zhang, X., and Banas, N. (2002). Coupling between the California current System and a coastal plain estuary in low riverflow conditions. *J. Geophys. Res.* 107:3166. doi: 10.1029/1999JC000160

Hillebrand, H., Dürselen, C.-D., Kirschel, D., Pollinger, U., and Zohary, T. (1999). Biovolume calculation for pelagic and benthic microalgae. *J. Phycol.* 35, 403–424. doi: 10.1046/j.1529-8817.1999.3520403.x

Janout, M. A., Aksenov, Y., Holemann, J. A., Rabe, B., Schauer, U., Polyakov, I. V., et al. (2015). Kara Sea freshwater transport through Vilkitsky Strait: variability, forcing, and further pathways toward the western Arctic Ocean from a model and observations. *J. Geophys. Res. Oceans* 120, 4925–4944. doi: 10.1002/2014JC010635

Kagan, B. A., Timofeev, A. A., and Sofina, E. V. (2010). Seasonal variability of surface and internal M2 tides in the Arctic Ocean. *Izv. Atmos. Ocean. Phys.* 46, 652–662. doi: 10.1134/S0001433810050105

Lange, X., and Burchard, H. (2019). The relative importance of wind straining and gravitational forcing in driving exchange flows in tidally energetic estuaries. *J. Phys. Oceanogr.* 49, 723–736. doi: 10.1175/jpo-d-18-0014.1

Lange, X., Klingbeil, K., and Burchard, H. (2020). Inversions of estuarine circulation are frequent in a weakly tidal estuary with variable wind forcing and seaward salinity fluctuations. *J. Geophys. Res. Oceans.* 125:e2019JC015789. doi: 10.1029/2019JC015789

Lapin, S. A. (2011). Hydrological characterization of the Ob' Inlet in the summer and autumn seasons. *Oceanology* 51, 925–934. doi: 10.1134/S0001437011060105

Lapin, S. A., Artamonova, K. V., Gangnus, I. A., and Kivva, K. K. (2015). Hydrological and chemical characteristics of the frontal zone in the Gulf of Ob in early autumn. *Probl. Arct. Antarct.* 3, 15–26.

Lentz, S. J., and Fewings, M. R. (2012). The wind- and wave-driven inner-shelf circulation. *Annu. Rev. Mar. Sci.* 4, 317–343. doi: 10.1146/annurev-marine-120709-142745

Li, C., White, J. R., Chen, C., Lin, H., Weeks, E., Galvan, K., et al. (2011). Summertime tidal flushing of Barataria Bay: transports of water and suspended sediments. *J. Geophys. Res. Oceans.* 116:C04009. doi: 10.1029/2010JC006566

Logvina, E. A., Gladysh, V. A., Kubyshkin, N. V., Nesterov, A. V., and Vinogradov, R. A. (2012). Estimation of sediment accumulation in the approach and maritime canals to the port of Sabetta (Yamal Peninsula). *Probl. Arct. Antarct.* 4, 105–118.

Makarevich, P. R. (2008). Annual successional cycle of pelagic phytocenoses in estuarine ecosystems of northern Russian seas. *Int. Algae. J.* 11, 57–63. doi: 10.1615/InterJAlgae.v11.i1.50

Makarevich, P. R., Larionov, V. V., Druzhkov, N. V., and Druzhkova, E. I. (2003). The role of phytoplankton from the Ob river in biological productivity of the Ob–Yenisei shoal. *Russ. J. Ecol.* 34, 86–90. doi: 10.1023/A:1023090812603

Miranda, L. B., Andutta, F. P., Kjerfve, B., and Filho, B. M. C. (2017). "Fundamentals of estuarine physical oceanography," in *Ocean Engineering & Oceanography*, Vol. 8, eds M. R. Dhanak and N. I. Xiros (Singapore: Springer), doi: 10.1007/978-981-10-3041-3

Moller, O. O., Castaing, P., Salomon, J. C., and Lazure, P. (2001). The influence of local and non-local forcing effects on the subtidal circulation of Patos Lagoon. *Estuaries* 24, 297–311. doi: 10.2307/1352953

Moller, O. O., Castello, J. P., and Vaz, A. C. (2009). The effect of river discharge and winds on the interannual variability of the pink shrimp Farfantepenaeus paulensis production in Patos Lagoon. *Estuar. Coasts* 32, 787–796. doi: 10.1007/s12237-009-9168-6

Monismith, S. G. (1986). An experimental study of the upwelling response of stratified reservoirs to surface shear stress. *J. Fluid Mech.* 171, 407–439. doi: 10.1017/S0022112086001507

Monteiro, P. M. S., and Largier, J. L. (1999). Thermal stratification in Saldanha Bay (South Africa) and subtidal, density-driven exchange with the coastal waters of the Benguela upwelling system. *Estuar. Coastal Shelf Sci.* 49, 877–890. doi: 10.1006/ecss.1999.0550

Nummelin, A., Ilicak, M., Li, C., and Smedsrud, L. H. (2016). Consequences of future increased Arctic runoff on Arctic Ocean stratification, circulation, and sea ice cover. *J. Geophys. Res. Oceans.* 121, 617–637. doi: 10.1002/2015JC011156

Oki, T., and Kanae, S. (2006). Global hydrological cycles and world water resources. *Science* 313, 1068–1072. doi: 10.1126/science.1128845

Olli, K., Ptacnik, R., Klais, R., and Tamminen, T. (2019). Phytoplankton species richness along coastal and estuarine salinity continua. *Am. Nat.* 194, E41–E51. doi: 10.1086/703657

Osadchiev, A. A. (2017). Spreading of the Amur river plume in the Amur Liman, the Sakhalin Gulf, and the Strait of Tartary. *Oceanology* 57, 376–382. doi: 10.1134/S0001437017020151

Osadchiev, A. A., and Korshenko, E. A. (2017). Small river plumes off the north-eastern coast of the Black Sea under average climatic and flooding discharge conditions. *Ocean Sci.* 13, 465–482. doi: 10.5194/os-13-465-2017

Osadchiev, A. A., and Sedakov, R. O. (2019). "Reconstruction of ocean surface currents using near simultaneous satellite imagery," in *Proceedings of the International Geosciences and Remote Sensing Symposium*, (Piscataway, NJ: Institute of Electrical and Electronics Engineers Inc.) 8078–8081. doi: 10.1109/IGARSS.2019.8898544

Osadchiev, A. A., Asadulin, E. E., Miroshnikov, A. Y., Zavialov, I. B., Dubinina, E. O., and Belyakova, P. A. (2019). Bottom sediments reveal inter-annual variability of interaction between the Ob and Yenisei plumes in the Kara Sea. *Sci. Rep.* 9:18642. doi: 10.1038/s41598-019-55242-3

Osadchiev, A. A., Frey, D. I., Shchuka, S. A., Tilinina, N. D., Morozov, E. G., and Zavialov, P. O. (2021a). Structure of the freshened surface layer in the Kara Sea during ice-free periods. *J. Geophys. Res. Oceans.* 126:e2020JC016486. doi: 10.1029/2020JC016486

Osadchiev, A. A., Frey, D. I., Spivak, E. A., Shchuka, S. A., Tilinina, N. D., and Semiletov, I. P. (2021b). Structure and inter-annual variability of the freshened surface layer in the Laptev and East-Siberian seas during ice-free periods. *Front. Mar. Sci.* Available online at: https://www.frontiersin.org/articles/10.3389/fmars.2021.735011/abstract

Osadchiev, A. A., Izhitskiy, A. S., Zavialov, P. O., Kremenetskiy, V. V., Polukhin, A. A., Pelevin, V. V., et al. (2017). Structure of the buoyant plume formed by Ob and Yenisei river discharge in the southern part of the Kara Sea during summer and autumn. *J. Geophys. Res. Oceans.* 122, 5916–5935. doi: 10.1002/2016JC012603

Osadchiev, A. A., Korotenko, K. A., Zavialov, P. O., Chiang, W.-S., and Liu, C.-C. (2016). Transport and bottom accumulation of fine river sediments under typhoon conditions and associated submarine landslides: case study of the Peinan River, Taiwan. *Nat. Haz. Earth Sys. Sci.* 16, 41–54. doi: 10.5194/nhess-16-41-2016

Osadchiev, A. A., Medvedev, I. P., Shchuka, S. A., Kulikov, M. E., Spivak, E. A., Pisareva, M. A., et al. (2020a). Influence of estuarine tidal mixing on structure and spatial scales of large river plumes. *Ocean Sci.* 16, 1–18. doi: 10.5194/os-16-1-2020

Osadchiev, A. A., Pisareva, M. N., Spivak, E. A., Shchuka, S. A., and Semiletov, I. P. (2020b). Freshwater transport between the Kara, Laptev, and East-Siberian seas. *Sci. Rep.* 10:13041. doi: 10.1038/s41598-020-70096-w

Osadchiev, A. A., Silvestrova, K. P., and Myslenkov, S. A. (2020c). Wind-driven coastal upwelling near large river deltas in the Laptev and East-Siberian seas. *Remote Sens.* 12:844. doi: 10.3390/rs12050844

Pavlov, V. K., Timokhov, L. A., Baskakov, G. A., Kulakov, M. Y., Kurazhov, V. K., Pavlov, P. V., et al. (1996). *Hydrometeorological regime of the Kara, Laptev, and East-Siberian seas*. Technical Memorandum, APL-UW TM 1-96, Applied Physics Laboratory. Washington: University of Washington.

Pogojeva, M., Zhdanov, I., Berezina, A., Lapenkov, A., Kosmach, D., Osadchiev, A., et al. (2021). Distribution of floating marine macro-litter in relation to oceanographic characteristics in the Russian Arctic seas. *Mar. Poll. Bull.* 166:112201. doi: 10.1016/j.marpolbul.2021.112201

Polukhin, A. (2019). The role of river runoff in the Kara Sea surface layer acidification and carbonate system changes. *Environ. Res. Lett.* 14:105007. doi: 10.1088/1748-9326/ab421e

Stigebrandt, A. (1990). On the response of the horizontal mean vertical density distribution in a fjord to low-frequency density fluctuations in the coastal water. *Tellus Ser. A* 42, 605–614. doi: 10.3402/tellusa.v42i5.11902

Sukhanova, I. N., Flint, M. V., Sakharova, E. G., Fedorov, A. V., Makkaveev, P. N., and Nedospasov, A. A. (2018). Phytocenoses of the Ob estuary and Kara Sea shelf in the late spring season. *Oceanology* 58, 802–816. doi: 10.1134/S0001437018060139

Sukhanova, I. N., Flint, V. M., Mosharov, S. A., and Sergeeva, V. M. (2010). Structure of the phytoplankton communities and primary production in the Ob River estuary and over the adjacent Kara Sea shelf. *Oceanology* 50, 743–758. doi: 10.1134/S0001437010050115

Voinov, G. N. (2016). Tides in the Gulf of Ob (Kara Sea). I. General characteristics of tide. *Sci. Notes RSHU* 44, 70–95.

Vvedensky, A. R., Diansky, N. A., Kabatchenko, I. M., Litvinenko, G. I., Reznikov, M. V., and Fomin, V. V. (2017). Calculation and analysis of the expected impact of the hydrotechnical construction on the environmental condition in the water area and bottom topography in case of the construction of the approach channel to the Sabetta Port. *Vestn. MGSU* 12, 480–489. doi: 10.22227/1997-0935.2017.5.480-489

Yakushev, E., Gebruk, A., Osadchiev, A, Pakhomova, S., Lusher, A., Berezina, A., et al. (2021). Microplastics distribution in the Eurasian Arctic is affected by Atlantic waters and Siberian rivers. *Comm. Earth Environ.* 2:23. doi: 10.1038/s43247-021-00091-0

Zavialov, I. B., Osadchiev, A. A., Sedakov, R. O., Barnier, B., Molines, J.-M., and Belokopytov, V. N. (2020). Water exchange between the Sea of Azov and the Black Sea through the Kerch Strait. *Ocean Sci.* 16, 15–30. doi: 10.5194/os-16-15-2020

Conflict of Interest: The authors declare that the research was conducted in the absence of any commercial or financial relationships that could be construed as a potential conflict of interest.

Publisher's Note: All claims expressed in this article are solely those of the authors and do not necessarily represent those of their affiliated organizations, or those of the publisher, the editors and the reviewers. Any product that may be evaluated in this article, or claim that may be made by its manufacturer, is not guaranteed or endorsed by the publisher.

Copyright © 2021 Osadchiev, Konovalova and Gordey. This is an open-access article distributed under the terms of the Creative Commons Attribution License (CC BY). The use, distribution or reproduction in other forums is permitted, provided the original author(s) and the copyright owner(s) are credited and that the original publication in this journal is cited, in accordance with accepted academic practice. No use, distribution or reproduction is permitted which does not comply with these terms.

frontiers in Marine Science

ORIGINAL RESEARCH
published: 16 December 2021
doi: 10.3389/fmars.2021.809566

Response of a Small River Plume on Wind Forcing

Alexander Osadchiev[1,2]*, *Roman Sedakov*[1] *and Alexandra Barymova*[3]

[1] Shirshov Institute of Oceanology, Russian Academy of Sciences, Moscow, Russia, [2] Moscow Institute of Physics and Technology, Dolgoprudny, Russia, [3] Marine Research Center at Lomonosov Moscow State University, Moscow, Russia

Wind forcing is the main driver of river plume dynamics. Direction and magnitude of wind determine position, shape, and size of a river plume. The response of river plumes on wind forcing was simulated in many numerical modeling studies; however, *in situ* measurements of this process are still very scarce. In this study, we report the first direct measurements of frontal movement of a small river plume under variable wind forcing conditions. Using quadcopters, we performed nearly continuous daytime aerial observations of the Bzyb river plume located in the non-tidal Black Sea. The aerial remote sensing was accompanied by synchronous *in situ* measurements of wind forcing. We assessed spreading patterns of the plume and evaluated movement velocity of its outer border with unprecedentedly high spatial (∼10 m) and temporal (∼1 min) resolution, which was not available in previous studies based on *in situ* measurements and satellite observations. Based on the collected data, we evaluated the time of response of plume spreading dynamics on changes in wind forcing conditions. The advection velocity of the outer plume border shows linear relation to wind speed with very small response time (10–20 min). The reversal between upstream/downstream plume spreading occurs during several hours under moderate wind forcing conditions. These reversals involve only near-field part of the plume, which cause detachment of the far-field part of the plume. The obtained results are crucial for understanding and simulating spreading dynamics of small river plumes worldwide.

Keywords: small river plume, wind forcing, coastal circulation, surface currents, aerial remote sensing, Black Sea

OPEN ACCESS

Edited by:
Juan Jose Munoz-Perez, University of Cádiz, Spain

Reviewed by:
Fialho Nehama, Eduardo Mondlane University, Mozambique
Wenping Gong, Sun Yat-sen University, China

***Correspondence:**
Alexander Osadchiev
osadchiev@ocean.ru

Specialty section:
This article was submitted to Coastal Ocean Processes, a section of the journal Frontiers in Marine Science

Received: *05 November 2021*
Accepted: *29 November 2021*
Published: *16 December 2021*

Citation:
Osadchiev A, Sedakov R and Barymova A (2021) Response of a Small River Plume on Wind Forcing. Front. Mar. Sci. 8:809566. doi: 10.3389/fmars.2021.809566

INTRODUCTION

Wind forcing and river discharge rate are two major factors that govern spreading of river plumes. Generally, spatial scales of a river plume are determined by river discharge rate, i.e., volume of fresh water that forms the plume. River discharge generally has large seasonal variability, which regulate seasonal variability of a river plume (Thomas and Weatherbee, 2006; Lihan et al., 2008; Saldias et al., 2012). Wind forcing generally governs synoptic variability of stratified river plumes (Liu et al., 2009; Horner-Devine et al., 2015). Temporal scales of discharge-driven and wind-driven variability decrease with for smaller spatial scales of river plumes. In particular, discharge-driven variability of small river plumes can be synoptic (Yankovsky et al., 2001; O'Callaghan et al., 2010; Yuan et al., 2018) and diurnal (Osadchiev and Korshenko, 2017; Cole et al., 2020), while wind forcing determine diurnal and even hourly variability of small river plumes (Pinones et al., 2005; Qu and Hetland, 2019; Osadchiev et al., 2020a, 2021a).

Wind impulse limitedly penetrates below the bottom boundary between a river plume and subjacent saline sea (Xia et al., 2011; Osadchiev and Zavialov, 2020). As a result, wind energy is concentrated in relatively shallow surface layer that causes more intense wind-driven advection of a river plume as compared to less stratified ambient sea. Similarly, ambient sea circulation affects river plume dynamics much less than wind forcing due to density gradient between a river plume and subjacent saline sea, which hinders upward flux of impulse (Osadchiev and Zavialov, 2013; Zu et al., 2014). Ambient currents can be the dominant driver of plume dispersal, albeit only for diluted outer parts of large plumes (Nikiema et al., 2007; Osadchiev, 2017; Osadchiev et al., 2020b; Nehama and Reason, 2021), while spreading of stratified river plumes is governed by wind forcing. As a result, wind-driven dynamics of a river plume is significantly different from that of the ambient saline sea. This feature strongly affects land-ocean exchange processes. Under strong wind forcing conditions, river-borne suspended and dissolved matter can be effectively transported within river plumes far off its sources in river estuaries as compared to suspended and dissolved material contained in saline sea water (Perianez, 2005; Shi and Wang, 2010; Osadchiev and Korshenko, 2017; Osadchiev et al., 2019; Korshenko et al., 2020).

Many previous works addressed wind-driven spreading of river plumes (e.g., Fong and Geyer, 2001; Berdeal et al., 2002; Hallock and Marmorino, 2002; Houghton et al., 2004; Lentz, 2004; Whitney and Garvine, 2005; Lentz and Largier, 2006; Choi and Wilkin, 2007; Williams et al., 2010; Rao et al., 2011; Lentz and Fewings, 2012; Moffat and Lentz, 2012; Zhao et al., 2018; Osadchiev and Sedakov, 2019; Osadchiev et al., 2020c). However, the majority of these works were based on numerical modeling of river plumes under different wind forcing conditions. Studies of this process based on *in situ* observations are still very scarce due to complexity of simultaneous thermohaline and velocity measurements at various plume regions with highly variable properties, positions, and circulation patterns. Nevertheless, *in situ* measurements of different plume characteristics (vertical structure, location of outer front, spreading direction, inner circulation, etc.), which change in response to changes in wind forcing conditions, are crucial for general understanding of spreading and mixing of river plumes. These measurements are essential for validation of numerical models and correct simulation of river plumes worldwide.

Quadcopters, which recently started to be applied in field surveys, provide unprecedented ability to continuously observe river plumes (Osadchiev et al., 2020a, 2021a,b). Aerial imagery and video records obtained by quadcopters can be used to reconstruct spatial and dynamical characteristics of river plumes with high spatial and temporal resolution. As a result, simultaneous measurements of wind forcing and continuous observations of a small river plume from a quadcopter provide ability for qualitative and quantitative assessment of response of a river plume on wind forcing. It is especially efficient for small river plumes, which can be almost completely observed from a single quadcopter from the altitudes of 100–500 m.

In this study, we report field measurements, which were performed in April 2021 at the Bzyb river plume located in the eastern part of the Black Sea (Osadchiev et al., 2020a, 2021a,b). Observations of the plume from a quadcopter at daytime during 3 days with variable wind forcing conditions were accompanied by wind measurements on-site, as well as thermohaline and current velocity measurements at the sea. Based on the collected data, we evaluated the time of response of plume spreading dynamics on changes in wind forcing conditions. In addition, we evaluated the dependence between spreading direction of the plume and movement velocity of its outer border on direction and magnitude of wind speed.

DATA AND METHODS

Field measurements analyzed in this study were performed on 14–17 April 2021 at the area adjacent to the Bzyb river mouth in the eastern part of the Black Sea (**Figure 1**). Aerial observations of the Bzyb plume by *DJI Mavik 2 Zoom* quadcopters equipped with a 12 MP/4K video cameras were performed during daytime (from 8 am to 7 pm). Quadcopters were lifted to the altitude of 500 m every 30–60 min from the spot located at the seashore 1 km northward from the river mouth (indicated by the red circle in **Figure 1C**) that provided opportunity to fix the observation point. Images of the plume at the angle ∼60° were taken every 3 s, quadcopter flights lasted 15–20 min. Usage of two quadcopters and multiple batteries provided ability to alternate their flights and to download data from one quadcopter during the flight of the other quadcopter. The resulting temporal coverage of the field survey period by images of the plume is shown by gray and black bands in **Figure 2**.

Wind forcing was measured by *Gill GMX200* wind speed and direction sensor located in the same place as the quadcopter spot (indicated by the red circle in **Figure 1**). The sensor was mounted to a pole and performed measurements at the altitude of 8 m with 1-min intervals. Satellite data used in this study include Landsat 8 optical image of the study area acquired on 14 April 2021 at 11:01 and Sentinel-2 optical image acquired on 15 April 2021 at 11:28 (indicated by black arrows in **Figure 2**). Note that these satellite images were acquired synchronously with aerial remote sensing. Therefore satellite data was used only to indicate the direction of plume movement, and no scientific analysis was made based on satellite images. Thermohaline and velocity measurements at the sea area adjacent to the Bzyb mouth were performed by *CastAway* CTD instrument and *Nortek Aquadopp* ADCP profiler.

The remote sensing data processing included georeferencing of the aerial imagery by direct projection into an earth-based Cartesian coordinate system using GPS and altimetry data from the quadcopter. The obtained projection was validated and corrected according to location of ground control points with well-known coordinates registered at the imagery, namely, river mouth capes, lakes near the river mouth, buildings. Georectification of the UAV imagery was performed based on the ground control points. The exact coordinates of the river mouth and sea shoreline at the georectified imagery were validated against the Sentiunel-2 satellite image (with 10 m spatial resolution) taken during the period of field work. This is an important issue due to regular morphologic changes induced by

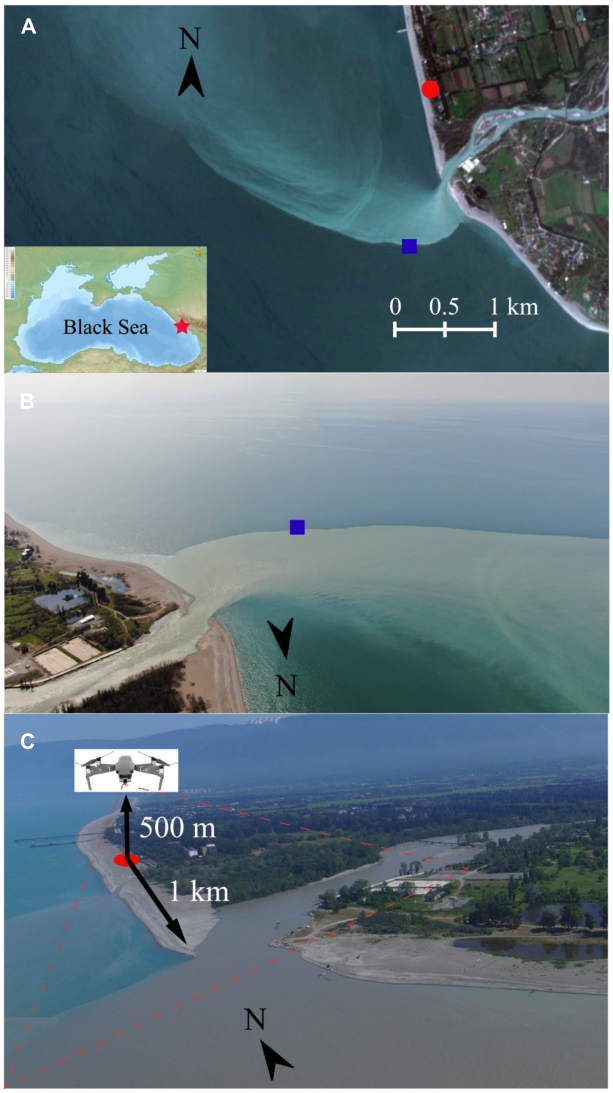


FIGURE 1 | Satellite **(A)** and aerial **(B)** images of the Bzyb plume acquired on 15 April 2021 at 11:20 **(B)** and 11:28 **(A)**, i.e., almost simultaneously. Scheme of quadcopter observations at the study area **(C)**. The red circles in the panels **(A,C)** indicate the place where the quadcopter spot and the meteorological station were located. The blue squares in the panels **(A,B)** indicate the place of ADCP measurements at the plume border. The red star at the inset in panel **(A)** indicates the location of the study area at the eastern part of the Black Sea. The dashed red triangle in the panel **(C)** indicates the quadcopter observation angle. Note that the aerial image shown in the panel **(C)** was taken during the other day that the almost simultaneous images shown in the panels **(A,B)**.

river channel processes, which are very intense in the study area. The vertical and horizontal accuracy of quadcopter positioning are 0.1 and 0.3 m, respectively. Once the remote sensing was performed from the altitude of 500 m on a distance of 1 km from the study area, the accuracy of direct projection is <1 m.

The choice of the point and angle of aerial remote sensing is crucial for this study. The observation area should cover the area of interest in the coastal sea. On the other hand, in order to obtain accurate georeferencing using multiple onshore ground control points, the observed area should partly cover the coast. The increase of altitude of remote sensing widens the observation area. However, this altitude is limited, first, by the camera resolution and, second, by regulations of national aviation administrations and quadcopter manufacturers, which seems to be more important. In particular, the *DJI* quadcopters used in our study have a hard-coded altitude limitation equal to 500 m, which was the exact operation altimetry in our study. The increase of the observation angle also widens the observation area, albeit only to a certain extent due to the projective distortion of the imagery.

In case of this study, the quadcopters observed the river mouth, the near-field part of the plume, and partly the far-filed plume. A small river plume generally has two types of outer border, namely, diffuse and sharp fronts (Osadchiev and Sedakov, 2019). A diffuse frontal zone is formed from the side of plume movement direction, i.e., in front of a spreading plume. A sharp frontal zone is formed from the opposite side, i.e., behind of a spreading plume. A sharp front is narrow (tens of centimeters for the Bzyb plume) and is distinctly visible in aerial imagery. As a result, motion of this part of the plume boundary could be accurately detected by aerial remote sensing, which is not the case of the diffuse front.

The main limitations of the described methodology, despite those related to altitude and observation area and described above, consist in turbidity of river water and weather conditions. The plume is visible at the aerial images due to its high turbidity, as compared to ambient seawater. However, low turbidity of river water limits detection of a river plume. Usage of quadcopters is hindered during rain and strong winds, which is a serious limitation for studying river plumes, because it inhibits observations of response of river plumes to strong winds and short-term rain-induced flooding events. Finally, aerial observations of river plumes are inhibited during dusk and under overcast sky conditions.

RESULTS

The field survey was carried during the spring freshet at the Bzyb River. Freshwater discharge rate reconstructed from direct velocity and depth measurements in the river mouth was ~200 m^3/s. According to CTD measurements and satellite observations, the Bzyb plume occupied area ~10 km^2, while the depth of the plume was 2–3 m. At the bottom boundary of the plume salinity abruptly increased by 2–3 units at the vertical distance of <1 m. Large salinity gradient was formed at the distinct outer border of the Bzyb plume near the river mouth, salinity in the surface layer increased from 4.5 in the plume to 15 in the ambient sea at the horizontal distance of 6 m. These large vertical and horizontal salinity gradients are typical for small mountainous river plumes formed in the northeastern part of the Black Sea (Osadchiev, 2018; Osadchiev et al., 2020a, 2021a).

Tidal circulation in the Black Sea is very low, tidal amplitudes in the study area are less than 6 cm (Medvedev et al., 2016; Medvedev, 2018). Ambient sea circulation in the study area also was low during the field survey. ADCP measurements performed

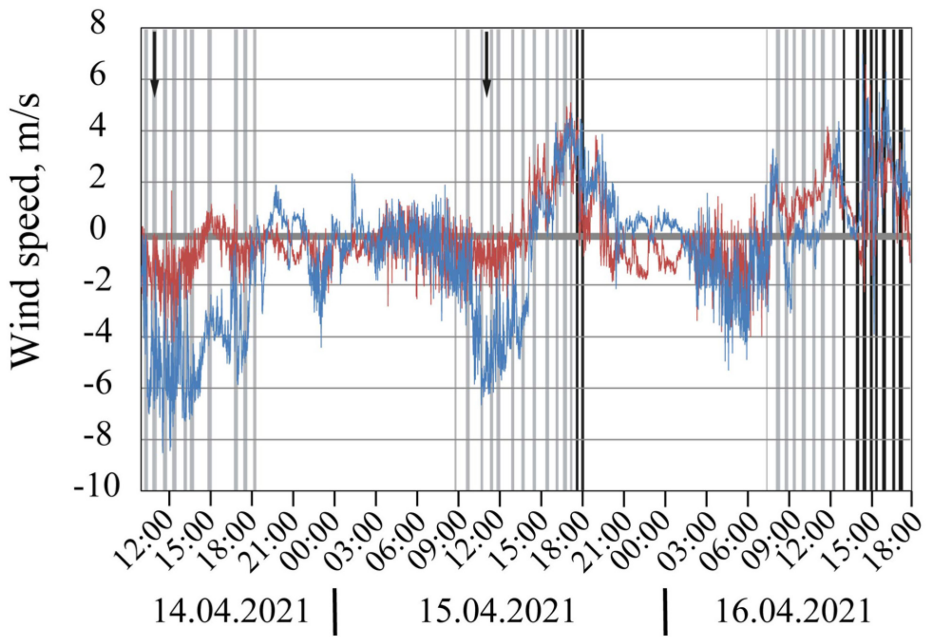


FIGURE 2 | Eastward (blue) and northward (red) components of wind speed on 14–16 August 2021 at the study area. Gray and black bands indicate periods of aerial observations of the Bzyb plume, gray band mark northward spreading of the plume, black bands mark southward spreading of the plume. Two black arrows indicate times of two satellite images of the study area acquired during the period of field survey.

500 m seaward from the Bzyb mouth showed that current velocity below the plume, i.e., at the depths >4 m, did not exceed 20 cm/s. As a result, the dynamics of the Bzyb plume during the considered period was governed by variability of wind forcing. Wind forcing during the field survey was moderate, wind speed was <5 m/s during 90% of the study period, average wind speed was 2.5 m/s (**Figure 2**).

The main advantage of the performed continuous aerial observations of the Bzyb plume (as compared to *in situ* measurements and satellite observations) consists in its potential to reveal the response of the plume dynamics on variability of wind forcing on small temporal scales, i.e., minutes and hours. The main observed feature of the plume dynamics on the hourly temporal scale consists in change of its spreading direction. The Bzyb plume was spreading northward during the majority of the observation periods (marked by gray bands in **Figure 2**). However, northward spreading of the plume twice switched to southward spreading at ∼18:00 on 15 April and at ∼15:00 on 16 April (marked by black bands in **Figure 2**). In both cases this process, was in detail registered by aerial observations (**Figure 3**). Northward spreading of the plume was distinctly associated with negative zonal component of wind speed, which dominated on 14 April (−2 to −6 m/s), at the first half of 15 April (−2 to −6 m/s), and at the first half of 16 April (−2 to −1 m/s). Once the zonal component of wind speed changed to positive at ∼15:00 on 15 April and at ∼11:00 on 16 April, it took 3–4 h for the Bzyb plume to change its spreading direction from northward to southward. In both cases, the observed quick reversal was induced by moderate wind forcing (1–4 m/s). The observed dependence of northward-southward spreading of the plume on the zonal wind component is caused by large values of the angle between wind direction and Ekman transport (up to 60–80°) within small and stratified river plumes, which was described in Osadchiev and Sedakov (2019). In this case, the positive/negative cross-shore wind component (u) corresponds to upwelling/downwelling favorable conditions.

In order to obtain quantitative assessments of the relation between wind forcing and plume spreading dynamics, we reprojected the aerial images (**Figures 3A,B**) to an earth-based Cartesian coordinate system (**Figures 3C,D**). At the georeferenced images we reconstructed the location of the distinct outer border of the plume, which can be located southward/northward from the river mouth in case of northward/southward spreading direction of the plume. Then we calculated motion direction and velocity of the plume outer border for all pairs of sequential images. The obtained velocities showed good agreement with synchronous ADCP measurements, which were performed near the plume border on 14 April (blue squares in **Figure 1**). Based on this data, we analyzed the response of the plume dynamics on variability of wind forcing on sub-hourly temporal scale (**Figure 4**).

On 14 April, the plume was spreading northward, its outer border steadily moved northward toward the river mouth under moderate offshore wind forcing (4–6 m/s). Once the wind switched to light onshore (0–2 m/s), the movement direction of the outer plume border changed to southward. On 15 April, the increase of offshore wind from 1–2 to 4–6 m/s also induced northward motion of the plume border. The following relaxation of the offshore wind to 3–4 m/s and then its change to light onshore wind (0–2 m/s) induced southward motion of the

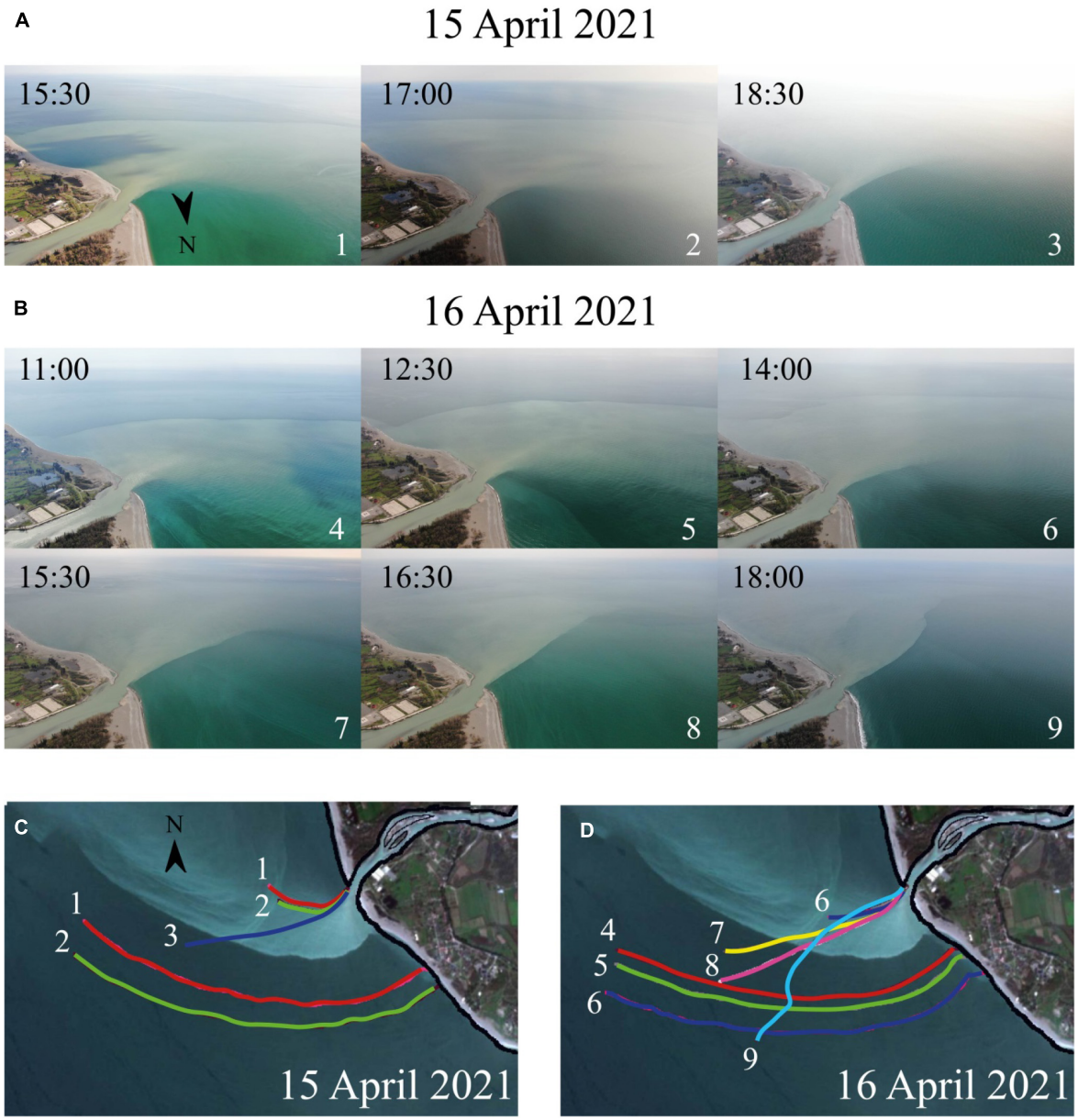


FIGURE 3 | Change of spreading direction of the Bzyb plume registered by aerial observations **(A,B)** and at the respective georeferenced images **(C,D)** on 15 April 2021 **(A,C)** and 16 April 2021 **(B,D)**. Colored lines and numbers in panels **(C,D)** represent the subsequent locations of the Bzyb plume border at time periods shown in panels **(A,B)**, respectively. The background image in panels **(C,D)** is the Sentinel-2 satellite image of the study area acquired on 15 April 2021 at 11:28.

plume border, which in several hours resulted in change of the plume spreading direction (**Figures 3A,C**). On 16 April, the plume border varied only slightly when wind forcing conditions changed between offshore and onshore (<2 m/s), then light onshore wind (2–4 m/s) caused southward motion and reversal of the plume (**Figures 3B,D**). During all 3 days, the observed response time of the motion of the outer plume border on changes in wind conditions were 10–20 min.

The reconstructed movement velocity of the Bzyb plume outer border during 3 days of the field survey provided the linear dependence $s = u/20$ between zonal wind speed u and advection velocity of the distinct southern border of the plume s (**Figure 4**). The Pearson correlation coefficient for this relation is equal to 0.85. The obtained relation demonstrates that even low wind forcing equal to 2–4 m/s results in relatively large movement velocity of the plume border equal to 0.1–0.2 m/s. Once the displacement of the plume border equal to ∼1 km results in reversal of northward/southward spreading direction of the plume, wind forcing of 2–4 m/s reverses the plume during 1.5–3 h. This temporal scale of the Bzyb plume reversal is consistent with aerial observations of this process. If the wind speed exceeds 5.5 m/s, the reversal occurs during less than an hour.

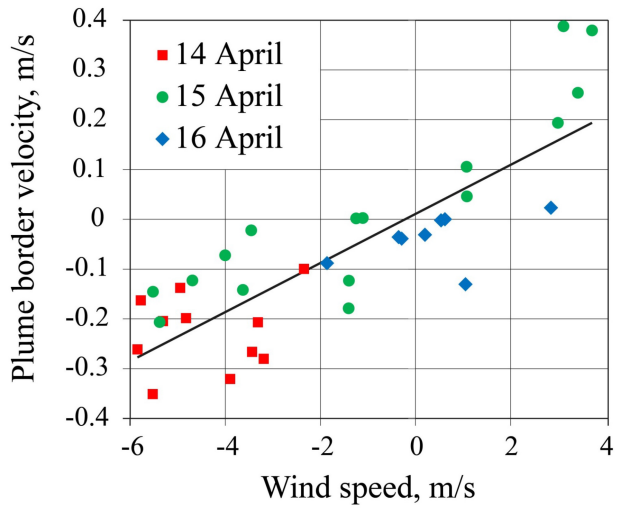


FIGURE 4 | Dependence between zonal wind speed and movement velocity of the plume outer border during the field survey. The black line indicates the linear trend.

DISCUSSION AND CONCLUSION

This work is focused on evaluation of response of a small river plume on variable wind forcing. For this purpose, we studied the Bzyb river plume located in the eastern part of the Black Sea. The field survey was performed during weak external forcing conditions, i.e., freshwater discharge ∼200 m^3/s, almost no tide, and light ambient coastal circulation. It provided opportunity to assess the effects of light and moderate wind forcing on river plume spreading using field observations.

We performed aerial remote sensing of the Bzyb river plume from the fixed point at the altitude of 500 m using quadcopters during the field survey on 14–16 April 2021. These observations provided almost continuous detection of position of the Bzyb plume during daytime of these 3 days with variable wind forcing conditions. The remote sensing of the plume was accompanied by wind measurements at the study area with temporal resolution of 1 min. Georeferencing of the obtained aerial imagery provides ability to qualitatively assess spreading patterns of the plume and evaluate movement velocity of its outer border. This methodology is relatively simple and straightforward, however, it provides very high spatial (∼10 m) and temporal (∼1 min) resolution of plume spreading variability, which was not available in previous studies based on *in situ* measurements and satellite observations of river plumes. Numerous previous studies used numerical modeling to quantify the response of a river plume on variable wind forcing; however, we are not aware of any study based on direct observations and measurements of this process at such small spatial and temporal scales. Nevertheless, precise description of this process is crucial for understanding and simulating spreading and mixing of river plumes worldwide.

During the study period, the zonal wind component determined position of the plume. The plume was spreading southward/northward along the shore under onshore/offshore wind. Changes in the wind direction resulted in reversal of spreading direction of the plume, which was observed several times during the field survey. The time differences between the observed reversals of motion direction of the plume border and the preceding changes in wind forcing were equal to 10–20 min. This very small time scale of response of the Bzyb plume spreading dynamics on wind forcing variability is the first main finding of this study.

The quick response of the Bzyb plume on wind forcing results in stable linear relation between advection velocity of the plume border and magnitude of zonal wind speed, which is the second main finding of this study. According to the obtained relation, velocity of the plume border is equal to zonal wind speed divided by 20; this relation is universal for both onshore and offshore winds. As a result, a shift between onshore and offshore wind even under low wind speed conditions (<5 m/s) results in total change of the plume spreading direction and, therefore, the plume position during less than several hours. Aerial imagery demonstrates that these plume reversals were limited to the relatively small near-field area of the plume and did not involve the majority of the far-field part of the plume. As a result, the wind-induced quick plume reversal induces formation of a new plume adjacent to the river mouth rather than changes position of the existing plume. In particular, the observed area of the Bzyb plume shortly after the northward-southward reversals reduced from ∼10 to ∼2.5 km^2. As a result, variability of wind direction is an important mechanism of detachment of the far-field part of the plume from its freshwater source, which results in its downstream advection of the old plume and presumably intensifies its mixing (Yankovsky et al., 2001; Mazzini and Chant, 2016; Yuan et al., 2018), which is the third main finding of this study.

The spreading dynamics of the small Bzyb plume continuously observed during 3 days clearly demonstrated the absence of a recirculating bulge near the river mouth even under low wind forcing conditions. The anticyclonic circulation within a plume under low external forcing (also called as the mid-field plume) is a common feature of classical idealized numerical models (Yankovsky and Chapman, 1997; Fong and Geyer, 2002; Horner-Devine et al., 2006; Choi and Wilkin, 2007), however, it is very rarely registered by *in situ* measurements and satellite observations (Horner-Devine, 2009; Osadchiev and Sedakov, 2019). Also, quick freshwater accumulation in the near-field part of the plume under low external forcing (also called as the plume ballooning), which was predicted by numerical and laboratory modeling (Nof and Pichevin, 2001; Fong and Geyer, 2002; Horner-Devine et al., 2006), was not observed at the Bzyb plume. The offset between the trend line and the point (0; 0) is small, almost equal to zero (**Figure 4**). It shows that the river plume has stable or almost stable position in case of very low wind forcing. However, we want to highlight that the location of the trend line could change to a certain extent in case of longer measurements and accumulation of more "wind speed—plume border velocity" points. As a result, the offset of the trend line from point (0; 0) also could change in case of longer measurements. However, we presume that this offset will remain rather small, i.e., <0.1 m/s for plume border velocity for zero wind forcing.

The response of the small Bzyb plume to upwelling/downwelling winds was significantly different to that described in conceptual models for large plumes based on analytical equations and numerical simulations (Fong and Geyer, 2001; Lentz, 2004; Lentz and Largier, 2006; Lentz and Fewings, 2012; Moffat and Lentz, 2012). The near-field part of the Bzyb plume responses very quickly to the changes in upwelling/downwelling winds because of re-shaping the new near-field plume with completely different spreading direction. As a result, the outer part of the plume (old plume) becomes detached from the near-field plume (new plume) due to their significantly different movement velocities. Aerial observations demonstrated that shortly after the plume reversal the detached outer part of the plume covers much wider area than the newly formed plume attached to the river mouth (**Figure 5A**). CTD measurements performed at the study area showed dramatic difference in vertical stratification at these water masses that determines difference in response of the new and old plumes to wind forcing (**Figure 5B**). In particular, the new plume spreading above the old plume forms a three-layered stratification (green vertical profile in **Figure 5B**). Similar vertical structure of the old and new plumes was previously observed at the small Kodor plume, which is located nearby the

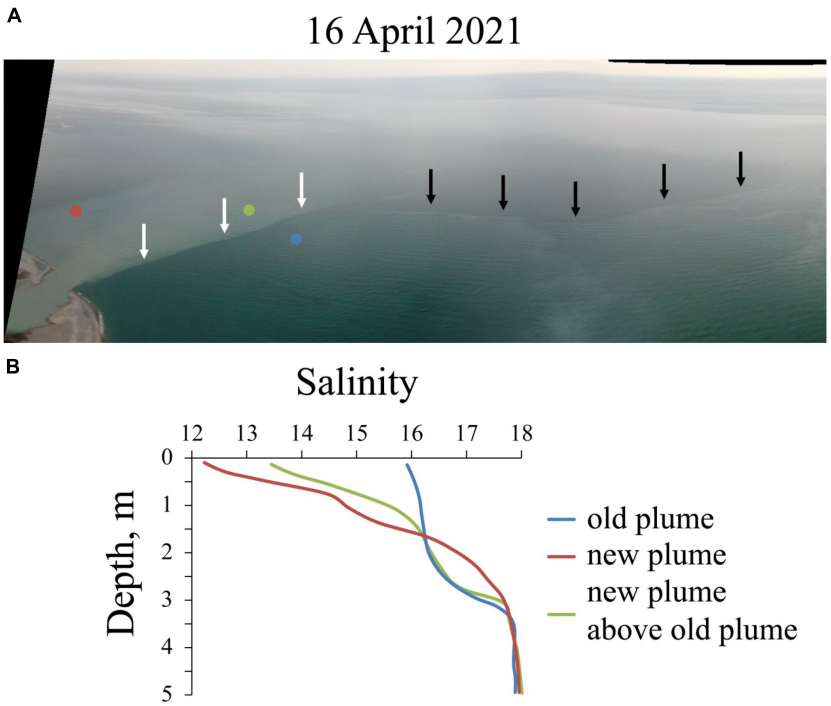


FIGURE 5 | Aerial panoramic image **(A)** and vertical salinity structure **(B)** of the near-field (new plume) and outer (old plume) parts of the Bzyb plume shortly after the plume reversal acquired on 16 April 2021 at 15:15. Colored dots in panel **(A)** indicate locations of vertical salinity measurements. White arrows indicate location of the border between the new plume and the old plume, black arrows indicate location of the border between the old plume and the ambient sea.

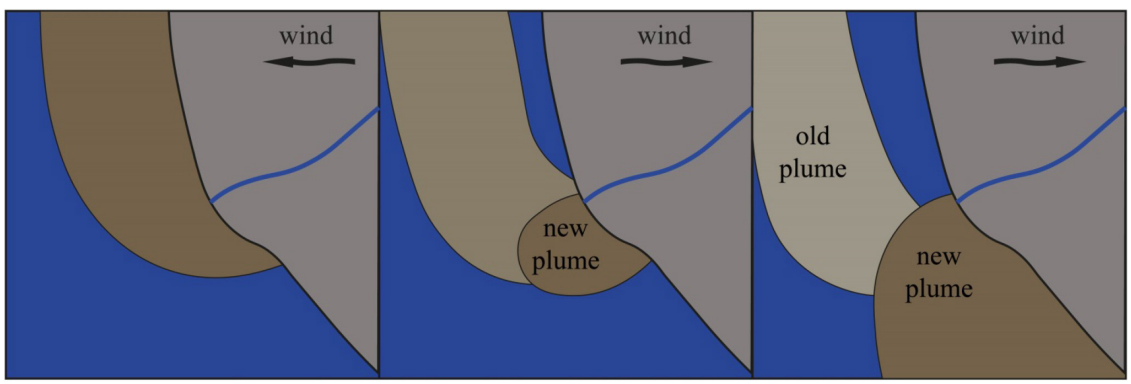


FIGURE 6 | The general scheme of the response of a small river plume to changes in upwelling/downwelling wind forcing.

study area and have similar properties to the Bzyb plume (see Figure 5 in Osadchiev et al., 2020a). The relatively slow changes of the outer plume thickness and its onshore/offshore advection in response to downwelling/upwelling winds is consistent with previous numerical studies of large plumes (Fong and Geyer, 2001; Lentz, 2004; Lentz and Largier, 2006; Moffat and Lentz, 2012), albeit the near-field plume processes are significantly different for the small and large plumes. The general scheme of response of the new and old plumes to wind forcing described above is summarized in **Figure 6**.

Qu and Hetland (2019) reported that the accuracy of numerical simulation of an idealized river plume depends on temporal resolution of the applied wind forcing, namely, it is proportional to the fraction of energy missing in the high-frequency wind absent from the forcing. However, they analyzed variability of wind speed and did not consider variability of wind direction. In this study, we demonstrate the importance of resolving wind direction variability for simulation of a small river plume, which requires significantly smaller time step than that for resolving wind speed variability based on the energy spectrum. Once 10 min is the temporal scale of plume response to variability of wind forcing and 1 h is the temporal scale of plume reversal and reshaping, these time scales should be resolved in numerical modeling of a small river plume. Therefore, the time step of 3–4 h considered by Qu and Hetland (2019) as reasonable for simulation the effects of wind speed variability is not sufficient to resolve the effects of wind direction variability.

The linear dependence between wind speed and the Bzyb plume movement velocity was obtained only for low and moderate wind forcing conditions (<6 m/s). Moreover, we considered only the fast changing wind. We presume that this linear relation would be distorted in case of durable onshore/offshore wind forcing. In this case, the plume is pressed to the shore and its outer border is stable, i.e., its advection velocity decreases to zero. In addition, the linear relation would be distorted in case of very strong wind, which induces intense mixing and dilution of the small river plume in ambient waters. The obtained relation could be different for different river plumes and, presumably, it depends on the vertical plume—sea salinity gradient, which is governed by river discharge rate. As a result, it can vary among different seasons for the individual river plume in case of large synoptic or seasonal variability of river discharge. Second, the Bzyb River inflows to sea area with quasi-linear shoreline and steep sea bottom slope, which is close to the idealized shoreline morphology and seafloor bathymetry. However, regional features of morphology and bathymetry can strongly modify the relation between wind speed and plume movement velocity. These issues require additional studies at different river plumes during different river discharge conditions. Usage of quadcopter to perform continuous aerial remote sensing of river plumes supported by synchronous *in situ* measurements holds promise to improve our understanding of spreading dynamics of river plumes worldwide.

DATA AVAILABILITY STATEMENT

The datasets presented in this study can be found in online repositories. The names of the repository/repositories and accession number(s) can be found below: https://doi.org/10.5281/zenodo.5641881.

AUTHOR CONTRIBUTIONS

AO designed the study and wrote the first draft of the manuscript. AO, RS, and AB performed the field work and organized the database. AO and RS performed the analysis of the *in situ* and meteorological data. All authors contributed to manuscript revision, read, and approved the submitted version.

FUNDING

This research was funded by the Ministry of Science and Higher Education of the Russian Federation, theme 0128-2021-0001 (collecting of *in situ* data), the Russian Science Foundation, research project 18-17-00156 (study of river plumes), and the Russian Foundation for Basic Research, research project 19-55-80004 (collecting and processing of aerial remote sensing data).

REFERENCES

Berdeal, G. I., Hickey, B. M., and Kawase, M. (2002). Influence of wind stress and ambient flow on a high discharge river plume. *J. Geophys. Res.* 107:3130. doi: 10.1029/2001JC000932

Choi, B.-J., and Wilkin, J. L. (2007). The effect of wind on the dispersal of the Hudson River plume. *J. Phys. Oceanogr.* 37, 1878–1897. doi: 10.1175/JPO3081.1

Cole, K. L., MacDonald, D. G., Kakoulaki, G., and Hetland, R. D. (2020). River plume source-front connectivity. *Ocean Model.* 150:101571. doi: 10.1016/j.ocemod.2020.101571

Fong, D. A., and Geyer, W. R. (2001). Response of a river plume during an upwelling favorable wind event. *J. Geophys. Res.* 106, 1067–1084. doi: 10.1029/2000jc900134

Fong, D. A., and Geyer, W. R. (2002). The alongshore transport of freshwater in a surface-trapped river plume. *J. Phys. Oceanogr.* 32, 957–972. doi: 10.1175/1520-04852002032<0957:TATOFI<2.0.CO;2

Hallock, Z. R., and Marmorino, G. O. (2002). Observations of the response of a buoyant estuarine plume to upwelling favorable winds. *J. Geophys. Res.* 107:3066. doi: 10.1029/2000JC000698

Horner-Devine, A. R. (2009). The bulge circulation in the Columbia River plume. *Cont. Shelf Res.* 29, 234–251. doi: 10.1016/j.csr.2007.12.012

Horner-Devine, A. R., Fong, D. A., Monismith, S. G., and Maxworthy, T. (2006). Laboratory experiments simulating a coastal river inflow. *J. Fluid Mech.* 555, 203–232. doi: 10.1017/S0022112006008937

Horner-Devine, A. R., Hetland, R. D., and MacDonald, D. G. (2015). Mixing and transport in coastal river plumes. *Annu. Rev. Fluid Mech.* 47, 569–594. doi: 10.1146/annurev-fluid-010313-141408

Houghton, R. W., Tilburg, C. E., Garvine, R. W., and Fong, D. A. (2004). Delaware river plume response to a strong upwelling-favorable wind event. *Geophys. Res. Lett.* 31:L07302. doi: 10.1029/2003GL018988

Korshenko, E. A., Zhurbas, V. M., Osadchiev, A. A., and Belyakova, P. A. (2020). Fate of river-borne floating litter during the flooding event in the northeastern part of the Black Sea in October 2018. *Mar. Pollut. Bull.* 160:111678. doi: 10.1016/j.marpolbul.2020.111678

Lentz, S. J. (2004). The response of buoyant coastal plumes to upwelling-favorable winds. *J. Phys. Oceanogr.* 34, 2458–2469. doi: 10.1175/JPO2647.1

Lentz, S. J., and Fewings, M. R. (2012). The wind- and wave-driven inner-shelf circulation. *Annu. Rev. Mar. Sci.* 4, 317–343. doi: 10.1146/annurev-marine-120709-142745

Lentz, S. J., and Largier, J. (2006). The influence of wind forcing on the Chesapeake Bay buoyant coastal current. *J. Phys. Oceanogr.* 36, 1305–1316. doi: 10.1175/JPO2909.1

Lihan, T., Saitoh, S. I., Iida, T., Hirawake, T., and Iida, K. (2008). Satellite-measured temporal and spatial variability of the Tokachi River plume. *Estuar. Coast. Shelf Sci.* 78, 237–249. doi: 10.1016/j.ecss.2007.12.001

Liu, Y., MacCready, P., Hickey, B. M., Dever, E. P., Kosro, P. M., and Banas, N. S. (2009). Evaluation of a coastal ocean circulation model for the Columbia River plume in summer 2004. *J. Geophys. Res.* 114:C00B04. doi: 10.1029/2008gl036447

Mazzini, P. L. F., and Chant, R. J. (2016). Two-dimensional circulation and mixing in the far field of a surface-advected river plume. *J. Geophys. Res.* 121, 3757–3776. doi: 10.1002/2015JC011059

Medvedev, I. P. (2018). Tides in the Black Sea: observations and numerical modeling. *Pure Appl. Geophys.* 175, 1951–1969. doi: 10.1007/s00024-018-1878-x

Medvedev, I. P., Rabinovich, A. B., and Kulikov, E. A. (2016). Tides in three enclosed basins: the Baltic, Black, and Caspian seas. *Front. Mar. Sci.* 3:46. doi: 10.3389/fmars.2016.00046

Moffat, C., and Lentz, S. (2012). On the response of a buoyant plume to downwelling-favorable wind stress. *J. Geophys. Res.* 42, 1083–1098. doi: 10.1175/JPO-D-11-015.1

Nehama, F. P. J., and Reason, C. J. C. (2021). Modelling the Zambezi River plume. *Afr. J. Mar. Sci.* 37, 593–604. doi: 10.2989/1814232X.2015.1113202

Nikiema, O., Devenon, J.-L., and Baklouti, M. (2007). Numerical modeling of the Amazon River plume. *Cont. Shelf Res.* 27, 873–899. doi: 10.1016/j.csr.2006.12.004

Nof, D., and Pichevin, T. (2001). The ballooning of outflows. *J. Geophys. Res.* 31, 3045–3058. doi: 10.1175/1520-04852001031<3045:TBOO<2.0.CO;2

O'Callaghan, J., Rickard, G., Popinet, S., and Stevens, C. (2010). Response of buoyant plumes to transient discharges investigated using an adaptive solver. *J. Geophys. Res.* 115:C11025. doi: 10.1029/2009JC005645

Osadchiev, A. A. (2017). Spreading of the Amur river plume in the Amur Liman, the Sakhalin Gulf, and the Strait of Tartary. *Oceanology* 57, 376–382. doi: 10.1134/S0001437017020151

Osadchiev, A. A. (2018). Small mountainous rivers generate high-frequency internal waves in coastal ocean. *Sci. Rep.* 8:16609. doi: 10.1038/s41598-018-35070-7

Osadchiev, A. A., and Korshenko, E. A. (2017). Small river plumes off the northeastern coast of the Black Sea under average climatic and flooding discharge conditions. *Ocean Sci.* 13, 465–482. doi: 10.5194/os-13-465-2017

Osadchiev, A. A., and Sedakov, R. O. (2019). Spreading dynamics of small river plumes off the northeastern coast of the Black Sea observed by Landsat 8 and Sentinel-2. *Remote Sens. Environ.* 221, 522–533. doi: 10.1016/j.rse.2018.11.043

Osadchiev, A. A., and Zavialov, P. O. (2013). Lagrangian model of a surface-advected river plume. *Cont. Shelf Res.* 58, 96–106. doi: 10.1016/j.csr.2013.03.010

Osadchiev, A. A., and Zavialov, P. O. (2020). "Structure and dynamics of plumes generated by small rivers," in *Estuaries and Coastal Zones - Dynamics and Response to Environmental Changes*, ed. J. Pan (London: IntechOpen).

Osadchiev, A. A., Asadulin, E. E., Miroshnikov, A. Y., Zavialov, I. B., Dubinina, E. O., and Belyakova, P. A. (2019). Bottom sediments reveal inter-annual variability of interaction between the Ob and Yenisei plumes in the Kara Sea. *Sci. Rep.* 9:18642. doi: 10.1038/s41598-019-55242-3

Osadchiev, A. A., Barymova, A. A., Sedakov, R. O., Zhiba, R. Y., and Dbar, R. S. (2020a). Spatial structure, short-temporal variability, and dynamical features of small river plumes as observed by aerial drones: case study of the Kodor and Bzyp river plumes. *Remote Sens.* 12:3079. doi: 10.3390/rs12183079

Osadchiev, A. A., Pisareva, M. N., Spivak, E. A., Shchuka, S. A., and Semiletov, I. P. (2020b). Freshwater transport between the Kara, Laptev, and East-Siberian seas. *Sci. Rep.* 10:13041. doi: 10.1038/s41598-020-70096-w

Osadchiev, A. A., Barymova, A. A., Sedakov, R. O., Rybin, A. V., Tanurkov, A. G., Krylov, A. A., et al. (2021a). Hydrophysical structure and current dynamics of the Kodor river plume. *Oceanology* 61, 1–14. doi: 10.1134/S000143702101015X

Osadchiev, A. A., Sedakov, R. O., Barymova, A. A., and Gordey, A. S. (2021b). Internal waves as a source of concentric rings within small river plumes. *Remote Sens.* 13:4275. doi: 10.3390/rs13214275

Osadchiev, A. A., Silvestrova, K. P., and Myslenkov, S. A. (2020c). Wind-driven coastal upwelling near large river deltas in the Laptev and East-Siberian seas. *Remote Sens.* 12:844. doi: 10.3390/rs12050844

Perianez, R. (2005). Modelling the dispersion of radionuclides by a river plume: application to the Rhone river. *Cont. Shelf Res.* 25, 1583–1603. doi: 10.1016/j.csr.2005.04.001

Pinones, A., Valle-Levinson, A., Narvaez, D. A., Vargas, C. A., Navarrete, S. A., Yuras, G., et al. (2005). Wind-induced diurnal variability in river plume motion. *Estuar. Coast. Shelf Sci.* 65, 513–525. doi: 10.1016/j.ecss.2005.06.016

Qu, L., and Hetland, R. D. (2019). Temporal resolution of wind forcing required for river plume simulations. *J. Geophys. Res.* 124, 1459–1473. doi: 10.1029/2018jc014593

Rao, S., Pringle, J., and Austin, J. (2011). Upwelling relaxation and estuarine plumes. *J. Geophys. Res.* 116, C09023. doi: 10.1029/2010JC006739

Saldias, G. S., Sobarzo, M., Largier, J., Moffat, C., and Letelier, R. (2012). Seasonal variability of turbid river plumes off central Chile based on high-resolution MODIS imagery. *Remote Sens. Environ.* 123, 220–233. doi: 10.1016/j.rse.2012.03.010

Shi, W., and Wang, M. (2010). Satellite observations of the seasonal sediment plume in central East China Sea. *J. Mar. Syst.* 82, 280–285. doi: 10.1016/j.jmarsys.2010.06.002

Thomas, A., and Weatherbee, R. A. (2006). Satellite-measured temporal variability of the Columbia River plume. *Remote Sens. Environ.* 100, 167–178. doi: 10.1016/j.rse.2005.10.018

Whitney, M. M., and Garvine, R. W. (2005). Wind influence on a coastal buoyant outflow. *J. Geophys. Res.* 110:C03014. doi: 10.1029/2003jc002261

Williams, W. J., Weingartner, T. J., and Hermann, A. J. (2010). Idealized two-dimensional modeling of a coastal buoyancy front, or river plume, under downwelling-favorable wind forcing with application to the Alaska Coastal Current. *J. Geophys. Res.* 40, 279–294. doi: 10.1175/2009jpo4206.1

Xia, M., Xie, L., Pietrafesa, L. J., and Whitney, M. M. (2011). The ideal response of a Gulf of Mexico estuary plume to wind forcing: its connection with salt flux and a Lagrangian view. *J. Geophys. Res.* 116:C08035. doi: 10.1029/2010JC006689

Yankovsky, A. E., and Chapman, D. C. (1997). A simple theory for the fate of buoyant coastal discharges. *J. Geophys. Res.* 27, 1386–1401. doi: 10.1175/1520-04851997027<1386:ASTFTF<2.0.CO;2

Yankovsky, A. E., Hickey, B. M., and Münchow, A. K. (2001). Impact of variable inflow on the dynamics of a coastal buoyant plume. *J. Geophys. Res.* 106, 19809–19824. doi: 10.1029/2001jc000792

Yuan, Y., Horner-Devine, A. R., Avener, M., and Bevan, S. (2018). The role of periodically varying discharge on river plume structure and transport. *Cont. Shelf Res.* 158, 15–25. doi: 10.1016/j.csr.2018.02.009

Zhao, J., Gong, W., and Shen, J. (2018). The effect of wind on the dispersal of a tropical small river plume. *Front. Earth Sci.* 12:170–190. doi: 10.1007/s11707-016-0628-6

Zu, T., Wang, D., Gan, J., and Guan, W. (2014). On the role of wind and tide in generating variability of Pearl River plume during summer in a coupled wide estuary and shelf system. *J. Mar. Syst.* 136, 65–79. doi: 10.1016/j.jmarsys.2014.03.005

Conflict of Interest: The authors declare that the research was conducted in the absence of any commercial or financial relationships that could be construed as a potential conflict of interest.

Publisher's Note: All claims expressed in this article are solely those of the authors and do not necessarily represent those of their affiliated organizations, or those of the publisher, the editors and the reviewers. Any product that may be evaluated in this article, or claim that may be made by its manufacturer, is not guaranteed or endorsed by the publisher.

Copyright © 2021 Osadchiev, Sedakov and Barymova. This is an open-access article distributed under the terms of the Creative Commons Attribution License (CC BY). The use, distribution or reproduction in other forums is permitted, provided the original author(s) and the copyright owner(s) are credited and that the original publication in this journal is cited, in accordance with accepted academic practice. No use, distribution or reproduction is permitted which does not comply with these terms.

frontiers in Marine Science

ORIGINAL RESEARCH
published: 21 January 2022
doi: 10.3389/fmars.2021.791956

Regulation of Algal Bloom Hotspots Under Mega Estuarine Constructions in the Changjiang River Estuary

Yanru He[1], Yihe Wang[1] and Hui Wu[1,2,3]**

[1] State Key Laboratory of Estuarine and Coastal Research, East China Normal University, Shanghai, China, [2] Southern Marine Science and Engineering Guangdong Laboratory, Zhuhai, China, [3] School of Marine Sciences, East China Normal University, Shanghai, China

Massive large-scale engineering projects have been built in river estuaries around the world, but their effects on environments in the surrounding coastal waters were less emphasized compared to those due to the watershed projects. In this study, we used the Changjiang River Estuary as an example to show that a significant consequence can be resulted in such a situation. Through analyzing the harmful algal bloom events data and the chlorophyll satellite data, we investigate the spatiotemporal variations of algal blooms in the estuary and its adjacent water. The results indicate that the location of algal bloom hotspot changed over the period of the estuarine constructions. Furthermore, using a well-validated numerical model, we explored the mechanisms responsible for such an ecosystem regime shift. It was found that after the estuarine constructions were built, the surface chlorophyll maximum was attenuated and part of it migrated landward north of the river mouth but was strengthened south of the river mouth and extended seaward. Alternations of the nutrient concentration distribution and turbidity distribution induced by river plume deviation are responsible for the redistribution of the high chlorophyll concentration area. By contrast, the direct impact of the Three Gorges Dam through changing the runoff and sediments flux, which has been highlighted in numerous studies, was less important than expected. Given the fact that Three Gorges Dam and mega estuarine constructions were built in a similar period, any observed regime shift of hydrodynamic and ecological status outside the estuary should be interpreted with particular caution.

Keywords: algal bloom hotspot, mega estuarine construction, Changjiang River Estuary, Three Gorges Dam, river plume dynamics, suspended sediments

OPEN ACCESS

Edited by:
Alexander Yankovsky, University of South Carolina, United States

Reviewed by:
Bin Zhao, Ocean University of China, China
Wei-dong Zhai, Shandong University (Qingdao), China

****Correspondence:***
Yihe Wang
wyhe11909045@gmail.com
Hui Wu
hwu@sklec.ecnu.edu.cn

Specialty section:
This article was submitted to Coastal Ocean Processes, a section of the journal Frontiers in Marine Science

Received: *09 October 2021*
Accepted: *08 December 2021*
Published: *21 January 2022*

Citation:
He Y, Wang Y and Wu H (2022) Regulation of Algal Bloom Hotspots Under Mega Estuarine Constructions in the Changjiang River Estuary. Front. Mar. Sci. 8:791956. doi: 10.3389/fmars.2021.791956

INTRODUCTION

The estuarine and coastal zone, which is a key area for human being inhabiting, is economically developed and densely populated. Various natural dynamic processes, including runoff, tide, wind, and shelf circulation, altogether transport nutrients and regulate the turbidity in the estuary, which is essential for algal growth, thereby controlling the aquatic ecosystem (Caffrey et al., 1998; Anderson et al., 2002; Gao and Song, 2005; Tang et al., 2006; Statham, 2012; Fan and Song, 2014; Liu et al., 2015; Wang et al., 2019a). In addition, poorly managed human activities have been recognized as another key driver to cause severe environmental issues, such as eutrophication, harmful algal

blooms, hypoxia, and habitat fragmentation, among many others (May et al., 2003; Chen et al., 2017; Zhang et al., 2018; Boesch, 2019).

The human activities that affect the estuarine environment can be classified into two categories in terms of the locations they take place. The first is conducted in the river basin, such as dam constructions, river diversion, and industrial or agricultural wastewater drainage, which directly scales up or down the amount of terrestrial freshwater and other materials entering the estuary (Humborg et al., 1997; Jiao et al., 2007). The other one occurs in the estuary, such as sea-crossing bridges, tidal flat reclamation, and deep-water channel constructions, which directly regulate the spatial characteristics of the hydrodynamic environment in the estuary and adjacent waters (Luan et al., 2016; Wu et al., 2018). Numerous attention have been paid to how the river basin engineering projects affect the physical processes and ecosystem in the receiving coastal waters (e.g., Humborg et al., 1997; Pelletier et al., 2016; Bargu et al., 2019). By contrast, the impacts of estuarine engineering constructions were often considered to be at a local scale, with very few studies discussing its far-reaching consequence in the coastal water. Several exceptions are as follows: the port expansion in the Ems River Estuary, which aggravated the estuarine eutrophication (Van Maren et al., 2015); the land reclamation in the Johor Estuary, which caused the adjacent aquatic environmental degradation (Wang et al., 2019c); and the wetlands reclamation and dike construction in the San Francisco Bay estuary which reduced the habitats for fish and waterfowl (Nichols et al., 1986).

The estuary is the starting point of the buoyant river plume, which is often nutrient-rich and turbid. A series of classic works indicated that the extension pathway and horizontal/vertical structure of the river plume are sensitive to the hydrodynamics and the geometric characteristics in the estuary. For example, the width and depth of river mouth essentially determine whether a river plume is surface-advected (i.e., floating on the surface with a strong stratification) or bottom-trapped (i.e., propagating along the coast with a strong horizontal front) (Yankovsky and Chapman, 1997), and the initial adjustment of river plume inside the river mouth can enhance the plume extension to the down-shelf direction (i.e., in the sense of Kelvin wave direction, with land on the right side in the Northern Hemisphere) (Garvine, 2001).

Estuarine engineering is a vital factor that regulates the geometry of estuaries, and thus induces hydrodynamic adjustments. One extreme example occurs in the Changjiang River Estuary. The mega-sized shipping channel constructions and the massive land reclamation on the tidal flats (**Figure 1**) substantially change the hydrodynamic structures in the estuary, thus regulating the Changjiang River plume extension in the adjacent sea with a much larger area than the estuary itself (Wu et al., 2018). Previous studies also showed that these engineering constructions have a remarkable impact on saltwater intrusion (Wu et al., 2010; Zhu L. et al., 2016) and sediment transport (Ma et al., 2013). The regulated plume extension (and thus, the nutrient it carries) and water turbidity could change the growth condition for the phytoplankton. However, these potential consequences have not received sufficient attention in the past.

To clarify whether and how the estuarine constructions change the characteristics of algal blooms in the vicinity of the large river estuary and to further demonstrate its contribution compared with the upstream constructions, here in this study, we investigated this question using the Changjiang River Estuary as an example. A multi-method investigation was carried out with numerical modeling, field data, and satellite remote sensing data. Details of the study area, data, model configuration, and validation were described in section "Materials and Methods." In section "Results," the interannual variation of harmful algal bloom events, the spatiotemporal distribution of algal bloom probability, which is derived from remote sensing chlorophyll, and the model results before and after the estuarine constructions were shown. The influences of human activities on the phytoplankton distribution were analyzed in detail in section "Discussion," including a comparison with the influence of the upstream project. Finally, conclusions were drawn in section "Summary".

MATERIALS AND METHODS

Study Area

This study focused on the vicinity of the Changjiang River Estuary, that is, the inner shelf of the East China Sea (**Figure 1**). The Changjiang River is the largest river in China and ranks the fifth in the world in terms of freshwater discharge with a huge amount of freshwater (900 km^3/year; Yang et al., 2015), sediments (1.52×10^8 tons/year; The Changjiang Water Resources Commission [CWRC] of The Ministry of Water Resources, 2016), and nutrients (nitrate of 1.15×10^{11} mol/year, phosphate of 1.05×10^9 mol/year; Gao et al., 2012). Due to the discharge of huge amounts of terrestrial materials by the Changjiang River, its estuary features a maximum turbidity zone around the river mouth and suffers from frequent harmful algal bloom and hypoxia events (Li and Zhang, 1998; Li et al., 2002; Chai et al., 2006; Wu et al., 2012; Zhu J. et al., 2016). It is reported that aquatic disasters have become systematically serious since 2000, as evidenced by nutrient characteristics and ratios (Chai et al., 2009), acceleration of eutrophication (Wang et al., 2021), and frequently occurred jellyfish blooms (Xian et al., 2005). One perspective is the increased frequency of harmful algal bloom. The main causative species is dinoflagellate during April to June and, in particular, the *Prorocentrum donghaiense* Lu and *Karenia mikimotoi* in recent decades (Tang et al., 2006; Zhou et al., 2017).

The Changjiang River is significantly regulated by upstream river dams and mega-sized estuarine engineering constructions. Among them, the Three Gorges Dam (TGD), the Deepwater Navigation Channel (DNC), and the Eastern Hengsha Reclamation (EHR) are representative. The upstream river dam, TGD, was closed in 2003. During a similar period, estuarine engineering was constructed. The DNC project was built in three phases. In the first phase (1998–2002), two 30-km-long dikes and 10 strips of groins were built on both flanks of the North Passage. In the second phase (2002–2005), the two guide dikes were lengthened to ∼50 km and nine additional strips of groins were constructed. The most important part of DNC project had been

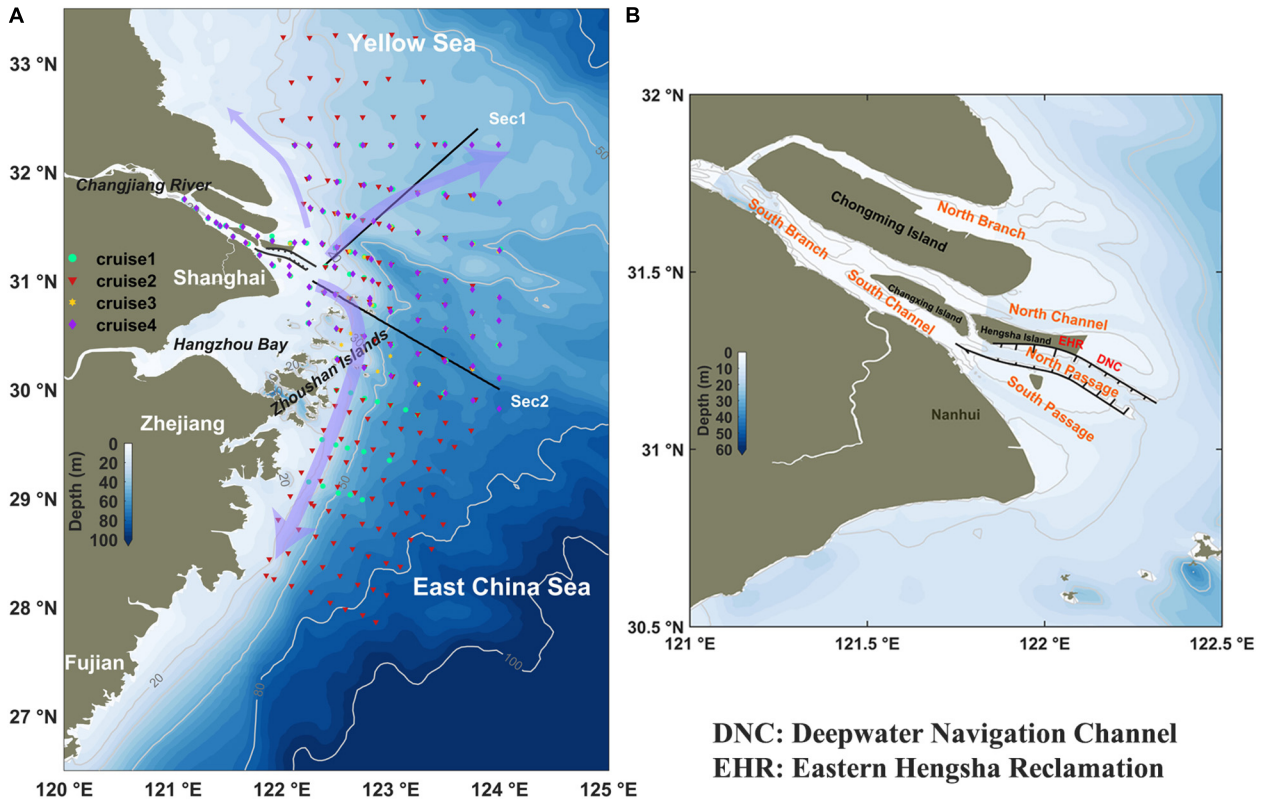


FIGURE 1 | (A) Map of the Changjiang River Estuary and its adjacent water. The arrows are the pathways of the Changjiang River plume. Dots denote the survey sites for the four cruises in 2016. The light gray lines represent the isobaths. Two solid black lines are the representative model output statistical sections discussed in the manuscript. **(B)** Zoom-in view map of the Changjiang River Estuary. The locations of the Deep Navigation Channel (DNC), the Eastern Hengsha Reclamation project (EHR), and four major outlets of Changjiang River Estuary are marked.

finished in phases one and two. In the third phase (2006–2010), the dikes were further elevated to 1.9 m above mean sea level. The EHR project also began to implement in this period, and now the large shallow tidal flat has become emerged land (**Figure 1**). In this study, we call all these engineering constructions as mega estuarine constructions (MEC).

Harmful Algal Bloom Event Data

Harmful algal bloom event data were collected in the spring season (April to June) from 2000 to 2010 in the vicinity of the Changjiang River Estuary to reveal interannual variations of phytoplankton distribution. The data sources were from Liang (2012) and Bulletin of China Marine Disasters (The Ministry of Natural Resources of the People's Republic of China, 2010). Key information on each harmful algal bloom event such as location, size, and occurrence period were recorded and displayed in **Figure 4**.

Satellite Remote Sensing Data

Chlorophyll is often used as a first-order proxy for phytoplankton biomass, and its concentration can be an effective description of biomass intensity for routine monitoring purposes (Morel, 1988). In this study, we collected surface chlorophyll concentration from Sea-viewing Wide Field-of-view Sensor (SeaWiFS) daily products during 1998–2010, and the Moderate Resolution Imaging Spectroradiometer (MODIS-Aqua) Level-3 standard mapped daily products from 2011 to 2016. The dataset from SeaWiFS has a spatial resolution of 9 km and that from MODIS-Aqua of 4 km. The accurate retrieval of remote sensing chlorophyll data in high turbid water is still under challenge (Shen et al., 2010, 2019; Le et al., 2013; Cui et al., 2020; Polikarpov et al., 2021). To reduce the disturbance signal of turbidity nearshore, a method of algal bloom occurrence probability was used. He et al. (2013) suggested that a credible threshold (e.g., 10 mg/m^3) is suitable for identifying algal blooms that can avoid false algal bloom signals caused by water turbidity.

The SeaWiFS product covered the period from August 1997 to December 2010. Due to the time-span limitation of the dataset, we shifted the remote sensing data source from SeaWiFS to MODIS-Aqua after 2010. The chlorophyll data was chosen during the period from May to June since 1998 when the algal bloom was dominated by dinoflagellate. Furthermore, to reduce the impact of cloud cover and invalid data, the monthly averaged chlorophyll concentration was calculated from the daily data. A threshold was set for each image to quantify the chlorophyll data availability retrieved by satellite. If the proportion of available data in the study area (121–125°E, 28–32.5°N) was greater than 50%, then it was used to calculate the long-term

mean. This method was consistent with that used in Chen et al. (2017). To ensure data consistency, we compared the SeaWiFS and MODIS data in the overlapped period of 2006–2010, and the results were qualitatively similar (not shown).

The remote sensing chlorophyll has a considerable error in its absolute value although numerous efforts have been made (Hu, 2009; Son and Kim, 2018). Hence, its long-term mean might be biased. As the focus of this study is the effect of the MEC on algal blooms, and also since the previous study (Wu et al., 2018) showed that its hydrodynamic consequence is to regulate the river plume transport pathway, we calculated the occurrence probability of high concentration of chlorophyll based on the remote sensing data. The probability of algal bloom occurrence was calculated as follows:

$$\mathrm{P(A)} = \frac{\sum_{i=1}^{N} p(A_i)}{\mathrm{N}} \times 100, \quad (1)$$

where A_i represents each pixel of the study area, P(A) is the probability of algal bloom occurrence, N is the number of valid chlorophyll data image at that pixel, and $p(A_i)$ is defined as follows:

$$p(A_i) = \begin{cases} 1, & Chl(A_i) \geq Chl_{threshold} \\ 0, & Chl(A_i) < Chl_{threshold} \end{cases}. \quad (2)$$

The threshold of chlorophyll was set to 10 mg/m^3 in this study. Such a threshold can reduce the interference of turbid water bodies (e.g., He et al., 2013).

In addition, the instantaneous Geo-stationary Ocean Color Imager (GOCI) data on May 12 and July 26 of 2016 were collected to validate the numerical model. The GOCI-L1B images were processed using the GOCI data processing system, and chlorophyll concentration was inverted using the Yellow Sea Large Marine Ecosystem Ocean Color Project (YOC) algorithm (Tassan, 1994; Siswanto et al., 2011).

Numerical Model

A hydrodynamics-sediments-ecosystem-coupled numerical model was used in this study. The hydrodynamic module was developed and explained in detail in previous studies (Wu et al., 2011, 2018). The model domain covered the entire East China Sea, Yellow Sea, Bohai Sea, and part of the northwestern Pacific Ocean. To better characterize the hydrological environment of the Changjiang River Estuary under the large-scale estuarine projects, we locally refined the model grid in the estuary with a resolution <500 m in the DNC area and 1–2 km in the near-field river plume area. The model was driven by realistic physical forcings to explore phytoplankton distribution characteristics in the Changjiang River Estuary before and after the MEC, including the hourly monitoring Changjiang River discharge at Datong Hydrological Station (∼630 km upstream of the river mouth), six hourly wind data, and other atmospheric parameters from the European Centre for Medium-Range Weather Forecasts (ERA-interim reanalysis products).

The ecosystem module used a vertical one-dimensional N2P2ZD model which was derived from the Flexible Biological Module in Finite-Volume Coastal Ocean Model (Chen et al., 2006) by Lin (2011). The state variables had two kinds of nutrients [dissolved inorganic nitrogen (DIN) and phosphate], two phytoplankton species (dinoflagellate and diatom), one zooplankton species, and one kind of detritus (Wang et al., 2019a). The settings of the upstream nutrient flux boundary used the data reported by Gao et al. (2012). Moreover, the initial and open boundary conditions for nutrients were derived from the climatological monthly World Ocean Atlas. For a complete set of biological equations, the readers are referred to Wang et al. (2019a).

The model includes a sediments transport module, with details described in Luo et al. (2017). The simulated suspended sediments concentration was used to calculate the light limitation for phytoplankton growth. Previous studies proved that the model has the capability of sediment simulation (Luo et al., 2017; Wang et al., 2019a). The settings of the upstream suspended sediment flux boundary used the data reported by Yang et al. (2015). The initial and open boundary conditions for suspended sediment were set to zero. The hydrodynamic model coupled with the sediment module was initiated in January 2014. After 1-year spin-up of the hydrodynamic model, the ecosystem model started to run. The model ended in December 2016. Hourly model output was used to analyze phytoplankton dynamics in 2016.

To assess the impact of MEC on ecological dynamic processes of the Changjiang River Estuary and its adjacent water, four experiments (Exps.) were configured (**Table 1**). In the control experiment (Exp. 1), the estuarine constructions were treated as land grid, and the river discharge used the realistic data in 2014–2016. In Exp. 2, the estuarine constructions (including the DNC and the EHR) were removed, i.e., the associated model grids were considered as water regions with natural water depth before the constructions. It should be noted that these engineering projects were built continuously since 1998, and we were unable to know their actual status in each year during this period. Hence, this experiment should be considered as a "natural" status, although for the purpose of comparison, we keep other conditions unchanged. Exps. 3 and 4 were designed to compare the relative influences of estuarine and upstream

TABLE 1 | Numerical experiments settings.

Experiment names	Major information	Upstream boundary conditions	MEC	Others
Exp. 1	After the MEC	Realistic	Land grid	Realistic
Exp. 2	Before the MEC	The same as Exp. 1	Water grid	The same as Exp. 1
Exp. 3	Before the TGD	+mean monthly runoff difference as **Figure 10** shown	Land grid	The same as Exp. 1
Exp. 4	Before the TGD	+200% sediment flux	Land grid	The same as Exp. 3

constructions. In Exp. 3, we changed the upstream freshwater discharge influenced by the TGD from Exp. 1. To do this, we added the runoff influence of the TGD to the realistic runoff in 2014–2016 according to the method of Wu et al. (2018). Details will be shown in section "Effect of the Three Gorges Dam-Induced Freshwater and Sediment Flux Variations." In Exp. 4, we further changed the upstream sediment flux influenced by TGD according to Yang et al. (2015) to estimate the effects of upper sediment flux changes on the turbidity, hence, the phytoplankton growth in the estuary and its adjacent water. Detailed settings of these experiments were shown in **Table 1**.

Model Validation

The numerical model used in this study has been extensively validated for hydrodynamics (e.g., Wu et al., 2011; Wu and Wu, 2018), sediments (Luo et al., 2017), and ecological variables (Wang et al., 2019a). Here in this study, we showed more validations on ecological variables. The model results were first compared with the remote sensing data derived from GOCI on May 12 and July 26 of 2016 (**Figure 2**).

TABLE 2 | Research cruise survey information.

Cruise number	Time	Research vessel
Cruise 1	March 7–19, 2016	R/V Runjiang
Cruise 2	May 6–25, 2016	R/V Zhehaike I
Cruise 3	July 4–15, 2016	R/V Runjiang
Cruise 4	July 19–28, 2016	R/V Runjiang

High chlorophyll concentration areas can be found with a couple of hotspots situating northeast to the river mouth and around the Zhoushan Islands (**Figures 2A,C**), which exhibited representative chlorophyll distribution characteristics as previous studies described (e.g., Chen et al., 2003; Tang et al., 2006; Zhou et al., 2008; Wang and Wu, 2009; Wang et al., 2019b). Model results well captured this pattern (**Figures 2B,D**).

The data collected onboard of the R/V Runjiang in March and July (twice) in 2016 and of the R/V Zhehaike I in May in 2016 (details in **Table 2**) were used for further validation. The former three cruises were supported by the National Natural Science

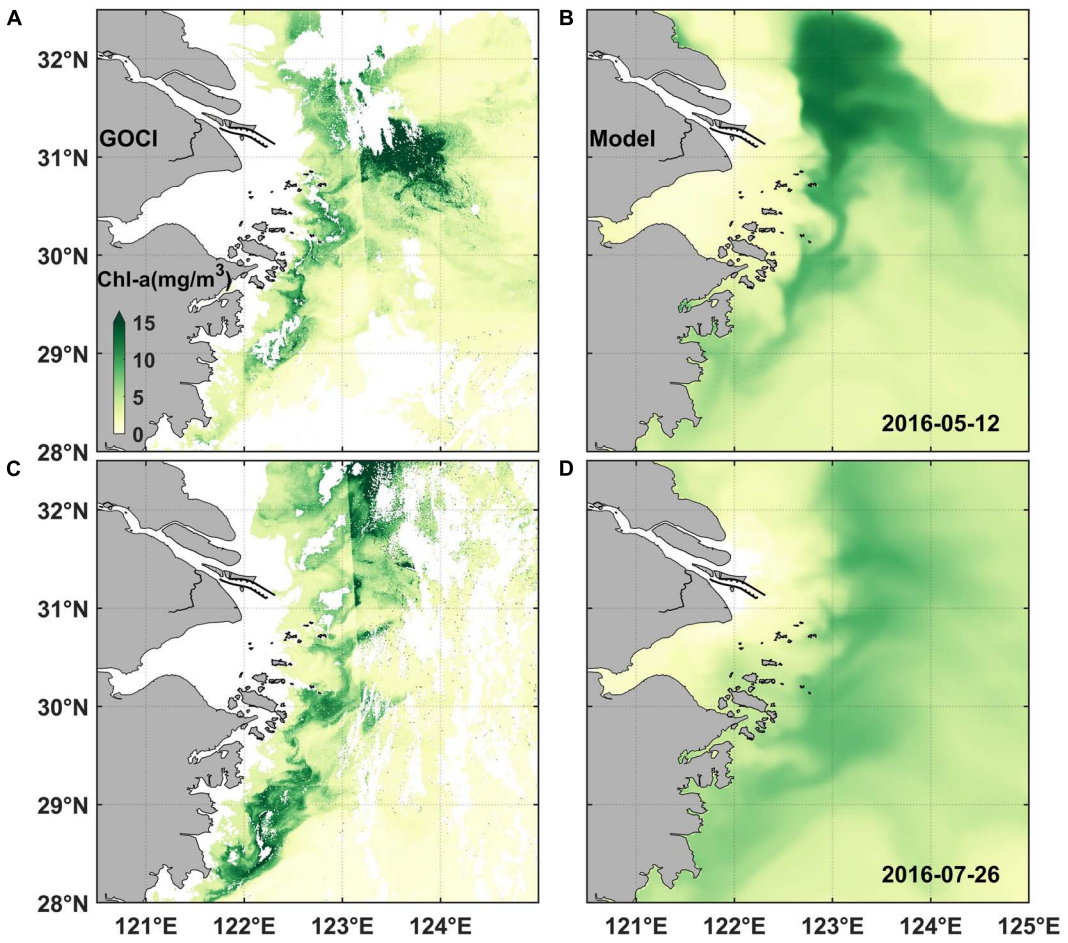


FIGURE 2 | Comparative snapshots of satellite-derived and modeled chlorophyll concentration images. **(A)** Geo-stationary Ocean Color Imager (GOCI) snapshot on May 12, 2016; **(B)** modeled chlorophyll concentration on May 12, 2016; **(C)** GOCI snapshot on July 26, 2016; and **(D)** modeled chlorophyll concentration on July 26, 2016. The white areas in the satellite-derived images indicate invalid data due to cloud shading.

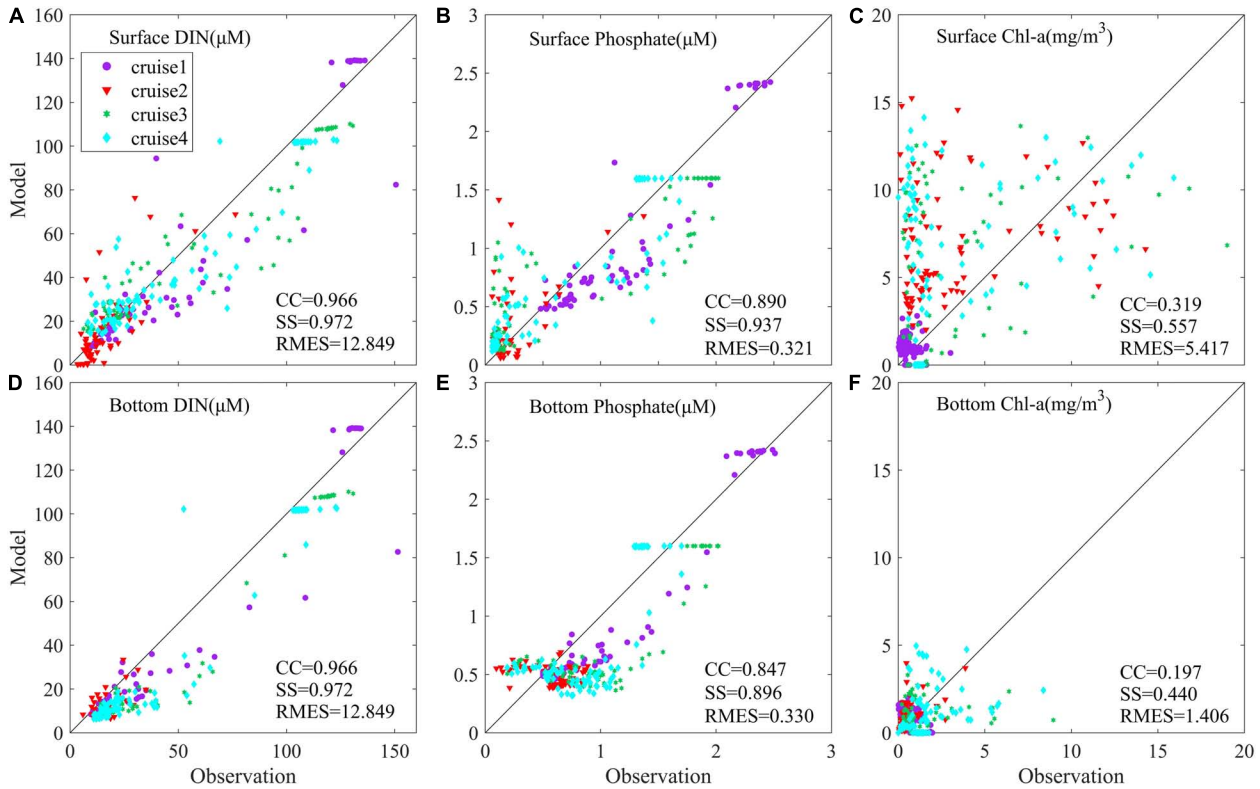


FIGURE 3 | Point-to-point comparison between modeled and observed nutrients and chlorophyll concentration. **(A)** Surface DIN, **(B)** surface phosphate, **(C)** surface chlorophyll concentration, **(D)** bottom DIN, **(E)** bottom phosphate and **(F)** bottom chlorophyll. CC is the correlation coefficient, RMSE is the root mean square error, and SS is the skill score.

Foundation of China, and the latter was conducted by the State Key Laboratory of Estuarine and Coastal Research, East China Normal University. To better quantify the simulated results, the following scatter diagram showed the observed and simulated data in March, May, and July of 2016 with some calculated metrics (**Figure 3**), including the correlation coefficient (CC), skill score (SS), and root mean square error (RMES). The SS (Murphy, 1988) was defined as:

$$SS = 1 - \frac{\sum_{i=1}^{N} (X_m - X_o)^2}{\sum_{i=1}^{N} (X_o - \overline{X_o})^2}, \quad (3)$$

where X_m is the modeled result, X_o is the observed data, $\overline{X_o}$ is the mean of observed data, and N is the number of samples.

The CC of DIN and surface phosphate were above 0.89 and SS was above 0.93, which implied that the nutrients simulation was in good agreement with the observed data (**Figure 3**). In addition, the modeled bottom phosphate concentration was relatively smaller than the observed data. The reason might be that phosphorus released from deposition (Meng et al., 2014) was not considered in the model simulation. The releasing phosphate flux is difficult to estimate in the model due to complicated environmental factors in the bottom layer. The simulated surface chlorophyll concentration was a bit high (**Figure 3C**). Overestimated model results of chlorophyll could be found in the offshore water (as seen in **Figure 2**). Riverine abundant nutrients were depleted and the phytoplankton growth condition became worse in the pelagic offshore water. Hence, the contribution of phytoplankton growth rate on biomass declined, and more other uncertain biological cycling processes took effect, which gave rise to more difficulty in biological parameterization. Given this complexity, an accurate simulation on phytoplankton growth remains a challenge. Nevertheless, the location of low chlorophyll concentration around the river mouth as well as the locations and patterns of surface chlorophyll maximum outside the river mouth were all well captured by the model, which was consistent with the remote sensing data (**Figure 2**). As our focus was on the location where algal bloom occurs, the model is suitable for the present study.

RESULTS

Long-Term Trend of Observed Algal Bloom Distribution

Two sets of observed data, i.e., harmful algal bloom events data and satellite derived chlorophyll, were used to analyze the long-term trend of algal bloom distribution. The harmful algal bloom event data from 2000 to 2010 in the spring season (April to June) showed that algae is likely to bloom along isobaths east and south of the Changjiang River mouth (**Figure 4**). The frequency is increased for the long-term trend, especially in the region

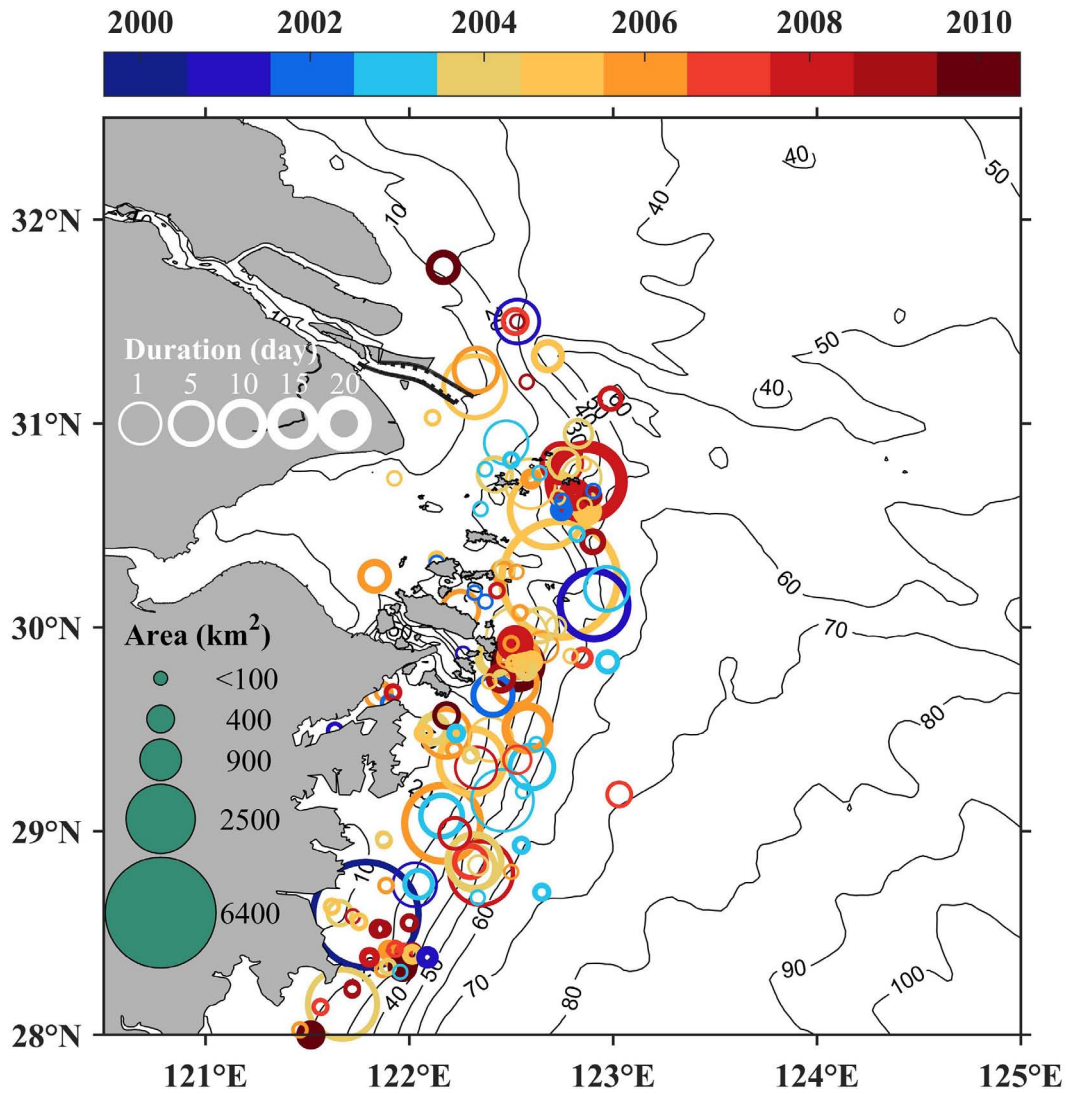


FIGURE 4 | Interannual variations of harmful algal bloom events during 2000 to 2010.

between 30°N and 32°N out of the Changjiang River mouth. Despite of strong randomness and variations, a landward shift trend can be observed with more events occurring in the region between 31°N and 32°N and a seaward shift trend appeared with more events and longer duration in the region between 30°N and 31°N.

The satellite-derived chlorophyll data from SeaWiFS and MODIS-aqua were also analyzed to get the long-term trend. A chlorophyll concentration threshold of 10 mg/m^3 was adopted to calculate the probability of algal bloom in the spring season (from May to June). The result indicated that algae were likely to bloom out of the Changjiang River Estuary along the coast (**Figure 5**). The seaward boundary of high probability was located around 123°E out of the Changjiang River mouth and tended to cling to the coast gradually toward the south. The patchy distribution of high probability (**Figure 5**), especially in the area adjacent the DNC, was in accordance with previous studies on the algal bloom distribution in this area (Zhou et al., 2008; Wang and Wu, 2009; Shen et al., 2011, 2019).

The algal bloom probability increased for the long-term trend in the Changjiang River Estuary region. The probability of algal bloom was rarely larger than 30% from 1998 to 2002. However, after 2002, some patches occurred east of the Changjiang River mouth and Zhoushan Islands where the probabilities were larger than 30%. The high probability area became even larger after 2006. Besides the temporal variation, the probability of algal bloom also had a spatial variation. The probability of algal bloom occurrence in the east and northeast of the Changjiang River mouth had been increased and moved landward especially after 2006 (**Figures 5B,C**). Meanwhile, in the direction of North Passage extension, a frequent algal bloom area was gradually formed after 2006 (**Figures 5B–D**). In the far field of the Changjiang River Estuary, including east and southeast of the Zhoushan Island

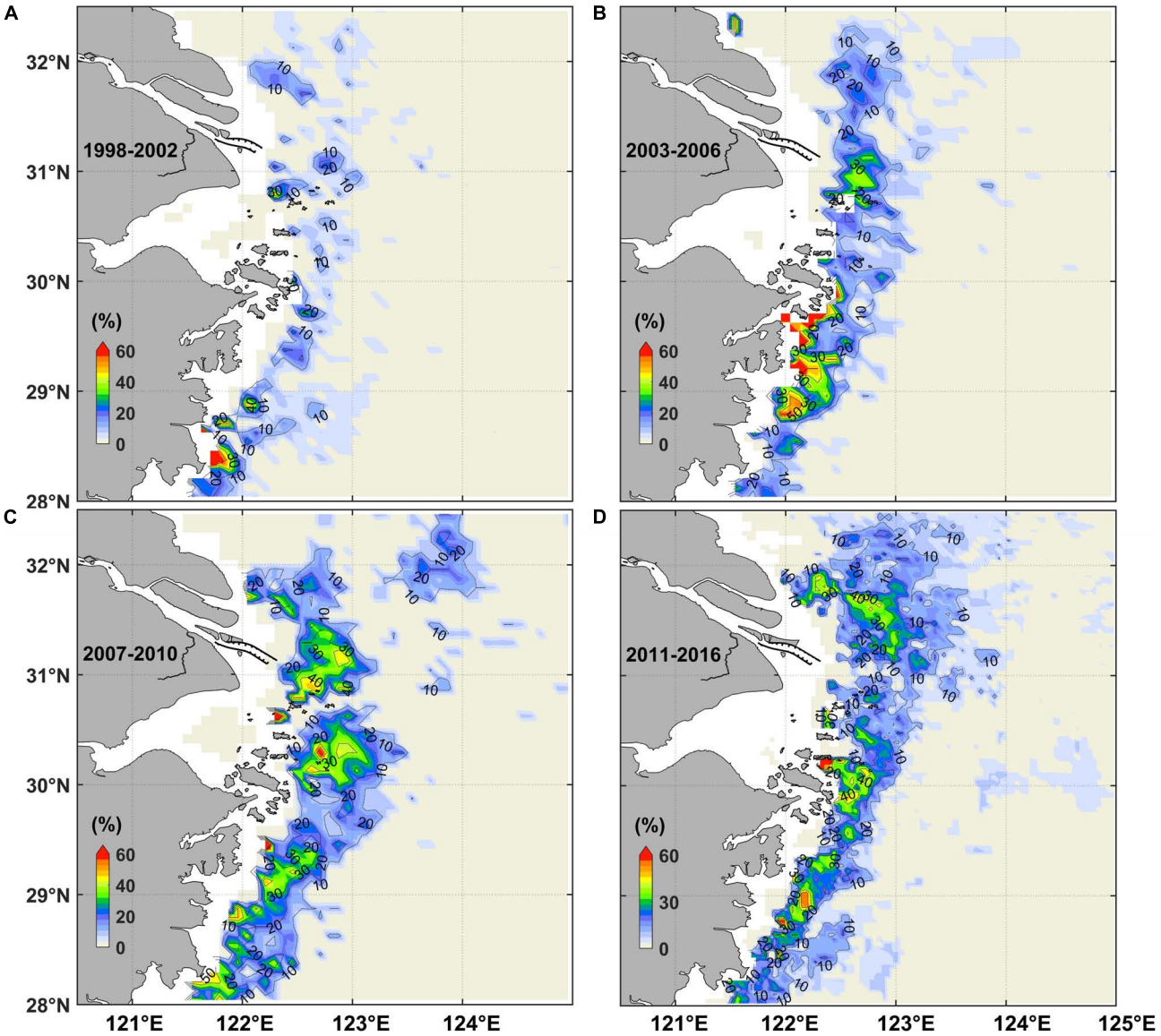


FIGURE 5 | The probability of algal bloom occurrence (the threshold of chlorophyll adopted 10 mg/m^3) based on satellite-derived chlorophyll concentration during **(A)** 1998–2002, **(B)** 2003–2006, **(C)** 2007–2010, **(D)** 2011–2016.

and the Jiangsu coastal water, the region of high probability emerged alternatively.

The long-term variation of satellite-derived chlorophyll showed a significant trend as described above. To characterize the spatiotemporal variation and to identify the influence of human activities, numerical experiments were further conducted.

Horizontal Variations Under the Influence of Mega Estuarine Constructions

Two sets of numerical experiments were conducted to explore the effect of MEC on variations of the phytoplankton spatial distribution and the hydrological and ecological environmental characteristics.

The tidal-averaged results in May 2016 were plotted to analyze their differences. Both model results with and without the MEC demonstrated that the surface chlorophyll maximum is distributed like a long-curved belt with a couple of hotspots some distance from the river mouth (**Figures 6A,B**). However, some subtle differences could be found. It indicated that after the MEC, the surface chlorophyll maximum was attenuated, part of which migrated landward north of the river mouth around 31.5°N. By contrast, south of the river mouth, the surface chlorophyll maximum was strengthened, and some of that extended seaward around 30.5°N (**Figure 6C**). In addition, in the far field of the Changjiang River Estuary, the shape of surface chlorophyll maximum was also slightly adjusted in response to the near-field variation after the MEC was built. These horizontal variation

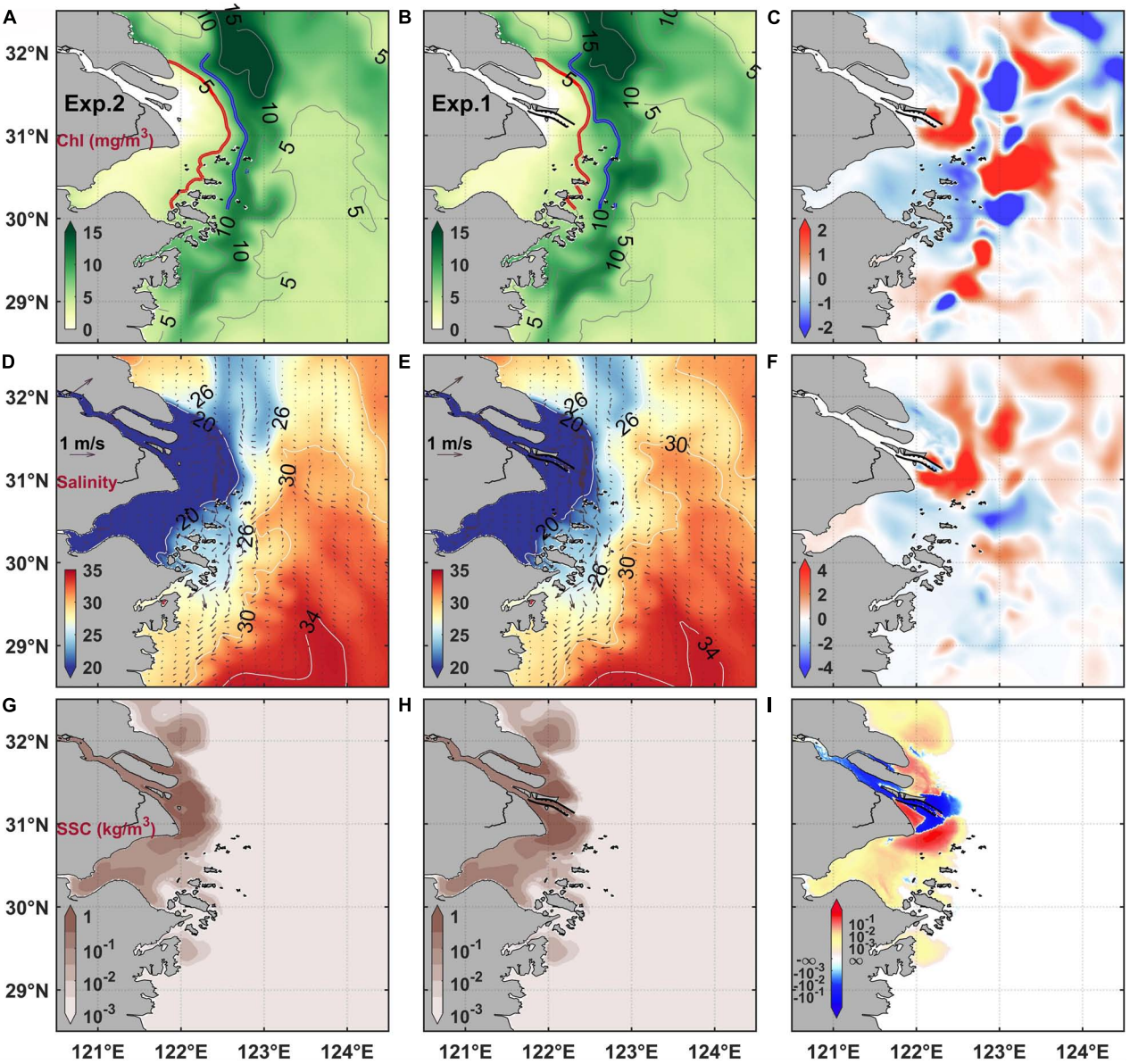


FIGURE 6 | Modeled tide-averaged surface **(A)** chlorophyll concentration (Chl) before the mega estuarine constructions (MEC), **(B)** chlorophyll concentration after the MEC, and **(C)** difference of chlorophyll concentration [**(B)** minus **(A)**]; salinity with residual current overlaid **(D)** before the MEC, **(E)** after the MEC, and **(F)** their difference [**(E)** minus **(D)**]; suspended sediment concentration (SSC) **(G)** before the MEC, **(H)** after the MEC, and **(I)** their difference [**(H)** minus **(G)**].

characteristics under the influence of MEC were similar to the long-term trend of satellite-derived chlorophyll data (**Figure 5**).

To explore the mechanism responsible for chlorophyll distribution variations, more numerical results were analyzed. Salinity manifests the extension of the Changjiang River plume. The numerical results showed that after the MEC, the surface salinity increased northeast to the river mouth and decreased southeast from the Hangzhou Bay to the Zhoushan Island adjacent waters. The variation of salinity distribution indicated that the northeastward extension of the Changjiang River plume was weakened, whereas its southward extension was strengthened (**Figures 6D–F**).

On the other hand, based on the results of numerical experiments, high suspended sediment concentration appeared inside the estuary and around the river mouth area. Remarkable variations of suspended sediment concentration could also be found adjacent to the DNC (**Figures 6G–I**). After the MEC, more suspended sediments were pushed out of the South Passage, whereas the suspended sediment concentration in the North Passage and the North Channel decreased. Notably, the sharp variation of suspended sediment occurred landward of the surface chlorophyll maximum (**Figure 6**).

The results of nutrient variations were also examined. The Changjiang River exported abundant nutrients (including DIN

and phosphate) to the sea, which caused sharp gradient of nutrients in the estuarine area (**Figure 7**). The terrigenous nutrients led to a large N/P ratio outside the estuary (**Figure 7**), which could form a phosphate limiting condition due to phytoplankton consumption. Under the influence of MEC, the surface DIN and phosphate concentration distribution both indicated that the nutrient concentration decreased northeast of the river mouth and increased southeast from the Hangzhou Bay to the Zhoushan Island (**Figure 7**). The results were similar to salinity distribution, which could be referred to the influence of deflection of plume extension. However, under the consumption of phytoplankton in the shelf, the nutrient variations, especially the N/P ratio variations, were highly correlated with the variations of chlorophyll concentration (**Figures 6C**, **7I**) in the surface chlorophyll maximum region.

Vertical Variations Under the Influence of Mega Estuarine Constructions

The model results demonstrated that different variations of plume extension and chlorophyll distributions in response to the MEC could be found in the northern and southern areas off the Changjiang River Estuary, respectively. Hence, two sections were selected to further illustrate the vertical

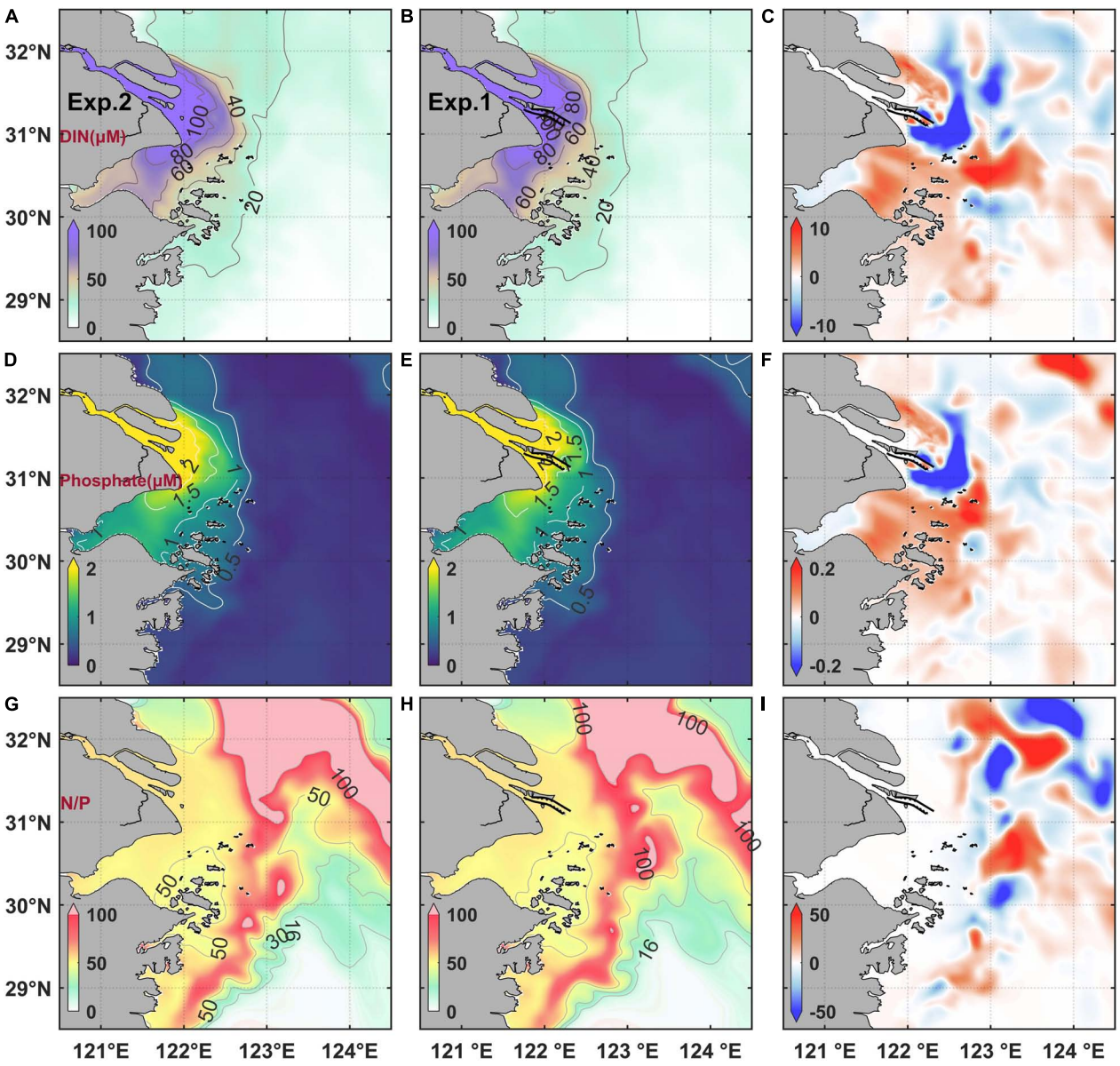


FIGURE 7 | Modeled tidal-averaged surface dissolved inorganic nitrogen concentration (DIN) **(A)** before the MEC, **(B)** after the MEC, and **(C)** their difference [**(B)** minus **(A)**]; phosphate concentration **(D)** before the MEC, **(E)** after the MEC, and **(F)** their difference [**(E)** minus **(D)**]. N/P ratio **(G)** before the MEC, **(H)** after the MEC, and **(I)** their difference [**(H)** minus **(G)**].

profiles. Sec1 and Sec2 were along the northeastward and southeastward extending direction of the Changjiang River plume, respectively (for location, see **Figure 1A**). The chlorophyll concentration, salinity, suspended sediment concentration, nutrients concentration, and euphotic depth were displayed on both sections (**Figures 8**, **9**). The euphotic depth is the layer in the water column where the sea surface light intensity attenuates to 1% (Strickland, 1958; Ralph et al., 2007). In the estuary region, the euphotic depth is mainly influenced by the suspended sediments.

Northeast to the Changjiang River Estuary, along the Sec1, the intensity of chlorophyll maximum decreased and a landward moving trend of high chlorophyll maximum emerged with a distance of ∼ 5 km after the MEC (**Figure 8A**). Similar landward moving trends of low salinity and high suspended sediment concentration were found (**Figures 8C,E**). The euphotic depth near the river mouth deepened (**Figure 8A**). Hence, after the MEC, the northeastern Changjiang River plume extension was weakened and light conditions for phytoplankton growth improved. The DIN and phosphate concentration inside the river mouth also decreased after the MEC due to the weakened river plume extension (**Figures 8B,D**). However, in the shelf region, the nutrients varied complicatedly due to superimposed biological cycling (**Figures 8B,D**).

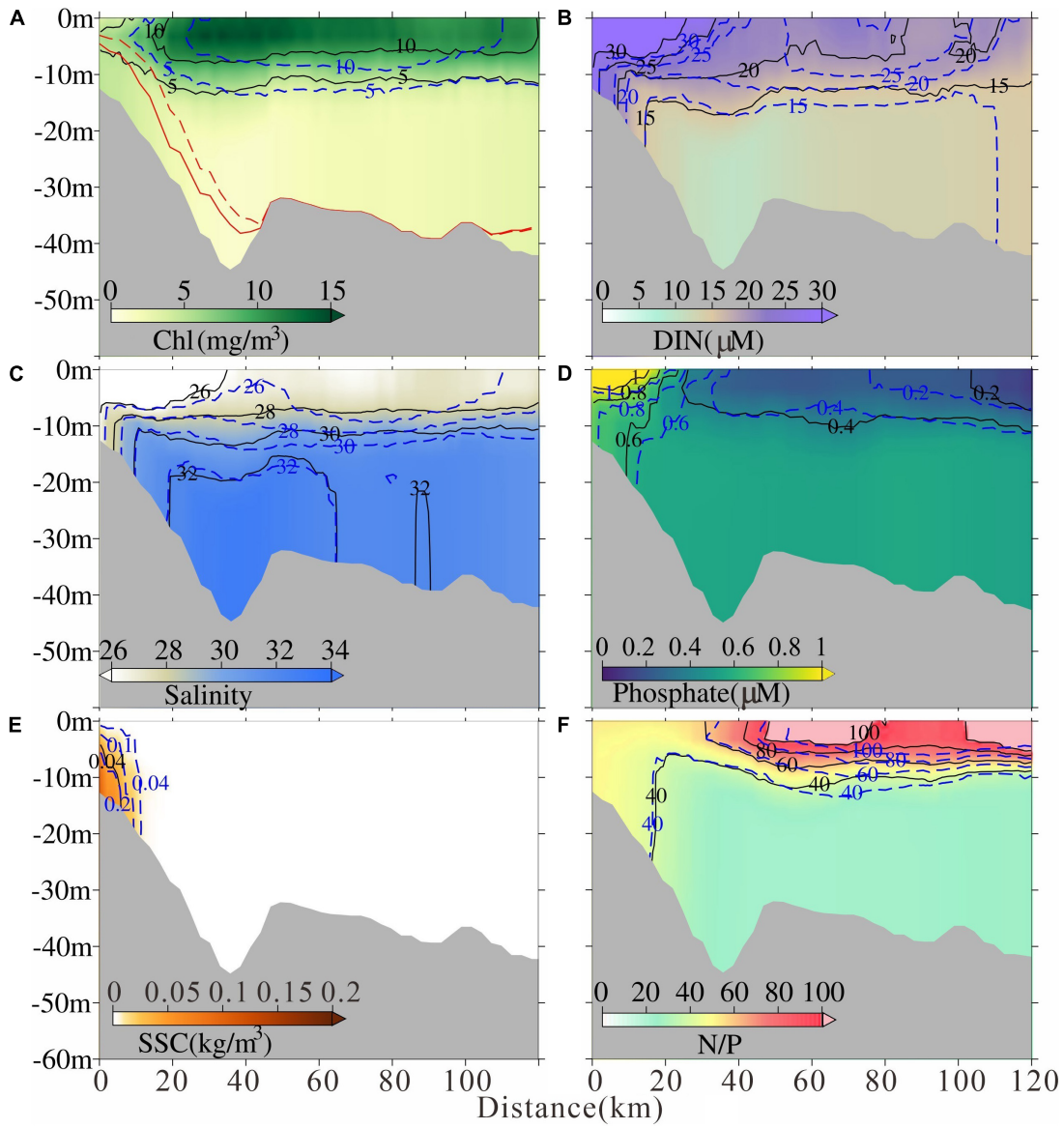


FIGURE 8 | Modeled tidal-averaged **(A)** chlorophyll concentration, **(B)** dissolved inorganic nitrogen concentration, **(C)** salinity, **(D)** phosphate, **(E)**suspended sediment concentration, and **(F)** N/P ratio in Sec1 after the MEC. The solid lines indicate the contour after the MEC and the dashed lines indicate the contour before the MEC, respectively. Euphotic depth was also marked in **(A)** with red lines.

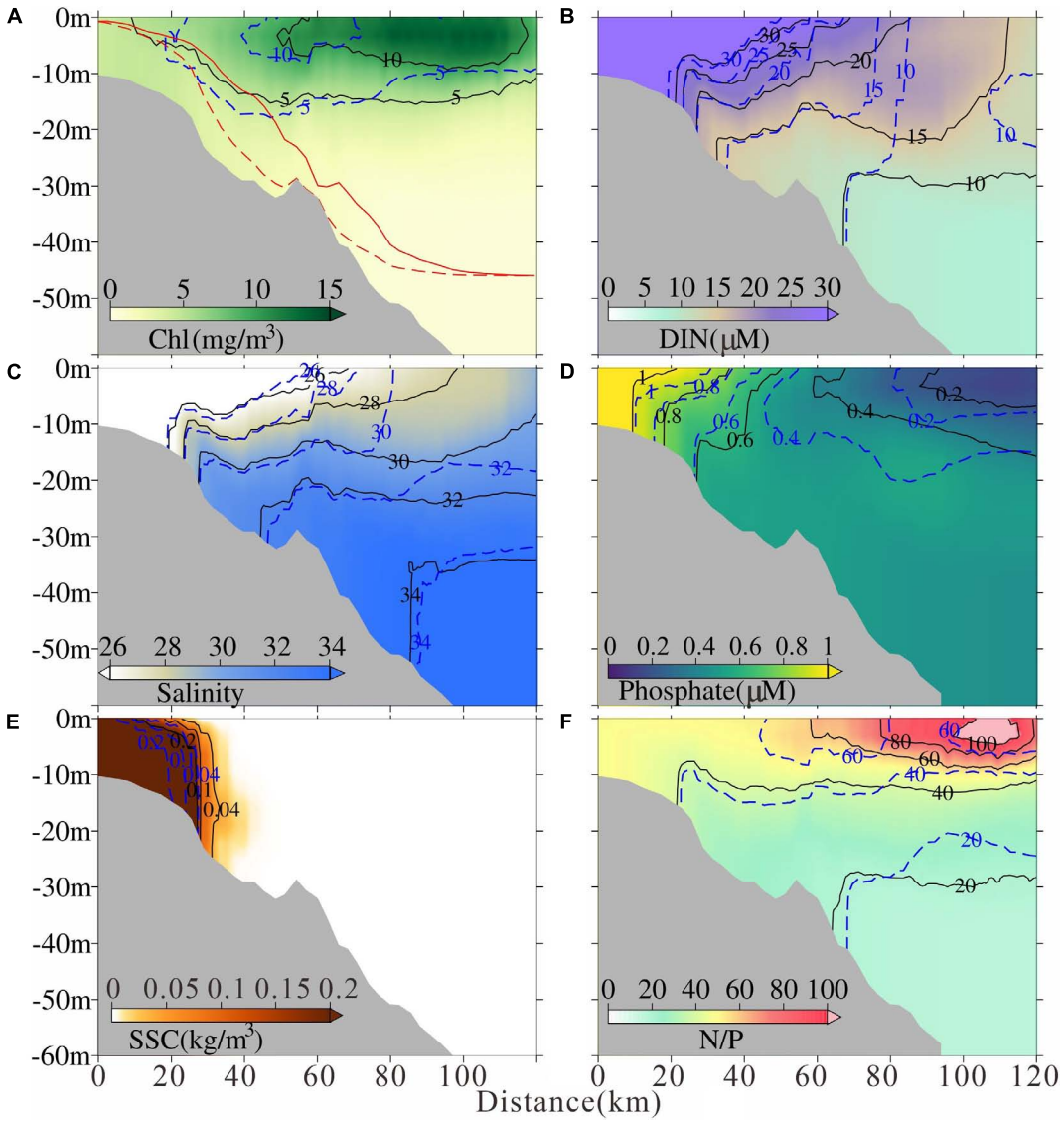


FIGURE 9 | Modeled tidal-averaged **(A)** chlorophyll concentration, **(B)** dissolved inorganic nitrogen concentration, **(C)** salinity, **(D)** phosphate, **(E)** suspended sediment concentration, and **(F)** N/P ratio in Sec2 after the MEC. The solid lines indicate the contour after the MEC and the dashed lines indicate the contour before the MEC, respectively. Euphotic depth was also marked in **(A)** with red lines.

By contrast, along Sec2, the 5 mg/m^3 contour of chlorophyll concentration moved landward, and the 10 mg/m^3 contour moved seaward after the MEC (**Figure 9A**). A seaward moving trend of low salinity and high suspended sediment concentration occurred (**Figures 9C,E**). The euphotic depth near the river mouth shoaled (**Figure 9A**). Previous study indicated that the southward Changjiang River plume extension was strengthened under the effect of MEC (Wu et al., 2018). Along Sec2, the DIN and phosphate concentration inside the river mouth also increased after the MEC due to the strengthened river plume extension (**Figures 9B,D**). The increasing trend could be found in the DIN concentration in the shelf region, while the phosphate concentration decreased (**Figures 9B,D**). The nutrient variation corresponded to the chlorophyll and plume variations based on the phosphate limiting condition in this area. The specific mechanism will be explored and discussed in the next section.

DISCUSSION

Effect of the Mega Estuarine Constructions-Induced Nutrient Distribution Variation

The numerical results indicated that, after the MEC, the intensity of surface chlorophyll maximum was weakened and the hotspot moved landward northeast of the Changjiang River Estuary, whereas it migrated seaward south of the river mouth. The

high chlorophyll concentration patches in the far field of the river plume were also modulated under the influence of MEC (**Figures 6**, **8**, **9**). The variation of chlorophyll distribution largely matched the long-term spatial variation trend of satellite-derived algal bloom probability (**Figure 5**), which indicated the influence of MEC on the variation of phytoplankton distribution. The underlying mechanisms were discussed as follows.

The numerical results of surface salinity indicated that, after the MEC, the river plume extension to the northeast was weakened, while that to the south was strengthened. Wu et al. (2018) suggested that the construction of these mega constructions block the lateral tide-induced residual transport among three estuarine outlets, and thus regulate the water diversion ratio between the North Channel and the South Channel. This modulation consequently strengthens the southward plume extension but weakens the northeastward one. The Changjiang River load is the dominant nutrient source in the estuarine area, especially in the river mouth region. Many studies have focused on the response of variation of riverine nutritional load on the phytoplankton species and abundance (Zhou et al., 2017; Ge et al., 2020; Xu et al., 2020). We believe that the modulation of plume structure could also induce the regulation of nutrient distribution, thus ultimately resulting in the variation of phytoplankton distribution.

The simulated results of nutrients revealed that under the modulation of plume extension, the DIN and phosphate concentration decreased northeast of the river mouth and increased south of the river mouth after the MEC. The adjustment of nutrient supplement caused the corresponding variant condition of phytoplankton growth and led to the variation of chlorophyll concentration. However, due to the consumption of phytoplankton and the potential phosphate limiting condition (Huang et al., 2007; Yang et al., 2013), the nutrient concentration further varied in the shelf region. The DIN concentration decreased and the phosphate concentration increased in the northeast, whereas the DIN concentration increased and the phosphate concentration decreased in the south. The sustenance of phytoplankton biomass relied on the biological recycling in the shelf region (Wang et al., 2019a). Hence, the far-field modulation of chlorophyll maximum alternatively occurred under this effect.

Effect of the Mega Estuarine Constructions-Induced Suspended Sediment Concentration Variation

The numerical results of suspended sediments indicated that the suspended sediment concentration decreased northeast of

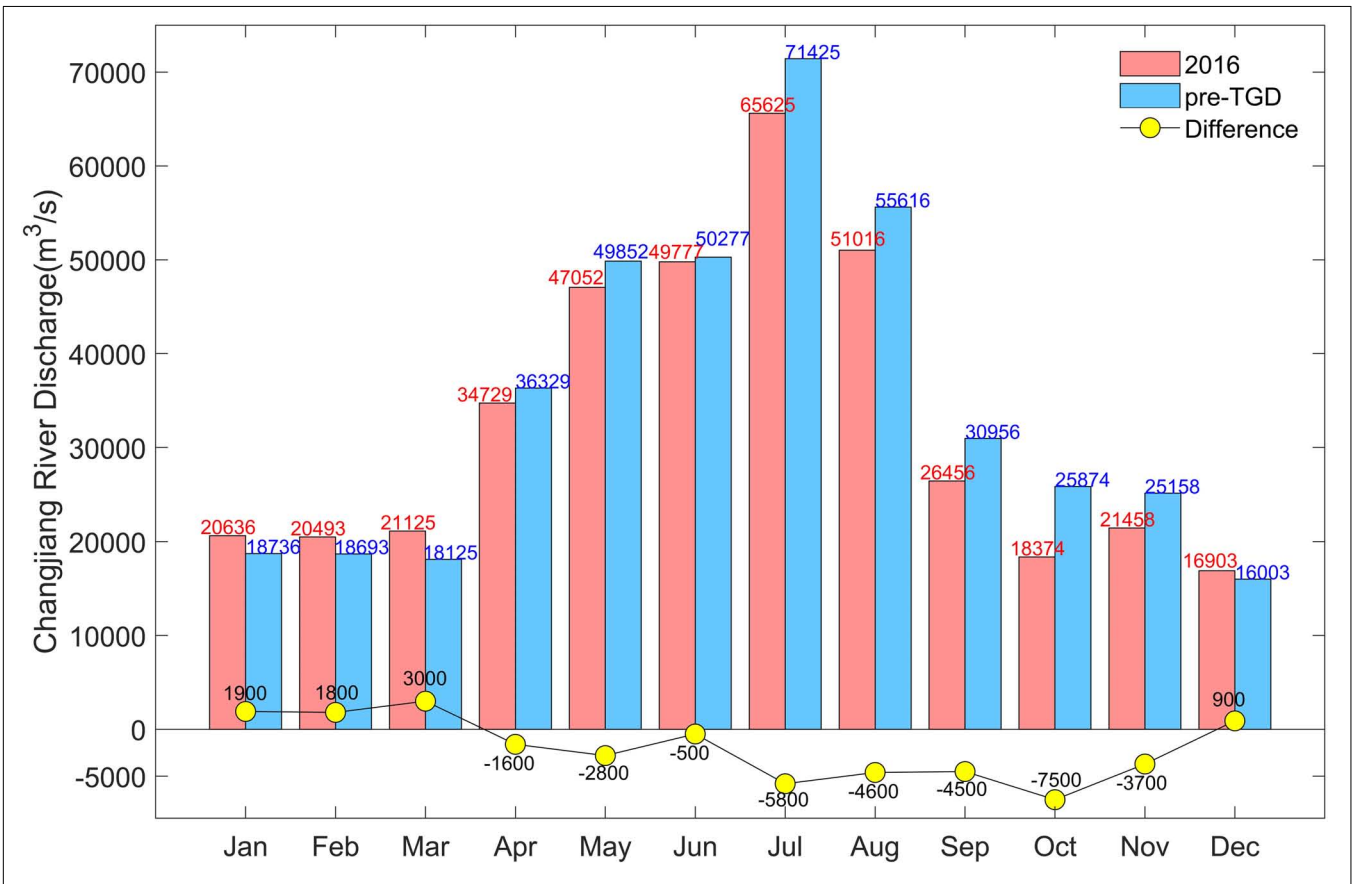


FIGURE 10 | Monthly Changjiang River discharges in 1950–2002 (before the TGD period, blue pillars) and in 2003–2015 (after TGD period, red pillars), respectively, and the yellow dots indicate the difference (red pillars minus blue pillars).

the river mouth and increased south of the river mouth after the MEC. The changed suspended sediment concentration regulated the turbidity distribution, which has a significant influence on the phytoplankton growth in the estuarine area (Kromkamp and Peene, 1995; Horemans et al., 2020). Zhu et al. (2009) demonstrated that high turbidity restrained the phytoplankton growth at the Changjiang River mouth, and a good correlation between turbidity and phytoplankton biomass can be established through seasonal field observations adjacent to the Changjiang River Estuary. Wang et al. (2019a) argued that the turbidity front could be the inner boundary of the surface phytoplankton maximum region under the plume regulating mechanisms. These are reasons we believe that the suspended sediment redistribution induced by the constructions of mega projects could adjust the light condition of phytoplankton growth.

The dynamic mechanisms of why the suspended sediments concentration distribution was changed were beyond the focus of this study; hence, readers are referred to previous studies (e.g., Zhu L. et al., 2016; Xie et al., 2017; Teng et al., 2021). Basically, it is a consequence of the change of currents. Our simulated results of euphotic depth exhibited the variations at the river mouth under the MEC. The euphotic depth deepened northeast of the river mouth and shoaled south of the river mouth. In addition, the corresponding chlorophyll variation was also coupled with the variation of light condition (**Figures 8A**, **9A**). However, it is notable that the numerical results of suspended sediment variations occurred mainly at the river mouth. Therefore, the

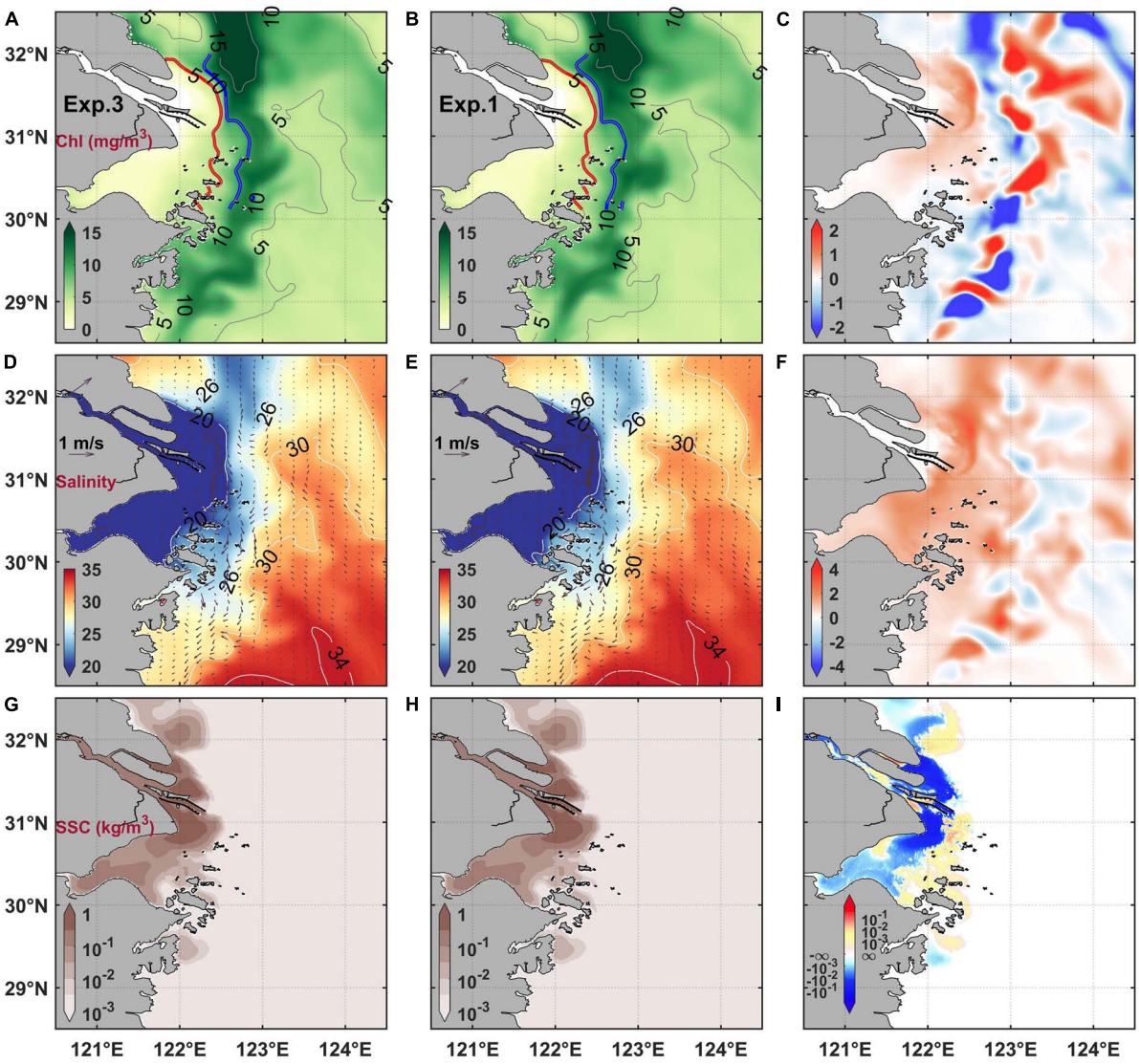


FIGURE 11 | Changes of chlorophyll concentration **(A–C)**, salinity **(D–F)**, and suspended sediment concentration **(G–I)** under the TGD-induced discharge change. The left column **(A,D,G)** are results with discharge subtracting the TGD influence (i.e., Exp. 3), the middle column **(B,E,H)** are results with realistic discharge (i.e., Exp. 1), and the right column are their difference (Exp. 1 minus Exp. 3).

modulation of plume structure and adjustment of nutrient condition should play a more important role in the variation of chlorophyll concentration on the shelf.

Besides the alternation of the growth environment of phytoplankton, the regulation of hydrodynamics could also induce the redistribution of phytoplankton. One representative hydrodynamic feature is the front. Previous studies suggested that algal blooms are prone to emerge in the front region (Franks, 1992; Tang et al., 2003). Phytoplankton blooms are often associated with fronts not only because of the optimal growth environment but also since hydrodynamics transport phytoplankton horizontally and aggregates phytoplankton in the front region (Tang et al., 2006; Wang et al., 2019b; Li et al., 2021). After the MEC, the plume structure was modulated, and the front region should also be dislocated. The simulated results showed that the front of the river plume migrated landward in the northeastward extension and moved seaward in the southward extension. It could also be one reason for the modulation of chlorophyll distribution.

Effect of the Three Gorges Dam-Induced Freshwater and Sediment Flux Variations

The well-known TGD was closed in 2003, hence, it is reasonable to infer that this huge riverine project could also influence the dynamics and environment in the estuary. In fact, previous studies often attributed many observed phenomena around the estuary to the influence of TGD (Chen et al., 2012). The MEC was constructed in a similar period as the TGD, hence, it is questionable to simply draw a conclusion that the observed changes must be a result of the TGD.

To clarify their relative significance, extra numerical experiments were conducted regarding the effect of the TGD. The first one was configured by altering the river discharge (Exp. 3 in **Table 1**), while the second one was set up by altering both the water discharge and sediment discharge (Exp. 4 in **Table 1**). The TGD-induced river runoff change was quantified with the method of Wu et al. (2018). The runoff difference was calculated by subtracting the monthly discharge in the period before the TGD construction (1950–2002) from the monthly river discharge since then (2003–2016) (**Figure 10**). Then, this difference was added to the realistic runoff in 2016. It was noted that after the completion of the TGD, the monthly discharge change increased from December to March (most notably in March, with an increase of ~3,000 m^3/s), whereas, it decreased from April to November. It was reported that after the TGD, the sediment flux was reduced from ~4.1 × 10^8 tons/year to ~1.2 × 10^8 tons/year (Yang et al., 2015). The TGD-induced sediment flux change was considered in Exp. 4. The upstream sediment flux in Exp. 4 is three times of that in Exp. 3.

The results of numerical experiments revealed that the surface chlorophyll maximum also migrated landward under the effect of TGD (**Figures 11A–C**), which was similar to the consequence of the MEC (**Figure 6C**). However, their differences were that the chlorophyll maximum on the southward

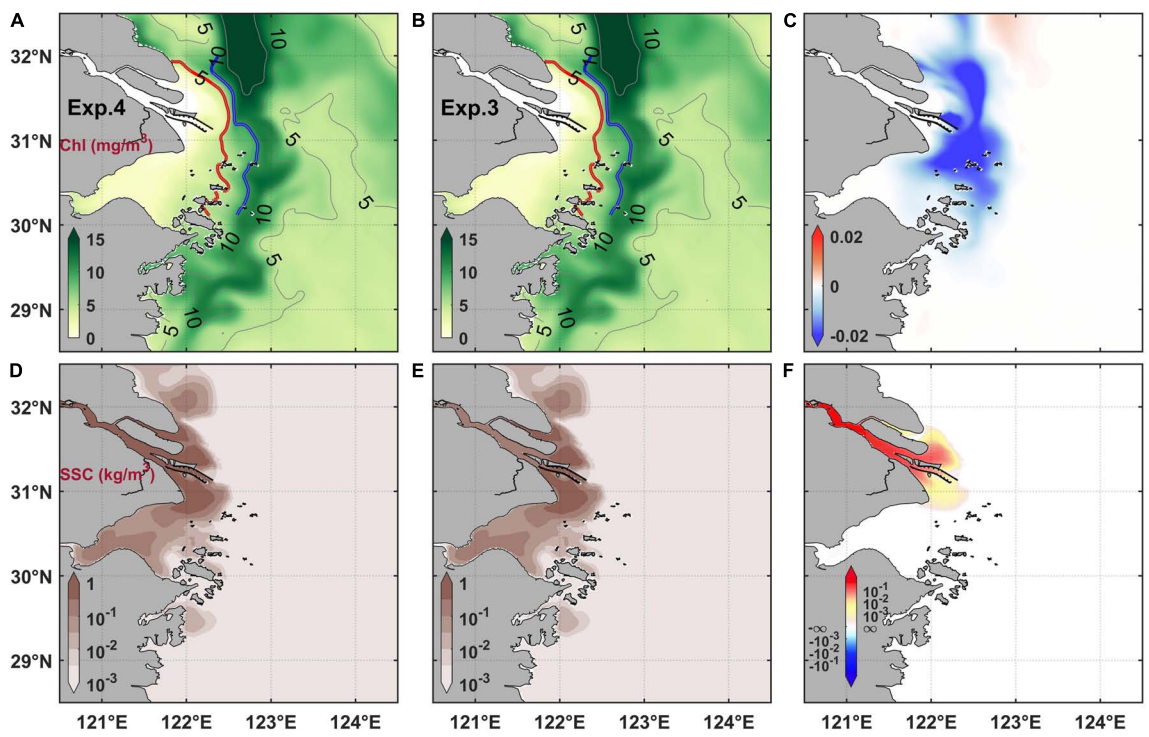


FIGURE 12 | Changes of chlorophyll concentration **(A–C)** and suspended sediment concentration **(D–F)** under the TGD-induced sediments flux change. The left column **(A,D)** are results with pre-TGD sediments flux (i.e. Exp. 4), the middle column **(B,E)** are results with post-TGD sediments flux (i.e. Exp. 3), and the right column are their difference (Exp. 4 minus Exp. 3).

plume branch also migrated landward after the TGD. On the other hand, the chlorophyll maximum area expanded landward both in the northeast and south parts of the estuary after the TGD (**Figure 11C**). Nevertheless, it should be emphasized that the TGD-induced variation was weaker than that due to the MEC (**Figures 6C**, **11C**). The surface salinity slightly increased and suspended sediment concentration decreased in the Changjiang River Estuary and its adjacent water after the TGD if only considering the change of runoff (**Figures 11D–I**). Even considering the change of sediment flux caused by the TGD (Exp. 4), the chlorophyll concentration in the Changjiang River Estuary was still only slightly affected (**Figure 12**). The chlorophyll differences with Exp. 4 minus Exp. 3 were 2 orders of magnitude less than the differences with Exp. 1 minus Exp. 3.

Some previous studies suggested that the decrease of watershed sediment flux induced by TGD has caused a decline of suspended sediment concentration in the Changjiang River Estuary (Hu et al., 2009; Li et al., 2012; Yang et al., 2015). However, some others demonstrated that there is still a deposition tendency in the delta area though the numerous watershed constructions have been built (Dai et al., 2014; Zhu L. et al., 2016). The long and short-term influences of TGD and other riverine constructions on the estuary are uncertain with controversy and is beyond the focus of this study. Here in this study, we only simplify the influence of TGD on the variations of the freshwater amount and watershed sediment flux. The subsequent transformation of bed sediment load is out of consideration. The long-term influence of TGD on the sediment variation in the estuary and the further influence on the ecosystem still need more exploration.

Nevertheless, our model results demonstrated that even the load of runoff and sediment flux changed significantly after the TGD, their influence on the plume diversion and suspended sediments concentration might not be seen immediately. Hence, the influence on the spatial phytoplankton variation could be less significant than expected.

Limitations

Based on the long-term trend of satellite-derived chlorophyll data and numerical modeling, we discussed the potential effects of engineering constructions. However, in such a complex circumstance, the mechanisms controlling the phytoplankton distribution and its interannual variation are far more complex.

The growth and distribution of phytoplankton in the estuaries are mainly affected by ecological and hydrodynamic factors such as nutrient, temperature, turbidity, and current. The variation of the estuarine ecological environment and hydrodynamics is determined by riverine and oceanic processes and sources, which are complicatedly influenced by climatic variation and anthropogenic factors. For riverine factors, previous studies have demonstrated that the variation of nutrient load and component has regulated the phytoplankton species and biomass in the Changjiang River Estuary (Tang et al., 2006; Zhou et al., 2019; Xu et al., 2020). The nitrogen and phosphorous concentrations and their ratio (N/P) in the persistent riverine load increased for a few decades, but silicon level remained constant (Jiang et al., 2014), which caused an alternation of dominant phytoplankton species from diatom to dinoflagellate and a significant biomass increase trend that is sustained in the East China Sea (Zhou et al., 2017; Ge et al., 2020). Regarding oceanic factors, for instance, Yang et al. (2013) suggested that the nutrient supplement induced by Kuroshio subsurface water intrusion partially influences the phytoplankton uptake and the distribution of primary production adjacent to the Changjiang River Estuary. Jiang et al. (2014) suggested that the variations of the summer phytoplankton community are highly related to the spatiotemporal variability in physiochemical properties that are controlled by the Taiwan Warm Current, which is the continuation of the Kuroshio intrusion on the shelf. It is reported that the intensity of the Kuroshio intrusion is also influenced by El Niño-Southern Oscillation and Pacific Decadal Oscillation (Qiu and Lukas, 1996; Wu, 2013), which has obvious interannual characteristics. The resultant interannual variation of sea surface temperature should also result in the response of phytoplankton growth (He et al., 2013).

Nevertheless, although this work can not completely answer the question of a long-term trend of phytoplankton variation in the Changjiang River Estuary, it highlighted the important influence of the MEC, which has been largely overlooked previously. The scale of estuarine projects will further expand in the foreseeable future. Hence, the result of this study reminds us to be very cautious about their potential consequences. More estuaries around the world are constructed with large-scale projects, and our study could provide a reference for other estuaries that also have mega constructions.

SUMMARY

Through analyzing the harmful algal bloom events data from bulletins during 2000–2010 and the spatiotemporal probability of algal blooms derived from chlorophyll remote sensing data from 1998 to 2016, we investigated the long-term trend of algal bloom distribution in the Changjiang River Estuary and its adjacent water. The results showed that the frequency of algal blooms east and northeast of the Changjiang River mouth had been increased and the high-value region moved landward gradually after 2003. Then, by using the model simulation, we explored the mechanisms of this variation before and after the MEC.

After the MEC, the river plume extensions were deflected, which is one main reason for the regulation of environmental elements distribution and high chlorophyll concentration area. Northeast to the river mouth, the terrigenous nutrients export declined, the suspended sediment concentration decreased, and, consequently, the high chlorophyll concentration area moved landward after the MEC due to the weakening of northward river plume extension. In contrast, the southward river plume extension was enhanced, carrying more riverine nutrients to the vicinity of the Zhoushan Islands, thus the corresponding algal bloom hotspots moved seaward.

The impact of the TGD on the phytoplankton distribution outside the Changjiang River Estuary was also discussed through numerical experiments. The variations of the freshwater amount and sediment discharge due to TGD constructions were considered in the experiments. The results indicated that the

river plume extension in the algal blooming season weakened, suspended sediment concentration decreased, and the high chlorophyll area integrally moved landward after the TGD, but these effects were less significant than that induced by the MEC.

Given the interaction of the above identified and unidentified processes, the phytoplankton distribution and its interannual variation in the estuarine area could be far more complex. Here in this study, we highlighted the influence of MEC on phytoplankton distribution, which could provide a new aspect on the long-term regulation of algal bloom in the coastal and estuarine area.

DATA AVAILABILITY STATEMENT

The raw data supporting the conclusions of this article will be made available by the authors, without undue reservation.

AUTHOR CONTRIBUTIONS

HW and YW designed the research and revised the manuscript. YH collected the remote sensing data, conducted the numerical experiments, and wrote an original draft of the manuscript. YH and YW analyzed the results. All authors contributed to the article and approved the submitted version.

FUNDING

This study was jointly supported by the project supported by the Innovation Program of Shanghai Municipal Education Commission (Grant No. 2021-01-07-00-08-E00102), the National Natural Science Foundation of China (Grant No. 42106162), Scientific Research Project of Shanghai Municipal Oceanic Bureau (Grant No. Huhaike-202105), and the Innovation Group Project of Southern Marine Science and Engineering Guangdong Laboratory (Zhuhai) (Grant No. 311020003).

ACKNOWLEDGMENTS

The sea surface wind and heat flux data obtained from European Centre for Medium-Range Weather Forecasts (ECMWF) are available at http://apps.ecmwf.int/datasets/. Initial and open ocean boundary conditions were derived from SODA at http://iridl.ldeo.columbia.edu/SOURCES/.CARTON-GIESE/.SODA/.v2p0p2-4/. The satellite-derived surface chlorophyll concentration data were obtained from the NASA Moderate Resolution Imaging Spectroradiometer (MODIS) and the Sea-viewing Wide Field-of-view Sensor (SeaWiFS) daily products at http://oceancolor.gsfc.nasa.gov/. And the instantaneous Geo-stationary Ocean Color Imager (GOCI) data and GOCI data processing system were obtained at http://kosc.kiost.ac.kr/.

SUPPLEMENTARY MATERIAL

The Supplementary Material for this article can be found online at: https://www.frontiersin.org/articles/10.3389/fmars.2021.791956/full#supplementary-material

REFERENCES

Anderson, D. M., Glibert, P. M., and Burkholder, J. M. (2002). Harmful algal blooms and eutrophication: nutrient sources, composition, and consequences. *Estuaries* 25, 704–726. doi: 10.1007/Bf02804901

Bargu, S., Justic, D., White, J. R., Lane, R., Day, J., Paerl, H., et al. (2019). Mississippi River diversions and phytoplankton dynamics in deltaic Gulf of Mexico estuaries: a review. *Estuar. Coast. Shelf Sci.* 221, 39–52. doi: 10.1016/j.ecss.2019.02.020

Boesch, D. F. (2019). Barriers and bridges in abating coastal eutrophication. *Front. Mar. Sci.* 6:123. doi: 10.3389/fmars.2019.00123

Caffrey, J. M., Cloern, J. E., and Grenz, C. (1998). Changes in production and respiration during a spring phytoplankton bloom in San Francisco Bay, California, USA:implications for net ecosystem metabolism. *Mar. Ecol. Prog. Ser.* 172:1998. doi: 10.3354/meps172001

Chai, C., Yu, Z., Shen, Z., Song, X., Cao, X., and Yao, Y. (2009). Nutrient characteristics in the Yangtze River Estuary and the adjacent East China Sea before and after impoundment of the Three Gorges Dam. *Sci. Total Environ.* 407, 4687–4695. doi: 10.1016/j.scitotenv.2009.05.011

Chai, C., Yu, Z., Song, X., and Cao, X. (2006). The status and characteristics of eutrophication in the Yangtze River (Changjiang) Estuary and the adjacent East China Sea, China. *Hydrobiologia* 563, 313–328. doi: 10.1007/s10750-006-0021-7

Chen, C., Cowles, G., and Beardsley, R. C. (2006). *An Unstructured Grid, Finite-Volume Coastal Ocean Model: FVCOM User Manual*, 2nd Edn. New Bedford, MA: School for Marine Science and Technology, University of Massachusetts Dartmouth, 315.

Chen, C. S., Zhu, J. R., Beardsley, R. C., and Franks, P. J. S. (2003). Physical-biological sources for dense algal blooms near the Changjiang river. *Geophys. Res. Lett.* 30, 405–414. doi: 10.1029/2002GL016391

Chen, J. Y., Pan, D. L., Liu, M. L., Mao, Z. H., Zhu, Q. K., Chen, N. H., et al. (2017). Relationships between long-term trend of satellite-derived chlorophyll-a and hypoxia off the Changjiang Estuary. *Estuar. Coasts* 40, 1055–1065. doi: 10.1007/s12237-016-0203-0

Chen, Y., Liu, R., Sun, C., Zhang, P., Feng, C., and Shen, Z. (2012). Spatial and temporal variations in nitrogen and phosphorous nutrients in the Yangtze River Estuary. *Mar. Pollut. Bull.* 64, 2083–2089. doi: 10.1016/j.marpolbul.2012.07.020

Cui, T. W., Zhang, J., Wang, K., Wei, J. W., Mu, B., Ma, Y., et al. (2020). Remote sensing of chlorophyll a concentration in turbid coastal waters based on a global optical water classification system. *ISPRS J. Photogramm. Remote Sens.* 163, 187–201. doi: 10.1016/j.isprsjprs.2020.02.017

Dai, Z. J., Liu, J. T., Wei, W., and Chen, J. Y. (2014). Detection of the Three Gorges Dam influence on the Changjiang (Yangtze River) submerged delta. *Sci. Rep.* 4:6600. doi: 10.1038/srep06600

Fan, W., and Song, J. B. (2014). A numerical study of the seasonal variations of nutrients in the Changjiang River estuary and its adjacent sea area. *Ecol. Modell.* 291, 69–81. doi: 10.1016/j.ecolmodel.2014.07.026

Franks, P. J. S. (1992). Phytoplankton blooms at fronts: patterns, scales, and physical forcing mechanisms. *Rev. Aquat. Sci.* 6, 121–137.

Gao, L., Li, D. J., and Zhang, Y. W. (2012). Nutrients and particulate organic matter discharged by the Changjiang (Yangtze River): seasonal variations and temporal trends. *J. Geophys. Res.* 117:G04001. doi: 10.1029/2012JG001952

Gao, X., and Song, J. (2005). Phytoplankton distributions and their relationship with the environment in the Changjiang Estuary, China. *Mar. Pollut. Bull.* 50, 327–335. doi: 10.1016/j.marpolbul.2004.11.004

Garvine, R. W. (2001). The impact of model configuration in studies of buoyant coastal discharge. *J. Mar. Res.* 59, 193–225. doi: 10.1357/002224001762882637

Ge, J. Z., Shi, S. Y., Liu, J., Xu, Y., Chen, C. S., Bellerby, R., et al. (2020). Interannual variabilities of nutrients and phytoplankton off the Changjiang Estuary in

response to changing river inputs. *J. Geophys. Res. Oceans* 125:e2019JC015595. doi: 10.1029/2019JC015595

He, X. Q., Bai, Y., Pan, D. L., Chen, C. T. A., Cheng, Q., Wang, D. F., et al. (2013). Satellite views of the seasonal and interannual variability of phytoplankton blooms in the eastern China seas over the past 14 yr (1998–2011). *Biogeosciences* 10, 4721–4739. doi: 10.5194/bg-10-4721-2013

Horemans, D. M. L., Meire, P., and Cox, T. J. S. (2020). The impact of temporal variability in light-climate on time-averaged primary production and a phytoplankton bloom in a well-mixed estuary. *Ecol. Modell.* 436:109287. doi: 10.1016/j.ecolmodel.2020.109287

Hu, B. Q., Yang, Z. S., Wang, H. J., Sun, X. X., and Bi, N. S. (2009). Sedimentation in the Three Gorges Dam and its impact on the sediment flux from the Changjiang (Yangtze river), china. *Hydrol. Earth Syst. Sci. Discuss.* 6, 5177–5204. doi: 10.5194/hessd-6-5177-2009

Hu, C. M. (2009). A novel ocean color index to detect floating algae in the global oceans. *Remote Sens. Environ.* 113, 2118–2129. doi: 10.1016/j.rse.2009.05.012

Huang, B. Q., Ou, L. J., Wang, X. L., Huo, W. Y., Li, R. X., Hong, H. S., et al. (2007). Alkaline phosphatase activity of phytoplankton in East China Sea coastal waters with frequent harmful algal bloom occurrences. *Aquat. Microb. Ecol.* 49, 195–206. doi: 10.3354/ame01135

Humborg, C., Ittekkot, V., Cociasu, A., and VonBodungen, B. (1997). Effect of Danube River dam on Black Sea biogeochemistry and ecosystem structure. *Nature* 386, 385–388. doi: 10.1038/386385a0

Jiang, Z. B., Liu, J. J., Chen, J. F., Chen, Q. Z., Yan, X. J., Xuan, J. L., et al. (2014). Responses of summer phytoplankton community to drastic environmental changes in the Changjiang (Yangtze River) estuary during the past 50 years. *Water Res.* 54, 1–11. doi: 10.1016/j.watres.2014.01.032

Jiao, N., Zhang, Y., Zeng, Y., Gardner, W. D., Mishonov, A. V., Richardson, M. J., et al. (2007). Ecological anomalies in the East China Sea: impacts of the Three Gorges Dam? *Water Res.* 41, 1287–1293. doi: 10.1016/j.watres.2006.11.053

Kromkamp, J. C., and Peene, J. (1995). Possibility of net phytoplankton primary production in the turbid Schelde Estuary (SW Netherlands). *Mar. Ecol. Prog. Ser.* 121, 249–259. doi: 10.3354/meps121249

Le, C. F., Hu, C. M., Cannizzaro, J., English, D., Muller-Karger, F., and Lee, Z. (2013). Evaluation of chlorophyll-a remote sensing algorithms for an optically complex estuary. *Remote Sens. Environ.* 129, 75–89. doi: 10.1016/j.rse.2012.11.001

Li, D., Zhang, J., Huang, D., Wu, Y., and Liang, J. (2002). Oxygen depletion off the Changjiang (Yangtze River) estuary. *Sci. China Ser. D Earth Sci.* 45, 1137–1146.

Li, J., and Zhang, C. (1998). Sediment resuspension and implications for turbidity maximum in the Changjiang Estuary. *Mar. Geol.* 148, 117–124.

Li, P., Yang, S. L., Milliman, J. D., Xu, K. H., Qin, W. H., Wu, C. S., et al. (2012). Spatial, temporal, and human-induced variations in suspended sediment concentration in the surface waters of the Yangtze Estuary and adjacent coastal areas. *Estuar. Coasts* 35, 1316–1327. doi: 10.1007/s12237-012-9523-x

Li, W. Q., Ge, J. Z., Ding, P. X., Ma, J. F., Glibert, P. M., and Liu, D. Y. (2021). Effects of dual fronts on the spatial pattern of Chlorophyll-a concentrations in and off the Changjiang River estuary. *Estuar. Coasts* 44, 1408–1418. doi: 10.1007/s12237-020-00893-z

Liang, Y. (2012). *China's Red Tide Disaster Survey and Evaluation (1933-2009)*. Beijing: Ocean Press. (In Chinese).

Lin, J. (2011). *A modeling Study of the Phytoplankton Dynamics off the Changjiang Estuary (in Chinese)*. Shanghai: East China Normal University.

Liu, X., Huang, B. Q., Huang, Q., Wang, L., Ni, X. B., Tang, Q. S., et al. (2015). Seasonal phytoplankton response to physical processes in the southern Yellow Sea. *J. Sea Res.* 95, 45–55. doi: 10.1016/j.seares.2014.10.017

Luan, H. L., Ding, P. X., Wang, Z. B., Ge, J. Z., and Yang, S. L. (2016). Decadal morphological evolution of the Yangtze Estuary in response to river input changes and estuarine engineering projects. *Geomorphology* 265, 12–23. doi: 10.1016/j.geomorph.2016.04.022

Luo, Z. F., Zhu, J. R., Wu, H., and Li, X. Y. (2017). Dynamics of the sediment plume over the Yangtze Bank in the Yellow and East China Seas. *J. Geophys. Res. Oceans* 122, 10073–10090. doi: 10.1002/2017jc013215

Ma, G. F., Shi, F. Y., Liu, S. G., and Qi, D. M. (2013). Migration of sediment deposition due to the construction of large-scale structures in Changjiang Estuary. *Appl. Ocean Res.* 43, 148–156. doi: 10.1016/j.apor.2013.09.002

May, C. L., Koseff, J. R., Lucas, L. V., Cloern, J. E., and Schoellhamer, D. H. (2003). Effects of spatial and temporal variability of turbidity on phytoplankton blooms. *Mar. Ecol. Prog. Ser.* 254, 111–128. doi: 10.3354/meps254111

Meng, J., Yao, P., Yu, Z., Bianchi, T. S., Zhao, B., Pan, H., et al. (2014). Speciation, bioavailability and preservation of phosphorus in surface sediments of the Changjiang Estuary and adjacent East China Sea inner shelf. *Estuar. Coast. Shelf Sci.* 144, 27–38. doi: 10.1016/j.ecss.2014.04.015

Morel, A. (1988). Optical modeling of the upper ocean in relation to its biogenous matter content (case I waters). *J. Geophys. Res.* 93:10749. doi: 10.1029/JC093iC09p10749

Murphy, A. H. (1988). Skill scores based on the mean square error and their relationships to the correlation coefficient. *Mon. Weather Rev.* 116, 2417–2424. doi: 10.1175/1520-049319881162.0.CO;2

Nichols, F. H., Cloern, J. E., Luoma, S. N., and Peterson, D. H. (1986). The modification of an estuary. *Science* 231, 567–573. doi: 10.1126/science.231.4738.567

Pelletier, M., El-Fityani, T., Graham, A., Rutter, A., Michelutti, N., Zeng, D. M., et al. (2016). Tracking pesticide use in the Saint Lawrence River and its ecological impacts during the World Exposition of 1967 in Montreal, Canada. *Sci. Total Environ.* 572, 498–507. doi: 10.1016/j.scitotenv.2016.08.064

Polikarpov, I., Al-Yamani, F., Petrov, P., Saburova, M., Mihalkov, V., and Al-Enezi, A. (2021). Phytoplankton bloom detection during the COVID-19 lockdown with remote sensing data: using Copernicus Sentinel-3 for north-western Arabian/Persian Gulf case study. *Mar. Pollut. Bull.* 171:112734. doi: 10.1016/j.marpolbul.2021.112734

Qiu, B., and Lukas, R. (1996). Seasonal and interannual variability of the North Equatorial Current, the Mindanao Current, and the Kuroshio along the Pacific western boundary. *J. Geophys. Res. Oceans* 101, 12315–12330. doi: 10.1029/95jc03204

Ralph, P. J., Durako, M. J., Enriquez, S., Collier, C. J., and Doblin, M. A. (2007). Impact of light limitation on seagrasses. *J. Exp. Mar. Biol. Ecol.* 350, 176–193. doi: 10.1016/j.jembe.2007.06.017

Shen, F., Tang, R. G., Sun, X. R., and Liu, D. Y. (2019). Simple methods for satellite identification of algal blooms and species using 10-year time series data from the East China Sea. *Remote Sens. Environ.* 235:111484. doi: 10.1016/j.rse.2019.111484

Shen, F., Zhou, Y. X., Li, D. J., Zhu, W. J., and Salama, M. S. (2010). Medium resolution imaging spectrometer (MERIS) estimation of chlorophyll-a concentration in the turbid sediment-laden waters of the Changjiang (Yangtze) Estuary. *Int. J. Remote Sens.* 31, 4635–4650. doi: 10.1080/01431161.2010.485216

Shen, L., Xu, H., Guo, X., and Li, M. (2011). Characteristics of large-scale harmful algal blooms (HABs) in the Yangtze River Estuary and the adjacent East China Sea (ECS) from 2000 to 2010. *J. Environ. Prot.* 02, 1285–1294. doi: 10.4236/jep.2011.210148

Siswanto, E., Tang, J., Yamaguchi, H., Ahn, Y.-H., Ishizaka, J., Yoo, S., et al. (2011). Empirical ocean-color algorithms to retrieve chlorophyll-a, total suspended matter, and colored dissolved organic matter absorption coefficient in the Yellow and East China Seas. *J. Oceanogr.* 67, 627–650. doi: 10.1007/s10872-011-0062-z

Son, Y. S., and Kim, H. C. (2018). Empirical ocean color algorithms and bio-optical properties of the western coastal waters of Svalbard, Arctic. *ISPRS J. Photogramm. Remote Sens.* 139, 272–283. doi: 10.1016/j.isprsjprs.2018.03.024

Statham, P. J. (2012). Nutrients in estuaries — an overview and the potential impacts of climate change. *Sci. Total Environ.* 434, 213–227. doi: 10.1016/j.scitotenv.2011.09.088

Strickland, J. D. H. (1958). Solar radiation penetrating the ocean. A review of requirements, data and methods of measurement, with particular reference to photosynthetic productivity. *J. Fish Res. Board Can.* 15, 453–493. doi: 10.1139/f58-022

Tang, D. L., Di, B. P., Wei, G. F., Ni, I. H., Oh, I. S., and Wang, S. F. (2006). Spatial, seasonal and species variations of harmful algal blooms in the South Yellow Sea and East China Sea. *Hydrobiologia* 568, 245–253. doi: 10.1007/s10750-006-0108-1

Tang, D. L., Kester, D. R., Ni, I. H., Qi, Y. Z., and Kawamura, H. (2003). *In situ* and satellite observations of a harmful algal bloom and water condition at the Pearl River estuary in late autumn 1998. *Harmful Algae* 2, 89–99. doi: 10.1016/S1568-9883(03)00021-0

Tassan, S. (1994). Local algorithms using SeaWiFS data for the retrieval of phytoplankton, pigments, suspended sediment, and yellow substance in coastal waters. *Appl. Opt.* 33, 2369–2378. doi: 10.1364/ao.33.002369

Teng, L. Z., Cheng, H. Q., de Swart, H. E., Dong, P., Li, Z. H., Li, J. F., et al. (2021). On the mechanism behind the shift of the turbidity maximum zone in response to reclamations in the Yangtze (Changjiang) Estuary. China. *Mar. Geol.* 440:106569. doi: 10.1016/j.margeo.2021.106569

The Changjiang Water Resources Commission [CWRC] of The Ministry of Water Resources (2016). *Changjiang Sediment Bulletin*. Available online at: http://www.cjw.gov.cn/zwzc/bmgb (accessed December 21, 2021).

The Ministry of Natural Resources of the People's Republic of China (2010). *Bulletin of China Marine Disasters*. Available online at: http://www.mnr.gov.cn/sj/sjfw/hy/gbgg/zghyzhgb/ (accessed December 21, 2021).

Van Maren, D. S., Van Kessel, T., Cronin, K., and Sittoni, L. (2015). The impact of channel deepening and dredging on estuarine sediment concentration. *Cont. Shelf Res.* 95, 1–14. doi: 10.1016/j.csr.2014.12.010

Wang, J., and Wu, J. (2009). Occurrence and potential risks of harmful algal blooms in the East China Sea. *Sci. Total Environ.* 407, 4012–4021. doi: 10.1016/j.scitotenv.2009.02.040

Wang, Y. H., Wu, H., Lin, J., Zhu, J. R., Zhang, W. X., and Li, C. (2019a). Phytoplankton blooms off a high turbidity estuary: a case study in the Changjiang River Estuary. *J. Geophys. Res. Oceans* 124, 8036–8059. doi: 10.1029/2019jc015343

Wang, Y. H., Wu, H., Gao, L., Shen, F., and Liang, X. S. (2019b). Spatial distribution and physical controls of the spring algal blooming off the Changjiang River Estuary. *Estuar. Coasts* 42, 1066–1083. doi: 10.1007/s12237-019-00545-x

Wang, X. G., Su, F. Z., Zhang, J. J., Cheng, F., Hu, W. Q., and Ding, Z. (2019c). Construction land sprawl and reclamation in the Johor River Estuary of Malaysia since 1973. *Ocean Coast. Manag.* 171, 87–95. doi: 10.1016/j.ocecoaman.2019.01.006

Wang, Y., Liu, D., Xiao, W., Zhou, P., Tian, C., Zhang, C., et al. (2021). Coastal eutrophication in China: trend, sources, and ecological effects. *Harmful Algae* 107:102058. doi: 10.1016/j.hal.2021.102058

Wu, C. R. (2013). Interannual modulation of the Pacific decadal oscillation (PDO) on the low-latitude western North Pacific. *Prog. Oceanogr.* 110, 49–58. doi: 10.1016/j.pocean.2012.12.001

Wu, H., Wu, T. N., and Bai, M. (2018). Mega estuarine constructions modulate the Changjiang River plume extension in adjacent seas. *Estuar. Coasts* 41, 1234–1252. doi: 10.1007/s12237-017-0357-4

Wu, H., Zhu, J. R., and Choi, B. H. (2010). Links between saltwater intrusion and subtidal circulation in the Changjiang Estuary: a model-guided study. *Cont. Shelf Res.* 30, 1891–1905. doi: 10.1016/j.csr.2010.09.001

Wu, H., Zhu, J. R., Shen, J., and Wang, H. (2011). Tidal modulation on the Changjiang River plume in summer. *J. Geophys. Res. Oceans* 116:C08017. doi: 10.1029/2011jc007209

Wu, J., Liu, J. T., and Wang, X. (2012). Sediment trapping of turbidity maxima in the Changjiang Estuary. *Mar. Geol.* 303, 14–25.

Wu, T. N., and Wu, H. (2018). Tidal mixing sustains a bottom-trapped river plume and buoyant coastal current on an energetic continental shelf. *J. Geophys. Res. Oceans* 123, 8026–8051. doi: 10.1029/2018jc014105

Xian, W., Kang, B., and Liu, R. (2005). Jellyfish blooms in the Yangtze Estuary. *Science* 307:41c. doi: 10.1126/science.307.5706.41c

Xie, D. F., Pan, C., Wu, X. G., Gao, S., and Wang, Z. B. (2017). The variations of sediment transport patterns in the outer Changjiang Estuary and Hangzhou Bay over the last 30 years. *J. Geophys. Res. Oceans* 122, 2999–3020. doi: 10.1002/2016jc012264

Xu, L. J., Yang, D. Z., Greenwood, J., Feng, X. R., Gao, G. D., Qi, J. F., et al. (2020). Riverine and oceanic nutrients govern different algal bloom domain near the Changjiang Estuary in summer. *J. Geophys. Res. Biogeosci.* 125:e2020JG005727. doi: 10.1029/2020JG005727

Yang, D. Z., Yin, B. S., Sun, J. C., and Zhang, Y. (2013). Numerical study on the origins and the forcing mechanism of the phosphate in upwelling areas off the coast of Zhejiang province, China in summer. *J. Mar. Syst.* 123, 1–18. doi: 10.1016/j.jmarsys.2013.04.002

Yang, S. L., Xu, K. H., Milliman, J. D., Yang, H. F., and Wu, C. S. (2015). Decline of Yangtze River water and sediment discharge: impact from natural and anthropogenic changes. *Sci. Rep.* 5:12581. doi: 10.1038/srep12581

Yankovsky, A. E., and Chapman, D. C. (1997). A simple theory for the fate of buoyant coastal discharges. *J. Phys. Oceanogr.* 27, 1386–1401. doi: 10.1175/1520-048519970272.0.CO;2

Zhang, W. X., Wu, H., and Zhu, Z. Y. (2018). Transient hypoxia extent off Changjiang River Estuary due to mobile Changjiang River plume. *J. Geophys. Res. Oceans* 123, 9196–9211. doi: 10.1029/2018jc014596

Zhou, M. J., Shen, Z. L., and Yu, R. C. (2008). Responses of a coastal phytoplankton community to increased nutrient input from the Changjiang (Yangtze) River. *Cont. Shelf Res.* 28, 1483–1489.

Zhou, Z. X., Yu, R. C., Sun, C. J., Feng, M., and Zhou, M. J. (2019). Impacts of Changjiang River discharge and Kuroshio intrusion on the Diatom and Dinoflagellate blooms in the East China Sea. *J. Geophys. Res. Oceans* 124, 5244–5257. doi: 10.1029/2019jc015158

Zhou, Z. X., Yu, R. C., and Zhou, M. J. (2017). Seasonal succession of microalgal blooms from diatoms to dinoflagellates in the East China Sea: a numerical simulation study. *Ecol. Modell.* 360, 150–162. doi: 10.1016/j.ecolmodel.2017.06.027

Zhu, J., Zhu, Z. Y., Lin, J., Wu, H., and Zhang, J. (2016). Distribution of hypoxia and pycnocline off the Changjiang Estuary, China. *J. Mar. Syst.* 154, 28–40. doi: 10.1016/j.jmarsys.2015.05.002

Zhu, L., He, Q., Shen, J., and Wang, Y. (2016). The influence of human activities on morphodynamics and alteration of sediment source and sink in the Changjiang Estuary. *Geomorphology* 273, 52–62. doi: 10.1016/j.geomorph.2016.07.025

Zhu, Z. Y., Ng, W. M., Liu, S. M., Zhang, J., Chen, J. C., and Wu, Y. (2009). Estuarine phytoplankton dynamics and shift of limiting factors: a study in the Changjiang (Yangtze River) Estuary and adjacent area. *Estuar. Coast. Shelf Sci.* 84, 393–401. doi: 10.1016/j.ecss.2009.07.005

Conflict of Interest: The authors declare that the research was conducted in the absence of any commercial or financial relationships that could be construed as a potential conflict of interest.

Publisher's Note: All claims expressed in this article are solely those of the authors and do not necessarily represent those of their affiliated organizations, or those of the publisher, the editors and the reviewers. Any product that may be evaluated in this article, or claim that may be made by its manufacturer, is not guaranteed or endorsed by the publisher.

Copyright © 2022 He, Wang and Wu. This is an open-access article distributed under the terms of the Creative Commons Attribution License (CC BY). The use, distribution or reproduction in other forums is permitted, provided the original author(s) and the copyright owner(s) are credited and that the original publication in this journal is cited, in accordance with accepted academic practice. No use, distribution or reproduction is permitted which does not comply with these terms.

frontiers in Marine Science

ORIGINAL RESEARCH
published: 31 January 2022
doi: 10.3389/fmars.2021.785967

Offshore Spreading of a Supercritical Plume Under Upwelling Wind Forcing: A Case Study of the Winyah Bay Outflow

Alexander E. Yankovsky[1], Diane B. Fribance[2], Douglas Cahl[1] and George Voulgaris[1]*

[1] School of the Earth, Ocean and Environment, University of South Carolina, Columbia, SC, United States, [2] Department of Marine Science, Coastal Carolina University, Conway, SC, United States

In this study, we present observations of the Winyah Bay (WB) plume (SC, United States) formed by high freshwater discharge and a moderate upwelling-favorable wind acting continuously for ∼1.5 days prior to the shipboard survey. If a similar wind forcing persists over a longer period, the plume turns upstream (against its natural propagation) and curves offshore forming a "filament" with minimal transverse spreading, as seen in numerous satellite images. The observed plume comprises a train of tidal sub-plumes undergoing rotational adjustment and being transported offshore by Ekman dynamics. The WB outflow is supercritical in terms of the interior Froude number. Moderate wind extends this supercritical regime farther offshore. The plume is characterized by interior fronts associated with consecutive tidal pulses. Age of the buoyant water can be distinguished by the buoyant layer mixing (evident in the layer's thickness and salinity anomaly) along with the transformation of its *TS* properties. However, relatively little transverse (lateral) spreading of buoyant water occurs: the equivalent freshwater layer thickness remains surprisingly consistent, approximately 0.8 m, over more than 20 km in the direction of the bulge extension. It is hypothesized that the supercritical regime constrains the transverse spreading of a plume. Microstructure measurements reveal higher dissipation rates below the base of the older (offshore) part of the plume. This is attributed to internal wave radiation from a newly discharged tidal pulse into an older plume, with the buoyant layer acting as a waveguide. Theoretical estimations of the internal wave properties show that the interior front is highly supercritical, while the observed dissipation maximum agrees with the theoretical wave structure.

Keywords: buoyant plume, coastal upwelling, tides, internal waves, mixing, turbulence

OPEN ACCESS

Edited by:
Alejandro Jose Souza, Center for Research and Advanced Studies – Mérida Unit, Mexico

Reviewed by:
Sutara Suanda, University of North Carolina at Wilmington, United States
James O'Donnell, University of Connecticut, United States

****Correspondence:***
Alexander E. Yankovsky
ayankovsky@geol.sc.edu

Specialty section:
This article was submitted to Coastal Ocean Processes, a section of the journal Frontiers in Marine Science

Received: *29 September 2021*
Accepted: *20 December 2021*
Published: *31 January 2022*

Citation:
Yankovsky AE, Fribance DB, Cahl D and Voulgaris G (2022) Offshore Spreading of a Supercritical Plume Under Upwelling Wind Forcing: A Case Study of the Winyah Bay Outflow. Front. Mar. Sci. 8:785967. doi: 10.3389/fmars.2021.785967

INTRODUCTION

Estuarine buoyant outflows are frequently modulated by tides, and run off on the continental shelf as energetic ebbing currents, sometimes further amplified by natural or artificial lateral constraints (e.g., jetties) at the mouth. Upon entering the shelf, the buoyant discharge detaches from the sloping bottom (a lift-off zone) and spreads laterally as a thin buoyant layer (e.g., Wright and Coleman, 1971; Garvine, 1974; MacDonald and Geyer, 2005; Branch et al., 2020). The lift-off renders the buoyant layer supercritical, that is, $F_i > 1$, where $F_i = U_s/\sqrt{g'h}$ is the internal Froude number, U_s is the surface velocity, h is the buoyant layer thickness, $g' = g\triangle\rho/\rho_0$ is the reduced gravity, g is the acceleration due to gravity, $\Delta\rho$ is the buoyant layer density anomaly, and ρ_0 is the ambient

seawater density. The lift-off depth depends on the flow characteristics in the estuarine channel and is inversely proportional to the outflow Froude number (where flow characteristics are taken at the mouth; e.g., Atkinson, 1993; Wang et al., 2015). Supercritical outflows undergo rapid lateral spreading, vigorous entrainment, and mixing until the buoyant layer transitions into subcritical regime (e.g., Hetland, 2005, 2010). After that, circulation in the plume is shaped by the Earth's rotation, leading to the formation of an anticyclonic bulge. Newly discharged water can recirculate around the bulge multiple times (feeding its growth) or can exit it and continue along the coast as a coastal buoyancy driven current (also referred to as a far field plume; e.g., Fong and Geyer, 2002; Horner-Devine et al., 2009). The natural propagation of the coastal current is in the direction of a Kelvin wave propagation (hereinafter referred to as downstream), but it can be reversed either by wind stress or by ambient shelf circulation (which in itself is frequently wind-driven). For instance, the Columbia River plume exhibits a bi-modal structure: it propagates to the north (downstream) during downwelling-favorable or light winds, and to the south (or upstream) during the upwelling season (e.g., Hickey et al., 1998, 2009).

In this study, we address the response of supercritical, tidally modulated estuarine outflow to upwelling favorable wind. Our study area is on the South Atlantic Bight (SAB) shelf, a shallow and broad continental shelf off the United States east coast with the shelf break lying more than 100 km offshore. Within this region, the largest buoyant outflow occurs from Winyah Bay (WB) and combines the freshwater discharge of several rivers: the Pee Dee (by far the largest contribution), Waccamaw, Sampit, and Black rivers. WB is a microtidal, partially mixed estuary with a narrow bay mouth and predominantly semidiurnal tides (Kim and Voulgaris, 2005).

A particularly interesting regime of the wind-forced WB plume has been noted when light-to moderate upwelling favorable winds are sustained for several days. Under such forcing, the plume turns upstream and/or offshore, detaches from the coast and crosses the shelf at an oblique angle; a pattern commonly seen in satellite imagery (**Figure 1**). In the three examples presented in **Figure 1**, the competition between buoyancy and wind forcing shifts toward the wind dominance from left panel to right. In the left panel, the freshwater discharge (represented by the Pee Dee River discharge only) exceeded 1000 m^3 s^{-1} several days prior to the image time and was subsiding, while upwelling favorable wind lasted for just over 2 days with an average wind stress of ∼0.04 Pa. Under these conditions, the plume exhibits a minimal upstream excursion near the mouth and then continues offshore while curving anticyclonically (downstream). As the strength and duration of the upwelling-favorable wind increases, and/or the freshwater discharge decreases, the plume tends to be swept upstream, but it still turns offshore (anticyclonically) as it moves away from the mouth (central and right panels in **Figure 1**). The important property of these cross-shelf plumes (as they will be referred to hereinafter) is their large length-to-width aspect ratio: the plume retains its tight width with the axial distance. If the buoyant water were advected as a passive tracer by the wind-induced Ekman dynamics, it would be reasonable to expect its transverse spreading (diffusion) with distance from the source, as can be seen in a smoke trail coming from a chimney. This does not happen here, which implies that the plume develops certain inherent dynamics not overwhelmed by the wind forcing. It should be noted that the images are only a proxy for the buoyant plume since they do not represent the salinity field, which warrants some caution in their interpretation.

Similar cross-shelf plume structures were reported previously in other regions. For instance, Li et al. (2003) presented satellite images of cross-shelf fronts, also in the SAB, but ∼200 km farther south from our study site. In that study the authors acknowledged the role of the wind forcing, but they did not link these features to estuarine outflows nearby. Other examples include the Columbia River plume studies, e.g., [Hickey et al., 1998 (their **Figure 5B**)], and [Hickey et al., 2009 (their **Figure 13**, central panel)], as well as the Fraser River plume observations reported by Kastner et al. (2018). In these studies, the observed offshore extension of buoyant water was due to the wind forcing opposing the natural downstream propagation of a plume. However, the continental shelf of the United States west coast is narrow so that the Columbia River plume is exposed to open ocean dynamics as it spreads offshore, while the cross-shore spreading of the Fraser River plume is limited by the width of the Strait of Georgia.

The response of a coastal plume to the upwelling-favorable wind has been extensively studied previously (e.g., Münchow and Garvine, 1993; Xing and Davies, 1999; García Berdeal et al., 2002; Whitney and Garvine, 2005; Lentz and Largier, 2006; Fisher et al., 2018; among others). Several works addressed the response of a far field (e.g., Fong and Geyer, 2001; Lentz, 2004) where the buoyant layer can be approximated by a slab model with horizontally uniform density. The buoyant water is transported offshore by the Ekman dynamics associated with the alongshore wind stress, while the mixing occurs at the offshore edge of a plume where the interface outcrops to the surface and consequently the bulk Richardson number drops below the critical value. Within the bulge area, both the alongshore and high-frequency cross-shore wind components can be important in transporting the buoyant water (e.g., Kakoulaki et al., 2014), while spatially homogeneous density field cannot be assumed due to the presence of a buoyancy source. Previously, Yankovsky and Voulgaris (2019) presented observations of the WB plume under light upwelling-favorable wind conditions and found the existence of interior fronts within the bulge. They hypothesized that interior fronts are formed by successive tidal pulses of the estuarine outflow undergoing rotational adjustment while being exposed to the wind-induced offshore transport. The proposed mechanism is somewhat similar to the formation of interior front discussed by O'Donnell (1990) (referred to as an interior jump herein), albeit under the influence of the alongshore mean flow, not the wind stress. Yankovsky and Voulgaris (2019) also argued that interior fronts are characterized by enhanced mixing due to the superposition of wind-induced and geostrophic shear; however, no mixing data were available for their study.

This study continues the investigation of the WB plume and its salient features under upwelling favorable wind forcing previously observed by Yankovsky and Voulgaris (2019).

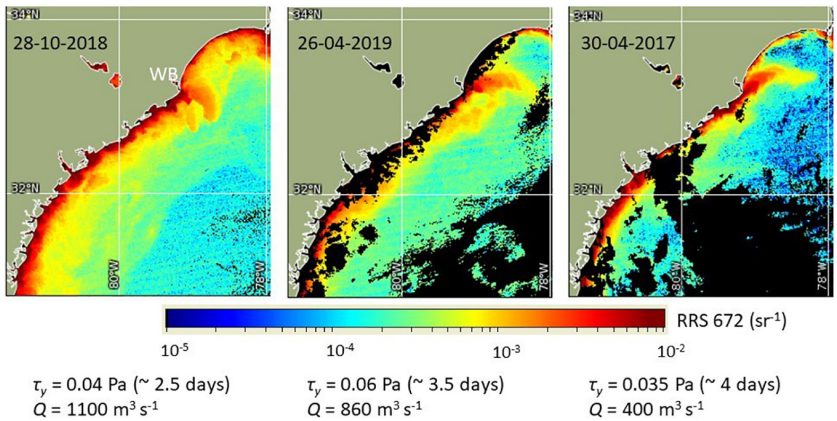


FIGURE 1 | VIIRS images of sediment index Rrs at 672 nm of the South Atlantic Bight shelf and the Winyah Bay (WB) plume. The forcing conditions shown below images are: freshwater discharge Q (Pee Dee only) over the preceding 5-day period, and the magnitude (duration) of the upwelling-favorable wind stress defined as its meridional component τ_y.

Measurement techniques are now expanded and yield additional information: near-surface salinity and velocity, as well as vertical profiles of the turbulent kinetic energy (TKE) dissipation ε. The supercriticality of a plume (and its interior front in particular) is assessed by solving a boundary problem for internal waves in the presence of the continuous stratification and sheared mean current. Most previous studies defined a supercritical regime in a highly simplified way, assuming a slab-like buoyant layer of a constant density and making a hydrostatic approximation. When these assumptions are relaxed, internal waves become dispersive, which implies that supercritical conditions can exist only for a limited range of wavenumbers. Moreover, change of the vertical shear with depth in the frontal current acts as a restoring force additional to the buoyancy effect (e.g., Baines, 1995).

The rest of the paper is organized as follows: section "Materials and Methods" describes the data collection and processing; section "Results" presents the results of data analysis; section "Internal Wave Properties" revisits the definition of the supercritical plume and delineates properties of internal waves under the observed conditions; and section "Discussion and Conclusion" discusses and summarizes the results. Derivation of the eigenvalue problem for internal waves in the presence of the mean sheared current and its numerical solution is described in Appendix.

MATERIALS AND METHODS

The WB plume was sampled on March 11, 2020 from 11:00 through 20:00 (all times are UTC) from the RV *Coastal Explorer*. A total of 16 stations were completed along a zonal transect running offshore from the WB mouth (**Figure 2**). The first station was conducted ∼1.1 km due east from the end of the southern (longer) jetty, or 8.1 km from the coast. Spatial separation between the stations was slightly less than 1 nautical mile. As seen from the inset in **Figure 2**, the transect was aligned with the direction of the plume's maximum offshore extent. The observations comprised ADCP measurements from the ship, microstructure profiling, CTD casts with the SBE 19plus v2 probe, and surface current measurements from a drone. The RV *Coastal Explorer* is a catamaran, and the 1200 kHz Workhorse Sentinel ADCP was deployed on a vertical pole between the bows with a bin size of 0.25 m and the center of the first bin referred at 2.58 m below the sea surface. The ship draft is 1.4 m, and hulls did not affect currents in the uppermost bin. ADCP sampling was interrupted from 16:38 through 17:18 (early station 10 through mid-station 11). Microstructure was sampled with two Rockland Scientific profilers: VMP-250 (downward profiles, stations 2–16) and MicroCTD (uprising profiles, stations 2–12). Both instruments had JFE-Advantech temperature and conductivity sensors which yielded temperature T and salinity s profiles in addition to the TKE dissipation rates. Microstructure profilers were deployed from a diver platform at the stern (facing upwind during sampling). Typically, three casts were completed with each instrument, which took on average 10 min. The ship was drifting predominantly downwind (not with the current) and if its position changed by 100 m or more during the sampling, it maneuvered back to the designated station location between the microstructure measurements and the CTD cast. The drone operations followed the CTD cast and were performed at stations 3 through 15.

Auxiliary data include freshwater discharge measurements from the USGS streamflow station 02135200 Pee Dee River at Highway 701 near Bucksport, SC (∼72 km from the WB mouth), sea level from the NOAA tide gauge station 8661070 at Springmaid Pier (33.655 N, 78.918 W), and offshore atmospheric forcing data from the NOAA buoy NDBC 41013 (33.441 N, 77.764 W) (**Figure 2**). Wind speed observations were available from the meteorological tower at the WB mouth (utilized in Yankovsky and Voulgaris, 2019) but no wind direction due to wildlife nesting. Comparison of wind velocity magnitude from the NOAA buoy and the tower show good agreement during the second half of March 10 through the first half of March 11 (wind forcing which affected the observed plume), while wind

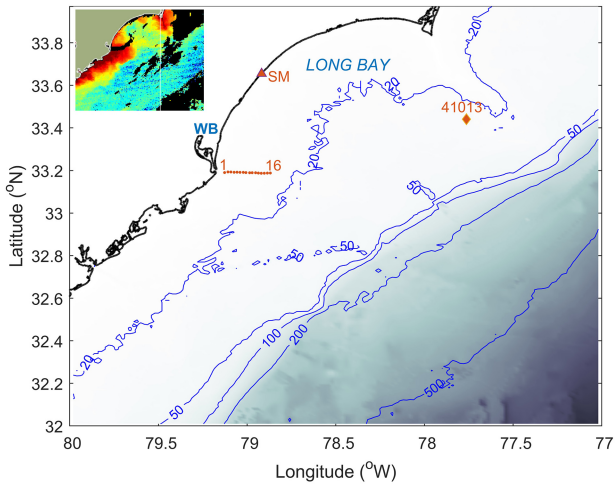


FIGURE 2 | Study area showing the data collection stations 1–16 (asterisks), NOAA NDBC buoy 41013, and the NOAA tide gauge station Springmaid Pier (SM). Isobaths are shown in meters. Inset is the satellite image (the same property and color scale as in **Figure 1**) corresponding to the map area and obtained on March 11, 2020 at 16:53–18:41. Images adapted from NOAA Coastwatch/Oceanwatch.

remained light during the mid-day of March 11 (**Figure 3**). Synthetic aperture radar (SAR) satellite image of the plume captured on March 12, when the forcing conditions remained similar to the period of shipboard observations, was obtained from the European Space Agency.

A straight line was fit to nominal locations of the stations (corresponding to CTD casts) and the projection of the measurement location on this line is referred to as the transect distance, with zero corresponding to the first station and the positive direction pointing eastward. A Cartesian coordinate system with x-, y-, and z-component pointing eastward, northward, and upward, respectively, is applied to vector quantities.

ADCP data were averaged over 5-min time intervals immediately preceding the drone sampling (and thus overlapping CTD casts). These ADCP profiles were combined with spatially averaged near-surface currents derived from the drone (see below). As an additional quality control, we estimated spatially averaged coordinates of the drone-derived surface currents (from drone GPS), and temporally averaged coordinates of the ADCP-derived currents (from the ship GPS). In almost all cases, their discrepancy was less than 100 m, typically ∼50 m or less, and in two cases as low as ∼ 10 m. The only exception is the separation of 240 m at station 10 due to the gap in ADCP record (so that earlier in time ADCP data were averaged, taken during the microstructure sampling).

The data from the two microstructure profilers were processed in similar ways to obtain estimates of ε. For efficiency, we will refer to the VMP-250 as dc (downcast) and the MicroCTD as uc (upcast). Dissipation estimates were obtained using Rockland Scientific processing tools (Lueck, 2016). Default cutoffs for spectral integration using the Nasmyth spectra vs. fitting to the inertial subrange were used. Each spectrum was the average of individual spectra obtained from 2-s segments with 50 and 75% overlap for the dc and uc systems, respectively. In order to maximize vertical resolution, in particular near the surface, a 4 s record was used for estimating the spectra. The minimum depth for evaluation was 1 m (dc) and 0 m (uc). Additionally, a minimum vertical velocity was set at 0.4 ms^{-1} (dc) and 0.45 ms^{-1} (uc). Terminal speeds were approximately 0.5 ms^{-1} (dc) and 0.6 ms^{-1} (uc). Dissipation estimates at the start of the uc cast (near bed) were manually removed if they did not agree with the dc estimates, or if there was high vibration, likely resulting from the instrument moving through its own wake after releasing its weight. Vertical tilt did not exceed 10° for either instrument. Each profiler was mounted with two perpendicular shear probes, and the two measurements were averaged for all analyses shown here. For salinity profiles obtained with JFE Advantech (JAC) sensors on MicroCTD, temperature and conductivity measurements were synchronized using the actual uprising velocity and following the procedure recommended by the manufacturer. The CTD sampling frequency was 4 Hz and the resulting profiles were averaged over 1-s time intervals.

Drone operations consisted of flying a DJI Phantom 4 Pro quadcopter with a 4k rectilinear video camera at the nominal altitude of 120 m (which slightly varied between the stations) and recording 30 seconds of video of the ocean surface with the camera pointed nadir. Video imagery was analyzed in order to identify the surface gravity wave parameters (wavelength, direction, and phase speed). Surface ocean currents produce a Doppler shift in the dispersion relation (change in phase speed) of linear surface gravity waves. The change in phase speed for a particular wave corresponds to the currents at a depth of approximately the wavelength divided by 4π (Stewart and Joy, 1974). The near-surface ocean current velocity was estimated by fitting the linear dispersion relation using the wavelength and phase speed values identified in the video imagery (Horstmann et al., 2017). We limit the wavelengths used in the analysis from 1 to 5 m, thereby providing an estimate of the ocean current at a depth between 0.08 and 0.40 m, with the average depth close to 0.18 m (but varying between stations). This methodology has shown to agree well (RMS differences below 0.1 m/s) with surface current estimates from a boat mounted ADCP (Streßer et al., 2017). The software used for this analysis was obtained from https://github.com/RubenCarrascoAlvarez/CopterCurrents.

The Sentinel-1 level 1 GRD product was processed using the European Space Agency's Sentinel Application Platform (SNAP[1]), following the generic workflow process described in Filipponi (2019). The steps included were (1) updating of the orbit state vectors for the image by applying the precise orbit available in SNAP; (2) thermal noise removal; (3) removal of low intensity noise and invalid data on the edges of the image (border noise removal); (4) conversion of the digital pixel values to radiometrically calibrated SAR backscatter using the calibration equation included within the Sentinel-1 GRD product; (5) removal of granular noise through Speckle filtering; (6) range

[1]http://step.esa.int

Doppler terrain correction to obtain a precise geolocation information; and (7) conversion of backscatter to dB.

RESULTS

The observed plume was formed under conditions of high discharge, moderate-to-light southwesterly wind (meteorological convention) and spring tides (**Figure 3**). In general, the upwelling conditions are associated with the alongshore wind stress component pointing upstream (i.e., northward), which causes a divergence in the corresponding cross-shore Ekman transport at the coast. The coastline orientation changes abruptly at the WB mouth (**Figure 2**). Since subinertial signals propagate along the shelf in the downstream (i.e., southward) direction only as coastally trapped waves (e.g., Yankovsky and Garvine, 1998) we assume that the upstream, meridionally oriented segment of the coastline adjacent to the WB mouth plays a more important role in controlling the upwelling conditions. Hence, we consider the northward component of the wind stress as upwelling-favorable. The upwelling-favorable wind event started at the end of March 9 and continued uninterrupted for ∼1.5 days by the beginning of data collection (**Figure 3A**). The alongshore wind stress was stronger (up to 0.1 Pa) on March 10 and subsided to less than 0.05 Pa on March 11, when the observations started. In addition, there were high frequency gusts in the eastward direction, which could also contribute to the offshore transport of the buoyant water. The tidally averaged Pee Dee River discharge prior to the observations was gradually decreasing from over 1000 m^3 s^{-1} in early March and attained near-constant values of 765–775 m^3 s^{-1} from the second half of March 8 through the period of observations. Both the discharge (assuming some delay between the discharge measurements and freshwater arrival on the shelf) and tidal amplitude were higher than those reported by Yankovsky and Voulgaris (2019). Overall, conditions were favorable for the formation of a cross-shelf plume although the duration of the upwelling favorable wind was shorter than in the cases from **Figure 1**. Hence, we assume that our observations represent an early stage of the cross-shelf plume formation, when its distinctive elongated shape has not yet been fully developed. This assumption is supported by the satellite image inset in **Figure 2**, showing a tendency for the offshore spreading of the WB plume. We also note that according to the scaling from Yankovsky and Voulgaris (2019) (their **Figure 11**), the observed conditions support the formation of interior fronts separating relatively older and younger tidally discharged water within the plume.

Before proceeding with presenting the *in situ* measurements, it is instructive to examine the spatial structure of the newly formed tidal plume observed on March 12 (**Figure 4**). The SAR image was obtained 2 h past the low tide (**Figure 3B**), thus the tidal pulse from the previous ebbing cycle was fully released, and the wind forcing at this time was very light, ∼0.02 Pa (**Figure 3A**). The width (i.e., its zonal dimension) of this tidal plume is 10–11 km, and the plume is clearly separated from the coast, which is likely due to the presence of jetties. Due to the similarity of forcing conditions, we assume that tidal pulses like this were present during the data collection period on March 11. Also, the tidal plume is shifted upstream (to the north) from the mouth, which further justifies the choice of the northward wind stress component as a proxy for the upwelling-favorable forcing.

The hydrographic structure of the water column was sampled with both the conventional lowered CTD probe and with two microstructure profilers; **Figure 5** compares the resulting salinity profiles. Only stations 2 through 12 are shown, where the MicroCTD data are available. There is a tendency in CTD measurements to indicate a deeper halocline compared to

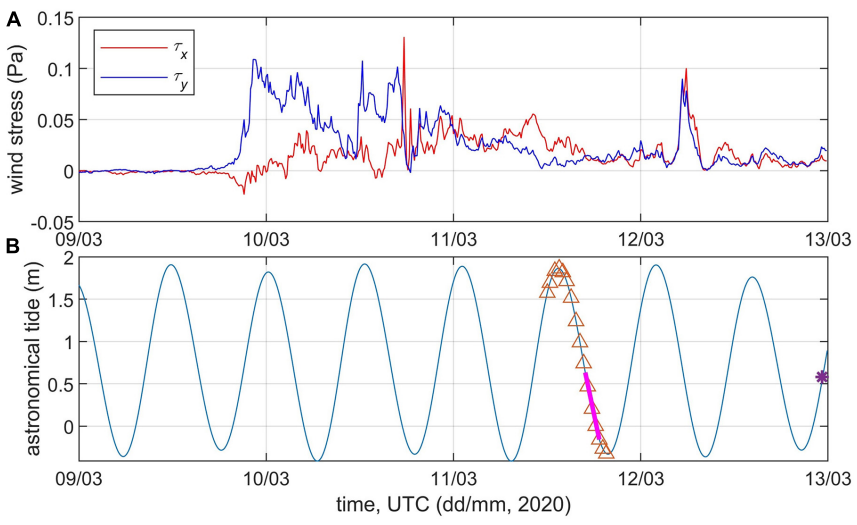


FIGURE 3 | Time series of **(A)** zonal (*x*) and meridional (*y*) components of the wind stress derived from the NDBC 41013 buoy data; **(B)** tidal sea level oscillations at Springmaid Pier station. Triangles, heavy magenta line and asterisk represent times for oceanographic stations, data collection for inset image in **Figure 2**, and SAR image, respectively.

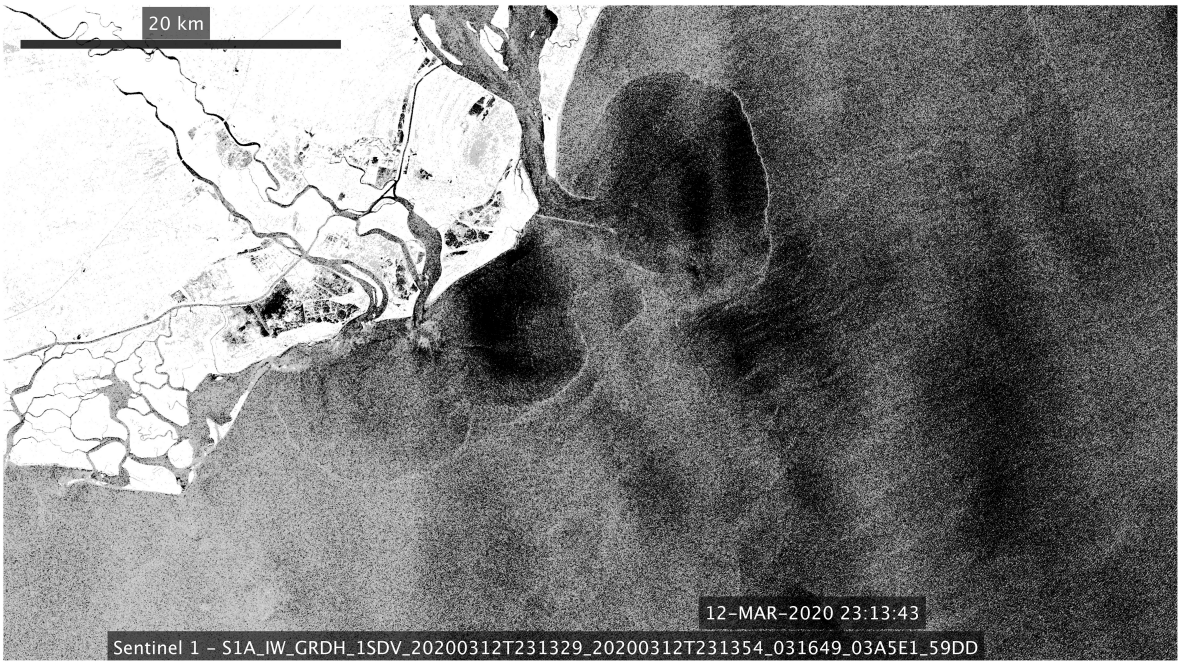


FIGURE 4 | Synthetic aperture radar image of the tidal plume off Winyah Bay obtained on March 12, 2020 at 23:14.

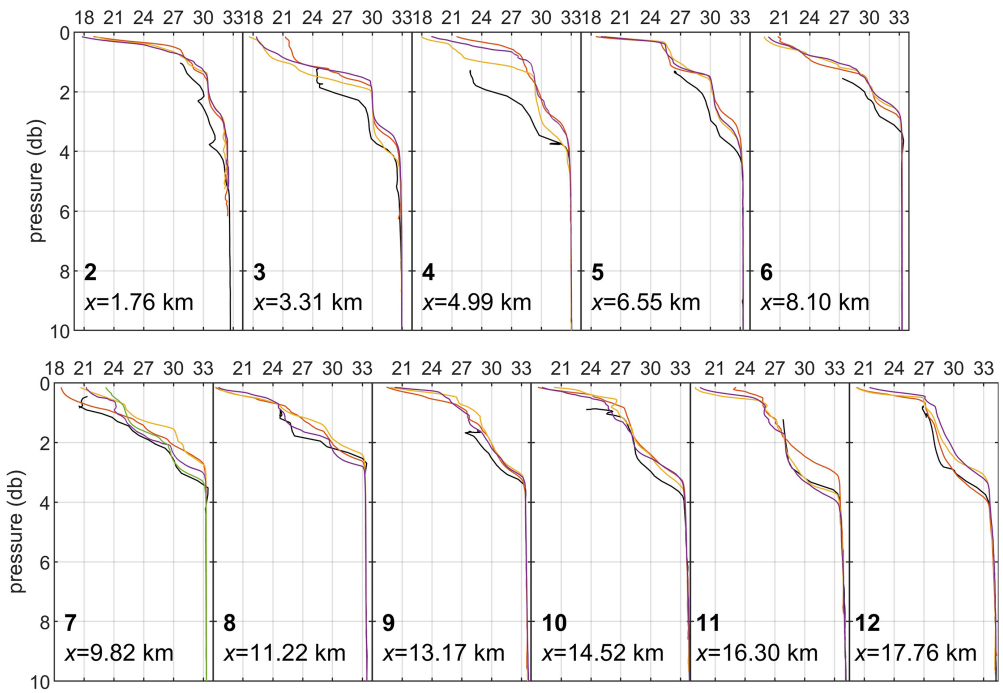


FIGURE 5 | Salinity profiles at stations 2–12: black – CTD casts, in colors – multiple MicroCTD casts. Salinity scale is the same in all panels. Station number and the corresponding transect distance are shown at the bottom of each panel.

MicroCTD profiles, especially at the nearshore stations 2 through 6, where the plume was shallower. This discrepancy is attributed to the ship's internal wake caused by its wind-induced drift (relative to the surface current). The MicroCTD profiler was deployed on a loose tether and surfaced at 5–10 m away from the ship, hence its data were less contaminated by ship's wake. Another advantage of the MicroCTD is that it sampled the near-surface layer up to 10–15 cm from the surface. VMP-250

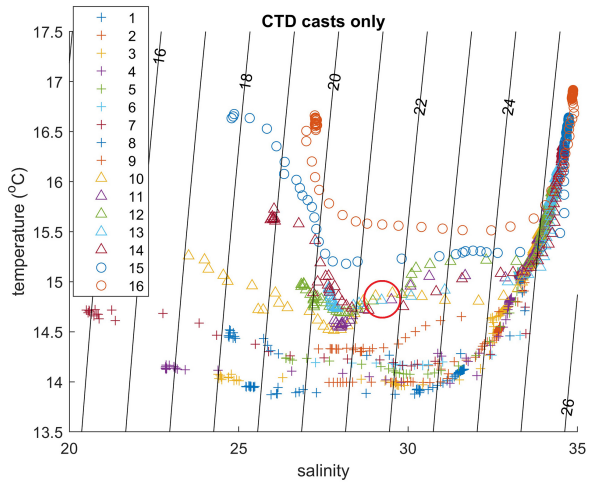


FIGURE 6 | *TS* diagram from CTD casts. Station numbers are shown in the legend; red circle emphasizes uniform *TS* properties of the buoyant layer between several stations.

salinity data are not discussed here because they do not offer any advantage over CTD due to its dc mode of sampling. The plume remained shallow, ∼4 m or less, with the 1–1.5 m deep, low salinity (minimum s ∼18–20) layer on top. Some profiles exhibit step-like structures (e.g., stations 3, 5, 10, 11) associated with more mixed, previously discharged buoyant water (recall a stronger wind forcing on the previous day, see **Figure 3A**).

Despite the potential influence of the ship's wake, CTD measurements are suitable for *TS* analysis (**Figure 6**) and reveal that the plume extended offshore past station 16 (with a corresponding transect distance of 24.06 km). This implies that the plume spread more than 30 km eastward from the coast, consistent with the satellite image inset in **Figure 2**. Water column stratification was primarily due to salinity, with temperature contribution being small. However, temperature is a good indicator for the age of the buoyant water, since the newly discharged water was cooler than the ambient shelf water. This is illustrated in the *TS* diagram of all 16 CTD stations shown in **Figure 6**, where data can be separated into three clusters according to the temperature range of the low-salinity buoyant layer. Stations 1–9 with the lowest T represent the newly discharged water, stations 10–14 represent intermediate age of the plume, and outer station 15–16 have the warmest and oldest water. Transition between these clusters is not abrupt: for instance, the lower part of the plume at station 9 has characteristics closer to the intermediate part of the plume (station 10), while the *TS* curve of station 15 also merges at some points with intermediate stations 14 and 12. However, stations 10–14 have almost identical *TS* indices of ∼14.8°C and ∼29, respectively (shown with red circle in **Figure 6**) indicating homogeneous water properties at some mid-depth layer of the plume. We deduce that this "mode water" in the intermediate part of the plume undergoes slower transformation than in the layers above or below.

The drone-derived surface currents exhibited a highly spatially variable, eddying flow regime near the mouth (stations 3–5, see examples in **Figures 7A,B**) with a predominantly offshore direction. The average radius of curvature r in surface currents at station 3 was ∼70 m and was determined from 8 pairs of vectors as $r = d/\tan(\Delta\varphi)$, where d is the distance between the two vector locations along the stream line, and $\Delta\varphi$ is the difference between their direction. Vortical structures seen at stations 3 and 4 cannot be directly caused by the energetic estuarine outflow because these samples were taken during the flood (**Figure 3B**). We believe they are associated with submesoscale processes on the inshore plume front under the upwelling wind forcing. From stations 6 through 15, the near surface flow was predominantly southeastward, consistent with the direction of the Ekman drift associated with the observed southwesterly winds (e.g., **Figure 7C**). Some directional variations in surface currents did

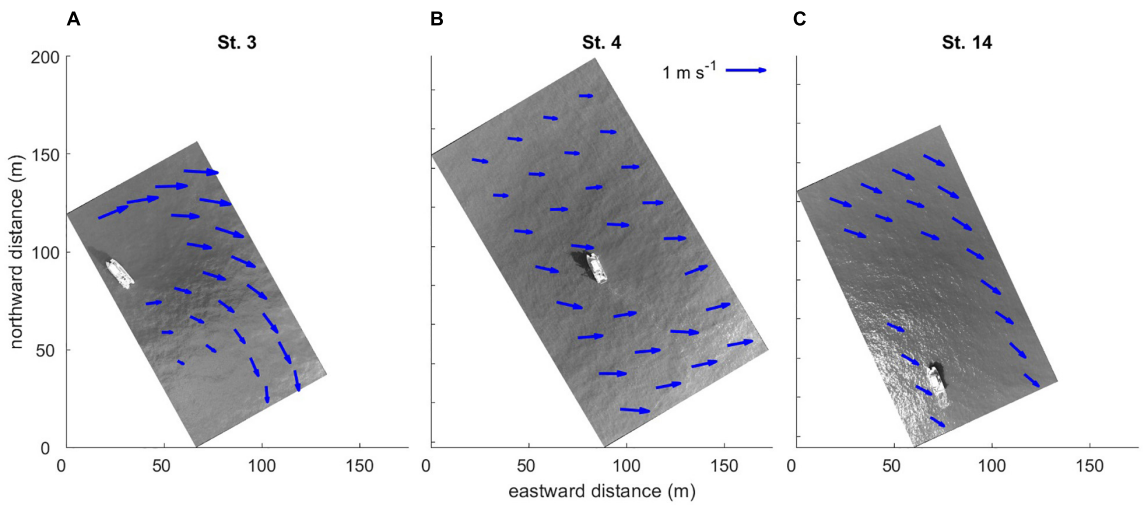


FIGURE 7 | Examples of drone-derived near-surface velocity field at **(A)** station 3; **(B)** station 4; **(C)** station 14.

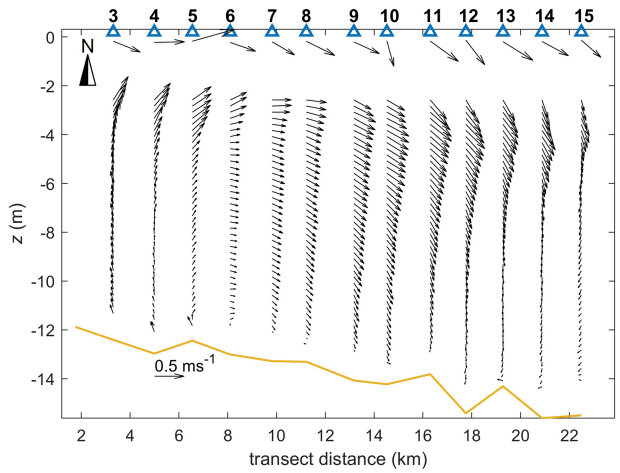


FIGURE 8 | Combined drone-ADCP vertical profiles of horizontal velocity vectors, stations 3–15. Heavy line is the bottom.

occur between the stations, since the wind stress-induced flow was not the only component present at the surface.

Combined drone-ADCP current profiles for all stations where drone data are available are presented in **Figure 8**. Drone-derived velocities are referred at near-surface depth varying from 0.13 to 0.22 m between different stations depending on spectral characteristics of the surface wave field. Near surface (drone-derived) currents have an offshore (eastward) component associated with the upwelling favorable wind. Since the prevailing wind was from southwest, the Ekman drift should have a southward component. Currents at 2.5–4 m depth show the anticyclonic flow pattern associated with the plume: the upstream flow at inshore stations 3–5 and the downstream flow at offshore stations 11–15. Strong vertical current shear is present in the upper part of the water column, apparently associated with the buoyant plume and the action of wind stress. The lower portion of the water column is dominated by tidal currents, which is evident in the vector rotation between the stations which follows the tidal stage: tidal currents turn seaward–southward–shoreward as tidal stage progresses from high tide to low tide (compare **Figure 8** and **Figure 3B** where timing of measurements is shown against the tidal stage). There is a velocity minimum in the lower part of the buoyant layer seen in the offshore stations 9–15. While this minimum is not fully resolved due to the vertical gap between the drone- and ADCP-derived currents, this feature is consistent with the presence of a homogeneous "mode" water at the mid-depth of the plume (stations 10–14).

The vertical distribution of salinity along the transect (**Figure 9A**) is constructed from MicroCTD casts. As explained earlier, these data are not contaminated by the ship's hull interference and also resolve the near-surface structure of the plume. For each station (2 through 12), individual casts were projected into 0.1 m vertical bins and averaged. **Figure 9** shows a newly formed tidal plume that occupies transect distances of ∼2–12 km as a thin (less than 2 m) buoyant layer with the lowest near-surface salinity below 20. Its cross-shelf length scale is comparable with that shown in the SAR image (**Figure 4**). The tidal plume is detached from the coast and forms an inshore front at ∼2 km. There is a convergence of buoyant water near the front, at 2–4 km. The vortical feature seen in surface currents (**Figure 7A**) at station 3 (x = 3.3 km) corresponds to this frontal convergence zone. The older, previously discharged buoyant water lies below and offshore of the new tidal plume, where another convergence zone exists at x = 12–14 km (stations 11–12). This feature appears to be an interior front similar to

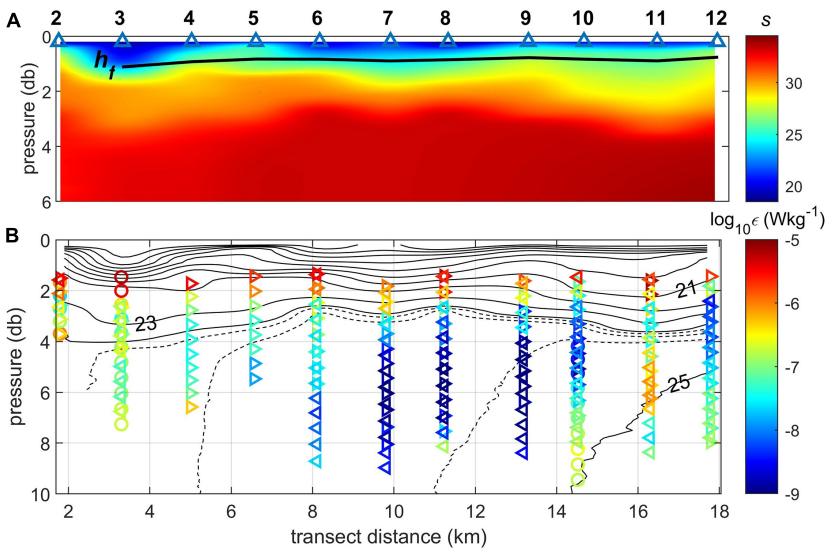


FIGURE 9 | Vertical transects derived from MicroCTD measurements, stations 2–12: **(A)** salinity with corresponding freshwater layer h_f; station locations are shown at the top; **(B)** TKE dissipation (color, different symbols represent different casts) and density σ_T (black contours). Contour intervals are 1 kg m^{-3} (solid line) and 0.25 kg m^{-3} (dashed line).

described in Yankovsky and Voulgaris (2019). At stations 11–12, the strongest stratification occurs at the base of the buoyant layer, while isohalines 28 and 30 (yellow–orange colors) have the widest separation. According to **Figure 6**, this is a layer occupied by the homogeneous "mode" water, and its depth of ∼1.9–2.5 m corresponds to the velocity minimum (**Figure 8**).

The spreading of the plume can be characterized by its freshwater content h_f which was estimated as

$$h_f = \int_{z_r}^{0} \frac{s_r - s}{s_r} dz, \tag{1}$$

where $z_r = -8$ m and $s_r = 34.9$ is the reference salinity (the highest salinity on the transect observed at station 16). The freshwater content was determined using the upper 8 m of the water column, roughly twice the depth of the plume. Higher values of h_f inshore ($x \leq 6.5$ km) are mostly due to lower salinity at depths 4–8 m, which does not necessarily represent the spreading of newly discharged water during the ongoing upwelling event. Farther offshore, h_f remains fairly uniform: the average of stations 5–12 is 0.84 m, with the maximum of 0.90 m found at station 11 ($x = 16.3$ km) and the minimum of 0.76 at station 12 ($x = 17.8$ km).

Next, we discuss the TKE dissipation rates. In general, VMP and MicroCTD profiles showed a good agreement. While the ε magnitude at specific depths varied between consecutive profiles due to high intermittency of turbulence in a highly stratified coastal environment (e.g., Huguenard et al., 2019), the shape of profiles remained remarkably consistent for each station. Since uprising profiles of MicroCTD provided better near-surface resolution (within the plume), only those are shown in **Figure 9B**. Although three MicroCTD profiles were conducted at each station (four at station 7), some of them were discarded due to the applied screening criteria. For this reason, we do not average individual profiles of ε for each station (as it was done for salinity) but show all of them with different symbols (**Figure 9B**). In the newly discharged buoyant water, high ε values of O(10^{-5}–10^{-6})W kg^{-1} penetrate to the base of the buoyant layer (especially at x = 8–11 km, **Figure 9B**), while below the plume ε drops to values lower by several orders of magnitude. In the intermediate age plume, ε decreases to $\sim 10^{-7}$ W kg^{-1} in the lower part of the plume where stronger stratification is present. Interestingly, there is a local maximum of ε below the base of the plume (∼5–7 m depth) at the location of the interior front ($x = 16.3$ km). This local maximum is also seen in two of three VMP profiles at station 11 (not shown), although the depth of the maximum, as well as its magnitude change between the individual profiles. This mid-depth maximum appears to be a robust feature and can be caused by the internal wave dynamics. It is well documented that energetic tidal pulses of buoyant discharge generate internal waves which radiate into an existing plume (e.g., Nash and Moum, 2005; Jay et al., 2009). Alternatively, ε mid-depth maximum can be present due to bottom friction of tidal currents, as reported by Spicer et al. (2021). However, no similar local maxima were observed inshore ($6 < x < 14$ km), where the water depth is approximately the same.

Vertical profiles of the horizontal velocity vector were projected on the direction of the integral depth-averaged velocity in the top 6 m layer (representative of the buoyant layer) for each station, and are referred to as maximum velocity profiles. They are shown in **Figure 10A** for offshore stations (starting from 8), where the subsurface velocity minimum occurred. While this velocity minimum is not fully resolved due to the vertical gap between the drone- and ADCP-derived currents, it is consistent with the presence of a homogeneous "mode" water at the mid-depth of the plume (stations 10–14). Its likely cause is the superposition of wind-induced shear stresses and the baroclinic pressure gradient. The former operates in the upper part of the plume which is evident in the vertical distribution of ε (**Figure 9B**) and causes the veering of the velocity vector with depth (**Figure 8**).

We deduce that in the older, offshore part of the plume ($x > 12$ km) the Ekman flow occupied only the upper part of the buoyant layer, which is evident in the decrease of ε, velocity minimum, and a more homogeneous "mode" water all occurring below 2 m, while the actual depth of the plume was ∼ 4 m. To further support this conclusion, we estimate the Ekman depth h_E as described below. We assume that the plume is linearly stratified with the constant buoyancy frequency N defined as

$$N^2 = \frac{g}{\rho} \frac{\triangle \rho_0 h_f}{h_p^2}, \tag{2}$$

where g is the acceleration due to gravity, where $\Delta\rho_0 = 25.84$ kg m^{-3} is the density anomaly of freshwater relative to the salinity at the base of the plume (assumed to be ∼34), ρ is the reference density and h_p is the depth of the plume. Next, we assume that the Ekman velocity changes linearly with depth and vanishes at the base of the Ekman layer h_E. With this assumption, the vertical shear u'_E is defined

$$u_E^{'} = \frac{2\tau}{\rho f h_E^2}, \tag{3}$$

where τ is the wind stress and f is the Coriolis parameter. Finally, we assume that the Ekman layer reaches the depth where the gradient Richardson number comes to its critical value of 0.25:

$$Ri = \frac{N^2}{u_E'^2} = 0.25, \quad \text{and so} \quad h_E^2 = \frac{\tau}{N\rho f}. \tag{4}$$

Using the following observed values: τ = 0.03 Pa, $h_p = 4$ m, $h_f = 0.84$ m, $f = 8 \times 10^{-5}$ s^{-1}, and ρ = 1020 kg m^{-3} yields $h_E = 1.8$ m, which is in a very good agreement with the observed structure of the plume.

Station 11 has been identified as the location of the interior front: it is characterized by the buoyant water convergence and the deepening of isopycnals. This station also has the fastest velocity of the buoyant layer as seen in the maximum velocity profiles (**Figure 10A**). We estimated geostrophic velocity between stations 11–12 using the observed v-component at mid-depth as a reference and integrating the geostrophic shear upward (**Figure 10B**). The geostrophic velocity in **Figure 10B** is compared against the observed v-component (average of velocity profiles from the two stations). Clearly, there is significant

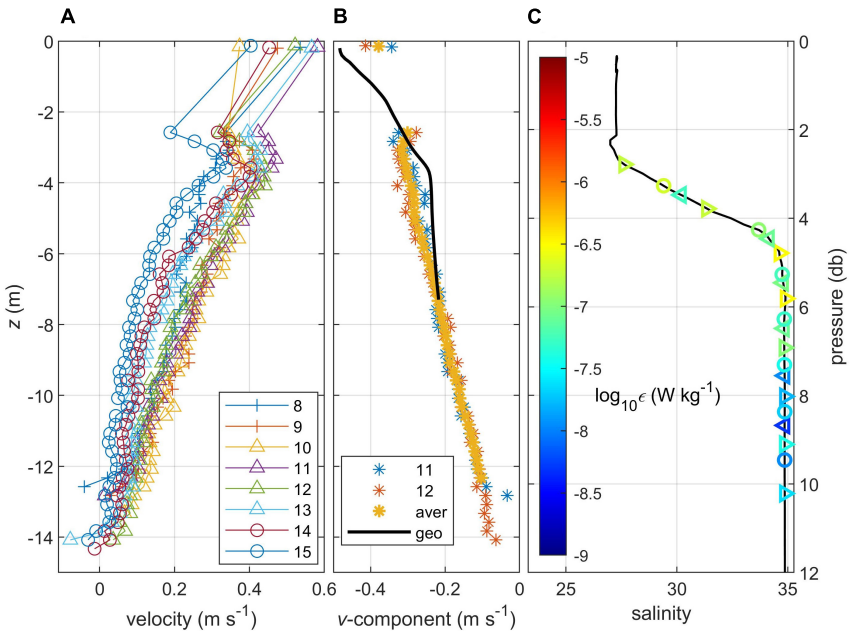


FIGURE 10 | Vertical profiles of **(A)** maximum velocity, stations 8–15; **(B)** meridional velocity component at the interior front, stations 11–12, their averaged value and geostrophic estimate; **(C)** salinity and TKE dissipation at station 16, different symbols indicate different casts. For comparison, the same color scale is used as in **Figure 9**.

geostrophic component in the observed velocity field at stations 11–12, although turbulent stresses tend to "smooth" the velocity profile and make it more linear with depth, as was also reported by Yankovsky (2006) and Mazzini et al. (2019).

Now we discuss the most seaward station 16 which lacks near-surface information as no drone or MicroCTD sampling took place. The CTD data reveal that the buoyant layer was well mixed (**Figure 10C**), thus it is permissible to calculate h_f by extrapolating s at constant value to the surface. This yields an h_f value of 0.80 m, which is close to the average of stations 5–12. TKE dissipation rates from the VMP-250 profiler reveal the mid-depth maximum at the base of the pycnocline in two of the three conducted profiles similar to that seen in **Figure 9B** (x = 16.3 km, station 11).

The observed values of h_f = 0.8–0.9 m, and the reduced gravity $g' = 0.25$ ms^{-2} associated with the freshwater relative to the ambient water of s = 34.9 density difference yield the internal wave phase speed $C = \sqrt{(g'h_f)} = 0.45 - 0.47$ ms^{-1}. This phase speed is less than the surface velocities from the maximum velocity profiles shown in **Figure 10A**, which implies that the plume remains supercritical. However, this is a crude estimate based on the slab-like approximation, and this conclusion is further investigated in the next section by considering internal wave properties.

INTERNAL WAVE PROPERTIES

In this section we consider characteristics of internal wave modes under the observed conditions, in the presence of the vertically sheared mean current. In particular, we focus on the interior front at station 11 where the accumulation of buoyant water occurred and the maximum velocity profile attained higher speed than at any other station. We numerically solve the wave problem Equations A7, A8 derived in Appendix, with H = 14 m, a spatial resolution Δz = 0.05 m, and the horizontal coordinate aligned with the direction of the maximum velocity. In order to elucidate the effect of mean sheared current, we start with somewhat idealized configuration of flow conditions as shown in the inset in **Figure 11A**: here, the water column is strongly stratified in the upper 4-m layer ($N^2 = 2.4 \times 10^{-2}$ s^{-2}) representing a plume, with weakly stratified lower part ($N^2 = 4.8 \times 10^{-4}$ s^{-2}). The mean current linearly increases toward the surface from 0.1 to 0.3 m s^{-1}, which is a smaller velocity range than observed. Without a mean current, two wave solutions are possible, forward- (i.e., $\theta = kx - \omega t$) and backward-propagating (i.e., $\theta = kx + \omega t$) with respect to the x-direction, where θ is the wave phase and the remaining variables are defined in Appendix. When a constant mean current U_0 is added, the dispersion relation $\omega = \omega(k)$ is modified as:

$$\omega^* = \omega + kU_0, \tag{5}$$

where asterisk denotes a Doppler-shifted wave frequency. However, when the mean current changes with depth, the Doppler shift is difficult to deduce without solving a wave problem, because the effective mean velocity depends on the interaction of the mean current with the wave structure (or, alternatively, with stratification). It also should be noted that propagating modes with real ω and k cannot exist with C within

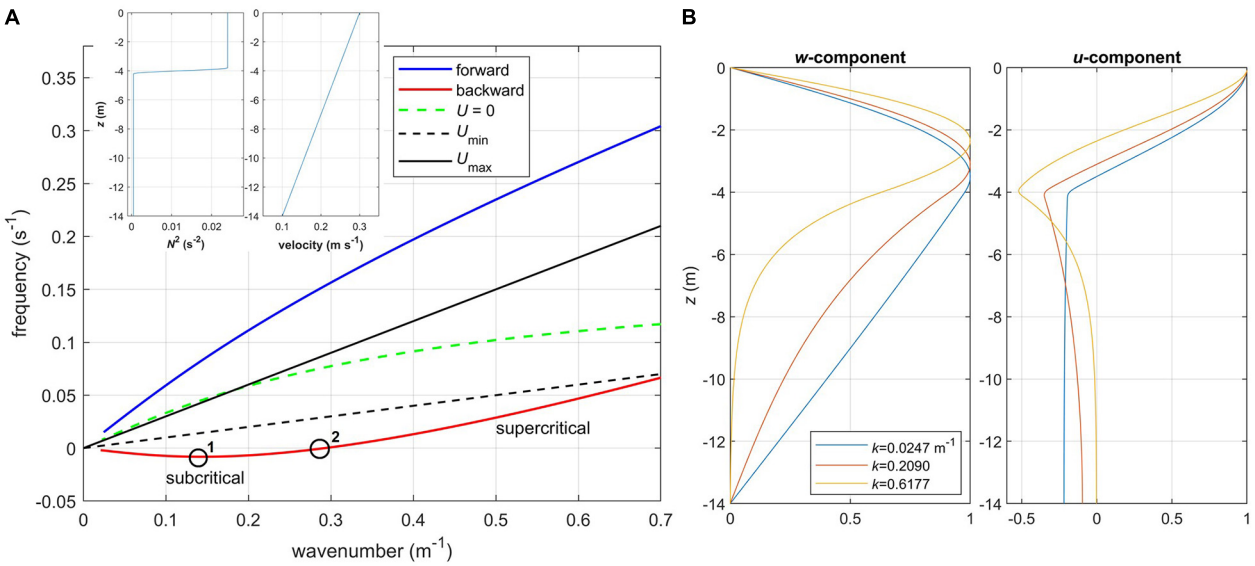


FIGURE 11 | Internal wave properties, case 1: **(A)** dispersion diagram for the first mode. Points 1 and 2 on the dispersion curve for backward propagating mode are $C_g = 0$ and $C = 0$, respectively. Inset shows profiles of buoyancy frequency squared (left) and mean velocity (right) specified in the wave Equation A7; **(B)** vertical profiles of vertical and horizontal velocity components normalized by their maximum values for various wavenumbers k, forward propagating mode.

the range of mean current velocities, that is, $U_{\min} \leq C \leq U_{\max}$, due to the presence of critical layers.

The resulting dispersion diagram for the first case is shown in **Figure 11A**; we consider only the first, gravest mode. The forward propagating mode without a mean current is shown as a green dashed line, while the not shown backward propagating mode is symmetric relative to $\omega = 0$. The waves are dispersive, that is, their phase speed $C = \omega/k$ decreases with the wave number. Once $U(z)$ is added, backward propagating mode shifts into a positive frequency domain for $k \geq 0.29$ m^{-1}, and remains in a negative frequency domain for lower k. In other words, the mean flow becomes supercritical for shorter waves, and remains subcritical for longer waves. The two points of special interest are those where $C = 0$ (no wave phase propagation, point 2 in **Figure 11A**) and where the group velocity $C_g = \partial\omega/\partial k$ becomes zero (no energy propagation, point 1 in **Figure 11A**).

It is also instructive to consider the vertical structure of the internal wave velocity field (**Figure 11B**). Due to the surface-intensified stratification, the wave structure concentrates in the upper layer: horizontal velocity u reaches maximum at the surface, and the u nodal point (where w reaches its maximum) is within the strongly stratified layer, gradually shifting upward with the increasing wavenumber (and frequency). Horizontal velocity of low-wavenumber waves does not change with depth in the weakly stratified layer ($z < -4$ m), but for waves with higher wavenumbers its magnitude decreases with depth after reaching a local maximum at $z = -4$m. This is because the wave frequency for such waves becomes higher than N in the lower layer, and the wave behavior there becomes evanescent, exponentially decaying with depth. Only forward-propagating modes are shown, but waves from the lower branch of dispersion diagram exhibit the same tendencies.

In the next example (**Figure 12**) the maximum U is increased to 0.5 m s^{-1}, which is closer to the observed values. The backward propagating mode is shifted into the positive frequency domain, that is, the mean current is supercritical for all wavelengths. Also, this mode has a high-wavenumber cutoff, where the dispersion curve merges with $U_{\min}$. In the backward propagating mode, u-component increases toward the bottom (**Figure 12B**), and this effect becomes significant as k approaches its cutoff value, that is, C comes close to $U_{\min}$.

Finally, the dispersion diagram (**Figure 13A**) is calculated for the observed profiles of stratification and maximum velocity from station 11. To better constrain a near-surface velocity, the second velocity value was derived from the drone data, for the longer wavelength band and the deeper corresponding reference depth. The mean current profile is approximated with an analytical function (a combination of polynomial and trigonometric functions), which yields its smooth second derivative in the wave Equation A7. Note that since $U(z)$ is now a non-linear function, d^2U/dz^2 acts as a restoring force for wave motions (in addition to the previously discussed Doppler shift). In this case, not only does the mean current become supercritical, but the backward propagating mode is completely eliminated (**Figure 13A**), while forward propagating waves have even stronger near-surface horizontal velocity maximum and shallower nodal point compared to the previous cases (**Figure 13B**).

Our observations lack a mooring deployment or any sampling specifically dedicated to observing the internal wave signal. However, elevated values of ε at the base of the plume (e.g., stations 11 and 16) suggest that internal waves can be contributing to the turbulence production in the middle of the water column. Here we deduce the wave signal from the shipboard ADCP data at station 12 ($x = 17.8$ km, at the vicinity of

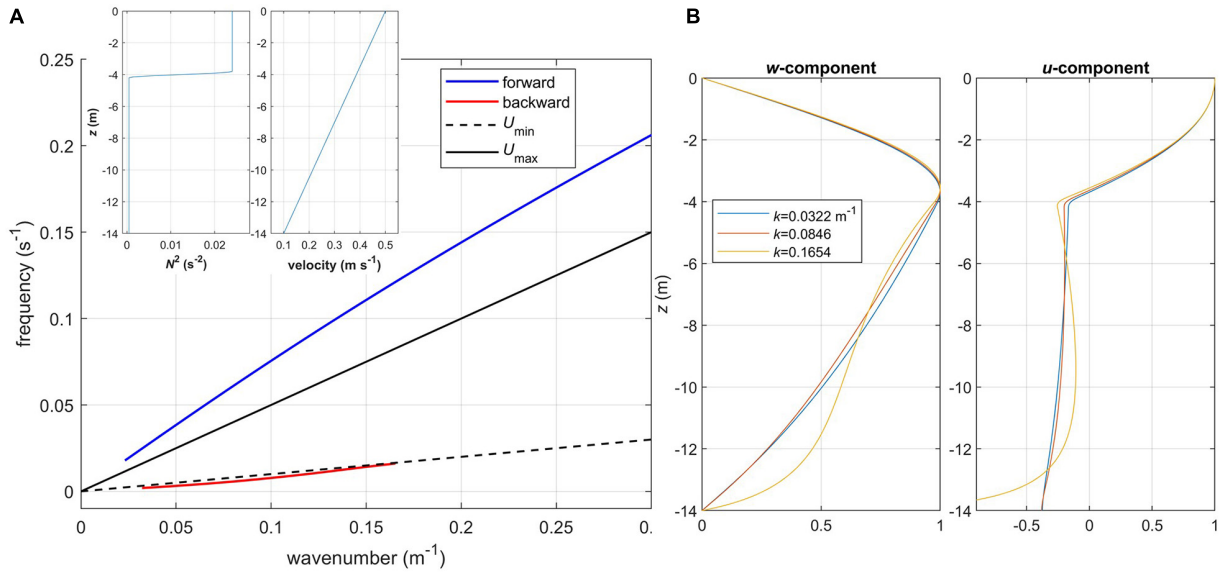


FIGURE 12 | Internal wave properties, case 2: **(A)** dispersion diagram for the first mode. Inset shows profiles of buoyancy frequency squared (left) and mean velocity (right) specified in the wave Equation A7; **(B)** vertical profiles of vertical and horizontal velocity components normalized by their maximum values for various wavenumbers k, backward propagating mode.

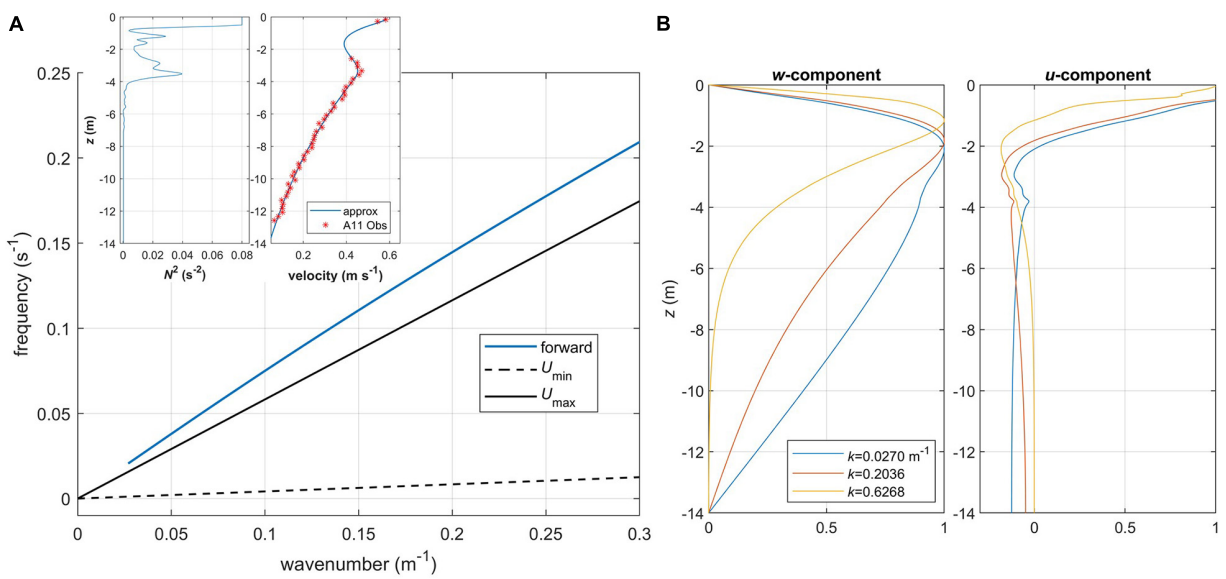


FIGURE 13 | Internal wave properties for realistic conditions from station 11, case 3: **(A)** dispersion diagram for the first mode. Inset shows specified in Equation A7 profiles of buoyancy frequency squared (left) and mean velocity (right), where asterisks/line show the observed/approximated values, respectively; **(B)** vertical profiles of vertical and horizontal velocity components normalized by their maximum values for various wavenumbers k, forward propagating mode.

the interior front) as follows. We project a velocity vector on the maximum velocity direction corresponding to the ∼15-min time interval when the ship was drifting (i.e., no maneuvering under propulsion). Mean values corresponding to this time interval are subtracted from each ADCP bin, and the resulting perturbed velocity is low-passed by applying a 2-min running mean in time and a weighted 5-bin averaging in vertical. The resulting band-passed depth-dependent time series is shown in **Figure 14**; it reveals sloping crisscrossing velocity bands implying a vertical propagation of the signal through the water column. To better visualize this effect, two black straight lines are drawn, but of course we should not expect that phase propagation occurs at a constant rate throughout the water column since it depends on local buoyancy frequency and mean current velocity. The vertical phase propagation is one of the fundamental internal wave properties. In the wave problem considered here (see Appendix),

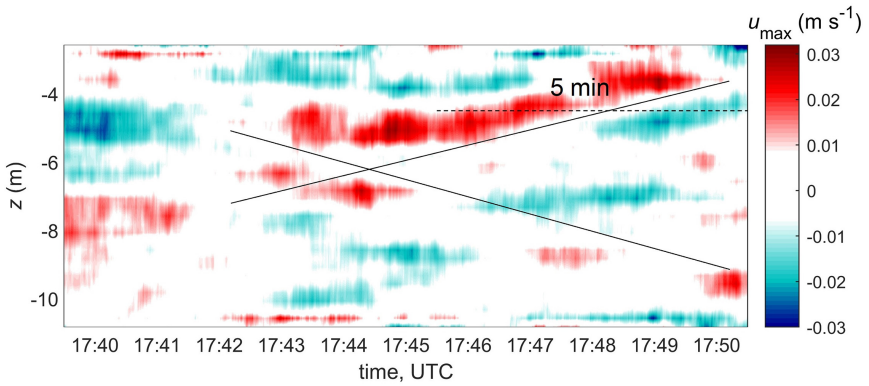


FIGURE 14 | Band-passed maximum velocity component from ADCP data at station 12. Black lines show approximate direction of the internal wave phase propagation; dashed line indicates the internal wave period.

we seek the normal mode solution assuming a flat bottom. Under this assumption, the vertical structure of the internal wave is a standing wave (hence, no phase propagation). However, in real conditions the bottom departs from its perfectly horizontal orientation often resulting in a vertically propagating signal.

The strongest vertically propagating signal is seen at 17:45–17:50, $z = -6$ to -4 m. The lowest frequency wave shown in **Figure 13** ($k = 0.027$ m^{-1}) has a wavelength of 233 m and a period of 5.1 min, roughly the same as the period of the perturbation in **Figure 14**. The horizontal velocity of this wave mode exhibits vertical shear at $z = -6$ to 4 m (similar to the observed), while the maximum vertical velocity occurs at $z = -4$ to 2 m (**Figure 13B**, blue profiles). Repeated MicroCTD salinity profiles (**Figure 5**) show vertical displacements of the pycnocline at 2–4 m depth at both frontal station 11 and 12, while inshore station 9 reveals neither such displacements nor elevated dissipation rates at the base of the plume. Although the data presented do not constitute an ultimate proof, they strongly suggest internal wave activity in the proximity of the interior front.

DISCUSSION AND CONCLUSION

In this study, we present observations of the WB plume formed by high freshwater discharge of O(1000) m^3 s^{-1} (all rivers combined) and a southwesterly upwelling-favorable wind acting continuously for ∼1.5 days prior to the survey. Such conditions, if the wind persists over several days, lead to the formation of cross-shelf plumes extending upstream and offshore as elongated "filaments" of buoyant water with minimal transvers spreading, as inferred from satellite images. The same feature appears to be present in observations reported here, where the freshwater content h_f remained nearly constant (∼0.8–0.9 m) over ∼20 km along the transect distance. The transect was aligned with the maximum offshore extent of the plume, as seen from **Figure 2**. This property contrasts the spreading of unforced supercritical plumes reported in modeling studies (e.g., Garvine, 1984; O'Donnell, 1990; Hetland, 2010) when the buoyant water spreads radially and the thinning of the buoyant layer does occur.

The observed plume comprises tidal pulses of different age distinguishable by their *TS* indices with older water being characterized by higher salinity and temperature. Tidal pulses are advected offshore and upstream by wind-induced currents, and are separated by interior fronts previously reported in Yankovsky and Voulgaris (2019). The present observations differ in that newer and older waters are separated not only in the horizontal but in the vertical as well with the newly released tidal plume spreading partially on top of the existing, previously released plume. This difference is likely caused by specifics of the wind forcing: in the present case, stronger wind stress was observed on the previous day, resulting in a deeper buoyant layer with lesser density anomaly. Vertical structures of velocity, salinity, and ε in the older (offshore) part of the plume imply that both the wind-induced shear stress and buoyancy (or, equivalently, pressure gradient force) affect plume spreading. However, stress divergence dominates in the upper part of the buoyant layer, while buoyancy is more pronounced in the lower part, with a velocity minimum found in the middle of the buoyant layer. This minimum velocity corresponds to the most homogeneous (with respect to the horizontal distance) part of the plume.

The observed plume is supercritical in the direction of the maximum depth-averaged velocity of the buoyant layer. In particular, for the observed interior front conditions, the backward propagating internal wave mode is not just reversed (as supercriticality implies) but is completely eliminated by the effect of the mean current shear. A supercritical regime in the plume can constrain the transverse spreading of the plume: since the interior front current flows in the upwind (i.e., downstream) direction, all pycnocline perturbations will ultimately radiate into the upwind edge of the plume and limit the plume's downwind spreading. The source of internal waves is likely the newly released tidal pulse, although any non-stationary current within the plume can radiate waves. Internal waves can approach the interior front at an arbitrary angle, but they will experience strong refraction on the frontal current (e.g., Duda et al., 2018), with a fraction of the incident energy flux still escaping farther offshore. In this way, an interior front can trap a substantial fraction of the internal wave energy flux and direct it downstream.

Internal waves are ubiquitous in buoyant plume dynamics. Radiation of high amplitude internal solitons (of pycnocline depression) by supercritical tidally modulated buoyant discharges is well documented by both observational (e.g., Nash and Moum, 2005; Jay et al., 2009; McPherson et al., 2020) and modeling (e.g., Stashchuk and Vlasenko, 2009) studies. These solitons propagate through the previously existing buoyant layer and disintegrate into trains of high-frequency internal waves. Internal waves associated with buoyant discharge are reported even in non-tidal seas (Osadchiev et al., 2020) or in subcritical discharges (Mendes et al., 2021). Interior fronts with associated supercritical currents can fundamentally alter the fate of arriving internal waves and their ultimate dissipation.

In conclusion, the cross-shelf plume described in this study represents a distinctive regime of coastal buoyant plume dynamics, corresponding to conditions where a supercritical buoyant outflow is exposed to moderate upwelling-favorable wind. The superimposed wind-driven currents transport tidal buoyant pulses offshore and, in combination with buoyancy-driven circulation, maintain a supercritical regime of the resulting plume. Under these conditions, internal waves can contribute to mixing processes and the entrainment of the ambient shelf water at the base of the plume. Dedicated modeling exercise is the next logical step in delineating the outlined regime.

DATA AVAILABILITY STATEMENT

Observational data presented in this study and a MATLAB code for solving the wave problem are available in Yankovsky et al. (2021); and https://zenodo.org/record/5796882. Auxiliary data are available at the following websites: VIIRS satellite images https://coastwatch.chesapeakebay.noaa.gov/region_cl.php; buoy wind data https://www.ndbc.noaa.gov/; tidal gauge data https://oceanservice.noaa.gov/facts/find-tides-currents.html; and freshwater discharge https://waterdata.usgs.gov/nwis/.

AUTHOR CONTRIBUTIONS

DF, AY, and DC collected the data. DF preprocessed and archived the data set and estimated the TKE dissipation. AY analyzed the CTD and velocity data, solved the wave problem, and drafted an early version. DC processed the drone data. GV produced the SAR image. All co-authors subsequently discussed, revised, and edited the manuscript. All authors contributed to the article and approved the submitted version.

FUNDING

Data collection was supported by the Office of the Vice President for Research of the University of South Carolina through funding from the Advanced Support for Innovative Research Excellence (ASPIRE) program.

ACKNOWLEDGMENTS

Seamanship and enthusiasm of James Phillips, Captain of RV *Coastal Explorer*, are greatly appreciated. Gabby Ricche compiled a series of satellite images with corresponding forcing conditions for the Winyah Bay plume. We are indebted to reviewers and Steve Dykstra for their insightful comments and suggestions.

REFERENCES

Atkinson, J. F. (1993). Detachment of buoyant surface jets discharged on slope. *J. Hydraul. Eng.* 119, 878–894. doi: 10.1061/(ASCE)0733-9429(1993)119:8(878)

Baines, P. G. (1995). *Topographic Effects in Stratified Flows*. Cambridge: Cambridge University Press, 482.

Branch, R. A., Horner-Devine, A. R., Kumar, N., and Poggioli, A. R. (2020). River plume liftoff dynamics and surface expressions. *Water Resour. Res.* 56:e2019WR026475. doi: 10.1029/2019WR026475

Duda, T. F., Lin, Y.-T., Buijsman, M., and Newhall, A. E. (2018). Internal tidal modal ray refraction and energy ducting in baroclinic Gulf Stream currents. *J. Phys. Oceanogr.* 48, 1969–1993. doi: 10.1175/JPO-D-18-0031.1

Filipponi, F. (2019). Sentinel-1 GRD preprocessing workflow. *Proceedings* 18:11. doi: 10.3390/ECRS-3-06201

Fisher, A. W., Nidzieko, N. J., Scully, M. E., Chant, R. J., Hunter, E. J., and Mazzini, P. L. F. (2018). Turbulent mixing in a far-field plume during the transition to upwelling conditions: microstructure observations from an AUV. *Geophys. Res. Lett.* 45, 9765–9773. doi: 10.1029/2018GL078543

Fong, D. A., and Geyer, W. R. (2001). Response of a river plume during an upwelling favorable wind event. *J. Geophys. Res.* 106, 1067–1084.

Fong, D. A., and Geyer, W. R. (2002). The alongshore transport of freshwater in a surface-trapped river plume. *J. Phys. Oceanogr.* 32, 957–972. doi: 10.1175/1520-0485(2002)032<0957:TATOFI>2.0.CO;2

García Berdeal, I., Hickey, B. M., and Kawase, M. (2002). Influence of wind stress and ambient flow on a high discharge river plume. *J. Geophys. Res.* 107:3130. doi: 10.1029/2001JC000932

Garvine, R. W. (1974). Physical features of the Connecticut River outflow during high discharge. *J. Geophys. Res.* 79, 831–846. doi: 10.1029/JC079i006p00831

Garvine, R. W. (1984). Radial spreading of buoyant, surface plumes in coastal waters. *J. Geophys. Res.* 89, 1989–1996. doi: 10.1029/JC089iC02p01989

Hetland, R. D. (2005). Relating river plume structure to vertical mixing. *J. Phys. Oceanogr.* 35, 1667–1688. doi: 10.1175/JPO2774.1

Hetland, R. D. (2010). The effects of mixing and spreading on density in near-field river plumes. *Dyn. Atmos. Ocean* 49, 37–53. doi: 10.1016/j.dynatmoce.2008.11.003

Hickey, B., McCabe, R., Geier, S., Dever, E., and Kachel, N. (2009). Three interacting freshwater plumes in the northern California Current System. *J. Geophys. Res.* 114:C00B03. doi: 10.1029/2008JC004907

Hickey, B. M., Peitrafesa, L. J., Jay, D. A., and Boicourt, W. C. (1998). The Columbia River plume study: subtidal variability in the velocity and salinity fields. *J. Geophys. Res.* 103, 10339–10368.

Horner-Devine, A. R., Jay, D. A., Orton, P. M., and Spahn, E. Y. (2009). A conceptual model of the strongly tidal Columbia River plume. *J. Mar. Syst.* 78, 460–475. doi: 10.1016/j.jmarsys.2008.11.025

Horstmann, J., Stresser, M., and Carrasco, R. (2017). "Surface currents retrieved from airborne video," in *Proceedings of the OCEANS 2017 – Aberdeen*, Aberdeen, 1–4. doi: 10.1109/OCEANSE.2017.8084957

Huguenard, K., Bears, K., and Lieberthal, B. (2019). Intermittency in estuarine turbulence: a framework toward limiting bias in microstructure measurements. *J. Atmos. Ocean. Technol.* 36, 1917–1932. doi: 10.1175/JTECH-D-18-0220.1

Jay, D. A., Pan, J., Orton, P. M., and Horner-Devine, A. R. (2009). Asymmetry of Columbia River tidal plume fronts. *J. Mar. Syst.* 78, 442–459. doi: 10.1016/j.jmarsys.2008.11.015

Kakoulaki, G., MacDonald, D., and Horner-Devine, A. R. (2014). The role of wind in the near field and midfield of a river plume. *Geophys. Res. Lett.* 41, 5132–5138. doi: 10.1002/2014GL060606

Kastner, S. E., Horner-Devine, A. R., and Thomson, J. (2018). The influence of wind and waves on spreading and mixing in the Fraser River plume. *J. Geophys. Res. Oceans* 123, 6818–6840. doi: 10.1029/2018JC013765

Kim, Y. H., and Voulgaris, G. (2005). Effect of channel bifurcation on residual estuarine circulation: Winyah Bay, South Carolina. *Estuar. Coast. Shelf Sci.* 65, 671–686. doi: 10.1016/j.ecss.2005.07.004

Lentz, S. (2004). The response of buoyant coastal plumes to upwelling-favorable winds. *J. Phys. Oceanogr.* 34, 2458–2469. doi: 10.1175/JPO2647.1

Lentz, S. J., and Largier, J. (2006). The influence of wind forcing on the Chesapeake Bay buoyant coastal current. *J. Phys. Oceanogr.* 36, 1305–1316. doi: 10.1175/JPO2909.1

Li, C., Nelson, J. R., and Koziana, J. V. (2003). Cross-shelf passage of coastal water transport at the South Atlantic Bight observed with MODIS Ocean Color/SST. *Geophys. Res. Lett.* 30:1257. doi: 10.1029/2002GL016496

Lueck, R. (2016). *Calculating the Rate of Dissipation of Turbulent Kinetic Energy. RSI Technical Note 028*. Victoria, BC: Rockland Scientific International Inc.

MacDonald, D., and Geyer, W. R. (2005). Hydraulic control of a highly stratified estuarine front. *J. Phys. Oceanogr.* 35, 374–387. doi: 10.1175/JPO-2692.1

Mazzini, P. L. F., Chant, R. J., Scully, M. E., Wilkin, J., Hunter, E. J., and Nidzieko, N. J. (2019). The impact of wind forcing on the thermal wind shear of a river plume. *J. Geophys. Res. Oceans* 124, 7908–7925. doi: 10.1029/2019JC015259

McPherson, R. A., Stevens, C. L., O'Callaghan, J. M., Lucas, A. J., and Nash, J. D. (2020). The role of turbulence and internal waves in the structure and evolution of a near-field river plume. *Ocean Sci.* 16, 799–815. doi: 10.5194/os-16-799-2020

Mendes, R., da Silva, J. C. B., Magalhaes, J. M., St-Denis, B., Bourgault, D., Pinto, J., et al. (2021). On the generation of internal waves by river plumes in subcritical initial conditions. *Sci. Rep.* 11:1963. doi: 10.1038/s41598-021-81464-5

Münchow, A., and Garvine, R. W. (1993). Buoyancy and wind forcing of a coastal current. *J. Mar. Res.* 51, 293–322. doi: 10.1357/0022240933223747

Nash, J. D., and Moum, J. N. (2005). River plumes as a source of large amplitude internal waves in the coastal ocean. *Nature* 437, 400–403. doi: 10.1038/nature03936

O'Donnell, J. (1990). The formation and fate of a river plume: a numerical model. *J. Phys. Oceanogr.* 20, 551–569. doi: 10.1175/1520-0485(1990)020<0551:TFAFOA>2.0.CO;2

Osadchiev, A., Barymova, A., Sedakov, R., Zhiba, R., and Dbar, R. (2020). Spatial structure, short-temporal variability, and dynamical features of small river plumes as observed by aerial drones: case study of the Kodor and Bzyp River plumes. *Remote Sens.* 12:3079. doi: 10.3390/rs12183079

Spicer, P., Cole, K. L., Huguenard, K., MacDonald, D. G., and Whitney, M. M. (2021). The effect of bottom-generated tidal mixing on tidally pulsed river plumes. *J. Phys. Oceanogr.* 51, 2223–2241. doi: 10.1175/JPO-D-20-0228.1

Stashchuk, N., and Vlasenko, V. (2009). Generation of internal waves by a supercritical stratified plume. *J. Geophys. Res.* 114:C01001. doi: 10.1029/2008JC004851

Stewart, R. H., and Joy, J. W. (1974). HF radio measurements of surface currents. *Deep Sea Res. Oceanogr. Abstr.* 21, 1039–1049. doi: 10.1016/0011-7471(74)90066-7

Streßer, M., Carrasco, R., and Horstmann, J. (2017). Video-based estimation of surface currents using a low-cost quadcopter. *IEEE Geosci. Remote Sens. Lett.* 14, 2027–2031. doi: 10.1109/LGRS.2017.2749120

Wang, J., MacDonald, D. G., Orton, P. M., Cole, K., and Lan, J. (2015). The effect of discharge, tides, and wind on lift-off turbulence. *Estuar. Coasts* 38, 2117–2131. doi: 10.1007/s12237-015-9958-y

Whitney, M. M., and Garvine, R. W. (2005). Wind influence on a coastal buoyant outflow. *J. Geophys. Res.* 110:C03014. doi: 10.1029/2003JC002261

Wright, L. D., and Coleman, J. M. (1971). Effluent expansion and interfacial mixing in the presence of a salt wedge, Mississippi River delta. *J. Geophys. Res.* 76, 8649–8661. doi: 10.1029/JC076i036p08649

Xing, J., and Davies, A. M. (1999). The effect of wind direction and mixing upon the spreading of a buoyant plume in a non-tidal regime. *Cont. Shelf Res.* 19, 1437–1483. doi: 10.1016/S0278-4343(99)00025-4

Yankovsky, A. E. (2006). On the validity of thermal wind balance in alongshelf currents off the New Jersey coast. *Cont. Shelf Res.* 26, 1171–1183. doi: 10.1016/j.csr.2006.03.008

Yankovsky, A. E., and Garvine, R. W. (1998). Subinertial dynamics on the inner New Jersey shelf during the upwelling season. *J. Phys. Oceanogr.* 28, 2444–2458. doi: 10.1175/1520-0485(1998)028<2444:SDOTIN>2.0.CO;2

Yankovsky, A. E., and Voulgaris, G. (2019). Response of a coastal plume formed by tidally-modulated estuarine outflow to light upwelling-favorable wind. *J. Phys. Oceanogr.* 49, 691–703.

Yankovsky, A., Fribance, D., Cahl, D., and Voulgaris, G. (2021). Data for the Paper in Front. Mar. Sci. doi: 10.3389/fmars.2021.785967 (v1.0) [Data set]. *Zenodo*. doi: 10.5281/zenodo.5796882

Conflict of Interest: The authors declare that the research was conducted in the absence of any commercial or financial relationships that could be construed as a potential conflict of interest.

Publisher's Note: All claims expressed in this article are solely those of the authors and do not necessarily represent those of their affiliated organizations, or those of the publisher, the editors and the reviewers. Any product that may be evaluated in this article, or claim that may be made by its manufacturer, is not guaranteed or endorsed by the publisher.

Copyright © 2022 Yankovsky, Fribance, Cahl and Voulgaris. This is an open-access article distributed under the terms of the Creative Commons Attribution License (CC BY). The use, distribution or reproduction in other forums is permitted, provided the original author(s) and the copyright owner(s) are credited and that the original publication in this journal is cited, in accordance with accepted academic practice. No use, distribution or reproduction is permitted which does not comply with these terms.

APPENDIX

We consider small-amplitude perturbations in the x–z plane to the mean flow conditions described by the density and horizontal velocity profiles, $\rho_0(z)$ and $U(z)$, respectively. The linearized equations of momentum balance, mass balance and continuity are:

$$\rho_0\left(\frac{\partial u}{\partial t}+U\frac{\partial u}{\partial x}+\frac{dU}{dz}w\right)=-\frac{\partial p}{\partial x}, \tag{A1}$$

$$\rho_0\left(\frac{\partial w}{\partial t}+U\frac{\partial w}{\partial x}\right)=-\frac{\partial p}{\partial z}-\rho g, \tag{A2}$$

$$\frac{\partial \rho}{\partial t}+U\frac{\partial \rho}{\partial x}+\frac{d\rho_0}{dz}w=0, \tag{A3}$$

$$\frac{\partial u}{\partial x}+\frac{\partial w}{\partial z}=0, \tag{A4}$$

where u and w are the x- and z-components of the perturbed velocity vector, ρ is the perturbed density, p is the perturbed pressure, and t is the time. The system Equations A1–A4 can be reduced to the following equation for w:

$$\left(\frac{\partial}{\partial t}+U\frac{\partial}{\partial x}\right)^2\left(\frac{\partial^2 w}{\partial x^2}+\frac{\partial^2 w}{\partial z^2}\right)+N^2\frac{\partial^2 w}{\partial x^2}-\frac{d^2U}{dz^2}\left(\frac{\partial}{\partial t}+U\frac{\partial}{\partial x}\right)\frac{\partial w}{\partial x}=0, \tag{A5}$$

where $N^2=-\frac{g}{\rho_0}\frac{d\rho_0}{dz}$ is the buoyancy frequency squared. We seek harmonic in time and in horizontal coordinate solution in the form:

$$w=\hat{w}(z)e^{i(kx-\omega t)}, \tag{A6}$$

where ω is the wave frequency and k is the wavenumber. Substituting Equation A6 into Equation A5 yields:

$$\frac{d^2\hat{w}}{dz^2}+\lambda\hat{w}=k^2\hat{w}, \text{ where } \lambda=\frac{N^2}{(U-C)^2}-\frac{1}{U-C}\frac{d^2U}{dz^2}. \tag{A7}$$

Here $C=\omega/k$ is the wave phase speed, and $\hat{w}$ is subject to boundary conditions:

$$\hat{w}=0(z=0,-H). \tag{A8}$$

For a fixed value of C, Equations A7, A8 form an eigenvalue problem for k^2 with the vertical profile of the w-component being the corresponding eigenvector. The u-component profile can be recovered from Equation A4. The problem is solved numerically for the arbitrary profiles of $N^2(z)$ and $U(z)$ by approximating derivatives with central differences. The problem is solved in MATLAB using its function **eig**. The accuracy of numerical solution was tested by using the analytical solution for constant N^2 and U. The dispersion curve $\omega=\omega(k)$ for the gravest first mode is recovered by repeating calculations for different values of C. Equation A7 is analogous to the well-known Taylor–Goldstein equation for the stratified parallel shear flow, except here the solution is sought in terms of vertical velocity rather than streamfunction. It should be noted that in the present problem formulation, internal waves become non-dispersive at low frequencies, that is, their dispersion curve becomes a linear function with constant C. Thus, the solution technique which we use cannot be applied in this situation. However, at low frequencies the waves also become affected by the Earth's rotation and so become dispersive again. In any case this low-frequency regime is beyond the scope of our study.

frontiers in Marine Science

ORIGINAL RESEARCH
published: 10 February 2022
doi: 10.3389/fmars.2021.793217

The Impacts of Freshwater Input and Surface Wind Velocity on the Strength and Extent of a Large High Latitude River Plume

J. Blake Clark[1,2,3]* *and Antonio Mannino*[1]

[1] Ocean Ecology Laboratory (Code 616), NASA Goddard Space Flight Center, Greenbelt, MD, United States, [2] NASA Postdoctoral Program, Goddard Space Flight Center, Universities Space Research Association, Greenbelt, MD, United States, [3] Goddard Earth Sciences Technology and Research II, University of Maryland, Baltimore County, MD, United States

Arctic Ocean physical and biogeochemical properties are strongly influenced by freshwater input from land and through the Bering Strait, where the mean currents transport water northward from the Bering Sea. The Yukon River is one of the largest rivers in North America and the Arctic, contributing large quantities of freshwater and terrigenous material to the coastal ocean in the northern Bering Sea. However, a detailed analysis of the coastal hydrodynamics at the outflow of the river has not been conducted in this remote but regionally important river. A three-dimensional hydrodynamic model was built to represent the lower Yukon River and coastal ocean for the ice-free months in 7 years. On average, a large anticyclonic eddy persisted at the main outflow of the Yukon that recirculates water back toward the coast where the currents converge to form a mean northward transport along the delta. Interannual spatial variance in salinity was relatively small, while there was substantial variance in *u* and *v* current velocity. *u* velocity spatial variance was correlated to the volume of freshwater discharge across years, while *v* velocity spatial variance was correlated to the N–S wind velocity. During strong wind events, plume structure was substantially altered: southerly winds deepened the plume and enhanced northward transport, while northerly winds shoaled and strengthened the pycnocline, and reversed the flow toward the south. The variability in plume dispersion on short time scales due to wind forcing has implications for where terrigenous material is processed in and settles out of the water column.

Keywords: river plume, stratification, Bering Sea, Arctic Ocean, Yukon River

OPEN ACCESS

Edited by:
Alexander Yankovsky, University of South Carolina, United States

Reviewed by:
Yusuke Kawaguchi, The University of Tokyo, Japan
Zhaoqing Yang, Pacific Northwest National Laboratory (DOE), United States

***Correspondence:**
J. Blake Clark
blake.clark@nasa.gov

Specialty section:
This article was submitted to Coastal Ocean Processes, a section of the journal Frontiers in Marine Science

Received: *11 October 2021*
Accepted: *16 December 2021*
Published: *10 February 2022*

Citation:
Clark JB and Mannino A (2022) The Impacts of Freshwater Input and Surface Wind Velocity on the Strength and Extent of a Large High Latitude River Plume. Front. Mar. Sci. 8:793217. doi: 10.3389/fmars.2021.793217

INTRODUCTION

The northern Bering Sea and Arctic Ocean are rapidly experiencing the effects of climate change, with increasing ocean temperatures (Grebmeier, 2012; Danielson et al., 2020), loss of sea ice (Stabeno et al., 2019), increasing river flow (Feng et al., 2021), and mobilization of long buried carbon from permafrost into aquatic systems (e.g., Rawlins et al., 2019). The relatively shallow bathymetry and large freshwater input make the Arctic the freshest of the major ocean basins, with riverine input of freshwater and terrestrial material imprinting on the Arctic Ocean physics

and biogeochemistry throughout the basin. A significant amount of organic matter is transported by these rivers into the ocean, including particulate organic carbon (POC; McClelland et al., 2016) which can be deposited into the shallow coastal seas, and dissolved organic carbon (DOC), which can be transported further from the coast and into deeper marine waters (Fichot et al., 2013). Historically, a large amount of ocean water (∼0.8 Sv; 1 Sv = 1 km^3 s^{-1}) (Roach et al., 1995) enters the Arctic through the Bering Strait, where the mean flow from the northern Bering Sea brings fresher continental runoff into the Arctic. In the last three decades there has been an increase of ∼20% in the northward transport of water through the Bering Strait, with flow increasing to 1.0 ± 0.05 Sv (Woodgate, 2018).

The input of freshwater and material along the Alaskan coast has the potential to be transported through the coastal current system into the Arctic, likely impacting the regional and global freshwater budgets and carbon cycles. Key processes related to POC and DOC transformations such as flocculation and settling occur in regions with strong salinity gradients within river plumes. The lack of knowledge of the spatial and temporal variability of the coastal currents in the northern Bering Sea at the outflow of the Yukon River make generalizations of the transport of riverine water and material from the Northern Bering Sea into the Arctic difficult. The coastal dynamics where the Yukon plume enters and mixes with marine water in the shallow and broad shelf are not thoroughly characterized even though the contribution to Arctic biogeochemical processes is likely large.

The Yukon River is the 5th largest river in North America, and the longest free-flowing river in the world (Yukon River Inter-Tribal Watershed Council, 2021). It is the 5th largest of the Arctic Great Rivers (Shiklomanov et al., 2021) by annual volume with a median discharge of 207 km^3 $year^{-1}$ from 1977 to 2019 (Clark and Mannino, 2021). Like other polar rivers, it is highly seasonal with discharge peaking in spring upon ice breakup, sustaining throughout the ice-free season with substantial interannual variability, and declining substantially from the fall into the winter. The Yukon has the highest sediment yield per unit watershed area for the six largest Arctic rivers, with 67 Mg km^{-2} $year^{-1}$ of total sediment entering the ocean on average (Piliouras and Rowland, 2020). In addition, DOC yield per watershed area is the third largest among the six largest Arctic rivers at 625 mg C m^{-2} $year^{-1}$ and 1.5 Tg C $year^{-1}$ of DOC is transported to the ocean from the Yukon basin on average (Holmes et al., 2012). With the mean northward current and shallow coastal bathymetry, a substantial portion of Yukon derived DOC may be transported through the Bering Strait contributing to the Arctic carbon budget. The time and space scales of transport of the riverine water along the coast likely exhibit substantial control on the quantity and composition of the material that flows through the Bering Strait into the Arctic as various biogeochemical reactions occur in and outside of the plume.

River plumes are highly complex hydrographic features in the coastal ocean where freshwater enters, stratifies, and mixes with oceanic water. River plume characterization exists along a continuum (Horner-Devine et al., 2015), and sampling and mathematical methods used to quantify the distribution of freshwater in the coast are varied and complex. The amount of freshwater and the geomorphology of the river channel adjacent to the coast are the first order controls; high discharge and a narrow channel will lead to a large plume and a prototypical river plume structure, while a large estuary or deltaic environment can lead to substantially different plume dynamics (Horner-Devine et al., 2015). External forcing such as tidal currents and wind stress can also affect how river plumes mix, evolve, and disperse in space and time in the ocean (e.g., Fong and Geyer, 2001; Pritchard and Huntley, 2006; Banas et al., 2009; Horner-Devine et al., 2015). The interplay of these external factors and the volume and timing of riverine discharge into the ocean will largely control the distribution of the plume from the outflow into deeper marine waters.

The main physical drivers of plume mixing dynamics shift as distance from the river mouth increases within large river plumes and other density stratified systems (Fong and Geyer, 2001; Hetland, 2005). Specific regions where mixing dynamics shift have been defined as the near-field, mid-field, and far-field areas, although the boundaries between these regions are rarely strongly delineated (Horner-Devine et al., 2015). In the near field just outside of the mouth, inertial flow from the momentum of river discharge dominates, and stratification is minimal as the water column remains vertically uniform and relatively fresh (Horner-Devine et al., 2015). Beyond this, stratification sets in as the bathymetry begins to slope away and buoyancy driven flow due to density stratification combined with the Coriolis force and centripetal acceleration can develop a large "bulge" offshore (Yankovsky and Chapman, 1997; Horner-Devine et al., 2015). Further offshore in the far-field of the plume, the Coriolis force and wind driven mixing exert a stronger influence on plume dispersion (Hetland, 2005; Horner-Devine et al., 2015). The balance between vertical shear, stratification, and inertial flow is critical in governing the overall structure of the plume as it evolves in space and time.

Wind stress is an important external forcing factor that can drive currents in the coastal ocean and affect how mixing occurs within a river plume (Hetland, 2005). The balance of wind-driven and buoyancy-driven flow will have a strong influence over how the plume is distributed in time and space for a given system beyond the frontal region (Whitney and Garvine, 2005). Wind regimes in the coast are generally categorized as "upwelling" or "downwelling" which refers to the wind's imparted effect on the coastal ocean currents either "pulling" water up from depth to the surface with a mean flow offshore, or "pushing" water down from the surface to depth with a mean flow onshore (Fong and Geyer, 2001). Downwelling winds tend to enhance the mean along shore current, increasing surface velocity within a plume while narrowing the horizontal extent of the plume and deepening the depth of the pycnocline (Fong and Geyer, 2001). Upwelling winds tend to have the opposite effect, narrowing the vertical extent of the plume while broadening the horizontal extent offshore due to the competing wind velocity and mean current flow and the Ekman transport of water offshore. The scales of mixing and how the plume currents and density respond to surface wind stress will likely impact coastal riverine material retention, distribution, and particulate deposition in the near shore region.

The hydrodynamic and circulation features of the lower Yukon River, delta, plume, Norton Sound and adjacent Bering Sea are understood only from a broad large-scale perspective with limited historical observational studies (e.g., Dean et al., 1989). In this study, a high-resolution numerical ocean model was constructed to characterize and predict fine-scale ocean hydrodynamics in the Yukon River plume, Norton Sound, and the coastal northern Bering Sea (hereinafter YukonFVCOM). The model was implemented over 7 years and used to estimate the hydrographic patterns at the outflow of the Yukon River. In addition, specific strong wind events were identified in each year to better estimate the effects of wind forcing on the plume structure and distribution. This allows a detailed characterization of the driving forces that govern the river plume structure in space and time.

MATERIALS AND METHODS

The Finite Volume Community Ocean Model Description

The Finite Volume Community Ocean Model version 4.3 (FVCOM) is an unstructured grid ocean model designed to simulate ocean physics in locations with complex geography and bathymetry (Chen et al., 2013). It is ideally suited for use in coastal ecosystems such as the Yukon River outflow where flexible model grid geometry allows for including the river delta in the model domain and shallow coastal bathymetry can be well represented. The FVCOM model has been implemented in the Arctic to simulate coastal currents and sea ice on multiple time and space scales and shows good agreement with observations in the region (Chen et al., 2016). FVCOM calculates velocity, momentum, density (ρ), temperature (T), and salinity (S) (among other hydrographic variables) in the water column and offers a prediction of the physical conditions in the coastal ocean. The YukonFVCOM grid is made of 756,241 elements connecting at 435,240 nodes spanning from ∼200 km upstream of the coast at Pilot Station, AK, to south of the Yukon delta northward to west of Nome, AK encompassing nearly all of Norton Sound and the Yukon delta (**Figure 1**). Grid spatial resolution stretches from ∼100 m in shallow coastal and deltaic areas to ∼2.5 km offshore (**Supplementary Figure 1**) with 10 vertical layers each comprising 10% of the water column at any given location. T, S, ρ, and sea surface height (η) are calculated at the nodes of the triangular mesh, and *u* and *v* current velocity vector components are calculated at the element centers. While intertidal wetting and drying is an important feature of FVCOM, we did not implement the scheme here as the focus of the study was in the ocean rather than intertidal regions.

To build the model grid, United States Geological Survey (USGS) HUC-8 watershed boundaries and Norton Sound coastline along with the USGS NED-8 Alaska digital elevation model were loaded into the Aquaveo® SMS meshing software to construct the unstructured triangular mesh based on the bathymetry. The model was built for the period of April 1 to September 30 for 7 years spanning various hydrological patterns (**Table 1**). The initial condition was set for every year using the output from September 30 of 2004 after three sequential simulations to equilibrate the salinity field. This was done for consistency upon initialization and with the assumption that by the time model analysis was initiated in May of each year, the ocean temperature would have equilibrated with the atmosphere and any residual salinity would have dissipated. The spring freshet generally occurs over May and early June (**Table 1**). Two anomalous years with regards to ice and river discharge were 2019 and 2005, respectively. In 2019, sea ice was virtually non-existent in Norton Sound (National Snow and Ice Data Index[1]), and the largest discharge on record occurred in 2005 with a very early ice break-up and spring freshet (**Table 1**).

The model was constructed and run on the NASA Center for Climate Simulation supercomputer *Discover* at NASA Goddard Space Flight Center. Forty compute nodes utilizing 28 out of 40 cores on each node were used for each simulation year taking 10–12 wall-clock hours to run with the 1,120 processes. The model internal time step was 6 s and the external time step was 2 s. Model output is in NetCDF format at hourly intervals and the output files were averaged as necessary using the NetCDF Operators (NCO) toolbox to generate monthly average composites[2].

Yukon River and Norton Sound Model Domain

The Yukon River is the 5th largest river routinely sampled as part of the Arctic Great Rivers Observatory (ArcticGRO) with daily gauge records going back to 1977. Under ArcticGRO, high quality biogeochemical observational data (Holmes et al., 2021) are collected at Pilot Station, AK, United States (61.9344°N, −162.881°W) (**Figure 1**) at USGS gauge station 15565447 making this an optimal Arctic River system for modeling hydrodynamic-biogeochemical interactions. Pilot Station is located ∼200 km upstream from the outflow of the delta region that drains into the shallow Norton Sound, with ∼95% of the 824,400 km^2 watershed located above the gauge station (**Figure 1B**). The watershed is underlain with 58% discontinuous permafrost (Holmes et al., 2012), and like other Arctic systems the discharge is highly seasonal with a peak occurring in late spring after ice break up and secondarily in later in the summer due to processes in the interior of Alaska such as rain events or melting snow and glaciers (Dornblaser and Striegl, 2009).

Tides, Meteorology, Open Boundary, and River Forcing

Four key external forcing factors are required to set up the FVCOM model. First, the open boundary surface elevation that drives the tidal elevation and tidal velocity in the coast was built using the TPXO software (Egbert and Erofeeva, 2002). This software is commonly used to predict tidal elevation in space and time throughout the globe. The model boundary node coordinates (n = 389) and hourly time intervals for each year were input to the software to predict the tidal elevation at each boundary node for the model time period.

[1]https://nsidc.org/data/seaice_index

[2]http://nco.sourceforge.net/

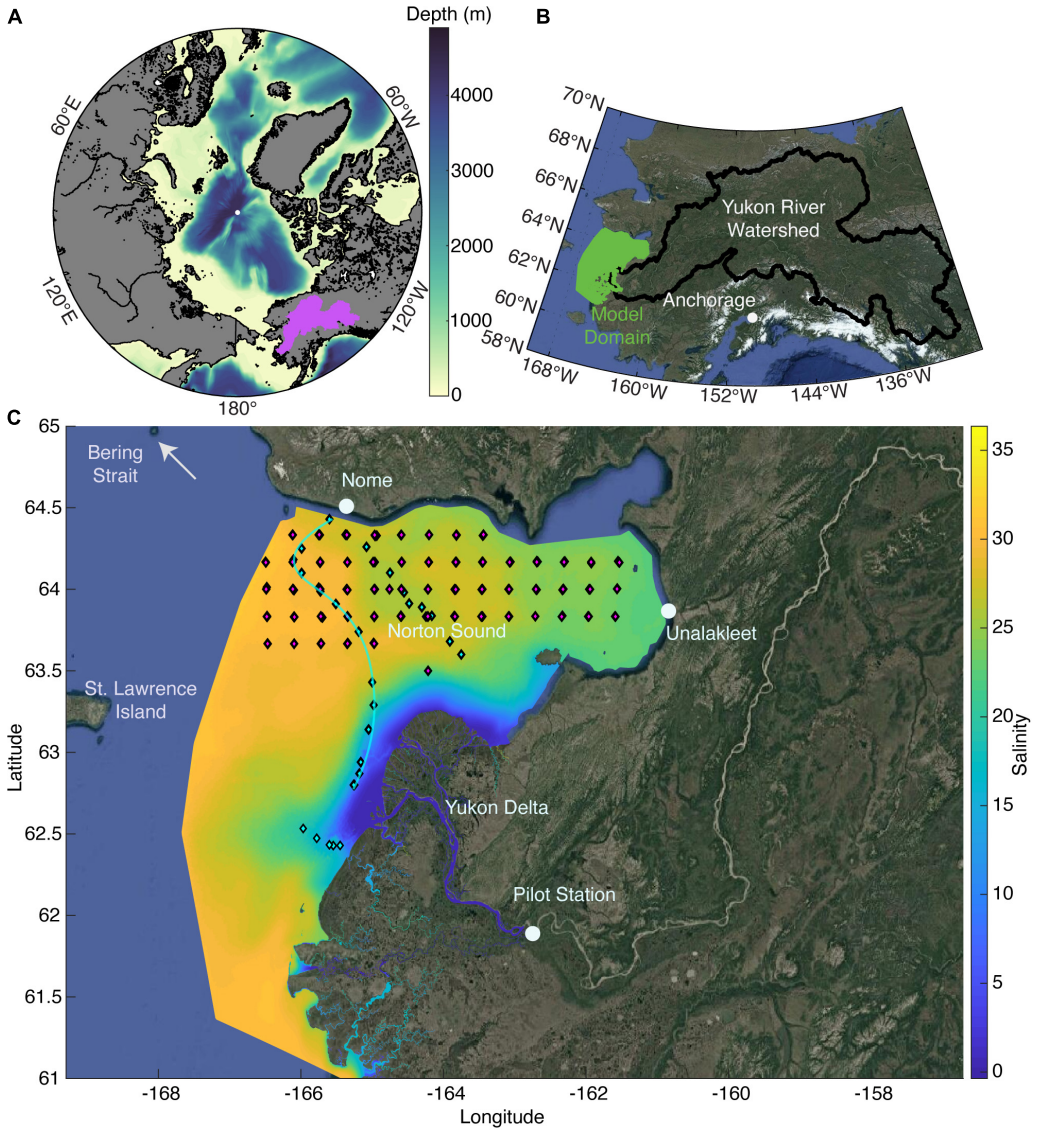


FIGURE 1 | (A) The Arctic Ocean showing the Yukon River watershed in purple; **(B)** Alaska and western Canada showing the Yukon watershed with the extent of the Yukon River FVCOM hydrodynamic model domain (YukonFVCOM); **(C)** the YukonFVCOM model domain with Alaska Department of Fish and Game (ADF&G) fishery survey stations as red markers and the stations sampled under the NASA RSWQ project in 2019 as cyan markers. The color contours are the average surface salinity predicted by the model for 2019. Panel **(A)** was created using the m_map toolbox (Pawlowicz, 2020) and the images in panels **(B,C)** were created using the MATLAB function Plot_Google_Map.m (Bar-Yehuda, 2021).

The surface meteorology was built for each year using daily predictions of weather conditions from the North American Regional Reanalysis (NARR; Mesinger et al., 2006). Wind vector velocity (m s^{-1}), air temperature (°C), relative humidity (%), surface pressure (Pa), and net short wave and long wave radiation (W m^{-2}) were used as the weather forcing of YukonFVCOM. Daily average wind velocity is used to predict wind-stress on the surface of the ocean model and wind roses for each year can be found in supporting information (**Supplementary Figure 2**). Relative humidity, air temperature, surface pressure, and radiation are used in the COARE2.6 algorithm (Fairall et al., 2003) to calculate the heat flux between the ocean and the atmosphere at each time step. To apply the 32 km NARR data to the high-resolution grid, all NARR grid points over the model domain were extracted for each variable. Next, the gridded weather data were interpolated onto each of the model triangular cells using a nearest-neighbor interpolation. Norton Sound is covered with sea ice in the winter and early spring, but dynamically modeled sea ice was excluded from this effort to reduce complexity, therefore model analysis (unless otherwise specified) began on May 1 after spin-up over the month of April and early May to allow the model to equilibrate.

The open boundary water column T and S fields were constructed using the World Ocean Atlas 2018 (WOA18)

TABLE 1 | Annual discharge (Q) and wind velocity vector components of each model year used in the FVCOM hydrodynamic model analysis.

Year	Cumulative Q[a]	Peak Q (date)[b]	Mean Q (date)[c]	*u* Wind[d] (σ)	*v* Wind[e] (σ)
2004	147.0	1.83 (June 12)	71.4 (June 25)	–0.48 (2.52)	–0.67 (3.39)
2005	193.6	3.34 (May 17)	99.0 (June 22)	0.51 (2.99)	–0.22 (4.50)
2015	151.8	1.75 (June 4)	64.7 (June 28)	0.99 (3.13)	–0.80 (3.45)
2016	183.1	1.70 (Aug. 30)	76.2 (July 4)	0.35 (2.89)	–1.05 (3.88)
2017	134.7	1.59 (June 1)	56.9 (July 2)	0.47 (2.52)	–1.39 (3.90)
2018	171.7	1.88 (June 8)	74.1 (June 28)	–0.16 (3.41)	–0.68 (3.24)
2019	151.0	1.83 (June 7)	68.7 (June 26)	0.18 (3.26)	–0.33 (4.22)

[a] *Total discharge over 183 day model period (km^3).*
[b] *Peak discharge (10^4 m^3 s^{-1}) and the date it occurred.*
[c] *Mean cumulative discharge (km^3) and the day of the year it was exceeded.*
[d] *Mean west–east vector wind velocity (m s^{-1}) and the standard deviation (σ), positive is westerly (from the west).*
[e] *Mean south–north vector wind velocity (m s^{-1}) and the standard deviation (σ), positive is southerly (from the south).*

TABLE 2 | Statistical metrics used to generate target diagrams (**Figures 3**, **4**).

Metric	11 μm MODIS-A[d]	11 μm SNPP[e]	4 μm MODIS-A[f]	CTD[g] Salinity	CTD[g] Stratification	CTD[g] Temperature
RMSD[a]	3.03 ± 1.45	2.63 ± 0.87	3.22 ± 0.91	2.92 ± 2.66	1.24 ± 0.85	4.45 ± 1.97
Bias[b]	–1.80 ± 1.70	–0.92 ± 1.49	–0.59 ± 2.06	0.68 ± 3.10	0.54 ± 0.51	–2.13 ± 2.41
r[c]	0.70	0.79	0.64	0.69	0.29	0.67

Values represent the mean across all comparisons for each statistic ±1 standard deviation.
[a] *Root mean square deviation (°C for temperature).*
[b] *Bias (difference between model and reference mean).*
[c] *Correlation coefficient.*
[d] *MODIS-Aqua sensor 11 μm (daytime) sea surface temperature satellite data product.*
[e] *Suomi-NPP VIIRS sensor 11 μm (daytime) sea surface temperature satellite data product.*
[f] *MODIS-Aqua sensor 4 μm (nighttime) sea surface temperature satellite data product.*
[g] *Conductivity, temperature, and depth sensor field data.*

T and S climatologies for each decade (Locarnini et al., 2018; Zweng et al., 2018). Monthly climatologies of each variable were downloaded and the closest points of the global WOA18 1° grid to the model boundary nodes were identified. For each month, WOA18 T and S were interpolated in three-dimensional space (longitude, latitude, and depth) onto the curved model boundary using the MATLAB® function *griddatan.m*. FVCOM linearly interpolates between input time points to match the time step within the model from the monthly climatological values.

Last, daily mean river discharge and water temperature at Pilot Station, AK were downloaded from the USGS[3] and implemented directly for each day in the model time frame. **Figure 2** shows the entire gauge record from 1977 to 1996 and 2001 to 2019. The daily discharge values were evenly split over the nine model nodes that makeup the landward model boundary which begins at Pilot Station and flow was evenly applied vertically in the water column. Substantial variability exists in the model years in timing and magnitude of the freshet, in addition to total discharge, offering a wide range of riverine conditions to assess how freshwater input can affect coastal ocean hydrography. **Table 1** provides a summary of freshwater input parameters and average wind vector velocities for each model period.

[3]https://waterdata.usgs.gov/nwis/inventory/?site_no=15565447

Model-Data Comparisons for Validation

Three sources of *in-situ* data were used to assess the predictability of the YukonFVCOM T and S fields in time and space. The Alaska Department of Fish and Game (ADF&G) conducted

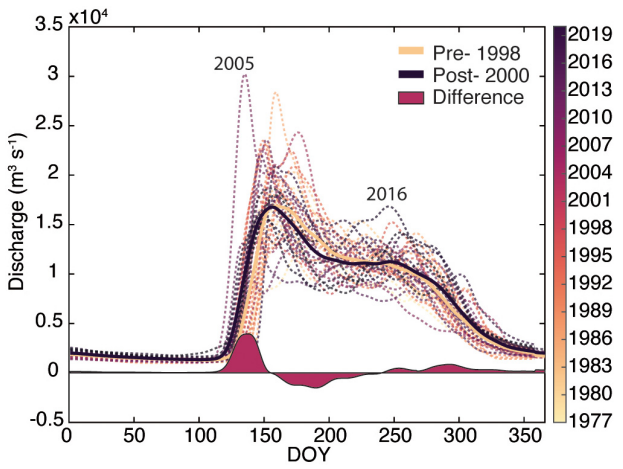


FIGURE 2 | United States Geological Survey (USGS) daily mean river discharge at Pilot Station, AK, United States for the period from 1977 to 2019. The difference is between the mean pre-1998 and post-2000 discharge.

surveys in 2017, 2018, and 2019 of fish stocks in Norton Sound where T and S vertical profiles were collected across Norton Sound during the summer (**Figure 1C**). In addition, 40 T and S vertical profiles were collected under the National Aeronautics and Space Administration (NASA) Remote Sensing of Water Quality (RSWQ2019) project #80NSSC18K0492 (PI Hernes, UC Davis) in late May and June of 2019 in the Yukon River delta and Norton Sound. All ADF&G and RSWQ2019 sampling stations used for the model skill assessment are shown in **Figure 1C**. The National Oceanographic and Atmospheric Administration Tides and Currents stations at Nome, AK and Unalakleet, AK were used to assess the models ability to predict η. The station at Nome is very close to the model boundary and therefore suffers some boundary effects, while the station at Unalakleet is deep in the model interior in Norton Sound and is therefore the best assessment of the predictive capacity of YukonFVCOM for η. The closest model nodes in space and time were matched with the CTD casts and the tide gauge stations for a statistical comparison using the correlation coefficient (*r*), Nash-Sutcliffe model efficiency (MEF), and RMSD as the primary metrics (Stow et al., 2009).

Sea surface temperature (SST) was validated for each year using satellite data acquired from the NASA Level 2 Ocean Color Browser (Nasa Goddard Space Flight Center, Ocean Ecology Laboratory, Ocean Biology Processing Group, 2020). Images with 100% spatial coverage over the model domain were downloaded at Level-2 daily for the 4 and 11μm temperature products from MODIS-Aqua (all years) and 11 μm VIIRS-Suomi-NPP (2015–2019) (JPL/OBPG/RSMAS, 2020). Monthly mean composites were constructed from each set of individual daily images by finding all images within a month and averaging through time. Each node in the model was assigned the closest satellite pixel in the image and the set of images were "stacked" in an array (number of model nodes × number of images) for each month. Finally, the monthly mean was taken excluding the points within each image that were masked to build a nearly complete monthly composite of SST over the ocean. Because of the large amount of satellite data and model output to compare (435,240 points × 5 months × 7 years), a target diagram approach was used to easily display the model-data comparison while assessing the predictive capacity of the model (Jolliff et al., 2009). The unbiased root mean square deviation (uRMSD) was scaled by the sign of the difference between modeled and observed standard deviation, so points on the left (right) of the origin indicate less (more) spatial variability in the modeled prediction vs. the observed. Bias is a measure of the direction and magnitude of the modeled SST relative to the observed with a negative bias indicating the model values are less than observations for that month. An example monthly satellite - YukonFVCOM SST comparison from August of 2019 can be found in **Supplementary Figure 3**. The same sign convention holds for the target diagram comparisons of the CTD casts.

Model Output Analysis

Monthly averaged model results were compiled for each year by averaging each NetCDF output file along the time dimension. A model transect was extracted along the blue-marked cruise track in **Figure 1C**, corresponding to the RSWQ2019 cruise from Nome toward the south Mouth of the Yukon River delta. This was done by finding the closest element centered points along the track evenly spaced at 200 m. To get element-centered T, S, and ρ, the average of the three nodes of each element were calculated. Much of the analysis related to plume dynamics and extent was reduced to this transect for simplicity, while maintaining a gradient from freshwater and across Norton Sound.

Multiple metrics related to the velocity field, density, and buoyancy were calculated to relate river forcing, wind velocity and coastal currents and plume distribution in the coastal ocean. First, vertical shear was calculated using Eq. 1 where u and v are the west–east and south–north (positive is north and east) current velocity vector components, z is the depth, and $dU\,dz^{-1}$ is the vertical shear. Equation 2 represents the formulation used to calculate the Brunt-Vaisala frequency, N^2 (s^{-2}) where g is the acceleration due to gravity (9.8 m s^{-2}), and ρ is the density calculated by the equation of state from the predicted T and S. The effect of pressure on density was assumed to be negligible because of the shallow depth of our study domain. All vertical gradients were calculated at model intra-sigma levels (n = 9). N^2 is a measure of the stratification stability of a water column with a greater N^2 indicating stronger stratification and water column stability.

Semi-variograms for u and v current velocity and salinity were calculated using the MATLAB file exchange toolboxes *variogram* and *variogramfit* (Schwanghart, 2020a,b). Variograms are a measure of the spatial autocorrelation of a dataset and are commonly used in geostatistical modeling to predict intermediate values in a sampled data set (Matheron, 1963). Here, the variograms were used to quantify the spatial variance for each year to assess the interannual similarity (or difference) in the spatial patterns of the salinity and velocity fields. Semi-variogram analysis was conducted by finding all pixels in the model where the salinity was greater than 2.0 to avoid issues relating to calculations occurring by relating points that are close in spatial proximity but are separated by land in portions of the delta. The semi-variogram, $\gamma(h)$, and lag distances, h, were input to *variogramfit* where an exponential model (Eq. 3) was iteratively fit to each experimental variogram by reducing the least-squares difference of the experimental and modeled variogram. The modeled variogram, $\gamma(h)$, is an exponential function of the sill, s, and the range, r. The range is a measure of the distance when values are no longer spatially autocorrelated, and the sill is the $\gamma(h)$ at the range. Finally, the range of each estimated variogram was compared to springtime cumulative river discharge, E–W wind velocity, and N–S wind velocity to assess how each forcing correlates to the spatial variance of the coastal ocean physical properties.

$$\frac{dU}{dz} = \frac{d\sqrt{u^2+v^2}}{dz} \tag{1}$$

$$N^2 = \frac{g}{\rho}\frac{d\rho}{dz} \tag{2}$$

$$\gamma(h) = s\left(1 - e^{\left(\frac{-r}{3}\right)}\right) \tag{3}$$

RESULTS AND DISCUSSION

River Discharge Variability

River discharge varied considerably between 1977 and 2019 and there was a subtle shift in discharge patterns over the gauge record (**Figure 2**). The difference between pre- and post-2000 (the middle of the gauge record) shows greater discharge earlier in the year post-2000 and a small increase in discharge in the later summer and early fall (**Figure 2**). The greatest discharge on record occurred in 2005 which also had the earliest discharge peak on May 17 (**Table 1**). Annual cumulative discharge was greatest in 2005 (247 km^3) and the second greatest was in 2016 (243 km^3) when discharge peaked on August 30, the only year where discharge peaked after July 12th. Maximum discharge from 2015 to 2019 averaged $17.5 \pm 1.15 \times 10^3$ m^3 s^{-1} while the average for the entire record is $20.3 \pm 4.9 \times 10^3$ m^3 s^{-1}. Contrarily, average total cumulative discharge from 2015 to 2019 was 217.3 ± 19.1 km^3 which is greater than the average of all years of 208.1 ± 18.5 km^3. This pattern indicates a broadening of the hydrograph, from a larger proportion of discharge occurring in late May and June historically, to a broader freshet that extends from the spring peak into the summer in more recent years. Relative to pre-1998 records, average cumulative discharge has increased 2.75% since 2000 (Clark and Mannino, 2021). This updated record adds to the growing body of evidence of river flow increasing into the Arctic Ocean (McClelland et al., 2006; Durocher et al., 2019; Feng et al., 2021).

Model Comparison With Satellite Sea Surface Temperature

YukonFVCOM has a good SST predictive capacity and relatively high inter-annual precision of estimating SST, especially in summer months, across all years (**Figure 3**). Overall, the model performance indicates that for most months the model is within 3°C of the observed average SST and model performance improves from spring into summer. There is a general cold bias in the model relative to satellite observations (mean of −1.2°C) but there is variance across seasons and sensors (**Table 2**). 4 μm SST matchups were substantially less biased than 11 μm MODIS-A and SNPP observations (−0.59° vs −1.80° and −0.92°) indicating that the bulk heating and cooling into the ocean is well captured. This is because 4 μm SST is measured at night and is therefore more representative of overall heat content and not as susceptible to diurnal temperature variance of the surface skin layer. Performance bias improves from spring into summer across sensors, with improvements from −3.01° to −0.99° for 11 μm MODIS-A, −1.33° to +0.90° for 4 μm MODIS-A, and −1.53° to −0.51° for 11 μm SNPP. Each sensor has a uRMSD < −2.5° for the spring months, indicating the model was more spatially uniform relative to observations. uRMSD improves substantially after June, especially for 11 μm MODIS-A and SNPP comparison (uRMSD = −0.08° and −0.81°, respectively). Jia and Mennet (2020) found that MODIS-A SST had a mean bias of −0.57°C across the Arctic when compared to in-water observations, which suggests that as waters warm from spring into summer, YukonFVCOM predictive capacity improves to be substantially less biased. Overall, the relatively low bias as SST increased and the ability for YukonFVCOM to more closely match with the 4μm SST indicates that the bulk formulations related to heating and cooling can capture the first order temperature variance in the model domain.

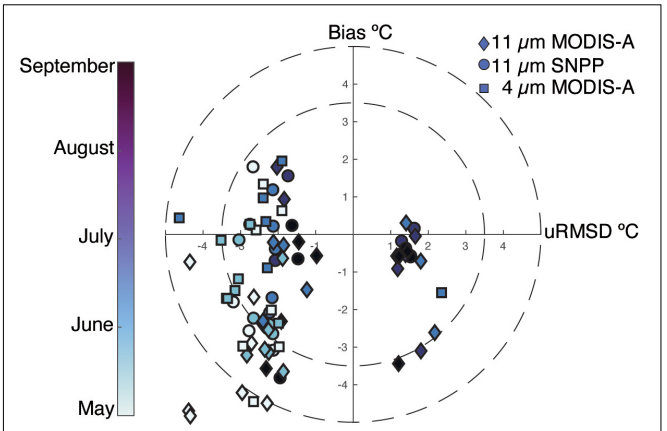


FIGURE 3 | Target diagram for each year of the 7 model run years (2004–2005 and 2015–2019) for 11 μm sea surface temperature for MODIS-Aqua (all years) and Suomi-NPP (2015–2019) observed SST (SST) compared with the FVCOM model predicted SST and 4 μm (night time) SST which was only acquired in May–July for each year from the MODIS-Aqua instrument. Negative bias indicates a colder model prediction relative to the observed, while negative unbiased root mean square deviation (uRMSD) indicates less variability in the model prediction vs. observed. The sign of the uRMSD is determined by the sign of the difference of the standard deviation of the predictions and observations (Jolliff et al., 2009).

The parameterization for horizontal and vertical diffusion was matched to the parameters from an ideal river plume simulation (Chen et al., 2013) and was kept constant between model years, although individual tuning for each year may be needed to achieve optimal solutions. In addition, the specific heat capacity of water used in the COARE2.6 algorithm is held constant at that of seawater although in reality it changes with salinity. To further improve the temperature and salinity predictions, fine parameter tuning for each year and updating the heating algorithm to have a variable specific heat capacity is likely necessary, in addition to using real-time model predicted boundary forcing from a global model. Developments are currently under way to implement the 1/12° global HYCOM model (Smedstad et al., 2008) as the open boundary T and S, rather than climatological forcing, in years when the simulations are available. While the contribution of temperature to density within the plume is likely small due to the large salinity gradients, a future detailed analysis on model temperature is warranted to better understand the physical forcing that may not be well represented in the model formulations. Future simulations that represent sea ice formation and melting will likely impact the early springtime temperature and density fields which may have residual effects into May. This would be crucial to better understand how coastal temperature may have varied in the past and may vary into the future in the northern Bering Sea as seasonal sea ice continues to decline.

Model Comparison With *in-situ* Temperature and Salinity Profiles and Tidal Elevation

Like the satellite SST, the model generally has a cold bias (–2.44°C) in temperature profiles and the bias decreases as temperature increases (**Figure 4A**). The cold bias is mainly due to an underprediction of temperature in the bottom half of the water column (bias = –5.01°C) while surface waters agree well with observations (bias = 0.13°C). The mean uRMSD of 3.20 indicates that temperature stratification is slightly greater in the model than the observations. Coupled with the greater bias in the bottom water, this indicates the temperature stratification is likely overpredicted and vertical heat transfer is underpredicted in YukonFVCOM. Salinity comparisons indicate that YukonFVCOM can simulate the salinity field quite well across years, with mean bias of 0.35 and only slight differences in bias between the surface (–0.76) and bottom (1.47) salinity. The low total bias indicates that salinity variability and stratification in the plume and beyond is well captured. Model results are encouragingly strong along the RSWQ2019 transect which crosses the plume water, with most of the locations with the strongest stratification (yellow and green stars in **Figure 4B**) showing little bias. Coupled with the temperature comparison, YukonFVCOM reasonably represented the salinity distribution and stratification from the plume into Norton Sound.

The unfiltered modeled and verified sea surface elevation values were well correlated across all years at Nome, AK (**Supplementary Figure 4**) and showed especially strong agreement for the tide station at Unalakleet at the interior edge of Norton Sound (**Supplementary Figure 5**). Near the model boundary at Nome, there was some difficulty in capturing high water events due the boundary SSH forcing constructed using the TPXO tidal predictions rather than a dynamically modeled product that accounts for SSH variation due to atmospheric effects. However, the strong performance at Unalakleet shows the YukonFVCOM model's ability to simulate atmospheric induced SSH changes across years and seasons, with a mean Nash-Sutcliffe model efficiency of 0.54 and a mean correlation coefficient of 0.7 (**Supplementary Table 1**). Future implementations that utilize a global model product that can incorporate dynamic atmospheric effects will allow for a more realistic representation of open boundary SSH.

Mean Hydrographic Variability

Average hydrographic features from May to July for all 7 years indicate spatial variability that is relatively typical for a large northern hemisphere river plume (**Figure 5**). Surface salinity varied from 0 continuously around the Yukon delta up to ~33 at the open ocean boundary toward the Bering Strait (**Figure 5A**). Salinity in Norton Sound was indicative of an estuarine environment with relatively low (<30) surface salinity and stratification persistent throughout the sound. The modeled salinity features are similar to surveys that were further out in Norton Sound toward the Bering Strait, with values near 30–32 at the surface and weakening vertical stratification further into the ocean (Dean et al., 1989). The freshwater plume extended furthest into the ocean at the outflow of the southern river mouth where the majority of freshwater exited the delta. The bulge at the south mouth is consistent with a prototypical plume (Horner-Devine et al., 2015) and is very similar to dynamics seen in other large western North American rivers such as the Columbia River (Hickey et al., 1998).

The vertically averaged velocity and sea surface height (η) show a pressure gradient from the delta and eastern edge of Norton Sound sloping toward the Bering Strait, in addition to a prominent eddy that persists at the outflow near the southern mouth of the delta (**Figure 5B**). The anti-cyclonic eddy off the coast of the south mouth coincides with an area of elevated η that extends from the south mouth toward the model boundary and continental shelf. Along the coast north

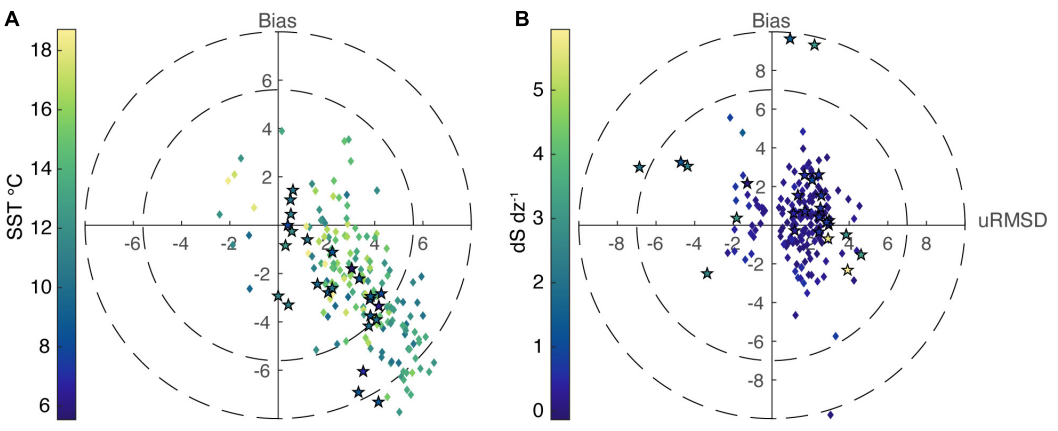


FIGURE 4 | Target diagrams comparing model results with all CTD vertical data collected for **(A)** temperature profiles and **(B)** salinity profiles at the locations in **Figure 1**. Comparisons were made by matching the closest model-observed points in time (daily averaged model output), space, and depth. Diamonds represent profile comparisons at ADF&G stations in Norton Sound and stars represent values collected on the RSWQ 2019 Norton Sound-Yukon plume cruise. The coloring of each marker indicated by the color bars to the left of each panel represents the sea surface temperature (SST) and depth averaged salinity stratification (dS dz^{-1}) at the time of collection.

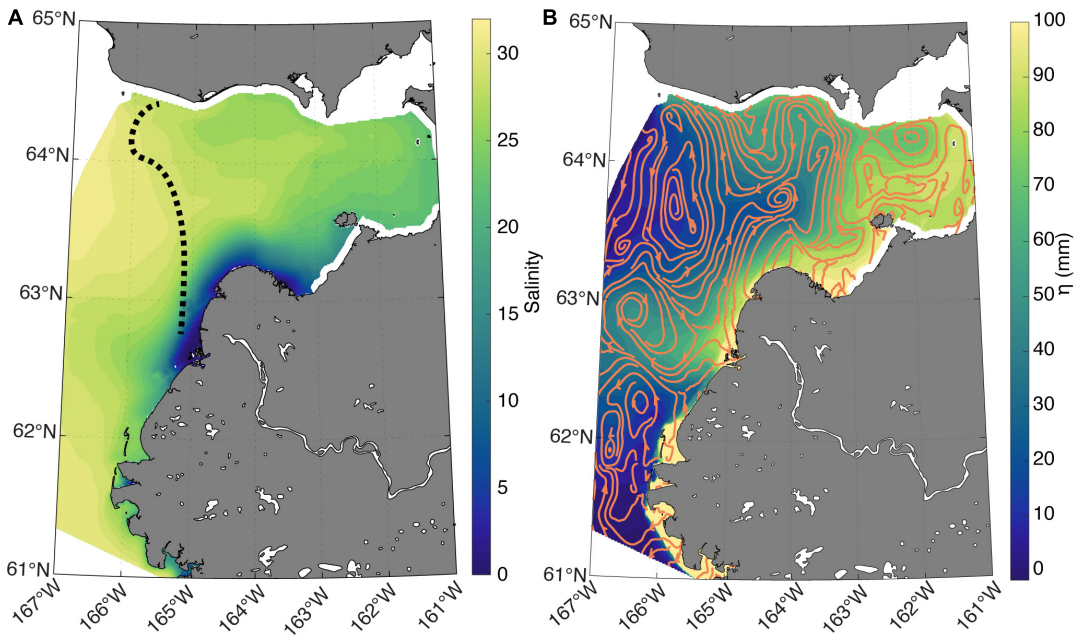


FIGURE 5 | Seven-year depth averaged May-July **(A)** salinity and **(B)** sea surface height (η) with the vertically averaged velocity field represented by the stream lines. The stream lines were derived using the built-in MATLAB function *streamslice.m*.

into Norton Sound, there is a strong northeastward current that pulls water from the eddy region (the bulge) and river delta toward the east side of Norton Sound. Velocity is predominantly northward bringing plume waters toward the north coast of Norton Sound where a strong coastal westward jet pushes water toward Bering Strait. This flow pattern toward the Bering Strait has been previously documented in studies looking at sediment distribution (Dupré, 1980) and a recent Saildrone survey also exhibited evidence of the bulge extending toward the west with the mean flow pulling freshwater back across the face of the delta toward the east into Norton Sound (Cokelet et al., 2015). The qualitative comparison of the YukonFVCOM mean flow and the historical surveys give confidence that the hydrographic patterns exhibited by YukonFVCOM are realistically capturing the flow patterns in the coastal ocean and that the model is a useful tool to analyze controls on the hydrographic variability under differential external forcing conditions.

The plume bulge eddy and coastal currents are typical of large river plumes where the balance between the Earth's rotation and the buoyancy and pressure gradient drives transport along the coast northward into Norton Sound (Hickey et al., 1998; Hetland, 2005). It has been shown that along shore flow of river plumes is governed by the rotation of the earth on longer time scales (Garvine, 1987; Yankovsky and Chapman, 1997) and that large river plumes with small estuaries typically exhibit the bulge feature at the river outflow (Yankovsky and Chapman, 1997; Horner-Devine et al., 2015). The Yukon plume is no exception, and plume dynamics related to the Earth's rotation such as bulge distribution and coastal current velocity are likely enhanced due to the high latitude. Shorter term variation due to wind forcing that undoubtedly affects river plume dynamics and distribution will be explored further in the following section.

Interannual Variation in Plume Dynamics

Salinity was more horizontally uniform relative to u and v currents with a greater average semi-variogram range (63.1 ± 4.4 km) (mean ± standard deviation, σ hereafter) and there were relatively similar values across all years, indicated by the similarity of the variograms (**Supplementary Figure 6A**) and the low relative σ of the range and sill (**Table 3**). u velocity was more spatially uniform (range = 32.5 ± 13.7 km) but had much greater interannual variation relative to v velocity (range = 19.2 ± 2.0 km) indicated by the greater σ. The small standard deviation (relative to the mean) in both salinity and v velocity indicate that interannual variability was relatively small and spatial variability of these quantities was consistent across the years even though there were substantial differences in discharge. Contrarily, the u velocity field had greater interannual variability, with 2005 and 2016 standing out as outliers with a much more uniform (larger range) u velocity field (**Table 3**), indicated by the shallower slope in the respective curves (**Supplementary Figure 6B**). These 2 years had the largest cumulative discharge (247 and 243 km^3, respectively) in the 37-year gauge record, suggesting that river flow may be an important predictor of u current velocity within the plume.

Comparisons of the semi-variogram range for u, v, and salinity with river discharge and wind velocity show that wind velocity and river discharge can have differential effects on river plume dynamics. Cumulative spring river discharge was not correlated with salinity or v semi-variogram range, but the u velocity range was significantly ($p < 0.05$) related to the cumulative discharge

TABLE 3 | Metrics used to model the variograms for the annual average May–July *u* and *v* surface velocity and salinity.

Year	*u* velocity range (km), sill ($\times 10^{-3}$)	*v* velocity range (km), sill ($\times 10^{-3}$)	Salinity range (km), sill
2004	21.2, 2.7	20.6, 1.7	65.7, 97.4
2005	55.8, 4.5	20.4, 2.0	62.0, 87.4
2015	33.2, 2.2	19.5, 1.7	55.0, 84.7
2016	46.7, 2.8	18.8, 1.7	62.3, 90.9
2017	23.8, 2.0	15.1, 1.7	69.2, 107.3
2018	21.2, 2.7	20.9, 1.7	62.2, 97.6
2019	25.5, 2.3	19.3, 1.6	65.3, 103.3
Mean	32.5, 2.8	19.2, 1.7	63.1, 95.5
σ	13.7, 0.8	2.0, 0.1	4.4, 8.3

Range is the distance where spatial autocorrelation declines and the sill is the variance of each variable at the range, and σ represents the standard deviation.

(**Figure 6A**). High discharge decreased the spatial variance of the *u* velocity field indicating cumulative spring discharge is likely a forcing factor that affects variance in the *u* velocity across years. Changes in plume velocity and salinity were not correlated with E–W wind velocity (**Figure 6B**), but there was a significant correlation between *v* current velocity range and N–S wind (**Figure 6C**). These results show that across years: (1) *u* current velocity variation is related to the total amount of freshwater entering the ocean; (2) *v* current velocity variation was related to the average N–S wind in the springtime across years; and (3) E–W wind velocity variance was not correlated to the mean salinity or current spatial variance. Wind velocity was typically northerly (wind toward the south from the Arctic Ocean; **Supplementary Figure 2**) and stronger northerly winds correlated with a decrease in the spatial variance in the *v* velocity field. Finally, salinity spatial variance was un-correlated with the three forcing variables analyzed here, and salinity was relatively stable across the 7 years (**Table 3**).

Velocity Structure in the Plume Across Norton Sound

Along the transect that follows the sampled cruise track from 2019 (**Figure 5A**), the mean *u* and *v* velocity fields were extracted for May–July across all years and the *u* and *v* velocity fields were averaged (n = 21; **Figures 7A,B**). To orient the reader, positive velocity is eastward or northward out of the page (*u*) or toward the right (*v*), while negative values are westward and

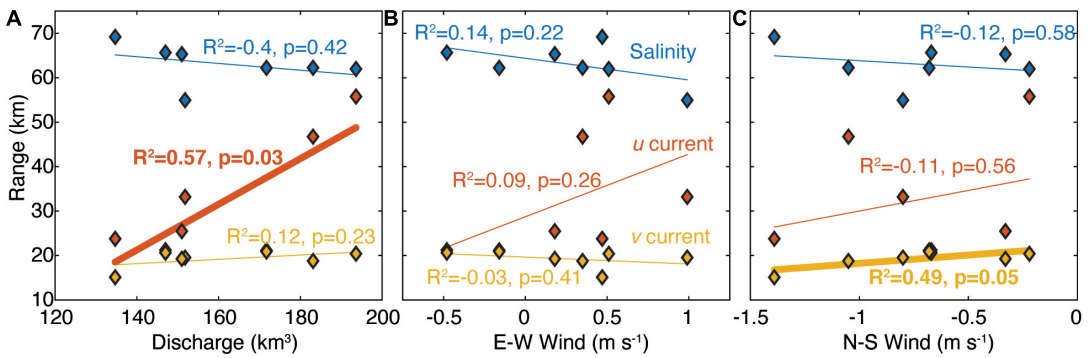


FIGURE 6 | Semi-variogram range for salinity, *u* (*west–east*), and *v* (*south–north*) current velocity as a function of **(A)** Yukon discharge, **(B)** East–west wind velocity and **(C)** North–south wind velocity. R^2 and p values are the coefficient of covariance and significance level determined by an ordinary least-squares linear regression. Bold values and lines are statistically significant ($p \leq 0.05$). Note the axis for E–W and N–S wind have different values.

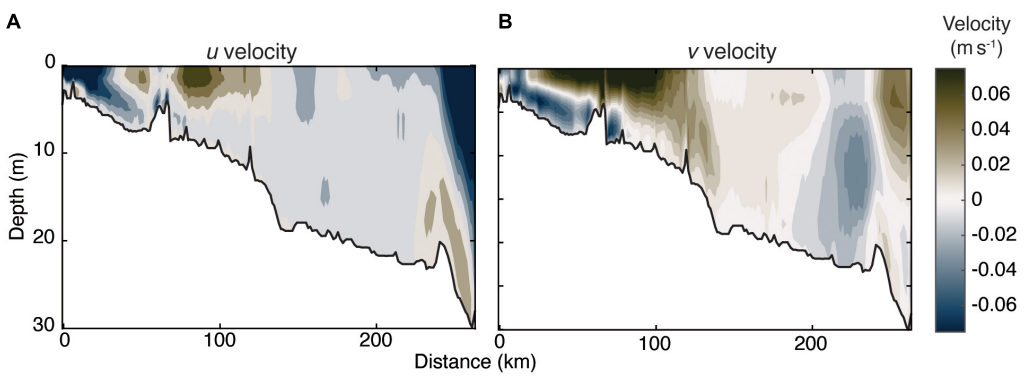


FIGURE 7 | Seven-year averaged May–July **(A)** *u* (west–east) and **(B)** *v* (south–north) current velocity along the transect that follows the western cruise track from the RSWQ June 2019 cruise.

southward into the page or toward the left. *u* velocity exhibited a strong rotational flow along the transect near the delta in the low salinity water of the plume with strong westward flow near the south river mouth and eastward flow ∼75 km down the transect to the north (**Figure 7A**). This corresponds with the anticyclonic eddy observed in the streamline velocity field in **Figure 5A**, along with the elevated η in the bulge region. Further into Norton Sound > 100 km away from the river mouth, the *u* velocity shifted from strong eastward to weakly westward with the mean flow out of Norton Sound toward the open ocean. The strong westward coastal jet along the north coast of Norton Sound observed in the surface velocity extended almost 20 m into the water column before dissipating and reversing eastward near the sea floor. The model does not include other small river and stream systems around Norton Sound, therefore the buoyancy driven flow patterns are solely due to the interaction of Yukon River and oceanic water. The opposing flow at the north edge of Norton Sound is indicative of two-layer circulation showing the estuarine nature of Norton Sound.

v Velocity within the plume exhibited strong two-layer circulation up to ∼100 km away from the river mouth (**Figure 7B**). The velocity remains weakly northward before strengthening near the north coast where the coastal jet turns toward the northwest and the Bering Strait. *v* Velocity began to reverse toward the south >200 km down-transect at >10 m deep which coincided with the bottom *u* current flowing back into Norton Sound. Combined with the *u* current field and the depth averaged velocity field (**Figure 5B**), there was a two-layer eddy with southwestward flow at the mouth, and northeastward flow further down transect into Norton Sound. There was also a topographic effect in the north-south direction where along-transect velocity had a persistent downwelling of strong surface velocity into the interior of the water column to >10 m of depth ∼125 km from the river mouth. The presence of these distinct features such as the anticyclonic eddy and two-layer circulation provide further evidence that the Yukon plume behaves as a prototypical river plume (Horner-Devine et al., 2015) and that Norton Sound has a density driven estuarine circulation. Analyzing the behavior of the Yukon plume during specific events can be potentially applicable for other high latitude rivers entering the ocean in shallow and broad shelf waters.

Plume Structure Is Strongly Influenced by Wind Velocity

There is a correlative link between north-south wind and surface ocean *v* velocity which manifested in the spatial variance analysis presented in **Figure 6C**, but the spatial variance of salinity appears to be unaffected by wind velocity when averaged over the freshet period for each year. However, short-term strong wind events likely affect the spatial density distribution and velocity fields within the plume, which has been documented from both field observations and numerical modeling studies in various coastal systems (Fong and Geyer, 2001; Whitney and Garvine, 2005; Horner-Devine et al., 2015). Wind storm events were predominantly southwesterly (toward the northeast) from the Bering Sea toward the North American Arctic land mass. The average duration of southwesterly storms was substantially longer (5.43 days; **Table 4**) than other directions, which averaged 2–3 days per event, and southwesterly wind events were the only type to occur in all 7 years. In this region, north winds are characterized as "upwelling" and south winds are characterized as "downwelling" due to the overall effect of the wind on the Ekman transport of coastal water. The strongest average wind magnitude during storms occurred from the northwest from the Arctic Ocean across Norton Sound with a mean velocity of 5.4 ± 0.85 m s^{-1} (**Table 4**). Overall, southwesterly wind events tended to occur earlier in the year with an average date of July 16; the other directional events tended to occur later into the summer in August and September when flow is typically lower (**Table 4**). Although there was substantial variability in wind direction throughout each year, the average non-storm wind blew from the Arctic over Norton Sound to the south but shifted year to year between westerly and easterly trajectories (**Table 1** and **Supplementary Figure 2**).

TABLE 4 | Parameters related to wind and current velocity and river plume extent and strength.

Direction	DOY, Nyears[a]	u_{wind}[b]	v_{wind}[c]	Ndays[d]	Q[e]	du dz^{-1}[f]	N2[g]	u[h]	v[i]	ρ_z[j]	ρ_{dz}[k]
Southwesterly	197, 7	4.72	4.00	5.43	11.0	0.005	0.014	0.020	0.077	6.68	18.48
Southeasterly	233, 4	–4.12	4.58	2.75	8.8	0.010	0.009	0.016	0.082	3.53	27.92
Northeasterly	222, 6	–2.61	–5.08	2.83	13.1	0.028	0.022	–0.032	–0.059	17.12	4.88
Northwesterly	214, 5	4.57	–4.93	2.20	10.1	0.012	0.016	–0.014	-0.054	13.71	7.46

All numbers are averaged over the 7 years and occurred during the maximum wind velocity duration (e.g., storms) for each direction. Variables f–k were calculated along the transects depicted in ***Figures 7***, ***9****.*

[a] *Average day of the Year and the number of years of occurrence.*
[b] *E–W wind velocity (m s^{-1}).*
[c] *N–S wind velocity (m s^{-1}).*
[d] *Average number of days per wind event.*
[e] *Previous 10 days cumulative Yukon River discharge at Pilot Station, AK (km^3).*
[f] *Vertical shear (m s^{-1} m^{-1}).*
[g] *Brunt-Vaisala frequency (s^{-2}).*
[h] *Average E–W current velocity (m s^{-1}).*
[i] *Average N–S current velocity (m s^{-1}).*
[j] *Maximum vertical density gradient (kg m^{-4}).*
[k] *Distance along the transect of maximum vertical density gradient (km)*

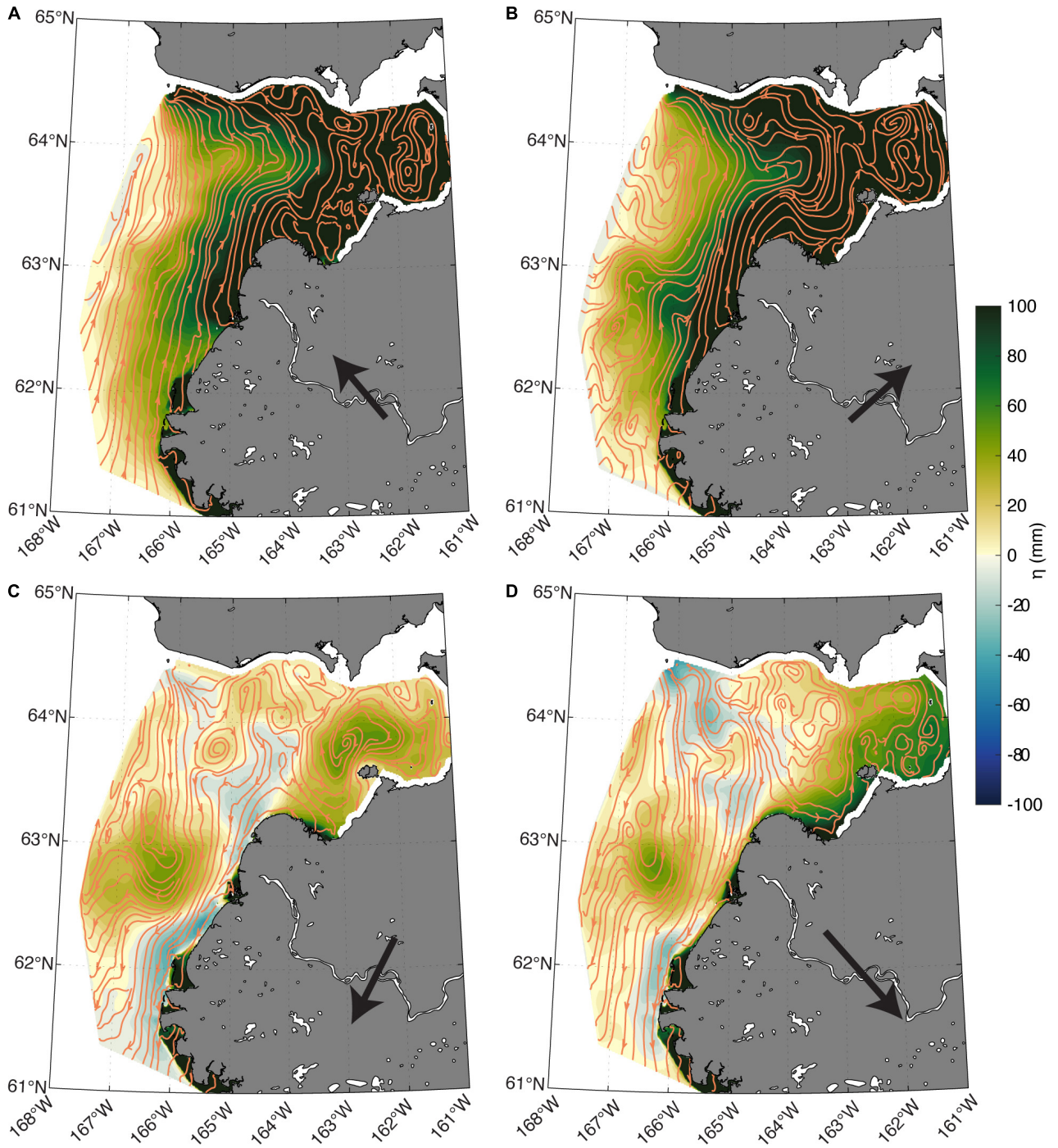


FIGURE 8 | Seven-year averaged surface height (η) for each year's longest duration wind event for **(A)** southeasterly, **(b)** southwesterly, **(C)** northeasterly, and **(D)** northwesterly. The streamlines are estimated from the depth-averaged *u* and *v* velocity fields and the arrows show the mean wind for each pattern.

The coastal currents differed substantially depending on the prevailing winds during storms. Analysis of the plume velocity during these wind events revealed that southerly (downwelling; **Figures 8A,B**) winds and northerly (upwelling; **Figures 8C,D**) winds substantially altered the depth-averaged current velocity. Downwelling wind pushed water near the coast toward the river delta and eastern edge of Norton Sound enhancing the mean flow pattern across the sound and toward the Bering Strait. The downwelling winds enhanced the northeastward flow with >20 cm s^{-1} flow in the surface toward the northeast and northward surface flow deepening $>$ 10 m into the water column over 150 km away from the south river mouth (**Figures 9A,B**).

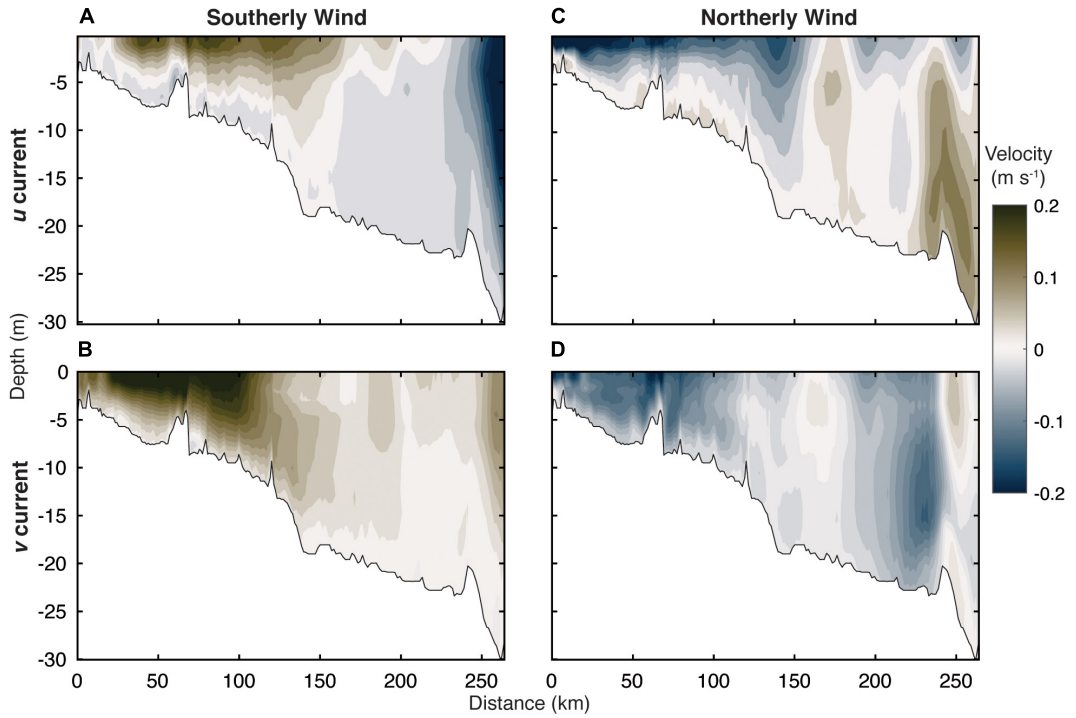


FIGURE 9 | Average southerly wind event **(A)** *u* and **(B)** *v* current velocity, and average northerly wind event **(C)** *u* and **(D)** *v* current velocity. Positive *u* is to the east (out of the page) and positive *v* is to the north (down the transect).

The mean *u* and *v* velocity was much greater than the annual average while occurring in the same direction showing that the downwelling winds substantially enhanced the plume circulation. This coincided with a large increase in η near the delta and in Norton Sound which likely enhanced the mean transport northwestward along the toward the Bering Strait down the pressure gradient. However, the prototypical bulge seen in the annual mean flow was largely diminished (**Figures 8A,B**) with the enhanced northward transport. The enhancement of velocity at depth away from the plume suggests that the currents could transport riverine material > 100 km offshore into deeper Norton Sound waters. The average current velocity <125 km from shore was 13.0 cm s^{-1} in the southerly wind events; a water mass leaving the southern end of the transect would take 11.1 days to be transported 125 km into the interior of Norton Sound, on average.

Upwelling winds from the north drove the depth averaged flow to completely reversed with currents moving southward against the northward flow typically seen (**Figures 8C,D**). There was a southwestward flow with a strong surface current in the nearshore < 150 km from the mouth pushing water toward the west in the near river plume region (**Figure 9C**). Strong westward currents (>20 cm s^{-1}) were confined to the upper 5 m of the water column within the plume and combine with weaker and more vertically homogenous southward currents (**Figure 9D**). Mean vertical shear was greatest in the northeasterly wind events at 2.8 cm s^{-1} m^{-1} (**Table 4**), compared to the southwesterly winds where the mean vertical velocity was more uniform (0.5 cm s^{-1} m^{-1}). The *v* current field has reversed and there is now a persistent southward flow at depth in Norton Sound 225 km down transect. Rather than the typical persistent coastal current along the north coast Norton Sound, an eastward current occurred at depth (**Figure 9C**), pulling water from the bottom near the Bering Strait into Norton Sound where it is advected southward back toward the river plume. The enhanced two-layer flow in Norton Sound with multiple regions of divergence in the *v* velocity field is indicative of strong upwelling: water is moving into Norton Sound along the bottom pushing deeper water from the Bering Strait shown in southwestward through Norton Sound.

The upwelling wind substantially depressed the elevated η along the coast (**Figure 8D**). The elevated η in the bulge region remained a substantial hydrographic feature with the velocity field still exhibiting some rotation around this area of high pressure before continuing toward the south in the direction of the wind field. Surprisingly, the upwelling wind driven mean current magnitude <125 km from the river mouth was 11.2 cm s^{-1} southward, only slightly less than 13.0 cm s^{-1} northward from the downwelling wind (**Figure 9D**). Wind was the predominant factor shifting the mean flow of water with downwelling winds enhancing the mean flow and upwelling winds shifting the flow in the opposite direction and transporting water southward away from the region of typical plume dispersion. The complete diminishment of the two-layer circulation and persistent southwestward flow within the plume during upwelling winds show that strong wind cannot only affect

the mixing in the far field of the plume (as described in Horner-Devine et al., 2015) but can also drive flow shifts in the near field at the plume front and at the outflow of the river.

Fong and Geyer (2001) showed that upwelling winds will diminish along shore flow in the mean plume direction and the Yukon plume not only exhibited a diminished dominant northeastward flow pattern but a complete reversal during upwelling events throughout the water column. The effect of wind forcing on the horizontal velocity occurred throughout the river plume, not just down transect away from the front in the far field. These flow patterns indicate that material that is transported from the river such as sediment and dissolved matter will be deposited and distributed in much different locations depending on the direction of the wind. Southerly winds transport a greater portion of plume water northeastward into Norton Sound at a much faster rate and deeper into the interior of the water column, potentially depositing finer sediment further offshore in deeper water in Norton Sound. Upwelling winds do the opposite, likely increasing coastal water residence time in the nearshore region before being transported through Norton Sound and toward the Bering Strait after wind slackens, and buoyancy and rotational flow begin to dominate again. This would likely

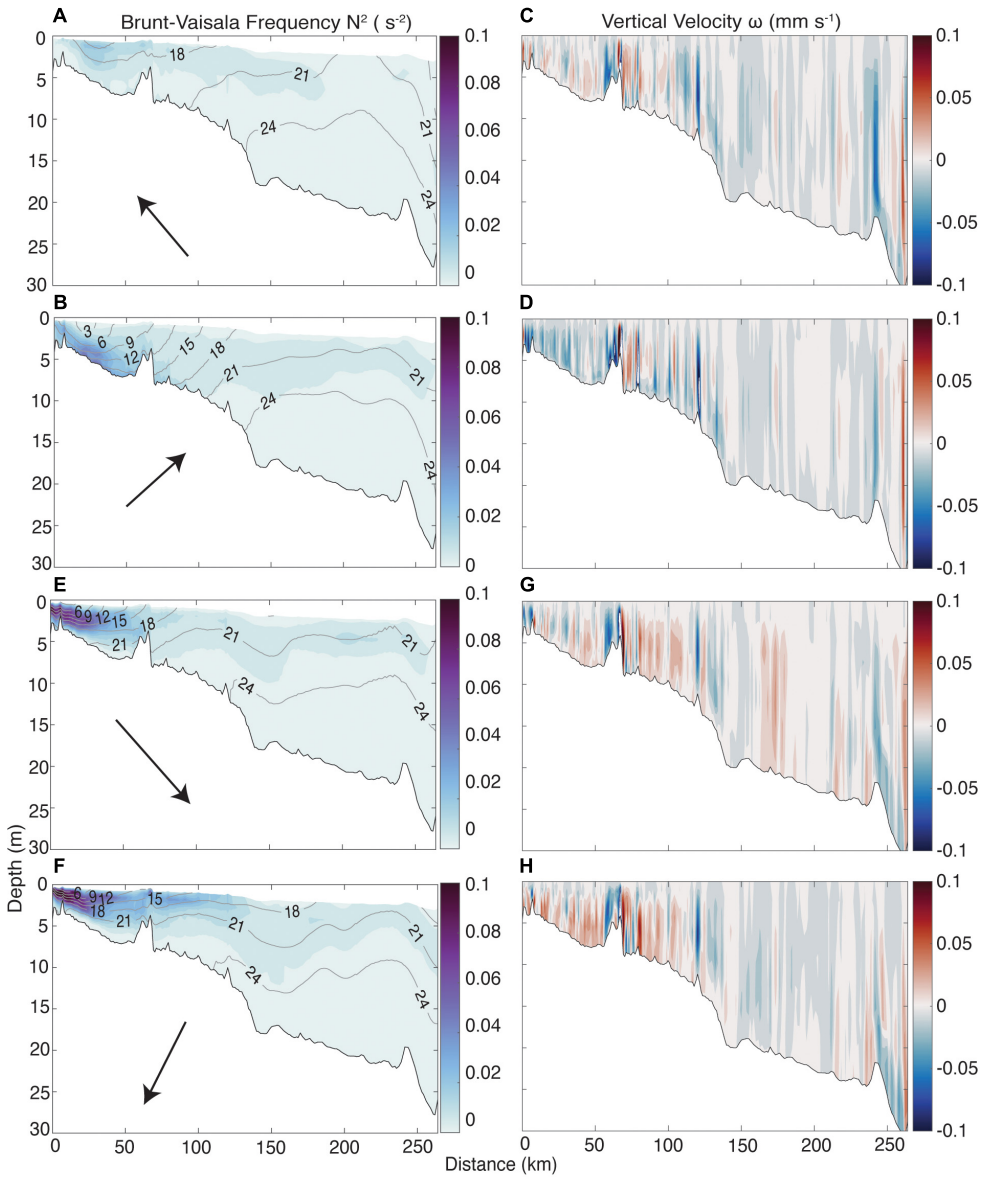


FIGURE 10 | Mean vertical Brunt-Vaisala frequency (N2) (first column) and vertical velocity (ω) (second column) for the mean of the southeasterly **(A,C)**, southwesterly **(B,D)**, northwesterly **(E,G)**, and northeasterly **(F,H)** wind events averaged across all years. The contour lines and labels in the first column depict the σθ (kg m-3) for each extracted transect. The arrows in the first column represent the average direction and magnitude of the wind for each row of plots, relative to north.

increase sediment deposition in the near field adjacent to the delta and offshore toward the west. Importantly, increased residence time of riverine water and the addition of upwelled deeper water at the coast will likely alter biogeochemical cycles such as increasing the breakdown of riverine organic matter and providing more nutrients to the surface ocean from depth. While *in-water* sampling would be dangerous and difficult during high wind-events, YukonFVCOM can provide a qualitative estimate of the spatial distribution of plume water for any scenario and provide a first-order estimate of where the plume frontal regions occur in short time frames.

Stratification as quantified by N^2 and vertical velocity (ω) within the plume had a similar, expected, response as the horizontal velocity field during wind events (**Figure 10**). Downwelling winds broadened the low-density plume waters northward (**Figures 10A,B**), and enhanced downward vertical velocity (**Figures 10C,D**). However, not all downwelling winds are the same with southeasterly and southwesterly winds showing a much different response in the magnitude of stratification and density. Southwesterly winds exhibited a much higher degree of stratification and lower density plume water extended further offshore as isopycnals bent upward (**Figure 10B**), and there was much greater downward vertical velocity in the near- and mid-field regions (**Figure 10D**). The downward velocity coincides with the deepened northeastward flow (**Figures 9A,B**) showing that plume water was advected further offshore and at a greater depth into the interior of Norton Sound relative to the mean. Stratification was greatest near the sea floor <50 km down transect with a relatively uniform and incremental increase in density up to 100 km. Southeasterly winds drove vertical shear to be ∼2× greater than southwesterly winds while the Brunt-Vaisala frequency was 36% less (**Table 4**) even though the southerly wind component was relatively similar to southwesterly winds (4.58 vs. 4.00 m s^{-1}). This suggests that the east-west wind velocity vector component contributed more to the variance in the current velocity and density fields during downwelling winds and that westerly wind components increased stratification and diminished mixing along the transect.

Upwelling winds shoaled the depth of greatest stratification toward the surface and near the plume outflow (**Figures 10E,F**) and drove upward transport of water within 125 km of the plume outflow (**Figures 10G,H**). The maximum vertical density gradients increased to 17.1 and 13.7 kg m^{-4} for northeasterly and northwesterly wind events, compared to 6.68 and 3.53 kg m^{-4} during downwelling wind events. The maximum vertical stratification occurred 4.9 and 7.5 km down the transect, compared to 18.5 and 27.9 km in the downwelling winds (**Table 4**). These circulation and stratification patterns show that upwelling-favorable winds increased river water retention near the surface and toward the southwest at the main river outflow by increasing stratification and shoaling the pycnocline. These flow patterns suggest that river water suspended material processing and deposition may increase in the near field while dissolved tracers may be confined to the near surface allowing for transport further offshore in surface waters toward the southwest away from the direction of the mean flow.

Finally, the difference in depth-averaged salinity between downwelling and upwelling winds shows the substantial spatial difference in plume water distribution under variable wind (**Figure 11**). The regions at the main outflow of the river at the south mouth and throughout the delta have a difference of >10 salinity with fresher water throughout the north edge of the delta during downwelling, coinciding with the enhanced northward transport. Downwelling winds also appeared to increase transport of more oceanic water into Norton Sound which logically follows the downward advection of water and

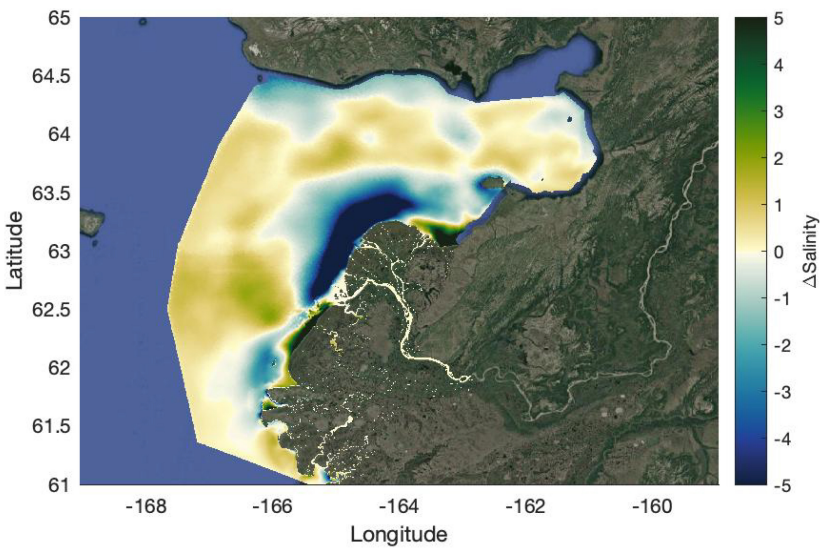


FIGURE 11 | The difference in the depth averaged salinity between the mean of the downwelling and upwelling wind events. Positive values indicated the downwelling has greater salinity and negative values indicate upwelling has greater salinity. Background image was created using the MATLAB function *Plot_Google_Map.m* (Bar-Yehuda, 2021).

replacement by marine water at the surface due to mass balance. Overall, upwelling and downwelling winds have a substantial effect on the short term spatial distribution of plume water throughout the region and can largely determine where the majority of river water is concentrated in the coastal ocean on short time scales.

Implications for Plume-Ocean Biogeochemistry

Wind direction has a strong influence on the plume strength and distribution in the coastal ocean which will determine the time and space scales of riverine material processing during coastal ocean transport. Depending on the interplay between river flow and wind velocity, material can be confined to the coast or transported far offshore which will alter regional sediment and dissolved matter biogeochemistry. Further analysis of long term model predictions in the context of inter-decadal weather variation could show if changes in regional wind patterns may effect plume dispersion on longer time scales and in the context of the changing Arctic climate. This will be key for generalizing how increasing river flow in the future will manifest in the plume impacts on coastal biogeochemical processes coupled with changes in regional atmospheric forcing.

Key processes such as sediment deposition, dissolved organic matter remineralization, and nutrient dispersion will therefore be governed by the wind forcing on the plume. Suspended sediment dynamics are difficult to characterize, especially in regions with strong coastal currents and a plume distribution that can vary by 100s of kilometers depending on the surface wind field. To characterize sediment deposition or resuspension in the Yukon Plume, a sampling scheme must be efficiently employed that can capture the full spatial variability of the plume in the near- and mid-field regions, independent of wind direction. By understanding the degree to which specific wind events determine the plume distribution, sampling schemes can be better informed to maximize effort where and when samples are collected. For example, if there was a strong upwelling event prior to a field expedition, it would be pertinent to focus sampling efforts near the mouth of the river and toward the south and southwest to capture the rapidly sinking/freshly deposited riverine sediment in the likely location they would be distributed.

Another important process in the transition from plume-to-ocean in the mid-field region of the plume is the mixing of freshwater derived dissolved organic carbon and marine water with high ionic strength. At this transition, high molecular weight compounds tend to precipitate out or bind with suspended matter into large colloids in a process known as flocculation (e.g., Sholkovitz et al., 1978; Verney et al., 2009; Asmala et al., 2014). External factors affecting the location of the plume transition zone will also affect flocculation as the plume front shifts under variable forcing. Capturing flocculation spatial patterns and rates of formation in the Yukon Plume and other large rivers is a high priority due to the very high sediment and organic loads to the coastal ocean. The strong seasonality and rapid transition from low to high flow during the freshet makes targeted sampling difficult without information on the real-time dynamics of the plume. However, representative and comprehensive sampling is critical to develop process-based experiments that estimate biogeochemical processes at the plume-ocean interface which can then inform biogeochemical models of these coastal regions. The wind patterns over the plume region before and during sampling can be used to qualitatively predict where the dominant plume front will occur and thus where sampling should be focused. While running the YukonFVCOM model in real time on a supercomputer is not configured (yet), combining the general knowledge of plume distribution in relation to wind forcing with remote measurements of ocean properties via satellites can lead to the efficient deployment of resources in this difficult to access environment. Finally, the characterization of the mean flow field will allow for future deployment of autonomous sampling platforms into locations to maximize sampling return. This is key in such a remote location that is rapidly undergoing climate change and where in-water observations are particularly sparse.

DATA AVAILABILITY STATEMENT

The FVCOM model output used in this study along with some post-processing scripts can be found at https://portal.nccs.nasa.gov/datashare/yukonriver/. The FVCOM source code version 4.3 is publicly available for download at http://fvcom.smast.umassd.edu/fvcom/. The river forcing for the Yukon River is available from the United States Geological Survey, the tidal prediction software is available at https://www.tpxo.net/global, the open boundary forcing is available through the World Ocean Atlas, and the model validation is available through the DAACs referenced in the main text.

AUTHOR CONTRIBUTIONS

JC constructed the model under the advise and expertise of AM. AM contributed substantially to the curation and editing of the manuscript and advice during model construction and analysis. Both authors contributed to the article and approved the submitted version.

FUNDING

This work was solely funded under the US National Aeronautics and Space Administration.

ACKNOWLEDGMENTS

We would like to acknowledge the Alaska Department of Fish and Game (ADF&G) and specifically Jenefer Bell for providing the CTD data used for model validation/calibration in Norton Sound, and the NASA RSWQ2019 award #80NSSC18K0492 to P. J. Hernes, RGM Spencer, and M. Tzortziou (UC Davis) and under funded program 281945 to AM (NASA GSFC) that provided support to acquire CTD data along the cruise track in 2019. Thank you to Peter Hernes and Maria Tzortziou for

helpful comments during the drafting of this manuscript. We also acknowledge Michael Novak for his leadership in the RSWQ2019 sampling effort and help with acquiring and processing data, and the NASA Center for Climate Simulation supercomputer *Discover* support team in help getting this model up and running and the allocation of resources they generously provide. Finally, we acknowledge the Native Alaskan village of Alakanuk for hosting us during our work in the Yukon Delta, especially Augusta Edmund and Captain Adam Boeckman of the Anchor Point for the Nome-Norton Sound portion of the RSWQ2019 field campaign. Thank you to two reviewers for helpful comments in improving this manuscript. The contribution of JC was primarily conducted under the NASA Postdoctoral Program, administered by Universities Space Research Association.

SUPPLEMENTARY MATERIAL

The Supplementary Material for this article can be found online at: https://www.frontiersin.org/articles/10.3389/fmars.2021.793217/full#supplementary-material

REFERENCES

Asmala, E., Bowers, D. G., Autio, R., Kaartokallio, H., and Thomas, D. N. (2014). Qualitative changes of riverine dissolved organic matter at low salinities due to flocculation. *J. Geophys. Res. Biogeosci.* 119, 1919–1933. doi: 10.1002/2014JG002722

Banas, N. S., MacCready, P., and Hickey, B. M. (2009). The columbia river plume as cross-shelf exporter and along-coast barrier. *Continental Shelf Res.* 29, 292–301. doi: 10.1016/j.csr.2008.03.011

Bar-Yehuda, Z. (2021). *zoharby/plot_google_map*. Availble online at: https://github.com/zoharby/plot_google_map, GitHub. (accessed December 13, 2021).

Chen, C., Beardsley, R. C., Cowles, G., Qi, J., Lai, Z., Gao, G., et al. (2013). *An Unstructured grid, finite-Volume Community Ocean Model FVCOM user Manual, SMAST. UMASSD Technical Report-13-0701*.

Chen, C., Gao, G., Zhang, Y., Beardsley, R. C., Lai, Z., Qi, J., et al. (2016). Circulation in the Arctic Ocean: results from a high-resolution coupled ice-sea nested global-FVCOM and Arctic-FVCOM system. *Prog. Oceanogr.* 141, 60–80. doi: 10.1016/j.pocean.2015.12.002

Clark, J. B., and Mannino, A. (2021). Preferential loss of Yukon river delta colored dissolved organic matter under nutrient replete conditions. *Limnol. Oceanogr.* 66, 1613–1626. doi: 10.1002/lno.11706

Cokelet, E. D., Meinig, C., Lawrence-Slavas, N., Stabeno, P. J., Mordy, C. W., Tabisola, H. M., et al. (2015). *The Use of Saildrones to Examine Spring Conditions in the Bering Sea*. Washington: OCEANS 2015 - MTS/IEEE, 1–7. doi: 10.23919/OCEANS.2015.7404357

Danielson, S. L., Ahkinga, O., Ashjian, C., Basyuk, E., Cooper, L. W., Eisner, L., et al. (2020). Manifestation and consequences of warming and altered heat fluxes over the Bering and Chukchi sea continental shelves. *Deep Sea Res. Part II Top. Stud. Oceanogr.* 177:104781. doi: 10.1016/j.dsr2.2020.104781

Dean, K. G., Mc Roy, C. P., Ahlniis, K., and Springer, A. (1989). The plume of the yukon river in relation to the oceanography of the bering sea. *Remote Sensing Environ.* 28, 75–84. doi: 10.1016/0034-4257(89)90106-5

Dornblaser, M. M., and Striegl, R. G. (2009). Suspended sediment and carbonate transport in the yukon river basin, alaska: fluxes and potential future responses to climate change. *Water Resour. Rese.* 45:7546. doi: 10.1029/2008wr007546

Dupré, W. R. (1980). *Yukon Delta Coastal Processes Study*. Houston, TX: Department of Geology, University of Houston.

Durocher, M., Requena, A., Burn, D. H., and Pellerin, J. (2019). Analysis of trends in annual streamflow to the Arctic Ocean. *Hydrol. Proc.* 33, 1143–1151. doi: 10.1002/hyp.13392

Egbert, G. D., and Erofeeva, S. Y. (2002). Efficient inverse modeling of barotropic ocean tides. *J. Atmospheric Oceanic Technol.* 19, 183–204. doi: 10.1175/1520-0426(2002)019<0183:EIMOBO>2.0.CO;2

Fairall, C. W., Bradley, E. F., Hare, J. E., Grachev, A. A., and Edson, J. B. (2003). Bulk parameterization of air–sea fluxes: updates and verification for the COARE algorithm. *J. Climate* 16, 571–591. doi: 10.1175/1520-0442(2003)016<0571:BPOASF>2.0.CO;2

Feng, D., Gleason, C. J., Lin, P., Yang, X., Pan, M., and Ishitsuka, Y. (2021). Recent changes to Arctic river discharge. *Nat. Commun.* 12:6917. doi: 10.1038/s41467-021-27228-1

Fichot, C. G., Kaiser, K., Hooker, S. B., Amon, R. M. W., Babin, M., Bélanger, S., et al. (2013). Pan-Arctic distributions of continental runoff in the Arctic Ocean. *Sci. Rep.* 3:1053. doi: 10.1038/srep01053

Fong, D. A., and Geyer, W. R. (2001). Response of a river plume during an upwelling favorable wind event. *J. Geophys. Res.* 106, 1067–1084. doi: 10.1371/journal.pone.0197627

Garvine, R. W. (1987). Estuary plumes and fronts in shelf waters: a layer model. *J. Phys. Oceanogr.* 17, 1877–1896. doi: 10.1175/1520-0485(1987)017<1877:EPAFIS>2.0.CO;2

Grebmeier, J. M. (2012). Shifting patterns of life in the pacific Arctic and sub-arctic seas. *Ann. Rev. Mar. Sci.* 4, 63–78. doi: 10.1146/annurev-marine-120710-100926

Hetland, R. D. (2005). Relating river plume structure to vertical mixing. *J. Phys. Oceanogr.* 35, 1667–1688. doi: 10.1038/s41598-019-55242-3

Hickey, B. M., Pietrafesa, L. J., Jay, D. A., and Boicourt, W. C. (1998). The columbia river plume study: subtidal variability in the velocity and salinity fields. *Journal of Geophysical Research* 103, 10339–10368. doi: 10.1029/97JC03290

Holmes, R. M., McClelland, J. W., Peterson, B. J., Tank, S. E., Bulygina, E., Eglinton, T. I., et al. (2012). Seasonal and annual fluxes of nutrients and organic matter from large rivers to the arctic ocean and surrounding seas. *Estuaries Coast*. 35, 369–382.

Holmes, R. M., McClelland, J. W., Peterson, B. J., Tank, S. E., Bulygina, E., Eglinton, T. I., et al. (2021). *Arctic Great Rivers Observatory. Water Quality Dataset, Version 20211213*.

Horner-Devine, A. R., Hetland, R. D., and MacDonald, D. G. (2015). Mixing and transport in coastal river plumes. *Ann. Rev. Fluid Mech.* 47, 569–594. doi: 10.1146/annurev-fluid-010313-141408

Jia, C., and Mennet, P. J. (2020). High latitude sea surface temperatures derived from MODIS infrared measurements. *Remote Sensing Environ.* 251:112094. doi: 10.1016/j.rse.2020.112094

Jolliff, J. K., Kindle, J. C., Shulman, I., Penta, B., Friedrichs, M. A. M., Helber, R., et al. (2009). Summary diagrams for coupled hydrodynamic-ecosystem model skill assessment. *J. Mar. Syst.* 76, 64–82. doi: 10.1016/j.jmarsys.2008.05.014

JPL/OBPG/RSMAS (2020). *GHRSST Level 2P Global Sea Surface Skin Temperature from the Visible and Infrared Imager/Radiometer Suite (VIIRS) on the Suomi-NPP satellite (GDS2). Version. 2016.2*.

Locarnini, R. A., Mishonov, A. V., Baranova, O. K., Boyer, T. P., Zweng, M. M., Garcia, H. E., et al. (2018). World Ocean Atlas 2018, volume 1: temperature. *Mishonov Technical. NOAA Atlas NESDIS* 81:52.

Matheron, G. (1963). Principles of geostatistics. *Econ. Geol. Bull. Soc. Econ. Geol.* 58, 1246–1266. doi: 10.2113/gsecongeo.58.8.1246

McClelland, J. W., Déry, S. J., Peterson, B. J., Holmes, R. M., and Wood, E. F. (2006). A pan-arctic evaluation of changes in river discharge during the latter half of the 20th century. *Geophys. Res. Lett.* 33:753. doi: 10.1029/2006GL025753

McClelland, J. W., Holmes, R. M., Peterson, B. J., Raymond, P. A., Striegl, R. G., Zhulidov, A. V., et al. (2016). Particulate organic carbon and nitrogen export from major Arctic rivers: POC and PN export from major Arctic rivers. *Global Biogeochem. Cycles* 30, 629–643. doi: 10.1002/2015GB005351

Mesinger, F., DiMego, G., Kalnay, E., Mitchell, K., Shafran, P. C., Ebisuzaki, W., et al. (2006). North American regional reanalysis. *Bull. Am. Meteorol. Soc.* 87, 343–360. doi: 10.1175/BAMS-87-3-343

Nasa Goddard Space Flight Center, Ocean Ecology Laboratory, Ocean Biology Processing Group (2020). *Reprocessing*. Greenbelt, MD: NASA OB.DAAC.

Pawlowicz, R. (2020). M_Map: A mapping package for MATLAB", Version 1.4m.

Piliouras, A., and Rowland, J. C. (2020). Arctic river delta morphologic variability and implications for riverine fluxes to the coast. *J. Geophys. Res.* 125:e2019JF005250. doi: 10.1029/2019JF005250

Pritchard, M., and Huntley, D. A. (2006). A simplified energy and mixing budget for a small river plume discharge. *J. Geophys. Res.* 111:301. doi: 10.1029/2005JC002984

Rawlins, M. A., Cai, L., Stuefer, S. L., and Nicolsky, D. (2019). Changing characteristics of runoff and freshwater export from watersheds draining Northern Alaska. *Cryosphere* 13:10144085. doi: 10.5194/tc-13-3337-2019

Roach, A. T., Aagaard, K., Pease, C. H., Salo, S. A., Weingartner, T., Pavlov, V., et al. (1995). Direct measurements of transport and water properties through the bering strait. *J. Geophys. Res.* 100:18443. doi: 10.1029/95JC01673

Schwanghart, W. (2020a). *Experimental (Semi-) Variogram*. Available online at: https://www.mathworks.com/matlabcentral/fileexchange/20355-experimental-semi-variogram (accessed July 23, 2020).

Schwanghart, W. (2020b). *Variogramfit*. Available online at: https://www.mathworks.com/matlabcentral/fileexchange/25948-variogramfit (accessed July 23, 2020).

Shiklomanov, A. I., Holmes, R. M., McClelland, J. W., Tank, S. E., and Spencer, R. G. M. (2021). *Arctic Great Rivers Observatory. Discharge Dataset, Version 20211116*.

Sholkovitz, E. R., Boyle, E. A., and Price, N. B. (1978). The removal of dissolved humic acids and iron during estuarine mixing. *Earth Planetary Sci. Lett.* 40, 130–136. doi: 10.1016/0012-821X(78)90082-1

Smedstad, O. M., Cummings, J. A., Metzger, E. J., Hogan, P. J., Hurlburt, H. E., Shriver, J. F., et al. (2008). *The 1/12 degree Global HYCOM Real-Time Nowcast/Forecast System*. Washington, DC: Naval Research Lab Stennis Space Center.

Stabeno, P. J., Bell, S. W., Bond, N. A., Kimmel, D. G., Mordy, C. W., and Sullivan, M. E. (2019). Distributed biological observatory region 1: physics, chemistry and plankton in the northern bering sea. *Deep Sea Res. Part II Top. Stud. Oceanogr.* 162, 8–21. doi: 10.1016/j.dsr2.2018.11.006

Stow, C. A., Jolliff, J., McGillicuddy, D. J. Jr., Doney, S. C., Allen, J. I., Friedrichs, M. A. M., et al. (2009). Skill assessment for coupled biological/physical models of marine systems. *J. Mar. Syst. J. Eur. Assoc. Mar. Sci. Tech.* 76, 4–15. doi: 10.1016/j.jmarsys.2008.03.011

Verney, R., Lafite, R., and Brun-Cottan, J.-C. (2009). Flocculation potential of estuarine particles: the importance of environmental factors and of the spatial and seasonal variability of suspended particulate matter. *Estuar. Coasts* 32, 678–693. doi: 10.1007/s12237-009-9160-1

Whitney, M. M., and Garvine, R. W. (2005). Wind influence on a coastal buoyant outflow. *J. Geophys. Res.* 110:2261. doi: 10.1016/j.scitotenv.2018.01.325

Woodgate, R. A. (2018). Increases in the pacific inflow to the arctic from 1990 to 2015, and insights into seasonal trends and driving mechanisms from year-round bering strait mooring data. *Progr. Oceanogr.* 160, 124–154. doi: 10.1016/j.pocean.2017.12.007

Yankovsky, A. E., and Chapman, D. C. (1997). A simple theory for the fate of buoyant coastal discharges. *J. Phys. Oceanogr.* 27, 1386–1401. doi: 10.1175/1520-0485(1997)027<1386:ASTFTF>2.0.CO;2

Yukon River Inter-Tribal Watershed Council (2021). https://www.yritwc.org/yukon-river-watershed. (accessed December 13, 2021).

Zweng, M. M., Reagan, J. R., Seidov, D., Boyer, T. P., Locarnini, R. A., Garcia, H. E., et al. (2018). *World Ocean Atlas 2018, Volume 2: Salinity*. Mishonov Technical. NOAA Atlas NESDIS 81:52.

Conflict of Interest: The authors declare that the research was conducted in the absence of any commercial or financial relationships that could be construed as a potential conflict of interest.

Publisher's Note: All claims expressed in this article are solely those of the authors and do not necessarily represent those of their affiliated organizations, or those of the publisher, the editors and the reviewers. Any product that may be evaluated in this article, or claim that may be made by its manufacturer, is not guaranteed or endorsed by the publisher.

Copyright © 2022 Clark and Mannino. This is an open-access article distributed under the terms of the Creative Commons Attribution License (CC BY). The use, distribution or reproduction in other forums is permitted, provided the original author(s) and the copyright owner(s) are credited and that the original publication in this journal is cited, in accordance with accepted academic practice. No use, distribution or reproduction is permitted which does not comply with these terms.

frontiers in Marine Science

ORIGINAL RESEARCH
published: 17 February 2022
doi: 10.3389/fmars.2022.791948

River Plume Rooted on the Sea-Floor: Seasonal and Spring-Neap Variability of the Pearl River Plume Front

Haihang Zhi[1], Hui Wu[1,3], Jiaxue Wu[2], Wenxia Zhang[1] and Yihe Wang[1]*

[1] State Key Laboratory of Estuarine and Coastal Research, East China Normal University, Shanghai, China, and Southern Marine Science and Engineering Guangdong Laboratory, Zhuhai, China, [2] Southern Marine Science and Engineering Guangdong Laboratory, Zhuhai, China, [3] School of Marine Sciences, East China Normal University, Shanghai, China

The buoyant river plume front exhibits substantial variability in the sea surface under energetic external forcing. Although highly dynamic, the river plume is often "rooted" at specific locations through the bottom river plume front. In this study, we addressed this mechanism using the Pearl River plume as an example based on a well-validated numerical model. With this model, we described the spatiotemporal characteristics of the Pearl River salinity front. It was found that, although the surface Pearl River plume features bimodal extension in summer and winter seasons, owing to the reversal of the seasonal monsoon wind, there is a relatively stable bottom front extending from the river mouth to the downstream region (i.e., in the direction of propagation of Kelvin Wave). The occurrence probability of the bottom front showed that the front location varies only slightly and fixes at ∼8-m isobath. The Empirical Orthogonal Function (EOF) analysis demonstrated that runoff, wind, and tide are major regulating factors. These three factors jointly control the strength and position of the bottom front. In particular, the bottom front moves offshore during the spring tide but onshore during the neap tide, respectively, indicating a different mechanism from the classic frontal trapping theory. The sensitivity experiment without tide indicated that the bottom plume front shrinks significantly, and the river plume becomes more dynamic since it is no longer rooted on the seafloor.

Keywords: Pearl River Estuary, river plume, salinity gradient, bottom front, tide

OPEN ACCESS

Edited by:
Alexander Yankovsky, University of South Carolina, United States

Reviewed by:
Gonzalo S. Saldías, University of the Bío Bío, Chile
Nadia K. Ayoub, UMR 5566 Laboratoire d'Études en Géophysique et Océanographie Spatiales (LEGOS), France

***Correspondence:**
Hui Wu
hwu@sklec.ecnu.edu.cn

Specialty section:
This article was submitted to Coastal Ocean Processes, a section of the journal Frontiers in Marine Science

Received: *09 October 2021*
Accepted: *28 January 2022*
Published: *17 February 2022*

Citation:
Zhi H, Wu H, Wu J, Zhang W and Wang Y (2022) River Plume Rooted on the Sea-Floor: Seasonal and Spring-Neap Variability of the Pearl River Plume Front. Front. Mar. Sci. 9:791948. doi: 10.3389/fmars.2022.791948

INTRODUCTION

The Pearl River is the second largest river in China in terms of freshwater discharge, with an annual-mean runoff of ∼10,000m^3/s (Gan et al., 2009). It discharges into the northern South China Sea (NSCS) through eight outlets which are Humen, Jiaomen, Hongqili, Hengmen, Modaomen, Jitimen, Hutiaomen and Yamen (**Figure 1**). The first four outlets enter a semi-enclosed estuarine bay, namely the Lingdingyang Bay or conventionally the Pearl River Estuary, which receives nearly half of the total upstream runoff (Lai et al., 2015). The Kelvin number of the Pearl River plume in the far-field is about 5 (estimated by the model result of this study), meaning that the plume is large-scale (Garvine, 1995). The average water depth of the Pearl River Estuary is ∼5 m with two deep channels (the West Channel and East Channel) exceeding 10 m. The length of the Pearl River Estuary is ∼60 km from the mouth up to Humen, and the width of its mouth is ∼50 km

(Zu and Gan, 2015). Because the Pearl River Estuary is wide relative to the baroclinic Rossby radius of deformation, the associated river plume has the characteristics of a buoyant coastal current inside the estuary that hugs the western flank (Dong et al., 2004). Once leaving the Pearl River Estuary, the buoyant low-salinity water spreads out over a broad continental shelf in the NSCS (Gan et al., 2009). Given the rich nutrients it carries, the Pearl River plume strongly impacts the adjacent coastal ocean through, for instance, harmful algal blooms (Wang et al., 2008) and hypoxia (Yu et al., 2020). Therefore, understanding the dynamic characteristics of the Pearl River plume front is a first step to resolving these environmental issues.

River plume features a low-salinity signature, and the surface water generally converges toward the front (Orton and Jay, 2005). Hence, the front often acts as a dynamic barrier to impede momentum and terrestrial materials from reaching the ocean. The structure of river plume fronts can be categorized into two types: surface-advected and bottom-trapped (Yankovsky and Chapman, 1997). The surface-advected plume floats over denser shelf water in a thin layer, with little contact with the bottom. Whereas a bottom-trapped plume forms a front from the surface to the bottom with a strong horizontal gradient, and its front is usually fixed at a depth deeper than the inflow depth. Previous studies have shown that bottom-trapped plume is influential in ecological processes. For example, the surface chlorophyll maximum near the estuary often occurs inside the salinity front (Franks, 1992), with a shoreward boundary at the location of the bottom front in turbid water (Wang et al., 2019). A large number of nutrients and pollutants carried by the river enter the Pearl River Estuary and extend in the shelf water along with the plume, which increases the nearshore productivity and produces a chlorophyll maximum zone at the front of the Pearl River Estuary (Hu and Li, 2009; Lu and Gan, 2015; Su et al., 2017). Stratification and multiple biogeochemical processes associated with the Pearl River plume also lead to the formation of hypoxic zones (Cui et al., 2019; Li et al., 2020). The spatial patterns of the high-value chlorophyll zone and the hypoxic zone in the Pearl River Estuary are closely related to the surface and bottom fronts of the Pearl River plume (Tang et al., 2003; Cui et al., 2019).

Numerous studies have been conducted on the Pearl River plume regarding its dynamics. Periodically variable runoff, monsoons and tides are recognized as important driving forces, which feature significant seasonal variability in the Pearl River. The summertime runoff is $\sim$20,000m^3/s in June and July but drops to $<$ 5,000m^3/s in January and February (**Figure 2**). The Pearl River Estuary region is affected by the East Asian Monsoon, with the southwesterly wind prevailing in summer and the northeasterly wind prevailing in winter (**Figure 2**). The tidal range outside the entrance of the Pearl River Estuary is $\sim$2 m during spring tide but increases gradually to $\sim$3 m from the entrance to the upper reaches. Due to the seasonal changes of these external forces (particularly the runoff and wind), the extension of the Pearl River plume shows significant seasonal variations. In winter, the Pearl River plume extends along the west coast under the northeasterly monsoon. However, in summer, its mainstream extends offshore to the east coast under the upwelling-favorable wind, but a small portion still extends to the west coast (Wong et al., 2003). Ou et al. (2007) categorized the summer Pearl River plume into four types according to the horizontal salinity distribution: offshore bulge spreading, westward alongshore spreading, eastward offshore spreading, and westward-eastward bidirectional alongshore spreading. Some studies have suggested that the coastal current driven by the seasonal monsoon causes the variation of the plume (Wong et al., 2003; Ou et al., 2009).

River plume dynamics have been explored extensively (e.g., Yankovsky and Chapman, 1997; Garvine, 1999; Lentz, 2001; Fong and Geyer, 2002; Whitney and Garvine, 2005; Moffat and Lentz, 2012; Molinas et al., 2014). The mixing and extension of the Pearl River plume under these external forces have also received extensive attention. Luo et al. (2012) suggest that runoff affects the size of the plume extension, while monsoon determines the shape and position of the plume. Zu and Gan (2009, 2015) and Zu et al. (2014) studied the impact of tide, runoff, and wind on the Pearl River plume from the perspective of energy and momentum balances. These studies indicate that tide hinders the extension of the plume, whereas the coastal currents driven by the monsoon cause the seasonal shift in its extension direction. In addition, these studies suggested that the primary energy source is the tide inside the estuary, whereas, on the shelf, it turns to the wind. The tidal mixing increases the thickness of freshwater but weakens the surface wind-induced Ekman transport (Zu et al., 2014). Pan et al. (2014) calculated tidal salt deficit flux and found its magnitude is related to tide strength, while its direction is affected by the wind.

It should be pointed out that previous studies mainly focused on the river plume in the surface layer. However, the role of the bottom plume front was rarely mentioned. In fact, some studies implied that the Pearl River plume could be locked by topography. For instance, the hypoxia areas associated with the Pearl River plume are distributed along specific topography (see **Figure 1**), which is recognized as the *coastal transition zone* (Li et al., 2020). Studies in other regions (e.g., Wang et al., 2019) suggest that such a topographic lock of phytoplankton bloom and associated environmental consequences can be linked to the bottom front. Hence, in this study, we investigated the spatiotemporal characteristics of bottom and surface fronts of the Pearl River plume, as well as its underlying dynamics, based on a validated numerical model. The remainder of this paper is organized as follows. In Section "Materials and Methods," the observed data, numerical model, and model validations are presented. The temporal and spatial characteristics of the surface and bottom front of the Pearl River plume are analyzed in Section "Results." These characteristics are based on statistical methods of front occurrence probability and Empirical Orthogonal Function. In Section "Discussion," dynamic factors that affect the plume front are discussed. Finally, we summarize our findings in section "Summary".

MATERIALS AND METHODS

Numerical Model

In this study, the Regional Ocean Modeling System (ROMS) (Shchepetkin and Mcwilliams, 2005) was configured with the

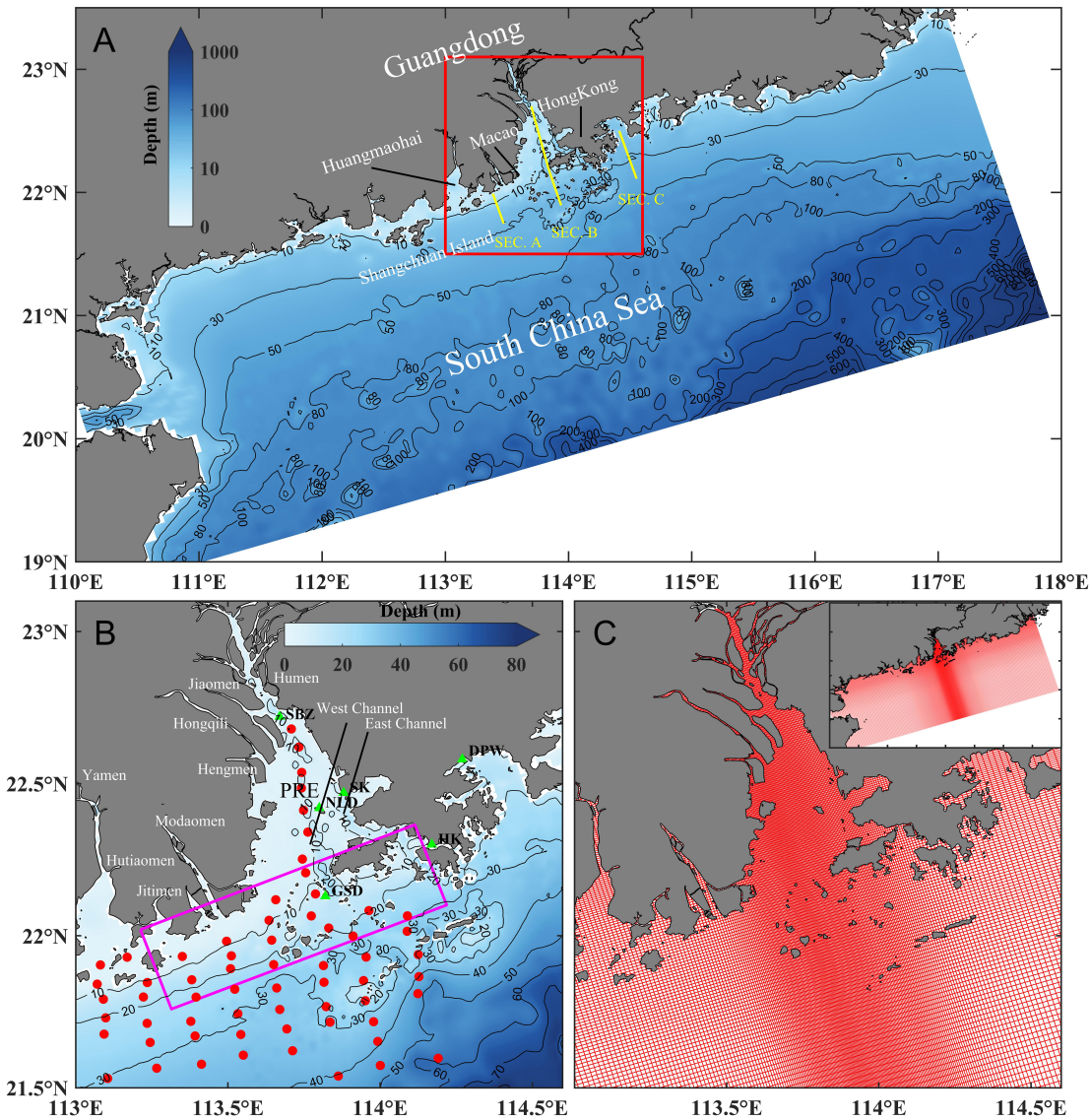


FIGURE 1 | (A) Map and bathymetry of the Pearl River Estuary and the ambient water. **(B)** Zoomed-in view of the bathymetry of the Pearl River Estuary, with the names of major outlets labeled. **(C)** Numerical model domain and grid. Three yellow lines in panel **(A)** denote sections used in later analysis. Magenta box in panel **(B)** is a coastal transition zone [modified from Li et al. (2020)]. Red dots and green triangles in panel **(B)** denote cruise stations and tide gauges, respectively (SBZ = Shanbanzhou, SK = Shekou, NLD = Neilingding, GSD = Guishandao, DPW = Dapengwan, HK = Hongkong). The solid black lines in panel **(A,B)** are isobaths.

model domain covering the Pearl River Estuary and its adjacent shelf (**Figure 1A**). The horizontal grid resolution was 500–800 m in the Pearl River Estuary and increased to 3–6 km in the open ocean. The eastern and western boundaries were perpendicular to the isobaths, while the southern boundary was located near the shelf break. The observed water depth data provided by Southern Marine Science and Engineering Guangdong Laboratory (Zhuhai) combined with the ETOPO2 data were interpolated to the model grids. A terrain-following S-coordinate (Song and Haidvogel, 1994) with 20 vertical levels was configured, and the surface and bottom layers were refined. A third-order HSIMT advection scheme developed by Wu and Zhu (2010) was selected for tracer advection simulation. Mellor and Yamada's level 2.5 turbulent closure scheme (Mellor and Yamada, 1982) and Smagorinsky scheme (Smagorinsky, 1963) were used to parameterize vertical mixing and horizontal mixing. The model was initialized with climatologic temperature and salinity from the Ocean General Circulation Model for the Earth Simulator (OFES) data. Open boundary conditions of temperature, salinity and shelf current were also obtained from OFES data. Thirteen tide constituents (M_2, S_2, N_2, K_2, K_1, O_1, P_1, Q_1, MF, MM, MN_4, M_4, and MS_4) extracted from Oregon State University (OSU) global inverse tidal model of TPXO8 (Egbert and Erofeeva, 2002) were used to provide tidal

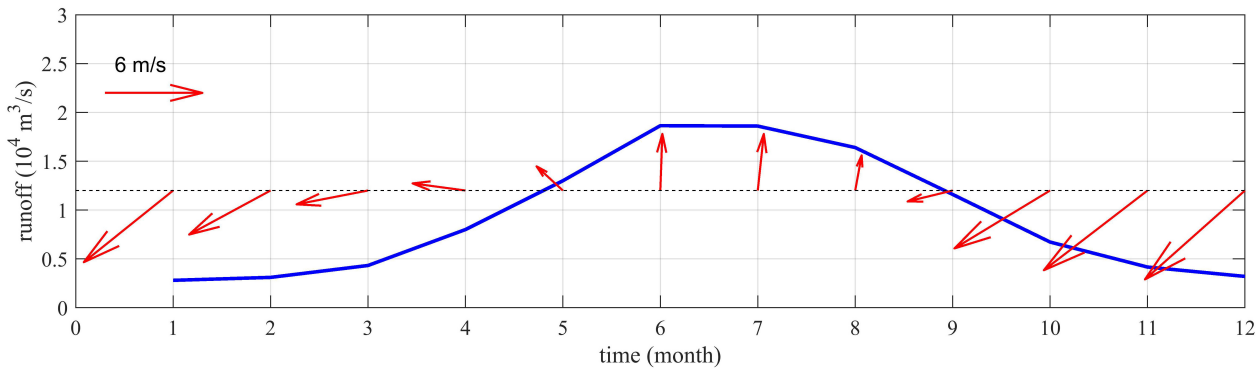


FIGURE 2 | Climatological monthly averaged runoff and wind vectors.

current and elevation for the open boundary. According to the diversion ratio suggested by Lu et al. (2013), the Pearl River runoff was distributed at eight major outlets. The atmospheric parameters (wind, air temperature, relative humidity, surface air pressure, cloud cover and net shortwave radiation) were provided by the European Centre for Medium-Range Weather Forecast (ECMWF) products (ERA-5 for realistic experiment and ERA-Interim for climatological experiment). The climatological experiment was driven by climatological monthly mean data of runoff, open boundary conditions, and atmospheric parameters. It was spun up for one year, and results of the second year were output for analysis. The configuration of the realistic experiment for model validation was the same as that of the climatological model except it was driven by 6-h atmospheric parameters.

Observed Data

Observed elevation and salinity data were used to validate the model. The elevation data used for comparison was observed during January 2008 at tide gauge stations that are marked with green triangles in **Figure 1B**. The salinity data were measured by a cruise organized by the Southern Marine Science and Engineering Guangdong Laboratory (Zhuhai). The cruise was conducted in the Pearl River Estuary and the adjacent shelf region from July 6 to 13, 2020. The sampling stations (as shown in **Figure 1B**) spanned from the Pearl River Estuary to the Huangmaohai and reached offshore to ∼50-m isobath.

Model Validation

Tides in the Pearl River Estuary and the adjacent water feature irregular semi-diurnal characteristics. K_1, O_1, M_2 and S_2 are the dominant tidal constituents in the NSCS, of which M_2 is the strongest. Harmonic analysis was conducted for observed and modeled elevation data to obtain the amplitude and phase of different tidal constituents. The vectorial difference (Foreman et al., 1993) was then used to compare the modeled results with the observation:

$$\mathrm{Diff} = [(a_0\cos g_0 - a_m\cos g_m)^2 + (a_0\sin g_0 - a_m\sin g_m)^2]^{1/2} \quad (1)$$

in which a_0 and g_0 are the observed harmonic tidal amplitude and phase, and a_m and g_m are the modeled counterparts. To normalize the results, the vectorial difference was further divided by the amplitude:

$$\mathrm{Rdiff} = \mathrm{Diff}/a_0 \quad (2)$$

The results of vectorial difference are listed in **Table 1**. The mean Diff of M_2 of all stations was 8.08 cm, and the mean Rdiff was 15.91%. The model simulated the M_2 constituent reasonably. The Diff of S_2 and K_1 were 5.73 cm and 7.35 cm, respectively, and the associated Rdiff did not exceed 25%. Rdiff of O_1 was 26.53% higher than other tidal constituents, but its absolute value was small given the small O_1 amplitude. Among the six tide gauge stations, the simulation at Shanbanzhou, located at the upper estuary inside the Humen, showed the largest error. The Rdiff of three harmonic tides (O_1, M_2 and S_2) exceeded 30% at this tide station. The tide in the river mouth is deformed to a certain extent, increasing the difficulty in accurate simulations. Given that the focus of this study was on the plume region, we did not further improve the validations. The overall model accuracy of simulating the tide was comparable with previous studies (e.g., Zu et al., 2014).

Observed data during July 2020 showed there was a low-salinity tongue outside the Pearl River Estuary (**Figure 3A**) and some researchers signify that the phenomenon is correlated to the West Channel geometry, estuarine outflow, tide, and wind (Pan et al., 2014; Liu et al., 2020). The surface plume extended in both directions to the east and west simultaneously (**Figure 3A**). The output data from the realistic forcing was compared with the observation (**Figures 3B,D**), showing reasonable skill in simulating the structure of the Pearl River plume both at the surface and the bottom. Inside the Pearl River Estuary, the shelf water intrusion simulated by the model was slightly weaker. Also, the modeled salinity near the Huangmaohai was relatively lower than the observation (**Figures 3C,D**). The reason could be that the model's runoff releasing position was too close to the ocean, resulting in insufficient mixing before leaving the estuary. Other than these two areas, the modeled salinity distribution was close to the observed data. Model performance was quantified via the correlation coefficient (CC), the root-mean-square

TABLE 1 | Comparison between the modeled and observed amplitude (A in cm) and phase (θ in deg) of four major tide constituents of K_1, O_1, M_2 and S_2.

Station	K_1(A/θ)				O_1(A/θ)				M_2(A/θ)				S_2(A/θ)			
	Model	Obs	Diff	RDiff(%)	Model	Obs	Diff	RDiff(%)	Model	Obs	Diff	RDiff(%)	Model	Obs	Diff	RDiff(%)
Shekou	37.90/326	37.64/312	9.07	24.09	29.62/250	30.39/263	7.06	23.24	61.19/299	53.26/296	8.57	16.08	25.21/337	27.78/336	2.60	9.37
Neilingding	37.32/326	41.83/312	10.74	25.67	29.24/249	29.45/258	4.59	15.60	58.51/299	53.17/302	5.93	11.15	24.00/337	22.07/330	3.57	16.19
Guishandao	35.95/316	37.25/309	5.12	13.75	27.66/238	30.24/253	7.66	25.31	47.00/275	44.76/281	5.63	12.57	17.77/309	21.06/316	4.06	19.26
Hongkong	34.97/313	28.96/302	8.24	28.45	26.51/236	28.16/249	6.44	22.87	42.00/264	38.47/269	5.28	13.73	16.21/297	18.95/301	3.08	16.23
Shanbanzhou	38.16/337	32.32/339	6.07	18.79	30.74/262	32.57/287	13.57	41.67	70.26/324	60.42/339	19.86	32.86	30.99/3	36.12 /31	17.11	47.36
Dapengwan	34.01/310	33.16/302	4.87	14.69	25.49/234	27.63/252	8.42	30.49	35.84/254	35.31/259	3.19	9.04	13.80/283	17.76/282	3.96	22.31
Mean			7.35	20.91			7.96	26.53			8.08	15.91			5.73	21.79

error (RMSE), and the skill score (SS). These metrics were calculated as follows:

$$CC = \frac{\sum_{i=1}^{N}(X_{mod} - \overline{X}_{mod})(X_{obs} - \overline{X}_{obs})}{\left[\sum_{i=1}^{N}(X_{mod} - \overline{X}_{mod})^2 \sum_{i=1}^{N}(X_{obs} - \overline{X}_{obs})^2\right]^{1/2}} \quad (3)$$

$$RMSE = \left[\sum_{i=1}^{N}(X_{mod} - X_{obs})^2/N\right]^{1/2} \quad (4)$$

$$SS = 1 - \frac{\sum_{i=1}^{N}(X_{mod} - X_{obs})^2}{\sum_{i=1}^{N}(X_{obs} - \overline{X}_{obs})^2} \quad (5)$$

in which X is the variable of interest and $\overline{X}$ is its mean. Model performance was categorized as excellent when SS $\geq$ 0.65, very good when 0.65 > SS $\geq$ 0.5, good when 0.5 > SS $\geq$ 0.2, and poor when SS < 0.2 (Maréchal, 2004; Allen et al., 2007). Although RMSE was greater than 3, the CC exceeded 0.9 and the SS was 0.8 in both the surface and bottom layers (**Figures 3E,F**). The relatively large RMSE but excellent CC and SS were caused by the strong spatial variability of salinity in the Pearl River Estuary. Therefore, the model was reliable and can be used for further investigation.

RESULTS

Variation of the Pearl River Plume

According to previous studies (Ou et al., 2009; Zu et al., 2014), the 32-psu isohaline can roughly denote the horizontal boundary of the Pearl River plume. We used the 75-h tidal-averaged salinity during the spring tides in different seasons to represent the seasonal variation of salinity distributions (**Figure 4**). In summer, as the runoff increased, the freshwater gradually extended outside the river mouth, and the prevailing southwesterly wind drove the coastal current to the northeast. The plume was thus brought to the eastern side of Pearl River Estuary. However, a portion of the plume extended toward the west coast simultaneously. The bottom plume, however, did not turn as did the surface. The bottom plume front existed only on the west coast of the Pearl River Estuary in summer, indicating that the plume extension to the east was surface-advected and that the extension to the west was bottom-trapped. The plume completely extended to the west in winter when the wind turned northeasterly. Its width was narrower than in summer. There were also seasonal variations inside the Pearl River Estuary. In summer, the surface plume filled the entire estuary, and the bottom shelf water intruded landward along two deep channels. In winter, the plume accumulated to the western side of the Pearl River Estuary, and the bottom shelf water intrusion that occupied the east side of the estuary was even more robust.

Whitney and Garvine (2005) suggested a wind index $W_s \equiv \frac{U_{wind}}{U_{buoyancy}}$, in which $U_{wind} \approx 2.65 \times 10^{-2} U$, $U_{buoyancy} = \frac{1}{K}(2g_r' Qf)^{1/4}$, U is along-shelf wind speed (up-shelf direction is positive in this study), K is internal Kelvin number, $g_r' = g(\rho_0 -$

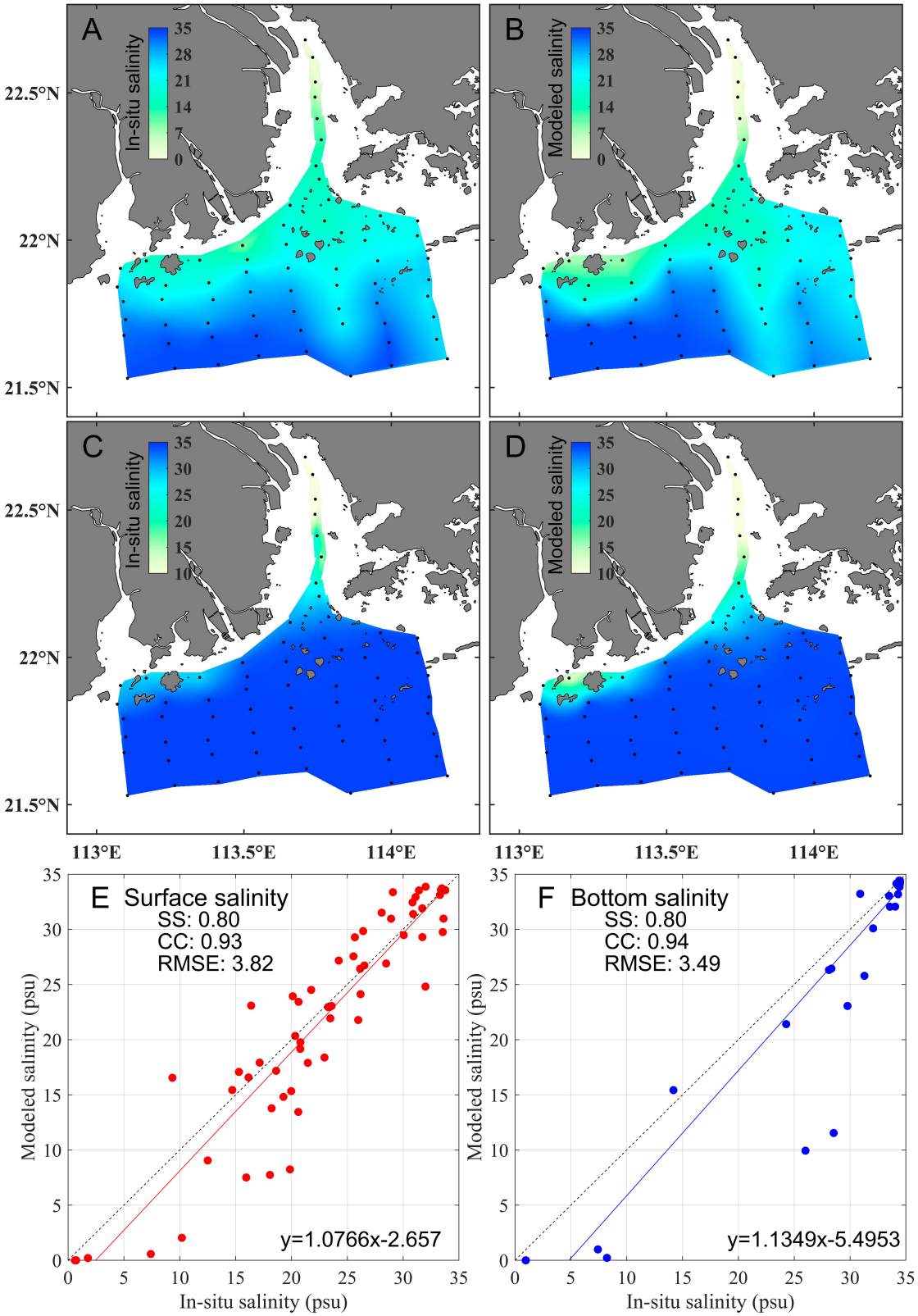


FIGURE 3 | Validation of the surface and bottom salinity during July 2020 (dots signify the sampling stations). **(A,C)** are surface and bottom observed salinity, respectively. **(B,D)** are modeled results, respectively. Scatterplots of model salinity and observed salinity are plotted in **(E,F)**.

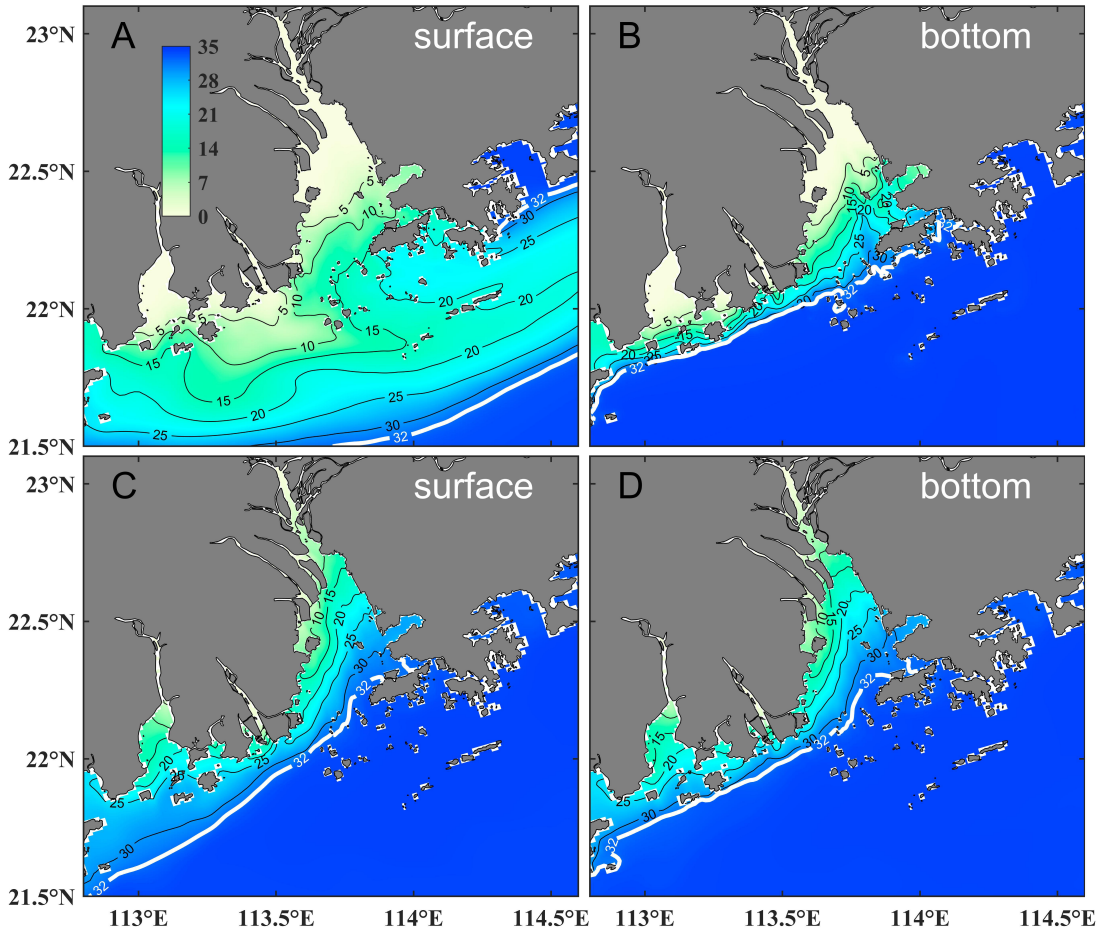


FIGURE 4 | Tidal-averaged surface and bottom salinity in summer **(A,B)** and winter **(C,D)** during spring tides. The solid black lines are isohaline and the 32-psu isohaline is highlighted by the thick white line.

$\rho_r)/\rho_0$ is the reduced gravity, ρ_0 is ambient seawater density, ρ_r is the freshwater density, Q is the runoff, and f is the Coriolis parameter. W_s quantifies the relative importance of wind stress and the down-shelf buoyancy-driven current. $|W_s|$ less than one indicates that the buoyancy-driven current is stronger than the wind-driven current. The calculated $|W_s|$ was ∼0.3 in summer but > 1 in winter. The existence of plume water along the west coast and the fact $|W_s| < 1$ in summer indicated that the extension of the Pearl River plume was controlled not only by the wind, but also by its baroclinicity.

The profile of Section A (**Figures 5A–D**) indicates that the river plume was bottom-trapped to the west of the Pearl River Estuary in summer and winter. The isohaline in winter was much sparser and more vertical than in summer. The isohaline during the spring tide was more vertical than during the neap tide. There was strong stratification in Section B in summer with a significant surface-to-bottom salinity difference. In winter, the isohaline in Section B was nearly vertical and the stratification was weakened significantly. In summer, the plume extended to the east coast under the upwelling-favorable summer monsoon (**Figures 5I,J**). A brackish water mass appeared in the offshore region as influenced by the surface-advected plume. In winter, Section C was occupied by high salinity water.

Salinity Gradient and Occurrence Probability of the Front

It is evident that the spatiotemporal variations of the Pearl River plume were very drastic. The surface-to-bottom salinity difference was also considerable in summer (**Figure 5**; later further shown in **Figure 13A**). Therefore, it is important to choose an appropriate method to describe the variability of the plume.

The gradient method is often used to identify fronts (Huang et al., 2010; He et al., 2016; Wu and Wu, 2018). In this study, the salinity gradient magnitude (SGM) was used to calculate the gradient in the surface and bottom layers of the Pearl River Estuary and its adjacent waters:

$$\mathrm{SGM} = \sqrt{(\Delta S_1/\Delta X_1)^2 + (\Delta S_2/\Delta X_2)^2} \tag{6}$$

In which ΔS_1 and ΔS_2 are the diagonal salinity difference of a 3×3 grid, while ΔX_1 and ΔX_2 are the diagonal distance between

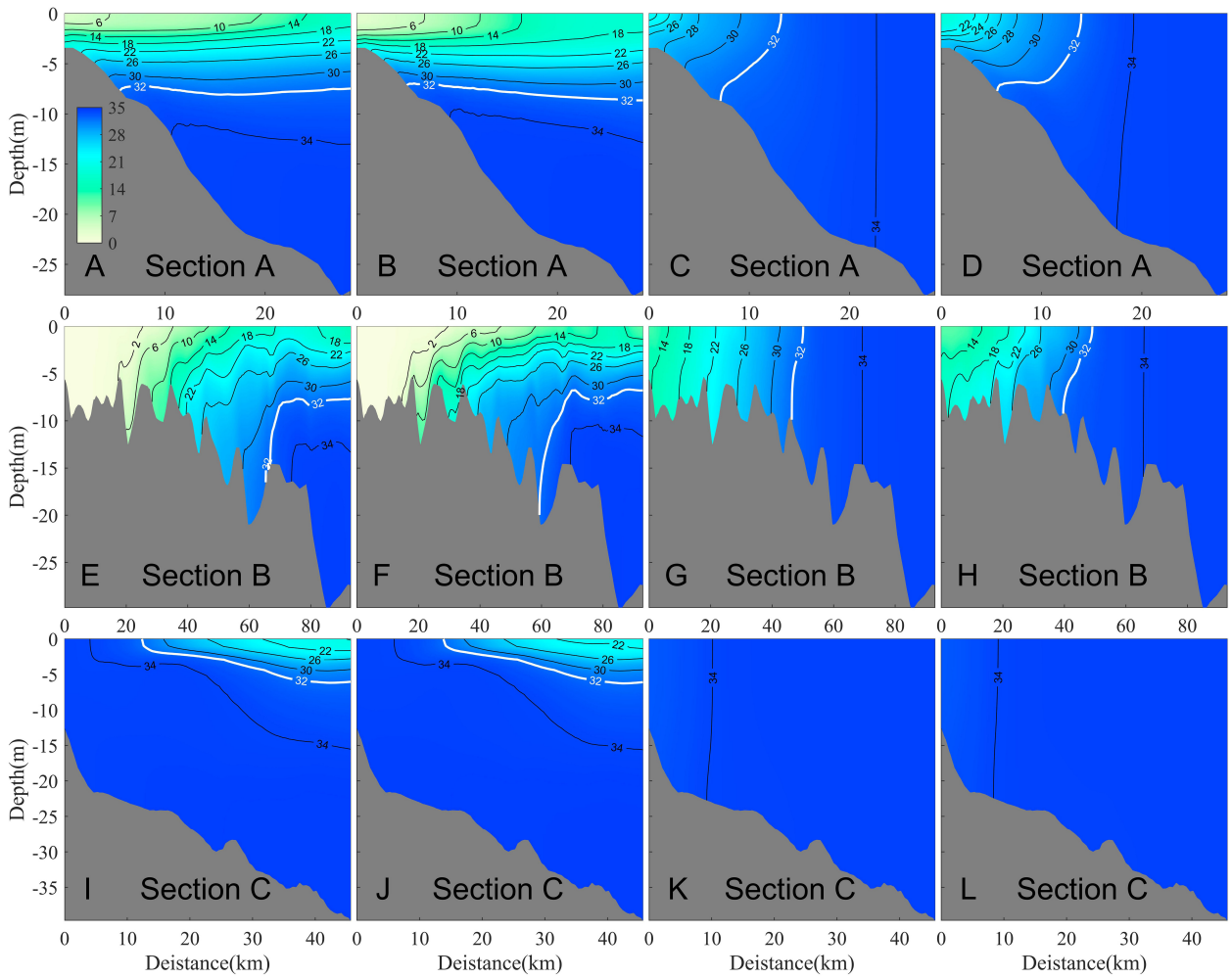


FIGURE 5 | Tidal-averaged salinity on the cross-shelf transections during the spring tide **(A,C,E,G,I,K)** and the neap tide **(B,D,F,H,J,L)** in summer **(A,B,E,F,I,J)** and winter **(C,D,G,H,K,L)**, respectively. The top row is section A, the middle is section B and the bottom is section C. The solid black lines are isohaline and the 32-psu isohaline is highlighted by the thick white line.

corners of the corresponding grids. The hourly modeled salinity was used to calculate SGM and then averaged over the period of interest. The seasonal and spring-neap cycles of the front are the main focus of this study. Annual-mean salinity gradient was used to indicate the average position of the front (**Figures 6A,B**). The surface salinity gradient in most areas of the model domain was small except in the Modaomen, Huangmaohai and Pearl River Estuary (**Figure 6A**). The bottom salinity gradient in the Pearl River Estuary and its adjacent coastal water was concentrated in a narrow region shoreward of ∼10-m isobath with a value up to 2 psu/km (**Figure 6B**). The distribution of the high bottom salinity gradient basically followed along the coastline. The standard deviation of the surface salinity gradient was large because the surface plume was affected by wind stress. Whereas in the bottom, the standard deviation of the salinity gradient was small, indicating the bottom plume front was more stable.

Summer (June to August) and winter (December to the next February) are flood and dry seasons, respectively. Therefore, these two seasons were selected as typical seasons to explore the cross-shelf variation in salinity gradients in Sections A, B, and C (**Figure 7**). The bottom front did not exist in Section C but occurred in Section A and Section B in winter and summer. Both the surface front and the bottom front had variations in intensity and spatial position. The bottom salinity gradients in Section A and Section B were stronger in summer than in winter on the seasonal scale. The surface and bottom front extended seaward in summer but shrank shoreward in winter. The seasonal cross-shelf movement of the surface front has a migration scale of ∼2 km in Section A and ∼20 km in Section B. The seasonal cross-shelf movement of the bottom front was smaller than that of the surface one, with Section A being ∼1.2 km and Section B being ∼10 km. In spring-neap tide cycles, the cross-shelf movement of the surface front was not obvious in Section B, although the phenomenon was apparent in Section A. The bottom front had a stronger intensity during the neap tides than during the spring. This was due to the increase of the tide mixing in the spring

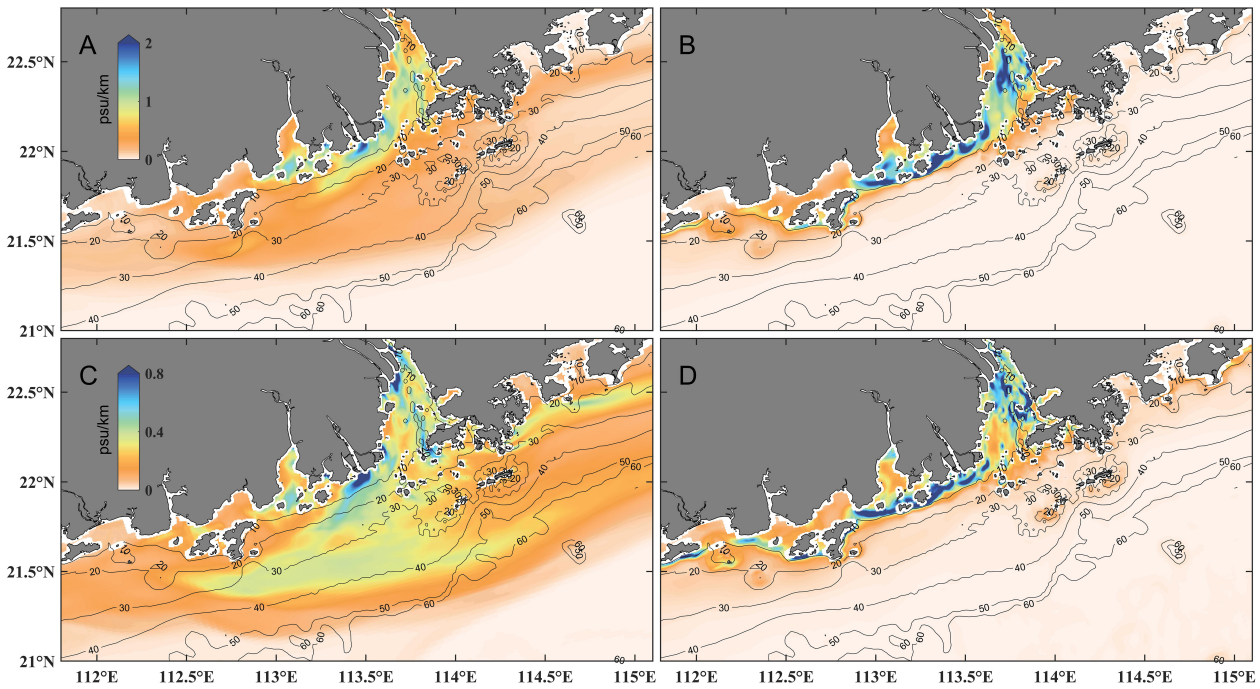


FIGURE 6 | Annual-averaged surface **(A)** and bottom **(B)** salinity gradient **(A,B)** and its standard deviation **(C,D)**. The solid black lines indicate isobaths.

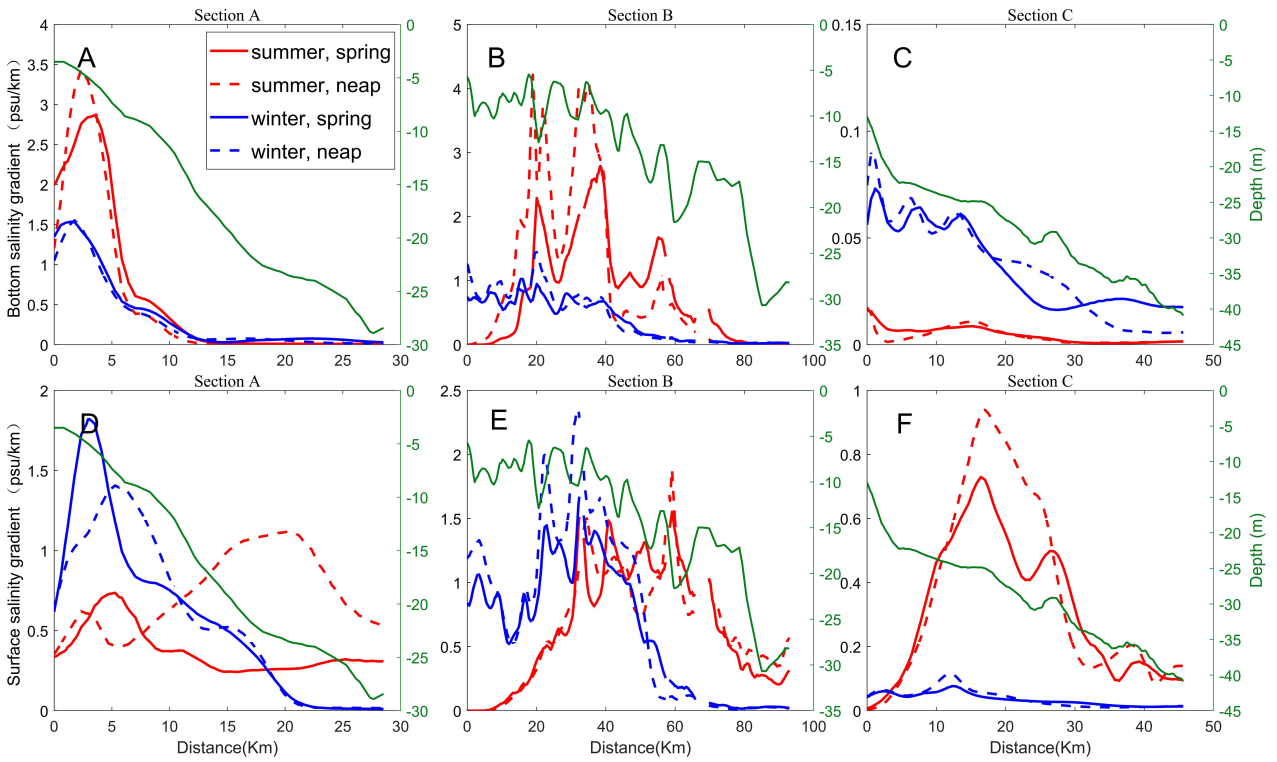


FIGURE 7 | Tidal-averaged cross-shelf bottom salinity gradient in Section A **(A,D)**, Section B **(B,E)** and Section C **(C,F)** during spring tide and neap tide in winter (December) and summer (July), respectively. The top row is for the bottom layer, and the bottom row is for the surface layer, respectively. Red and blue colors indicate results in summer and winter, respectively. Green lines signify section depth. Solid and dotted lines represent results in spring tide and neap tide, respectively.

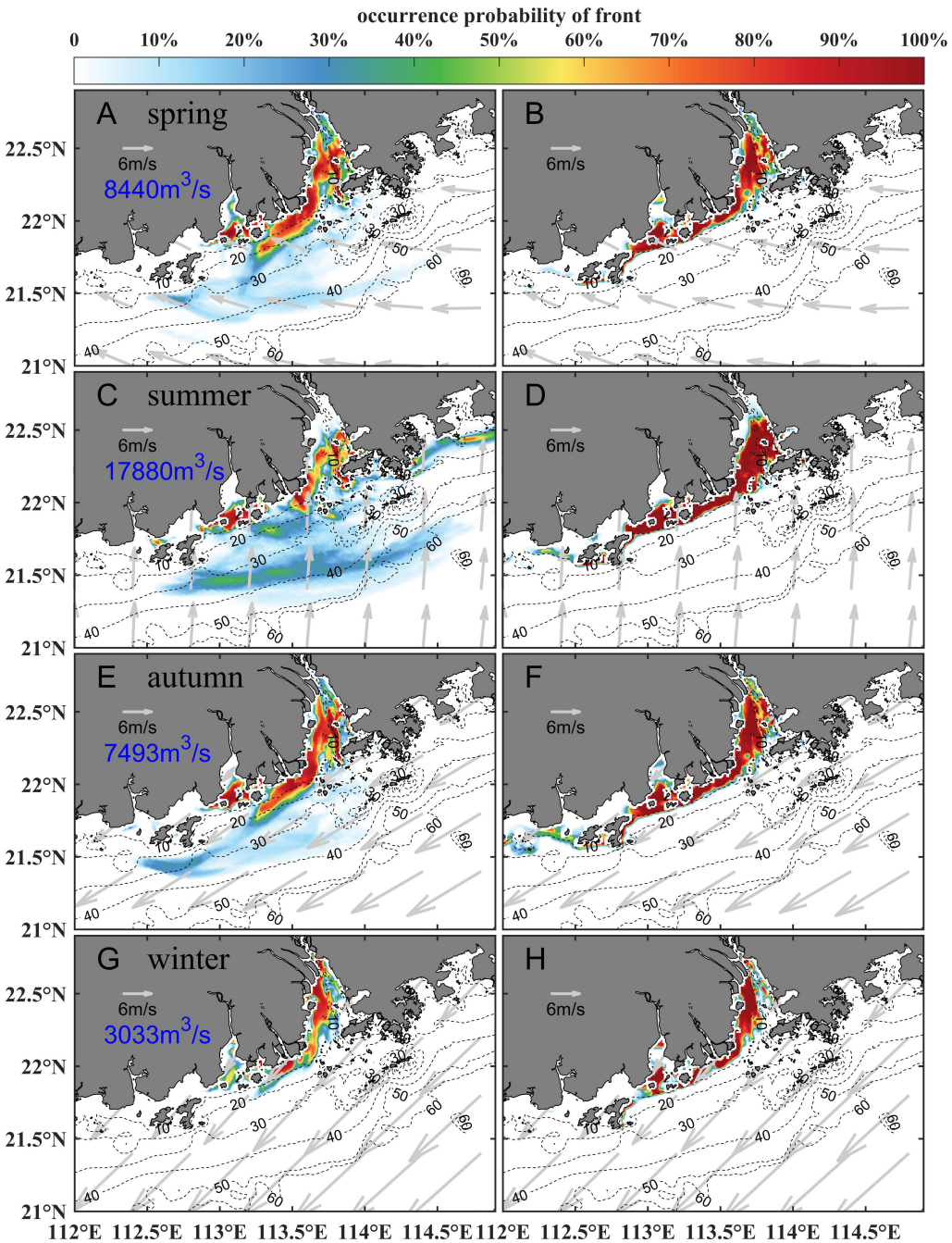


FIGURE 8 | Seasonal occurrence probability of surface **(A,C,E,G)** and bottom **(B,D,F,H)** fronts in spring **(A,B)**, summer **(C,D)**, autumn **(E,F)**, and winter **(G,H)**, respectively. The left column is the surface layer, and the right column is the bottom layer. Seasonal mean runoff and wind field are also labeled. The black dotted lines are isobaths.

tide inducing more vigorous shear dispersion that decreased the horizontal gradient. There were three extreme values on the bottom front at Section B and their positions correspond to the bathymetric variations. The bottom front moved seaward during the spring tides and landward during the neap tides. The migration scale of the bottom front in neap-spring cycles in Section A was ∼0.8 km in summer and ∼0.4 km in winter. The migration scale in neap-spring cycles in Section B was relatively larger than in Section A with ∼3 km in summer and ∼1 km in winter, respectively. The migration of the front depends not only on the strength of the external forces but also on the seafloor slope. According to the Yankovsky and Chapman (1997) theory, under the same external force, the greater the seafloor slope the smaller the horizontal migration distance of the front.

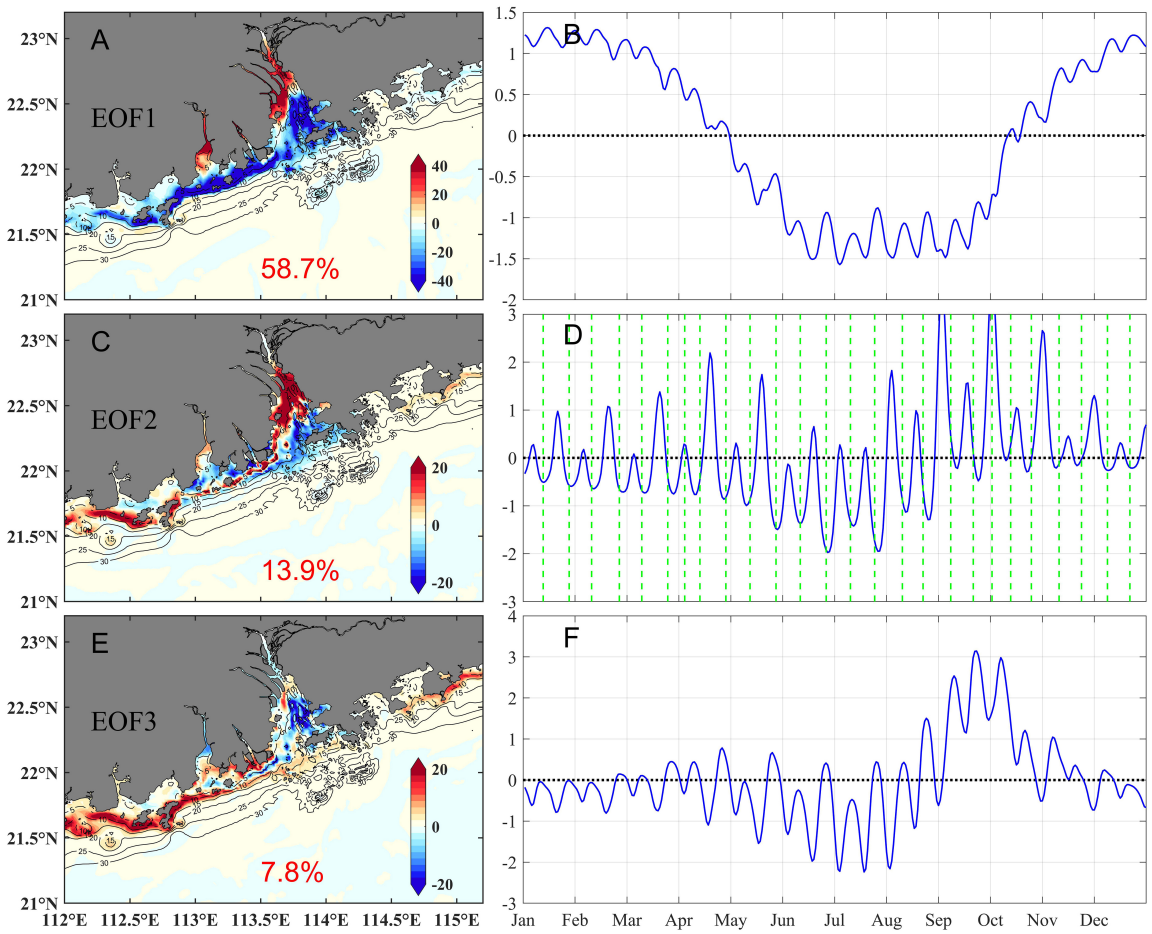


FIGURE 9 | Three leading EOF modes [Mode 1: **(A,B)**; Mode 2: **(C,D)**; Mode3: **(E,F)**] of the bottom salinity gradient. The green dotted lines in panel **(D)** denote the spring tides. The solid black lines **(A,C,E)** are isobaths.

The annual-mean salinity gradient and its standard deviation (**Figure 6**) provided basic information of the Pearl River plume front. However, averaging over a long-time span may obscure the actual intensity of the front. Therefore, we further calculated the occurrence probability of the plume front when its intensity exceeded a given threshold. Fedorov threshold (Fedorov, 1986)-i.e., ten times the average salinity gradient in the study area-was often used to detect the front (Fedorov, 1986). However, it should be noted that the Fedorov threshold is sensitive to the domain selected. To reflect the position of the front in different seasons more reasonably, we choose 0.8 psu/km as the threshold according to **Figure 7**. Counting the time of which the salinity gradient is greater than 0.8 psu/km in the four seasons, and then dividing it by the total time span, we got the occurrence probability of the salinity front (**Figure 8**) in four seasons (i.e., spring, summer, autumn and winter). In summer, the surface front existed in the east coast and moved offshore significantly; hence, there was a large area with a noticeable occurrence probability. The surface front also existed in the offshore region in spring and autumn; however, the probability dropped to ∼10%. In winter, the surface salinity front entirely extended to the west coast. In this period, the coastal extension of the front is the shortest, shrinking to the position around 113°E.

Whereas for the bottom front, the high occurrence probability area was distributed in a more narrow region and was nearly identical throughout four seasons (**Figure 8**). This indicated that the bottom front was strongly "rooted" on the seafloor. The occurrence of the surface front in the west region opposite to the wind direction in summer could be closely linked to the formation of the bottom front, as indicated by previous studies (e.g., Wu and Wu, 2018).

Empirical Orthogonal Function Analysis

To infer the formation dynamics of such a stable bottom front, the variability of the bottom salinity gradient was further analyzed by the EOF method. Before doing the EOF, the bottom salinity gradient was low-pass filtered (with a cut-off window of 72 h) to remove the strong intra-tidal signal, and then the long-term mean was further subtracted from the data. Hence, EOF analysis was performed on the anomaly field of the bottom salinity gradient. The results are shown in **Figure 9**. The three leading EOF modes contributed 58.7%, 13.9% and 7.8% of the

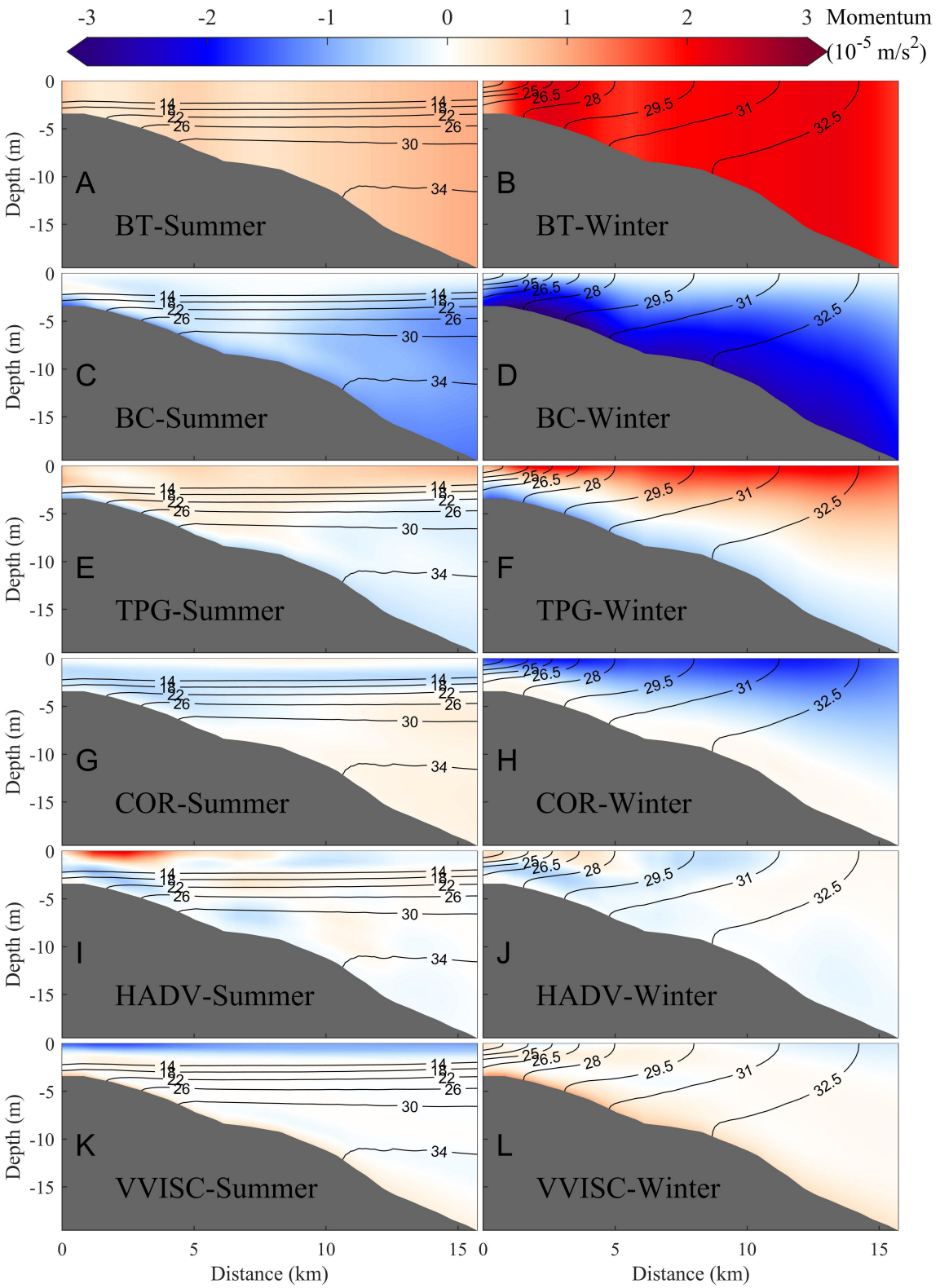


FIGURE 10 | Cross-shelf component of tidal-averaged momentum terms in Section A during summer (July) and winter (January) spring tides, respectively. **(A,B)** barotropic pressure gradient force; **(C,D)** baroclinic pressure gradient force; **(E,F)** total pressure gradient force; **(G,H)** Coriolis force; **(I,J)** horizontal momentum advection; **(K,L)** vertical turbulent viscous term. The solid black lines are isohalines.

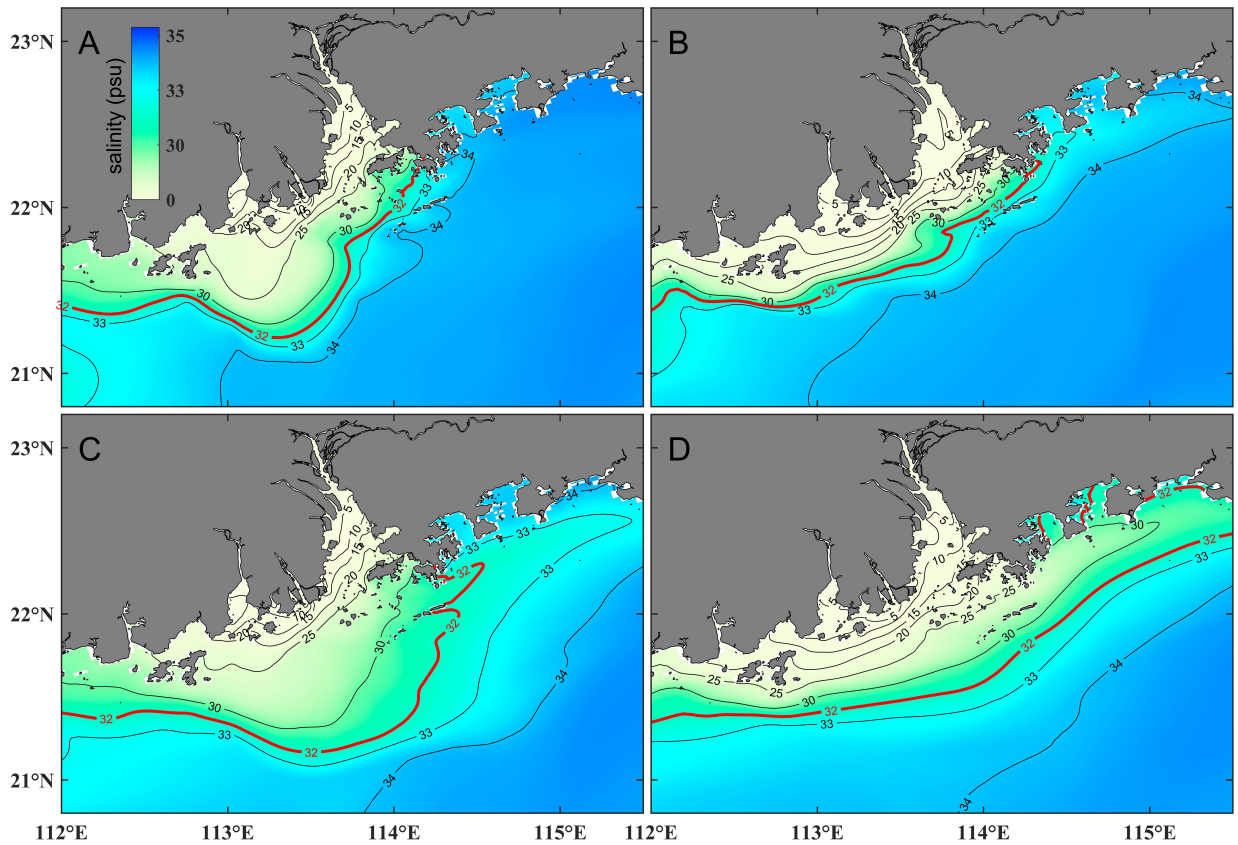


FIGURE 11 | Averaged surface salinity in April **(A,B)** and the entire spring season **(C,D)** with **(A,C)** and without **(B,D)** tide, respectively. The solid black lines are isohaline and the 32-psu isohaline is highlighted by the thick red line.

total variance, respectively, totaling 80.4%, which represented most of the variance in the bottom salinity gradient in the Pearl River Estuary.

Mode 1 showed a notable seasonal variation of the bottom front. During the spring and winter seasons, the bottom front shrank toward the coast, but it moved toward the sea during the summer and autumn seasons. This mode was mainly related to runoff and along-shelf wind with a correlation coefficient of -0.95 and -0.87, respectively. In summer and autumn, the runoff was large; meanwhile, the bottom front moved toward the sea. Correspondingly, the runoff was small in spring and winter, and the bottom front moved toward the land.

Mode 2 indicated a significant spring-neap cross-shelf movement. The correlation coefficient between Mode 2 and the tidal range was -0.57. The bottom front moved seaward during the spring tide, whereas it moved shoreward during the neap tides. It can also be seen that the influence of tide on the bottom front was the strongest in August and September, in consistence with the amplification of the tidal range around the autumnal equinox. West of ∼113.5°E, the spatial mode was different from that on the east side because there were freshwater sources from other tributaries of the estuary.

Mode 3, which contributed to the total variance less significantly, peaked during September and October. Its correlations with wind, runoff or tidal forcing were not as apparent as previous two modes. We inferred it was caused by the transition of the summer plume to the winter plume. In summer, a large area of river plume was surface advected due to the large river discharge and the upwelling-favorable summer monsoon. Then in autumn, the remainder of this plume was transported to the west coast, which supplied excess plume water that favored the formation of a strong bottom front.

DISCUSSION

Momentum Balance

Momentum terms from the model were used to diagnose the dynamic characteristics of the Pearl River plume. The average momentum terms over 75 h were used to remove tidal oscillations. The coordinate was rotated to represent the along-shelf (x) and cross-shore (y) directions.

The tidal-averaged momentum equation across the shelf reads:

$$0 = -\vec{V}\cdot\nabla v - fu - g\frac{\partial \eta}{\partial y} - \frac{g}{\rho_0}\int_z^{\eta}\frac{\partial \rho}{\partial y}dz + \frac{\partial}{\partial z}\left(A_z\frac{\partial v}{\partial z}\right) \quad (7)$$

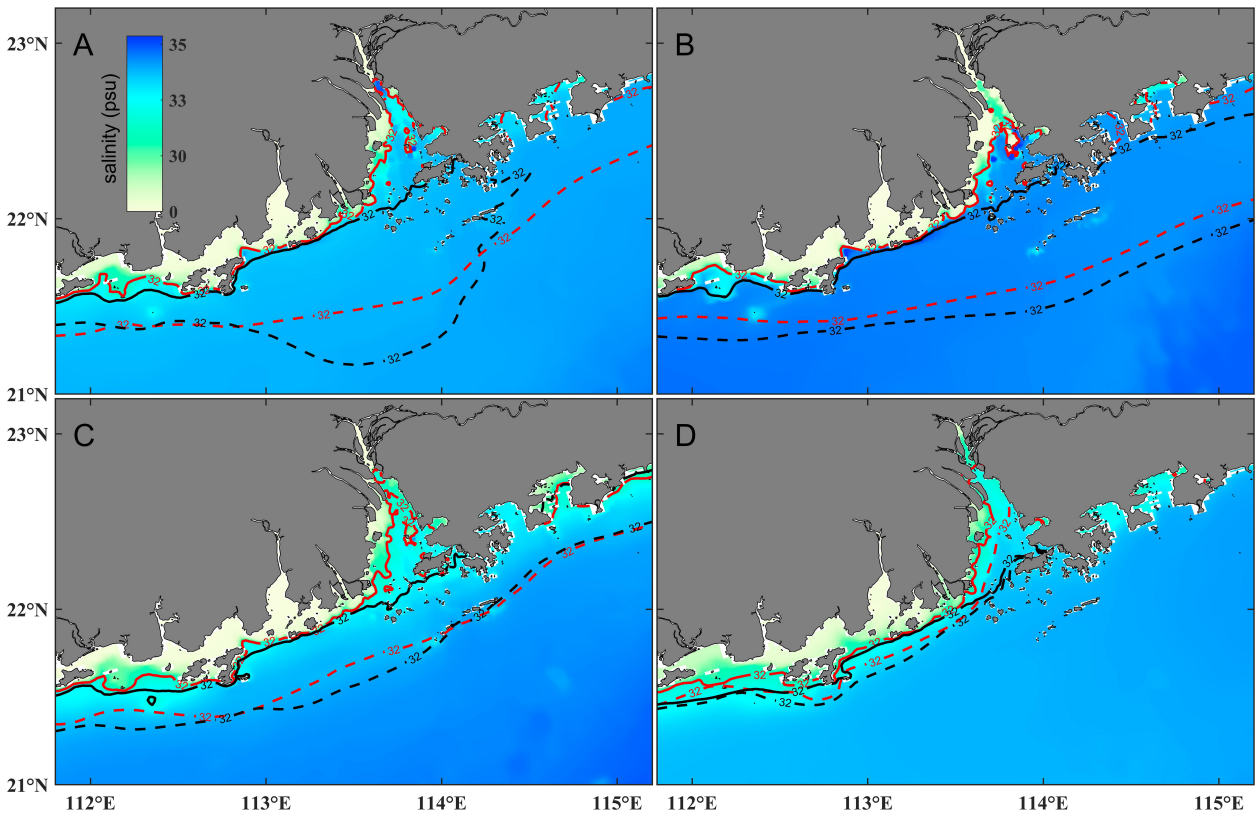


FIGURE 12 | Distribution of the bottom salinity in the presence and absence of tide in spring **(A)**, summer **(B)**, autumn **(C)** and winter **(D)**, respectively. The color shading is the salinity in the absence of tide, the dashed and solid lines are the 32-psu contours in the surface layer and the bottom layer, respectively. The black lines and red lines denote the result with and without tide, respectively.

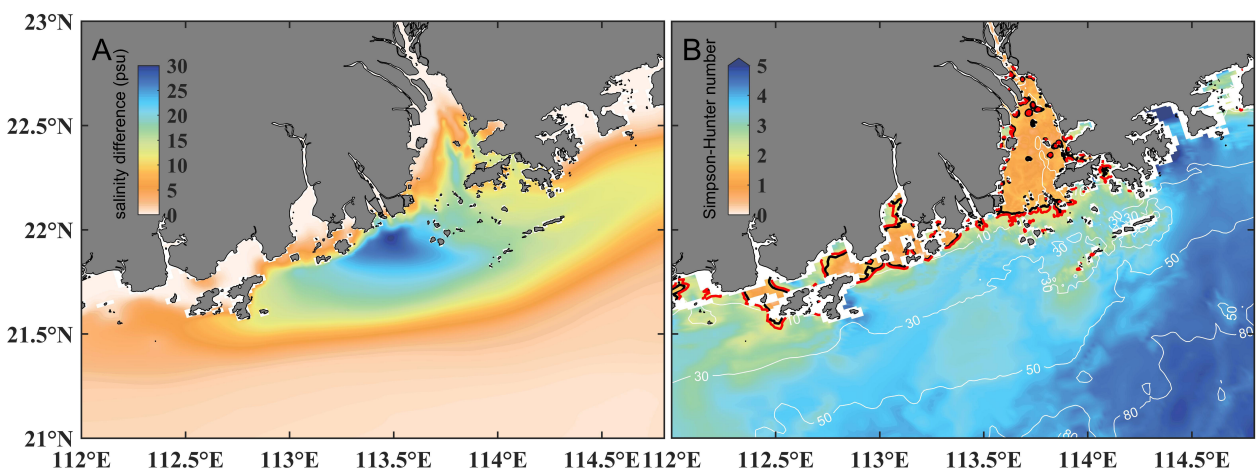


FIGURE 13 | Averaged surface-to-bottom salinity difference during the entire summer season **(A)** and the distribution of Simpson-Hunter number **(B)**. The black and red solid lines in **(B)** are the contours of SH = 1.7 and SH = 2, respectively.

in which the tidal-averaging operator was omitted. The terms on the right-hand side are the advection, Coriolis force, barotropic pressure gradient force, baroclinic pressure gradient force, and vertical friction force, respectively. The horizontal diffusion term was neglected because it was much smaller than the vertical diffusion.

Results across Section A during the spring tide in summer and winter seasons are shown in **Figure 10**. The barotropic pressure

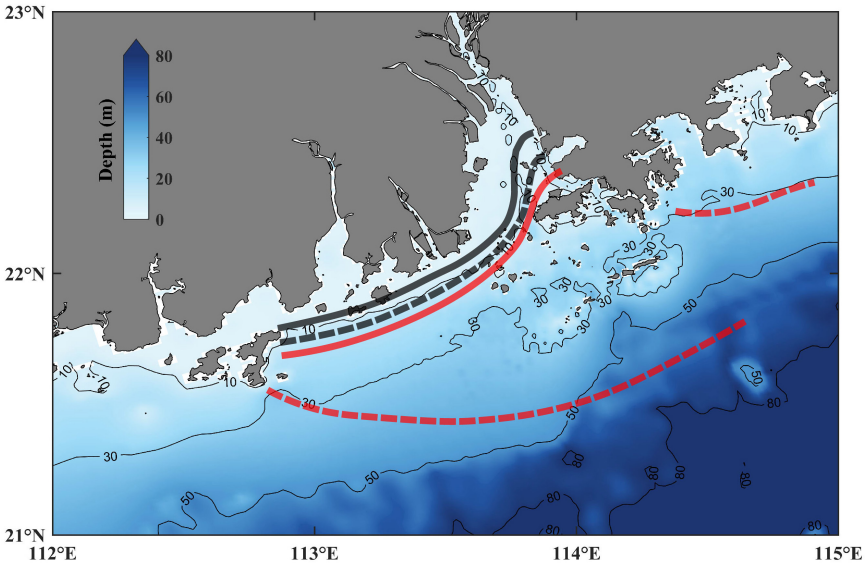


FIGURE 14 | Schematic map of the spatiotemporal distribution of the front. The solid thick lines are the bottom front position, and the dashed thick lines are the surface front position, respectively. The red color and black color represent summer and winter seasons, respectively. The solid black lines signify the isobaths.

gradient force was seaward (positive value) and the baroclinic pressure gradient force was landward (negative value). The total pressure gradient force and Coriolis force were largely balanced in the cross-shelf direction. This momentum balance in winter was more in line with the thermal wind balance than in summer. The advection term also has larger values on the surface layers and at the top of the bottom boundary layer, indicating strong nonlinearity. The vertical friction of the surface layer was strong in summer, and the friction of the bottom boundary layer was strong in winter. Overall, the momentum balance was more geostrophic in the winter season, while the nonlinear momentum advection and friction became important in summer. This was apparently related to the different front shapes in these two seasons. Nevertheless, from **Figure 10**, it is clear that the locations associated with maximum bottom salinity gradient were similar in winter and summer, regardless of contrast dynamic balances. This seems consistent with the dynamics of EOF mode 2. The cross-shelf location was controlled by tidal forcing, which remains largely unchanged during different seasons.

Tidal Modulation on the River Plume

The EOF analysis, as well as the above momentum balance analysis, indicated that tide was a dominant forcing determining the cross-shelf position of the bottom front. This, however, was in contrast to the previous conclusion that was derived from a non-tidal river plume (Chapman and Lentz, 1994; Yankovsky and Chapman, 1997). In these studies, the cross-shelf position was controlled by river discharge and wind through the bottom Ekman dynamics.

Hence, a sensitivity experiment with tide excluded was configured to further explore the role of the tide in controlling the bottom front in the Pearl River Estuary. The average surface salinity in April and the entire spring season are shown in **Figure 11**. The model results showed that dramatic differences can be found with tidal forcing removed. In the absence of tide, the Pearl River plume also extended to the upstream, in consistence with the findings in other estuaries (e.g., Guo and Valle-Levinson, 2007; Wu et al., 2011). With tide included, the surface plume extended further to the sea.

The difference between tidal and non-tidal simulations in all four seasons is shown in **Figure 12**. The bottom 32-psu contour was roughly located along the line connecting Macao and Hong Kong in the tide's presence. In the absence of tide, a large amount of shelf water intruded into the Pearl River Estuary, hence, the bottom front moved shoreward. This was due to the enhanced estuarine circulation under weak mixing, thus strong stratification (Gong et al., 2018). The difference in the 32-psu contours in the shelf region was small between the two sensitivity experiments, indicating that the impact of the tide on the front weakened in the offshore region.

The spring-neap migration of the bottom front implied that it could be linked to the tidal front due to differential mixing over topography (Simpson and Hunter, 1974; Wu and Wu, 2018). Simpson-Hunter (SH) number can be used to compare the relative strength of the mixing caused by tidal current and by stratification (Simpson and Hunter, 1974),

$$\mathrm{SH} = \log\left(\frac{h}{U_T^3}\right) \tag{8}$$

in which h is the water depth, U_T is the maximum tidal velocity during the spring tide. The smaller the SH number is, the more likely the tidal mixing can overcome vertical stratification. An SH number between 1.7 and 2 was commonly taken as the position of the tidal-induced mixing front (Beardsley et al., 1985; Loder and Greenberg, 1986; Wu and Wu, 2018). As shown in

Figure 13B, the SH number in the Pearl River Estuary was less than 2, indicating that tide could thoroughly mix the entire water column. In the coastal area from the entrance of the Pearl River Estuary to the west coast, SH number value was between 1.7 and 2. Thus, there was a boundary between stratified and mixed waters at the entrance of the Pearl River Estuary. This place was consistent with the region with a high occurrence probability of the bottom front (**Figure 7**). This indicated that the formation and maintenance of the bottom plume front were closely linked to the tidal mixing, which was similar to the Changjiang River plume (Wu and Wu, 2018).

SUMMARY

A numerical model with high resolution in the Pearl River Estuary was configured to explore the spatiotemporal distribution of the Pearl River plume front. The model validation indicated that it can reasonably reproduce the structure of the Pearl River plume. The salinity gradient magnitude and the occurrence probability of the front were used to identify the mean and standard deviation of the plume front both at the surface and the bottom. The results indicated that a year-round bottom front existed in the Pearl River Estuary and the west coast, while the surface front was much more variable. The spatial position of the Pearl River plume front is summarized in **Figure 14**.

Empirical Orthogonal Function (EOF) analysis indicated that the Pearl River discharge was the primary external forcing regulating the bottom front intensity. With a larger discharge, the bottom front became stronger and moved seaward. Additionally, the tide was a significant factor affecting the cross-shelf position of the bottom front, moving to the sea during the spring tides but to the land during the neap tides. The cross-shelf movement of the bottom front was more pronounced in August and September, consistent with the amplification of the tidal range around the autumnal equinox. Momentum analysis signified that the Coriolis force and the total pressure gradient force balance dominated in the study region, and the nonlinear advection term and friction term became important in summer.

Experiments with and without tide were further conducted to explore the tidal influence on the Pearl River plume front. In the absence of tides, the river plume also extended to the upstream even though the wind was not upwelling-favorable, and the bottom front moved landward. It can be seen from the Simpson-Hunter number that tide can overcome the influence of stratification, causing differential mixing over topography, thus producing a tidal front that sustained the Pearl River plume front. Consequently, the Pearl River plume front was rooted on the seafloor, which should be essential for the frequent occurrence of hypoxia in certain areas.

DATA AVAILABILITY STATEMENT

The raw data supporting the conclusions of this article will be made available by the authors, without undue reservation.

AUTHOR CONTRIBUTIONS

HW designed the research. HZ conducted the numerical experiments and wrote the first draft of the manuscript. HZ and YW analyzed the results. All authors contributed extensively to the interpretation of results and approved the submitted version.

FUNDING

This study was supported by Innovation Group Project of Southern Marine Science and Engineering Guangdong Laboratory (Zhuhai) (Grant No. 311020003), the Innovation Program of Shanghai Municipal Education Commission (Grant Nos. 2021-01-07-00-08-E00102), the National Natural Science Foundation of China (Grant Nos. 42106162 and 41776101).

REFERENCES

Allen, J. I., Somerfield, P. J., and Gilbert, F. J. (2007). Quantifying uncertainty in high-resolution coupled hydrodynamic-ecosystem models. *J. Mar. Syst.* 64, 3–14. doi: 10.1016/j.jmarsys.2006.02.010

Beardsley, R. C., Limeburner, R., Yu, H., and Cannon, G. A. (1985). Discharge of the Changjiang (Yangtze River) into the East China Sea. *Cont. Shelf Res.* 4, 57–76. doi: 10.1016/0278-4343(85)90022-6

Chapman, D. C., and Lentz, S. J. (1994). Trapping of a coastal density front by the bottom boundary layer. *J. Phys. Oceanogr.* 24, 1464–1479.

Cui, Y. S., Wu, J. X., Ren, J., and Xu, J. (2019). Physical dynamics structures and oxygen budget of summer hypoxia in the Pearl River Estuary. *Limnol. Oceanogr.* 64, 131–148. doi: 10.1002/lno.11025

Dong, L. X., Su, J. L., Wong, L. A., Cao, Z. Y., and Chen, J. C. (2004). Seasonal variation and dynamics of the Pearl River plume. *Cont. Shelf Res.* 24, 1761–1777. doi: 10.1016/j.csr.2004.06.006

Egbert, G. D., and Erofeeva, S. Y. (2002). Efficient inverse modeling of Barotropic Ocean tides. *J. Atmos. Ocean. Technol.* 19, 183–204. doi: 10.1175/1520-0426(2002)019<0183:eimobo>2.0.co;2

Fedorov, K. N. (1986). *The Physical Nature and Structure of Oceanic Fronts*. New York, NY: Springer-Verlag.

Fong, D. A., and Geyer, W. R. (2002). The alongshore transport of freshwater in a surface-trapped river plume*. *J. Phys. Oceanogr.* 32, 957–972.

Foreman, M. G. G., Henry, R. F., Walters, R. A., and Ballantyne, V. A. (1993). A finite element model for tides and resonance along the north coast of British Columbia. *J. Geophys. Res.* 98, 2509–2531. doi: 10.1029/92JC02470

Franks, P. J. S. (1992). Phytoplankton blooms at fronts: patterns, scales, and physical forcing mechanisms. *Rev. Aquat. Sci.* 6, 121–137.

Gan, J. P., Li, L., Wang, D. X., and Guo, X. G. (2009). Interaction of a river plume with coastal upwelling in the northeastern South China Sea. *Cont. Shelf Res.* 29, 728–740. doi: 10.1016/j.csr.2008.12.002

Garvine, R. W. (1995). A dynamical system for classifying buoyant coastal discharges. *Cont. Shelf Res.* 15, 1585–1596. doi: 10.1016/0278-4343(94)00065-U

Garvine, R. W. (1999). Penetration of buoyant coastal discharge onto the continental shelf: a numerical model experiment. *J. Phys. Oceanogr.* 29, 1892–1909. doi: 10.1175/1520-048519990292.0.CO

Gong, W. P., Lin, Z. Y., Chen, Y. Z., Chen, Z. Y., and Zhang, H. (2018). Effect of winds and waves on salt intrusion in the Pearl River estuary. *Ocean Sci.* 14, 139–159. doi: 10.5194/os-14-139-2018

Guo, X. Y., and Valle-Levinson, A. (2007). Tidal effects on estuarine circulation and outflow plume in the Chesapeake Bay. *Cont. Shelf Res.* 27, 20–42. doi: 10.1016/j.csr.2006.08.009

He, S. Y., Huang, D. J., and Zeng, D. Y. (2016). Double SST fronts observed from MODIS data in the East China Sea off the Zhejiang–Fujian coast, China. *J. Mar. Syst.* 154, 93–102. doi: 10.1016/j.jmarsys.2015.02.009

Hu, J. T., and Li, S. Y. (2009). Modeling the mass fluxes and transformations of nutrients in the Pearl River Delta, China. *J. Mar. Syst.* 78, 146–167. doi: 10.1016/j.jmarsys.2009.05.001

Huang, D. J., Zhang, T., and Zhou, F. (2010). Sea-surface temperature fronts in the Yellow and East China Seas from TRMM microwave imager data. *Deep Sea Res. II Top. Stud. Oceanogr.* 57, 1017–1024. doi: 10.1016/j.dsr2.2010.02.003

Lai, Z. G., Ma, R. H., Gao, G. Y., Chen, C. S., and Beardsley, R. C. (2015). Impact of multichannel river network on the plume dynamics in the Pearl River estuary. *J. Geophys. Res. Oceans* 120, 5766–5789. doi: 10.1002/2014JC010490

Lentz, S. J. (2001). The influence of stratification on the wind-driven cross-shelf circulation over the North Carolina Shelf*. *J. Phys. Oceanogr.* 31, 2749–2760.

Li, D., Gan, J. P., Hui, R., Liu, Z. Q., Yu, L. Q., Lu, Z. M., et al. (2020). Vortex and biogeochemical dynamics for the hypoxia formation within the coastal transition zone off the Pearl River estuary. *J. Geophys. Res. Oceans* 125:e2020JC016178. doi: 10.1029/2020JC016178

Liu, X. C., Gu, Y. Z., Li, P. L., Liu, Z. Z., Zhai, F. G., and Wu, K. J. (2020). A tidally dependent plume bulge at the Pearl River Estuary mouth. *Estuar. Coast. Shelf Sci.* 243:106867. doi: 10.1016/j.ecss.2020.106867

Loder, J. W., and Greenberg, D. A. (1986). Predicted positions of tidal fronts in the Gulf of Maine region. *Cont. Shelf Res.* 6, 397–414. doi: 10.1016/0278-4343(86)90080-4

Lu, L. Y., Zhan, J. M., and Geng, B. X. (2013). Study of the Pearl River plume dispersion based on flux budget analysis [in Chinese]. *J. Hydrodyn.* 28, 252–259. doi: 10.3969/j.issn1000-4874.2013.03.002

Lu, Z. M., and Gan, J. P. (2015). Controls of seasonal variability of phytoplankton blooms in the Pearl River Estuary. *Deep Sea Res. II Top. Stud. Oceanogr.* 117, 86–96. doi: 10.1016/j.dsr2.2013.12.011

Luo, L., Zhou, W., and Wang, D. (2012). Responses of the river plume to the external forcing in Pearl River Estuary. *Aquat. Ecosyst. Health Manage.* 15, 62–69. doi: 10.1080/14634988.2012.655549

Maréchal, D. (2004). *A Soil-Based Approach to Rainfall-Runoff Modeling in Ungauged Catchments for England and Wales.* dissertation's thesis. Bedford: Cranfield University.

Mellor, G. L., and Yamada, T. (1982). Development of a turbulence closure model for geophysical fluid problems. *Rev. Geophys.* 20, 851–875. doi: 10.1029/RG020i004p00851

Moffat, C., and Lentz, S. J. (2012). On the response of a buoyant plume to downwelling-favorable wind stress. *J. Phys. Oceanogr.* 42, 1083–1098. doi: 10.1175/JPO-D-11-015.1

Molinas, E., Vinzon, S. B., Vilela, C., and Gallo, M. N. (2014). Structure and position of the bottom salinity front in the Amazon Estuary. *Ocean Dyn.* 64, 1583–1599. doi: 10.1007/s10236-014-0763-0

Orton, P. M., and Jay, D. A. (2005). Observations at the tidal plume front of a high-volume river outflow. *Geophys. Res. Lett.* 32, 1–16. doi: 10.1029/2005GL022372

Ou, S. Y., Zhang, H., and Wang, D. X. (2007). Horizontal characteristics of buoyant plume off the Pearl River Estuary during summer. *J. Coast. Res. SI* 50, 652–657.

Ou, S. Y., Zhang, H., and Wang, D. X. (2009). Dynamics of the buoyant plume off the Pearl River Estuary in summer. *Environ. Fluid Mech.* 9, 471–492. doi: 10.1007/s10652-009-9146-3

Pan, J. Y., Gu, Y. Z., and Wang, D. X. (2014). Observations and numerical modeling of the Pearl River plume in summer season. *J. Geophys. Res. Oceans* 119, 2480–2500. doi: 10.1002/2013JC009042

Shchepetkin, A. F., and Mcwilliams, J. C. (2005). The regional oceanic modeling system (ROMS): a split-explicit, free-surface, topography-following-coordinate oceanic model. *Ocean Model.* 9, 347–404. doi: 10.1016/j.ocemod.2004.08.002

Simpson, J. H., and Hunter, J. R. (1974). Fronts in the Irish Sea. *Nature* 250, 404–406. doi: 10.1038/250404a0

Smagorinsky, J. (1963). General circulation experiments with the primitive equations. *J. Mon. Weather Rev* 91, 99–164. doi: 10.1115/1.4027610

Song, Y., and Haidvogel, D. (1994). A semi-implicit ocean circulation model using a generalized topography-following coordinate system. *J. Comput. Phys.* 115, 228–244. doi: 10.1006/jcph.1994.1189

Su, J. Z., Dai, M. H., He, B. Y., Wang, L. F., Gan, J. P., Guo, X. H., et al. (2017). Tracing the origin of the oxygen-consuming organic matter in the hypoxic zone in a large eutrophic estuary: the lower reach of the Pearl River Estuary, China. *Biogeosciences* 14, 1–24. doi: 10.5194/bg-2017-43

Tang, D. L., Kester, D. R., Ni, I. H., Qi, Y. Z., and Kawamura, H. (2003). In situ and satellite observations of a harmful algal bloom and water condition at the Pearl River estuary in late autumn 1998. *Harmful Algae* 2, 89–99. doi: 10.1016/S1568-9883(03)00021-0

Wang, S. F., Tang, D. L., He, F. L., Fukuyo, Y., and Azanza, R. V. (2008). Occurrences of harmful algal blooms (HABs) associated with ocean environments in the South China Sea. *Hydrobiologia* 596, 79–93. doi: 10.1007/s10750-007-9059-4

Wang, Y. H., Wu, H., Gao, L., Shen, F., and Liang, X. S. (2019). Spatial distribution and physical controls of the spring algal blooming off the Changjiang river estuary. *Estuar. Coasts* 42, 1066–1083. doi: 10.1007/s12237-019-00545-x

Whitney, M. M., and Garvine, R. W. (2005). Wind influence on a coastal buoyant outflow. *J. Geophys. Res. Oceans* 110:C03014. doi: 10.1029/2003JC002261

Wong, L. A., Chen, J. C., Xue, H., Dong, L. X., Guan, W. B., and Su, J. L. (2003). A model study of the circulation in the Pearl River Estuary (PRE) and its adjacent coastal waters: 2. Sensitivity experiments. *J. Geophys. Res. Oceans* 108:3157. doi: 10.1029/2002JC001452

Wu, H., and Zhu, J. R. (2010). Advection scheme with 3rd high-order spatial interpolation at the middle temporal level and its application to saltwater intrusion in the Changjiang Estuary. *Ocean Model.* 33, 33–51. doi: 10.1016/j.ocemod.2009.12.001

Wu, H., Zhu, J. R., Shen, J., and Wang, H. (2011). Tidal modulation on the Changjiang River plume in summer. *J. Geophys. Res. Oceans* 116:C08017. doi: 10.1029/2011JC007209

Wu, T. N., and Wu, H. (2018). Tidal mixing sustains a bottom-trapped river plume and buoyant coastal current on an energetic continental shelf. *J. Geophys. Res. Oceans* 123, 9061–9081. doi: 10.1029/2018JC014105

Yankovsky, A. E., and Chapman, D. C. (1997). A simple theory for the fate of buoyant coastal discharges. *J. Phys. Oceanogr.* 27, 1386–1401.

Yu, L. Q., Gan, J. P., Dai, M. H., Hui, C. R., Lu, Z. M., and Li, D. (2020). Modeling the role of riverine organic matter in hypoxia formation within the coastal transition zone off the Pearl River Estuary. *Limnol. Oceanogr.* 66, 452–468.

Zu, T. T., and Gan, J. P. (2009). Process-Oriented study of the river plume and circulation in the Pearl River estuary: response to the wind and tidal forcing. *Adv. Geosci.* 12, 213–230. doi: 10.1142/9789812836168_0015

Zu, T. T., and Gan, J. P. (2015). A numerical study of coupled estuary-shelf circulation around the Pearl River Estuary during summer: responses to variable winds, tides and river discharge. *Deep Sea Res. II Top. Stud. Oceanogr.* 117, 53–64. doi: 10.1016/j.dsr2.2013.12.010

Zu, T. T., Wang, D. X., Gan, J. P., and Guan, W. B. (2014). On the role of wind and tide in generating variability of Pearl River plume during summer in a coupled wide estuary and shelf system. *J. Mar. Syst.* 136, 65–79. doi: 10.1016/j.jmarsys.2014.03.005

Conflict of Interest: The authors declare that the research was conducted in the absence of any commercial or financial relationships that could be construed as a potential conflict of interest.

Publisher's Note: All claims expressed in this article are solely those of the authors and do not necessarily represent those of their affiliated organizations, or those of the publisher, the editors and the reviewers. Any product that may be evaluated in this article, or claim that may be made by its manufacturer, is not guaranteed or endorsed by the publisher.

Copyright © 2022 Zhi, Wu, Wu, Zhang and Wang. This is an open-access article distributed under the terms of the Creative Commons Attribution License (CC BY). The use, distribution or reproduction in other forums is permitted, provided the original author(s) and the copyright owner(s) are credited and that the original publication in this journal is cited, in accordance with accepted academic practice. No use, distribution or reproduction is permitted which does not comply with these terms.

frontiers in Marine Science

ORIGINAL RESEARCH
published: 08 March 2022
doi: 10.3389/fmars.2022.836739

Long-Term Variability on Suspended Particulate Matter Loads From the Tributaries of the World's Largest Choked Lagoon

Eduardo C. Bortolin[1], Juliana Távora[2] and Elisa H. L. Fernandes[1]*

[1] Laboratório de Oceanografia Costeira e Estuarina (LOCOSTE), Instituto de Oceanografia, Universidade Federal do Rio Grande (FURG), Rio Grande, Brazil, [2] Faculty of Geo-Information Science and Earth Observation, University of Twente, Enschede, Netherlands

OPEN ACCESS

Edited by:
Alexander Yankovsky, University of South Carolina, United States

Reviewed by:
Andrew M. Fischer, University of Tasmania, Australia
Mukesh Gupta, Catholic University of Louvain, Belgium

***Correspondence:**
Eduardo C. Bortolin
edubortolin@gmail.com

Specialty section:
This article was submitted to Coastal Ocean Processes, a section of the journal Frontiers in Marine Science

Received: *15 December 2021*
Accepted: *17 January 2022*
Published: *08 March 2022*

Citation:
Bortolin EC, Távora J and Fernandes EHL (2022) Long-Term Variability on Suspended Particulate Matter Loads From the Tributaries of the World's Largest Choked Lagoon. Front. Mar. Sci. 9:836739. doi: 10.3389/fmars.2022.836739

Continental freshwater contributions are the main long-term control on the variability of suspended particulate matter (SPM) concentrations in choked lagoons. The current work aims to assess the seasonal to interdecadal variability in SPM concentrations from Patos Lagoon tributaries, as a case study towards the understanding of tributaries contributions to coastal lagoons. Thus, an interdecadal dataset (1984–2020) was collected in the region of the tributaries of Patos Lagoon (southern Brazil), integrating Landsat series (653 scenes) and *in situ* measurements. SPM concentrations were estimated from the scenes using a semi-analytical multiwavelength algorithm, applied in the regions of the lower course of the tributaries. Results identified SPM concentrations variability in seasonal scales, enhanced by El Niño Southern Oscillation (ENSO) in interannual time scales, also influencing in interdecadal trends. The seasonal SPM concentration variability reached 50 $g.m^{-3}$ to each tributary. Higher SPM concentration values occurred from winter to spring, enhanced during El Niño periods and frequently reaching annual means higher than 100 $g.m^{-3}$. Periods from summer to autumn, however, presented lower SPM concentrations, especially during La Niña periods, when the mean annual SPM concentration remained mostly below 50 $g.m^{-3}$. Seasonal and interannual (ENSO) forcings combined developed configurations of high input periods (HIP) and low input periods (LIP). During the LIP, the river plumes are limited to their tributary zone of influence and the whole lagoon has reduced SPM concentrations. During the HIP, the river plumes spread over the lagoon sub-environments, and the SPM concentrations of all tributaries reach the estuarine zone and the ocean. Thus, the mentioned natural phenomena influence the river plumes spreading, the SPM concentrations in the lagoon, and the export to the Atlantic Ocean in time scales varying from seasonal to interdecadal.

Keywords: river plumes, landsat, Patos Lagoon, remote sensing, ENSO (El Nino/Southern Oscillation), tributaries, freshwater contribution, suspended particulate matter

INTRODUCTION

The drainage systems transport sediments to the coastal environments, developing particularly high suspended particulate matter (SPM) concentrations in shallow transitional environments (Miller and McKee, 2004; Lihan et al., 2008), often higher than in the coastal sea (Eisma, 1993). Estuaries and coastal lagoons are key transitional environments for monitoring processes influencing the SPM dynamics, as these water bodies have ecological significance, shelter harbors, and regulate the export to the ocean. The amount of SPM concentrations in the water column affects water quality parameters (Bilotta et al., 2012), and can be associated with pollutants and modify the subaquatic behavior of the light (reflectance and absorption), which can impact aquatic life and water potability (Wilkinson et al., 2017). Understanding the variability of SPM concentrations reaching transitional systems is a complex challenge, because the fluxes respond in different temporal and spatial scales and to multiple natural or anthropogenic forcings.

The SPM loads from tributaries to coastal systems have been studied by different approaches in the last decades. Earlier investigations focused on assessing SPM associated with the variability of chemical elements (Rostad and Leenheer, 1997; Rachold, 1999; Schäfer et al., 2002; Gordeev et al., 2004), dissolved nutrients (Ward and Twilley, 1986), and isotopic composition promoted by the tributary's influxes (Rachold et al., 1997). Recent studies, however, have longer data sets available and rely on more advanced technology (e.g., more satellite products), allowing the survey of historical changes and long-term analysis of SPM behavior (Choi et al., 2012; Kreiling and Houser, 2016; Park et al., 2018; Ryberg et al., 2018). Despite advances, studies analyzing seasonal to decadal variability on SPM concentrations rarely used datasets longer than 35 years, with few exceptions (Dang et al., 2010). This represents a gap in the literature and also can lead to interpretations based on the trend of a specific decade. Moreover, studies concerning SPM in river plumes focused on tidally influenced environments (Hetland and Hsu, 2013; Horner-Devine et al., 2015; Shanmugam, 2018). This kind of study, however, is uncommon for microtidal environments, sheltered from tidal influence by sandy barriers (Liu et al., 1997).

Coastal lagoons in particular represent a path towards the coast for the concentrations of SPM received from the drainage basin through the tributaries. Choked lagoons are composed of a series of elliptical cells, and these systems are connected to the ocean through a single and narrow channel, which limits tidal currents and water-level fluctuations in the lagoon (Kjerfve, 1994). Patos Lagoon is the largest choked coastal lagoon in the world (Kjerfve, 1986; **Figure 1**), covering about 10.000 km^2, draining almost 200.000 km^2, with 6 m average depth, connected to the Atlantic Ocean through a single narrow inlet (< 700 m wide), which was stabilized by jetties built-in 1911 (Toldo et al., 2000). Salinity in Patos Lagoon ranges from 0 to 34, mostly limited to the estuarine zone, which is about 55 km from the mouth (Moller et al., 2001). The concentration of dissolved organic matter (CDOM) in the estuarine zone is inversely correlated with salinity, with mean concentrations ranging from 13.07 to 18.26 mg.m^{-3} (Rodrigues et al., 2012). Measurements

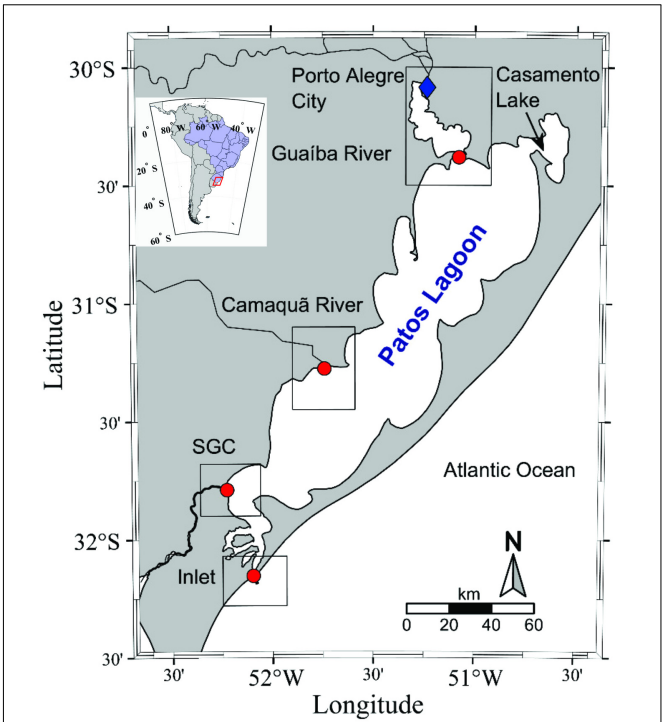


FIGURE 1 | Patos Lagoon detailing the investigated area of each tributary (rectangular boxes). The mouth of the main tributaries is marked by red dots.

from 1986 to 2008 revealed mean Chlorophyll *a* concentrations of 7.31 μg L^{-1} (SD = ± 9.75) in this region (Abreu et al., 2010).

This important depositional basin receives SPM from three main tributaries Guaíba and Camaquã rivers, and the São Gonçalo Channel (SGC), which connects Patos and Mirim Lagoons, which together cover 14,000 km^2 (Bortolin et al., 2020). Once inside the lagoon, the coarser fractions of suspended sediment tend to deposit in the upper course of the system and the SPM fine fraction is either transported in suspension or deposited in preferential zones, responding to autogenic forcings (Bortolin et al., 2020), such as the variability in freshwater discharges and wind action (Távora et al., 2019; Bitencourt et al., 2020). The fine SPM fraction which reaches Patos Lagoon estuary moves towards the coast through Rio Grande Channel, which has predominant ebb flow (Moller et al., 2001; Fernandes et al., 2002), but is also subject to flocculation processes during flood flows (Ávila et al., 2021).

The system is under a microtidal regime of 30 cm amplitude, and its dynamic is driven by freshwater discharges and winds (Moller et al., 2001). The wind influence becomes more relevant at shorter timescales and during periods of reduced freshwater discharges (<2,000 m^3.s^{-1}) (Moller et al., 2001; Távora et al., 2020b). Two predominant wind directions in the region are NE (22.3%) and SW (13.5%) (Tomazelli, 1993). NE winds are predominant along the year (5 m.s^{-1} mean velocity) driven by the Atlantic Anticyclone, and SW winds occur secondarily in a higher intensity (8 m.s^{-1}) mainly during winter (Stech and Lorenzetti, 1992). The mean annual freshwater discharge in Patos

Lagoon is about 2,400 $m^3.s^{-1}$ (Vaz et al., 2006), however, such conditions change according to ENSO events (Fernandes et al., 2002), with lower inflows during La Niña events, contrasting with peaks reaching 12,000 $m^3.s^{-1}$ during El Niño events (Moller et al., 1996). These driving forces behave according to well-studied cycles, whose periods are recognized in seasonal and interannual scales (Vaz et al., 2006; Jung et al., 2020), as well as El Niño-Southern Oscillation (ENSO) (Vaz et al., 2006; Távora et al., 2019, 2020b; Bitencourt et al., 2020).

The freshwater inputs from the tributaries are assumed as the main control in SPM concentrations in Patos Lagoon during long time scales (seasonal and interannual), with high SPM concentrations proportional to peaks in freshwater discharges related to the ENSO cycle (Moller et al., 2001; Távora et al., 2019, 2020b; Bitencourt et al., 2020). A recent study has proposed the prediction of SPM concentrations by the tributaries of Patos Lagoon in short time scales, based on the time series of freshwater discharge from the tributaries and the rating-curves approach (Jung et al., 2020). However, an assessment of measured SPM concentrations from the Patos Lagoon tributaries reaching the interdecadal time scale is still a gap of knowledge in this system and in coastal lagoons in general, especially in South America (Beltrame et al., 2009; Bitencourt et al., 2020; Távora et al., 2020b). Thus, the aim of the current work is to contribute towards the understanding of the long-term variability (covering seasonal, interannual, and interdecadal time scales) of SPM concentrations from tributaries towards coastal lagoons, by using high spatial resolution remote sensing reflectance (Rrs) measurements from Patos Lagoon as a case study.

In this context, remote sensing represents a low-cost and trustworthy tool for monitoring SPM concentrations in large coastal environments (Matthews, 2011; Choi et al., 2012; Távora et al., 2020b), with the advantage of providing long-term data. Despite the methodological benefits, few studies investigated SPM in Patos Lagoon using remote sensing. General characterizations of the suspended sediment dynamics were carried out (e.g., Pagot et al., 2007; Fassoni-Andrade et al., 2015), but these studies investigated a short-term period of about 2 years. Recent studies analyzed the behavior of SPM concentrations inside Patos Lagoon using a Moderate Resolution Imaging Spectroradiometer (MODIS) satellite, which has a high temporal resolution (daily satellite overpass). Although with low spatial resolution, such recent studies investigated shorter periods than the present work, as follows, 8 years (Távora et al., 2019), and 17 years period (Távora et al., 2020b). None of them, however, focused on the Patos Lagoon tributaries, and for that, the high spatial resolution provided by Landsat products is required.

During the last decade, generically applicable algorithms have been developed to model SPM concentrations from Rrs in coastal water bodies (Nechad et al., 2010; Han et al., 2016; Novoa et al., 2017). The performance of those algorithms was compared for Patos Lagoon, presenting different results depending on the region of the lagoon (Távora et al., 2020b). A recent advance was achieved by the multi-wavelength semi-analytical method proposed by Távora et al. (2020a), which estimates SPM concentrations with its uncertainties and has shown satisfactory performance in comparison to the algorithms mentioned above.

The algorithm proposed by Távora et al. (2020a) was applied to the Patos Lagoon tributaries in the current study, using high spatial resolution satellite images (Landsat 5, 7, and 8) from 1984 to 2020 to model long-term SPM concentrations from the tributaries contributing to the lagoon. The present investigation covered the longest timescale analysis of SPM concentrations in the tributaries of Patos Lagoon, and accounts for the higher spatial resolution satellites already used for this purpose in the area, which is ideal for capturing small scale details in specific environments (such as meandering rivers). The combination of *in situ* and modeled results was a useful strategy to fill gaps in the SPM concentrations from each tributary. Furthermore, it was possible to propose conceptual models about the behavior of long-term SPM concentrations during periods of high and low continental contributions from the tributaries.

MATERIALS AND METHODS

The flowchart in **Figure 2** summarizes the main steps adopted in the present work, from the scenes acquisition to the final image processing stages.

Atmospheric Correction

Satellite scenes from Landsat 5, 7, 8 (hereon L5, L7, L8) were acquired through the Earth Explorer data collection of the United States Geological Survey (USGS)[1], encompassing the years 1984 to 2020. The atmospheric correction from Level 1 to Level-2 was processed with the freely available software ACOLITE (version 20210114.0), developed by the Royal Belgian Institute of Natural Sciences (RBINS)[2], which also merged the tiles to fit the study area (29.9°32.5° S; 50.5°–52.5° W). The high spatial resolution of the satellites allowed the selection of smaller boxes to investigate each tributary region (**Figure 1**), as follows: Guaíba (29.9°–30.67° S; 50.87°–51.34° W), Camaquã (30.98°–31.52° S; 51.59°–52.10° W), SGC (31.68°–31.90° S; 52.06°–52.36° W) and inlet (32.07°–32.28° S; 51.93°–52.13° W).

ACOLITE provides two atmospheric correction schemes: dark spectrum fitting (DSF) (Vanhellemont and Ruddick, 2018; Vanhellemont, 2019) and exponential extrapolation (EXP) (Vanhellemont and Ruddick, 2014, 2015, 2016). The manufacturer recommends the use of the DSF, while the EXP can be considered as a complementary tool. Both were tested for the study area to check the best performance. The two models were applied to nine randomly picked satellite scenes, collected in different years, with distinct turbidity and cloud conditions. The DSF performed better, showing less masked data for highly turbid waters and cloudy days.

After performing the atmospheric correction, the scenes were selected to avoid evidence of signal disturbance, such as suspicious noise, remaining clouds, and haze. After this quality control, all scenes from the Red to the Short Wave Infra-red (SWIR) were used, following the methods described in the algorithm proposed by Távora et al. (2020a).

[1]https://earthexplorer.usgs.gov/ (Accessed August 31, 2021).

[2]https://odnature.naturalsciences.be/remsem/software-and-data/acolite (Accessed August 31, 2021).

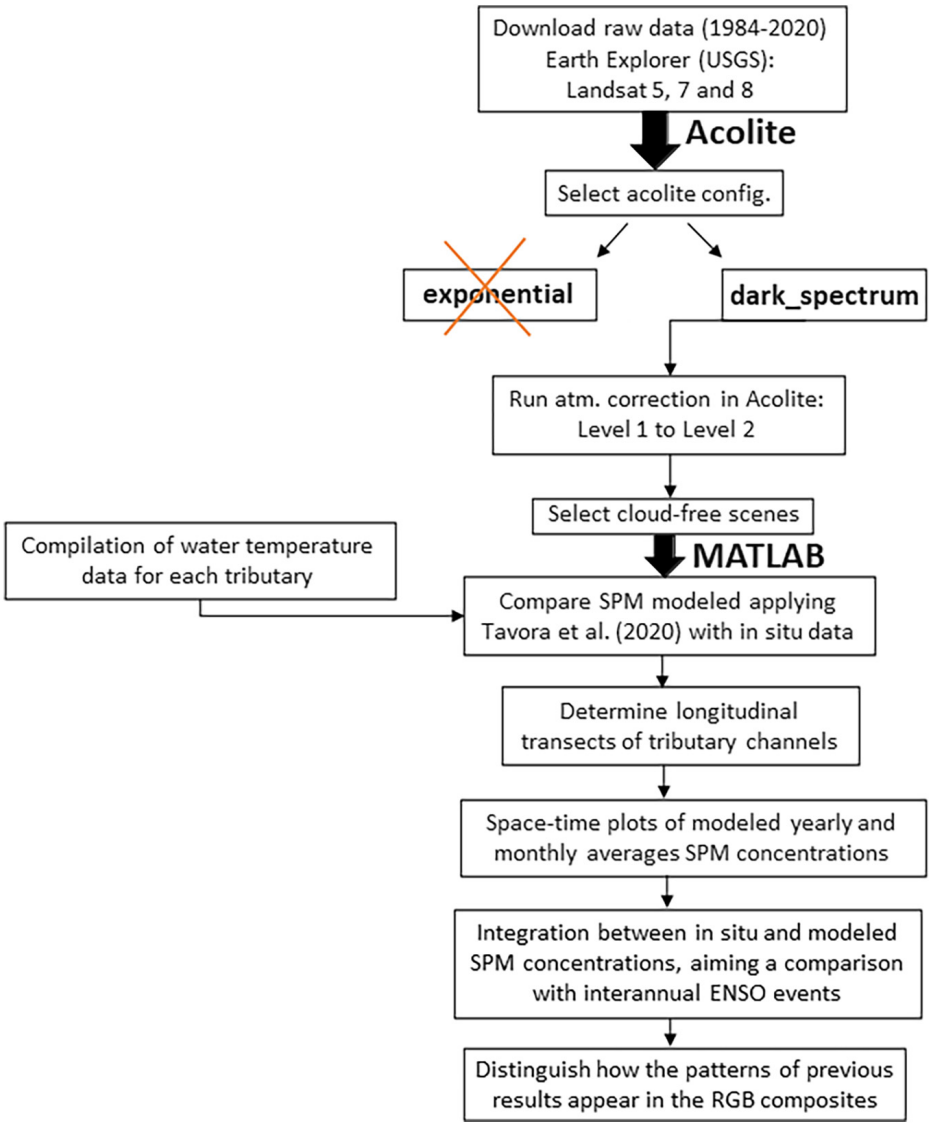


FIGURE 2 | Flowchart representing a schematic processing sequence developed in Acolite and MATLAB. The upper portion of the flowchart represents the atmospheric correction (see section "Atmospheric Correction") processing developed in the ACOLITE software. The lower portion summarizes the modeling of SPM concentrations (see section "Multi-Proxy Suspended Particulate Matter Estimates"), the integration with *in situ* data (see section "Multi-Proxy Suspended Particulate Matter Estimates"), and the comparison with environmental forcings [see sections "El Niño-Southern Oscillation Index (MEI v.2) and Discharges From Tributaries" and "Spectral Method (Lomb-Scargle Periodogram)"] developed in MATLAB.

Multi-Proxy Suspended Particulate Matter Estimates

Concentrations of SPM have been measured in Patos Lagoon over the last four decades during surveys and monitoring programs. This dataset, together with the respective methodological description and protocol analysis, was organized in a compendium (Távora et al., 2020c, 2021), and used here to select the collection campaigns suitable for comparison with the SPM estimates derived from satellite scenes. This dataset presented concentrations of SPM ranging from 4 up to 700 gm^{-3}, which are compatible with the algorithm developed by Távora et al. (2020a).

The algorithm used for modeling SPM concentrations is a semi-analytical multi-wavelength method, which calculates the SPM concentrations providing the uncertainties derived from measurements, which can be applied to any ocean color sensor (Távora et al., 2020a). The performance of the algorithm applied in this work was previously evaluated to a variety of coastal environments (Távora et al., 2020a), based on 420 *in situ* measurements. The SPM concentration underestimation was avoided by removing solutions where the saturation reflectance threshold is higher than 50% for each specific band.

This method also considers the water temperature, which was acquired by *in situ* measurements and made available

by the *Departamento Municipal de Águas e Esgotos* (DMAE)[3] from Porto Alegre, the *Agência Nacional das Águas* (ANA)[4] for Camaquã River, the *Sistema de Monitoramento da Costa Brasileira* (SiMCosta)[5] and the *Pesquisa Ecológica de Longa Duração no Estuário da Lagoa dos Patos e Costa Marinha Adjacente* (PELD-ELPA)[6], the last two sources being from the estuarine zone. Additionally, an online historical database[7] provided daily water temperature since 2007 for three cities close to the tributaries (**Table 1**), such a dataset was used to fill gaps when *in situ* observations were not available. This website gets data from the Operational Sea Surface Temperature and Ice Analysis (OSTIA), which combines satellite data provided by the Group for High-Resolution Sea Surface Temperature (GHRSST), together with *in situ* measurements to determine the water temperature.

The high spatial resolution of the Landsat series allowed SPM concentration estimates even in the narrowest sections of the SGC channels (∼380 m width, or about 12–13 pixels) and Camaquã River (∼150 m width, or 5 pixels). Longitudinal transects were established throughout each tributary channel towards the lagoon (**Figure 3**). Their lengths varied according to the channel morphology; for example, the Camaquã River presents the shortest transect because of the increasing sinuosity in the upstream channel, which did not allow avoiding the river margins. The transect points were selected to respect what we called "a safe distance" from the margin of the rivers in order to prevent the adjacency effects (Bulgarelli et al., 2017) which compromises the Rrs signal. Land masks were also applied, creating a buffer around the river margins. The mean SPM concentration was modeled to each point of the transect, on 10-x-10 pixel boxes, providing satisfactory accuracy when compared with *in situ* measurements. Based on these transects, it was possible to assess SPM concentrations variability from each tributary towards the lagoon.

The SPM concentrations calculated along the transects presented a percentage of gaps in each tributary as follows, Guaíba (66%), Camaquã (73%), SGC (67%), and Inlet (67%). The mean SPM concentrations were calculated for each tributary region, respecting the determined box (see section "Atmospheric Correction"), then the *in situ* observed SPM concentration was also considered to reduce the percentage of gaps in the time series on each tributary. SPM concentrations both *in situ* and satellite-calculated were then integrated in a daily timestep. This strategy reduced the gaps in the SPM datasets, reaching more suitable percentages to Guaíba (39%), Camaquã (66%), SGC (63%), and Inlet (55%). This data integration strategy was only possible after assuring the accuracy of the satellite-derived SPM concentration estimates (see **Supplementary Material**). These results were compared with RGB true-color composite images processed by ACOLITE, allowing the development of a conceptual model about the SPM concentration behavior under periods of low and high freshwater discharges.

[3]http://www2.portoalegre.rs.gov.br/dmae/ (Accessed August 31, 2021).

[4]https://www.snirh.gov.br/hidroweb/mapa (Accessed August 31, 2021).

[5]https://simcosta.furg.br/home (Accessed August 31, 2021).

[6]https://peld.furg.br/ (Accessed August 31, 2021).

[7]World Sea Water Temperatures. https://seatemperature.info/ (Accessed August 07, 2021).

TABLE 1 | Water temperature sources for each region.

Data source (*in situ*)	Tributary to Patos Lagoon	Close cities (seatemperature.info)
DMAE	Guaíba River	Porto Alegre
ANA	Camaquã River	Pelotas
SiMCosta	Inlet/SGC	Rio Grande/Pelotas
PELD-ELPA	Inlet/SGC	Rio Grande/Pelotas

The first column represents the in situ collection source. The second column shows the tributary for which temperature was searched. The third column is the nearest city from each tributary mouth with available data in the seatemperature.info website, which were applied when occurred in situ collection gaps.

El Niño-Southern Oscillation Index (MEI v.2) and Discharges From Tributaries

The Multivariate ENSO Index (MEI.v2) data is provided by the Physical Sciences Laboratory of National Oceanic and Atmospheric Administration (NOAA)[8], calculated for twelve-time intervals, in a bi-monthly arrangement. The MEI.v2 index can be considered one of the most representative ENSO indexes. It is calculated from the Empirical Orthogonal Function (EOF) combining five variables (i.e., sea level pressure, sea surface temperature, zonal and meridional components of the surface wind, and outgoing longwave radiation over the tropical Pacific basin). The MEI.v2 index indicates the intensity and phase of ENSO. Significant positive values indicate El Niño (warm) events, in contrast, La Niña phases are represented by significant negative values.

The Camaquã, Guaíba, and Inlet discharges were acquired from the ANA dataset, available online[9]. The Guaíba River discharge was calculated from the sum of Jacuí and Taquari freshwater discharges, which represent 85% of the Guaíba freshwater discharge input (Vaz et al., 2006). The SGC water level was provided by *Agência de Desenvolvimento da Lagoa Mirim* (ALM), and from this data it is possible to assess the SGC discharge based on a Rating Curve Method (Oliveira et al., 2015).

Spectral Method (Lomb-Scargle Periodogram)

Coastal systems are dynamic, respond to deterministic (e.g., tidal effects) and stochastic forcings (e.g., river load and wind). Spectral methods have been used to recognize periodicity in coastal events and identify the respective processes responsible for changes (Jalón-Rojas et al., 2016). The selection of a method should consider the percentage of gaps in the data, its sampling frequency, and the aim of the analysis, which in our case is

[8]Physical Sciences Laboratory of National Oceanic and Atmospheric Administration (NOAA). https://psl.noaa.gov/enso/mei/ (Accessed August 07, 2021).

[9]Agência Nacional das Águas. https://www.snirh.gov.br/hidroweb/mapa (Accessed August 07, 2021).

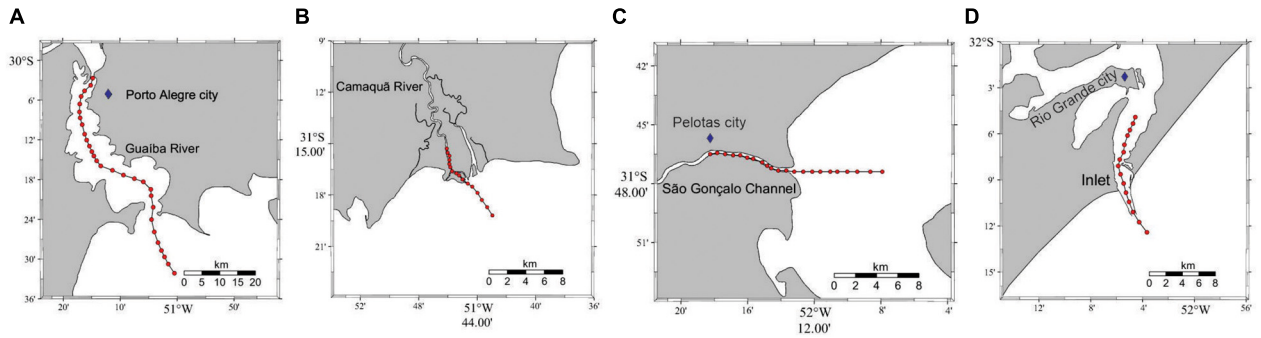


FIGURE 3 | Representation of the points of the 10-x-10 pixel boxes which compose the transects determined for each tributary: **(A)** Guaíba River, **(B)** Camaquã River, **(C)** SGC, and **(D)** Inlet.

to recognize the most energetic cyclicities in each of the Patos Lagoon tributaries.

The Lomb-Scargle Periodogram (LSP) (Lomb, 1976; Scargle, 1982) is considered the best-known method to detect periodicity in time series on unevenly sampled parameters, where the signal is processed in a Fourier-like power spectrum representing the periods of oscillation (VanderPlas, 2018). The MATLAB function *plomb* (Signal Processing Toolbox), introduced in R2014b[10], was used in the present work, providing the significance levels of energy, where peak values over the determined threshold can be interpreted as reliable signals, not incidental fluctuations or any noise. This method can identify significant periodicity in multiannual time series with more than 70% randomly missing data. However, following previous studies, when gaps surpass 50% the method is more reliable in time series of at least 10–15 years (Jalón-Rojas et al., 2016).

The LSP was applied to the calculated mean SPM concentrations for each tributary region, with a significance level of 95% ($\alpha = 0.05$) and only peaks over this limit were considered. The freshwater discharge exerts a direct influence on SPM concentration, and for complementary comparison, the LSP was also applied to this dataset with a threshold of 95% confidence ($\alpha = 0.05$). In respect to the criteria previously described, spectral methods were not used for the Inlet discharge, because it has 61% of missing data over 6 years, exceeding the limitations of the method. In contrast, the other tributaries have at least 20 years of freshwater discharge data with a low percentage of gaps [i.e., Guaíba (23%), Camaquã (0.4%), and SGC (21%)]. The equation 1/peak frequency was calculated to convert frequencies to periods.

RESULTS

Accuracy of Suspended Particulate Matter Concentration Estimates

The investigated 37 years period resulted in 653 cloud-free scenes, after image processing and selection. This amount represents the sum of the scenes from the area determined for each tributary, Guaíba (174 scenes), Camaquã (146 scenes), SGC (165 scenes), and Inlet (168 scenes).

The data set reached 47 match-ups, which represent sampling simultaneity (same day) between satellite scenes and *in situ* data (see text footnote 3, respectively). These match-ups were more frequent for Guaíba (43), secondarily for Camaquã (4), while it was absent for the Inlet and SGC, due to few *in situ* measurements at these locations. The match-ups were used for algorithm validation purposes, testing the accuracy associated with these atmospherically corrected satellite scenes, respecting the saturation threshold of 50% (see section "Multi-Proxy Suspended Particulate Matter Estimates"), assessing the modeled mean SPM value in 10-x-10 pixel boxes, and achieving satisfactory results (see **Supplementary Material**).

Periodicity in Suspended Particulate Matter Concentrations Variability

Figures 4A–D represents signals of the freshwater discharge and SPM concentrations periodograms (LSP) for each tributary. Results suggest that both parameters show a similar power behavior, with corresponding general trends and peaks. The dashed lines illustrate the significance threshold for SPM concentrations (black lines) and freshwater discharges (red lines), and peaks reaching these limits represent 95% significance. Peaks are marked on the y-axis and the period of occurrence is checked on the x-axis when it achieves the threshold lines. The SPM concentration peaks reach the significance level less often than the discharge peaks because of the larger percentage of gaps.

The three main tributaries (Guaíba, Camaquã, and SGC) present a well-marked 1-year peak above the confidence limit, and such power cyclicity is recognized for SPM concentrations and for freshwater discharge. In addition to the 1-year peak, other cyclicities are detected in the SPM signal, encompassing longer periods. One cycle of 16 years is marked for Guaíba River and Inlet, reaching the significance level, while for the other tributaries this peak presents a smaller magnitude, but the signal is also present. Camaquã highlights a 7 years cyclicity for SPM concentrations, and such peak is also detected on the other tributaries, though lower and not statistically significant.

[10]MathWorks. https://www.mathworks.com/help/signal/ref/plomb.html (Accessed August 07, 2021).

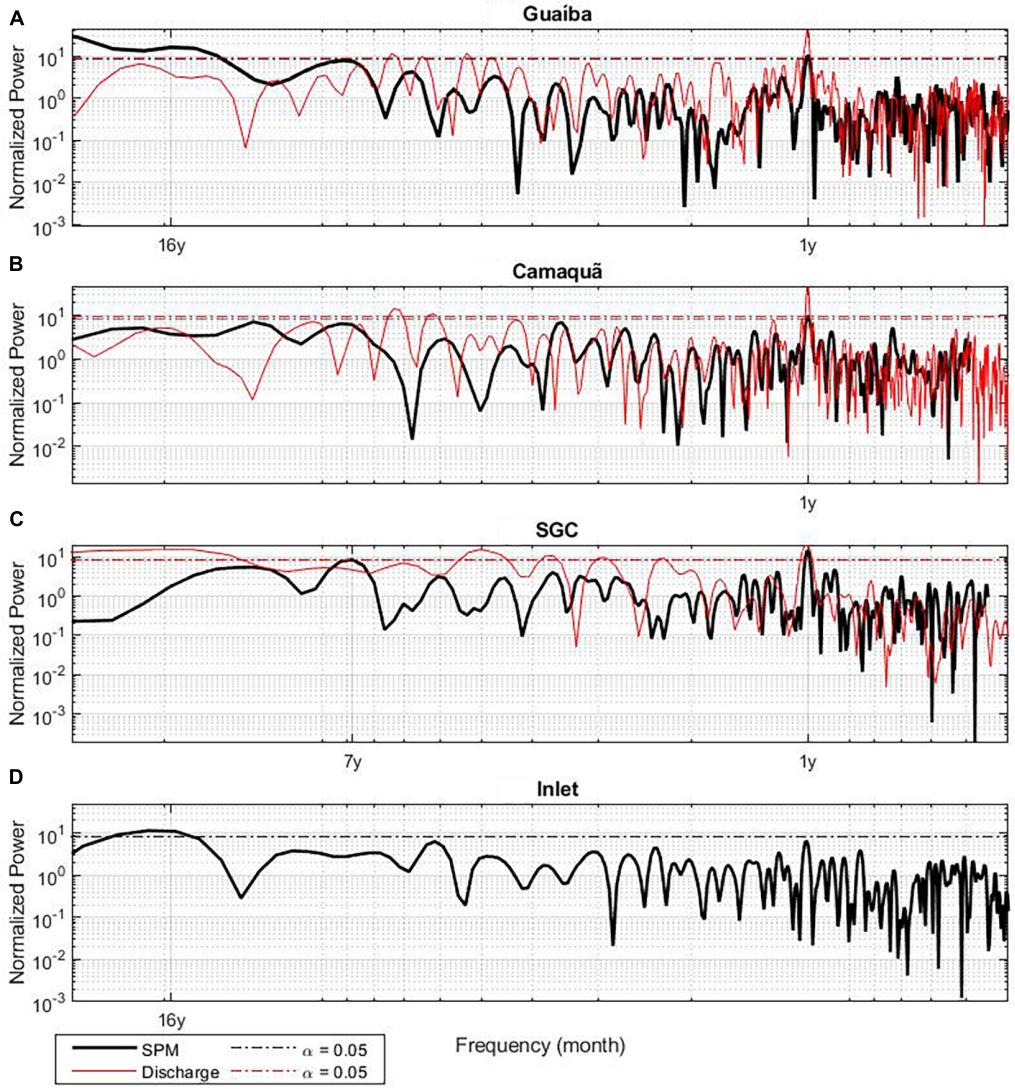


FIGURE 4 | Lomb-Scargle periodograms of the discharge (red solid line) and mean SPM concentration (black solid line) for each tributary region [**(A)** Guaíba River, **(B)** Camaquã, **(C)** SGC, and **(D)** Inlet], encompassing the whole time series (1984–2020). The dashed lines represent the confidence threshold, red lines for discharge and black for SPM mean concentration, both with 95% reliability. The axes are on a logarithmic scale.

Relationship Between El Niño-Southern Oscillation Index and Environmental Parameters

Figure 5 presents the relationship between environmental variables (freshwater discharges and SPM concentrations) and ENSO effects (**Figure 5A**). The yearly mean SPM concentrations which were calculated for each tributary region (see section "Atmospheric Correction") is represented by the gray bars; their discharges also were expressed yearly (black dotted line) and monthly (gray line). Gray rectangles highlight the most significant El Niño event periods (MEI index around 2).

Long-term (decadal scale) changes in SPM concentrations following ENSO oscillations are observed in **Figure 5**. The end of the last century (1984–2000) had more expressive El Niño events than the more recent decades (**Figure 5A**). Such behavior is reflected in the SPM concentrations, presenting values that frequently overpass 100 $g.m^{-3}$ (**Figures 5B–E**). This same period also shows a higher mean in comparison with the following decades. Non-significant El Niño events characterize the interval from 1999 to 2015, contrasting with more expressive La Niña periods, which present low SPM concentrations among all the tributaries, rarely reaching 100 $g.m^{-3}$.

There is also a relationship regarding short-term variability (yearly scales), where peaks in El Niño events are synchronous with positive values of SPM concentrations, and valleys are linked to La Niña periods (**Figures 5**, **6**). This positive association is best observed during extreme El Niño events, which occurred in 1986–1987, 1991–1992, 1997–1998, 2015–2016 (**Figure 6**). The

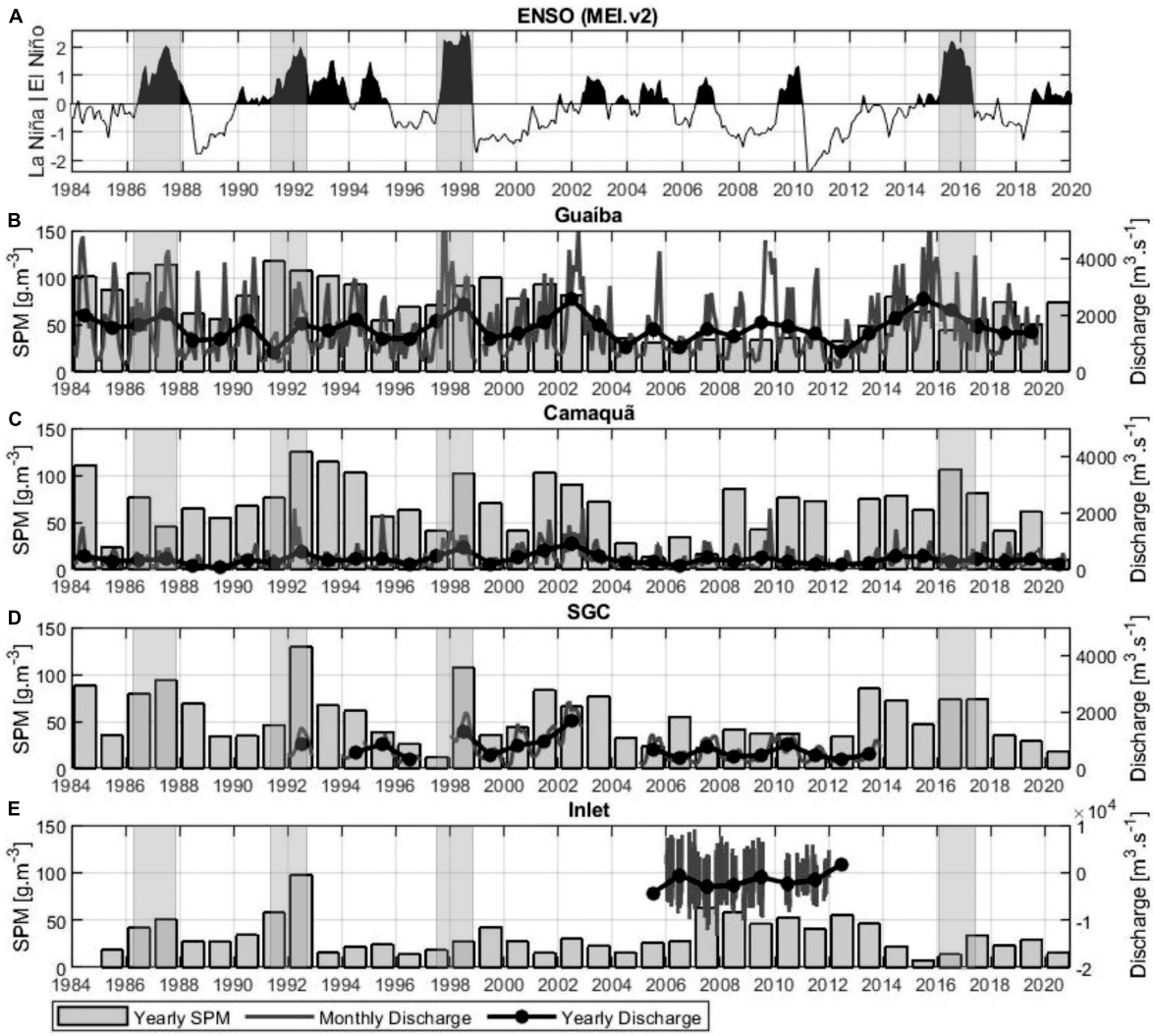


FIGURE 5 | Comparison between ENSO phenomena, SPM concentrations (*in situ* + modeled), yearly and monthly discharges of each tributary. The ENSO index is represented on the top panel **(A)**, where the periods of expressive El Niño events (MEI v.2 around 2) are highlighted by gray rectangles. The MEI v.2 positive values represent El Niño periods and the negative represent La Niña periods. The following panels represent the mentioned parameters for each tributary, Guaíba River **(B)**, Camaquã River **(C)**, SGC **(D)**, and Inlet channel **(E)**. The SPM concentration ($g.m^{-3}$) is expressed by gray bars, with two exceptions without any data (SPM or scenes), one for Camaquã River in 2012, and the other for Inlet channel in 1984. The mean yearly discharge ($m^3.s^{-1}$) is illustrated by a black dotted line and the mean monthly discharge ($m^3.s^{-1}$) is demonstrated by the dark gray line.

overall maximum values of SPM concentrations of each tributary occurred in the 1991–1992 El Niño event, as follows: Guaíba River 117.6 $g.m^{-3}$ in 1991, Camaquã River 125.2 $g.m^{-3}$ in 1992, SGC 129.5 $g.m^{-3}$ in 1992, Inlet 97.56 $g.m^{-3}$ in 1992.

The tributaries have particularities when responding to ENSO cycles, and some present a more direct relationship than others. Guaíba River has less pronounced variability, and among the tributaries presented more homogeneous concentrations, with values usually over 50 $g.m^{-3}$, except for the 10 years from 2003 to 2013, when La Niña events prevailed. Camaquã River and SGC have marked variabilities, whose averages oscillated more than 50 $g.m^{-3}$ from 1 year to another, mainly when El Niño periods occurred. The two higher yearly mean SPM concentrations were calculated for SGC (129.5 $g.m^{-3}$) and Camaquã (125.2 $g.m^{-3}$) for the year 1992. The Inlet usually presents higher SPM concentrations at the end of El Niño periods and increasing trends from the peaks of each La Niña period, and such trends remained until the following El Niño peak. Thus, the increasing pattern in SPM concentrations is observed in all tributaries, although not so well defined in all of them.

Spatial and Temporal Suspended Particulate Matter Variability at the Tributaries

The interannual SPM variability (from 1984 to 2020) along the transects of each tributary is represented in **Figures 6A–D**, also evidencing relationship with the ENSO phenomena. The El Niño

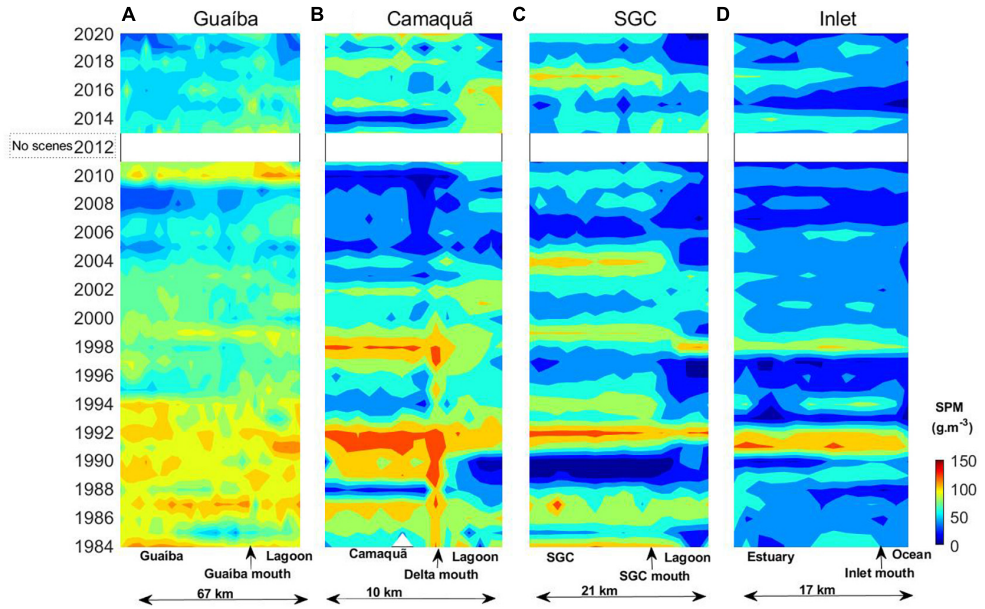


FIGURE 6 | Space-time representation of mean SPM concentration (g.m^{-3}) through the longitudinal transects of each tributary. The y-axis show the years of the time series (1984–2020), while the x-axes represent the spatial variation with plotted key points. Each tributary configuration is illustrated in a single panel, Guaíba River **(A)**, Camaquã River **(B)**, SGC **(C)**, and Inlet channel **(D)**. No scenes are available for the year 2012.

events in 1986–1987, 1991–1992, 1997–1998 are well marked in all the transects, mainly in the upstream portions. The 80s and 90s (last century) presented higher SPM concentrations, contrasting with the lower SPM concentrations of the first decade of the XXI century, in agreement with the previous section observations. SPM concentrations are relatively more homogeneous in Guaíba River across the years in comparison with the southward tributaries, where the peaks and low values are more contrasting. Regarding all the tributaries, the SPM concentrations are relatively higher northward, and the peaks of all of them are reflected in the inlet contribution.

Figures 7A–D presents the monthly mean SPM concentration throughout the 1984–2020 time series, allowing the identification of seasonal variability on the loads of the tributaries. The tributaries presented strong seasonality with relatively higher SPM concentration contributions from June to December (from winter to spring) and lower concentrations measured from January to May (from summer to autumn).

The mouth of the tributaries represents a key point (**Figures 6**, **7**) beyond which SPM concentration patterns usually switch from high SPM concentration (upstream) to low (downstream). However, high concentration rates remained basinward to which years of expressive SPM concentration coincide with El Niño events or occur from June to December.

DISCUSSION

The SPM concentration in Patos Lagoon is mainly controlled by the freshwater discharge of the tributaries and secondarily by the winds (Moller et al., 2001; Távora et al., 2019, 2020b; Bitencourt et al., 2020). The long-term (1984–2020) period analyzed in the present study allows reliable interpretations of the seasonal, interannual and interdecadal SPM concentrations and spatial patterns. At these long timescales, the freshwater input is an important forcing on exchanges with the ocean, while winds are the main control at short time scales (Távora et al., 2019).

Cyclicity in Environmental Parameters From 1984 to 2020

The 1-year peak was the main signal variability recorded in the discharge and SPM concentrations for all the main tributaries (**Figure 4**), which means that there is a high energy cyclicity once a year when the discharges and SPM concentrations are higher. This cyclical time scale is associated with seasonal deterministic forcings (Jalón-Rojas et al., 2016), such as the increase in river flow (rainy seasons) on austral winters (21 Jun–21 Sep) and springs (21 Sep–21 Dec). In general, there is a good agreement between discharge and SPM concentration signals (**Figure 4**), however, the discharge reached the significance limit more often, probably due to fewer gaps in the dataset.

The observed long-term cyclicity (∼ 16 years) is likely related to stochastic discharge events and ENSO cycles. The Guaíba River has a secondary SPM concentration peak (**Figure 4A**), detected at about 16 years, and although the discharge is not a statistically significant threshold, it presents a relatively high power during this period. This 16 years peak is also well marked in the other tributaries, but only reached the significance level at the Inlet (**Figure 4D**). This signal was probably detected in response to the El Niño phases of 1998–2015, and 1986–2002 (**Figure 5A**), both spaced about 16 years, and it is not expected to represent a coastal

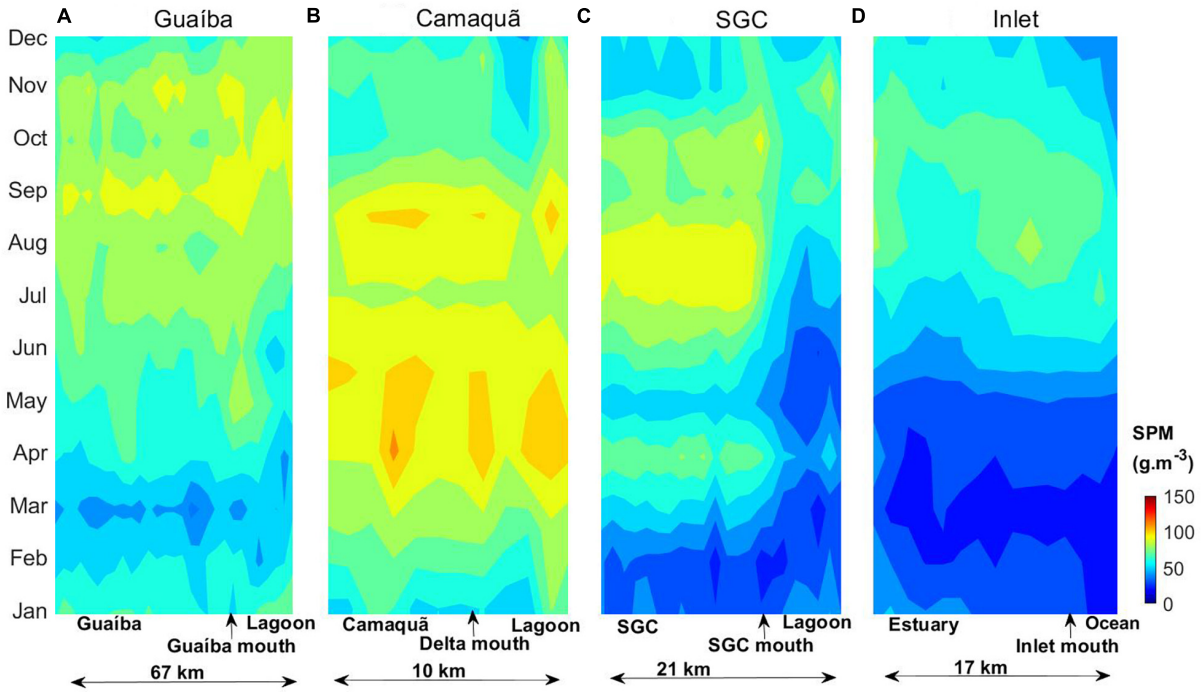


FIGURE 7 | Spatial and temporal representation of mean SPM concentration (g.m^{-3}) through the longitudinal transects of each tributary. The y-axis show the mean monthly SPM concentration, while the x-axes represent the spatial variation with plotted key points. Each tributary configuration is illustrated in a single panel, Guaíba River **(A)**, Camaquã River **(B)**, SGC **(C)**, and Inlet channel **(D)**.

process. The SGC tributary presents SPM concentration peaks around 7 years (**Figure 4C**), which can be linked to the spacing between ENSO cycles (**Figure 5A**) at the end of the last century (1986/1987–1991/1992–1997/1998), whose intervals correspond roughly to this scale. These 7-years peaks are marked in all the tributaries, although only the SGC had enough power to attain the significance level.

Seasonal to Interdecadal Response of Suspended Particulate Matter Concentrations to El Niño-Southern Oscillation

Each study area presents a peculiar response to ENSO, relying on the drainage basin characteristic, anthropogenic structural changes, agricultural land use, deforestation, mining, and urban expansion (Hestir et al., 2013; Dogliotti et al., 2016; Bueno et al., 2021). The environmental changes associated with the ENSO phenomenon have been studied in coastal systems from seasonal to decadal time scales (Hestir et al., 2013; Gray et al., 2015; Dogliotti et al., 2016; Bitencourt et al., 2020; Távora et al., 2020b; Karl et al., 2021). Interdecadal sampling, however, allows reliable interpretations about natural processes trends, as otherwise the interannual analysis can be based on the trends of a specific decade (Gray et al., 2015). Interdecadal studies already reported an increase of about 10 times in sediment transport of a coastal river during El Niño years (Gray et al., 2015). Other environments, however, observed low turbidity values associated with different responses of tributaries to interdecadal events (Dogliotti et al., 2016). Thus, study cases reporting the behavior of tributaries on interdecadal observations are crucial for monitoring the global scale ENSO influence on suspended sediment fluxes and climate variability (Rühl et al., 2021).

The El Niño events occurred with higher intensity for longer periods and more often during the last 16 years of the XX century (**Figure 5A**) than in the XXI century, as indicated by the proportional relationship between discharges, SPM concentrations, and ENSO positive peaks (**Figure 5**). The higher SPM concentrations of each tributary were measured during this 16 years period of intense El Niño events, while the following 16 years are marked by significant La Niña and moderate El Niño events, producing lower discharges and SPM concentrations, especially between 2003 and 2013. This decadal variability is also noted in **Figure 6**, where the longitudinal transects show higher SPM concentrations before 2000. The variability of SPM concentrations seems to behave in interannual trends. The increasing trends in SPM concentration from La Niña peaks to El Niño peaks are not well recognized in the XXI century because such a period is marked by the absence of expressive El Niño events.

The SPM concentrations also respond on a yearly scale to the El Niño events (**Figures 5**, **6**). However, the magnitude of the response of each tributary relies on the characteristics of their watersheds and drainage morphology. The relatively more homogeneous SPM concentrations of Guaíba River (**Figures 5B**, **6A**) are probably due to its broad depositional basin

morphology ($\leq$ 20 km width), which is similar to a lake and less vulnerable to flow variations. In addition, this water body has a residence time of about 10 days (Toldo and Almeida, 2009) and the deposited sediments are prone to resuspension by wind action (Nicolodi et al., 2013). This pattern can also result from its wide drainage basin[11], which is about 84,763 km^2, delivering the non-synchronized loads from nine sub-basins (Scottá et al., 2019).

The Camaquã River is a tributary with morphology and discharge behavior typical of fluvial systems, showing a good yearly proportion between ENSO events and SPM concentrations (**Figures 5C**, **6B**). The Camaquã drainage basin (see text footnote 6) is about 21,657 km^2, with a narrow river channel ($\sim$ 150 m), turning it more susceptible to changes in water quality following discharge pulses. The SGC has a unidirectional flow through a narrow channel ($\sim$350 m), developed by differences in water level between Patos Lagoon and Mirim Lagoon (Oliveira et al., 2015; Oliveira et al., 2019), whose watershed encompasses (see text footnote 6) 28,499 km^2. The outflow through the channel is also controlled by wind effects (Oliveira et al., 2019). Nevertheless, the El Niño effects are well marked in the region (**Figures 5D**, **6C**). Freshwater discharges over 3,000 m^3.s^{-1} limit the inflow of seawater, which is also minimized by the microtidal regime (Moller et al., 2001; Fernandes et al., 2002). The prevailing ebb flow favors the export to the ocean, and the higher SPM concentrations at the Inlet have good correspondence with El Niño cycles (**Figures 5E**, **6D**).

The SPM concentrations represented through the transects in **Figure 6** show the contrast between the El Niño/La Niña periods. Years that represent intense El Niño events (1986–1987, 1991–1992, 1997–1998, 2015–2016) usually have high SPM concentrations, except for the years 2015–2016. Recent studies suggest that the 2015–2016 El Niño event might be overestimated (Van Oldenborgh et al., 2021), in agreement with what is observed in the present work and with Bitencourt et al. (2020). During years of El Niño events, SPM concentrations remained relatively high even downstream from the river mouth, evidencing the development of river plumes. Thus, these periods have a more significant load contribution to the lagoon and consequently to the Atlantic Ocean.

Seasonality of freshwater discharge is also very well marked in the SPM concentrations along the transects (**Figure 7**). Periods of higher discharges in the mid-latitude rivers (austral winter and spring) (Vaz et al., 2006; Marques and Moller, 2008) recorded the higher SPM concentrations for all the tributaries, with subtle variations according to each drainage basin characteristic, as discussed before. After the river load reaches the lagoon, solids in suspension can be deposited and the exceeding material is exported towards the ocean. Bortolin et al. (2020) showed that this fine suspended load is deposited inside Patos Lagoon forming mud depocenters established according the hydrodynamic conditions. The Inlet panel (**Figure 7D**) shows that from June to November the export of SPM to the Atlantic Ocean is higher.

[11]Fundação Estadual de Proteção Ambiental Henrique Luiz Roessler—RS. http://ww2.fepam.rs.gov.br/bcrs25/ (Accessed August 07, 2021).

Conceptual Model About the Dynamics of Suspended Particulate Matter Load

The SPM load in a choked lagoon under a microtidal regime is regulated by the discharge of the tributaries (Kjerfve, 1986, 1994). El Niño events and seasonal discharges are the main control to the SPM contribution of the tributaries, as they will drive the sediment export to the lagoon and later to the ocean. The El Niño cycles control the intensity and frequency of the discharge events, directly influencing the yearly mean SPM concentrations delivery to Patos Lagoon in a stochastic frequency (**Figures 5**, **6**). The seasonality promotes SPM loads reaching the lagoon in a deterministic pattern (**Figure 7**), where the lower SPM concentrations occur during austral summer and autumn, while the higher concentrations are related to the winter and spring discharges (Vaz et al., 2006).

The tributary plumes behave differently during low input periods (LIP) and high input periods (HIP), whose conceptual models are illustrated in **Figures 8A,B**, respectively. These models were developed based on the interpretation of the spatial-temporal variability of SPM concentrations responding to ENSO and seasonal forcings described in the current work. Moreover, the dynamics of the discharged SPM was also characterized by: (1) examining Red-Green-Blue true-color composite images (hereon RGB composites) and (2) analyzing studies which also investigated the behavior of the SPM reaching Patos Lagoon (e.g., Pagot et al., 2007; Fassoni-Andrade et al., 2015; Távora et al., 2019, 2020b) and exported to Atlantic Ocean (Marques et al., 2009, 2010; Vinzon et al., 2009; Marta-Almeida et al., 2021).

The LIP (**Figure 8A**) presents reduced SPM concentrations through the lagoon, with limited environments where the plumes of the tributaries exert influence, which can be observed in the RGB composite images created by ACOLITE (**Supplementary Material**). During the LIP, the reduced SPM load remains in the sub environments (mud depocenters) of Patos Lagoon. Consequently, the low export to the Atlantic Ocean is controlled mainly by the SGC, which is in the estuarine zone. The HIP (**Figure 8B**) is developed by periods of intense and frequent discharges of the tributaries, where these loads increase the turbidity throughout Patos Lagoon, which has a residence time longer than the discharge frequency of the tributaries (Toldo et al., 2000; Toldo and Almeida, 2009). The plumes of all the tributaries reach the estuarine zone during the HIP, which increases the export to the Atlantic Ocean and also the size of the Inlet plumes. The SPM behavior in both proposed conceptual models (LIP and HIP) will be detailed below.

Both scales of variability (ENSO and seasonal) act combined to develop different concentration gradients throughout the lagoon body. Therefore, it is common for El Niño years to have occasionally low SPM concentrations during the dryer season (austral summer and autumn), as it is common to have high SPM concentrations during the wet seasons (austral winter and spring) even in the course of La Niña events, although the HIP configuration is more frequent and more intense during El Niño years. According to previous studies, the material reaching the lagoon is distributed by internal currents developed by wind effects (Bortolin et al., 2020), which control the sedimentation

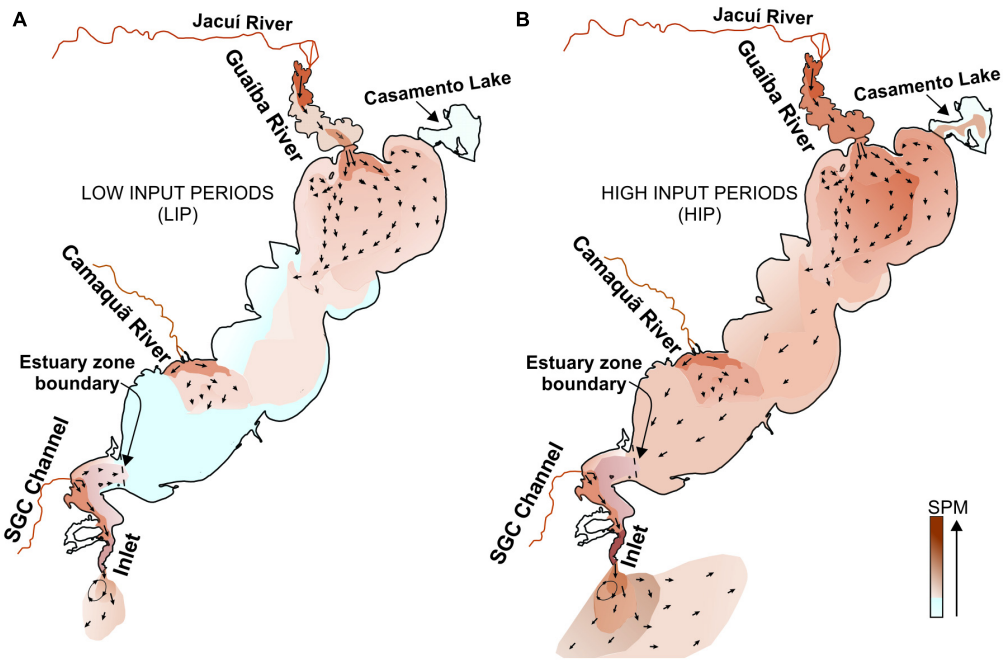


FIGURE 8 | (A) Conceptual model developed for the regular behavior of each tributary SPM load during low input periods (LIP). **(B)** Conceptual model developed for the regular behavior of each tributary SPM load during high input periods (HIP).

processes (Távora et al., 2019) and enhances or reduces the discharge to the Ocean (Moller et al., 2001).

The river plumes are usually investigated concerning the flow types in environments with tidal mixing and salinity variations (Hetland and Hsu, 2013; Horner-Devine et al., 2015; Shanmugam, 2018; Osadchiev and Zavialov, 2020). Such condition is, however, negligible nearby the main tributaries of this broad back-barrier environment, which is almost isolated from the ocean tides and currents, providing a singular opportunity to investigate the SPM behavior modulated by freshwater discharges and wind effects.

The Guaíba plume covers the largest area in comparison with the other tributaries reaching Patos Lagoon (**Figures 8A,B**), and is composed mainly of fine sediments (silt and clay), because the Guaíba river traps most of the coarse grains (Toldo et al., 2000; Vaz et al., 2006; Nicolodi et al., 2013). The Guaíba River has a residence time of about 10 days (Toldo and Almeida, 2009), and the variability on Guaíba River SPM concentration is mainly controlled by Jacuí River discharges (Vaz et al., 2006). During periods of low frequency (from January to June) in Jacuí River discharge, Guaíba river can become a low or moderate turbidity environment (**Figure 9A**), responding to each new Jacuí discharge (**Figure 9B**).

The dynamic regions of a plume can be characterized by the distance that it reaches from the mouth of the tributaries, as follow, near-field, mid-field, and far-field (Hetland and Hsu, 2013). The fine grain composition of this plume associated with the wide river mouth of Guaíba River favors the plume dispersion, usually without developing a strong jet at the near-field. At the mid-field a recirculation feature (called bulge) is currently developed after the spit-bank structures of the northern cell of the lagoon (**Figures 9A,B**). The plume evolves its far-field towards the southern cells of Patos Lagoon (**Figure 8**), enhanced by the predominant NE winds (frequent during summer) (Hetland and Hsu, 2013; Távora et al., 2019). Although the Guaíba River contributes with almost 61% of the suspended load delivered to Patos Lagoon (Vaz et al., 2006), the suspended material has to be transported for more than 200 km to be exported to the ocean (Fernandes et al., 2002), and part of the fine material remains in the lagoon, mainly in the northern cell (Bortolin et al., 2020). Previous studies already reported decreasing sedimentation rates from the northern cell to the southern cell of the lagoon (Ivanoff et al., 2020).

During the LIP (**Figures 8A**, **9A**), this far-field plume can be directed by NE winds, diluting gradually in the central cells (Távora et al., 2019), reaching the southern depositional environments but rarely attaining to the estuarine zone and the Casamento Lake (**Figure 1**). The Patos Lagoon reaches longer residence times (∼ 108 days) (Toldo et al., 2000; Fernandes et al., 2002), especially during low discharge circumstances, and this low discharge can cause a delay in the spread of the SPM plume towards the south. For this reason, material discharged during austral spring can be dissipated southward by NE wind-driven currents (Bortolin et al., 2020); a low discharge pattern that lasts until summer (Távora et al., 2019). Therefore, the fine sediments discharged tend to remain and accumulate in the mud depocenters of Patos Lagoon, especially in the northern cell (Bortolin et al., 2020). During the HIP (**Figure 8B**) this plume is spread throughout the lagoon, reaching all the lagoon cells, Casamento Lake, and the inlet.

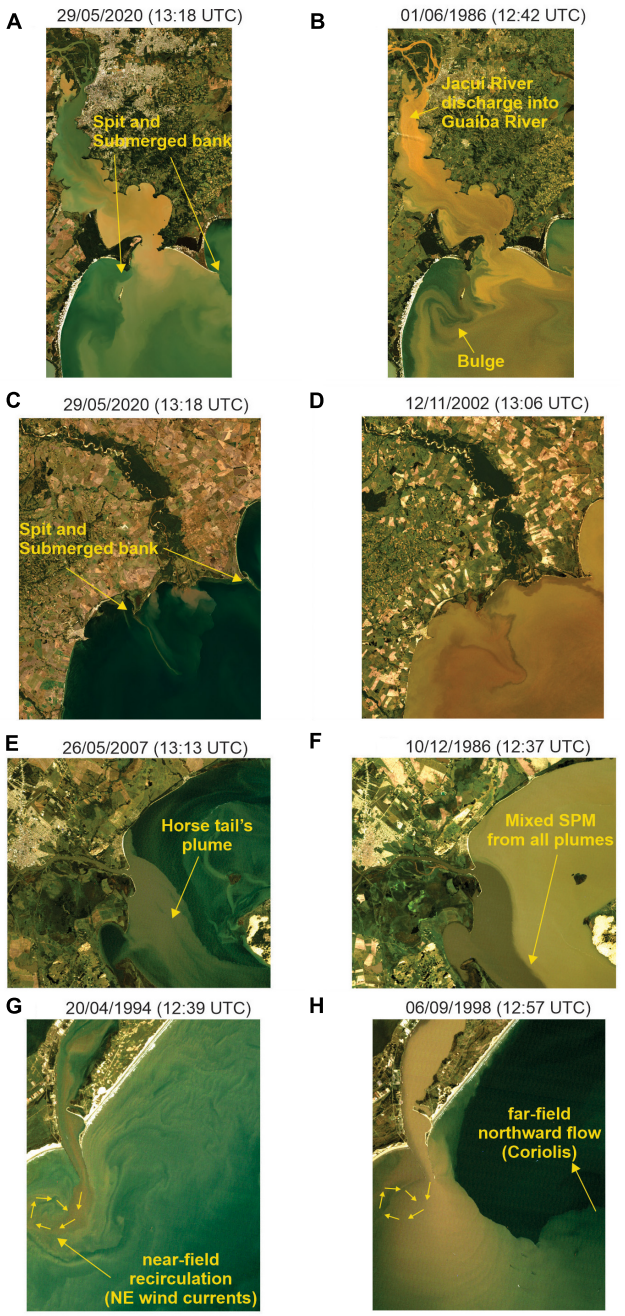


FIGURE 9 | Landsat images representing the main characteristics described during the low input periods (LIP, left panels) and the high input periods (HIP, right panels) for each tributary. **(A)** Represents the load of Guaíba plume dissipating in the northern cell of Patos Lagoon between the two submerged banks which follow the spits. **(B)** Represents the development of a bulge of the Guaíba river plume, also evidences the contrasting color of a new Jacuí River load into Guaíba. **(C)** Camaquã River plume during the LIP, limited by the submerged banks. **(D)** Camaquã River load spreading over the region limited by the submerged banks. **(E)** Typical SGC plume during LIP. **(F)** Mixing between the plumes of all tributaries in the lower estuarine zone. **(G)** Recirculation at the near-field plume developed by NE wind-generated currents. **(H)** Represents the near-field recirculation under NE winds influence, while the far-field reached due to the development of larger plumes during HIP flow northward influenced by the Coriolis force.

Camaquã River plumes are usually limited between the sandy spits and the respective submerged banks during the LIP (**Figure 9C**). Its plume presents near-field hyperpycnal flow developed due to the sandy load of Camaquã River (Toldo et al., 2000), and a dissipating characteristic offshore from which the buoyant portion eventually reaches 16 km from the mouth. Camaquã River is smaller than Guaíba River and has a shorter residence time, hence has more drastic flow changes and its plume can change characteristics with each outflow episode. This significant variability in the plumes characteristics according to flow changes is typical in small rivers (Osadchiev and Zavialov, 2020). Such stronger variability is noticed in the SPM concentrations represented in **Figures 5–7**, as discussed in the last section. During the HIP, the magnitude and frequency of freshwater discharge increases, forcing the far-field plume to move to the southern cell (**Figure 9D**), and mixing with the material discharged from Guaíba and flowing towards the Inlet (**Figure 8B**).

The SGC plume is at the estuarine zone (**Figure 8**) and has a high occurrence frequency throughout the year combined with higher SPM concentrations during El Niño years (**Figure 6**). Although its SPM concentration is lower in comparison with the other tributaries (**Figure 5**), this plume has a horse tail's shape (Shanmugam, 2018) and deflects directly towards the inlet region (**Figure 9E**). The SGC plume can be interpreted as the main plume influencing the inlet during summer, autumn, and the first winter month (July)—during this period SPM from the other tributaries usually remains limited to their area of influence. The plumes of the other tributaries finally reach the estuarine zone during winter, moved by the increase in discharge, and are mixed with the SGC plume (**Figure 9F**). Hence, during winter all the tributaries influence the export to the Atlantic Ocean.

The concentration of SPM at the inlet is proportional to the amount of the exceeding fine material exported to the ocean. Previous studies reported that the freshwater discharge is the main control on Patos Lagoon plumes size (Marques et al., 2009, 2010). Wind action exerts a secondary influence, because the lagoon axis is parallel to the prevailing wind direction (NE-SW) (Bitencourt et al., 2020; Bortolin et al., 2020). The fine SPM which did not deposit in the Patos Lagoon mud depocenters and remained in suspension is mostly clay (Bortolin et al., 2020).

The inlet plumes spread near the coast (**Figure 9G**), mainly controlled by wind effects, where NE winds are more frequent and drive the plumes southward due to the alongshore currents, while south-quadrant winds are less common and deflect the plumes northward (Moller et al., 2001; Marques et al., 2009). The southward plume deflection causes a recirculation bulge in the zone sheltered by the jetties (**Figure 9G**), developing areas prone to flocculation and deposition of fine SPM (Vinzon et al., 2009; Marques et al., 2010). The relatively high SPM concentration conditions occur preferably during El Niño periods (**Figure 6**), and austral winter and spring seasons (**Figure 7**). The high SPM concentration once aligned with NE winds enhances the export flows. These circumstances develop larger plumes in which the far-field portion deflects northward forced by the Coriolis effect (**Figure 9H**), independently of the direction of deflection of the near-field plume (Marques et al., 2009, 2010). Therefore, the

discharge, winds and Coriolis forces together develop different configurations of the inlet plumes, according to the distance each plume reaches off the coast (Monteiro et al., 2011).

Our results suggest that Landsat satellites can provide long-term monitoring of SPM concentrations with detailed spatial resolution to allow estimates in narrow channels (as narrow as 200 m). Thus, they proved ideal for investigating the seasonal, interannual and interdecadal variability throughout decades on coastal systems. However, the temporal resolution of Landsat sensors is low compared to other satellites such as Moderate Resolution Imaging Spectroradiometer (MODIS). The latter offers daily temporal resolution, ideal to investigate shorter-term events, and might be more suitable to characterize episodic variations in the main lagoon water body, as long as those variations are larger than 250–1,000 m depending on the band of choice. The granulometry of the sediments discharged by each tributary also is a gap in knowledge and remote sensing methods are a promising possibility in future studies.

CONCLUSION

Patos Lagoon can be understood as a laboratory for studying the SPM contribution from tributaries and their plumes behavior under negligible tidal effects. The following topics represent the main conclusions achieved by the current work:

- A decadal variability is observed in SPM concentrations from the tributaries, which was associated with the intensity and magnitude of ENSO phases. Regarding the investigated period (1984–2020), the last two decades of the XX century were subject to El Niño events with higher intensity and duration than the XXI century.
- The SPM concentrations also respond yearly according to ENSO phases. The magnitude of the responses to ENSO is regulated by the characteristics of the watershed and the morphology of the tributary.
- Tributaries with narrow channels and typical discharge behavior of a fluvial system, such as Camaquã River, presented a proportion between ENSO events and SPM concentrations. The other tributaries were also influenced by other conditionings, as winds and residence time.
- The El Niño periods favor the development of the tributary's plumes entering the Patos Lagoon and the Atlantic Ocean.
- Austral winter and spring are the seasons of higher SPM concentrations, and such amounts are enhanced during El Niño events.
- The ENSO and seasonal forcings combined regulate the delivery of SPM from the tributaries to Patos Lagoon and the fine sediments export to the Atlantic Ocean. These scales of variability led us to propose two conceptual models for Patos Lagoon, called Low Input Periods (LIP) and High Input Periods (HIP), based on the SPM load from tributaries and the SPM concentration gradient.
- The LIP is characterized by a reduced SPM concentration throughout the lagoon, and by the plumes of each tributary exerting local influence. During the LIP, there is a low export of SPM to the Ocean, when the SGC plume influences the estuarine zone the most, because the SPM from the other tributaries does not reach the estuarine area.
- The HIP present plumes spread throughout Patos Lagoon, and the whole water body becomes a turbid environment. The plumes of all the tributaries reach the estuarine zone. The Guaíba River plume is the largest plume of all tributaries. It develops a far-field portion towards the south and has to be transported about 200 km to reach the inlet. This plume influences the most Patos Lagoon exportation during the HIP periods, which represent the main export to the Atlantic Ocean. These periods develop larger plumes, where the far-field are under Coriolis effect, independently from the near-field portion which is influenced by wind action.

DATA AVAILABILITY STATEMENT

The original contributions presented in the study are included in the article/**Supplementary Material**, further inquiries can be directed to the corresponding author/s.

AUTHOR CONTRIBUTIONS

EB: intellectual development, writing, developing figures, and data collection and interpretation. JT: intellectual development, creating main MATLAB scripts, developing figures, and review. EF: intellectual development, writing, data interpretation, review, and discussion of ideas. All authors contributed to the article and approved the submitted version.

FUNDING

The authors are grateful to the LOAD Project—LOng-term analysis of Suspended Particulate Matter concentrations Affecting port areas in Developing countries (Office of Naval Research, Contract N62909-19-1-2145), for sponsoring this research; and to the SUNSET Project—SoUth BraziliaN ShElf Sediment Transport: sources and consequences, sponsored by the CAPES-COFECUB collaboration.

ACKNOWLEDGMENTS

We thank Isabel Jalon Rojas from Environnements et Paléoenvironnements Océaniques et Continentaux (EPOC-Université de Bordeaux) for the advices about the spectral methods.

SUPPLEMENTARY MATERIAL

The Supplementary Material for this article can be found online at: https://www.frontiersin.org/articles/10.3389/fmars.2022.836739/full#supplementary-material

REFERENCES

Abreu, P. C., Bergesch, M., Proença, L. A., Garcia, C. A. E., and Odebrecht, C. (2010). Short- and Long-Term Chlorophyll a Variability in the Shallow Microtidal Patos Lagoon Estuary. Southern Brazil. *Estuaries Coasts* 33, 554–569. doi: 10.1007/s12237-009-9181-9

Ávila, R. A., Orozco, P. M. S., Andrade, M. M., and Möller, O. O. (2021). Temporal variability of suspended-solids concentration in the estuarine channel of patos lagoon, southern Brazil. *Water* 13, 1–13. doi: 10.3390/w13050646

Beltrame, M. O., De Marco, S. G., and Marcovecchio, J. E. (2009). Dissolved and particulate heavy metals distribution in coastal lagoons. A case study from Mar Chiquita Lagoon, Argentina. *Estuar. Coast. Shelf Sci.* 85, 45–56. doi: 10.1016/j.ecss.2009.04.027

Bilotta, G. S., Burnside, N. G., Cheek, L., Dunbar, M. J., Grove, M. K., Harrison, C., et al. (2012). Developing environment-specific water quality guidelines for suspended particulate matter. *Water Res.* 46, 2324–2332. doi: 10.1016/j.watres.2012.01.055

Bitencourt, L. P., Fernandes, E. H., da Silva, P. D., and Möller, O. (2020). Spatio-temporal variability of suspended sediment concentrations in a shallow and turbid lagoon. *J. Mar. Syst.* 212:103454. doi: 10.1016/j.jmarsys.2020.103454

Bortolin, E. C., Weschenfelder, J., Fernandes, E. H., Bitencourt, L. P., Möller, O. O., García-Rodríguez, F., et al. (2020). Reviewing sedimentological and hydrodynamic data of large shallow coastal lagoons for defining mud depocenters as environmental monitoring sites. *Sediment. Geol.* 410:105782. doi: 10.1016/j.sedgeo.2020.105782

Bueno, C., Alves, F. L., Pinheiro, L. M., Perez, L., Agostini, V. O., Fernandes, E. H. L., et al. (2021). The effect of agricultural intensification and water-locking on the world's largest coastal lagoonal system. *Sci. Total Environ.* 801:149664. doi: 10.1016/j.scitotenv.2021.149664

Bulgarelli, B., Kiselev, V., and Zibordi, G. (2017). Adjacency effects in satellite radiometric products from coastal waters: a theoretical analysis for the northern Adriatic Sea. *Appl. Opt.* 56:854. doi: 10.1364/ao.56.000854

Choi, J. K., Park, Y. J., Ahn, J. H., Lim, H. S., Eom, J., and Ryu, J. H. (2012). GOCI, the world's first geostationary ocean color observation satellite, for the monitoring of temporal variability in coastal water turbidity. *J. Geophys. Res. Ocean* 117, 1–10. doi: 10.1029/2012JC008046

Dang, T. H., Coynel, A., Orange, D., Blanc, G., Etcheber, H., and Le, L. A. (2010). Long-term monitoring (1960-2008) of the river-sediment transport in the Red River Watershed (Vietnam): temporal variability and dam-reservoir impact. *Sci. Total Environ.* 408, 4654–4664. doi: 10.1016/j.scitotenv.2010.07.007

Dogliotti, A. I., Ruddick, K., and Guerrero, R. (2016). Seasonal and inter-annual turbidity variability in the Río de la Plata from 15 years of MODIS: El Niño dilution effect. *Estuar. Coast. Shelf Sci.* 182, 27–39. doi: 10.1016/j.ecss.2016.09.013

Eisma, D. (ed.) (1993). *Suspended Matter in the Aquatic Environment*. Berlin Heidelberg: Springer, doi: 10.1007/978-3-642-77722-6

Fassoni-Andrade, A. C., Guasselli, L. A., Toniolo, G. R., and Moreira, A. A. (2015). "Dinâmica espacial e temporal de sedimentos em suspensão na região estuarina da Lagoa dos Patos - RS, a partir de dados do sensor OLI, Landsat-8," in *Anais XVII Simposio Brasileiro De Sensoriamento Remoto* (João Pessoa: Simpósio Brasileiro de Sensoriamento Remoto), 1953–1960.

Fernandes, E. H. L., Dyer, K. R., Moller, O. O., and Niencheski, L. F. H. (2002). The Patos Lagoon hydrodynamics during an El Niño event (1998). *Cont. Shelf Res.* 22, 1699–1713. doi: 10.1016/S0278-4343(02)00033-X

Gordeev, V. V., Rachold, V., and Vlasova, I. E. (2004). Geochemical behaviour of major and trace elements in suspended particulate material of the Irtysh river, the main tributary of the Ob river, Siberia. *Appl. Geochem.* 19, 593–610. doi: 10.1016/j.apgeochem.2003.08.004

Gray, A. B., Pasternack, G. B., Watson, E. B., Warrick, J. A., and Goñi, M. A. (2015). Effects of antecedent hydrologic conditions, time dependence, and climate cycles on the suspended sediment load of the Salinas River, California. *J. Hydrol.* 525, 632–649. doi: 10.1016/j.jhydrol.2015.04.025

Han, B., Loisel, H., Vantrepotte, V., Mériaux, X., Bryère, P., Ouillon, S., et al. (2016). Development of a semi-analytical algorithm for the retrieval of suspended particulate matter from remote sensing over clear to very turbid waters. *Remote Sens.* 8:211. doi: 10.3390/rs8030211

Hestir, E. L., Schoellhamer, D. H., Morgan-King, T., and Ustin, S. L. (2013). A step decrease in sediment concentration in a highly modified tidal river delta following the 1983 El Niño floods. *Mar. Geol.* 345, 304–313. doi: 10.1016/j.margeo.2013.05.008

Hetland, R. D., and Hsu, T. J. (2013). "Freshwater and sediment dispersal in large river plumes," in *Biogeochemical Dynamics at Large River-Coastal Interfaces: linkages With Global Climate Change*, eds T. S. Bianchi, M. A. Allison and W. J. Cai (New York: Springer), 55–85. doi: 10.1017/cbo9781139136853.006

Horner-Devine, A. R., Hetland, R. D., and MacDonald, D. G. (2015). Mixing and transport in coastal river plumes. *Annu. Rev. Fluid Mech.* 47, 569–594. doi: 10.1146/annurev-fluid-010313-141408

Ivanoff, M. D., Toldo, E. E., Figueira, R. C. L., de Ferreira, P. A. L. (2020). Use of 210 Pb and 137 Cs in the assessment of recent sedimentation in Patos Lagoon, southern Brazil. *Geo-Mar. Lett.* 40, 1057–1067. doi: 10.1007/s00367-019-00633-8

Jalón-Rojas, I., Schmidt, S., and Sottolichio, A. (2016). Evaluation of spectral methods for high-frequency multiannual time series in coastal transitional waters: advantages of combined analyses. *Limnol. Oceanogr. Methods* 14, 381–396. doi: 10.1002/lom3.10097

Jung, B. M., Fernandes, E. H., Möller, O. O., and García-Rodríguez, F. (2020). Estimating suspended sediment concentrations from river discharge data for reconstructing gaps of information of long-term variability studies. *Water* 12:2382. doi: 10.3390/W12092382

Karl, D. M., Letelier, R. M., Bidigare, R. R., Björkman, K. M., Church, M. J., Dore, J. E., et al. (2021). Seasonal-to-decadal scale variability in primary production and particulate matter export at Station ALOHA. *Prog. Oceanogr.* 195:102563. doi: 10.1016/j.pocean.2021.102563

Kjerfve, B. (1986). "Comparative Oceanography of Coastal Lagoons," in. *Estuarine variability*, ed. D. Wolfe (Waltham, USA: Academic Press), 63–81. doi: 10.1016/b978-0-12-761890-6.50009-5

Kjerfve, B. (1994). "Coastal Lagoons," in *Coastal lagoon processes*, ed. B. Kjerfve (Amsterdam: Elsevier)

Kreiling, R. M., and Houser, J. N. (2016). Long-term decreases in phosphorus and suspended solids, but not nitrogen, in six upper Mississippi River tributaries, 1991–2014. *Environ. Monit. Assess.* 188, 1–19. doi: 10.1007/s10661-016-5464-3

Lihan, T., Saitoh, S. I., Iida, T., Hirawake, T., and Iida, K. (2008). Satellite-measured temporal and spatial variability of the Tokachi River plume. *Estuar. Coast. Shelf Sci.* 78, 237–249. doi: 10.1016/j.ecss.2007.12.001

Liu, J. T., Zarillo, G. A., and Surak, C. R. (1997). The influence of river discharge on hydrodynamics and mixing in a subtropical lagoon. *J. Coast. Res.* 13, 1016–1034. doi: 10.1016/S0967-0653(98)80018-5

Lomb, N. R. (1976). Least-squares frequency analysis of unequally spaced data. *Astrophys. Space Sci.* 39, 447–462. doi: 10.1007/BF00648343

Marques, W., and Moller, O. O. (2008). Variabilidade Temporal em Longo Período da Descarga Fluvial e Níveis de Água da Lagoa dos Patos, Rio Grande do Sul, Brasil. *Rev. Bras. Recur. Hídr.* 13, 155–163. doi: 10.21168/rbrh.v13n3.p155-163

Marques, W. C., Fernandes, E. H., Monteiro, I. O., and Möller, O. O. (2009). Numerical modeling of the Patos Lagoon coastal plume, Brazil. *Cont. Shelf Res.* 29, 556–571. doi: 10.1016/j.csr.2008.09.022

Marques, W. C., Fernandes, E. H. L., Moraes, B. C., Möller, O. O., and Malcherek, A. (2010). Dynamics of the Patos Lagoon coastal plume and its contribution to the deposition pattern of the southern Brazilian inner shelf. *J. Geophys. Res. Ocean* 115, 1–22. doi: 10.1029/2010JC006190

Marta-Almeida, M., Dalbosco, A., Franco, D., and Ruiz-Villarreal, M. (2021). Dynamics of river plumes in the South Brazilian Bight and South Brazil. *Ocean Dyn.* 71, 59–80. doi: 10.1007/s10236-020-01397-x

Matthews, M. W. (2011). A current review of empirical procedures of remote sensing in Inland and near-coastal transitional waters. *Int. J. Remote Sens.* 32, 6855–6899. doi: 10.1080/01431161.2010.512947

Miller, R. L., and McKee, B. A. (2004). Using MODIS Terra 250 m imagery to map concentrations of total suspended matter in coastal waters. *Remote Sens. Environ.* 93, 259–266. doi: 10.1016/j.rse.2004.07.012

Moller, O. O. Jr., Castaing, P., Salomon, J.-C., and Lazure, P. (2001). The Influence of Local and Non-Local Forcing Effects on the Subtidal Circulation of Patos Lagoon. *Estuaries* 24, 297–311. doi: 10.2307/1352953

Moller, O. O., Lorenzzentti, J. A., Stech, J. L., and Mata, M. M. (1996). The Patos Lagoon summertime circulation and dynamics. *Cont. Shelf Res.* 16, 335–351. doi: 10.1016/0278-4343(95)00014-R

Monteiro, L. O., Marques, W. C., Fernandes, E. H., Gonçalves, R. C., and Möller, O. O. Jr. (2011). On the effect of earth rotation, river discharge, tidal oscillations, and wind in the dynamics of the Patos Lagoon coastal plume. *J. Coast. Res.* 27, 120–130. doi: 10.2112/JCOASTRES-D-09-00168.1

Nechad, B., Ruddick, K. G., and Park, Y. (2010). Calibration and validation of a generic multisensor algorithm for mapping of total suspended matter in turbid waters. *Remote Sens. Environ.* 9, 854–866.

Nicolodi, J. L., Toldo, E. E., and Farina, L. (2013). Dynamic and resuspension by waves and sedimentation pattern definition in low energy environments: guaíba lake (Brazil). *Braz. J. Oceanogr.* 61, 55–64. doi: 10.1590/S1679-87592013000100006

Novoa, S., Doxaran, D., Ody, A., Vanhellemont, Q., Lafon, V., Lubac, B., et al. (2017). Atmospheric corrections and multi-conditional algorithm for multi-sensor remote sensing of suspended particulate matter in low-to-high turbidity levels coastal waters. *Remote Sens.* 9:61. doi: 10.3390/rs9010061

Oliveira, H. A., Helena, E., Fernandes, L., Olinto, M. O. Jr., and Collares, G. L. (2015). Processos Hidrológicos e Hidrodinâmicos da Lagoa Mirim. *Rev. Bras. Recur. Hídr.* 20, 34–45.

Oliveira, H., Fernandes, E., Möller, O., and García-Rodríguez, F. (2019). Relationships between wind effect, hydrodynamics and water level in the world's largest coastal lagoonal system. *Water* 11:2209. doi: 10.3390/w11112209

Osadchiev, A., and Zavialov, P. (2020). "Structure and Dynamics of Plumes Generated by Small Rivers," in Estuaries and Coastal Zones–Dynamics and Response to Environmental Changes, eds J. Pan and A. Devlin (London: IntechOpen). doi: 10.5772/intechopen.87843

Pagot, M., Rodríguez, A., Hillman, G., Corral, M., Oroná, C., and Niencheski, L. F. (2007). Remote Sensing Assessment of Suspended Matter and Dynamics in Patos Lagoon. *J. Coast. Res.* 10047, 116–129. doi: 10.2112/1551-5036-47.sp1.116

Park, J., Kal, B., and Kim, S. (2018). Long-term Trend Analysis of Major Tributaries of Nakdong River Using Water Quality Index. *J. Wetl. Res.* 20, 201–209.

Rachold, V. (1999). "Major, Trace and Rare Earth Element Geochemistry of Suspended Particulate Material of East Siberian Rivers Draining to the Arctic Ocean," in *Land-Ocean Systems in the Siberian Arctic*, eds H. Kassens, H. A. Bauch, I. A. Dmitrenko, H. Eicken, H. W. Hubberten and M. Melles (Berlin: Springer), 1993–1994.

Rachold, V., Eisenhauer, A., Hubberten, H., Hansen, B., Meyer, H. (1997). Sr Isotopic Composition of suspended particulate material (SPM) of East Siberian Rivers: sediment transport to the Arctic Ocean. *Arct. Alp. Res.* 29, 422–429. doi: 10.2307/1551990

Rodrigues, J. P., Araujo, M. L. V., Emerich, P., Ávila, R., and Garcia, C. A. E. (2012). "Absorção e atenuação sa luz e sua relação com os (Rs-Brasil)," in *Proceedings of the Congresso Brasileiro de Oceanografia (Rio de Janeiro: Associação Brasileira de Oceanografia (AOCEANO))*, 1615–1629.

Rostad, C., and Leenheer, J. (1997). Organic Carbon and Nitrogen Content Associated with Colloids and Suspended Particulates from the Mississippi River and Some of Its Tributaries. *Environ. Sci. Technol.* 31, 3218–3225.

Rühl, S., Thompson, C. E. L., Queirós, A. M., and Widdicombe, S. (2021). Decadal patterns and trends in benthic-pelagic exchange processes. *J. Mar. Syst.* 222:103595. doi: 10.1016/j.jmarsys.2021.103595

Ryberg, K. R., Blomquist, J. D., Sprague, L. A., Sekellick, A. J., and Keisman, J. (2018). Modeling drivers of phosphorus loads in Chesapeake Bay tributaries and inferences about long-term change. *Sci. Total Environ.* 616–617, 1423–1430. doi: 10.1016/j.scitotenv.2017.10.173

Scargle, J. D. (1982). Studies in astronomical time series analysis. II. Statistical aspects of spectral analysis of unevenly spaced data. *Astrophys. J.* 263, 835–853. doi: 10.1086/160554

Schäfer, J., Blanc, G., Lapaquellerie, Y., Maillet, N., Maneux, E., and Etcheber, H. (2002). Ten-year observation of the Gironde tributary fluvial system: fluxes of suspended matter, particulate organic carbon and cadmium. *Mar. Chem.* 79, 229–242.

Scottá, F. C., Andrade, M. M., Silva Junior, V. O., Oliveira, N., Weschenfelder, J., Bortolin, E. C., et al. (2019). Geoacoustic patterns of the guaíba river bottom and subbottom and their relationship with sedimentary and hydrodynamic processes. *Rev. Bras. Geofis.* 37, 105–120. doi: 10.22564/rbgf.v37i1.1991

Shanmugam, G. (2018). A global satellite survey of density plumes at river mouths and at other environments: plume configurations, external controls, and implications for deep-water sedimentation. *Pet. Explor. Dev.* 45, 640–661. doi: 10.1016/S1876-3804(18)30069-7

Stech, J. L., and Lorenzetti, J. A. (1992). The response of the South Brazil Bight to the passage of wintertime cold fronts. *J. Geophys. Res.* 97, 9507–9520. doi: 10.1029/92JC00486

Távora, J., Fernandes, E. H., Paranhos Bitencourt, L. B., and Mulattieri Suarez Orozco, P. (2020b). El-Niño Southern Oscillation (ENSO) effects on the variability of Patos Lagoon Suspended Particulate Matter. *Reg. Stud. Mar. Sci.* 40:101495. doi: 10.1016/j.rsma.2020.101495

Távora, J., Boss, E., Doxaran, D., and Hill, P. (2020a). An algorithm to estimate suspended particulate matter concentrations and associated uncertainties from remote sensing reflectance in coastal environments. *Remote Sens.* 12, 1–24. doi: 10.3390/rs12132172

Távora, J., Fernandes, E. H. L., and Möller, O. O. (2020c). *Data Publisher for Earth and Environmental Science*. PANGAEA. Available online at: https://doi.pangaea.de/10.1594/PANGAEA.920924 (accessed August 7, 2021).

Távora, J., Fernandes, E. H., and Moller, O. O. (2021). Patos Lagoon, Brazil, Suspended Particulate Matter (SPM) data compendium. *Geosci. Data J.* 1–24. doi: 10.1002/gdj3.134

Távora, J., Fernandes, E. H. L., Thomas, A. C., Weatherbee, R., and Schettini, C. A. F. (2019). The influence of river discharge and wind on Patos Lagoon, Brazil, Suspended Particulate Matter. *Int. J. Remote Sens.* 40, 4506–4525. doi: 10.1080/01431161.2019.1569279

Toldo, E., and Almeida, L. E. S. B. (2009). *Rio Guaíba*. Available Online at: http://lproweb.procempa.com.br/pmpa/prefpoa/dmae/usu_doc/rioguaiba_eliriotoldojr.pdf (accessed August 31, 2009).

Toldo, J., Dillenburg, S. R., Correa, I. C. S., and Almeida, L. E. S. B. (2000). Holocene sedimentation in Lagoa dos Pantos Lagoon, Rio Grande do Sul, Brazil. *J. Coast. Res.* 16, 816–822.

Tomazelli, L. (1993). O Regime dos Ventos e a Taxa de Migração das Dunas Eólicas Costeiras do Rio Grande do Sul, Brasil. *Pesqui. em Geociênc.* 20, 18–26. doi: 10.22456/1807-9806.21278

Van Oldenborgh, G. J., Hendon, H., Stockdale, T., Heureux, M. L., De Perez, E. C., Singh, R., et al. (2021). Defining El Niño indices in a warming climate. *Environ. Res. Lett.* 16:044003.

VanderPlas, J. T. (2018). Understanding the Lomb–Scargle Periodogram. *Astrophys. J. Suppl. Ser.* 236:16. doi: 10.3847/1538-4365/aab766

Vanhellemont, Q. (2019). Adaptation of the dark spectrum fitting atmospheric correction for aquatic applications of the Landsat and Sentinel-2 archives. *Remote Sens. Environ.* 225, 175–192. doi: 10.1016/j.rse.2019.03.010

Vanhellemont, Q., and Ruddick, K. (2014). Turbid wakes associated with offshore wind turbines observed with Landsat 8. *Remote Sens. Environ.* 145, 105–115. doi: 10.1016/j.rse.2014.01.009

Vanhellemont, Q., and Ruddick, K. (2015). Advantages of high quality SWIR bands for ocean colour processing: examples from Landsat-8. *Remote Sens. Environ.* 161, 89–106. doi: 10.1016/j.rse.2015.02.007

Vanhellemont, Q., and Ruddick, K. (2016). "Acolite for Sentinel-2: aquatic applications of MSI imagery," in *Proceedings of the ESA Living Planet Symposium*, ed. L. Ouwehand (Prague: ESA), 740, 9–13.

Vanhellemont, Q., and Ruddick, K. (2018). Atmospheric correction of metre-scale optical satellite data for inland and coastal water applications. *Remote Sens. Environ.* 216, 586–597. doi: 10.1016/j.rse.2018.07.015

Vaz, A. C., Möller, O. O. jr., and de Almeida, T. L. (2006). Análise quantitativa da descarga dos rios afluentes da Lagoa dos Patos. *Atlântica* 28, 13–23.

Vinzon, S. B., Winterwerp, J. C., Nogueira, R., and de Boer, G. J. (2009). Mud deposit formation on the open coast of the larger Patos Lagoon-Cassino Beach system. *Cont. Shelf Res.* 29, 572–588. doi: 10.1016/j.csr.2008.09.021

Ward, L., and Twilley, R. R. (1986). Seasonal Distributions of Suspended Particulate Material and Dissolved Nutrients in a Coastal Plain Estuary. *Estuaries* 9, 156–168.

Wilkinson, J. L., Hooda, P. S., Swinden, J., Barker, J., and Barton, S. (2017). Spatial distribution of organic contaminants in three rivers of Southern England bound to suspended particulate material and dissolved in water. *Sci. Total Environ.* 593–594, 487–497. doi: 10.1016/j.scitotenv.2017.03.167

Conflict of Interest: The authors declare that the research was conducted in the absence of any commercial or financial relationships that could be construed as a potential conflict of interest.

Publisher's Note: All claims expressed in this article are solely those of the authors and do not necessarily represent those of their affiliated organizations, or those of the publisher, the editors and the reviewers. Any product that may be evaluated in this article, or claim that may be made by its manufacturer, is not guaranteed or endorsed by the publisher.

Copyright © 2022 Bortolin, Távora and Fernandes. This is an open-access article distributed under the terms of the Creative Commons Attribution License (CC BY). The use, distribution or reproduction in other forums is permitted, provided the original author(s) and the copyright owner(s) are credited and that the original publication in this journal is cited, in accordance with accepted academic practice. No use, distribution or reproduction is permitted which does not comply with these terms.

frontiers in Marine Science

ORIGINAL RESEARCH
published: 28 March 2022
doi: 10.3389/fmars.2022.863540

Impact of Wave–Current Interactions on the Detachment of Low-Salinity Water From Changjiang River Plume and Its Subsequent Evolution

Zhipeng Jiang[1,2,3], Dehai Song[1,2], Qinsheng Wei[4,5] and Yang Ding[1,2]*

[1] Frontier Science Center for Deep Ocean Multispheres and Earth System and Physical Oceanography Laboratory, Ocean University of China, Qingdao, China, [2] Laboratory for Ocean Dynamics and Climate, Qingdao National Laboratory for Marine Science and Technology, Qingdao, China, [3] College of Oceanic and Atmospheric Sciences, Ocean University of China, Qingdao, China, [4] First Institute of Oceanography, Ministry of Natural Resources, Qingdao, China, [5] Laboratory for Marine Ecology and Environmental Science, Qingdao National Laboratory for Marine Science and Technology, Qingdao, China

OPEN ACCESS

Edited by:
Alexander Yankovsky,
University of South Carolina,
United States

Reviewed by:
Hui Wu,
East China Normal University, China
Douglas Cahl,
University of South Carolina,
United States

***Correspondence:**
Dehai Song
songdh@ouc.edu.cn

Specialty section:
This article was submitted to Coastal Ocean Processes, a section of the journal Frontiers in Marine Science

Received: 27 January 2022
Accepted: 25 February 2022
Published: 28 March 2022

Citation:
Jiang Z, Song D, Wei Q and Ding Y (2022) Impact of Wave–Current Interactions on the Detachment of Low-Salinity Water From Changjiang River Plume and Its Subsequent Evolution. Front. Mar. Sci. 9:863540. doi: 10.3389/fmars.2022.863540

The evolution of low-salinity water (LSW) detached from river plumes is critical to coastal systems and inner-shelf biogeochemical processes. In this study, the impact of wave–current interactions on the LSW detachment from the Changjiang River plume and its subsequent evolution is explored. Waves can advance the detachment of LSW through enhancing the vertical mixing, the northward intrusion of the inshore branch of the Taiwan Warm Current, and the upwelling. The wave-enhanced vertical mixing increases the core salinity of the initially isolated LSW and the growth rate of the core salinity during its subsequent evolution. Waves can lengthen the journey of the isolated LSW and accelerate its movement. Five wave–current interaction processes are compared and it is found that the wave-induced form drag contributes the most to the LSW detachment and its subsequent evolution. It enhances the vertical mixing and alters the wave-driven flow through the vertical transfer of wave-generated pressure to the momentum equation and the turbulent kinetic energy (TKE) equations. The wave dissipation working in the TKE equations weakens the northeastward flow off the Changjiang River estuary, which restrains the diluted water expansion. The current advection and refraction of wave energy contribute most to the enhancement of the double-core upwelling system.

Keywords: low-salinity water, Changjiang River plume, wave–current interactions, form drag, detachment

INTRODUCTION

The detachment of low-salinity water (LSW) from river plumes has been observed globally, such as the Changjiang River (Lie et al., 2003; Chen et al., 2008; Moon et al., 2010; Rong and Li, 2012; Xuan et al., 2012; Ge et al., 2015; Wei et al., 2017; Qu et al., 2019), the Yellow River (Yu et al., 2020), the Pearl River (Gan et al., 2009; Shu et al., 2011; Chen et al., 2016), the Block Island Sound (Liu et al., 2017), the Columbia River, and the Hudson River (Yankovsky et al., 2001; García Berdeal et al., 2002; Jurisa and Chant, 2012). After detachment, the isolated LSW still keeps some plume features with moderate nutrient concentration and sufficient light intensity and thus is often related to red

tide patches or high chlorophyll-a patches in surrounding waters, which could further contribute to the formation of bottom hypoxia (Wei et al., 2017, 2020; Qu et al., 2019). Therefore, exploring the formation and expansion of detached LSW provides a better understanding of the dynamical and biogeochemical processes at river plume fronts. Several mechanisms on LSW detachment have been proposed, such as the bathymetry gradient (Chen et al., 2016), river discharge (Yankovsky et al., 2001; Jurisa and Chant, 2012), tide and tidal mixing (Moon et al., 2010; Rong and Li, 2012; Liu et al., 2017; Yu et al., 2020), wind and wind-induced upwelling (Jurisa and Chant, 2012; Xuan et al., 2012; Ge et al., 2015; Chen et al., 2016), and baroclinic instability (Chen et al., 2008).

The LSW detachment from the Changjiang River plume has been frequently reported in summer by regional surveys or real-case numerical simulations (Beardsley et al., 1985; Lie et al., 2003; Chen et al., 2008; Moon et al., 2010; Xuan et al., 2012; Zhang et al., 2014; Ge et al., 2015; Wei et al., 2017). However, this phenomenon was not captured every summer and the occurrence time and location reported in previous studies seems irregular. Southerly or southeasterly wind usually plays a crucial role on the LSW detachment at the Changjiang River plume. Chen et al. (2008) showed that the input of wind in numerical models is conducive to strengthening the offshore detachment. Xuan et al. (2012) suggested that wind mixing, wind-driven northward current, and wind-induced upwelling are three important driving forcings on the detachment; and a southeasterly wind speed of 8 ms^{-1} was given as a critical value for the detachment. Ge et al. (2015) showed that the LSW detachment can only be generated by a non-uniform wind in summer. However, Moon et al. (2010) found the detachment can also be generated under a constant uniform northwestward wind.

Intensified tide-induced vertical mixing during the spring tide is another explanation of the LSW detachment (Moon et al., 2010; Wu et al., 2011; Rong and Li, 2012; Zhang et al., 2014). Zhang et al. (2014) found that during the transition from neap tide to spring tide, the tidal mixing is strengthened more quickly in shallow water than that in deep water, and the surface salinity is thus increased more quickly in shallow water, which promotes the LSW detachment. Moon et al. (2010) showed that the stratification is destroyed at the slope region during spring tides; the bottom boundary layer can reach the surface here and well mix the water column, which separates the main body of the Changjiang diluted water (CDW) and the LSW. But Xuan et al. (2012) found that the tidal currents alone are not the main controlling factor due to the detachment events not always occurring on spring tides, and they also confirmed that tidal mixing at the detachment region could not lead to a completely mixed water column.

Large river discharge could promote the LSW offshore extending by intensifying the subsurface current (Chen et al., 2008). River discharge can affect the core salinity of the LSW and the detachment time, but not the pattern of the LSW (Zhang et al., 2014). Given a model with a horizontal resolution of less than 1 km, Chen et al. (2008) regarded the LSW detachment as a result of baroclinic instability, which could be strengthened by the southerly wind and formed a chain of anticyclonic eddies to carry the CDW offshore. But Xuan et al. (2012) found that baroclinic instability frequently occurs in the Changjiang River estuary (CRE) in summer while the detachment has been rarely observed. Wei et al. (2017) pointed out that the offshore LSW is induced by the double-core upwelling structure combined with the prevailing southerly wind and the anticyclonic eddy off the CRE. The double-core upwelling structure refers to the two upwelling zones off the CRE: the southern one correlated with the northward intrusion of the Taiwan Warm Current and the northern one at the boundary of the bottom cold-water mass in the northern East China Sea (ECS).

Despite some disputes still remaining on the detachment of LSW, winds and tides have been generally accepted as the main physical mechanisms. However, the waves' effects on the detachment of LSW and its subsequent evolution have been less documented in previous studies, which may have important impacts on the detachment. Wave effects on the river plume have been studied in several estuaries. Gerbi et al. (2013) found that the breaking surface waves can cause the river plume to be thicker and narrower and to propagate offshore more slowly; in this situation the plume has much smaller vertical gradients of salinity and velocity, leading to the decreased importance of shear dispersion. Rong et al. (2014) investigated the wave–current interactions on the Mississippi-Atchafalaya River plume in the Texas-Louisiana Shelf and they found that wave-enhanced bottom stress can restrict the offshore transport in the Chenier Shelf; meanwhile, the wave mixing and three-dimensional wave forces can weaken the stratification in the Louisiana Bight. Delpey et al. (2014) found that wave-induced alongshore currents can hinder the fluvial outflow in a small bay in northwestern of France. Schloen et al. (2017) showed that wave-induced salt transport changes the horizontal salinity distribution in the coastal zone of the southern North Sea and wind waves can destroy the weak stratification and thus modify the estuarine circulation. Akan et al. (2017) studied the impacts of wave–current interactions on the Columbia River plume dynamics, and they found that the plume is shifted in the down-wave direction due to the Stokes velocity induced alongshore advection. Gong et al. (2018) found the enhancement of bottom stress is the most important process influencing the Pearl River plume. However, there are few studies focused on the wave effects on the Changjiang River plume, still less on the offshore detachment of LSW.

In this study, a two-way coupled wave–current model is applied to investigate the wave effects on the detachment of LSW from the Changjiang River plume in summer. Contributions of different wave–current interactions to the LSW detachment are quantified. The paper is organized as follows: the Section "Study Site and Observations" gives a brief description of the study area and the LSW detachment observed in July 2006. The model configuration and validation, as well as the numerical experiments, are given in Section "Model Configuration and Experiments." The wave effects on river plumes and LSW detachment are discussed in Section

"Discussion." In "Conclusion" section, the conclusion of this study is presented.

STUDY SITE AND OBSERVATIONS

Study Site

The Changjiang River, more than 6,300 km in length, is the longest river in Asia and is the third-longest in the world. The CRE, a 90-km-wide river mouth, is divided by the Chongming Island into the South Branch and North Branch (**Figure 1A**). Due to the silted state of the North Branch, the South Branch becomes the main channel of the CDW. The CRE is characterized by its huge river discharge, large number of sediments, and considerable tidal range; thus, the CDW mixed with ambient saline water has a great influence on salinity distribution and flow field in the ECS. It has become one of the dominant hydrodynamic features in the ECS (e.g., Beardsley et al., 1985; Su and Wang, 1989; Wu et al., 2021).

The circulation in the ECS is basically composed of the Kuroshio main stream in the Okinawa Trough, Kuroshio branch currents on the outer shelf, and coastal currents on the inner and middle shelves (Lie and Cho, 2016). The Taiwan Warm Current (TWC) flows off the southeastern Chinese coast with high temperatures and high salinity (Guan and Fang, 2006). It bifurcates into two branches near 28°N: the inshore branch flows northward along the 50 m isobath off the Zhejiang-Fujian coast and turns to the northeast of the CRE, and the offshore branch flows eastward and finally joins the western flank of the Kuroshio (Wang et al., 2019). Due to prevailing southeasterly wind in summer, the northward intrusion of the TWC inshore branch can reach the CRE and Jiangsu coast (Beardsley et al., 1985; Chen et al., 1994; Zhu et al., 2004). In summer, the coastal currents on the inner shelf tend to flow northward along the Jiangsu coast as a portion of the CDW plume. Although the magnitude of this branch is much smaller than the northeast branch, it could be an important nutrient source for the frequent algal bloom there (Pu, 1981; Pu and Xu, 1983; Zhao et al., 1995; Wu et al., 2014; Zhu and Wu, 2018). The coastal currents flow northeastward along the Zhejiang-Fujian coast, which intensifies the northeastward TWC, and flow northward or northeastward on the shallow Changjiang Bank (Lie and Cho, 2016). The structure and pathway of the CDW show significant seasonal variations. It is weak and generally trapped alongshore with a southward extension along the Zhejiang-Fujian coast in the winter, but is stronger and more unstable with a northeastward extension toward the Cheju Island in summer (e.g., Beardsley et al., 1985; Lie et al., 2003; Wu et al., 2014).

In the ECS, wind waves also exhibit significant seasonal variability: southward waves driven by the prevailing northerly winds in winter and northward waves by southerly winds in summer. *In situ* observations showed that the significant wave height (H_s) is larger in winter and autumn than that in summer and spring, with the maximum H_s occurring in winter; and the climatological monthly mean H_s from 1988 to 1999 was 1.20 m in July and 1.70 m in January (He et al., 2018). Furthermore, the ECS is well known for its significant tidal motions dominated by semi-diurnal tides, which propagate from the open ocean (Song et al., 2013). Strong tidal currents not only strengthen vertical mixing but also induce strong residual currents, which are comparable to wind-driven currents on the inner shelf (e.g., Guo and Yanagi, 1998; Kang et al., 1998).

Observations

In this study, two cruise measurements were collected. The first was conducted onboard the R/V *Dongfanghong2* from June 28 to July 16, 2006 in the southern Yellow Sea and ECS (**Figure 1A**). The second was conducted onboard the R/V *Beidou* in the southern Yellow Sea (**Figure 2A**) from July 18 to 24, 2006. Both cruises measured the physical parameters (temperature, salinity, density) using the Seabird Series Conductivity-Temperature-Depth (CTD). The parameters were measured in full water depth with a 1-m vertical resolution during the first cruise, but we only obtained the surface, 10 m, 30 m, and bottom-layer data during the second cruise. During the second cruise, the measured sea surface salinity (SSS) shows two low-salinity patches (**Figure 2C**): one off the CRE with a salinity low to 24 psu and the other far away from the CRE with a salinity of 27 psu. The former was due to the northeastward extension of the Changjiang River plume and the latter was regarded as the detachment of LSW from the plume (Wei et al., 2017). Xuan et al. (2012) also found the same detachment event during this period using the satellite-derived sea surface temperature and a real-case numerical simulation. Based on the cruise time and the SSS pattern, we speculate that the isolated LSW had existed for several days, and the detachment should occur before July 17, which is consistent with Xuan et al. (2012). Based on the second cruise measurement, Wei et al. (2017) found a double-core upwelling system and an anticyclonic eddy off the CRE, which favors the LSW detachment from the CDW plume under the prevailing southerly winds.

MODEL CONFIGURATION AND EXPERIMENTS

Model Setup

Circulation Model

The circulation model used in this study is the unstructured-grid, Finite-Volume, primitive-equation Community Ocean Model (FVCOM, Chen et al., 2003). The ECS FVCOM was established by Ding et al. (2018) to study the Yellow Sea Warm Current, the synoptic current fluctuations in the Bohai Strait (Ding et al., 2019), and also the marine heatwaves in the ECS and southern Yellow Sea (Gao et al., 2020). In this study, we carry the ECS FVCOM forward with a refined mesh grid in the CRE. The model domain (21°N∼41°N, 117°E∼138°E) covers the Bohai Sea, the Yellow Sea, the ECS, and part of the northwest Pacific; the open boundary is exactly the same as those in previous studies (**Figure 1A**). However, to better represent the CDW, the Changjiang River is extended upstream from the Xuliujing hydrologic station to the Datong hydrologic station (approximately 620 km away from the estuary). There is a

total of 81,411 nodes and 154,079 triangular elements in the model domain and 31 layers in the vertical. The horizontal resolution is 20 km at the open boundary and about 400 m in the CRE (**Figure 1B**), where the Deep Navigation Channel and the dykes can be well distinguished (**Figure 1C**). The bathymetry data reads from the China coastal sea marine charts and the DBDB5 database (US Naval Oceanographic Office, and the US Naval Ocean Research, and Development Activity, 1983). The daily Changjiang River discharge is derived from the Datong hydrologic station[1] and employed in the model with a salinity of 0 psu. The tidal forcing at the open boundary is derived from the TPXO9-atlas-v2 global barotropic model[2], consisting of three diurnal tides (K_1, O_1, Q_1), three semi-diurnal tides (M_2, S_2, N_2), and three shallow-water tides (M_4, MS_4, MN_4). Daily temperature, salinity, non-tidal current, and sea surface height obtained from the Hybrid Coordinate Ocean Model (HYCOM[3]) are employed as corresponding boundary conditions. Surface forcing includes longwave and shortwave radiation, sea surface pressure, air temperature, evaporation and precipitation, and relative humidity, which are obtained from the National Centers for Environmental Prediction (NCEP) Climate Forecast System Reanalysis (CFSR) hourly products (Saha et al., 2010). The heat flux is thus calculated using the bulk formula (Fairall et al., 1996) based on the above datasets. The hourly surface wind is obtained from the fifth generation of atmospheric reanalysis (ERA5) in the European Center for Medium-Range Weather Forecasts (ECMWF[4]). The external forcings employed in this model are also the same as those used in previous studies (Ding et al., 2018, 2019). The model is cold started with the initial temperature and salinity obtained from the HYCOM and run from January 1, 2004 to January 1, 2007.

Wave Model

The Mellor-Donelan-Oey (MDO) wave model proposed by Mellor et al. (2008) is employed in this study and coupled with the abovementioned circulation model. The wave energy in the model is a function of the wave propagation direction θ, the horizontal coordinates (x, y), and time t; and the wave frequency σ is an independent variable but depends on θ. The MDO wave model adopts the spectrum of Donelan et al. (1985), which is based on the Joint North Sea Wave Project (JONSWAP) spectrum. The directionally dependent wave energy equation in a sigma coordinate system is given as (Mellor et al., 2008):

$$\begin{aligned}&\frac{\partial E_\theta}{\partial t}+\frac{\partial}{\partial x_\alpha}\left[\left(\bar{c}_{g\alpha}+\bar{u}_{A\alpha}\right)E_\theta\right]+\frac{\partial}{\partial\theta}\left(\bar{c}_\theta E_\theta\right)+\int_{-1}^{0}\bar{S}_{\alpha\beta}\frac{\partial U_\alpha}{\partial x_\beta}Dd\varsigma\\&\quad=S_{\theta\mathrm{in}}-S_{\theta\mathrm{Sdis}}-S_{\theta\mathrm{Bdis}}\end{aligned}\tag{1}$$

where E_θ is the spectrally integrated wave energy:

$$E_\theta\equiv\int_0^\infty E_{\theta,S}d\sigma\tag{2}$$

and $E_{\theta,S}$ is the directional spectrum of the kinematic energy divided by the water density. x_α and x_β is the horizontal coordinate ($\alpha = x, y$ and $\beta = x, y$); c_g is the group speed, and the overbar represents a spectral average; u_A is the Doppler velocity given by Mellor (2003, 2008); c_θ is the refraction velocity; U_α is the ocean current plus the Stokes drift; ς is the sigma variable; $D = h + \eta$ is the total water depth, with h the local water depth and η the water elevation. The three terms on the right-hand side (RHS) of Equation (1) are the wind growth source term $S_{\theta\ in}$, the dissipation terms due to wave processes at the surface $S_{\theta\ Sdis}$ and bottom $S_{\theta\ Bdis}$, respectively; details about the three source terms can be found in Mellor et al. (2008). $S_{\alpha\ \beta}$ is the depth-dependent wave radiation stress term given by Mellor (2015).

Considering the wave effects, the momentum and continuity equations in the circulation model can be rewritten as:

$$\frac{\partial\eta}{\partial t}+\frac{\partial DU_\alpha}{\partial x_\alpha}+\frac{\partial\omega}{\partial\varsigma}=0\tag{3}$$

$$\begin{aligned}&\frac{\partial(DU_\alpha)}{\partial t}+\frac{\partial\left(DU_\alpha U_\beta\right)}{\partial x_\beta}+\frac{\partial\left(DS_{\alpha\beta}\right)}{\partial x_\beta}+\frac{\partial(\omega U_\alpha)}{\partial\varsigma}+DF_f\\&\quad=-gD\frac{\partial\eta}{\partial x_\alpha}-\frac{gD^2}{\rho_0}\int_{-1}^{0}\left(\frac{\partial\rho}{\partial x_\alpha}-\frac{\varsigma}{D}\frac{\partial D}{\partial x_\alpha}\frac{\partial\rho}{\partial\varsigma}\right)d\varsigma+DF_h\\&\quad+\frac{\partial\tau_{T\alpha}}{D\partial\varsigma}+\frac{\partial\tau_{P\alpha}}{D\partial\varsigma}\end{aligned}\tag{4}$$

where ω is the vertical velocity in sigma coordinate; ρ is the water density; ρ_0 is the reference density; F_f is the Coriolis force vector ($-fv$, fu) and f is the Coriolis parameter; g is the gravitational acceleration; F_h is the horizontal diffusion terms, calculated by the Smagorinsky eddy parameterization (Smagorinsky, 1963); $\tau_{T\alpha}$ is the turbulent-viscous part of the wind stress or skin friction, defined as $K_m(\partial U_\alpha/\partial\varsigma)$, where K_m is calculated using the Mellor-Yamada level 2.5 turbulence closure model (Mellor and Yamada, 1982); $\tau_{P\alpha}$ is the wind stress induced by form drag (Mellor et al., 2008):

$$\tau_{P\alpha}=\frac{\cosh\left[2kD\left(1+\varsigma\right)\right]}{2\pi\sinh\left(2kD\right)}\int_0^{2\pi}P_{w0}\sin\phi\frac{\partial\hat{\eta}}{\partial x_\alpha}d\theta\tag{5}$$

where P_{w0} is the wind pressure at the surface; $\hat{\eta}=a\cos\phi$ is the wave setup with a the amplitude and φ the phase.

Considering the input of τ_T and τ_P, the turbulence kinetic energy (TKE) equation can be rewritten as (Mellor, 2013):

$$\begin{aligned}&\frac{\partial q^2D}{\partial t}+\frac{\partial q^2U_\alpha D}{\partial x_\alpha}+\frac{\partial q^2\omega}{\partial\varsigma}=\frac{\partial}{\partial\varsigma}\left(\frac{K_q}{D}\frac{\partial q^2}{\partial\varsigma}\right)\\&\quad+2\tau_{T\alpha}\frac{\partial U_\alpha}{\partial\varsigma}+2\tau_{P\alpha}\frac{\partial U_\alpha}{\partial\varsigma}+2K_h\frac{g}{\rho_0}\frac{\partial\rho}{\partial\varsigma}-\frac{2Dq^3}{B_1l}+F_q\end{aligned},\ and\tag{6}$$

$$\begin{aligned}&\frac{\partial q^2lD}{\partial t}+\frac{\partial q^2lU_\alpha D}{\partial x_\alpha}+\frac{\partial q^2l\omega}{\partial\varsigma}=\frac{\partial}{\partial\varsigma}\left(\frac{K_q}{D}\frac{\partial q^2l}{\partial\varsigma}\right)\\&\quad+E_1l\left(\tau_{T\alpha}\frac{\partial U_\alpha}{\partial\varsigma}+\tau_{P\alpha}\frac{\partial U_\alpha}{\partial\varsigma}+E_3K_h\frac{g}{\rho_0}\frac{\partial\rho}{\partial\varsigma}\right)\tilde{w}-\frac{Dq^3}{B_1}+F_l\end{aligned}\tag{7}$$

where q^2 is twice the turbulence energy and l is the turbulence length scale; K_q is the mixing coefficient and K_h is the vertical thermal diffusion coefficient; $\tilde{w}$is the so-called wall proximity function defined in Mellor and Yamada (1982); F_q and F_l are the horizontal diffusion terms for the q^2 and q^2l; E_1, E_3, and B_1 are

[1]http://www.cjh.com.cn/sssqcwww.html

[2]https://www.tpxo.net/

[3]https://www.hycom.org/

[4]https://www.ecmwf.int/en/forecasts/datasets/reanalysis-datasets/era5

empirical constants (Mellor and Yamada, 1982; Galperin et al., 1988).

The turbulence kinetic flux q^2 induced by surface wave dissipation was given by Mellor and Blumberg (2004):

$$\begin{cases} \frac{\partial q^2}{\partial z} = \frac{2\alpha_{CB} u_\tau^3}{K_q} \\ l = \max(\kappa z_w, \kappa z) \end{cases} \quad at\ z = \zeta(x, y, t) \tag{8}$$

where α_{CB} is a parameter related to wave age and u_τ is the waterside friction velocity; $\kappa = 0.41$ is the von Karman number, and $z_w = 0.85H_s$ is the wave-related roughness. The turbulence kinetic flux q^2 induced by the bottom wave dissipation was given by Mellor (2013):

$$\begin{cases} \frac{\partial q^2}{\partial z} = \int_{-\pi}^{\pi} S_{\theta \mathrm{Bdis}} d\theta \\ l = 0 \end{cases} \quad at\ z = -h(x, y) \tag{9}$$

Thus, the wave–current interacts through depth-dependent wave radiation stress, Stokes drift, vertical transfer of wave-generated pressure to the mean momentum equation caused by form drag, wave dissipation as a source term in the TKE equation, mean current advection, and refraction of wave energy (Mellor, 2003, 2015; Mellor et al., 2008). The combined wave–current induced bottom shear stress is also calculated using Soulsby's (1995) method. More details on the model coupling can be found in Gao et al. (2018) and Song et al. (2021). The significant wave height, peak wave direction, and peak wave period are obtained from the WaveWatch III (WW3) global wave model[5], which are employed to generate a full-wave spectrum along the open boundary as:

$$\begin{aligned} E(\sigma, \theta) &= g\left(\frac{H_s}{4}\right)^2 \times f_{spr} \\ \sigma_\theta &= \frac{2\pi}{T_p} \end{aligned} \tag{10}$$

where H_s is the significant wave height, σ_θ is the wave direction-dependent frequency, T_p is the peak wave period, and f_{spr} is the so-called spreading function:

$$f_{spr} \equiv \begin{cases} \frac{\beta}{2} \sec h^2 [\beta(\theta - \theta_w)]; & |\theta - \theta_w| \le \frac{\pi}{2} \\ 0; & |\theta - \theta_w| > \frac{\pi}{2} \end{cases} \tag{11}$$

with $\beta = 2.2$ and θ_w is the direction of incoming/outgoing waves. Details can be found in Mellor et al. (2008). It has been shown that it is better to recreate full-wave spectra from WW3 bulk parameters for accurate wave models (Kumar et al., 2017).

The two-way coupling between the MDO wave model and the FVCOM circulation model has been proved computationally efficient, based on which several works have been published, e.g., the oil spills transport (Wang and Shen, 2010), the wave simulation in the Gulf of Mexico during Hurricane Katrina (Wang and Shen, 2012), the suspended sediment transport in Jiaozhou Bay, China (Gao et al., 2018), and the bay-shelf exchange in the northern South China Sea (Song et al., 2021).

[5]https://polar.ncep.noaa.gov/waves/wavewatch/

TABLE 1 | Summary of experiment settings.

Experiment	Description
Exp1 (CR)	Control run with all wave–current interactions
Exp2 (NoWave)	Same as Exp1 but no wave
Exp3 (NoCWCBS)	Same as Exp1 but no combined wave–current bottom stress
Exp4 (NoFormDrag)	Same as Exp1 but no form drag
Exp5 (NoWDinTKE)	Same as Exp1 but no wave dissipation in turbulence kinetic energy equation
Exp6 (NoWRS)	Same as Exp1 but no depth-dependent wave radiation stress
Exp7 (NoCARWE)	Same as Exp1 but no current advection and refraction of wave energy

Experiment Configuration

In this study, seven numerical experiments are conducted to quantify the effect of the overall and individual wave–current interaction process (**Table 1**). Exp1 is the control run (CR), which considers all the wave–current interaction processes. Exp2 (NoWave) is the same as Exp1 but the exclusion of waves. This and the following experiments are hot started from 2006 based on the first-2 year run in Exp1. In Exp3 (NoCWCBS), the impact of the combined wave–current bottom stress (CWCBS) is replaced by current-induced bottom stress. In Exp4 (NoFormDrag), the form drag $\tau_{P\alpha}$ is not considered, i.e., the last term on the RHS of Equation (4) and the third term on the RHS of Equations (6) and (7). In Exp5 (NoWDinTKE), the source term equal to wave dissipation is removed from the TKE equation, and thus Equations (8) and (9) is changed to:

$$\begin{cases} \frac{\partial q^2}{\partial z} = 0 \\ l = 0 \end{cases} \quad at\ z = \zeta(x, y, t), and \tag{12}$$

$$\begin{cases} \frac{\partial q^2}{\partial z} = 0 \\ l = 0 \end{cases} \quad at\ z = -h(x, y) \tag{13}$$

In Exp6 (NoWRS), the depth-dependent wave radiation stress (WRS) is removed from the momentum equation, i.e., the third term on the left-hand side (LHS) of Equation (4). In Exp7 (NoCARWE), the current advection and refraction of wave energy (CARWE) is excluded in Equation (1), i.e., the second and third terms on the LHS of Equation (1).

The configurations of each experiment are summarized in **Table 1**. In this study, the Stokes drift is not discussed as it is not separated from the ocean current in the MDO wave model (Mellor et al., 2008).

Model Validation

The ECS FVCOM has been well-validated in Ding et al. (2018, 2019) and Gao et al. (2020). In this study, the model result of the control run is further validated for the wave performance and the accuracy to reproduce the detachment of LSW. Three methods are employed to quantify the differences between the observations and simulations: the determination coefficient R^2, the root mean square error (RMSE), and the correlation coefficient (CC) with a 95% confidence interval.

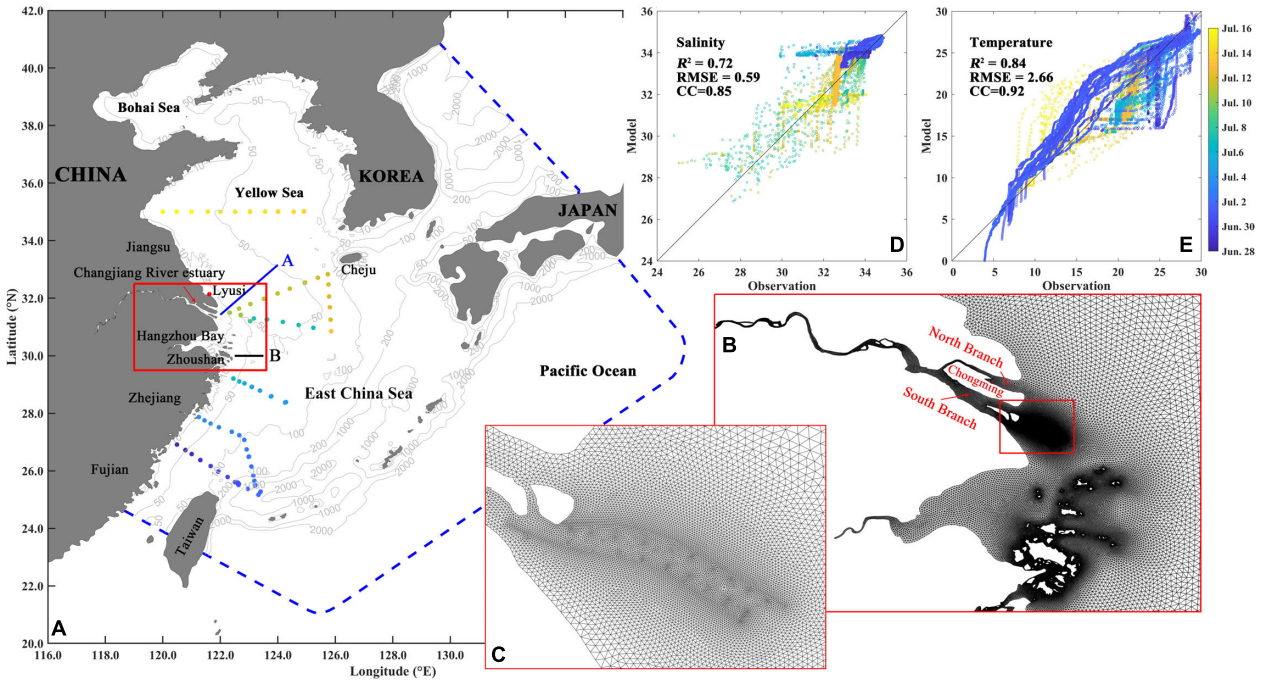


FIGURE 1 | (A) The model coverage with the observation stations during the first cruise from June 28 to July 16, 2006, two cross-sections A/B in blue/black solid lines, and zoom-in mesh-grids in **(B)** the Changjiang River estuary [red box in panel **(A)**] and **(C)** the Deep Navigation Channel [red box in panel **(B)**]. The comparison between the observed and modeled **(D)** salinity and **(E)** temperature during the first cruise. Color in panels **(A,D,E)** indicate the date of measurements.

The modeled salinity and temperature according to the observation time, station, and water depth are given in **Figures 1**, **2**. The comparison between the model results and measured profiles during the first cruise gives R^2 = 0.72, RMSE = 0.59 psu, and CC = 0.85 for salinity (**Figure 1D**) and R^2 = 0.84 RMSE = 2.66°C, and CC = 0.92 for temperature (**Figure 1E**). The comparison between the model results and *in situ* measurement during the second cruise gives R^2 = 0.80, RMSE = 0.87 psu, and CC = 0.89 for salinity (**Figure 2B**). The simulated SSS (**Figure 2D**) has a similar pattern to the observations (**Figure 2C**), with the river plume expanding northeastward and an isolated LSW at the eastern part of the cruise route. But the isolated LSW is slightly southward with a little higher salinity and a smaller salinity gradient, compared to the observations. The salinity distribution in the four cross-sections along 32.3°N, 32.7°N, 33.0°N, and 33.3°N (**Figure 3**) is also compared to the observations (see Figure 5 in Wei et al., 2017). It indicates the model can also reproduce the vertical structure of the CDW and reproduces the detachment of LSW.

To evaluate the performance of wave simulation, the simulated H_s is compared with the remote-sensed H_s by Jason-1[6]. The satellite-derived wave data is fixed on the specific orbit in the study area (**Figure 4A**). A total of 857 samples of the along-tracked H_s is collected during July 2006 and compared with the model results (**Figures 4B,C**). The comparison indicates a reasonable model performance on wave simulation, with R^2 = 0.80, RMSE = 0.33 m, and CC = 0.91. Overall, we think the model results are reasonable and agree well with the observations; thus, the model can be used to study the wave effects on the detachment of LSW.

Model Results

The daily averaged SSS in the control run shows two LSW detachment events started on July 13 and July 28, respectively, when the 24 psu (25 psu for the second event) isohaline closed and just disconnected with the river plume front. Xuan et al. (2012) also confirmed these two events happened in July, but they used the date of "complete detachment," which is usually some days later after the detachment begins. As the first event was more obvious and this isolated LSW existed longer than the second one, in this study, we will focus on the first detachment event from July 11 to July 19. The wind turned southerly on July 10 and kept increasing until July 15, and then decreased gradually until July 19 (**Figure 5A**). Correspondingly, the wave propagated from south to north, and the H_s increased from July 13 to 15 but then decreased.

Before the occurrence of the LSW detachment, the CDW main body extended northward under the southerly winds on July 11 (**Figure 6A**). Due to the Coriolis force, the CDW front turned to the southeast (**Figure 6G**). The TWC flowed northeastward and its inshore branch was rather weak (**Figure 6M**). As the wind speed began to increase on July 12 (**Figure 6B**), the CDW main body turned northeast and extended further northeastward (**Figure 6H**). The CDW with salinity less than 26 psu evidently covered a much larger area than that on July

[6]https://podaac.jpl.nasa.gov/

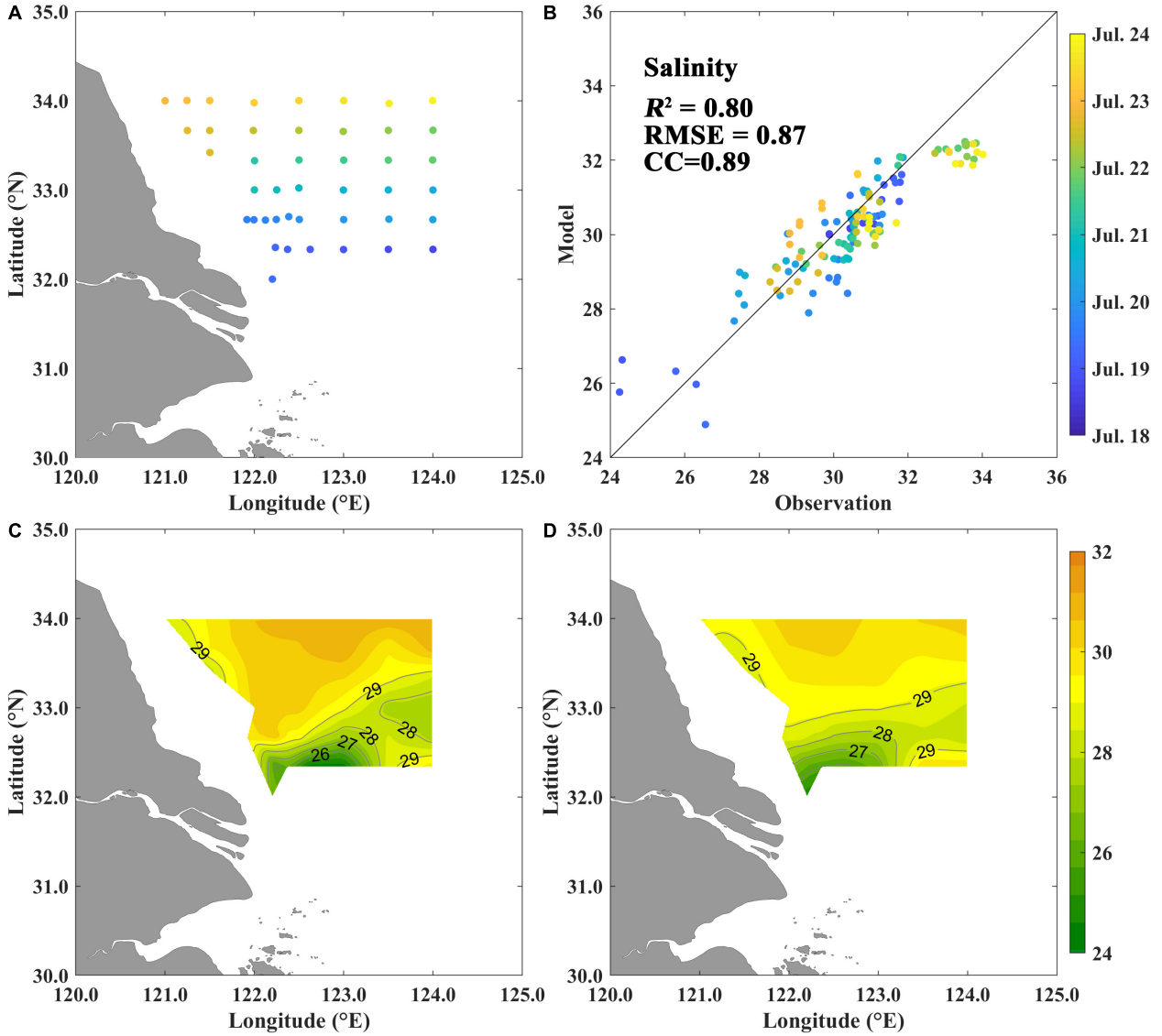


FIGURE 2 | (A) Distribution of the observation stations and **(B)** the comparison between the **(C)** observed and **(D)** modeled salinity during the second cruise from July 18 to 24, 2006. Color in panels **(A,B)** indicate the date of measurement.

11 and its front reached 123°E. The southeastward extension of the CDW front was also weakened. The TWC inshore branch was slightly increased (**Figure 6N**). In the next day, wind speed continued to grow and the wind direction was almost unchanged (**Figure 6C**). A strong wind speed of 12 ms^{-1} prevailed south of the river estuary, and the wind speed was over 8 ms^{-1} in the north of the river estuary. The CDW front with 26 psu moved further northeastward and became narrow, which was more easily extruded and penetrated by saline water. As proposed by Xuan et al. (2012), an isolated low-salinity lens was detached from the CDW front under a critical wind speed of 8 ms^{-1}, with a core salinity of 23.96 psu; and the CDW less than 20 psu retreated sharply (**Figure 6I**). The TWC was enhanced due to the enlarged southeasterly wind, and the northward flow pushed the CDW to the north (Figure 6O).

The wind speed reached a maximum on July 14 and a wind speed over 12 ms^{-1} prevailed in most study areas on July 14 (**Figure 6D**). The isolated LSW kept developing and moving northeastward under the strong southeasterly wind (**Figure 6J**). The TWC was obviously enhanced and widened, but the direction of its inshore branch gradually turned northeastward (**Figure 6P**). The core salinity of the LSW was a bit higher (26.14 psu), and its size was also significantly increased. Then on July 15, the wind speed was still high (~11 ms^{-1}) but the direction turned from southeasterly to southerly (**Figure 6E**). The TWC was still strong, but the direction of its inshore branch mostly turned to northeastward (**Figure 6Q**). The CDW main

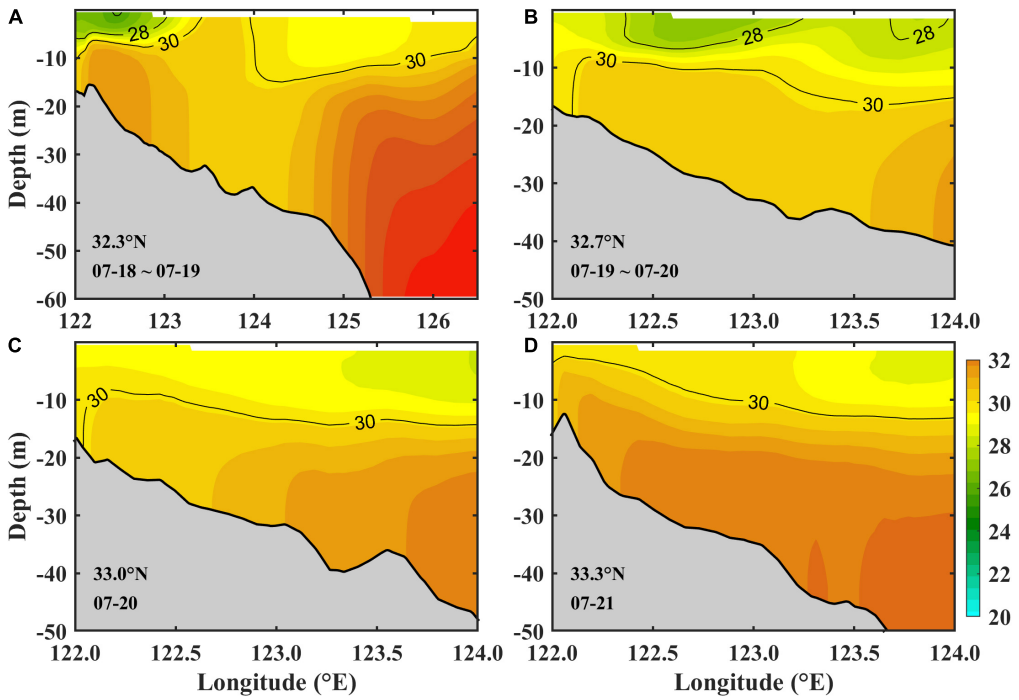


FIGURE 3 | The model result of the cross-sectional distribution of salinity corresponding to the observations in Wei et al. (2017) with **(A)** along 32.3°N during July 18 and 19, **(B)** along 32.7°N during July 19 and 20, **(C)** along 33.0°N on July 20, and **(D)** along 33.3°N on July 21.

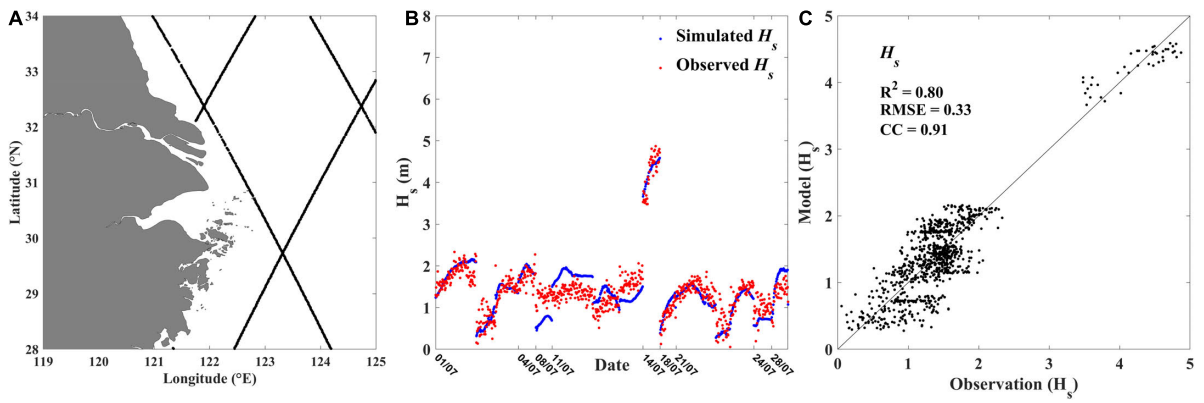


FIGURE 4 | (A) The distribution of observation points along the satellite orbit over the East China Sea during July 2006. **(B,C)** The comparison between the observed and simulated significant wave height (H_S).

body became narrower with a northward movement and the core salinity of the LSW was increased to 27.42 psu (**Figure 6K**). The wind speed quickly decreased to below 10 ms^{-1} and the wind kept southerly until July 16 (**Figure 6F**). It was still conducive to the LSW detachment. The TWC also began to decrease (**Figure 6R**). The CDW main body became narrower and further northward. The size of the LSW became smaller and its core salinity reached 27.75 psu (**Figure 6L**). In addition, another small isolated low-salinity lens was detached from the plume front. After July 16, the isolated LSW still existed for a long time. The salinity of the LSW kept increasing.

The LSW detachment can be seen more clearly through the cross-sectional view (**Figures 7A–F**). From July 11 to 13, the CDW extended offshore and became thinner. The LSW was detached from the main body on July 13 with a core salinity of 23.96 psu. The CDW main body retreated on July 14 with the plume front of about 28 psu and the isolated LSW moved further offshore with the core salinity rising to 26.14 psu. On July 15, the CDW main body moved back to the estuary, and the high salinity water over 30 psu pushed the CDW northward. The isolated LSW became thicker and moved away from the selected cross-section A.

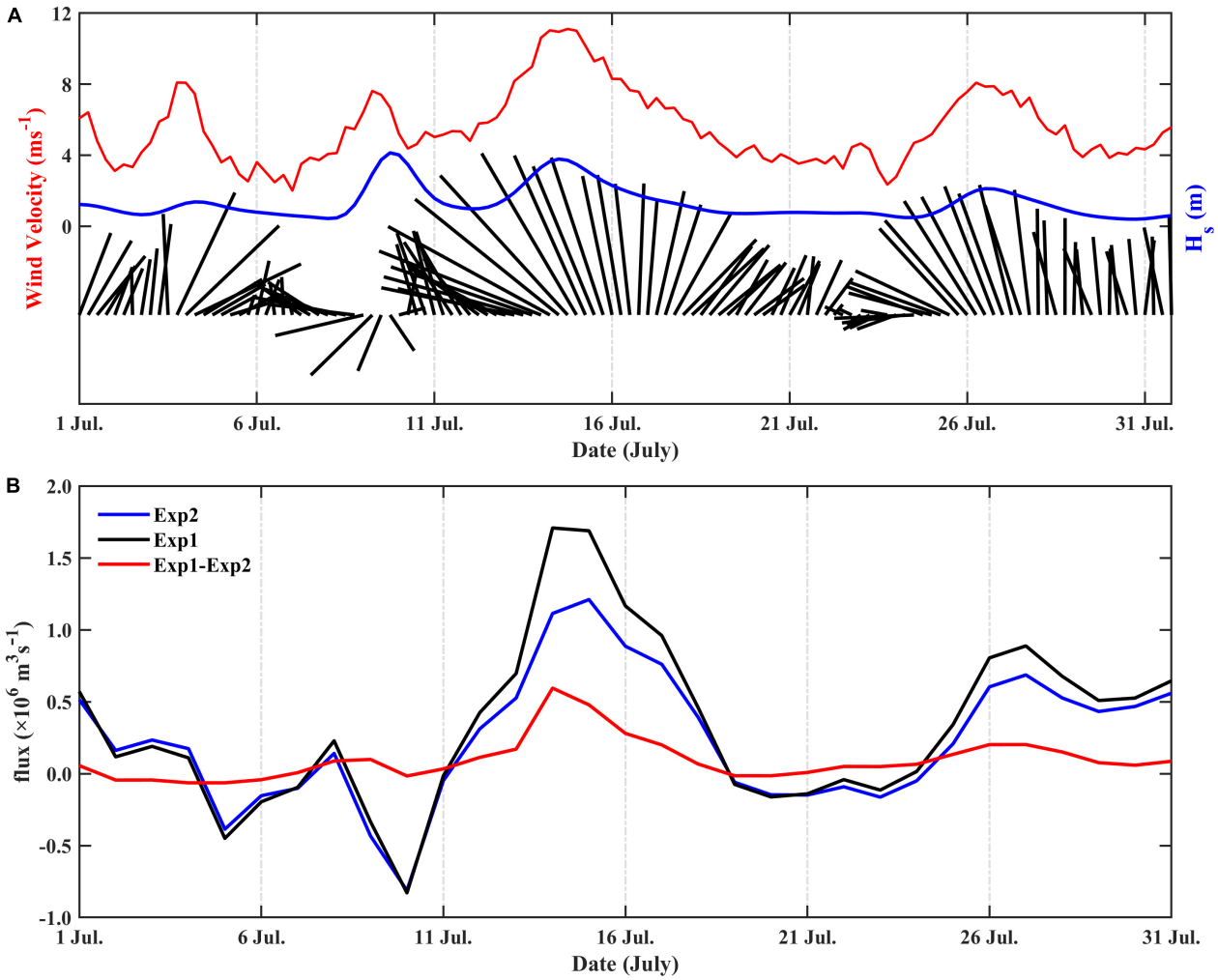


FIGURE 5 | (A) The wind vector (black), magnitude (red), and simulated significant wave height (blue) in the Changjiang River estuary (spatially-averaged within the range of **Figure 4A**) during July 2006. **(B)** The daily-averaged current flux across the cross-section B (30°N, 122.5∼123.5°E) during July 2006. Positive indicates northward flux.

The snapshot of vertical velocity along the cross-section A is given in **Figures 7G–L**. An upwelling was formed on July 11 with a strong core of 122.3°E. The system became weak from July 11 to July 13 but then was enhanced from July 14. A double-core upwelling system was formed on July 15, with one core on 122.3°E and another on 122.5°E. The two upwelling cores were clearer on July 16.

DISCUSSION

Wave Effects on the Detachment of Low-Salinity Water

Salinity and Wave-Induced Mixing

In Exp1, the control run, the averaged SSS between July 11 and 19 shows a northeastward extension of the CDW due to the prevailing southerly wind during the same period (**Figure 8A**). The waves enhanced the surface mixing, which increases the surface salinity but slightly decreases the salinity below the nearshore surface; thus, the CDW main body is less extended (**Figures 8A,B**). The difference of SSS between Exp1 and Exp2 (Exp1–Exp2) illustrates that the SSS is notably increased off the CRE and the Hangzhou Bay, but decreased on the southern Jiangsu coast due to the northward migration of the CDW (**Figure 8C**).

Here, ΔS is used to represent the vertical mixing in the water column, which is calculated as the bottom salinity minus surface salinity. Compared to Exp2, the retreated CDW reduces the surface salinity in the river estuary and thus increases ΔS there in Exp1 (**Figures 8D,E**). The ΔS is reduced due to the wave-induced surface mixing in the most inner-shelf region, but increased off the southern Jiangsu coast. The difference of ΔS between Exp1 and Exp2 (**Figure 8F**) is similar to that of SSS (**Figure 8C**), which indicates that the surface salinity varies more than the bottom salinity due to the inclusion of waves in the model. The bottom salinity is increased nearshore

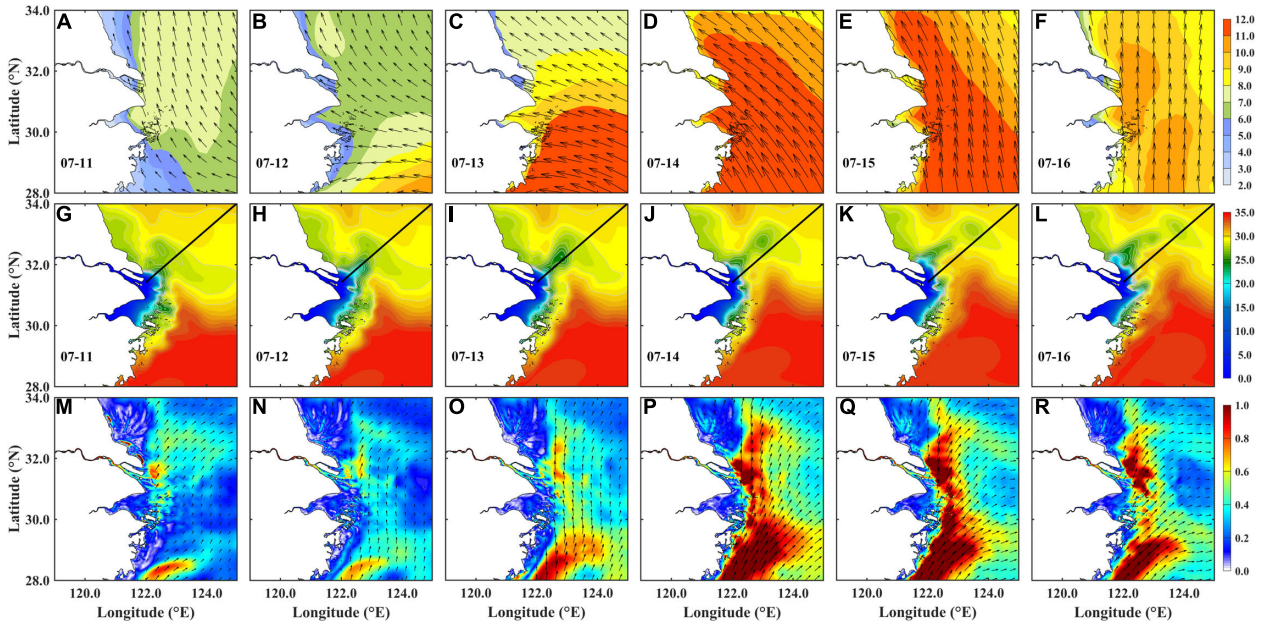


FIGURE 6 | The daily-averaged **(A–F)** wind (unit: ms^{-1}), **(G–L)** surface salinity, and **(M–R)** surface current (unit: ms^{-1}) from July 11 to 16, 2006 in Exp1. The black line indicates the cross-section A; color indicates magnitude and arrow for direction.

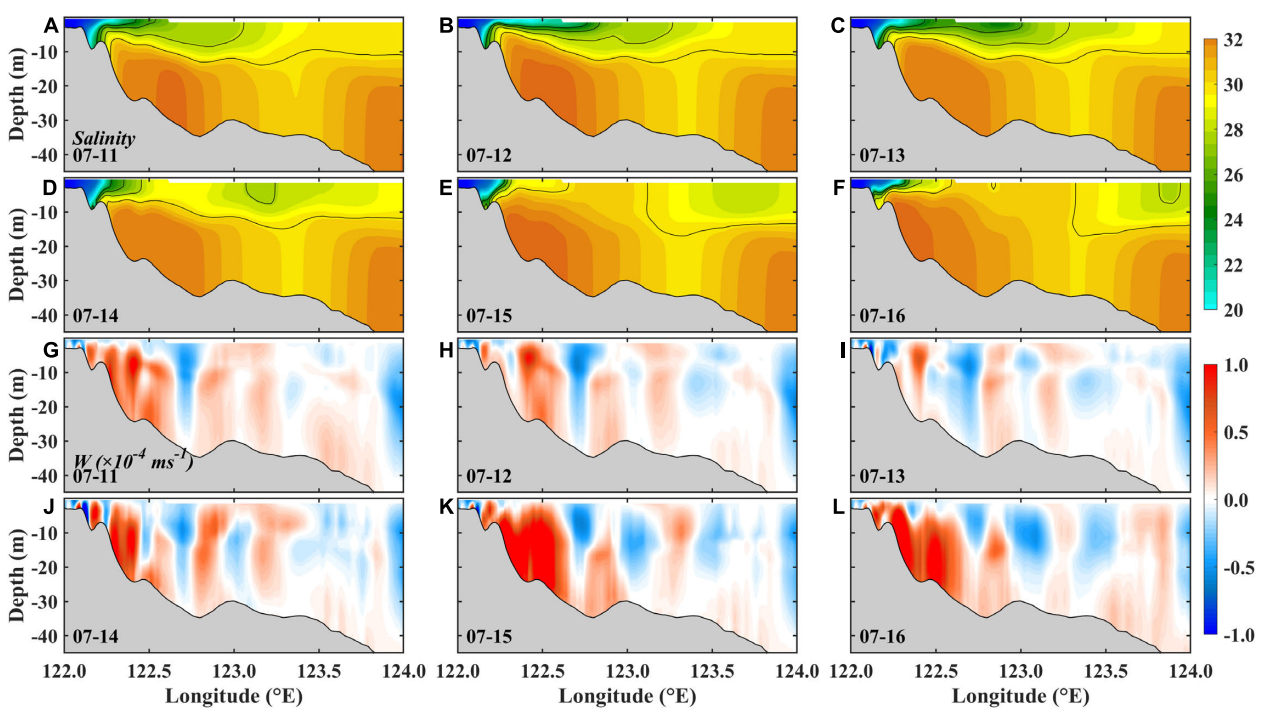


FIGURE 7 | (A–F) The daily-averaged salinity (black lines indicate 24, 26, 28, and 30 psu) and **(G–L)** vertical velocity (unit: $\times 10^{-4}$ ms^{-1}) along the cross-section A from July 11 to 16, 2006.

from the CRE to the Zhejiang coast but slightly decreased offshore, and the difference between Exp1 and Exp2 is less than 3 psu (not shown).

Wave-Driven Flow

The wave-driven surface flow (Exp1-Exp2) enhances the northward TWC inshore branch (**Figures 8G–I**), which brings

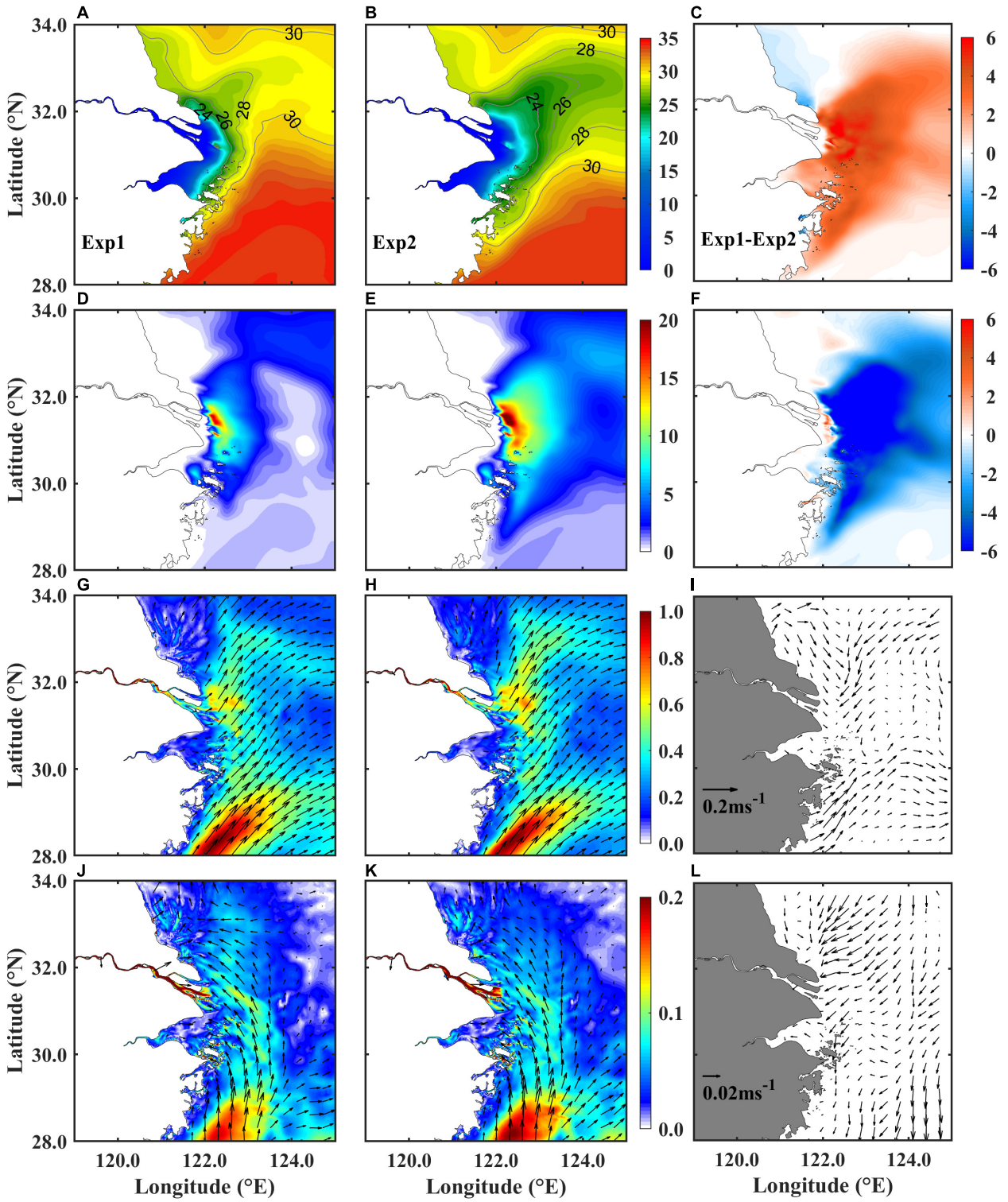


FIGURE 8 | The **(A–C)** surface salinity, **(D–F)** difference between the bottom and surface salinity (bottom minus surface), **(G–I)** surface current, and **(J–L)** bottom current (unit: ms^{-1}) averaged from July 11 to 19 in **(A,D,G,J)** Exp1 (CR), **(B,E,H,K)** Exp2 (NoWave), and **(C,F,I,L)** Exp1–Exp2. Color indicates magnitude and arrows for direction.

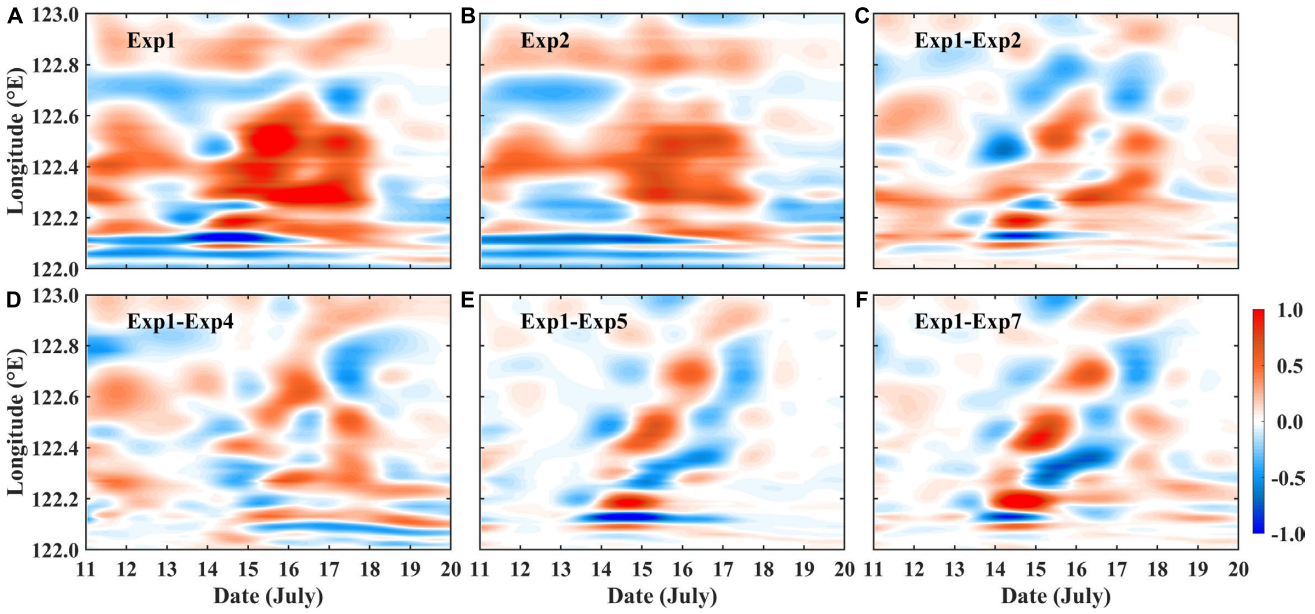


FIGURE 9 | The vertically-averaged vertical velocity (unit: $\times 10^{-4}$ ms^{-1}, upward positive) along the cross-section A during from July 11 to 19, 2006 in **(A)** Exp1 (CR), **(B)** Exp2 (NoWave), **(C)** Exp1–Exp2, **(D)** Exp1–Exp4 (NoFormDrag), **(E)** Exp1–Exp5 (NoWDinTKE), and **(F)** Exp1–Exp7 (NoCARWE).

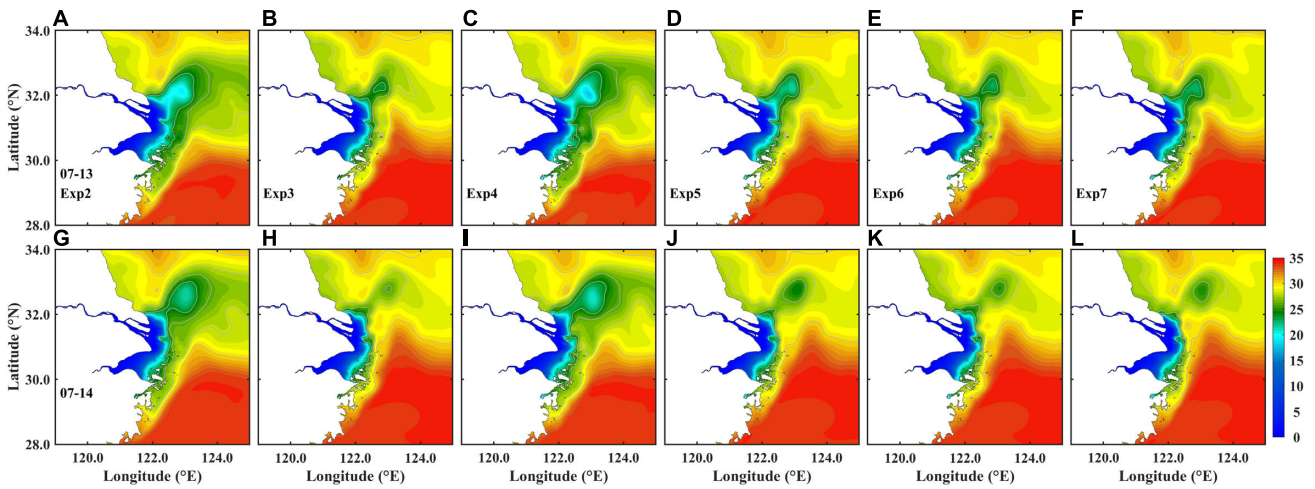


FIGURE 10 | The daily-averaged surface salinity (gray lines indicate 24, 26, 28, and 30 psu) on July 13 (upper panel) and 14 (lower panel) in **(A,G)** Exp2 (NoWave), **(B,H)** Exp3 (NoCWCBS), **(C,I)** Exp4 (NoFormDrag), **(D,J)** Exp5 (NoWDinTKE), **(E,K)** Exp6 (NoWRS), and **(F,L)** Exp7 (NoCARWE), respectively.

the high salinity water northward, and thus the CDW is migrated northward (**Figure 8C**). Influenced by the adjustment of the CDW plume structure, the northeastward surface flow is reduced along the CDW pathway, which is consistent with the restrained CDW plume (**Figures 8A,B**). Meanwhile, the bottom current is generally enhanced in Exp2 due to the removal of combined wave–current bottom stress (**Figures 8J,K**). However, the bottom wave-driven flow is less than 0.05 ms^{-1} in magnitude, which is much smaller than the surface wave-driven flow (**Figure 8L**).

The flux of wave-driven flow through the cross-section B is calculated to show its daily variation. On most days, the wave-driven flow traveled along the coast from south to north, which reached a maximum of 5.9×10^5 m^{3}s^{-1} on July 14 (**Figure 5B**), when the southerly wind also reached a maximum (**Figure 5A**). During the second LSW detachment event, the flux of wave-driven flow also increased as the wind speed increasing. The flux through cross-section B well correlates to the wind with a CC = 0.83 (95% confidence interval). It indicates the wave-driven flow benefits for the detachment of LSW.

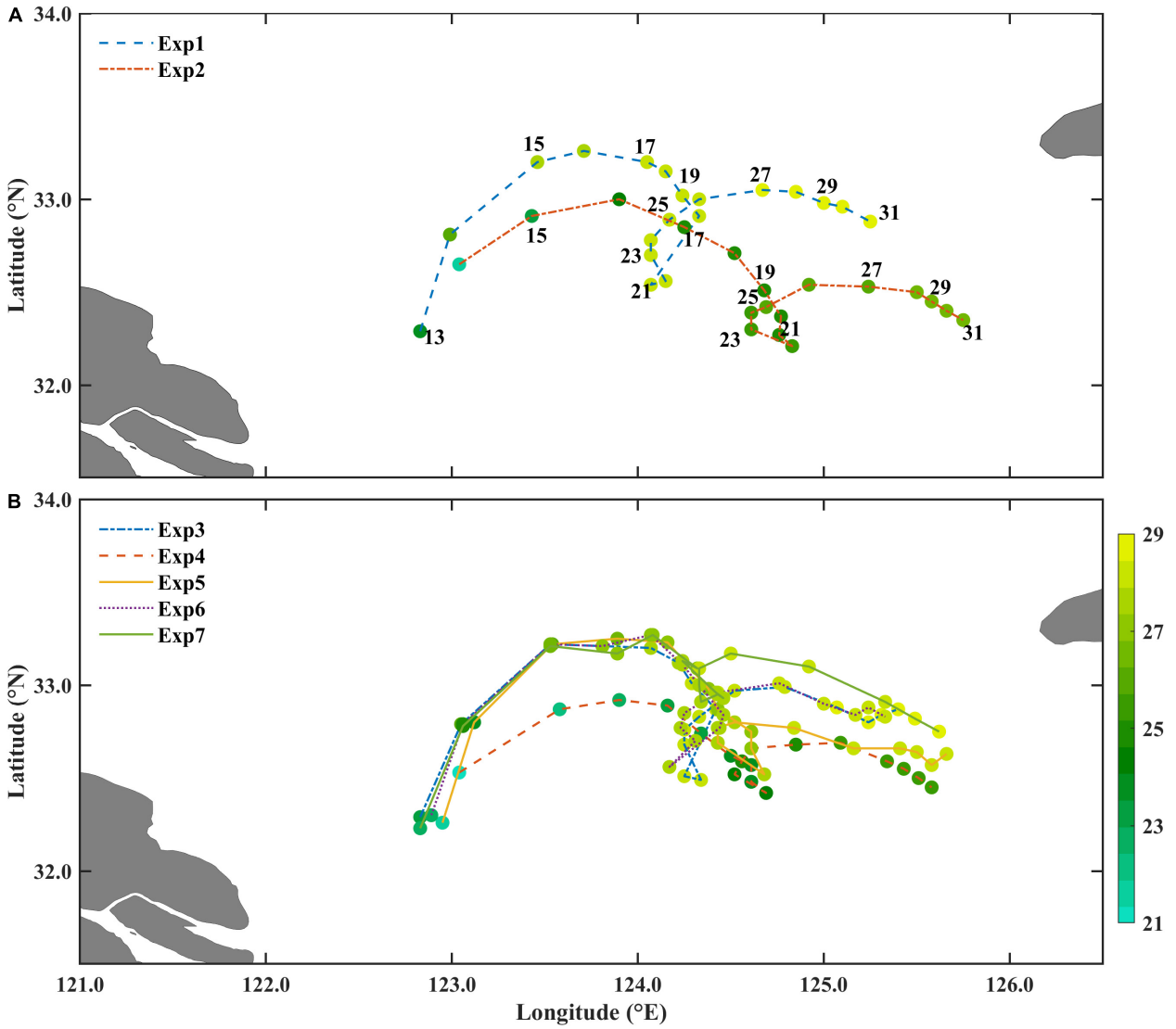


FIGURE 11 | The trajectory of the LSW center since the detachment in **(A)** Exp1 (CR) and Exp2 (NoWave), and **(B)** Exp3 (NoCWCBS), Exp4 (NoFormDrag), Exp5 (NoWDinTKE), Exp6 (NoWRS), and Exp7 (NoCARWE), respectively. Color circles indicate the core salinity of the LSW and the numbers indicate the day of July.

Upwelling

The vertically-averaged vertical velocity is calculated along the cross-section A between 122°E and 123°E, and its temporal variation from July 11 to 19 is plotted in **Figure 9**. It illustrates that the upwelling is enhanced and the double-core structure is formed during the detachment event, which is consistent with the observations by Wei et al. (2017). The temporal variation of the upwelling is similar in Exp1 (**Figure 9A**) and Exp2 (**Figure 9B**), which indicates the double-core structure is determined by winds rather than waves, i.e., the wind-enhanced TWC inshore branch. However, compared to Exp2, the upwelling can be further enhanced by 30% during the detachment events in Exp1 (**Figure 9C**) due to the enhanced onshore bottom wave-driven flow along this cross-section (**Figure 8L**).

Detachment and Movement of Low-Salinity Water

Both the SSS in Exp1 and Exp2 (NoWave) show that the wave effects can greatly affect the detachment of LSW (compare **Figures 6I,J**, **10A,G**). Exclusion of waves in the model, the detachment of LSW is 16 h delayed with a lower core salinity of the isolated LSW. As the isolated LSW lens still has a non-negligible impact on the surrounding seawater, attention is still paid to its evolution after the detachment. According to the simulated daily SSS distribution, the core salinity and position of the isolated LSW are employed to represent its evolution (**Figure 11A**). In Exp1 the core salinity of the LSW was 23.96 psu on July 13 and 28.81 psu on July 31; while in Exp2, it was 21.47 psu on July 14 and 26.55 psu on July 31. As the waves can affect the salinity distribution in the entire region, the growth rate of the core salinity is divided by the bottom-surface salinity

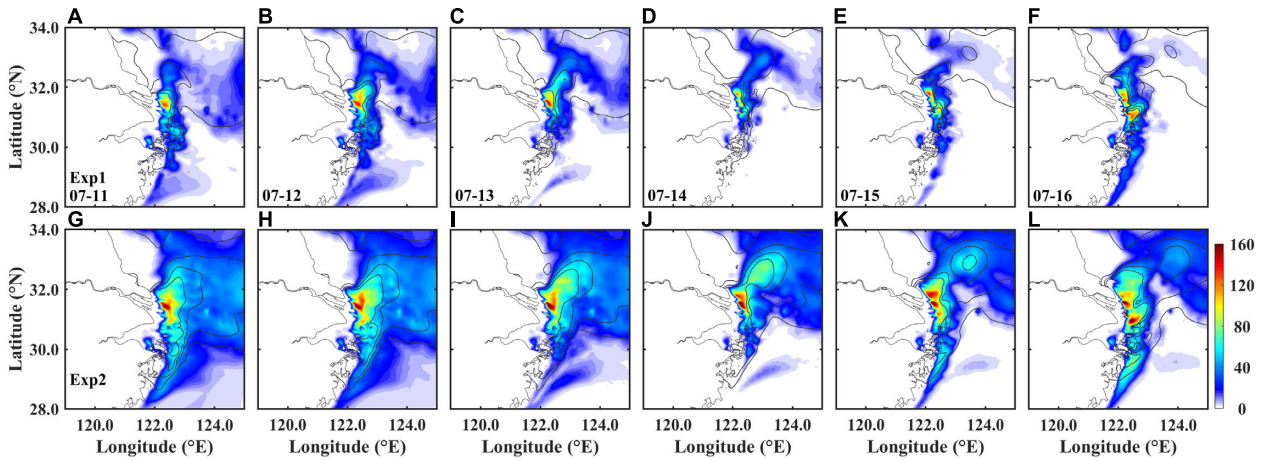


FIGURE 12 | The daily-averaged surface salinity (black lines indicate 24, 26, 28, and 30 psu) and PEA (unit: kg·m^{-1}s^{-2}) calculated from July 11 to 16 in **(A–F)** Exp1 (CR) and **(G–L)** Exp2 (NoWave).

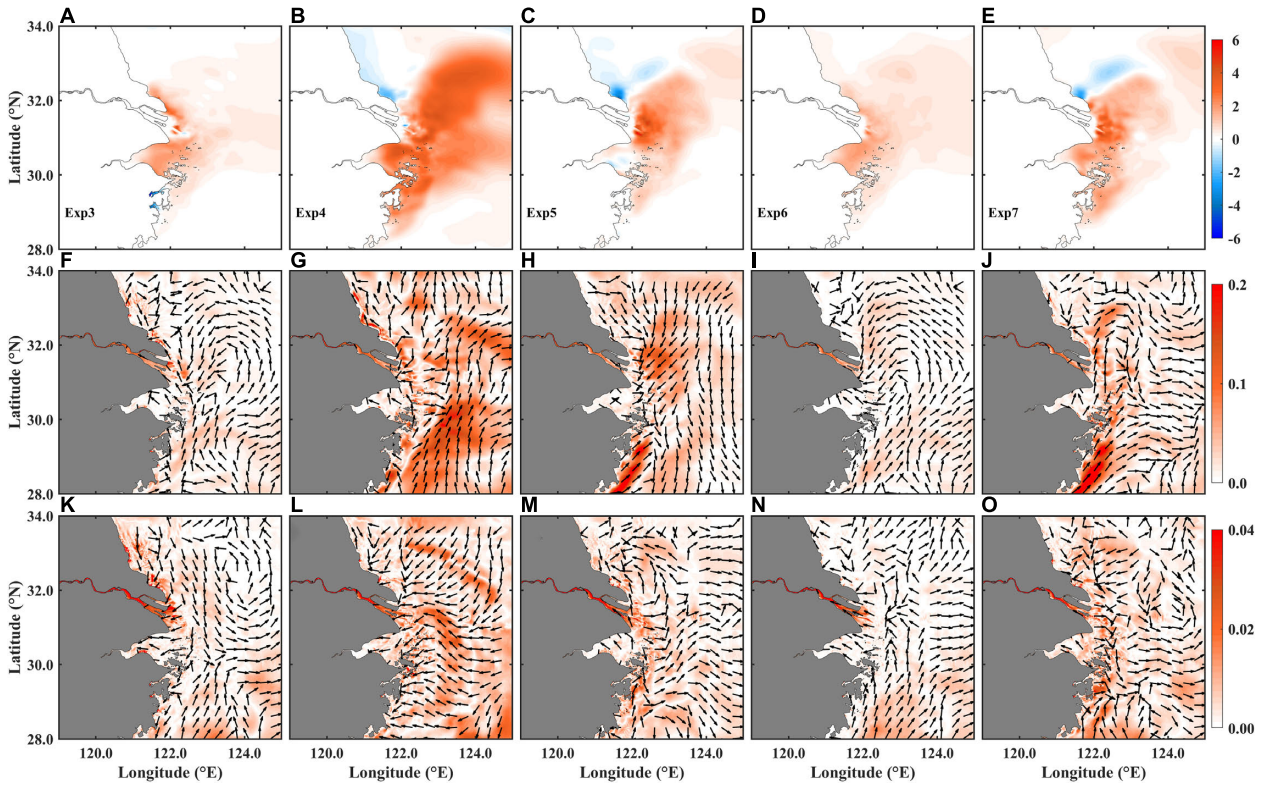


FIGURE 13 | The difference of **(A–E)** surface salinity, **(F–J)** surface current, and **(K–O)** bottom current (unit: ms^{-1}) averaged from July 11 to 19, 2006 in **(A,F,K)** Exp1 (CR) –Exp3 (NoCWCBS), **(B,G,L)** Exp1–Exp4 (NoFormDrag), **(C,H,M)** Exp1–Exp5 (NoWDinTKE), **(D,I,N)** Exp1–Exp6 (NoWRS), and **(E,J,O)** Exp1–Exp7 (NoCARWE). Color indicates magnitude and arrows for direction.

difference. The average growth rate of the core salinity was 0.052 from July 13 to 31 in Exp1 and 0.039 from July 14 to 31 in Exp2. It indicates that the core salinity was increased more quickly in Exp1 than that in Exp2 due to the wave-enhanced vertical mixing. Due to the wave effects, the isolated LSW moves more northward in Exp1 than that in Exp2. Compared to their initial detachment position, the LSW lens moved northeastward from July 13 to July 31 in Exp1, but southeastward in Exp2 (**Figure 11A**). The trajectory of the isolated LSW is almost dominated by the wind direction; and when the wind turned to easterly on July 22, the

LSW also traveled westward. The isolated LSW moved a total of 427 km (22.47 km·d^{-1}) in distance (not displacement) from July 13 to July 31 in Exp1 and 373 km (20.72 km·d^{-1}) from July 14 to July 31 in Exp2 along the trajectory. It indicates that the wave effects lengthen the LSW journey and accelerate its movement.

The potential energy anomaly (PEA) proposed by Simpson (1981) is calculated to explain the detachment:

$$\Phi = \frac{1}{h}\int_{-h}^{0}(\bar{\rho}-\rho)\,gzdz \tag{14}$$

where

$$\bar{\rho} = \frac{1}{h}\int_{-h}^{0}\rho dz.$$

The PEA reflects the energy required for mixing the water column to be vertically homogeneous, and a higher PEA indicates a stronger stratification. As we only concern the mixing in the upper layer of the water column, h is set to be 10 m for deep water. The 10 m is selected according to the thickness of CDW with a salinity less than 30 psu and the thickness of the isolated low-salinity lens, which is consistent with the snapshot of salinity along the cross-section A (**Figures 7A–F**). If Φ is calculated as the integration from the bottom to the surface, the bottom water will largely affect the PEA than the surface LSW. The snapshots of the PEA distribution are given in **Figure 12**. It shows the CDW has the highest PEA when leaving the river estuary. The isolated LSW companied with a relative higher PEA when detached from the river plume. Apparently, the ambient well-mixed surface water (low PEA) began to squeeze the CDW from both sides since July 11, and the CDW front became narrower in the horizontal and thinner in the vertical. Then the low PEA water worked like a scalpel cutting off the CDW front and the high PEA lens was completely detached on July 15.

The vertical mixing, the northward flow, and the upwelling, all enhanced by waves, promote the detachment of the LSW. Comparison between Exp1 and Exp2 shows the CDW has a higher PEA in Exp2 than that in Exp1. The squeezing between the northward flow and the Subei coastal water becomes more difficult in Exp2 and thus it needs 16 h more to finish the detachment. Furthermore, the isolated LSW also has a higher PEA in Exp2 than that in Exp1.

Comparison Between Different Wave–Current Interactions

Salinity and Vertical Mixing

Comparison between the five wave–current interaction processes on SSS indicates the form drag (Exp1–Exp4, CR–NoFormDrag) varied the SSS most (**Figure 13B**). It increases the SSS by 1∼4 psu following the CDW pathway and in Hangzhou Bay; and the SSS in the southern Jiangsu coast and the CRE is decreased. The combined wave–current bottom stress (CWCBS), calculated as Exp1-Exp3 (CR-NoCWCBS), increases the SSS by 2∼3 psu off the CRE and in Hangzhou Bay, and by about 1 psu on the shelf. The SSS is decreased in some small bays at the south of Hangzhou Bay (**Figure 13A**). The wave dissipation on turbulence, calculated as Exp1-Exp5 (CR–NoWDinTKE), shows the SSS is increased off the river estuary by more than 1 psu but decreased off the Lyusi area (**Figure 13C**). The wave radiation stress (WRS), calculated as Exp1–Exp6 (CR–NoWRS), raises the SSS in almost the study area (**Figure 13D**), but the increment is the least among Exp3∼Exp7. The SSS variation induced by the current advection and refraction of wave energy (CARWE), calculated as Exp1–Exp7 (CR–NoCARWE), is quite similar to that induced by the wave dissipation on turbulence (**Figure 13E**). To quantify the contribution of each wave–current interaction process on SSS, the root mean square (RMS) of the SSS difference between the control run and each experiment is calculated (**Table 2**). A larger RMS indicates a more inhomogeneous difference and thus a greater impact of the wave–current interaction process. The results in **Table 2** indicate the form drag has the most significant impact on the SSS distribution in the studied area, followed by the wave dissipation on turbulence, the CARWE, the CWCBS and the WRS.

Compared to the SSS, the bottom salinity varies less in all five experiments (not shown). It has a relatively large difference nearshore but a small difference in deep water. The RMSs of the bottom salinity difference between the control run and each experiment are also given in **Table 2**. It indicates the wave effects on the bottom salinity are much less than those on SSS; and the form drag still has the greatest impact on the bottom salinity distribution.

The difference of vertical mixing represented by ΔS between the control run and the five experiments is similar to the SSS difference (not shown), but a positive SSS difference (enhanced SSS) usually indicated a negative ΔS difference (enhanced vertical mixing). The RMSs of the ΔS difference between the control run and each experiment (**Table 2**) indicate the form drag has the major contribution to the vertical mixing, followed by the wave dissipation on turbulence, the CARWE and the WRS. The CWCBS has a minor contribution to the vertical mixing.

Wave-Driven Flow

The CWCBS (Exp1-Exp3) generates northward currents along the coast and a weakly anticlockwise circulation off the CRE (**Figure 13F**). The largest CWCBS-induced surface flow is about 0.07 ms^{-1} along the Jiangsu coast. The form drag (Exp1–Exp4) can generate the largest surface flow (0.14 ms^{-1} in maximum), which flows northward to northeastward (**Figure 13G**). The wave dissipation in the TKE equation (Exp1–Exp5) can induce southward surface flow with a magnitude of 0.10 ms^{-1}, which is basically opposite to that induced by the form drag (**Figure 13H**). The WRS (Exp1–Exp6) also generates weak surface flow in the study area. Similar to the flow induced by the CWCBS, the WRS can generate an anticlockwise circulation off the CRE (**Figure 13I**). The CARWE (Exp1–Exp7) generates northeastward surface flow along the Zhejiang coast but southward flow along the Jiangsu coast (**Figure 13J**). There is also a northward surface flow from the Hangzhou Bay to the CRE along 122°E until 33°N, which turns sharply to the southward on 123°E. All the wave–current interaction processes can enhance the TWC inshore branch. The CWCBS, the wave dissipation on turbulence, and the WRS work together to weaken the

TABLE 2 | The root mean square (RMS) of the difference between the control run and each experiment on surface salinity, bottom salinity, ΔS, vertical velocity, and low-salinity water (LSW) core salinity, and the detachment time and L_x calculated by Equation (13) in each experiment.

Experiment	RMS					Detachment time	L_x (km)
	Surface salinity	Bottom salinity	ΔS	Vertical velocity	LSW core salinity		
Exp3 (NoCWCBS)	0.5379	0.4118	0.3093	0.1132	0.25	10:00 July 13	13.71
Exp4 (NoFormDrag)	1.7806	0.6187	1.8351	0.1823	4.11	23:00 July 13	50.55
Exp5 (NoWDinTKE)	0.8030	0.3841	0.6623	0.1754	1.13	20:00 July 13	36.97
Exp6 (NoWRS)	0.5107	0.3207	0.3488	0.0549	0.70	11:00 July 13	13.18
Exp7 (NoCARWE)	0.7899	0.4558	0.6174	0.2017	0.72	16:00 July 13	26.99

northeastward surface flow along the CDW pathway (**Figure 8I**), which in turn is enhanced by the form drag and the CARWE.

The wave-driven flow in the bottom layer is much weaker in magnitude, only about 19% of the surface wave-driven flow in average. The bottom flow generated by the CWCBS is similar to that on the surface (**Figure 13K**). The form drag induces a landward bottom flow, which has a relatively large speed of 0.02 ms^{-1} compared to the other experiments (**Figure 13L**). The bottom flow induced by the wave dissipation on turbulence (**Figure 13M**) and the WRS (**Figure 13N**) have similar patterns, which enhances the TWC inshore branch. The CARWE generates a southward coastal flow from the Jiangsu coast to the Hangzhou Bay and an anticlockwise circulation offshore (**Figure 13O**). The combination of the flow driven by each wave–current interaction process differs from the wave-driven flow calculated by Exp1-Exp2 (**Figures 8I,L**), which indicates the strong non-linear interactions between those individual processes.

Upwelling

The difference of the vertical-averaged vertical velocity along the cross-section A between the control run and each wave–current interaction experiment is calculated from July 11 to 19 (**Figures 9D–F**). The CWCBS and the WRS only enhanced the upwelling on 122.1°E from July 13 to 15 (not shown), which cannot support the double-core upwelling system. The wave dissipation (**Figure 9E**) and CARWE (**Figure 9F**) have a similar impact on the upwelling. They strengthened the upwelling from July 13 to 15, when the double-core upwelling was formed: one core was on 122.2°E and the other one was initially formed on 122.4°E but gradually moved eastward and decayed. It indicates the retreat of TWC inshore branch due to decrease of southerly wind (Wang et al., 2019). The effect of form drag on upwelling is complicated (**Figure 9D**). It enhanced the cores on 122.1°E and 122.2°E from July 14 until July 19; and another core appeared on 122.3°E from July 14 to 19 and it extended eastward on July 16.

Similarly, the RMSs of the wave-induced upwelling difference between the control run and each experiment are also given in **Table 2**. It indicates the CARWE has the largest impact on the wave-induced upwelling in five experiments. The form drag and the wave dissipation have less but comparable impact on the upwelling, followed by the CWCBS and WRS.

Detachment and Movement of Low-Salinity Water

To compare the effect of individual wave–current interaction process on the LSW detachment, the occurrence time of the detachment in each experiment is compared in **Table 2**. The SSS on July 13 and 14 in each experiment is also plotted in **Figure 10**. It shows that the LSW closed by 22 psu isohaline was detached on 23:00 July 13 in Exp2, meanwhile the LSW closed by 24 psu isohaline was detached on 07:00 July 13 in Exp1. Excluding the form drag in Exp4, the LSW closed by 22 psu isohaline left the CDW main body on 23:00 July 13 (**Figures 10C,I**); meanwhile in the other experiments, the LSW was detached with a closed 24 psu isohaline (**Figure 10**). Compared to the control run, it was 3 h, 13 h, 4 h, and 9 h delayed in Exp3 (NoCWCBS), Exp5 (NoWDinTKE), Exp6 (NoWRS) and Exp7 (NOCARWE), respectively. It indicates the form drag affects the detachment most, followed by the wave dissipation on turbulence, the CARWE, the WRS and the CWCBS.

The trajectories of the isolated LSW in Exp3∼Exp7 are shown in **Figure 11B**. The trajectory in Exp4 (NoFormDrag) is most similar to that in Exp2 (NoWave), while the others are similar to that in Exp1 (CR). To quantify the difference between the experiments, the following calculation is used:

$$L_x = \frac{\sum_{i=1}^{N} |L_{xi} - L_{1i}|}{N} \tag{15}$$

where L_{xi} is the location of the isolated LSW center on the ith day in experiment x, i.e., Exp3∼Exp7; L_{1i} is the location of the isolated LSW center on the ith day in Exp1; and N is the total days since the LSW detached to July 31. L_x represents the similarity of trajectory between the individual wave–current interaction experiment and the control run; and a larger L_x indicates the wave–current interaction process plays a more important role in the LSW migration. The result is given in **Table 2**. It indicates the form drag (Exp4) is the most important process to impact the LSW migration, followed the wave dissipation on turbulence (Exp5), the CARWE (Exp7). The CWCBS (Exp3) and WRS (Exp6) have the least influence on the LSW movement.

Similarly, the RMSs of daily-averaged LSW core salinity difference after the detachment between the control run and individual wave–current interaction process experiment are calculated and listed in **Table 2**. Also, a larger RMS indicates the wave–current interaction process has a more important effect on the variation of LSW core salinity. The results indicate the form drag (Exp4) has the greatest influence on the core salinity, followed by the wave dissipation on turbulence (Exp5), the CARWE (Exp7) and the WRS (Exp6). The CWCBS (Exp3) has the least influence on the LSW core salinity.

CONCLUSION

In this paper, the wave effects on LSW detachment from the Changjiang River plume are evaluated in the view of wind-enhanced vertical mixing, northward flows intrusion and upwelling. Further comparison between the experiments considering and not considering waves indicates waves are not the controlling factor of the LSW detachment, but they can accelerate the detachment of LSW from the river plume. Using PEA, the detachment of LSW can be explained as the low PEA water squeezing the high PEA water. Influenced by the waves' adjustment to the shelf circulation, wave-enhanced double-core upwelling squeezes the CDW vertically and reduces the thickness of CDW; strengthened northward flow brings south saline seawater here and intrudes the CDW front; and the enhanced vertical mixing increases the surface salinity. To summarize, the non-uniform impacts of waves promote the non-uniform variations at the CDW front, which is conducive to the LSW detachment. The wave-enhanced vertical mixing will enlarge the core salinity of the isolated LSW when detached; furthermore, it will accelerate the growth rate of the core salinity during its subsequent evolution. Waves also affect the trajectory of the isolated LSW, which is moved further northward and travels faster.

The comparison among experiments driven by different wave–current interaction processes illustrates the form drag almost dominates the wave effects on the river plume, the detachment, and the movement of LSW. It works through the wind-induced pressure and the wave setup in the momentum Equation (4) and the TKE Equations (6) and (7). The wave-weakened northeastward surface flow along the CDW pathway, which confines the CDW extension, is mainly caused by the wave dissipation in the TKE equations. The CARWE obviously enhances the magnitude of the double-core upwelling system. But this effect declines with the decaying wave-driven flow. It indicates the interrelationship between those individual wave–current interactions. The waves affect the salinity mainly on the CDW pathway, but the wave-driven flow and the wave-enhanced upwelling are dramatical within 50 m isobath. The wave effects on the isolated LSW continue until the LSW disappears. Previous work to quantify the individual wave–current interaction process by using the FVCOM-MDO model shows that the CWCBS plays the most important role in suspended sediment transport in coastal seas (Gao et al., 2018), and the WRS dominates the bay-shelf exchange (Song et al., 2021). However, in this study, it shows that form drag is the most significant wave effect on the detachment and movement of the LSW, mostly because it occurs in the surface layer. It also confirms that waves are important to several ocean processes, but the dominant wave–current interaction mechanisms are different (Song et al., 2021).

As the offshore LSW is significant to inner-shelf biogeochemical processes (Wei et al., 2017, 2020; Qu et al., 2019), the existence duration and pathway of the isolated LSW seems important to the water quality and the harmful algae bloom. Therefore, the impact of wave effects on the biogeochemical process will be further explored.

DATA AVAILABILITY STATEMENT

The datasets presented in this study can be found in online repositories. The names of the repository/repositories and accession number(s) can be found below: https://doi.org/10.6084/m9.figshare.13649780.v2.

AUTHOR CONTRIBUTIONS

ZJ contributed to the software, formal analysis, and writing – original draft. DS contributed to the conceptualization, methodology, and writing – review and editing. QW contributed to the investigation and resources. YD contributed to the software and writing – review and editing. All authors contributed to the article and approved the submitted version.

FUNDING

This study was financially supported by the National Natural Science Foundation of China (Grant Numbers 41876088 and 41876085) and the Ocean University of China and Woods Hole Oceanographic Institution Collaborative Project (Grant Number 23427).

ACKNOWLEDGMENTS

The numerical simulation was conducted at the High-Performance Scientific Computing and System Simulation Platform of Pilot National Laboratory for Marine Science and Technology (Qingdao).

REFERENCES

Akan, Ç, Moghimi, S., Özkan-Haller, H. T., Osborne, J., and Kurapov, A. (2017). On the dynamics of the Mouth of the Columbia River: results from a three-dimensional fully coupled wave-current interaction model. *J. Geophys. Res. Oceans* 122, 5218–5236. doi: 10.1002/2016jc012307

Beardsley, R. C., Limeburner, R., Yu, H., and Cannon, G. A. (1985). Discharge of the Changjiang (Yangtze River) into the East China Sea. *Continental Shelf Res.* 4, 57–76. doi: 10.1016/0278-4343(85)90022-90026

Chen, C., Beardsley, R. C., Limeburner, R., and Kim, K. (1994). Comparison of winter and summer hydrographic observations in the Yellow and East China Seas and adjacent Kuroshio during 1986. *Continental Shelf Res.* 14, 909–929. doi: 10.1016/0278-4343(94)90079-90075

Chen, C., Liu, H., and Beardsley, R. C. (2003). An unstructured grid, finite-volume, three-dimensional, primitive equations ocean model: application to coastal ocean and estuaries. *J. Atmospheric Oceanic Technol.* 20, 159–186. doi: 10.1175/1520-0426(2003)020<0159:augfvt>2.0.co;2

Chen, C., Xue, P., Ding, P., Beardsley, R. C., Xu, Q., Mao, X., et al. (2008). Physical mechanisms for the offshore detachment of the Changjiang Diluted Water in the East China Sea. *J. Geophys. Res.* 113, 1–17. doi: 10.1029/2006jc003994

Chen, Z., Pan, J., and Jiang, Y. (2016). Role of pulsed winds on detachment of low salinity water from the Pearl River Plume: upwelling and mixing processes. *J. Geophys. Res. Oceans* 121, 2769–2788. doi: 10.1002/2015jc011337

Delpey, M. T., Ardhuin, F., Otheguy, P., and Jouon, A. (2014). Effects of waves on coastal water dispersion in a small estuarine bay. *J. Geophys. Res. Oceans* 119, 70–86. doi: 10.1002/2013JC009466

Ding, Y., Bao, X., Yao, Z., Bi, C., Wan, K., Bao, M., et al. (2019). Observational and model studies of synoptic current fluctuations in the Bohai Strait on the Chinese continental shelf. *Ocean Dynam.* 69, 323–351. doi: 10.1007/s10236-019-01247-1245

Ding, Y., Bao, X., Yao, Z., Song, D., Song, J., Gao, J., et al. (2018). Effect of coastal-trapped waves on the synoptic variations of the Yellow Sea Warm Current during winter. *Continental Shelf Res.* 167, 14–31. doi: 10.1016/j.csr.2018.08.003

Donelan, M. A., Hamilton, J., Hui, W. H., and Stewart, R. W. (1985). Directional spectra of wind-generated ocean waves. *Philos. Trans. R. Soc. London. Series A Mathematical Phys. Sci.* 315, 509–562. doi: 10.1098/rsta.1985.0054

Fairall, C. W., Bradley, E. F., Rogers, D. P., Edson, J. B., and Young, G. S. (1996). Bulk parameterization of air-sea fluxes for tropical ocean-global atmosphere coupled-ocean atmosphere response experiment. *J. Geophys. Res. Oceans* 101, 3747–3764. doi: 10.1029/95JC03205

Galperin, B., Kantha, L. H., Hassid, S., and Rosati, A. (1988). A quasi-equilibrium turbulent energy model for geophysical flows. *J. Atmospheric Sci.* 45, 55–62. doi: 10.1175/1520-0469(1988)045<0055:aqetem>2.0.co;2

Gan, J., Li, L., Wang, D., and Guo, X. (2009). Interaction of a river plume with coastal upwelling in the northeastern South China Sea. *Continental Shelf Res.* 29, 728–740. doi: 10.1016/j.csr.2008.12.002

Gao, G. D., Wang, X. H., Song, D., Bao, X., Yin, B. S., Yang, D. Z., et al. (2018). Effects of wave-current interactions on suspended-sediment dynamics during strong wave events in Jiaozhou Bay, Qingdao, China. *J. Phys. Oceanography* 48, 1053–1078. doi: 10.1175/jpo-d-17-0259.1

Gao, G., Marin, M., Feng, M., Yin, B., Yang, D., Feng, X., et al. (2020). Drivers of Marine Heatwaves in the East China Sea and the South Yellow Sea in Three Consecutive Summers During 2016-2018. *J. Geophys. Res. Oceans* 125, 1–19. doi: 10.1029/2020jc016518

García Berdeal, I., Hickey, B. M., and Kawase, M. (2002). Influence of wind stress and ambient flow on a high discharge river plume. *J. Geophys. Res. Oceans* 107:13-11-13-24. doi: 10.1029/2001JC000932.

Ge, J., Ding, P., and Chen, C. (2015). Low-salinity plume detachment under non-uniform summer wind off the Changjiang Estuary. *Estuarine Coastal Shelf Sci.* 156, 61–70. doi: 10.1016/j.ecss.2014.10.012

Gerbi, G. P., Chant, R. J., and Wilkin, J. L. (2013). Breaking surface wave effects on river plume dynamics during upwelling-favorable winds. *J. Phys. Oceanography* 43, 1959–1980. doi: 10.1175/jpo-d-12-0185.1

Gong, W., Lin, Z., Chen, Y., Chen, Z., Shen, J., and Zhang, H. (2018). Effect of waves on the dispersal of the Pearl River plume in winter. *J. Mar. Systems* 186, 47–67. doi: 10.1016/j.jmarsys.2018.05.003

Guan, B., and Fang, G. (2006). Winter counter-wind currents off the southeastern China coast: a review. *J. Oceanography* 62, 1–24. doi: 10.1007/s10872-006-0028-28

Guo, X., and Yanagi, T. (1998). Three-dimensional structure of tidal current in the East China Sea and the Yellow Sea. *J. Oceanography* 54, 651–668. doi: 10.1007/BF02823285

He, H., Song, J., Bai, Y., Xu, Y., Wang, J., and Bi, F. (2018). Climate and extrema of ocean waves in the East China Sea. *Sci. China Earth Sci.* 61, 980–994. doi: 10.1007/s11430-017-9156-9157

Jurisa, J. T., and Chant, R. (2012). The coupled Hudson River estuarine-plume response to variable wind and river forcings. *Ocean Dynamics* 62, 771–784. doi: 10.1007/s10236-012-0527-527

Kang, S. K., Lee, S.-R., and Lie, H.-J. (1998). Fine grid tidal modeling of the Yellow and East China Seas. *Cont. Shelf Res.* 18, 739–772. doi: 10.1016/S0278-4343(98)00014-4

Kumar, N., Cahl, D. L., Crosby, S. C., and Voulgaris, G. (2017). Bulk versus spectral wave parameters: implications on stokes drift estimates, regional wave modeling, and HF radars applications. *J. Phys. Oceanography* 47, 1413–1431. doi: 10.1175/JPO-D-16-0203.1

Lie, H.-J., and Cho, C.-H. (2016). Seasonal circulation patterns of the Yellow and East China Seas derived from satellite-tracked drifter trajectories and hydrographic observations. *Prog. Oceanography* 146, 121–141. doi: 10.1016/j.pocean.2016.06.004

Lie, H.-J., Cho, C.-H., Lee, J.-H., and Lee, S. (2003). Structure and eastward extension of the Changjiang River plume in the East China Sea. *J. Geophys. Res.* 108, 1–14. doi: 10.1029/2001jc001194

Liu, Q., Rothstein, L. M., and Luo, Y. (2017). A periodic freshwater patch detachment process from the Block Island Sound estuarine plume. *J. Geophys. Res. Oceans* 122, 570–586. doi: 10.1002/2015JC011546

Mellor, G. (2003). The three-dimensional current and surface wave equations. *J. Phys. Oceanography* 33, 1978–1989. doi: 10.1175/1520-0485(2003)033<1978:ttcasw>2.0.co;2

Mellor, G. (2015). A combined derivation of the integrated and vertically resolved, coupled wave-current equations. *J. Phys. Oceanography* 45, 1453–1463. doi: 10.1175/jpo-d-14-0112.1

Mellor, G. L. (2008). The depth-dependent current and wave interaction equations: a revision. *J. Phys. Oceanography* 38, 2587–2596. doi: 10.1175/2008JPO3971.1

Mellor, G. L. (2013). Pressure-slope momentum transfer in ocean surface boundary layers coupled with gravity waves. *J. Phys. Oceanogr.* 43, 2173–2184. doi: 10.1175/JPO-D-13-068.1

Mellor, G. L., and Yamada, T. (1982). Development of a turbulence closure model for geophysical fluid problems. *Rev. Geophys. Space Phys.* 20, 851–875. doi: 10.1029/RG020i004p00851

Mellor, G. L., Donelan, M. A., and Oey, L.-Y. (2008). A surface wave model for coupling with numerical ocean circulation models. *J. Atmospheric Oceanic Technol.* 25, 1785–1807. doi: 10.1175/2008jtecho573.1

Mellor, G., and Blumberg, A. (2004). Wave breaking and ocean surface layer thermal response. *J. Phys. Oceanography* 34, 693–698. doi: 10.1175/2517.1

Moon, J.-H., Hirose, N., Yoon, J.-H., and Pang, I.-C. (2010). Offshore detachment process of the low-salinity water around Changjiang Bank in the East China Sea. *J. Phys. Oceanography* 40, 1035–1053. doi: 10.1175/2010jpo4167.1

Pu, Y. (1981). Surface water mass and circulation in the northern East China Sea. *Mar. Sci. Bull.* 5, 23–36.

Pu, Y., and Xu, X. (1983). The expansion of diluted water in the Changjiang (Yangtz River) as seen from the variations in the runoff, water level and salinity. *Mar. Sci. Bull.* 2, 1–7.

Qu, D., Yu, H., Sun, Y., Zhao, Y., Wei, Q., Yu, H., et al. (2019). Numerical study on the summertime patches of red tide in the adjacent sea of the Changjiang (Yangtze) River Estuary, China. *Mar. Pollution Bull.* 143, 242–255. doi: 10.1016/j.marpolbul.2019.04.027

Rong, Z., and Li, M. (2012). Tidal effects on the bulge region of Changjiang River plume. *Estuarine Coastal Shelf Sci.* 97, 149–160. doi: 10.1016/j.ecss.2011.11.035

Rong, Z., Hetland, R. D., Zhang, W., and Zhang, X. (2014). Current-wave interaction in the Mississippi-Atchafalaya river plume on the Texas-Louisiana shelf. *Ocean Modell.* 84, 67–83. doi: 10.1016/j.ocemod.2014.09.008

Saha, S., Moorthi, S., Pan, H. L., Wu, X., Wang, J., Nadiga, S., et al. (2010). The NCEP climate forecast system reanalysis. *Bull. Am. Meteorol. Soc.* 91, 1015–1058. doi: 10.1175/2010bams3001.1

Schloen, J., Stanev, E. V., and Grashorn, S. (2017). Wave-current interactions in the southern North Sea: the impact on salinity. *Ocean Modell.* 111, 19–37. doi: 10.1016/j.ocemod.2017.01.003

Shu, Y., Wang, D., Zhu, J., and Peng, S. (2011). The 4-D structure of upwelling and Pearl River plume in the northern South China Sea during summer 2008 revealed by a data assimilation model. *Ocean Modell.* 36, 228–241. doi: 10.1016/j.ocemod.2011.01.002

Simpson, J. H. (1981). The shelf-sea fronts: implications of their existence and behaviour. *Philos. Trans. R. Soc. London. Series A Mathematical Phys. Sci.* 302, 531–546. doi: 10.1098/rsta.1981.0181

Smagorinsky, J. (1963). General circulation experiments with the primitive equations: I. the basic experiment. *Monthly Weather Rev.* 91, 99–164. doi: 10.1175/1520-0493(1963)091<0099:gcewtp>2.3.co;2

Song, D., Wang, X. H., Zhu, X., and Bao, X. (2013). Modeling studies of the far-field effects of tidal flat reclamation on tidal dynamics in the East China Seas. *Estuarine Coastal Shelf Sci.* 133, 147–160. doi: 10.1016/j.ecss.2013.08.023

Song, D., Wu, W., and Li, Q. (2021). Effects of wave-current interactions on bay-shelf exchange. *J. Phys. Oceanography* 51, 1637–1654. doi: 10.1175/JPO-D-20-0222.1

Soulsby, R. L. (1995). "Bed shear-stresses due to combined waves and currents," in *Advances in Coastal Morphodynamics*, eds M. Stive, J. Fredsøe, L. Hamm, R. Soulsby, C. Teisson, and J. Winterwerp (Delft: Delft Hydraulics).

Su, J., and Wang, K. (1989). Changjiang river plume and suspended sediment transport in Hangzhou Bay. *Continental Shelf Res.* 9, 93–111. doi: 10.1016/0278-4343(89)90085-X

US Naval Oceanographic Office, and the US Naval Ocean Research, and Development Activity (1983). *DBDB5 (Digital Bathymetric Data Base-5 minute grid)*. Bay St. Louis: US N.O.O.

Wang, J., and Shen, Y. (2010). Modeling oil spills transportation in seas based on unstructured grid, finite-volume, wave-ocean model. *Ocean Modell.* 35, 332–344. doi: 10.1016/j.ocemod.2010.09.005

Wang, J., and Shen, Y. (2012). On the development and verification of a parametric parallel unstructured-grid finite-volume wind wave model for coupling with ocean circulation models. *Environ. Modell. Software* 37, 179–192. doi: 10.1016/j.envsoft.2012.03.019

Wang, J., Yu, F., Ren, Q., Si, G., and Wei, C. (2019). The observed variations of the north intrusion of the bottom Taiwan Warm Current Inshore Branch and its response to wind. *Reg. Stud. Mar. Sci.* 30:100690. doi: 10.1016/j.rsma.2019.100690

Wei, Q., Wang, B., Zhang, X., Ran, X., Fu, M., Sun, X., et al. (2020). Contribution of the offshore detached Changjiang (Yangtze River) Diluted Water to the formation of hypoxia in summer. *Sci. Total Environ.* 764:142838. doi: 10.1016/j.scitotenv.2020.142838

Wei, Q., Yu, Z., Wang, B., Wu, H., Sun, J., Zhang, X., et al. (2017). Offshore detachment of the Changjiang River plume and its ecological impacts in summer. *J. Oceanography* 73, 277–294. doi: 10.1007/s10872-016-0402-400

Wu, H., Shen, J., Zhu, J., Zhang, J., and Li, L. (2014). Characteristics of the Changjiang plume and its extension along the Jiangsu Coast. *Continental Shelf Res.* 76, 108–123. doi: 10.1016/j.csr.2014.01.007

Wu, H., Zhu, J., Shen, J., and Wang, H. (2011). Tidal modulation on the Changjiang River plume in summer. *J. Geophys. Res.* 116, 1–21. doi: 10.1029/2011jc007209

Wu, R., Wu, H., and Wang, Y. (2021). Modulation of shelf circulations under multiple river discharges in the East China Sea. *J. Geophys. Res. Oceans* 126:e2020JC016990. doi: 10.1029/2020JC016990

Xuan, J.-L., Huang, D., Zhou, F., Zhu, X.-H., and Fan, X. (2012). The role of wind on the detachment of low salinity water in the Changjiang Estuary in summer. *J. Geophys. Res. Oceans* 117:C10004. doi: 10.1029/2012jc008121

Yankovsky, A. E., Hickey, B. M., and Münchow, A. K. (2001). Impact of variable inflow on the dynamics of a coastal buoyant plume. *J. Geophys. Res. Oceans* 106, 19809–19824. doi: 10.1029/2001JC000792

Yu, X., Guo, X., and Gao, H. (2020). Detachment of low-salinity water from the Yellow River plume in summer. *J. Geophys. Res. Oceans* 125:e2020JC016344. doi: 10.1029/2020jc016344

Zhang, W.-J., Zhu, S.-X., Li, X.-Q., Ruan, K., Guan, W.-B., and Peng, J. (2014). Numerical simulation and dynamical analysis for low salinity water lens in the expansion area of the Changjiang diluted water. *China Ocean Eng.* 28, 777–790. doi: 10.1007/s13344-014-0060-61

Zhao, B., Fang, G., and Cao, D. (1995). Characteristics of tidal residual currents and their relations with coastal current transports in the Bohai Sea. Yellow Sea and East China Sea. *Stud. Mar. Sin.* 36, 1–11.

Zhu, J., Chen, C., Ding, P., Li, C., and Lin, H. (2004). Does the Taiwan warm current exist in winter? *Geophys. Res. Lett.* 31:L12302. doi: 10.1029/2004GL019997

Zhu, P., and Wu, H. (2018). Origins and transports of the low-salinity coastal water in the southwestern Yellow Sea. *Acta Oceanol. Sinica* 37, 1–11. doi: 10.1007/s13131-018-1200-x

Conflict of Interest: The authors declare that the research was conducted in the absence of any commercial or financial relationships that could be construed as a potential conflict of interest.

Publisher's Note: All claims expressed in this article are solely those of the authors and do not necessarily represent those of their affiliated organizations, or those of the publisher, the editors and the reviewers. Any product that may be evaluated in this article, or claim that may be made by its manufacturer, is not guaranteed or endorsed by the publisher.

Copyright © 2022 Jiang, Song, Wei and Ding. This is an open-access article distributed under the terms of the Creative Commons Attribution License (CC BY). The use, distribution or reproduction in other forums is permitted, provided the original author(s) and the copyright owner(s) are credited and that the original publication in this journal is cited, in accordance with accepted academic practice. No use, distribution or reproduction is permitted which does not comply with these terms.

frontiers | Frontiers in Marine Science

ORIGINAL RESEARCH
published: 08 April 2022
doi: 10.3389/fmars.2022.881383

Differential Impact of the Khatanga and Lena (Laptev Sea) Runoff on the Distribution and Grazing of Zooplankton

Anna Pasternak, Alexander Drits, Elena Arashkevich and Mikhail Flint*

Shirshov Institute of Oceanology, Russian Academy of Sciences, Moscow, Russia

The ecosystems of the Arctic Ocean and their expected changes in a context of Global climate processes are crucially dependent on the freshwater input. The freshwater signal is assumed to be the main structuring factor for the marine fauna on the shallow shelf of the Siberian Arctic seas. The Laptev Sea, as a part of the world's widest continental shelves surrounding the Arctic Ocean, is a key area for understanding the land–ocean interaction in high latitude regions. The largest freshwater input is provided by the deltaic Lena river followed by the estuarine Khatanga river. The plumes of these rivers differ considerably in their hydrophysical characteristics, suggesting differential impacts on ecosystems of the adjacent shelf. The key component of pelagic ecosystems is zooplankton, which transfers energy from primary producers to higher trophic levels and modifies sedimentations processes. This study is focused on the influence of river discharge on zooplankton in the Laptev Sea at the end of productive season. We studied zooplankton biomass, species composition, distribution patterns of the dominant species and assessed herbivorous feeding rates and grazing pressure of these species along a transect from the inner Khatanga Gulf northward to the continental slope, and a transect in the Lena plume influenced area in August-September 2017. Despite large spatial extension of the Khatanga plume, the impact of river discharge on zooplankton species composition was restricted mainly to the inner Gulf where the brackish species shaped the community. Contrary to the Khatanga input, the Lena freshwater inflow was highly variable and under certain conditions (discharge rate, wind forcing) governed the structure of zooplankton community over a vast shelf area. Distribution patterns of zooplankton biomass, ingestion rates and grazing impact of the dominant species on phytoplankton over the shelf influenced by the Khatanga and Lena plumes were similar. Analysis of our results on demographic structure of *Calanus glacialis* suggests that seasonal development of the population was largely controlled by the time of ice retreat. Observed climatic changes in the Arctic were not reflected in the total zooplankton biomass and composition of the dominant species.

Keywords: Laptev sea, zooplankton distribution, Khatanga, Lena, river plume, herbivorous feeding, gazing impact

OPEN ACCESS

Edited by:
Alexander Yankovsky, University of South Carolina, United States

Reviewed by:
Atsushi Yamaguchi, Hokkaido University, Japan
Joshua Stone, University of South Carolina, United States

****Correspondence:***
Anna Pasternak
pasternakanna@hotmail.com

Specialty section:
This article was submitted to Coastal Ocean Processes, a section of the journal Frontiers in Marine Science

Received: *22 February 2022*
Accepted: *18 March 2022*
Published: *08 April 2022*

Citation:
Pasternak A, Drits A, Arashkevich E and Flint M (2022) Differential Impact of the Khatanga and Lena (Laptev Sea) Runoff on the Distribution and Grazing of Zooplankton. Front. Mar. Sci. 9:881383. doi: 10.3389/fmars.2022.881383

INTRODUCTION

The present day condition of the Arctic Ocean and its changes in a context of Global climatic processes are crucially dependent on the freshwater input which is mainly derived from river discharge. Overall freshwater delivery to the Arctic is ~3300 km^3 y^{-1} which makes up 11% of Global river run-off, although Arctic holds only 1% of the global ocean volume (McClelland et al., 2011). Among these 11% of the river discharge, more than 6% is accepted by the Siberian Arctic Seas (Fütterer and Galimov, 2003).

Freshwater discharge in the Arctic strongly influences hydrophysical, hydrochemical and biological processes not only in the estuarine areas, but also over the wide shelf areas (Fütterer and Galimov, 2003; Flint et al., 2018; Flint et al., 2021). The freshening effect and the formed long living freshened "lenses" usually extend as far north as the continental slope (Flint et al., 2018; Flint et al., 2021). River discharge plays a pivotal role in the interaction between terrestrial and marine environments which is a process of Global importance, especially in the Arctic, where it acts as a mechanism of delivery of climatic signal to high latitudes.

The rivers' inflows create an extremely variable environment for pelagic communities in terms of salinity, temperature, turbidity, and nutrients. The enhanced delivery of nutrients to the phytoplankton populations, the basis of the aquatic trophic webs, could increase the resource for primary production. A spatio-temporally resolved biogeochemical model estimated that river input of carbon and nutrients to the Arctic Ocean fuels 28–51% of the current annual Arctic Ocean net primary production (Terhaar et al., 2021). A vast amount of the allochthonous organic matter is transformed in the shelf areas adjacent to the large rivers' mouths (Gordeev et al., 1996). In the processes of transformation of organic matter, an essential role belongs to mesozooplankton which transfers energy from primary producers to higher trophic levels and modifies sedimentations processes, either enhancing retention in the upper water layer, or increasing sedimentation rates (Steinberg and Landry, 2017). Freshwater signal was shown to determine the structure (species composition, distribution, biomass) (e.g., Abramova and Tuschling, 2005; Hirche et al., 2006; Flint et al., 2010) and foraging activity (e.g., Drits et al., 2017; Arashkevich et al., 2018; Drits et al., 2020) of zooplankton in the river plume-affected areas. One of the remarkable consequences of the river runoff influence on zooplankton is formation of dense aggregations with extremely high biomass associated with high gradient zones (Vinogradov et al., 1995; Flint et al., 2010; Drits et al., 2017). Such dense aggregations determine high efficiency of the so-called "pelagic biofilter", where a considerable part of the organic matter discharged by the river is utilized (Flint et al., 2010). Impact of the freshwater discharge on zooplankton may vary depending of the runoff volume and seasonal regime, bathymetry and orography of estuaries, hydrographical structure of the plumes. As annual Arctic river inflow is expected to increase by 10–20% under a doubled CO_2 scenario (ACIA, 2005), impact of freshwater discharge on zooplankton could be more pronounced, e.g., expanding over larger shelf areas.

The Laptev Sea, as a part of the world's widest continental shelves surrounding the Arctic Ocean, is a key area for understanding the land–ocean interaction in high latitude regions.

The Laptev Sea receives annually 820 km^3 of the river runoff which is the second (after the Kara Sea) freshwater contribution to the Arctic seas (Gordeev et al., 1996; Williams and Carmack, 2015). The majority of these volumes is provided by discharges from the large deltaic Lena river (590 km^3 y^{-1}) which inflows to the southeastern Laptev Sea and estuarine Khatanga river (105 km^3 y^{-1}) which inflows to the southwestern Laptev Sea. Plumes of these two rivers do not merge (Fofonova et al., 2015) and have an influencing control over the environment of this Arctic marginal sea, which is ice-covered during most of the year. River runoff noticeably contributes to ice melting in the Siberian Arctic seas (Eicken et al., 1997; Nghiem et al., 2014). In the Laptev Sea, Lena warm water is an important heat source for the early local breakup of ice cover (Bauch et al., 2013), which, in turn, could regulate seasonal phytoplankton bloom and development of pelagic biota.

The results of the studies on zooplankton in the Laptev Sea indicate the importance of the freshwater discharge for composition, distribution and abundance of mesozooplankton communities (Kosobokova et al., 1998; Lischka et al., 2001; Abramova and Tuschling, 2005; Arashkevich et al., 2018). Freshwater discharge forms a salinity gradient along which different zooplankton assemblages change in turn from freshwater/brackish to euryhaline and marine assemblage (Jashnov, 1940; Kosobokova et al., 1998; Lischka et al., 2001). While the western and northeastern Laptev Sea shelf is dominated by a marine–neritic fauna, the central part is inhabited by a transitional brackish–marine assemblage. A brackish–neritic community characterizes the eastern and southeastern regions, where lowest salinities usually prevail. Closer to estuaries, the summer zooplankton consists of both freshwater and brackish-water species, whereas in winter, brackish-water species are dominant (Abramova and Tuschling, 2005). Highest zooplankton biomass was reported in the northern and northeastern parts of the

Laptev Sea, as well as close to the river inflows (Kosobokova et al. 1998; Lischka et al., 2001; Arashkevich et al., 2018). investigated zooplankton composition and biomass in the slope region and the outer Laptev Sea in the direction of the Nansen Basin and concluded that zooplankton standing stock was lower than in the other Arctic seas. It may be, however, connected with the study area, as shallow shelf areas with enhanced zooplankton biomass were not included in this study (Lischka et al., 2001).

The majority of the data on zooplankton in the shallow Laptev Sea shelf were obtained in the eastern and central parts of the sea influenced by the Lena plume. Little is known about pelagic fauna in the Khatanga region. The structure and abundance of zooplankton in the inner Khatanga Gulf was not studied at all. Knowledge on species composition and abundance

of the communities in the shelf area influenced by the Khatanga plume is based on only few stations in the cited studies (Kosobokova et al., 1998; Lischka et al., 2001; Abramova and Tuschling, 2005).

To our knowledge, no data exist on grazing rates of zooplankton and grazing impact on phytoplankton in this area. There are only two studies on feeding patterns of zooplankton in the Laptev Sea, and they were performed in the eastern and central parts of the sea. These studies assessed diets of the dominant species on the basis of the analysis of the fatty acid composition (Peters et al., 2004) and estimated herbivorous ingestion rates of zooplankton and grazing impact on phytoplankton (Arashkevich et al., 2018).

Plumes formed by the estuarine Khatanga and deltaic Lena discharges differ by their hydrographical structure (Osadchiev et al., 2020; Osadchiev et al., 2021). The Lena discharge enters the sea undiluted from multiple channels and forms a shallow river plume (5-8 m depth) spreading over extremely large area. Shallow Lena plume is significantly affected by wind forcing conditions, which results in large inter-annual variability of its position and spatial extent (Osadchiev et al., 2021). Freshwater discharge from the Khatanga River, on the other hand, experiences strong tidal mixing in the Khatanga Gulf. As a result, the Khatanga plume is formed by relatively small volume of freshwater mixed with large volume of saline water. The weakly stratified Khatanga plume despite relatively low runoff rate (more than 5 times less than that of Lena) occupies large area (up to a distance of 150–250 km from the Khatanga Gulf) (Osadchiev et al., 2020). We hypothesize that in the Khatanga area strong tidal mixing could prevent propagation of brackish zooplankton over the shelf despite a pronounced plume extension. On the contrary, in the Lena area, the distribution of the different zooplankton assemblages is determined by the plume extension, and, under certain wind forcing conditions, brackish species could occupy a vast shelf area.

To address this hypothesis, we

1. Studied the structure of zooplankton community and distribution of dominant species along the transect from the inner Khatanga Gulf northward to the ice edge at the end of the productive season and compared these features with those obtained in the Lena plume affected area.
2. Followed the influence of temporal variability of the river plume extension on the composition and abundance of zooplankton at the repeated stations at each transect.
3. Estimated herbivorous feeding rates of the dominant zooplankton and grazing impact on phytoplankton biomass and production.

Additionally, the data obtained on the demographic structure of the population of *Calanus glacialis* allowed us to follow the influence of the timing of ice retreat on seasonal development of the population. This paper fills in the gap in understanding how composition, distribution and grazing of zooplankton communities are modified by river discharge with different hydrographical characteristics. The obtained results contribute to spatial coverage with data on zooplankton in the Laptev Sea and describe the state-of-the-art species composition, distribution and feeding in the river plume affected areas, which could serve as a benchmark in future studies.

MATERIALS AND METHODS

Zooplankton Sampling

The material was collected during cruise # 69 of the RV "Akademik Mstislav Keldysh" to the Laptev Sea from 31 August to 20 September 2017. In the western part of the Laptev Sea, a transect of 11 stations from the inner Khatanga Gulf northward to the continental slope was performed (**Figure 1**). The northernmost station 5635 was located at the ice edge. Two of the stations (5591_2 and 5590_2) were sampled at the same locations where the pilot stations 5591 and 5590 have been sampled two weeks earlier to follow a short-term variability in zooplankton composition and abundance. To estimate if there were diel changes in the vertical distribution of zooplankton, day and night sampling was done at the pilot station 5591.

In the eastern part of the Laptev Sea, three stations were carried out in the shelf adjacent to the Lena Delta on 2-3 September. Two of the stations (5596 and 5592) were repeated on 15-16 September, and one more station (5623), furthest from the Lena delta, was sampled on 15 September (**Figure 1**).

Simultaneously, data on temperature, salinity, and chlorophyll fluorescence were obtained from vertical CTD sounding with the SeaBird 19+ probe at all the stations.

Mesozooplankton was sampled using a Juday closing net (0.1 m^2 mouth area, 180 μm mesh size) towed vertically from 2-3 m above the bottom to the surface at all shallow stations. At deeper shelf stations, the layers below and above the pycnocline, which was determined according to the CTD profiles, were usually sampled. Five separate layers were sampled with a MultiNet multiple plankton sampler (mouth area 0.125 m^2, mesh size 180 μm) at the deepest station 5635 (**Table 1**). The volume of filtered water was calculated by multiplying mouth area value by the sampled depth layer. For determination of zooplankton abundance and biomass, samples were preserved in 4% borax-buffered formalin. Zooplankton were identified, staged, measured and counted in the laboratory under a stereomicroscope under x40 magnification. Not numerous large specimens (the older stages of *Calanus* spp., *Oikopleura vanhoeffeni, Limacina helicina, Parasagitta elegans*) were counted in the whole samples, while more numerous forms were counted in subsamples so as not less than 50 specimens were recorded. The copepodites of the closely related copepod species *Calanus finmarchicus* and *C. glacialis* were distinguished according to morphology and prosome lengths (Kwasniewski et al., 2003). For *Calanus* spp., all copepodite stages were distinguished, for *Pseudocalanus* spp. and *Drepanopus bungei*, copepodite stages CI to CIV were pooled. The wet weight (WW) of each species was calculated using nomograms by Chislenko (1968). These tables (1968; www.twirpx.com/file/1588162/) allow the calculation of biovolume (wet weight, WW) of

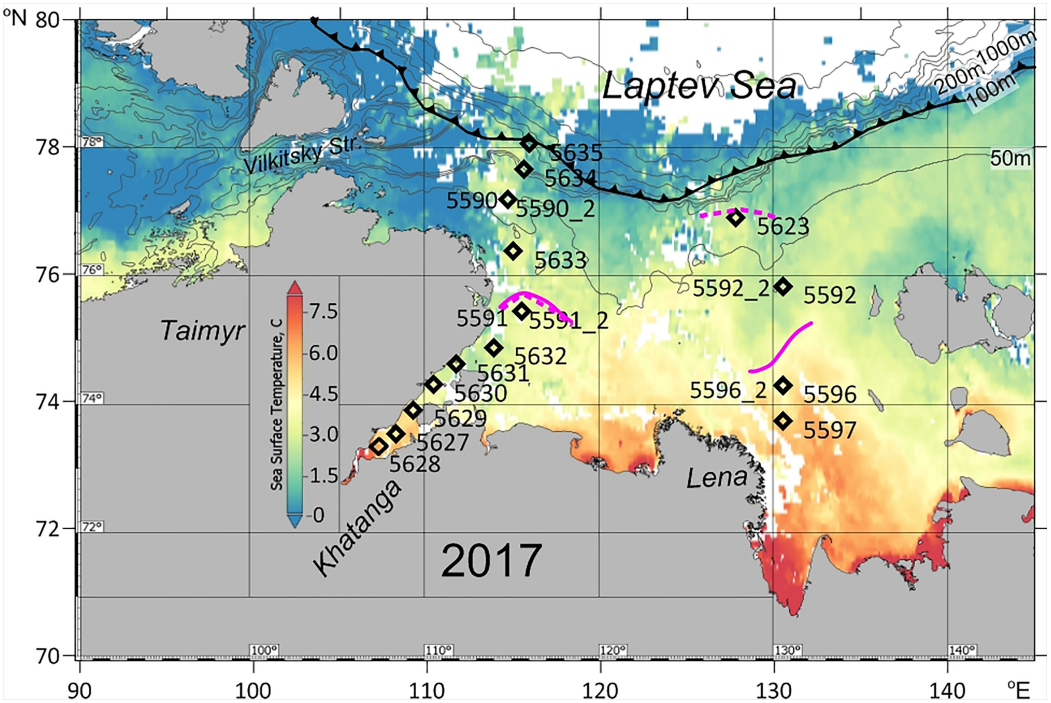


FIGURE 1 | Map of the study area with location of the stations. Sea surface temperature (° C) distribution: average for 29 August – 6 September 2017 (at 11 microns, MODIS-Aqua_L3_SST_8d_4km vR2019.0) (Berrick et al., 2009). Bold lines show the position of the ice boundary (http://www.aari.ru). Magenta lines indicate river plume extension (isohaline of 25): solid line - at the time of first sampling (31.08-3.09. 2017), dashed line - at the time of the repeated sampling (14.09-20.09.2017). Contour depths in meters. When sampling was repeated, the Lena plume considerably extended to the north, while Khatanga plume remained at the same position.

TABLE 1 | Sampling details and environmental characteristics at stations in the Khatanga and Lena areas.

Sampling area	Station	Latitude	Date	Time	Depth	Layer	Chl[a]	PP[b]
Khatanga area	5628	73.45	17.09.17	17:20	10	0-8	1.9	14
	5627	73.60	17.09.17	15:30	14	0-12	1.9	17
	5629	73.86	17.09.17	21:15	20	0-18	1.0	24
	5630	74.25	18.09.17	2:30	26	0-23	0.9	21
	5631	74.60	18.09.17	7:00	28	0-10, 10-25	0.9	49
	5632	74.83	18.09.17	17:20	32	0-10, 10-29	0.2	28
	5591	75.40	01.09.17	22:00, 10:00	43	0-10, 10-40	0.1	
	5591_2	75.40	18.09.17	17:40	43	0-10, 10-40	0.1	32
	5633	76.35	19.09.17	7:00	44	0-10, 10-41	0.3	20
	5590	77.15	31.08.17	20:00	58	0-20, 20-55	0.1	
	5590_2	77.15	19.09.17	13:00	66	0-20, 20-64	0.2	20
	5634	77.60	19.09.17	20:30	180	0-20, 20-40, 40-115, 115-175	0.2	48
	5635	77.90	20.09.17	9:30	840	0-20, 20-40, 40-100, 100-200, 200-700, 700-820	0.4	52
Lena area	5597	73.70	03.09.17	18:00	22	0-20	0.2	52
	5596	74.10	03.09.17	12:30	23	0-10. 10-20	0.1	22
	5596_2	74.10	14.09.17	8:30	23	0-10. 10-20	0.8	28
	5592	75.65	02.09.17	23:00	43	0-15, 15-40	0.1	10
	5592_2	75.65	14.09.17	20:30	43	0-15, 15-41	0.1	32

[a]*Data from Demidov et al., 2019.*

[b]*Data from Demidov et al., 2020 (Khatanga area) and Demidov A.B., personal communication (Lena area).*

Depth – depth (m) of the station, Layer – layers (m) of zooplankton sampling, Chl a – mean concentration of chlorophyll a (mg m^{-3}) in the photosynthetic layer, PP – primary production (mg C m^{-2} d^{-1}).

aquatic organisms on the basis of the body shape and length. Dry weight (DW) of crustacean plankton was estimated as 0.16 WW (Vinogradov and Shushkina, 1987), DW of chaetognaths was calculated according to Matthews and Hestad (1977), larvaceans – to Hopcroft et al. (1998). To compare seasonal development of *C.glacialis* population at different stations, a mean developmental stage index (DSI) was calculated as abundance weighted average:

$$DSI = \frac{\sum i \times n_i}{\sum n_i}$$

where i is copepodite stage number from 1 to 6, n_i is abundance of stage i, and summations are for i from 1 to 6 (Skjoldal et al., 2021).

Feeding of Zooplankton

Feeding rates of dominant herbivorous zooplankton (C. glacialis, C. finmarchicus, C. hyperboreus, Limnocalanus macrurus, Senecella siberica, Pseudocalanus spp., Drepanopus bungei, Jaschnovia tolli, Oithona similis, Oikopleura vanhoeffeni, Limacina helicina) were assessed with the gut fluorescence method (Mackas and Bohrer, 1976). This approach was subject to discussion because of the possibility of pigment destruction during the passage through the gut (e.g., Båmstedt et al., 2000). There is no general agreement as to extent of pigment degradation, with values ranging from 0 to 95% (Pasternak, 1994). On the other hand, when different methods to estimate feeding were directly compared, reliable results were obtained with the gut fluorescence (Baars and Franz, 1984; Tiselius, 1988; Peterson et al., 1990; see also Pasternak, 1994). This suggests that high degradation rates are not the rule. Therefore, the gut fluorescence method continues to be a highly valuable tool for studies of zooplankton feeding (e.g., Saiz and Calbet, 2011; Valdés et al., 2017; D'souza and Gauns, 2018), and is still the only method that provides information on the in situ feeding rates and feeding impact of herbivorous zooplankton on phytoplankton assemblage.

Zooplankton for the gut pigment analysis was sampled from the layers above and below the pycnocline similarly to collection for the identification. The content of the cod-end was diluted in a 1L plastic bucket and the zooplankters were immediately anaesthetized with carbonated seawater. Undamaged animals were then sorted under a dissecting microscope and 1 to 50 animals per replicate, depending on size/stage, were picked with forceps and placed in test tubes with 3 ml of 90% acetone. Two to five replicates, if possible, for each species/stage were analyzed. Pigments were extracted for 24 h at 5 ° C in the dark. Chl *a* and phaeopigments were measured by a standard fluorometric procedure (Holm-Hansen et al., 1965) with a Trilogy fluorometer (Turner Designs) before and after acidification with 1 N HCl. Gut content of the animals (G) in units of Chl *a* equiv. ind^{-1} was calculated as G = (Chl *a* +1.51 x Phaeopigment) (Dagg and Wyman, 1983). The amount of pigment ingested daily (I, ng Chl *a* ind^{-1} day^{-1}) was estimated as: $I = G^{*}24/GPT$, where GPT is the gut passage time (hours). We used the gut passage values obtained in our previous studies and the published data (**Table 2**). We could not find published data on the gut passage time in Clausocalanidae *D. bungei*, so the value of 0.9 h obtained for the related *Clausocalanus laticeps* (Atkinson et al., 1996) was used. All the data on GPT were adjusted to the temperature of the habitat where the animals were collected with the Q_{10} = 2.2 (Irigoien, 1998). To assess ingestion rates of zooplankton in carbon units, we calculated the phytoplankton carbon (C, mg m^{-3}) to Chl *a* (mg m^{-3}) ratio of 15 ± 7 (n=11) in the Khatange region and 18 ± 8 (n=6) in the Lena region. Phytoplankton biomass and Chl *a* concentration were assessed from the same samples. The data on phytoplankton biomass in carbon units calculated according to Menden-Deuer and Lessard (2000) were taken from Sukhanova et al. (2019) for the Khatanga and I.N. Sukhanova (personal communication) for the Lena region. Chl *a* was assessed fluorometrically by Demidov et al. (2019).

Grazing Impact

Grazing impact of each of the dominant species on the integrated (0-bottom) Chl *a* content (E_{Chl}, mg Chl *a* m^{-2}) was estimated using the individual ingestion rates (I_i, ng Chl *a* ind^{-1} d^{-1}) and the abundance of the given species (N_i, ind m^{-2}):

$$E_{Chl} = \sum_{i=1}^{n} I_i N_i$$

where i is the layer number, n is the total number of layers. Grazing impact on primary production was assessed with the use of the obtained C: Chl *a* ratio. We used the data on primary production measured in this cruise using on-deck ^{14}C incubations (Demidov et al., 2020 for the Khatanga region and A.B. Demidov, personal communication, for the Lena region).

RESULTS

Study Area

Detailed description of the hydrography of the studied areas is given in (Flint et al., 2018; Osadchiev, 2020). Here, we present the features of physical environment which are most important for zooplankton.

Khatanga Transect. Hydrography of the studied area was strongly influenced by the river run-off. Variations of surface salinity and temperature along the transect are shown in

TABLE 2 | Gut passage time (GPT, h) of the dominant zooplankton.

Species	GPT	T	Reference
Calanus glacialis	0.84	8	Drits et al., 2015
C. hyperboreus	0.9	8	Pasternak et al., 2008
Metridia longa	1.5	8	Pasternak et al., 2008
Limnocalanus macrurus	1.3	7	Drits et al., 2016
Senecella siberica	1.3	7	Drits et al., 2016
Jaschnovia tolli	1.2	3	Our unpublished data
Pseudocalanus spp.	0.67	8	Pasternak et al., 2008
Oithona simils	1.7	8	Pasternak et al., 2008
Oikopleura vanhoeffeni	0.79	1-6	Bochdansky et al., 1998
Limacina helicina 4.5-5.5 mm	14.4	4-5	Pasternak et al., 2017
L. helicina 1.3-1.6 mm	8.7	4-5	Pasternak et al., 2017

Experimental temperature (T °C) in the cited studies is indicated.

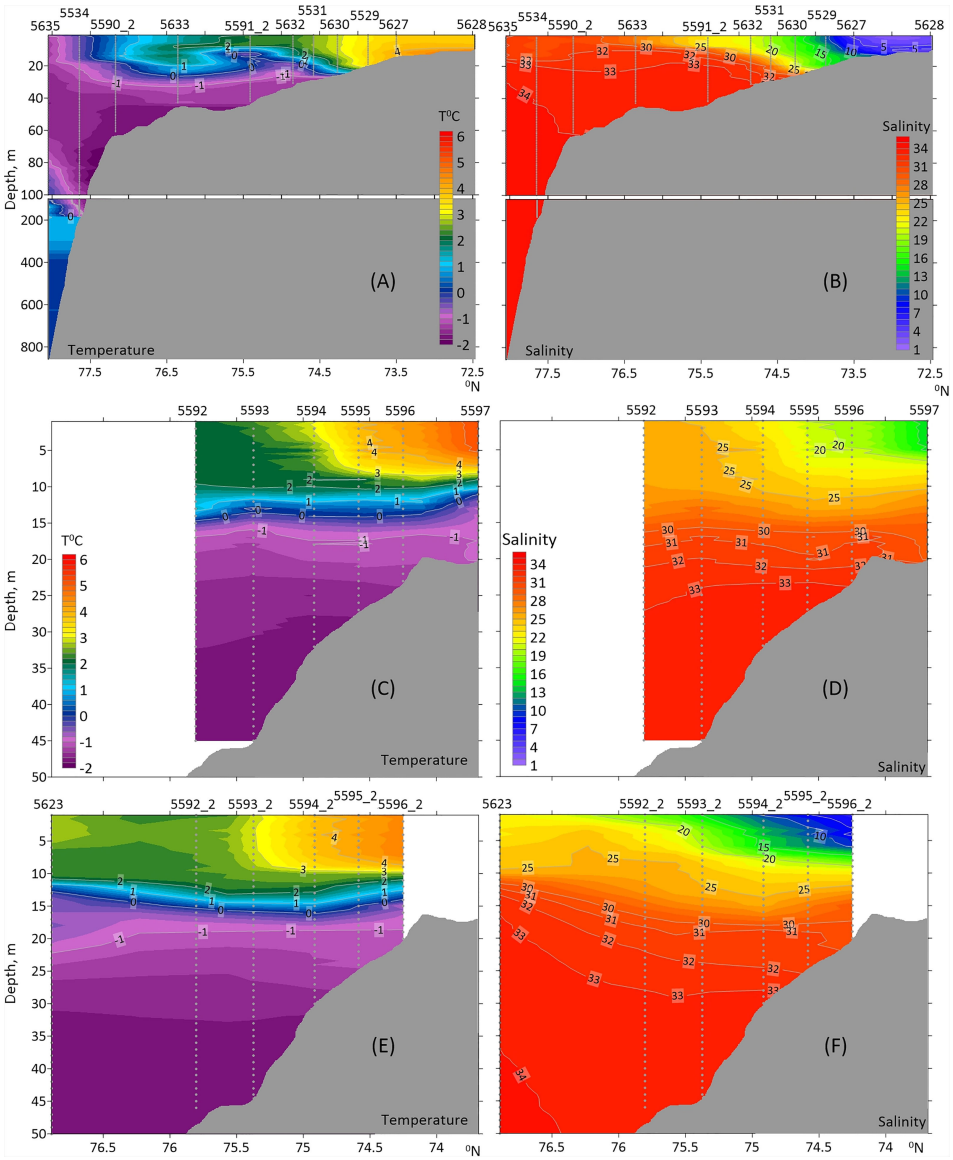


FIGURE 2 | Distribution of salinity (left) and temperature (right) along the transects. **(A, B)** – Khatanga transect (17-20 September); **(C, D)** – Lena transect (2-3 September); **(E, F)** – Lena transect (14-15 September). Redrawn from: Flint et al., 2018. Considerable changes in the distribution of the freshened upper mixed layer are recognized in the Lena area at the second sampling. The distribution of salinity – temperature parameters in the Khatanga area could not be presented as only two stations were repeated.

Figures 2A, B. Salinity and temperature of the upper mixed layer along the Khatanga transect varied from 3.4 and +3.6 °C at st. 5628 (Khatanga Gulf) to 32.2 and -1.3 °C at st. 5635 (slope area). According to the changes in salinity, three zones could be distinguished: inner Khatanga Gulf (st. 5627-5629, surface salinity from 3.4 to 11), shelf zone influenced by the Khatanga plume (st. 5630-5591_2, surface salinity from 17 to 21), shelf-and-slope zone outside the plume (st. 5633-5635, salinity > 27). Chlorophyll a concentration varied from 1-1.9 mg m^{-3} (inner Gulf) to 0.1-0.9 mg m^{-3} (plume zone) and 0.2-0.4 (shelf-and-slope zone outside the plume) (**Table 1**). At the shallow stations in the Khatanga Gulf, there was no pronounced vertical stratification. It was recorded at all stations outside the Gulf (**Figures 2A, B**). Salinity in the upper mixed layer at stations 5590_2 and 5591_2 was similar to that measured at these locations at the corresponding pilot stations two weeks earlier (32.1 and 31.5, 21.5 and 22.3, respectively).

Lena Transect. Two zones could be distinguished along the Lena transect, shelf zone influenced by the Lena plume and shelf zone outside the plume. At the first sampling, two of the stations (5597 and 5596) were located inside the Lena plume where salinity and temperature in the upper layer varied from 13.4 and 5.3 °C at

the closest to the Lena Delta st. 5597 to 21.8 and 3.9 °C at st. 5596 (**Figures 2C, D**). Station 5592 with temperature of 2.1 °C and salinity of 25.7 was outside the plume. Two weeks later, salinity of the upper layer at st. 5596 decreased from 21.8 to 6.6 psu, while temperature increased from 3.9 to 4.6 °C. At another repeated station (st. 5592), changes in hydrographical parameters were less pronounced: salinity decreased from 25.8 to 19, while temperature remained almost unchanged (about 2.1 °C, **Figures 2E, F**). Chlorophyll *a* concentration increased by almost an order of magnitude at st. 5596 and did not change at st. 5592 (**Table 1**).

Zooplankton Biomass and Composition

Two peaks of total zooplankton biomass (DW, mg m^{-3}) were recorded along the Khatanga transect: the first, in the inner Khatanga Gulf (st. 5627-5629), and second, at the shelf edge (st. 5590_2). Biomass values were more than 50 mg DW m^{-3} in both areas. In the plume zone, biomass was much lower, constituting, on average, 17 mg DW m^{-3} (**Figure 3A**). Minimum of 2.2 mg DW m^{-3} was recorded at the most oceanic station 5635.

Species composition of zooplankton along the Khatanga transect changed with the distance from the river mouth. *Limnocalanus macrurus* which was responsible for the first maximum of zooplankton biomass dominated inside the Khatanga Gulf. It was followed by *Drepanopus bungei*. At the two stations closest to the river, *Senecella siberica* played a significant role (**Figure 3**). When moving seaward, *Calanus* spp. accounted for a larger share of zooplankton biomass (15-60%). In this area, copepods of the genus Pseudocalanus and chaetognaths *Parasagitta elegans* contributed substantially to zooplankton biomass. *Metridia longa* made up 27% of zooplankton biomass at the slope stations. Comparison of zooplankton composition and biomass at the repeated stations revealed that composition of the dominant species did not change in two weeks, while biomass increased by a factor of 1.8 to 2.6. Increase of biomass was mostly due to *C. glacialis* at st. 5590_2 and *C. glacialis* together with *P. elegans* at st. 5591_2 (**Figure 3**).

Zooplankton biomass and composition at the three stations in the Lena area performed on 2-3 September were pretty similar.

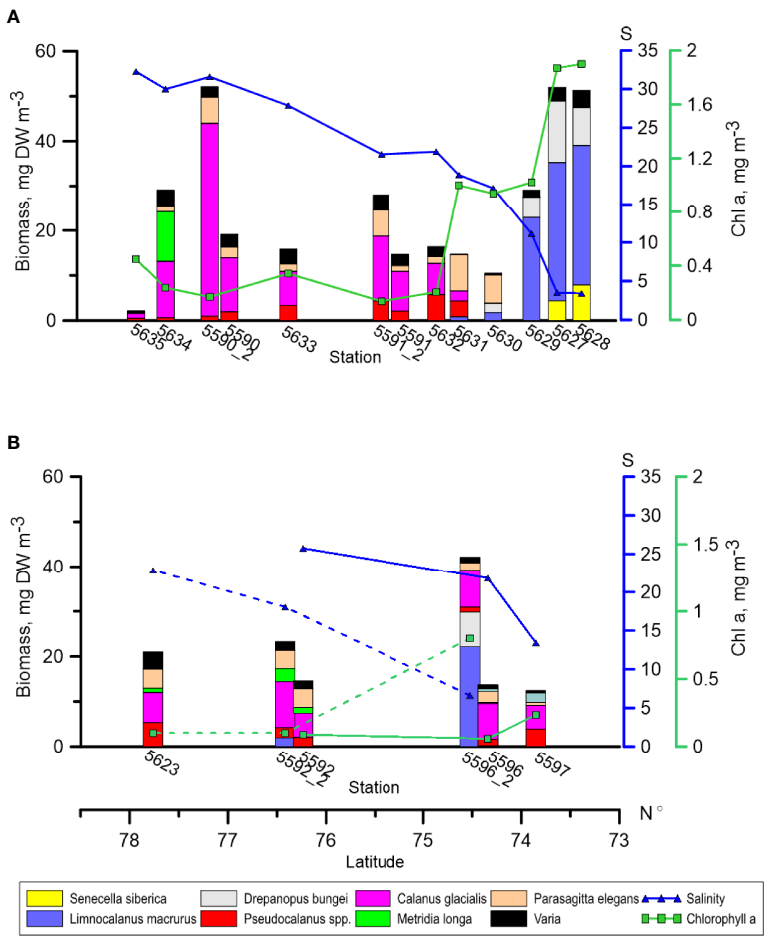


FIGURE 3 | Distribution of zooplankton biomass, surface salinity and Chlorophyll a (0-bottom at the shallow station, 0-50 m at the deep stations) along the transects. **(A)** – Khatanga transect, **(B)** – Lena transect. Bars – zooplankton biomass, blue line - salinity (S), green line - chlorophyll a Dashed lines – salinity and chlorophyll *a* at the repeated stations along the Lena transect. At the repeated stations along the Khatanga transect, the values of salinity and chlorophyll a almost did not change and thus are not shown. Note considerable changes in species composition and biomass at st. 5596_2 compared with st. 5596.

Calanus glacialis, *Pseudocalanus* spp. and *P. elegans* played the most pronounced roles at these stations (**Figure 3**). Beside them, *O. vanhoeffeni* were important at the nearest to the delta st. 5597. When sampling was repeated two weeks later, both composition and biomass of zooplankton demonstrated considerable changes. The most striking changes considered st. 5596_2: total biomass there turned out to be three times that at st. 5596. High abundance of *L. macrurus* at st. 5596_2, which was not found at all at the first sampling, was mostly responsible for this difference. *Drepanopus bungei* also contributed to biomass increase at this station, although to a lesser extent than *L. macrurus*. The latter was also found at another repeated station (5592_2), but its biomass was much less than at st. 5596_2.

Vertical Distribution

Vertical distribution of zooplankton biomass at the pilot stations 5591 and 5590 was similar irrespective of the time of the day (**Figure 4**). This suggests that zooplankton did not ascend into the upper layer at night, at least, at the shelf shallow water stations. Relatively high biomass of *C. glacialis* in the upper layer at these stations at all times of the day is associated with high abundance of the young development stages (CI-CIII) of this copepod.

Vertical distribution of zooplankton biomass on the shallow shelf depended on the vertical distribution of salinity and temperature. In both of the areas, the bulk of the biomass was concentrated in the layer below the pycnocline regardless of Chl *a* vertical distribution and time of the day. In the relatively warm freshened upper mixed layer, biomass of zooplankton was lower (**Figures 5**, **6**). The biomass maximum was determined mostly by the vertical distribution of *Calanus glacialis*, *Pseudocalanus* spp. and *Parasagitta elegans*. The only exception was st. 5596_2 in the Lena influenced area where biomass in the upper layer was twice that in the lower layer. *Limnocalanus macrurus*, which strongly dominated zooplankton biomass at this station, occupied the upper 10-0 m layer inhabited also by the second important species, *D. bungei* (**Figure 6**).

In the shelf edge and slope region, the biomass in the upper mixed layer was low (**Figure 5**). The higher values were recorded in the 40-20 m layer below pycnocline. *Calanus glacialis*, *C. hyperboreus* and *M. longa* were responsible for this biomass increase. An increase of zooplankton biomass related to these species was recorded in the near-bottom layer at these stations (**Figure 5**).

Age Structure of *Calanus glacialis*

The demographic structure of the population of *C. glacialis* changed from the south to the north, with similar trends in the both studied regions. At the southernmost stations where *C. glacialis* was first found (the species did not inhabit strongly freshened regions), the population consisted of only older stages (mainly, CV) (**Figures 7A–C**). To the north, the share of younger stages gradually increased. The youngest population was observed at the ice edge (st. 5635) where CI and CII comprised more than a half of the population abundance and the role of CV decreased to less than 5% (**Figure 7A**). Note that at this station a high abundance of *Calanus* spp. nauplii was recorded, up to 600 ind m^{-3} in the 0-20 m layer. Distinct demographic changes were also recognized when comparing the population structure at the repeated stations: in two weeks, the share of the younger stages decreased, and the older stages increased. Thus, at st. 5591 the share of CI-CIII decreased from 11 to 3%, at st. 5590 – from 62 to 18%, at st. 5596 – from 37 to 0%, at st. 5592 – from 46 to 10% (**Figures 7B–D**). To follow the ageing of the population, we calculated the mean developmental stage index (DSI), which varied from 2.2 at the ice edge to 4.5-5.2 at the southernmost stations (**Table 3**). At the repeated stations 5590, 5592, 5596, DSI in two weeks increased from 3.1-3.8 to 4.4-5.0 and almost did not change (4.7 to 4.9) at st. 5591. At the latter station, abundance of *C. glacialis* increased by a factor of 2 (from 710 to 1500 ind m^{-2}), while no significant changes in abundance were found at the

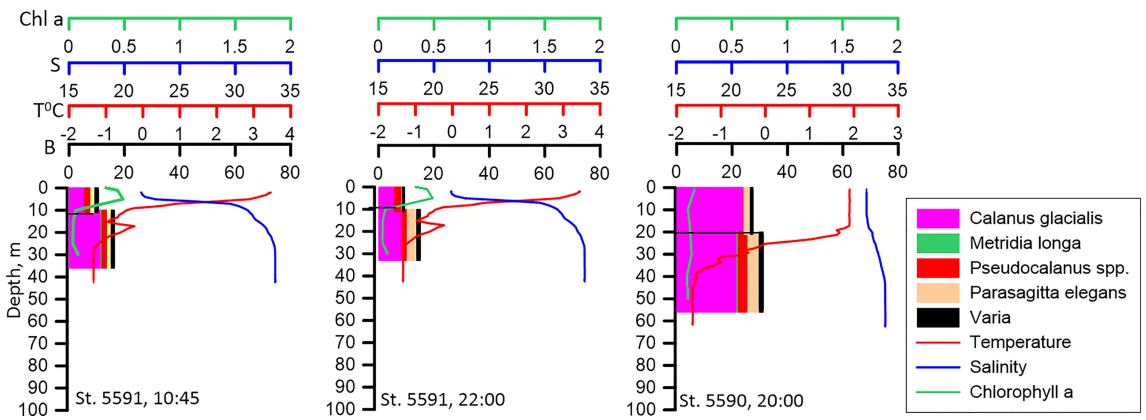


FIGURE 4 | Vertical distribution of biomass of the dominant species (B, mg DW m^{-3}) at different time of the day at the neighboring stations. No diel re-distribution of biomass could be detected. Vertical profiles of temperature (T° C), salinity (S) and Chlorophyll *a* (Chl, mg m^{-3}) distribution are presented.

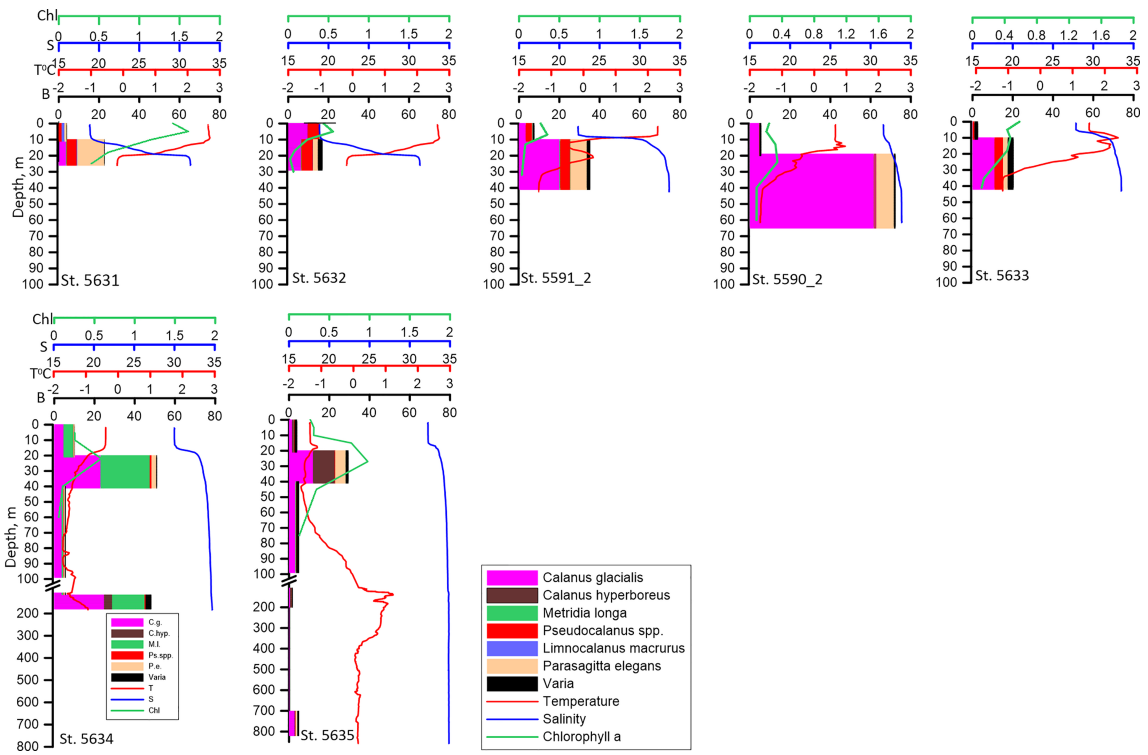


FIGURE 5 | Vertical distribution of biomass of the dominant species (B, mg DW m^{-3}), temperature (T° C), salinity (S) and Chlorophyll a (Chl, mg m^{-3}) along the Khatanga transect. Note that the bulk of the biomass occupies the layer below the pycnocline.

other three repeated stations (st. 5590: 9500 and 9700 ind m^{-2}, st. 5592: 1000 and 1200 ind m^{-2}, st. 5596: 670 and 440 ind m^{-2}, **Table S2**) which suggests that the observed demographic changes were related rather to the ageing of the population than to advection. We noted clear positive effect of temperature on the DSI (DSI = 0.344 t + 0.346, R^2 = 0.38; n = 14; p = 0.017).

Feeding

Overall, gut pigment content of dominant zooplankters in both regions was not high, usually, not exceeding 3 ng Chl ind^{-1} (**Table S1**). Higher gut pigment content (> 10 ng Chl ind^{-1}) was recorded in large copepods *C. hyperboreus* and in large (> 2 mm) larvaceans *O. vanhoeffeni*. The maximum values (> 1000 ng Chl ind^{-1}) were measured in large (4-6 mm diameter) specimens of pteropods *L. helicina*.

Specific daily rations of small-sized copepods (including the young stages of *C. glacialis*) through herbivory varied from less than 1% to 4% (**Table 4**). Specific rations of large copepods made up around 1%. Contrary to copepods, both large pteropods and larvaceans demonstrated high values of specific rations: from 24% to 45% and 11% to 20%, respectively (**Table 4**).

Given the low feeding activity demonstrated by the main groups of zooplankton grazers and their not very high biomass, it is no surprise that grazing pressure was not high. It was less than 1% of chlorophyll in the inner Khatanga Gulf and at the ice edge, while consistuted about 3% in the plume-affected shelf area. At the pilot st. 5590, grazing impact reached maximum of 8%. In the Lena area, grazing imact was 1.5-2% with one exception of 6% at st. 5623 close to the Lena plume periphery (**Figure 8**). Grazing impact at the repeated stations decreased by a factor of 2. Grazing pressure on primary production varied from 1.4 to 13% at most of the stations with the maximum of 29% at st. 5590_2 (outer shelf off Khatanga) and 72% at st. 5623. The grazing pressure within the distinguished zones was determined by different consumers. *Limnocalanus macrurus* and *D. bungei* were the main grazers in the inner Khatanga Gulf and at st 5596_2 in the Lena plume area. Larvaceans *O. vanhoeffeni* contributed 99% to total grazing at the southernmost station in the Lena plume. At all of other stations, *C. glacialis* and *Pseudocalanus* spp. were the main grazers.

DISCUSSION

Biomass and Composition of Zooplankton.

Several previous studies estimated zooplankton biomass and composition in the Lena influenced area (Jashnov, 1940; Kosobokova et al., 1998; Abramova, 1999; Abramova and Sokolova, 1999; Lischka et al., 2001; Abramova and Tuschling, 2005; Arashkevich et al., 2018) but the data in the Khatanga plume area are scarce (Jashnov, 1940; Kosobokova et al., 1998) and no data, to our knowledge, were so far obtained for the

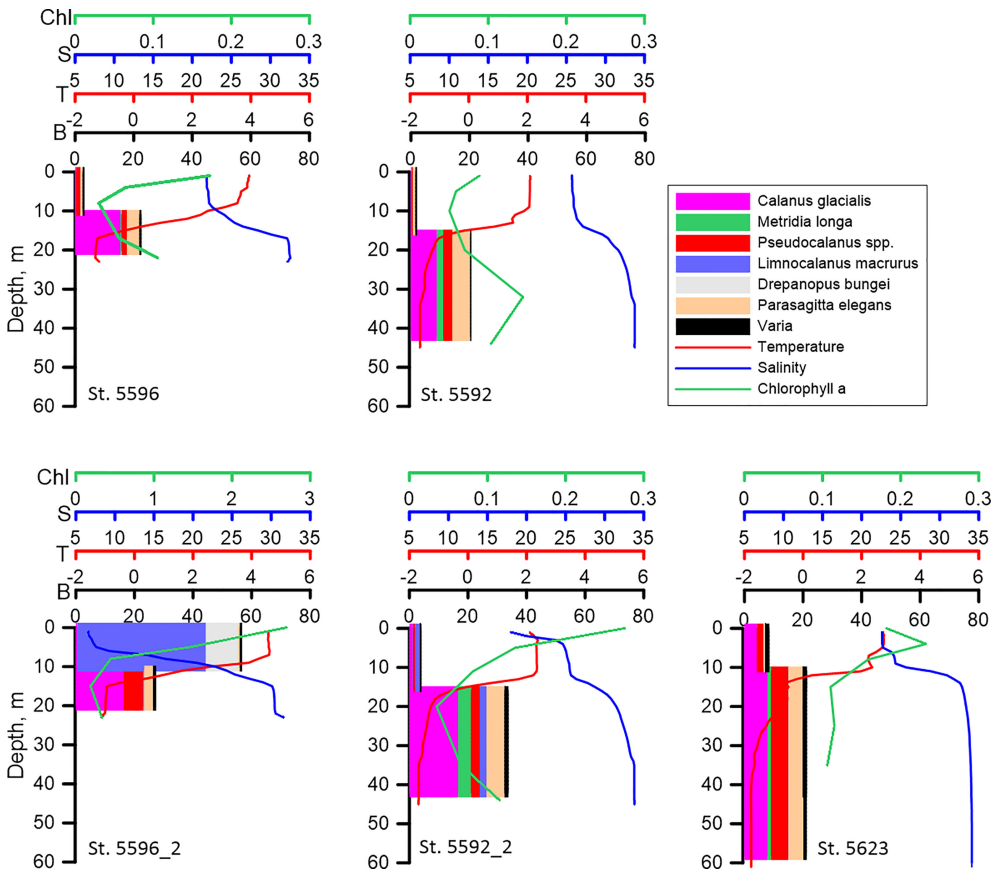


FIGURE 6 | Vertical distribution of biomass of the dominant species (B, mg DW m^{-3}), temperature (T° C), salinity (S) and Chlorophyll a (Chl, mg m^{-3}) along the stations influenced by the Lena plume. Upper panel: sampling on 2-3 September; lower panel: sampling on 14-15 September. Considerable changes in the vertical distribution of zooplankton at the repeated st. 5596_2 are seen.

Khatanga Gulf. Our values for zooplankton biomass in the Khatanga plume area (11-28 mg DW m^{-3}) are close to the values (18-36 mg DW m^{-3}) reported by Kosobokova et al. (1998) for the same season. Lower biomass values of 0.3-6 mg DW m^{-3} reported by Lischka et al. (2001) were probably connected with the later sampling in this study (October). Our estimates of the biomass in the Lena plume area (12-42 mg DW m^{-3}) are similar to those reported for this region by Lischka et al. (2001) in August-September and Arashkevich et al. (2018) in September: 15-60 and 10-30 mg DW m^{-3}, respectively. Similar values of around 23 mg DW m^{-3} were recalculated from the data by (Sorokin and Sorokin, 1996). Lower values (2-13 mg DW m^{-3}) were obtained for the same season by Kosobokova et al. (1998) which was explained by the scarcity of sampling in the shallow water region (Lischka et al., 2001). In the outer shelf/slope zone outside the Khatanga plume, our estimates (2-52 mg DW m^{-3}) are close to the values of 4-25 mg DW m^{-3} presented by Kosobokova et al. (1998). Thus, the comparison of the data obtained in 1991, 1993, 1995 and in 2015, 2017 did not reveal considerable trends in changes of the biomass of zooplankton in the studied regions of the Laptev Sea, despite the fast warming of the Arctic and ice cover decrease (e.g., Perovich et al., 2019; Overland et al., 2019; Timofeeva and Sharatunova, 2021).

In general, our results on the species composition and zooplankton assemblages in the distinguished zones are in accordance with the previous studies in the Siberian Arctic seas (e.g., Vinogradov et al., 1995; Lischka et al., 2001; Fetzer et al., 2002; Abramova and Tuschling, 2005; Hirche et al., 2006; Arashkevich et al., 2010; Drits et al., 2020). Brackish species *Limnocalanus macrurus*, *Senecella siberica* and *Drepanopus bungei* made up the bulk of biomass in the most freshened areas closer to the river mouth. Their role decreased in the plume-affected areas where *Pseudocalanus* spp. and *Calanus glacialis* contributed significantly to total biomass. In the outer shelf/slope outside the plume, *C. glacialis* was by far the most important species, followed by *M. longa* and *P. elegans*.

Differential Influence of the Khatanga and Lena Runoff on Zooplankton

The freshwater discharge into the Laptev Sea forms a salinity gradient over the shelf and, to a large extent, determines the structure and functioning of zooplankton community

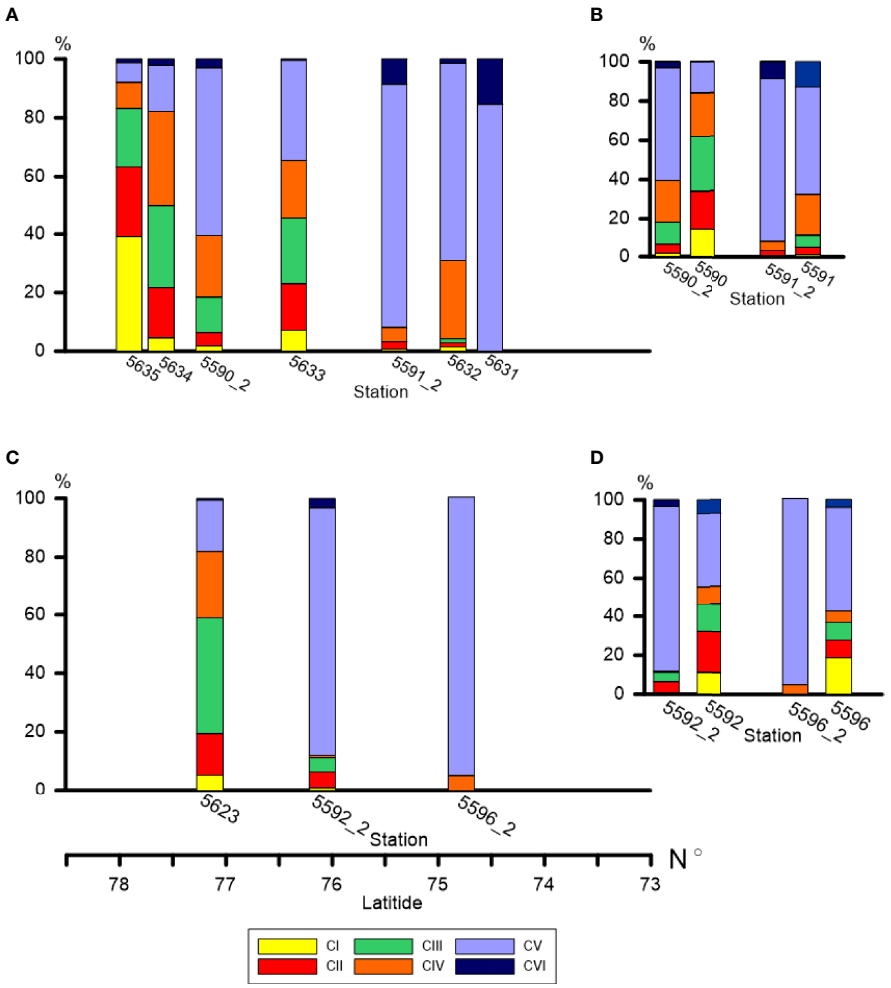


FIGURE 7 | Demographic structure of *C. glacialis* population (relative abundance of each copepodite stage as percent of total population abundance) along the Khatanga **(A)** and Lena **(C)** transects and at the repeated stations in the Khatanga area **(B)** and in the Lena area **(D)**. Spatial and temporal changes in dominance of consecutive copepodite stages is clearly recognized.

(Jashnov, 1940; Kosobokova et al., 1998; Lischka et al., 2001; Abramova and Tuschling, 2005; Arashkevich et al., 2018, and others). Most of the data were obtained close to the Lena Delta and in the shelf plume-affected area. Our results make it possible to track if the influence of the Khatanga discharge on zooplankton community differs from that of the Lena. Despite large spatial extension of the Khatanga plume, the impact of Khatanga discharge on zooplankton species composition was restricted mainly to the inner Gulf where the brackish species (*S. siberica, L. macrurus, D. bungei*) shaped the community. These species were almost absent in the shelf plume area. The specific feature of the Khatanga estuary is a strong tidal forcing (Osadchiev et al., 2020) which could constitute the base of the mechanism of zooplankton retention (Gagnon and Lacroix, 1983; Morgan et al., 1997; Menéndez et al., 2012) within the Gulf. As an indirect support of this suggestion, results on zooplankton distribution in the not-so-far located Yenisei gulf in the Kara Sea which is similar in size, geomorphology, and climatic conditions to the Khatanga Gulf are considered. Contrary to the latter, the Yenisei Gulf is less affected by tidal mixing due to low tidal velocities (Osadchiev et al., 2020), and the distribution of the brackish zooplankton is not limited to the gulf. Instead, they inhabit the extended area of the shelf affected by the river plume (Vinogradov et al., 1995; Fetzer et al., 2002; Hirche et al., 2006). Similarly, the brackish species are distributed far to the north within the Lena plume area (Lischka et al., 2001; Abramova and Tuschling, 2005; Arashkevich et al., 2018). Our results showed highly variable pattern of spatial distribution of the brackish zooplankton assemblage: at the first sampling (1-2 September), when northern boundary of the plume was located at 75° N, the distribution resembled that in the Khatanga plume area. Neither *L. macrurus* nor *D. bungei* were found even at the closest to the Lena Delta station 5597, instead, *C. glacialis*, *Pseudocalanus* spp. and *O. vanhoeffeni* formed the bulk of the biomass. Two weeks later, when the Lena plume extended

TABLE 3 | Development stage index of *Calanus glacialis* population (DSI) in the Khatanga and Lena affected areas.

Area	Station	Date	T°C	DSI
Khatanga	5590	31.08.17	1.9	3.1
	5590_2	19.09.17	0.7	4.4
	5591	01.09.17	3.4	4.7
	5591_2	18.09.17	2.3	4.9
	5631	18.09.17	2.6	5.2
	5632	18.09.17	2.2	4.6
	5633	19.09.17	1.5	3.6
	5634	19.09.17	-0.39	3.4
	5635	20.09.17	-1.35	2.2
Lena	5592	02.09.17	2.1	3.6
	5592_2	14.09.17	2.1	4.7
	5596	03.09.17	3.9	3.8
	5596_2	17.09.17	4.6	4.95
	5623	15.09.17	2.6	3.4

northward up to 77° N, *L. macrurus* constituted more than 50% of zooplankton biomass at 100 km distance from the Lena Delta and was found as far as 75.5° N. The wide distribution of brackish zooplankton in the plume area indicates that there are no mechanisms of zooplankton retention in the vicinity of the Lean Delta. Thus, contrary to the Khatanga input, the Lena freshwater discharge governs the structure of zooplankton community over a vast shelf area. Position and area occupied by the Lena plume strongly depend on the local wind forcing conditions (Osadchiev et al., 2021). In particular, meridional extension of the plume at the repeated sampling was related to the prevailing eastern and south-eastern winds in this area at the time of the study (Flint et al., 2018).

Distribution of total zooplankton biomass along the Khatanga transect is similar to that reported in the Lena area in autumn (Arashkevich et al., 2018). In both cases, biomass over the shelf influenced by the river plume was twice lower than in the vicinity of the freshwater inflow. Increased biomass of zooplankton close to the Lena Delta was also noted by Lischka et al. (2001) who explained this by better feeding conditions, increased water temperature and local hydrography. In our study, chlorophyll concentration and temperature were higher in the inner Khatanga Gulf which is in agreement with this explanation. In the Khatanga plume zone, besides lower chlorophyll concentration, its maximum was in the upper layer above pycnocline, the layer avoided by the marine species. This further worsened feeding conditions of herbivores in the plume-affected shelf area.

The vertical distribution pattern of zooplankton biomass in most of the cases resembled the pattern found in the Laptev Sea by Jaschnov (1940) and Kosobokova et al. (1998). They reported that biomass was confined mainly to the layer below pycnocline while the surface layer in the Lena and Khatanga plumes was poor. However, our results show that under increased spreading

TABLE 4 | Daily ingestion of autotrophic phytoplankton (I, μg C ind^{-1}d $^{-1}$) and specific daily ration (I/W, % body carbon) of the dominant zooplankters in different habitats.

		Khatanga area						Lena area	
		Inner Gulf		Plume-affected shelf		Slope		Plume-affected shelf	
Species	W_c	I	I/W	I	I/W	I	I/W	I	I/W
Senecella siberica	130	0.42	0.3						
Limnocalanus macrurus	118	0.28	0.2					0.68	0.6
Drepanopus bungei	6	0.07	1.2	0.17	2.7			0.02	0.3
Jaschnovia tolli	27	1.01	3.8	1.19	4.4				
Oithona similis	0.3			0.01	2.6	0.01	2.7	0.01	4.2
Pseudocalanus spp. CII-CIV	4			0.06	1.4	0.01	0.2	0.05	1.2
Pseudocalanus spp. CV-fem	7			0.11	1.6			0.10	1.5
Calanus glacialis CI	3.2					0.04	1.4		
C. glacialis CII	9.6			0.32	3.3	0.20	2.1		
C. glacialis CIII	21			0.38	1.8	0.27	1.3	0.24	1.1
C. glacialis CIV	75			0.52	0.7	0.45	0.6	0.92	1.2
C. glacialis CV	128			0.55	0.4	0.45	0.3	0.92	0.7
C. glacialis fem	320			0.73	0.2				
C. hyperboreus CIV	126					0.20	0.2		
C. hyperboreus CV	520					0.74	0.1		
C. hyperboreus fem	1506					2.17	0.1		
Metridia longa CV	48					0.18	0.4		
M. longa fem	196					0.26	0.1		
Limacina helicina 0.4-0.5 mm	5							3.56	1.5
L. helicina 4-5 mm	172					41.95	24.4		
L. helicina 5-6 mm	245							110.60	45.1
Oikopleura vanhoeffeni 0.5-1 mm	1.7							0.35	20.4
O. vanhoeffeni 1-2 mm	22							4.56	16.9
O. vanhoeffeni 2-4 mm	162							8.58	11.0

W_c – body carbon, μg C ind $^{-1}$.

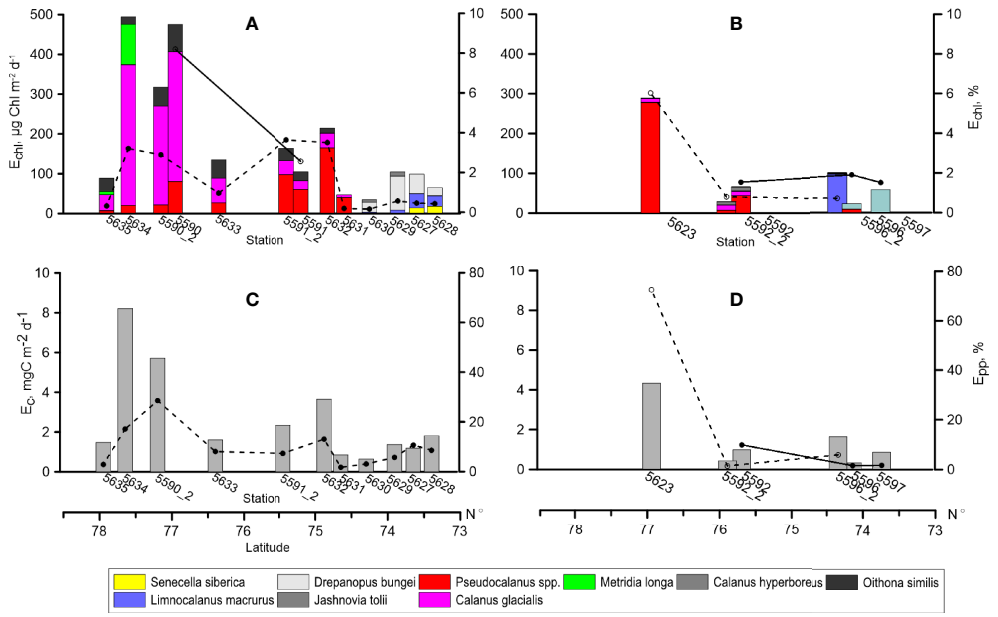


FIGURE 8 | Grazing of dominant zooplankton species in terms of Chl a (E_{chl}), **(A, B)** and organic carbon (E_c), **(C, D)**, bars. Lines: daily grazing impact on phytoplankton standing stock (E_{chl}, %) and grazing as percentage of primary production (E_{pp}, %). Solid line - first sampling (31.08-3.09. 2017), dashed line - repeated sampling (14.09-20.09.2017). Left: Khatanga area, right: Lena area.

of freshened upper layer in the Lena plume, the vertical distribution pattern changed: maximum of zooplankton biomass made up by the brackish species, *L. macrurus* and *D. bungei*, was found in the layer above pycnocline.

Ice Melting Regime and Development of *C. glacialis* Population

Timing of ice retreat is among the main factors controlling seasonal development of the dominant copepod populations in the Arctic seas (Kosobokova and Hirche, 2001; Leu et al., 2011; Drits et al., 2020; Rogachev et al., 2021). According to Kosobokova and Hirche (2001), spawning of *C. glacialis* in the Laptev Sea occurred at the ice edge, and ageing of the population followed ice retreat. These authors noted that reproduction and development of *C. glacialis* differed between the eastern and western parts of the Laptev Sea in September 1993. In the east, where a large area extending northward from the mouth of Lena was open by the beginning of August 1993, the young stages CI-CIII constituted up to 40-60% of the population. In the western sea, almost completely covered with ice in early September, the older stages CIV- CVI dominated (Kosobokova and Hirche, 2001). The authors assumed that under the ice conditions in the western sea, reproduction and recruitment of *C. glacialis* has a sporadic character. Delays in *C. glacialis* reproduction and population developments due to inter-annual/geographical differences in sea ice conditions were recorded both in the Canadian and Eurasian Arctic (Kwasniewski et al., 2003; Søreide et al., 2008; Leu et al., 2011).

In our study, both eastern and western areas of the Laptev Sea were open from the second week of August in 2017 (http://www.aari.ru/). Demographic structure of *C. glacialis* did not reveal pronounced differences between the Khatanga and Lena areas at the beginning of September. At the southernmost stations, the population consisted totally of the overwintering stages (CIV-CVI). Northward, the contribution of younger stages gradually increased. Our results on demographic structure of *C. glacialis* along the Khatanga transect enabled us to follow population advancement in relation to timing of ice retreat. At the southernmost stations, the ice breakup occurred at the beginning of August, while at the northernmost ice-edge station, about 30-35 days later (http://www.aari.ru/). The development stage index of the population at these sites was 5.2 and 2.2, respectively. The positive correlation between DSI and temperature of the upper mixed layer agrees with delayed population development under late ice retreat and low temperatures. The question arises whether the population which we observed in the vicinity of the ice at the second half of September would be able to reach an overwintering stage (CV or CIV) before the formation of solid ice. The calculated duration of a copepodite stage (assuming equal development time of each stage) was around 12 days at the repeated stations. Our estimate is in accordance with other studies stating that *C. glacialis* needs approximately 2 months to develop from CI to their overwintering stages CIV and CV at 3° C (McLaren and Corkett, 1981; Corkett et al., 1986). This means that development from CII to CIV (the overwintering stage) will take about 24 days at surface temperature about 2-4 °C. Since the ontogenetic development of *Calanus* spp. is strongly temperature dependent (McLaren and Corkett, 1981; Skjoldal et al., 2021), the development of *C. glacialis* to the overwintering stage in the marginal ice zone (with the surface temperature below -1°C) is likely too slow to succed before the solid ice cover was formed by the midle of October. Suboptimal conditions for *C. glacialis* in this zone

suggest that only a minor portion of the population survives through the winter season.

Feeding and Grazing Pressure

The herbivorous feeding rates of the dominant copepods did not reveal any influence of the river discharge. Specific daily rations on the algal food in the overwhelming majority of cases were less than 2% and did not exceed 4% body carbon. Assuming assimilation of phytoplankton of 0.6 (Mauchline, 1998), energy input through herbivory did not cover the metabolic requirements of these copepods (2-10% body carbon) calculated according to Ikeda (2001) with regard to water temperature and body weight. This pattern is similar to what was described by Arashkevich et al. (2018) in the Lena plume area in September 2015: the lack of pronounced river influence on feeding rates, and low daily rations. The estimated budgets showed that during the post-bloom period, ingestion through herbivory could not provide the necessary carbon to sustain the demands of growth and metabolism. Interestingly, that despite low herbivorous feeding, the population of *C. glacialis* grew and developed. This means that their energy input was supplemented by other sources, such as ciliates (e.g., Levinsen et al., 2000) and detritus (e.g., van der Jagt et al., 2020). For rough estimation of daily rations of copepods on all these sources (phytoplankton, ciliates and detritus), Arashkevich et al. (2018) calculated *C. glacialis* ingestion rates using suspended POC/Chl (besides C_{phyt}/Chl) ratio at the stations along the Lena transect. This resulted in an almost an order of magnitude higher daily energy input which considerably exceeded metabolic requirements. Thus, given the observed development of the *C. glacialis* population in our study, we suggest that the copepods successfully exploited additional food sources beside phytoplankton.

Contrary to copepods, the two other groups of dominant zooplankton, large size larvaceans and pteropods, demonstrated high rates of phytoplankton consumption (**Table 4**). We assume that this is related to their specific feeding mechanism – unselected collection of particles from the large water volume with mucous net (*L. helicina*) or "house" (*O. vanhoeffeni*). Even under low phytoplankton concentrations in autumn, these groups not only met the metabolic demands calculated as 6-9% and 3-5% of body carbon (after Lombard et al., 2005; Pasternak et al., 2017), but seemed to provide fast growth through solely herbivorous feeding.

The present study is the first attempt to estimate grazing impact on autotrophic phytoplankton in the Khatanga Gulf and adjacent shelf. Influence of the river runoff is manifested in the lowest grazing pressure (mean impact equaled 0.4% of Chl a) in the inner Gulf despite high zooplankton biomass. This is the result of the two main factors: first, an increased phytoplankton biomass (mainly, the freshwater assemblage) carried by the river runoff (Sukhanova et al., 2019), and second, negligible feeding rates of the absolute zooplankton dominant, *L. macrurus*. Age composition (solely adults) and low feeding rates point to the final phase of seasonal development of the population found in other estuarine arctic regions in September (Hirche et al., 2003; Drits et al., 2016). As the influence of the river discharge weakened, phytoplankton biomass decreased and grazing in the shelf area constituted, on average, 4% of Chl a. The mean consumption of the newly produced organic carbon by zooplankton over the shelf was also higher than in the Gulf (15 and 6% of primary production, accordingly) but the difference was not significant (p=0.07).

Grazing impact of copepods depends on phytoplankton size structure (e.g., Finkel et al., 2010) as the majority of these grazers consume particles <5 μm less efficiently than larger items (Levinsen et al., 2000). Size structure of phytoplankton communities in the Siberian Arctic seas varies depending on the impact of the river discharge, with larger phytoplankton cells (> 3 μm) prevailing under low salinity and relatively high water temperature in the estuaries, and picophytoplankton (< 3 μm) prevailing under high salinity and low water temperature on the shelf (Belevich et al., 2021; Demidov et al., 2021). Specifically, in the Khatnga Gulf, the share of picophytoplankton was about 10% of total Chl *a*, while on the shelf, the contribution increased to 35% (Belevich et al., 2021). If we re-calculate the estimated grazing pressure considering Chl *a* content of only the larger phytoplankton, the values will increase to 7% in the shelf area while will remain almost unchanged in the Gulf.

Zooplankton grazing pressure, assessed with the gut fluorescence approach in the Lena area in September 2015 (Arashkevich et al., 2018), followed the same trend: the lowest values (2% of Chl *a* and 1% of primary production) were found at low salinity and high temperature at closest to the Lena Delta stations. The values gradually increased up to 5% of Chl *a* and 6% of primary production with increase of salinity and decrease of temperature with the distance from the Delta. Similarly, our estimates showed highest grazing pressure of 4% of Chl *a* and 72% of primary production at the Lena plume edge (st. 5623) under higher salinity. Within the plume-influenced area, grazing impact did not exceed 1% of Chl *a* and 10% of primary production. Note that contrary to the negligible role of grazing by *L. macrurus* in September 2015 (Arashkevich et al., 2018), the species determined the total zooplankton grazing at st. 5596_2, most influenced by an increased freshwater inflow.

CONCLUSION

The results provide new information on the distribution, herbivorous feeding and grazing impact of the dominant zooplankton species in the poorly studied Khatanga as well as in the better studied Lena regions of the Laptev Sea at the end of the productive season.

We demonstrated that the influence of the Khatanga discharge on zooplankton composition differed from that of Lena. Strong tidal forcing which is a specific feature of the Khatanga estuary assumingly created a retention mechanism that prevented propagation of brackish zooplankton into the adjacent shelf area. As a result, the impact of Khatanga discharge on zooplankton composition was restricted mainly to the inner Gulf and was poorly recognized in the shelf area. On the contrary, Lena freshwater inflow governs the structure of zooplankton community over a vast shelf area. The wide distribution of brackish zooplankton within the shallow undiluted Lena plume indicates that there are no mechanisms of zooplankton retention in the vicinity of the Lena

Delta. Distribution pattern of brackish species is highly variable in the Lena area due to variability in the plume extension largerly determined by wind forcing. Contrary to our expectations, zooplankton biomass and distribution of total biomass as well as grazing impact on phytoplankton over the shelf influenced by the Khatanga and Lena plumes were similar.

Analysis of our results on demographic structure of *C. glacialis* confirmed that timing of ice retreat is among the main factors controlling seasonal development of the population. A late ice breakup significantly impairs the chances of reaching the overwintering stage and surviving through winter. Comparison of our results with those obtained at the end of the previous century did not reveal considerable changes either in the composition of the dominant species or in the biomass of zooplankton under the impact of ongoing Arctic amplification.

DATA AVAILABILITY STATEMENT

The original contributions presented in the study are included in the article/**Supplementary Material**. Further inquiries can be directed to the corresponding author.

AUTHOR CONTRIBUTIONS

AP and AD equally contributed to the design of the study. AD, EA and MF performed the field data collection and and samples treatment. AP, AD and EA preapred and analyzed the data. AP and AD wrote the first draft of the manuscript. All authors contributed to manuscript revision, read, and approved the submitted version.

FUNDING

This work was performed according to State assignment of the Ministry of Science and Higher Education of the Russian Federation # FMWE-2021-0007.

SUPPLEMENTARY MATERIAL

The Supplementary Material for this article can be found online at: https://www.frontiersin.org/articles/10.3389/fmars.2022.881383/full#supplementary-material

REFERENCES

Abramova, E. N. (1999). ""Composition, Abundance and Population Structure of Spring-Time Zooplankton in the Shelf Zone of Laptev Sea"," in *Land–Ocean Systems in the Siberian Arctic: Dynamics and History*. Eds. H. Kassens, H. A. Bauch, I. Dmitrenko, H. Eicken, H.-W. Hubberten, M. Melles, et al (Berlin: Springer-Verlag), 161–168.

Abramova, E. N., and Sokolova, V. A. (1999). About Findings and Life Cycle of Limnocalanus Johanseni (Copepoda, Calanoida) in the Lena Delta. *Zoologicheskii Zhurnal.* 78, 1360– 1363.

Abramova, E., and Tuschling, K. (2005). A 12-Year Study of the Seasonal and Interannual Dynamics of Mesozooplankton in the Laptev Sea: Significance of Salinity Regime and Life Cycle Patterns. *Global Planet. Change* 48, 141–164. doi: 10.1016/j.gloplacha.2004.12.010

ACIA: Arctic Climate Impact Assessment – Scientific Report.(2005). Cambridge University Press, Cambridge

Arashkevich, E. G., Drits, A. V., Pasternak, A. F., Flint, M. V., Demidov, A. B., Amelina, A. B., et al. (2018). Distribution and Feeding of Herbivorous Zooplankton in the Laptev Sea. *Oceanology*. 58, 381–395. doi: 10.1134/S0001437018030013

Arashkevich, E. G., Flint, M. V., Nikishina, A. B., Pasternak, A. F., Timonin, A. G., Vasilieva, J. V., et al. (2010). The Role of Zooplankton in the Transformation of the Organic Matter in the Ob Estuary, on the Shelf, and in the Deep Regions of the Kara Sea. *Oceanology* 50, 780–792. doi: 10.1134/S0001437010050140

Atkinson, A., Ward, P., and Murphy, E. J. (1996). Diel Periodicity of Subantarctic Copepods: Relationships Between Vertical Migration, Gut Fullness and Gut Evacuation Rate. *J. Plank. Res.* I8, 1387–1405. doi: 10.1093/plankt/18.8.1387

Baars, M. A., and Franz, H. G. (1984). Grazing Pressure of Copepods on the Phytoplankton Stock of the Central North Sea. *Neth. J. Sea Res.* 18, 120–142. doi: 10.1016/0077-7579(84)90028-0

Båmstedt, U., Gifford, D. J., Irigoien, A., Atkinson, A., and Roman, M. (2000). ""Feeding"," in *ICES Zooplankton Methodology Manual*. Eds. R. Harris, P. Wiebe, J. Lenz, H. R. Skjoldal and M. Huntley (Amsterdam: Elsevier), 297–399.

Bauch, D., Hölemann, J. A., Nikulina, A., Wegner, C., Janout, M. A., Timokhov, L. A., et al. (2013). Correlation of River Water and Local Sea-Ice Melting on the Laptev Sea Shelf (Siberian Arctic). *J. Geophys. Res. Oceans* 118, 550–561. doi: 10.1002/jgrc.20076

Belevich, T. A., Demidov, A. B., Makkaveev, P. N., Shchuka, S. A., and Flint, M. V. (2021). Picophytoplankton Distribution Along Khatanga Bay-Shelf-Continental Slope Environment Gradients in the Western Laptev Sea. *Heliyon* 7, 1–9, e06224. doi: 10.1016/j.heliyon.2021.e06224

Berrick, S. W., Leptoukh, G., Farley, J. D., Rui, H., and Hualan, R. (2009). Giovanni: A Web service workflow-based data visualization and analysis system.. *IEEE Transactions on Geoscience and Remote Sensing* 47, 106–113. doi: 10.1109/TGRS.2008.2003183

Bochdansky, A. B., Deibel, D., and Hatfield, E. A. (1998). Chlorophyll a Conversion and Gut Passage Time for the Pelagic Tunicate *Oikopleura Vanhoeffeni* (Appendicularia). *J. Plank. Res.* 20, 2179–2197. doi: 10.1093/plankt/20.11.2179

Chislenko, L. L. (1968). *Nomograms for Determination of Weight of Aquatic Organisms by Size and Body Shape* (Leningrad: Nauka (in Russian).

Corkett, C. J., McLaren, I. A., and Sevigny, J.-M. (1986). The Rearing of the Marine Calanoid Copepods *Calanus Finmarchicus* (Gunnerus), *C. Glacialis* Jaschnov and *C. Hyperboreus* Krøyer, With Comment on the Equiproportional Rule. *Sylleogeus* 58, 539–546.

Dagg, M. J., and Wyman, K. D. (1983). Natural Ingestion Rates of the Copepods Neocalanus Plumchrus and Neocalanus Cristatus Calculated From Gut Contents. *Mar. Ecol. Prog. Ser.* 13, 37–46. doi: 10.3354/meps013037

Demidov, A. B., Gagarin, V. I., Arashkevich, E. G., Makkaveev, P. N., Konyukhov, I. V., Vorobieva, O. V., et al. (2019). Spatial Variability of Primary Production and Chlorophyll in the Laptev Sea in August–September. *Oceanology* 59, 678–691. doi: 10.1134/S0001437019050047

Demidov, A. B., Sheberstov, S. V., and Gagarin, V. I. (2020). Interannual Variability of Primary Production in the Laptev Sea. *Oceanology* 60, 50–61. doi: 10.1134/S0001437020010075

Demidov, A. B., Sukhanova, I. N., Belevich, T. A., Flint, M. V., Gagarin, V. I., Sergeeva, V. M., et al. (2021). Size-Fractionated Surface Phytoplankton in the Kara and Laptev Seas: Environmental Control and Spatial Variability. *Mar. Ecol. Prog. Ser.* 664, 59–77. doi: 10.3354/meps13652

Drits, A. V., Pasternak, A. F., and Flint, M. V.. (2021). Size-Fractionated Surface Phytoplankton in the Kara and Laptev Seas: Environmental Control and Spatial Variability. *Mar. Ecol. Prog. Ser.* 664, 59–77. doi: 10.3354/meps13652

Drits, A. V., Arashkevich, E. G., Nikishina, A. B., Sergeeva, V. M., Solovyev, K. A., and Flint, M. V. (2015). Feeding of Dominant Zooplankton Species and Their Grazing Impact on Autotrophic Phytoplankton in the Yenisei Estuary in Autumn. *Oceanology* 55, 573–582. doi: 10.1134/S0001437015040049

Drits, A. V., Pasternak, A. F., Arashkevich, E. G., Poyarkov, S. G., and Flint, M. V. (2020). Distribution and Grazing of the Dominant Mesozooplankton Species in the Yenisei Estuary and Adjacent Shelf in Early Summer (July 2016). *Cont. Shelf. Res.* 201, 104133. doi: 10.1016/j.csr.2020.104133

Drits, A. V., Pasternak, A. F., Nikishina, A. B., Semenova, T. N., Sergeeva, V. M., Polukhin, A. A., et al. (2016). The Dominant Copepods Senecella Siberica and Limnocalanus Macrurus in the Ob Estuary: Ecology in a High-Gradient Environment. *Polar Biol.* 39, 1527–1538. doi: 10.1007/s00300-015-1878-6

D'souza, A., and Gauns, M. (2018). Temporal Variability in Copepod Gut Pigments Over the Central Western Continental Shelf of India. *J. Mar. Biol. Assoc. U. K.* 98 (1), 149–159. doi: 10.1017/S0025315416001144

Eicken, H., Reimnitz, E., Alexandrov, V., Martin, T., Kassens, H., and Vieho, T. (1997). Sea Ice Processes in the Laptev Sea and Their Importance for Sediment Transport. *Cont. Shelf Res.* 17, 205–233. doi: 10.1016/S0278-4343(96)00024-6

Fetzer, I., Hirche, H.-J., and Kolosova, E. G. (2002). The Influence of Freshwater Discharge on the Distribution of Zooplankton in the Southern Kara Sea. *Polar Biol.* 25, 404–415. doi: 10.1007/s00300-001-0356-5

Finkel, Z. V., Beardall, J., Flynn, K. J., Quigg, A., Rees, T. A. V., and Raven, J. A. (2010). Phytoplankton in a Changing World: Cell Size and Elemental Stoichiometry. *J. Plank. Res.* 32, 119–137. doi: 10.1093/plankt/fbp098

Flint, M. V., Anisimov, E. M., Arashkevich, E. G., Artemiev, V. F., Bezzubova, E. M., Belevich, T. A., et al. (2021). *Ecosystems of the Kara and Laptev Seas* (Moscow: Erokhova Publ).

Flint, M. V., Arashkevich, E. G., Artemiev, V. F., Baranov, B. V., Bezzubova, E. M., Belevich, T. A., et al. (2018). *Ecosystems of the Siberian Arctic Seas* (Moscow: APR).

Flint, M. V., Semenova, T. N., Arashkevich, E. G., Sukhanova, I. V., Gagarin, V. I., Kremenetskiy, V. V., et al. (2010).Structure of the zooplankton communities in the region of the Ob River's estuarine frontal zone. *Oceanology* 50;766779doi: 10.1134/S0001437010050139

Fofonova, V., Danilov, S., Androsov, A., Janout, M., Bauer, M., Overduin, P., et al. (2015). Impact of Wind and Tides on the Lena River Freshwater Plume Dynamics in the Summer Sea. *Ocean Dyn.* 65, 951–968. doi: 10.1007/s10236-015-0847-573

Fütterer, D. K., and Galimov, E. M. (2003). ""Siberian River Run-Off Into the Kara Sea: Characterization, Quantification, Variability and Environmental Significance – an Introduction"," in *Siberian River Run-Off in the Kara Sea*. Eds. R. Stein, K. Fahl, D. K. Fütterer, E. M. Galimov and O. V. Stepanets (Amsterdam: Elsevier Science), 1-8).

Gagnon, M., and Lacroix, G. (1983). Distribution and grazing of dominant zooplankton species in the Ob Estuary: influence of the runoff regime.. *Estuar. Coast.* 40, 1082–1095. doi: 10.1007/s12237-016-0201-2

Gordeev, V. V., Martin, J. M., Sidorov, I. S., and Sidorova, M. V. (1996). A Reassessment of the Eurasian River Input of Water, Sediment, Major Elements, and Nutrients to the Arctic Ocean. *Am. J. Sci.* 296, 664–691. doi: 10.2475/ajs.296.6.664

Hirche, H. J., Fetzer, I., Graeve, M., and Kattner, G. (2003). Limnocalanus Macrurus in the Kara Sea (Arctic Ocean): An Opportunistic Copepod as Evident From Distribution and Lipid Patterns. *Polar Biol.* 26, 720–726. doi: 10.1007/s00300-003-0541-9

Hirche, H. J., Kosobokova, K. N., Gaye-Haake, B., Harms, I., Meon, B., and Nothig, E.-M. (2006). Structure and Function of Contemporary Food Webs on Arctic Shelves: A Panarctic Comparison. The Pelagic System of the Kara Sea – Communities and Components of Carbon Flow. *Prog. Oceanogr* 71, 288–313. doi: 10.1016/j.pocean.2006.09.010

Holm-Hansen, O., Lorenzen, C. J., Holmes, R. W., and Strickland, J. D. H. (1965). Fluorometric Determination of Chlorophyll. *J. Conseil* 30, 3–15. doi: 10.1093/icesjms/30.1.3

Hopcroft, R. R., Roff, J. C., and Bouman, H. A. (1998). Zooplankton Growth Rates: The Larvaceans Appendicularia, Fritillaria and Oikopleura in Tropical Waters. *J. Plank. Res.* 20, 539–555. doi: 10.1093/plankt/20.3.539

Ikeda, T., Kanno, Y., Ozaki, K., and Shinada, A. (2001). Metabolic Rates of Epipelagic Copepods as a Function of Body Mass and Temperature. *Mar. Biol.* 139, 587–596. doi: 10.1007/s002270100608

Irigoien, X. (1998). Gut Clearance Rate Constant, Temperature and Initial Gut Contents: A Review. *J. Plank. Res.* 20, 997–1003. doi: 10.1093/plankt/20.5.997

Jashnov, V. A. (1940). *Plankticheskaya Produktivnost' Severnykh Morei SSSR (Plankton Productivity of the Northern Seas of the USSR)* (Moscow: MOIP (in Russian).

Kosobokova, K. N., Hanssen, H., Hirche, H.-J., and Knickmeier, K. (1998). Composition and Distribution of Zooplankton in the Laptev Sea and Adjacent Nansen Basin During Summer. *Polar Biol.* 19, 63–76. doi: 10.1007/s003000050216

Kosobokova, K., and Hirche, H. J. (2001). Reproduction of Calanus Glacialis in the Laptev Sea, Arctic Ocean. *Polar Biol.* 24, 33–43. doi: 10.1007/s003000000171

Kwasniewski, S., Hop, H., Falk-Petersen, S., and Pedersen, G. (2003). Distribution of Calanus Species in Kongsfjorden, a Glacial Fjord in Svalbard. *J. Plank. Res.* 25, 1–20. doi: 10.1093/plankt/25.1.1

Leu, E., Søreide, J. E., Hessen, D. O., Falk-Petersen, S., and Berge, J. (2011). Consequences of Changing Sea-Ice Cover for Primary and Secondary Producers in the European Arctic Shelf Seas: Timing, Quantity, and Quality. *Prog. Oceanogr* 90, 18–32. doi: 10.1016/j.pocean.2011.02.004

Levinsen, H., Turner, J. T., Nielsen, T. G., and Hansen, B. W. (2000). On the Trophic Coupling Between Protists and Copepods in Arctic Marine Ecosystems. *Mar. Ecol. Prog Ser.* 204, 65–77. doi: 10.3354/meps204065

Lischka, S., Knickmeier, K., and Hagen, W. (2001). Mesozooplankton Assemblages in the Shallow Arctic Laptev Sea in Summer 1993 and Autumn 1995. *Polar Biol.* 24186–, 199. doi: 10.1007/s003000000195

Lombard, F., Sciandra, A., and Gorsky, G. (2005). Influence of Body Mass, Food Concentration, Temperature and Filtering Activity on the Oxygen Uptake of the Appendicularian Oikopleura Dioica. *Mar. Ecol. Prog. Ser.* 301, 149–158. doi: 10.3354/meps301149

Mackas, D. L., and Bohrer, R. N. (1976). Fluorescence Analysis of Zooplankton Gut Contents and Investigation of Diel Feeding Patterns. *J. Exp. Mar. Biol. Ecol.* 25, 77–85. doi: 10.1016/0022-0981(76)90077-0

Matthews, J. B. L., and Hestad, L. (1977). Ecological Studies on the Deep-Water Pelagic Community of Korsfjorden, Western Norway. Length/weight Relationships for Some Macroplanktonic Organisms. *Sarsia* 63, 57–63. doi: 10.1080/00364827.1977.10411322

Mauchline, J. (1998). The Biology of Calanoid Copepods. *Adv. Mar. Biol.* 33, 176–219.

McClelland, J. W., Holmes, R. M., Dunton, K. H., and Macdonald, R. W. (2011). The Arctic Ocean Estuary. *Estuaries Coasts* 35, 353–368. doi: 10.1007/s12237-010-9357-3

McLaren, I., and Corkett, C. (1981). Temperature-Dependent Growth and Production by a Marine Copepod. *Can. J. Fish. Aquat. Sci.* 38, 77–83. doi: 10.1139/F81-010

Menden-Deuer, S., and Lessard, E. J. (2000). Carbon to Volume Relationships for Dinoflagellates, Diatoms, and Other Protist Plankton. *Limnol. Oceanogr* 45, 569–579. doi: 10.4319/lo.2000.45.3.0569

Menéndez, M. C., Piccolo, M. C., and Hoffmeyer, M. S. (2012). Short-Term Variability on Mesozooplankton Community in a Shallow Mixed Estuary (Bahía Blanca, Argentina): Influence of Tidal Cycles and Local Winds. *Est. Coast. Shelf Sci.* 112, 11–22. doi: 10.1016/j.ecss.2011.08.014

Morgan, C. A., Cordell, J. R., and Simenstad, C. A. (1997). Sink or Swim? Copepod Population Maintenance in the Columbia River Estuarine Turbidity-Maxima Region. *Mar. Biol.* 129, 309–317. doi: 10.1007/s002270050171

Nghiem, S. V., Hall, D. K., Rigor, I. G., Li, P., and Neumann, G. (2014). Effects of Mackenzie River Discharge and Bathymetry on Sea Ice in the Beaufort Sea. *Geophys. Res. Lett.* 41, 873–879. doi: 10.1002/2013GL058956

Osadchiev, A., Frey, D., Spivak, E., Shchuka, S., Tilinina, N., and Semiletov, I. (2021). Structure and Inter-Annual Variability of the Freshened Surface Layer in the Laptev and East-Siberian Seas During Ice-Free Periods. *Front. Mar. Sci.* 8. doi: 10.3389/fmars.2021.735011

Osadchiev, A. A., Medvedev, I. P., Shchuka, S. A., Kulikov, M. E., Spivak, E. A., Pisareva, M. N., et al. (2020). Influence of Estuarine Tidal Mixing on Structure and Spatial Scales of Large River Plumes. *Ocean Sci.* 16, 1–18. doi: 10.5194/os-16-1-2020

Overland, J., Hanna, E., Hanssen-Bauer, I., Kim, S.-J., Walsh, J., Wang, M., et al. (2019). [The Arctic] Surface Air Temperature [in "State of the Climate in 2018"]. *Bull. Amer. Meteor. Soc* 100 (9), S142– S144. doi: 10.1175/2019BAMSStateoftheClimate.1

Pasternak, A. F. (1994). Gut Fluorescence in Herbivorous Copepods: An Attempt to Justify the Method. *Hydrobiologia*, 292/293 241–248. doi: 10.1007/BF00229947

Pasternak, A., Arashkevich, E., Reigstad, M., Wassmann, P., and Falk-Petersen, S. (2008). Dividing Mesozooplankton Into Upper and Lower Size Groups:

Applications to the Grazing Impact in the Marginal Ice Zone of the Barents Sea. *Deep-Sea Res. II.* 55, 2245–2256. doi: 10.1016/j.dsr2.2008.05.002

Pasternak, A. F., Drits, A. V., and Flint, M. V. (2017). Feeding, Egg Production, and Respiration Rate of Pteropods *Limacina* in Arctic Seas. *Oceanology* 57, 122–129. doi: 10.1134/S000143701701012X

Perovich, D., Meier, W., Tschudi, M., Farrell, S., Hendricks, S., Gerland, S., et al. (2019). [The Arctic] Sea Ice Cover [in "State of the Climate in 2018"]. *Bull. Amer. Meteor. Soc* 100 (9), S146– S150. doi: 10.1175/2019BAMSStateoftheClimate.1

Peterson, W. T., Painting, S., and Barlow, R. (1990). Feeding Rates of Calanoides Carinatus: A Comparison of Five Methods Including Evaluation of the Gut Fluorescence Method. *Mar. Ecol. Prog. Ser.* 63, 85–92. doi: 10.3354/meps063085

Peters, J., Tuschling, K., and Brandt, A. (2004). Zooplankton in the Arctic Laptev Sea - Feeding Ecology as Indicated by Fatty Acid Composition. *J. Plank. Res.* 26, 227–234. doi: 10.1093/plankt/fbh017

Rogachev, K. A., Pomerleau, C., Shlyk, N. V., and Carmack, E. C. (2022). Joint Effects of Sea Ice Melt, Freshwater Discharge and Tidal Currents on Zooplankton Abundance in the Sea of Okhotsk: 2004 and 2013. *Polar Sci.* 31100781. doi: 10.1016/j.polar.2021.100781

Søreide, J. E., Falk-Petersen, S., Hegseth, E. N., Hop, H., Carroll, M. L., Hobson, K. A., et al. (2008). Seasonal Feeding Strategies of *Calanus* in the High-Arctic Svalbard Region. *Deep-Sea Res. II.* 55, 2225–2244. doi: 10.1016/j.dsr2.2008.05.024

Saiz, E., and Calbet, A. (2011). Copepod Feeding in the Ocean: Scaling Patterns, Composition of Their Diet and the Bias of Estimates Due to Microzooplankton Grazing During Incubations. *Hydrobiologia* 666, 181–196. doi: 10.1007/s10750-010-0421-6

Skjoldal, H. R., Aarflot, J. M., Bagøien, E., Skagseth, Ø., Rønning, J., and Lien, V. S. (2021). Seasonal and Interannual Variability in Abundance and Population Development of Calanus Finmarchicus at the Western Entrance to the Barents Se–2019. *Prog. Oceanogr* 195, 102574. doi: 10.1016/j.pocean.2021.102574

Sorokin, Y. I., and Sorokin, P. Y. (1996). Plankton and Primary Production in the Lena Delta Estuary and in the South-Eastern Laptev Sea. *Estuar. Coast. Shelf Sci.* 43, 399–418. doi: 10.1006/ecss.1996.0078

Steinberg, D. K., and Landry, M. R. (2017). Zooplankton and the Ocean Carbon Cycle. *Annu. Rev. Mar. Sci.* 9, 413–444. doi: 10.1146/annurev-marine-010814-015924

Sukhanova, I. N., Flint, M. V., Fedorov, A. V., Sakharova, E. G., Artemyev, V. A., Makkaveev, P. N., et al (2019). Phytoplankton of the Khatanga Bay, Shelf and Continental Slope of the Western Laptev Sea. *Oceanology* 59, 648–657. doi: 10.1134/S0001437019050205

Terhaar, J., Lauerwald, R., Regnier, P., Gruber, N., and Bopp, L. (2021). Around One Third of Current Arctic Ocean Primary Production Sustained by Rivers and Coastal Erosion. *Nat. Commun.* 12, 169. doi: 10.1038/s41467-020-20470-z

Timofeeva, A. B. , and Sharatunova, M. V. (2021). Multiyear Variability of the Fast Ice Thickness in the Laptev Sea According to the Polar Station Data. *Russian Arctic* 12, 62–76. doi: 10.24412/2658-4255-2021-1-62-76

Tiselius, P. (1988). Effects of Diurnal Feeding Rhythms, Species Composition and Vertical Migration on the Grazing Impact of Calanoid Copepods in the Skagerrak and Kattegat. *Ophelia* 28 (3), 215–230. doi: 10.1080/00785326.1988.10430814

Valdés, V., Escribano, R., and Vergara, O. (2017). Scaling Copepod Grazing in a Coastal Upwelling System: The Importance of Community Size Structure for Phytoplankton C Flux. *Lat. Am. J. Aquat. Res.* 45 (1), 41–54. doi: 10.3856/vol45-issue1-fulltext-5

van der Jagt, H., Wiedmann, I., Hildebrandt, N., Niehoff, B., and Iversen, M. H. (2020). Aggregate Feeding by the Copepods Calanus and Pseudocalanus Controls Carbon Flux Attenuation in the Arctic Shelf Sea During the Productive Period. *Front. Mar. Sci.* 7. doi: 10.3389/fmars.2020.543124

Vinogradov, M. E., and Shushkina, E. A. (1987). *Functioning of the Plankton Communities in Ocean Pelagic* (Moscow: Nauka (in Russian).

Vinogradov, M. E., Shushkina, E. A., Lebedeva, L. P., and Gagarin, V. I. (1995). Mesoplankton of the East Kara Sea and the Ob and Yenisei River Estuaries. *Oceanology* 34, 646–652.

Williams, W. J., and Carmack, E. C. (2015). The 'Interior' Shelves of the Arctic Ocean: Physical Oceanographic Setting, Climatology and Effects of Sea-Ice Retreat on Cross-Shelf Exchange. *Progr. Oceanogr* 139, 24–31. doi: 10.1016/j.pocean

Conflict of Interest: The authors declare that the research was conducted in the absence of any commercial or financial relationships that could be construed as a potential conflict of interest.

Publisher's Note: All claims expressed in this article are solely those of the authors and do not necessarily represent those of their affiliated organizations, or those of the publisher, the editors and the reviewers. Any product that may be evaluated in this article, or claim that may be made by its manufacturer, is not guaranteed or endorsed by the publisher.

Copyright © 2022 Pasternak, Drits, Arashkevich and Flint. This is an open-access article distributed under the terms of the Creative Commons Attribution License (CC BY). The use, distribution or reproduction in other forums is permitted, provided the original author(s) and the copyright owner(s) are credited and that the original publication in this journal is cited, in accordance with accepted academic practice. No use, distribution or reproduction is permitted which does not comply with these terms.

frontiers | Frontiers in Marine Science

TYPE Original Research
PUBLISHED 10 August 2022
DOI 10.3389/fmars.2022.896163

Check for updates

OPEN ACCESS

EDITED BY
Alexander Yankovsky,
University of South Carolina,
United States

REVIEWED BY
Steven Figueroa,
Chungnam National University, South Korea
Ewa Szymczak,
University of Gdansk, Poland

*CORRESPONDENCE
Z. Safar
z.safar@tudelft.nl
C. Chassagne
C.Chassagne@tudelft.nl

SPECIALTY SECTION
This article was submitted to Coastal Ocean Processes, a section of the journal Frontiers in Marine Science

RECEIVED 14 March 2022
ACCEPTED 29 June 2022
PUBLISHED 10 August 2022

CITATION
Safar Z, Chassagne C, Rijnsburger S, Sanz MI, Manning AJ, Souza AJ, van Kessel T, Horner-Devine A, Flores R, McKeon M and Pietrzak JD (2022) Characterization and classification of estuarine suspended particles based on their inorganic/organic matter composition.
Front. Mar. Sci. 9:896163.
doi: 10.3389/fmars.2022.896163

COPYRIGHT
© 2022 Safar, Chassagne, Rijnsburger, Sanz, Manning, Souza, van Kessel, Horner-Devine, Flores, McKeon and Pietrzak. This is an open-access article distributed under the terms of the Creative Commons Attribution License (CC BY). The use, distribution or reproduction in other forums is permitted, provided the original author(s) and the copyright owner(s) are credited and that the original publication in this journal is cited, in accordance with accepted academic practice. No use, distribution or reproduction is permitted which does not comply with these terms.

Characterization and classification of estuarine suspended particles based on their inorganic/organic matter composition

Z. Safar[1]*, C. Chassagne[1]*, S. Rijnsburger[1], M. Ibanez Sanz[2], A. J. Manning[1,3,4,5], A.J. Souza[6], T. van Kessel[7], A. Horner-Devine[8], R. Flores[9], M. McKeon[10] and J.D. Pietrzak[1]

[1]Section of Environmental Fluid Mechanics, Department of Hydraulic Engineering, Delft university of technology, Delft, Netherlands, [2]Antea group, Antwerpen, Belgium, [3]HR Wallingford Ltd, Coasts & Oceans Group, Wallingford, United Kingdom, [4]Energy and Environment Institute, University of Hull, Hull, United Kingdom, [5]Universiy of Plymouth, Plymouth, United Kingdom, [6]CINVESTAV, Merida, Yucatan, Mexico, [7]Deltares, Delft, Netherlands, [8]Department of Civil Engineering, University of Washington, Seattle, WA, United States, [9]Departamento de Obras Civiles, Universidad Tecnica Federico Santa Maria, Valparaiso, Chile, [10]Pacific Northwest National Laboratory, Portland, OR, United States

An 11 hours survey was performed on the 17th of September 2014 in the Rhine Region Of Freshwater Influence (Rhine-ROFI) about 10 km downstream of the mouth of the Rotterdam Waterway during calm weather conditions. Suspended Particle Matter (SPM) measurements were performed during a full tidal cycle, near the seabed, at neap tide, and samples were taken at 0.6 meter above bed for on-board analysis. The measurements were performed with (a) LISST 100X, a submersible particle size analyzer, (b) LISST-HOLO, a submersible digital holographic camera, (c) a home-made underwater camera and (d) an on-board LabSFLOC2 video microscopy equipment that used *in-situ* collected samples. The first aim of the present study was to compare the results obtained from the different monitoring techniques and to characterize the different types of suspended particles found in-situ. It was found that that the highly anisotropic particles present in the water column lead to multiple peaks in the Particle Size Distributions (PSD) found using the LISST 100X. Using the LISST-HOLO, underwater camera and LabSFLOC2 camera these particles could properly be imaged and meaningful PSD's were obtained using these techniques in the size range > 20 μm. LabSFLOC2, LISST-HOLO and the underwater camera moreover provide information on the size and aspect ratio of particles. On the other hand, LISST 100X can be used to detect the fine fraction (<20 μm), a size range that is not accessible for the other techniques. From the analysis of the data on the survey day, three classes of particles were identified, based on composition rather than size (the sizes given here are purely indicative): (1) mineral (inorganic) sediment particles in the range size 5 - 20 μm, (2) organic/inorganic aggregates in the size range 20 - 200 μm and (3) organic particles in the size range > 200 μm. A large range of settling velocities (0.1 - 10 mm/s) and aspect ratios between 1 and 10 were

recorded by video microscopy (LabSFLOC2). This spreading in settling velocities and aspect ratio was due to the different properties (shape, effective density and size) of the particles in the water column. The second aim of the study was to reproduce the flocs found *in-situ* in the lab and investigate the kinetics of flocculation between inorganic and living organic matter. Laboratory experiments were conducted with grab samples obtained from Port of Rotterdam harbour and living microalgae (*Skeletonema costatum*). The results of these experiments showed a shift in effective density upon addition of living algae to the sediment, which confirmed the flocculation ability between sediment and microalgae. The flocculation occured on a timescale of minutes and lead to flocs having a large spread in density for a given size, due to the heteregeous inorganic/organic composition of the flocs. This spread in density was at the origin of the large range of settling velocities for a given floc size observed in-situ, which leads to conclude that organic matter should be an important input parameter in sediment transport models.

KEYWORDS

Flocculation, SPM, ROFI, aggregation, algae, settling velocity, density

1 Introduction

Floc properties (size, shape, density) depend on parameters such as salinity (Lee et al., 2016), pH (Mietta et al., 2009), polymeric substances (Shakeel et al., 2020) and hydrodynamic shear (Verney et al., 2011). The conditions in which flocs were formed and the shear stress they experienced when they were created determine the flocs' structure (Shakeel et al., 2020). Sediment transport models that account for flocculation need to incorporate the key parameters that will lead to predictive models. These parameters should be measurable, so that the models can be validated. A new flocculation model was presented in (Chassagne and Safar, 2020) that is based on parameters measurable in-situ, in particular by laser diffraction (LISST 100X). The remaining parameters (linked to flocculation kinetics) can be found by laboratory experiments. Settling velocity of flocs, which is an input parameter in sediment transport models, is often obtained by estimating the density of flocs based on *in-situ* measurements. The mean density of flocs is usually obtained by assuming that all flocs (represented by a mean size i.e. a D50) have the same density (Fettweis, 2008; Many et al., 2016). Even though this assumption may be valid for some (large) aquatic regions, it is questionable whether this can apply to estuarine areas. In Regions Of Freshwater Influence (ROFI) in particular, it is generally observed that at the top of the water column, the Suspended Particulate Matter (SPM) concentration, in terms of inorganic sediment, is much lower than in the ambient coastal water during stratified water column conditions (Pietrzak et al., 2011). However, biological algal species and organic particles can be advected by the freshwater plume (De Ruyter van Steveninck et al., 1992; Schofield et al., 2013; Cross et al., 2015; Deng et al., 2019). Coastal waters are nutrient-rich and their shallowness provides good light penetration. They are suitable environments for micro-organisms such as diatoms, bacteria, dinoflagellates, phytoplankton and zoo-plankton (Van de Meent, 1982; De Ruyter van Steveninck et al., 1992; van Leussen, 1999; Lartiges et al., 2001; Roozen, 2005; van der Hout et al., 2012). A wide variety of diatoms, dinoflagellates and flagellates are for instance found in the Dutch coastal area of the North Sea. Most abundant are *Skeletonema costatum, Rhizosolenia delicatula, Chaetoceros and Paralia* (Rijstenbil, 1987; Prins et al., 2012; Blauw, 2015). These micro-organisms are important in the formation of estuarine aggregates. Aggregates (flocs) are formed in the water column, when organic matter, from the top of the water column, and inorganic matter, found in deeper water layers, meet (Deng et al., 2019). Both living and dead organic matter contribute to this process. By colonizing and growing on the nutrient-rich sediment particles microorganisms form aggregates of different size, shape, density and settling velocity (Logan et al., 1995; Razaz et al., 2015; Lee et al., 2017; Schwarz et al., 2017). Studies have shown that the algal mucous secretion and cell protuberance lead to entanglement and aggregate formation of algae during sinking, and that these 'sticky' aggregates scavenge minerals and other particles during settling, which further increases the settling velocity (Pavoni et al., 1972; Alldredge and Gotschalk, 1989; Passow et al., 1994; Dam and Drapeau, 1995). Even small-celled diatoms such as

Skeletonema costatum, the microalgae that we used in laboratory studies, attain high settling velocities due to their formation in chains and their ability to aggregate (Malone, 1980; Smetacek, 1985; Manning et al., 2017). The dead cells of the algae can also accumulate as particulate organic matter. This organic matter will be a source of sticky material that also aggregate with clay minerals and sediment particles to form flocs. Some of the particulate organic matter will be microbially decomposed into dissolved organic matter in the water column as well as in the sediment bed (Foree and McCarty, 1970). The near-bottom water flow transports (in)organic matter and microorganisms and is therefore another driving mechanism for sediment transport along many coasts, where both advection and resuspension occur (Ganaoui et al., 2007). The organic matter present in the water column is time and space dependent (Khelifa and Hill, 2006; Maggi, 2007; Fettweis and Baeye, 2015; Fettweis and Lee, 2017). When aggregated with mineral clay it will be shown that the produced flocs can have variety of shapes. This shape will be discussed in terms of particles aspect ratio in the present article.

The aim of this study is to investigate the properties of particles in the Rhine ROFI (size, shape, composition, density and settling velocity) and categorize those particles accordingly. These classes of particles will serve as input parameters for anticipated modelling studies (Chassagne and Safar, 2020). The one-day survey that was chosen to perform the analysis was a calm weather day. The low energetic conditions (neap tide) during the survey day led to the presence of very anisotropic particles in the water column and low SPM concentrations, which makes the interpretation of the *in-situ* data by diffraction techniques challenging. Studying the particles characteristics during these conditions is however interesting because at higher energetic conditions, mineral sediment particles dominate the Particle Size Distribution (PSD) close to the bed, where the measurements were performed. This would not allow the study of organic matter-based particles, which have typically a low concentration but play an important role in the flocculation and resuspension processes.

Four different in-situ/on board instruments, based on optical techniques, were used simultaneously during this one day boat survey in the Rhine-ROFI to perform this analysis. It will be shown that the combination of instruments enables to give an accurate overview of the different types of particles found in-situ, ranging from organic highly anisotropic particles to quasi-spherical mineral clay particles. In particular, it will be shown that the use of an underwater camera enables to clearly identify particles in the range of 10 μm — 1000 μm. The use of underwater cameras was long limited to size analysis of objects larger than hundreds of microns (Van Leussen and Cornelisse, 1993; Sternberg et al., 1999). Due to the latest development in camera specifications, it is nowadays possible to use underwater cameras with a much better resolution and light sensitivity (Benson and French, 2007; Smith and Friedrichs, 2015; Shen and Maa, 2016), which enables to assess particles larger than 10 μm.

Additional laboratory experiments have been performed to try to reproduce the flocs observed in-situ. The kinetics of flocculation are studied using static light scattering and the steady-state population of flocs is observed by video microscopy.

2 Materials and methods

2.1 *In-situ* measurements

2.1.1 Survey site and hydrodynamic conditions

An 11 hour boat survey (6:00 - 17:00 GMT) was performed on the 17th of September 2014 in the Rhine Region of Freshwater Influence (Rhine-ROFI) about 10 km downstream of the mouth of the Rotterdam Waterway during calm weather conditions. This field survey was part of a large field campaign that was conducted in September-October 2014 in the mid-field region of the Rhine ROFI (Flores et al., 2017), close to the Sand Engine (Stive et al., 2013). A mooring and two frames were deployed at 12 m depth as part of the Stratification Impact on Near-shore Sediment Transport (STRAINS II) experiment (Flores et al., 2017; Horner-Devine et al., 2017; Rijnsburger et al., 2018). In Figure 1 the position of the survey vessel is indicated by the capital letter S and cross. The mooring and two frames location is indicated by the capital letter M and the dot.

The tidal elevation at Hoek van Holland was between 0.85 m and -0.62 m, and the wind speed stayed below 6 m/s coming from the east. In addition, the significant wave height was below 0.5 m, which was retrieved from a wave rider buoy 1 km south from the survey site. The total river discharge from the Rhine and Meuse River was about 1500 m^3/s, for that day. The boat survey started at flood tide, before the flood peak. The water column was weakly stratified with a salinity difference of 2 PSU (Practical Salinity Unit) between surface and bottom. The water column was divided into different salinity layers after a front arrival 2 hours later. The stratification prevailed almost the whole day as it was a neap tide day with low energetic mixing conditions. Note that the salinity close to the bottom remained close to 30 PSU.

The one day field-survey was used to study SPM in the near bed part of the water column. Several *in-situ* instruments, based on optical techniques, were used simultaneously during this day. Two of these instruments (LISST 100X and LISST-HOLO) were on a frame in the vicinity of the survey vessel whereas the underwater camera was operated from the vessel and the LabSFLOC2 camera set-up was used on board. The samples studied with the LabSFLOC2 camera were collected using a Van Dorn sampler and analysed as soon as the sampler was retrieved.

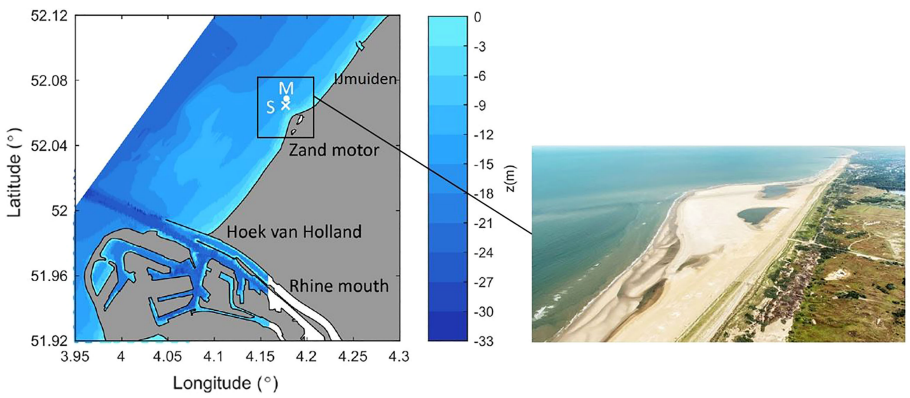


FIGURE 1
Left figure: Measurement position is given by (x), position of the survey vessel (S, cross), and the mooring and frames (M, dot). Right figure: Aerial view of the Sand Engine close to which the field survey was conducted (Photo: Rijkswaterstaat).

2.1.2 LISST 100X

LISST 100X (Laser *In-Situ* Scattering and Transmissometry) uses laser diffraction to determine the volume concentrations of particles in 32 logarithmically spaced effective spherical diameter classes. The obtained Particle Size Distribution (PSD) ranges for the 100X type from 2.5 – 500 μm (Traykovski et al., 1999; Agrawal, 2001). The LISST 100X was placed on the bottom frame, 1.65 m above the bed (mab) and measurements were taken every 10 seconds. The data was averaged over 10 minutes bursts.

2.1.3 LISST-HOLO

LISST-HOLO (Submersible Digital Holographic Camera) is an *in-situ* digital holographic technology that uses solid state diode laser at 658 nm and 4.4 μ m pixel size digital camera (1600 × 1200 pixels). It measures equivalent spherical diameters in the size range of 25-2500 μ m, within 50 log spaced size classes. The LISST- HOLO was placed at 1.40 mab on one of the two frames and took a picture every 5 minutes. The LISST-HOLO was tuned to get the most appropriate values for *clean stack* and *threshold* parameters (Davies et al., 2011). *Clean Stack* 3% and default *threshold* of 0.15 were found to give the best pictures and were used to process the raw data (LISST HOLO manual). The particle density can be estimated from the *solidity* calculated by the LISST-HOLO software. The *solidity* is defined as the solid fraction of a given particle, and can be related to the porosity of that particle (Choi et al., 2018). A fully solid particle will have a *solidity* of 1, whereas a *solidity* close to 0 will indicate a very porous particle. The *solidity* is obtained by dividing the black area of a particle (A_B=N×r^2 where r^2 is the area of a black pixel and N the number of black pixels within a particle) by the total area (A) of that particle. We assume that the volume of the particle is given by V=A×c , where c is the dimension of the particle perpendicular to the field of view of the camera, and V_B=A_B×c is the volume of the black area. Assuming that the particles properties do not change along the direction indicated by c, we can express *solidity* as function of the volume of the particle by:

$$S = \frac{A_B \times c}{A \times c} = \frac{V_B}{V} \tag{1}$$

The density ρ_p of a particle is given by:

$$\rho_p = \rho_s \frac{V_B}{V} + \frac{(V - V_B)}{V} \rho_w \tag{2}$$

where ρ_s is the absolute density of the solid part and ρ_w is the absolute density of water (that fills the voids). It is assumed that no air is trapped in the flocs. From this we can deduce that the effective density of a floc is given by:

$$\rho_e = \rho_p - \rho_w = (\rho_s - \rho_w)S \tag{3}$$

The density of the solid fraction ρ_s (represented by black pixels) is at this stage unknown. For mineral sediment flocs it can be expected to be close to 2600 kg m^{-3} and for organic rich particles, expected to be much lower (1016-1600 kg m^{-3}) (Deng et al., 2019; Chassagne et al., 2021; Deng et al., 2021). Note that the assumption that the particle's properties do not change along the direction indicated by c can lead to erroneous estimations.

2.1.4 LabSFLOC2 settling column camera system

The water samples were taken at 0.6 mab depth and were analysed using the LabSFLOC2 camera system (Laboratory Spectral Flocculation Characteristics, version 2) that recorded the settling velocity of particles from a pipetted amount of sample. The particle size, shape and effective density were estimated from the settling velocity (Manning et al., 2007b; Manning et al., 2010; Manning et al., 2017).

LabSFLOC2 was developed by Manning (Manning and Dyer, 2002; Benson and Manning, 2013; Manning et al., 2017), and it utilizes a high magnification 2.0 MP Grasshopper monochrome digital video camera (Manning and Dyer, 2002) to observe individual flocs as they settle in a 350 mm high by 100 mm square Perspex settling column. The video camera, positioned nominally 75 mm above the base of the column, views all particles in the center of the column that pass within a 1 mm depth of field, 45 mm from the Sill TZM 1560 Telecentric (maximum pixel distortion of 0.6%), 0.66 (1:1.5) magnification, F4, macro lens fitted behind a 5 mm thick glass face-plate.

During sampling, a modified pipette is used to carefully extract a floc sub-sample from the Van Dorn chamber and is filled to produce a fluid head of 50 mm, which results in a video image control sample volume nominally of 400 mm^3 (1 mm image depth and 8 mm nominal video image width, with a nominal 50 mm high suspension extracted with a modified pipette). This controlled volume permits in principle LabSFLOC2 calculated floc mass to be compared and calibrated directly to ambient SSC. In the present study, this was not performed.

The pipette sub-sample is immediately transferred to the LabSFLOC2 settling chamber, whereby the aperture of the pipette was brought into contact with the LabSFLOC2 settling column water surface and permitted the flocs to pass from the vertically held pipette to the chamber and settle solely under gravity, i.e. naturally and unassisted. Thus, the flocs allowed to pass into the settling column were naturally segregated as they fell by the process of differential settling; i.e. the fastest falling aggregates would be observed first.

Settling flocs are viewed as silhouettes (to reduce image smearing) resulting from a CCS LDL-TP-43/35-BL, 43 x 35 mm, homogeneous blue (470 nm) back-illumination LED panel, located at the rear of the settling column. The video images are streamed in real time as AVI files to a laptop PC *via* a FireWire-B PCI card interface. The digital floc images are captured at a frame rate of 25 Hz (one frame is 0.04 s), at a resolution of 1600 × 1200 pixels, with an individual pixel nominally representing 5 μ m (confirmed by independent calibration). The AVI files are not Codec compressed, so they could be analysed with MATLAB software routines. During post-processing, the HR Wallingford Ltd DigiFloc software - version 1.0 (Benson and Manning, 2013; Manning et al., 2017), is then used to semi-automatically process the digital recordings to obtain floc size and settling velocity spectra.

The sphere-equivalent floc diameter, D , was calculated from the measured major and minor axis of each observed two-dimensional floc by (Manning and Schoellhamer, 2013):

$$D = (D_{major} \times D_{minor})^{0.5} \tag{4}$$

Each floc settling velocity was determined by measuring the vertical distance that the floc travels between a sequence of frames. Stokes Law then enables an estimation of individual floc effective density (Manning and Schoellhamer, 2013),

$$\rho_e = \rho_p - \rho_w = \frac{18 W_s \mu}{g D^2} \tag{5}$$

where W_s is the settling velocity, μ is the water viscosity and g is the gravitational acceleration.

During the survey day, 26 samples were analyzed using the LabSFLOC2 camera system.

2.1.5 Underwater video camera

A video camera mounted under the Van Dorn sampler was lowered at each sampling time, to take videos of the particles at the sample location. The camera was an Imaging source GigE color camera, I/O Aptina CMOS MT9P031, with a maximum resolution of 2592 × 1944. The pixel size is $2\mu m \times 2\mu m$. The videos taken with the underwater camera were used for qualitative analysis of the flocs and not for quantitative size analysis.

2.2 Laboratory measurements

Based on the observed field results, additional laboratory experiments were conducted to study flocculation of Port of Rotterdam (PoR) sediment as function of microalgae concentration. Seawater (filtered through a 5 μ m filter) was used as the suspending medium.

2.2.1 Sediment suspensions

The experiments were conducted with grab samples taken in the neighborhood of the survey (at the mooring indicated on the map and defined as PoR sediment.The samples were kept in a dark refrigerated room for two weeks before being used. The samples were sieved so as to remove particles coarser than 125 μm.

2.2.2 Algae

The microalgae *Skeletonema costatum* was chosen in the study, as being one of the most predominant algae species in the coastal area (Rijstenbil, 1987). The algae was obtained from the hatchery Roem van Yerseke B.V. The concentration of the algae stock suspension was about 5×10^6 cells/mL and was kept in a dark environment to avoid photosynthesis and limit changes in concentration. The algae stock was refreshed every two weeks.

2.2.3 Particle size measurements

The Particle Size Distribution of samples was obtained by Static Light Scattering (SLS) using a Malvern Mastersizer 2000 which provides a full PSD every 30 s. The size range of the SLS device is 0.01-10000 μ m in 100 logarithmic-spaced bins. The samples are stirred in a 1L-jar at a constant rate of 35 rpm (Shear rate = 30 s^{-1}), and pumped through pipes to and from the SLS device at a constant rate of 10 rotation per minute (rpm) which is about 12 s^{-1} . The set-up is the same as the one used by Ibanez

et al. (Ibanez Sanz). The shear rates used are usually higher than those observed in the field (which are of the order of 0–10 s^{-1}), especially at neap. However, these rates were determined in preliminary experiments to ensure a minimal breakage of the aggregated fractions and avoid settling in the pipes.

When a steady-state PSD was reached for a given algae concentration, the concentration of algae was adjusted to a higher content. The percentage of algae content was increased in steps to get concentrations of 10, 20 and 30 volume %. A separate measurement was done for a concentration of 5 volume %. Each percentage corresponds to the volume taken from the microalgae stock suspension divided by the total volume in the jar. At steady-state, some sub-samples have been pipetted and studied with the LabSFLOC2 camera system that was mounted in the laboratory. The description of the LabSFLOC2 camera system is given in Section 2.14. In order to obtain a good signal to noise ratio by SLS we used sediment and algae concentrations that are 100 times more concentrated than the ones observed *in-situ* during our one-day survey. The time scale of aggregation is therefore not be representative of *in-situ* conditions but an indicator whether flocculation is (or not) taking place.

3 Results and discussion

3.1 Field survey results

3.1.1 Classes of particles

From the underwater camera records and the LISST-HOLO pictures, different types of particles are identified, as shown in Figure 2. One type corresponds to (mineral) sediment-rich flocs, having an effective density close to 1600 kg m^{-3} with settling velocity of 1 - 10 mm/s. These particles have compact form and dark color (high density). An other particle type corresponds to organic matter-rich particles having an effective density between 16 - 160 kg m^{-3} with a settling velocity of 0.1 - 1 mm/s. These particles display an open or anisotropic structure and have a lighter color (low density). They are likely composed of inorganic and organic particles such as Transparent Extracellular Polymeric (TEP) substances (Jarvis et al., 2005; Spencer et al., 2010). For some of these flocs, the elongated algae structure is still recognizable, although the algae is coated with (in)organic debris and can be in some state of coiling. The third type corresponds to bare algae, or algae bound to very little amount of sediment, which have a very low density of about 16 kg m^{-3} with low settling velocity, mostly around 0.1 - 0.5 mm/s. The microalgae *Skeletonema costatum*, for instance, is known to form elongated strings (Karp-Boss et al., 2007; Many et al., 2019). Despite having such different settling velocities and densities, all these particles are composed of different amounts of organic and inorganic matter. As detailed in (Chassagne et al., 2021), flocs composed in part of organic and inorganic particles are defined as Class 2 particles, whereas pure organic particles (like microalgaes) are defined as belonging to Class 3. Class 1 particles are defined as pure mineral clay particles, and none of the particles observed using video techniques were belonging to this class. As the survey day was very calm, only very small clay particles (<1 μ m) are expected to be in suspension.

The LabSFLOC2 camera cannot measure sizes below 10 μ m, a range that is accessible to the LISST-HOLO. This implies that

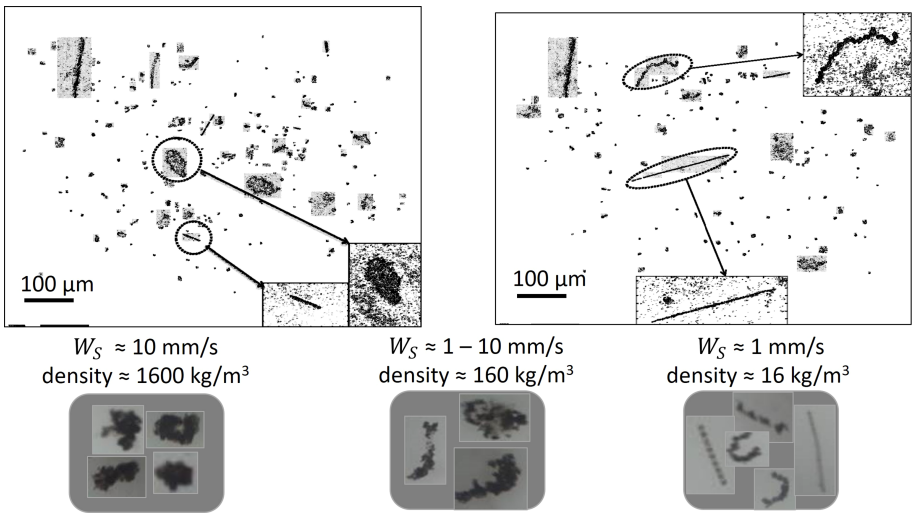


FIGURE 2
Different particles identified by LISST-HOLO (top figures) and underwater camera (bottom pictures) recordings. The indicated settling velocities and derived densities are found by LabSFLOC2 measurements. All the flocs illustrated here belong to the size range of 20 - 200 μ m. The flocs composed of inorganic/organic particles belong to Class 2 (left and middle pictures, some flocs on the right picture), whereas the bare algae (strings devoid of mineral sediment that are seen on the right picture) belong to Class 3.

in Figure 3 no particle below 10 μ m are recorded using the LabSFLOC2. As it was a calm day, not many particles were recorded, and a large spread in settling velocity was recorded the whole day. On the other hand, with the LabSFLOC2 technique, more large particles (> 100 μ m) were observed than with LISST-HOLO. This can partially be due to the fact that differential settling is occurring while particles are left to settle after being pipetted into the settling column. This would also lead to the cluster of fast-settling particles observed at 10:40 for example (also seen at 12:30) in Figure 3. Another possibility for these fast-settling particles is the coiling of flocs under shear that occurs continuously and lead to flocs as illustrated in Figure 2, at the bottom left. In Figure 4 a large spread in density for a given floc size is observed (left panel) - this spread is related to the spread in settling velocity for a given floc size, as shown in Figure 3. This spread was also observed in many studies, see for instance (Manning et al., 2007a; Manning and Schoellhamer, 2013). The spread in density for a given size can be attributed to two factors: first, the composition of a floc (the relative amount of mineral and organic matter within a floc) and second, a conversation artifact due to the shape of a floc. For highly anisotropic particles such as algae, the equivalent diameter will be estimated by:

$$D = D_{minor} \times \sqrt{AR} \tag{6}$$

where the AR the aspect ratio. For a 1 mm long algae, with AR=10 , this gives an equivalent diameter of about 100 μ m, which is the size that many flocs of aspect ratio close to 1 also have. Plotting the density as a function of the particle major axis can therefore help to better differentiate the different types of particles as illustrated in Figure 4, right panel where some elongated particles are now visible in the LISST-HOLO plot.

3.1.2 Density of particles

Particle density estimations are given in Figure 4 for the samples measured at 10:40 by LabSFLOC2 and LISST-HOLO. The data for that time is representative for all the three main type of particles found during the survey day. The density of the flocs recorded using the LabSFLOC2 was evaluated using the method described in Section 2.1.4. The density of the flocs recorded using the LISST-HOLO was evaluated using the method described in Section 2.1.3. This method requires the solid fraction density ρ_s as input, see eq.(3). From Figure 4, it can be seen that for particles having a major axis D_{major}<300 μm, the data found by LISST-HOLO and by LabsFLOC match when ρ_s is taken to be the one for mineral clay (which is done for the data plotted in the left panel as well as the one indicated as ρ_s = 2600 kg m^{-3} in the right panel), whereas for particles having a major axis D_{major}>300 μ m, the data found by LISST-HOLO and by LabsFLOC match when ρ_s is taken to be close to the density of organic material (which was taken to be 1016 kg m^{-3}). This is done in the right panel (ρ_s = 1016 kg m^{-3}). This implies that a black/white scale to estimate the solidity as proposed in Section 2.1.3 is not appropriate to estimate densities and that a proper

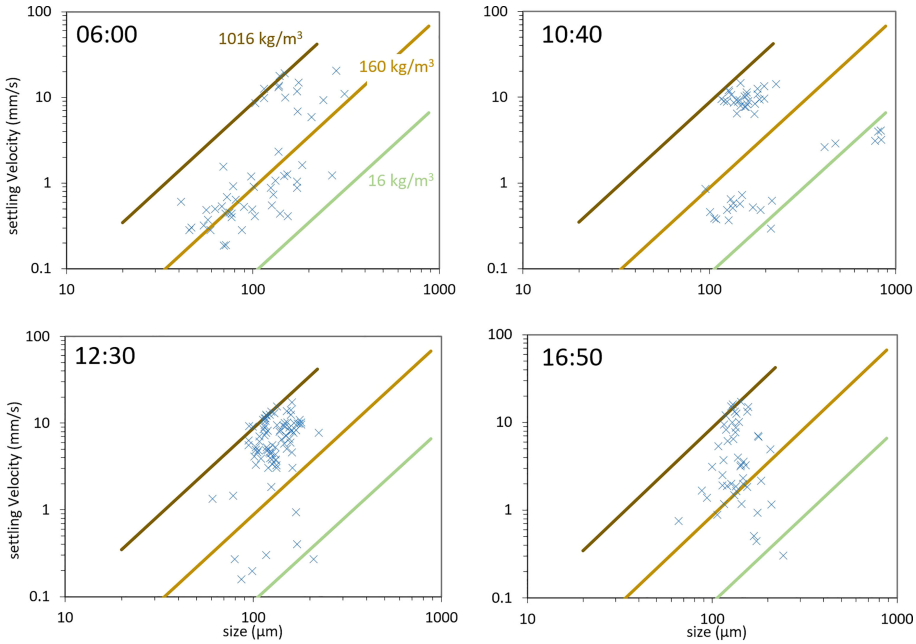


FIGURE 3
Settling velocities as function of equivalent diameter, as determined by LabSFLOC2 measurements at different GMT times of the survey day.

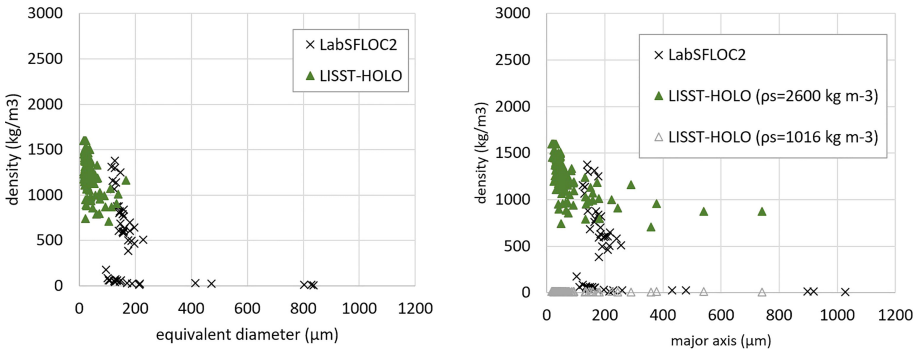


FIGURE 4
Density of particles as function of size, determined by LabSFLOC2 and LISST-HOLO measurements for survey time 10:40 (GMT). Left figure: as function of particle equivalent diameter, right figure: as function of particle major axis. See text for details about the derivation of the density from LISST-HOLO data.

greyscale analysis should be performed, whereby the greyscale would be calibrated with the inorganic/organic composition of a floc. This can not be done at present, as this analysis requires a proper calibration of the greyscale colours based on more extended research.

The fact that density of flocs decreases with size has been reported by numerous studies (Gibbs, 1985: Al Ani et al., 1991; Vaezi et al., 2011; Mehta et al., 2014; Ramirez Mendoza). This density/size dependence is usually modelled using the relation

$$\rho_e = (\rho_s - \rho_w)\left(\frac{D}{D_0}\right)^{D_f-3} \quad (7)$$

where D is the particle diameter evaluated according to eq.(4) and D_0 is a reference size, usually taken to be the one of a primary particle. The parameter D_f found from fitting the data is often refered to as a fractal dimension. As we now have seen, even though eq.(7) usually models well the data, no information can be gained from D_f as in the situations where organic matter plays a role in flocculation, ρ_s will be a decreasing function of D.

3.1.3 Particle Size Distribution (PSD) with various techniques

As the size of the particles did not change significantly during the whole day, the PSD data from the LISST 100X, the LISST-HOLO and the LabSFLOC2 camera system were averaged over the entire day for each instrument. This enabled having a statistically significant data set, as the amount of particles detected was low during the day. Figure 5 shows the day average particle size distributions estimated by the three techniques. Although the LabSFLOC2 camera data are not

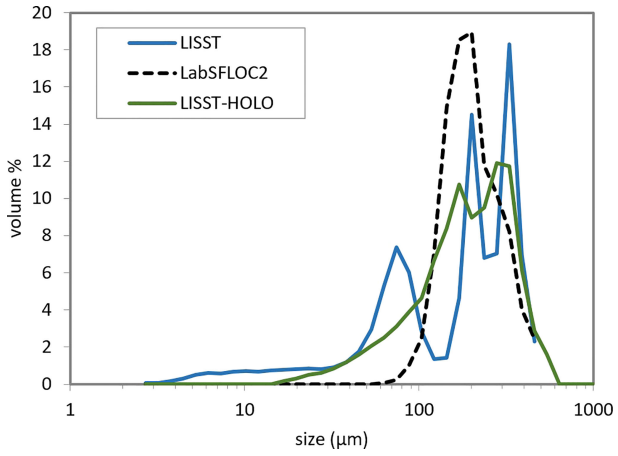


FIGURE 5
Comparison between the PSD's obtained from three measurement techniques. Each PSD is the average of the data collected during the 11 hour survey.

directly comparable with the LISST data due to differences between the two techniques (Mikkelsen et al., 2005), the overall mean size of the particles obtained from the LabSFLOC2 camera correlates with the mean particle size obtained from the LISST data and fluctuates between 150 and 220 μ m.

The clay-silt fraction (< 10 μ m) can only be assessed by LISST 100X and is out of the LISST-HOLO and LabSFLOC2 system range.

The averaged PSD measured by LISST 100X is trimodal with peaks in particle sizes at 300, 200 and 70 μ m. It was shown by Karp-Boss et al. that biological species cause trimodal distributions in LISST 100 data due to their very anisotropic shape (Karp-Boss et al., 2007). The PSD measured by LISST-HOLO displays two marked peaks which overlap the 200 μ m and 300 μ m LISST 100X size peaks. Graham et al. showed that the PSD produced by LISST-HOLO usually indeed overlap with the PSD of LISST 100X in the size range (20-500 μ m) (Graham et al., 2012). The LabSFLOC2 data on the other hand displays one wide peak that tends to be bimodal, overlapping mainly the 200 μ m peak and slightly the 300 μ m peak. Graham and Nimmo Smith (2010), who compared the LISST-HOLO PSD with the Malvern Hydro 2000G PSD, have found that the LISST-HOLO PSD showed multiple modes as compared to the monomodal PSD produced by the Malvern Hydro 2000G, which were attributed to overlapping large particles in the field of view of the holographic system. In our case, the presence of highly anisotropic particles leads to same kind of effect. The PSD found using the LabSFLOC2 technique is based on the particle size estimation given by eq.(4). Both minor and major axis are visually determined and therefore no error is made when identifying the particles.

Agrawal et al. inverted the data found by LISST 100X using different kernel matrix to produce particle size distribution for non-spherical particles (Agrawal et al., 2008). However their method does not apply to very anisotropic particles such as bare algae and flocculated algae as are present in our observations. This is why a combination of holographic pictures and/or other video or camera recording, are necessary to interpret the LISST 100X PSD as was also concluded by Graham et al. (2012).

3.2 Laboratory Experiments results

From laboratory experiments it is possible to study the time evolution of the clay-algae floc size distributions without the technical problems encountered with the *in-situ* LISST (Graham and Nimmo Smith, 2010). The untreated PoR sediment obtained from grab samples and the microalage were suspended in seawater as described in Section 2.2. The PSD was measured during flocculation.

Figure 6 shows the SLS (Malvern 2000) measurements of the mean particle sizes (D50) evolution in time until reaching a steady-state. The corresponding PSDs are given in Figure 7.

The flocculation rate of PoR sediment particles (no added algae) is low, as is usually observed for sediment suspensions in saline water. It has been shown that salt-induced flocs are extremely fragile, and that their (fully reversible), growth/break-up is proportional to shear stress (Mietta et al., 2009). The organic matter originally present in the PoR samples is decayed, as the samples have been stored for quite some time in a fridge. It is unclear at this stage whether this organic matter (originally present in PoR sample) plays a role in the flocculation process. After reaching steady-state, Living Algae (LA) is added to the suspension to produce a 10% LA + 0.2 g/L PoR sediment suspension. After reaching a steady-state more LA is added to produce a 20% LA + 0.17 g/L PoR sediment suspension. This procedure is repeated to produce a 30% LA + 0.15 g/L PoR sediment suspension. A separate measurement (open symbols) was performed for a 5% LA + 0.21 g/L PoR sediment suspension. In the presence of algae, the mean particle size shifts towards higher particle sizes in a few minutes, indicating that the sediment

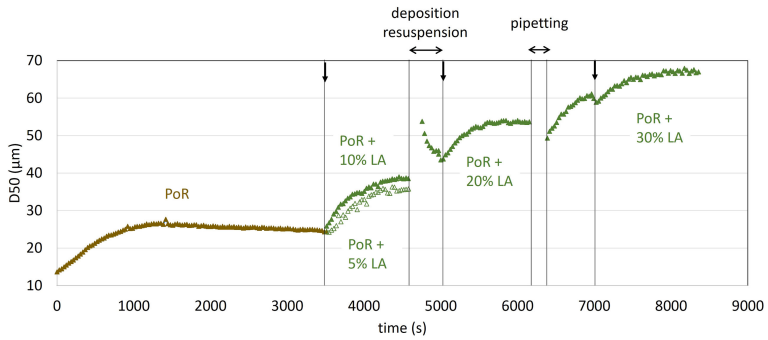


FIGURE 6
Mean particle size (D50) evolution as function of time. The vertical arrows indicate injection of Living Algae (LA). See text for details.

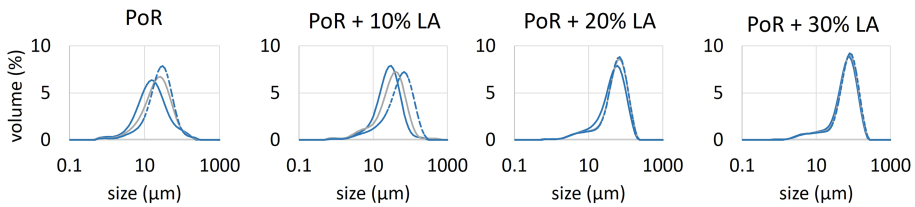


FIGURE 7
Particle size distributions as function of time. Full blue curve: after injection of algae; grey curve: 500 s after injection; dashed blue curve: before sampling for LabSFLOC2 measurements (when steady-state is reached).

particles are binding to the algae. From Figure 7, it can be seen that the Particle Size Distribution (PSD) of the samples remain fairly monomodal, even just after injection of microalgae. In contrast to *in-situ* measurements, the algae used in the lab experiments is rather monodisperse and in the micron-size range. This explains why flocs grow monotonically over time, as more microalgae and sediment particles stick together. After reaching each steady-state a sample was taken to be analysed with the LabSFLOC2 camera system, see Figure 8.

Besides the mean size of particles, the aspect ratio of each particle was also determined and the density of each particle evaluated using Stokes Law. The results are given in Figure 9. A distinction is made in that figure between particles having an effective density larger or lower than 160 kg m^{-3} . The value of 160 kg m^{-3} corresponds to the middle line in Figure 8.

The PoR sediment sample displays particles in the size range 20-350 μ m with a wide range of settling velocities (between 0.01 - 10 mm/s), aspect ratio (AR = 1 - 3) and absolute densities (0 - 2500 kg m^{-3}). In the sample with 5% LA content, the particles have aggregated with algae of lower density and hence the settling velocity range becomes (0.01 - 0.5 mm/s). The estimated densities are now in the range (0 - 1500 kg m^{-3}). One large cluster with effective density between 160 kg m^{-3} and 16 kg m^{-3} is found in the size range > 100 μ m, see Figure 9. These low density particles can be attributed to microalgae which have aggregated with themselves.

Upon addition of LA, the density/size profile changes in shape and resembles more an exponential decreasing density function of size, as it is usually observed in estuarine conditions (Manning and Schoellhamer, 2013). The PoR sample has a much wider spread in density for a given particles size compared with sediment and living algae. This is consistent with the fact that the the LA binds to the mineral sediment particles, hereby reducing the density of the particles. As was discussed in the previous subsection, eq.(7) cannot be used to estimate a meaningful fractal dimension, as ρ_s depends on particle size.

The sample with 30% LA shows a large number of clusters, with a large spread in settling velocities (0.01 - 10 mm/s). A large amount of particles are found in the effective density range 160 - 16 kg m^{-3} and sizes > 100 μ m, which indicates that these particles are algae-rich. These particles are also elongated (AR > 1), see Figure 9. The AR is not as high as the ones observed in-situ, due to the shear imposed in the jar, which prevents flocs to grow anisotropically. This condition is different in-situ, where the shear is usually milder and differential settling can occur, whereby particles can "catch-up" with each other (Deng et al., 2021).

When pippeting the samples for the LabSFLOC2 experiments in the presence of algae, the stirrer twice needed to be stopped in the jar, resulting in the deposition of flocs at the bottom of the jar (see "deposition/resuspension" and "pipeting" in Figure 6). When the stirrer was set in motion again, flocs were resuspended and it was assumed that aggregation had occured

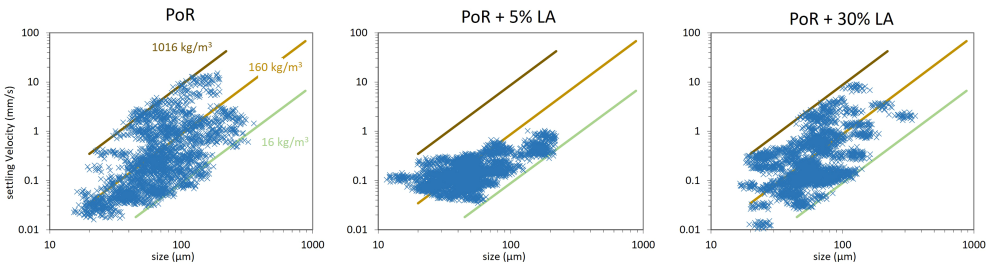


FIGURE 8
Settling velocity as function of mean size (equivalent diameter) determined by LabSFLOC2 experiments.

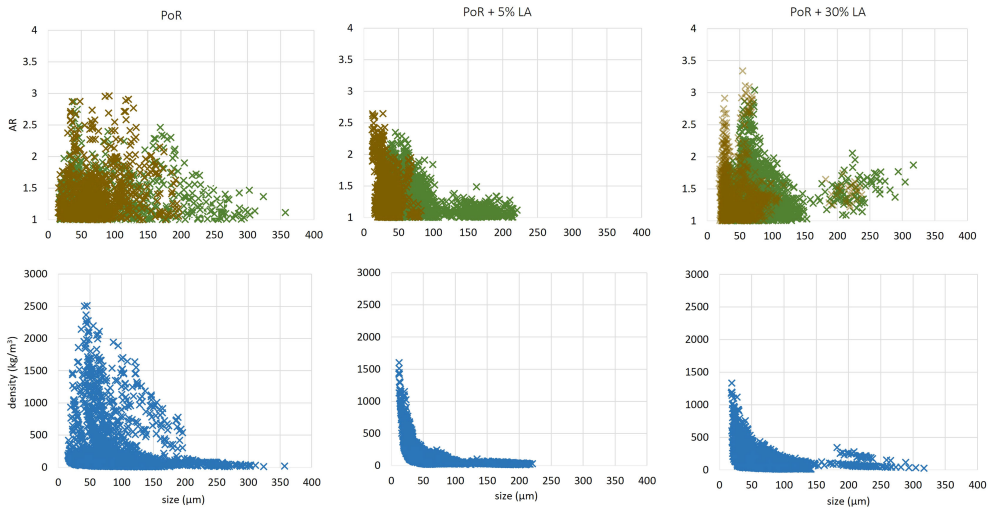


FIGURE 9
Top panel: Aspect Ratio (AR) as function of equivalent diameter. The brown color represents particles of effective density larger than 160 kg m^{-3} and the green colour particles of density lower than 160 kg m^{-3} . Bottom panel: absolute density as function of equivalent diameter. The data is obtained by LabSFLOC2 experiments.

between flocs that had been in contact at the bottom of the jar. This resulted in the large size increase upon resuspension observed after "deposition/resuspension". Very rapidly, due to shear, the mean size decreased towards the steady-state value found before the stirrer was stopped. At "pipetting" the stirrer was only very briefly stopped. Despite the fact that the D50 had reached a steady-state prior the pipeting, some size increase was observed after the stirrer was set in motion again.

4 Conclusion

In this study, we have presented the SPM characteristics of a one-day field survey in the Rhine ROFI, during neap tide calm weather conditions with a variety of techniques. Videos from the underwater camera and LISST-HOLO data show the presence of many algae particles in the bottom water layer. These particles can be found in the form of elongated chains, or bound to debris and mineral particles in different degrees of coiling. From sample analysis done on board with a LabSFLOC2 camera, the aspect ratio of the particles could be quantified and was found to be close on average to 2 for the lightest particles (effective density < 160 kg m^{-3}) even though aspect ratios between 3 and 8 were also observed for this class of particles. All the other particles have in good approximation an aspect ratio close to 1. According to their density estimations, and confirmed visually from the LISST-HOLO and underwater camera video recordings, these lightest particles were algae-rich flocs or bare algae particles.

The particle density was estimated using Stokes Law from the LabSFLOC2 data. It could in principle also be estimated from the solidity derived from the LISST-HOLO data, however due to presence of organic rich particles, the conversion is not straightforward, as the density of organic and inorganic particles are very different. Further research is required to find a proper calibration between the gray-scale recorded from LISST-HOLO and density.

The fact that particles are highly anisotropic leads to multiple peaks in the PSD found using the LISST 100X. These peaks could lead to the erroneous interpretation that they correspond to meaningful particle size distributions. Comparison between instruments (LISST with LabsFLOC2 and underwater camera) has demonstrated that the combination of instrument leads to better data interpretation. The mean particle size obtained by LISST 100X for the larger flocs is however in agreement with the mean particle size obtained with the LISST-HOLO and LabsFLOC camera system.

The use of different measurement techniques provide a full spectrum of particle size distribution: LISST 100X can be used to detect the fine fraction (< 20 μ m), while LabSFLOC2, LISST-HOLO and the underwater camera provide information about the coarser fraction, in particular the particles' shape. From the LabSFLOC2, both size and settling velocity can be estimated, from which density can be assessed.

Based on these findings the *in-situ* SPM particles are categorized into three classes. These classes are defined as follows:

(Class 1): Sediment inorganic particles (clay minerals): the particles in this class have high effective density and small aspect ratio. Class 1 particles can flocculate with organic matter to form Class 2 particles. They belong to the size range < 20 μ m.

(Class 2): Flocculated particles: this class has a wide distribution in sizes (20 - 200 μ m), effective densities and settling velocities (0.1 - 10 mm/s). Their properties depend on the availability of the other classes, the floc history and hydrodynamic conditions.

(Class 3): Living (microalgae) or dead organic matter (exopolymers): particles in this class have low effective density, can have a high aspect ratio and can flocculate with sediment particles. The largest microalgae recorded *in-situ* have sizes > 200 μ m, however microalgaes and expopolymers can have sizes in the range (100 nm - 20 μ m).

The size ranges given in the present article (< 20 μ m, 20 - 200 μ m, > 200 μ m) are purely indicative. Shen et al. (2018) for instance uses the size ranges 0.25-4 μ m for primary particles and 4 - 20 μ m for microflocs. They discuss the fact that microflocs are generally stable and compact, whereas the sizes of macroflocs and megaflocs (sometimes referred to as microflocs and macroflocs if only two classes are considered) varies for different studies. The critical diameter that separates macroflocs and megaflocs (microflocs and macroflocs) is in the range 133 - 500 μ m.

In future studies, the role of organic matter should be better integrated. Recently, such a study has for instance been done in the Southern Bight of the North Sea (Fettweis et al., 2022). The authors have analyzed the seasonal variations in concentration of Transparent Exopolymer Particles (TEPs), particulate organic carbon (POC) and particulate organic nitrogen (PON) were investigated together with floc size and the concentration of suspended particulate matter (SPM) along the cross-shore gradient, from the high turbid nearshore toward the low-turbid offshore waters. They found in particular that, despite a constantly high abundance of total TEP throughout the entire year, it is its fresh organic matter fraction (i.e. produced during phytoplankton blooms) that promotes the formation of larger and faster sinking biomineral flocs, thereby contributing to reducing the SPM concentration in the water column over spring and summer. Clearly, the seasonal variations in organic matter properties hence impact the suspended sediment properties, such as floc composition, size, shape and density in particular.

Complementary laboratory experiments have confirmed that sediment inorganic particles bind to living microalgae: the flocculation time between inorganic and organic (algae) particles is less than a few minutes. In the laboratory experiments, no floc or algae strain had an aspect ratio larger than 3, suggesting that the creation of highly anisotropic particles, as observed in field data, is occuring in environmental conditions that are different from the lab. Due to technical constraints, high and continuous shears need to be applied in the lab, whereas differential settling and lower shears *in-situ* lead to the creation of more elongated and open flocs. This study helped us to rethink our laboratory set-up and design a new one that will enable to study the growth and decay of flocs in conditions that are closer to *in-situ* conditions.

The main finding of this study is that flocs (Class 2 particles) which are found in the size range 20-200 μ m and which corresponds to the size range of most particles found in-situ, have a very large spread in density due to their organic/inorganic composition. This suggests that the organic fraction should be an input parameter in any realistic flocculation model. A more in-depth discussion, that put the work presented here in a broader context can be found in (Chassagne et al., 2021). The new flocculation model presented in (Chassagne and Safar, 2020; Chassagne et al., 2021) can be parameterized by laboratory experiments involving suspensions of mineral sediment and organic matter (living or dead) - which will be the topic of a forthcoming article. The model is based on parameters measurable in-situ, in particular by laser diffraction (LISST 100X), which enables it to be tested. This model can easily be implemented in large-scale sediment transport models (Chassagne and Safar, 2020).

Data availability statement

The original contributions presented in the study are included in the article/supplementary material. Further inquiries can be directed to the corresponding authors.

Author contributions

ZS: data analysis and writing. CC: writing and supervision. SR: data collection and processing. MS: data collection and processing. AM: data collection and processing. JP: supervising. AS: data analysis revision and writing revision. TK: data analysis revision. AH-D: data collection. RF: data collection. MM: data collection. All authors contributed to the article and approved the submitted version.

Funding

This work has been performed in the frame of the grant NWO 869.15.011, entitled “Flocs and fluff in the Delta” and the MUDNET academic network (https://www.tudelft.nl/mudnet/).

Conflict of interest

Author MS was employed by company Antea Group, and author AM was employed by company HR Wallingford Ltd.

The remaining authors declare that the research was conducted in the absence of any commercial or financial relationships that could be construed as a potential conflict of interest.

Publisher's note

All claims expressed in this article are solely those of the authors and do not necessarily represent those of their affiliated organizations, or those of the publisher, the editors and the reviewers. Any product that may be evaluated in this article, or claim that may be made by its manufacturer, is not guaranteed or endorsed by the publisher.

References

Agrawal, Y. C. (2001). Traykovski p. particles in the bottom boundary layer: Concentration and size dynamics through events. *J. Geophys. Res.: Oceans.* 106 (C5), 9533–9542. doi: 10.1029/2000JC900160

Agrawal, Y. C., Whitmire, A., Mikkelsen, O. A., and Pottsmith, H. C. (2008). Light scattering by random shaped particles and consequences on measuring suspended sediments by laser diffraction. *J. Geophys. Res.: Oceans.*, 113(C4). doi: 10.1029/2007JC004403

Al Ani, S., Dyer, K. R., and Huntley, D. A. (1991). Measurement of the influence of salinity on floc density and strength. *Geo-Marine. Lett.* 11 (3), 154–158. doi: 10.1007/BF02431002

Alldredge, A. L., and Gotschalk, C. C. (1989). Direct observations of the mass flocculation of diatom blooms: characteristics, settling velocities and formation of diatom aggregates. *Deep. Sea. Res. Part A. Oceanographic. Res. Papers.* 36 (2), 159–171. doi: 10.1016/0198-0149(89)90131-3

Benson, T., and French, J. R. (2007). InSiPID: A new low-cost instrument for *in situ* particle size measurements in estuarine and coastal waters. *J. Sea. Res.* 58 (3), 167–188. doi: 10.1016/j.seares.2007.04.003

Benson, T., and Manning, A. J. (2013). *DigiFloc: the development of semi-automatic software to determine the size and settling velocity of flocs* (HR Wallingford Report DDY0427-Rt001).

Blauw, A. N. (2015). *Monitoring and prediction of phytoplankton dynamics in the north Sea* (Universiteit van Amsterdam [Host]) UvA-DARE (Digital Academic Repository).

Chassagne, C., and Safar, Z. (2020). Modelling flocculation: Towards an integration in large-scale sediment transport models. *Mar. Geol.* 430, 106361. doi: 10.1016/j.margeo.2020.106361

Chassagne, C., Safar, Z., Deng, Z., He, Q., and Manning, A. (2021). "Flocculation in estuaries: Modeling, laboratory and in-situ studies," in *Sediment transport - recent advances* (IntechOpen). doi: 10.5772/intechopen.100404

Choi, S. M., Seo, J. Y., Ha, H. K., and Lee, G. H. (2018). Estimating effective density of cohesive sediment using shape factors from holographic images. *Estuarine. Coast. Shelf. Sci.* 215, 144–151. doi: 10.1016/j.ecss.2018.10.008

Cross, J., Nimmo-Smith, W. A., Hosegood, P. J., and Torres, R. (2015). The role of advection in the distribution of plankton populations at a moored 1-d coastal observatory. *Prog. Oceanography.* 137, 342–359. doi: 10.1016/j.pocean.2015.04.016

Dam, H. G., and Drapeau, D. T. (1995). Coagulation efficiency, organic-matter glues and the dynamics of particles during a phytoplankton bloom in a mesocosm study. *Deep. Sea. Res. Part II.: Topical. Stud. Oceanography.* 42 (1), 111–123. doi: 10.1016/0967-0645(95)00007-D

Davies, E. J., Nimmo-Smith, W. A., Agrawal, Y. C., and Souza, A. J. (2011). Scattering signatures of suspended particles: an integrated system for combining digital holography and laser diffraction. *Optics. Express.* 19 (25), 25488–25499. doi: 10.1364/OE.19.025488

Deng, Z., He, Q., Chassagne, C., and Wang, Z. B. (2021). Seasonal variation of floc population influenced by the presence of algae in the changjiang (Yangtze river) estuary. *Mar. Geol.* 440, 106600. doi: 10.1016/j.margeo.2021.106600

Deng, Z., He, Q., Safar, Z., and Chassagne, C. (2019). The role of algae in fine sediment flocculation: *In-situ* and laboratory measurements. *Mar. Geol.* 413, 71–84. doi: 10.1016/j.margeo.2019.02.003

De Ruyter van Steveninck, E. D., Admiraal, W., Breebaart, L., Tubbing, G. M., and Van Zanten, B. (1992). Plankton in the river Rhine: structural and functional changes observed during downstream transport. *J. Plankton. Res.* 14 (10), 1351–1368. doi: 10.1093/plankt/14.10.1351

Fettweis, M. (2008). Uncertainty of excess density and settling velocity of mud flocs derived from *in situ* measurements. *Estuarine. Coast. Shelf. Sci.* 78 (2), 426–436. doi: 10.1016/j.ecss.2008.01.007

Fettweis, M., and Baeye, M. (2015). Seasonal variation in concentration, size, and settling velocity of muddy marine flocs in the benthic boundary layer. *J. Geophys. Res.: Oceans.* 120 (8), 5648–5667. doi: 10.1002/2014JC010644

Fettweis, M., and Lee, B. J. (2017). Spatial and seasonal variation of biomineral suspended particulate matter properties in high-turbid nearshore and low-turbid offshore zones. *Water* 9 (9), 694. doi: 10.3390/w9090694

Fettweis, M., Schartau, M., Desmit, X., Lee, B. J., Terseleer, N., van der Zande, D., et al. (2022). Organic matter composition of biomineral flocs and its influence on suspended particulate matter dynamics along a nearshore to offshore transect. *J. Geophys. Res.: Biogeosci.* 127 (1), e2021JG006332. doi: 10.1029/2021JG006332

Flores, R. P., Rijnsburger, S., Horner-Devine, A. R., Souza, A. J., and Pietrzak, J. D. (2017). The impact of storms and stratification on sediment transport in the r hine region of freshwater influence. *J. Geophys. Res.: Oceans.* 122 (5), 4456–4477. doi: 10.1002/2016JC012362

Foree, E. G., and McCarty, P. L. (1970). Anaerobic decomposition of algae. *Environ. Sci. Technol.* 4 (10), 842–849. doi: 10.1021/es60045a005

Ganaoui, O. E., Schaaff, E., Boyer, P., Amielh, M., Anselmet, F., and Grenz, C. (2007). Erosion of the upper layer of cohesive sediments: characterization of some properties. *J. Hydraulic. Eng.* 133 (9), 1087–1091. doi: 10.1061/(ASCE)0733-9429(2007)133:9(1087)

Gibbs, R. J. (1985). Estuarine flocs: their size, settling velocity and density. *J. Geophys. Res.: Oceans.* 90 (C2), 3249–3251. doi: 10.1029/JC090iC02p03249

Graham, G. W., Davies, E. J., Nimmo-Smith, W. A., Bowers, D. G., and Braithwaite, K. M. (2012). Interpreting LISST-100X measurements of particles with complex shape using digital in-line holography. *J. Geophys. Res.: Oceans.* 117 (C5), C05034. doi: 10.1029/2011JC007613

Graham, G. W., and Nimmo Smith, W. A. (2010). The application of holography to the analysis of size and settling velocity of suspended cohesive sediments. *Limnol. Oceanography.: Methods* 8 (1), 1–5. doi: 10.4319/lom.2010.8.1

Horner-Devine, A. R., Pietrzak, J. D., Souza, A. J., McKeon, M. A., Meirelles, S., Henriquez, M., et al. (2017). Cross-shore transport of nearshore sediment by river plume frontal pumping. *Geophys. Res. Lett.* 44 (12), 6343–6351. doi: 10.1002/2017GL073378

Ibanez Sanz, M. E. (2018). *Flocculation and consolidation of cohesive sediments under the influence of coagulant and flocculant* (Delft University of Technology).

Jarvis, P., Jefferson, B., and Parsons, S. A. (2005). Breakage, regrowth, and fractal nature of natural organic matter flocs. *Environ. Sci. Technol.* 39 (7), 2307–2314. doi: 10.1021/es048854x

Karp-Boss, L., Azevedo, L., and Boss, E. (2007). LISST-100 measurements of phytoplankton size distribution: Evaluation of the effects of cell shape. *Limnol. Oceanography.: Methods* 5 (11), 396–406. doi: 10.4319/lom.2007.5.396

Khelifa, A., and Hill, P. S. (2006). Models for effective density and settling velocity of flocs. *J. Hydraulic. Res.* 44 (3), 390–401. doi: 10.1080/00221686.2006.9521690

Lartiges, B. S., Deneux-Mustin, S., Villemin, G., Mustin, C., Barres, O., Chamerois, M., et al. (2001). Composition, structure and size distribution of suspended particulates from the Rhine river. *Water Res.* 35 (3), 808–816. doi: 10.1016/S0043-1354(00)00293-1

Lee, B. J., Hur, J., and Toorman, E. A. (2017). Seasonal variation in flocculation potential of river water: Roles of the organic matter pool. *Water* 9 (5), 335. doi: 10.3390/w9050335

Lee, J., Liu, J. T., Hung, C. C., Lin, S., and Du, X. (2016). River plume induced variability of suspended particle characteristics. *Mar. Geol.* 380, 219–230. doi: 10.1016/j.margeo.2016.04.014

LISST HOLO manual. V.3.0 (Sequoia Scientific) (2014).

Logan, B. E., Passow, U., Alldredge, A. L., Grossartt, H. P., and Simont, M. (1995). Rapid formation and sedimentation of large aggregates is predictable from coagulation rates (half-lives) of transparent exopolymer particles (TEP). *Deep. Sea. Res. Part II.: Topical. Stud. Oceanography.* 42 (1), 203–214. doi: 10.1016/0967-0645(95)00012-F

Maggi, F. (2007). Variable fractal dimension: A major control for floc structure and flocculation kinematics of suspended cohesive sediment. *J. Geophys. Res.: Oceans.* 112 (C7), C7012. doi: 10.1029/2006JC003951

Malone, T. C. (1980). Algal size [Influence on response to environment, physiological processes]. *Stud. Ecol. (USA).* 7, 456–463.

Manning, A. J., and Dyer, K. R. (2002). The use of optics for the *in situ* determination of flocculated mud characteristics. *J. Optics. A.: Pure. Appl. Optics.* 4 (4), S71. doi: 10.1088/1464-4258/4/4/366

Manning, A. J., Friend, P. L., Prowse, N., and Amos, C. L. (2007a). Estuarine mud flocculation properties determined using an annular mini-flume and the LabSFLOC system. *Continental. Shelf. Res.* 27 (8), 1080–1095. doi: 10.1016/j.csr.2006.04.011

Manning, A. J., Friend, P. L., Prowse, N., and Amos, C. L. (2007b). Preliminary findings from a study of Medway estuary (UK) natural mud floc properties using a laboratory mini-flume and the LabSFLOC system. *Continental. Shelf. Res. BIOFLOW. SI.* 1080-95. doi: 10.1016/j.csr.2006.04.011

Manning, A. J., and Schoellhamer, D. H. (2013). Factors controlling floc settling velocity along a longitudinal estuarine transect. *Mar. Geol.* 345, 266–280. doi: 10.1016/j.margeo.2013.06.018

Manning, A. J., Schoellhamer, D. H., Mehta, A. J., Nover, D., and Schladow, S. G. (2010). "Video measurements of flocculated sediment in lakes and estuaries in the USA," in *Proceedings of the joint federal interagency conference on sedimentation and hydrologic modeling* (Nevada, USA: Riviera Hotel, Las Vegas).

Manning, A. J., Whitehouse, R. J., and Uncles, R. J. (2017). Suspended particulate matter: the measurements of flocs. ECSA practical handbooks on survey and analysis methods. *Estuar. Coast. Hydrography. Sedimentol.* 17, 211–260. doi: 10.1017/9781139644426.009

Many, G., Bourrin, F., de Madron, X. D., Pairaud, I., Gangloff, A., Doxaran, D., et al. (2016). Particle assemblage characterization in the Rhone river ROFI. *J. Mar. Syst.* 157, 39–51. doi: 10.1016/j.jmarsys.2015.12.010

Many, G., de Madron, X. D., Verney, R., Bourrin, F., Renosh, P. R., Jourdin, F., et al. (2019). Geometry, fractal dimension and settling velocity of flocs during flooding conditions in the rhône ROFI. *Estuarine. Coast. Shelf. Sci.* 219, 1–3. doi: 10.1016/j.ecss.2019.01.017

Mehta, A. J., Manning, A. J., and Khare, Y. P. (2014). A note on the krone deposition equation and significance of floc aggregation. *Mar. Geol.* 354, 34–39. doi: 10.1016/j.margeo.2014.04.002

Mietta, F., Chassagne, C., Manning, A. J., and Winterwerp, J. C. (2009). Influence of shear rate, organic matter content, pH and salinity on mud flocculation. *Ocean Dynamics.* 59 (5), 751–763. doi: 10.1007/s10236-009-0231-4

Mikkelsen, O. A., Hill, P. S., Milligan, T. G., and Chant, R. J. (2005). *In situ* particle size distributions and volume concentrations from a LISST-100 laser particle sizer and a digital floc camera. *Continental. Shelf. Res.* 25 (16), 1959–1978. doi: 10.1016/j.csr.2005.07.001

Passow, U., Alldredge, A. L., and Logan, B. E. (1994). The role of particulate carbohydrate exudates in the flocculation of diatom blooms. *Deep. Sea. Res. Part I.: Oceanographic. Res. Papers.* 41 (2), 335–357. doi: 10.1016/0967-0637(94)90007-8

Pavoni, J. L., Tenney, M. W., and Echelberger, W. F.Jr. (1972). Bacterial exocellular polymers and biological flocculation. *J. (Water. pollut. Control. Federation).* 1, 414–431.

Pietrzak, J. D., de Boer, G. J., and Eleveld, M. A. (2011). Mechanisms controlling the intra-annual mesoscale variability of SST and SPM in the southern north Sea. *Continental. Shelf. Res.* 31 (6), 594–610. doi: 10.1016/j.csr.2010.12.014

Prins, T. C., Desmit, X., and Baretta-Bekker, J. G. (2012). Phytoplankton composition in Dutch coastal waters responds to changes in riverine nutrient loads. *J. sea. Res.* 73, 49–62. doi: 10.1016/j.seares.2012.06.009

Ramirez Mendoza, R. (2015). *Flocculation controls in a hypertidal estuary* (University of Liverpool).

Razaz, M., Kawanisi, K., and Nistor, I. (2015). Tide-driven controls on maximum near-bed floc size in a tidal estuary. *J. Hydro-environment. Res.* 9 (3), 465–471. doi: 10.1016/j.jher.2014.04.001

Rijnsburger, S., Flores, R. P., Pietrzak, J. D., Horner-Devine, A. R., and Souza, A. J. (2018). The influence of tide and wind on the propagation of fronts in a shallow river plume. *J. Geophys. Res.: Oceans.* 123 (8), 5426–5442. doi: 10.1029/2017JC013422

Rijstenbil, J. W. (1987). Phytoplankton composition of stagnant and tidal ecosystems in relation to salinity, nutrients, light and turbulence. *Netherlands J. Sea. Res.* 21 (2), 113–123. doi: 10.1016/0077-7579(87)90027-5

Roozen, F. C. (2005). *Transparency of floodplain lakes: a study of plankton and suspended matter along the lower Rhine* (Wageningen University and Research).

Schofield, O., Moline, M., Cahill, B., Frazer, T., Kahl, A., Oliver, M., et al. (2013). Phytoplankton productivity in a turbid buoyant coastal plume. *Continental. Shelf. Res.* 63, S138–S148. doi: 10.1016/j.csr.2013.02.005

Schwarz, C., Cox, T., Van Engeland, T., Van Oevelen, D., Van Belzen, J., Van de Koppel, J., et al. (2017). Field estimates of floc dynamics and settling velocities in a tidal creek with significant along-channel gradients in velocity and SPM. *Estuarine. Coast. Shelf. Sci.* 197, 221–235. doi: 10.1016/j.ecss.2017.08.041

Shakeel, A., Safar, Z., Ibanez, M., van Paassen, L., and Chassagne, C. (2020). Flocculation of clay suspensions by anionic and cationic polyelectrolytes: A systematic analysis. *Minerals* 10 (11), 999. doi: 10.3390/min10110999

Shen, X., Lee, B. J., Fettweis, M., and Toorman, E. A. (2018). A tri-modal flocculation model coupled with TELEMAC for estuarine muds both in the laboratory and in the field. *Water Res.* 145, 473–486. doi: 10.1016/j.watres.2018.08.062

Shen, X., and Maa, J. P. (2016). A camera and image processing system for floc size distributions of suspended particles. *Mar. Geol.* 376, 132–146. doi: 10.1016/j.margeo.2016.03.009

Smetacek, V. S. (1985). Role of sinking in diatom life-history cycles: ecological, evolutionary and geological significance. *Mar. Biol.* 84 (3), 239–251. doi: 10.1007/BF00392493

Smith, S. J., and Friedrichs, C. T. (2015). Image processing methods for *in situ* estimation of cohesive sediment floc size, settling velocity, and density. *Limnol. Oceanography.: Methods* 13 (5), 250–264. doi: 10.1002/lom3.10022

Spencer, K. L., Manning, A. J., Droppo, I. G., Leppard, G. G., and Benson, T. (2010). Dynamic interactions between cohesive sediment tracers and natural mud. *J. Soils Sediments.* 10 (7), 1401–1414. doi: 10.1007/s11368-010-0291-6

Sternberg, R. W., Berhane, I., and Ogston, A. S. (1999). Measurement of size and settling velocity of suspended aggregates on the northern California continental shelf. *Mar. Geol.* 154 (1-4), 43–53. doi: 10.1016/S0025-3227(98)00102-9

Stive, M. J., De Schipper, M. A., Luijendijk, A. P., Aarninkhof, S. G., van Gelder-Maas, C., Van Thiel de Vries, J. S., et al. (2013). A new alternative to saving our beaches from sea-level rise: the sand engine. *J. Coast. Res.* 29 (5), 1001–1008. doi: 10.2112/JCOASTRES-D-13-00070.1

Traykovski, P., Latter, R. J., and Irish, J. D. (1999). A laboratory evaluation of the laser in situ scattering and transmissometery instrument using natural sediments. *Mar. Geol.* 159 (1-4), 355–367. doi: 10.1016/S0025-3227(98)00196-0

Vaezi, F., Sanders, R. S., and Masliyah, J. H. (2011). Flocculation kinetics and aggregate structure of kaolinite mixtures in laminar tube flow. *J. Colloid. Interface Sci.* 355 (1), 96–105. doi: 10.1016/j.jcis.2010.11.068

Van de Meent, D. (1982). Particulate organic matter in the river Rhine delta: Its role in trace metal scavenging. *Netherlands*.

van der Hout, C. M., Witbaard, R., Duineveld, G., Groot, L., and Bergman, M. (2012). "Variability of suspended particulate matter composition at egmond, the Netherlands," in *Particles in Europe*, ICM, Barcelona, Spain: Royal Netherlands Institute for Sea Research (NIOZ) Vol. 17. 1.

van Leussen, W. (1999). The variability of settling velocities of suspended fine-grained sediment in the ems estuary. *J. sea. Res.* 41 (1-2), 109–118. doi: 10.1016/S1385-1101(98)00046-X

Van Leussen, W., and Cornelisse, J. M. (1993). The determination of the sizes and settling velocities of estuarine flocs by an underwater video system. *Netherlands J. Sea. Res.* 31 (3), 231–241. doi: 10.1016/0077-7579(93)90024-M

Verney, R., Lafite, R., Brun-Cottan, J. C., and Le Hir, P. (2011). Behaviour of a floc population during a tidal cycle: laboratory experiments and numerical modelling. *Continental. Shelf. Res.* 31 (10), S64–S83. doi: 10.1016/j.csr.2010.02.005

Advantages of publishing in Frontiers

OPEN ACCESS
Articles are free to read for greatest visibility and readership

FAST PUBLICATION
Around 90 days from submission to decision

HIGH QUALITY PEER-REVIEW
Rigorous, collaborative, and constructive peer-review

TRANSPARENT PEER-REVIEW
Editors and reviewers acknowledged by name on published articles

Frontiers
Avenue du Tribunal-Fédéral 34
1005 Lausanne | Switzerland

Visit us: www.frontiersin.org
Contact us: frontiersin.org/about/contact

REPRODUCIBILITY OF RESEARCH
Support open data and methods to enhance research reproducibility

DIGITAL PUBLISHING
Articles designed for optimal readership across devices

FOLLOW US
@frontiersin

IMPACT METRICS
Advanced article metrics track visibility across digital media

EXTENSIVE PROMOTION
Marketing and promotion of impactful research

LOOP RESEARCH NETWORK
Our network increases your article's readership